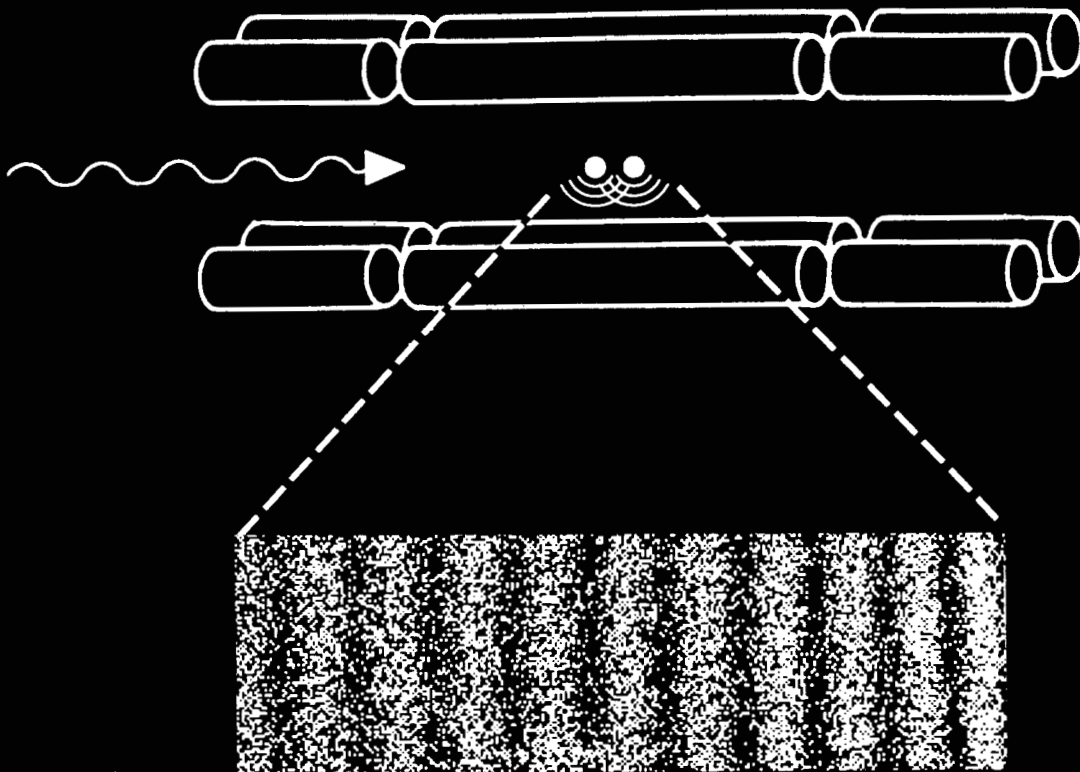




United States Department of Commerce
Technology Administration
National Institute of Standards and Technology

NIST Technical Note 1380

Trapped Ions and Laser Cooling IV



Selected publications of the
Ion Storage Group
Time and Frequency Division
NIST
Boulder, Colorado

Edited by: James C. Bergquist
John J. Bollinger
Wayne M. Itano
Christopher R. Monroe
David J. Wineland

Technical Note 1380

Trapped Ions and Laser Cooling IV

Selected publications of the Ion Storage Group of the Time and Frequency Division

Edited by

James C. Bergquist
John J. Bollinger
Wayne M. Itano
Christopher R. Monroe
David J. Wineland

Time and Frequency Division
Physics Laboratory
National Institute of Standards and Technology
325 Broadway
Boulder, Colorado 80303

Supported in part by

U.S. Office of Naval Research
800 North Quincy
Arlington, Virginia 22217

U.S. Army Research Office
P.O. Box 12211
Research Triangle Park, North Carolina 27709

January 1996



U.S. DEPARTMENT OF COMMERCE, Ronald H. Brown, Secretary
TECHNOLOGY ADMINISTRATION, Mary L. Good, Under Secretary for Technology
NATIONAL INSTITUTE OF STANDARDS AND TECHNOLOGY, Arati Prabhakar, Director

**National Institute of Standards and Technology Technical Note
Natl. Inst. Stand. Technol., Tech. Note 1380, 204 pages (January 1996)
CODEN:NTNOEF**

**U.S. GOVERNMENT PRINTING OFFICE
WASHINGTON: 1996**

For sale by the Superintendent of Documents, U.S. Government Printing Office, Washington, DC 20402-9325

PREFACE

This collection of papers represents the work of the Ion Storage Group, Time and Frequency Division, National Institute of Standards and Technology, from May 1992 to January 1996. It follows the collections of papers contained in NBS Technical Note 1086, *Trapped Ions and Laser Cooling* (June 1985), NIST Technical Note 1324, *Trapped Ions and Laser Cooling II* (September 1988), and NIST Technical Note 1353, *Trapped Ions and Laser Cooling III* (April 1992). Although the primary goal of this work has been the development of techniques necessary for achieving high resolution spectroscopy, we have also been able to investigate related areas of research.

Papers listed on page viii were published or prepared during the period May 1992 to January 1996 but are not included here. Copies can be obtained on request. We intend to update this publication periodically to include new work. We hope this collection of papers will be useful to our colleagues in this and related fields.

We acknowledge the contributions of many colleagues to this collection. In particular, we thank Amy Barton, Ed Bell, Dana Berkeland, Flavio Cruz, Dan Dubin, Ulli Eichmann, Jon Gilligan, Phil Gould, Dan Heinzen, Steve Jefferts, Brana Jelenković, Brian King, Dawn Meekhof, John Miller, Fred Moore, Martin Poitzsch, Mark Raizen, Norman Ramsey, Max Rauner, Andy Steinbach, Carl Weimer, and Joseph Tan. We gratefully acknowledge the continued support of the U.S. Office of Naval Research and the U.S. Army Research Office. We thank Wendy Ortega Henderson for assembling this collection.

James C. Bergquist
John J. Bollinger
Wayne M. Itano
Christopher R. Monroe
David J. Wineland

Boulder, Colorado
February 1996

CONTENTS

LIST OF ADDITIONAL PUBLICATIONS	viii
FREQUENCY STANDARDS AND METROLOGY	
1. "Laser stabilization to a single ion," J. C. Bergquist, W. M. Itano, and D. J. Wineland, in <i>Frontiers in Laser Spectroscopy</i> , proc. International School of Physics <<Enrico Fermi>>, Course CXX, ed. by T. W. Hänsch and M. Inguscio (North Holland, Amsterdam, 1994), pp. 359-376.	TN-1
2. "Ionic crystals in a linear Paul trap," M. G. Raizen, J. M. Gilligan, J. C. Bergquist, W. M. Itano, and D. J. Wineland, <i>Phys. Rev. A</i> <u>45</u> , 6493-6501 (1992).	TN-19
3. "Cryogenic linear ion trap for accurate spectroscopy," M. E. Poitzsch, J. C. Bergquist, W. M. Itano, and D. J. Wineland, <i>Rev. Sci. Instrum.</i> <u>67</u> , 129-134 (1996).	TN-28
4. "Minimizing the time-dilation shift in Penning-trap atomic clocks," J. N. Tan, J. J. Bollinger, and D. J. Wineland, Proc., Conf. on Precision Electromagnetic Meas., Boulder, CO, June, 1994; <i>IEEE Trans. on Instrum. Meas.</i> <u>44</u> , 144-147 (1995).	TN-34
5. "High-magnetic-field corrections to cesium hyperfine structure," W. M. Itano, Proc., Fifth Symp. Freq. Standards and Metrology, Woods Hole, MA, Oct. 1995 (World Scientific).	TN-38
6. "Application of laser-cooled ions to frequency standards and metrology," D. J. Wineland, J. C. Bergquist, D. J. Berkeland, J. J. Bollinger, F. C. Cruz, W. M. Itano, B. M. Jelenković, B. E. King, D. M. Meekhof, J. D. Miller, C. Monroe, and J. N. Tan, <i>ibid.</i>	TN-40
7. "Accurate measurement of time," W. M. Itano and N. F. Ramsey, <i>Sci. Am.</i> <u>269</u> (1), 56-59 and 62-65 (July 1993).	TN-49
LASER COOLING AND QUANTUM STATE CONTROL	
1. "Resolved-sideband Raman cooling of a bound atom to the 3-D zero-point energy," C. Monroe, D. M. Meekhof, B. E. King, S. R. Jefferts, W. M. Itano, D. J. Wineland, and P. Gould, <i>Phys. Rev. Lett.</i> <u>75</u> , 4011-4014 (1995).	TN-57

2. "Quantum projection noise: population fluctuations in two-level systems," W. M. Itano, J. C. Bergquist, J. J. Bollinger, J. M. Gilligan, D. J. Heinzen, F. L. Moore, M. G. Raizen, and D. J. Wineland, *Phys. Rev. A* 47, 3554-3570 (1993). TN-61
3. "Spin squeezing and reduced quantum noise in spectroscopy," D. J. Wineland, J. J. Bollinger, W. M. Itano, F. L. Moore, and D. J. Heinzen, *Phys. Rev. A* 46, R6797-R6800 (1992). TN-78
4. "Squeezed atomic states and projection noise in spectroscopy," D. J. Wineland, J. J. Bollinger, W. M. Itano, and D. J. Heinzen, *Phys. Rev. A* 50, 67-88 (1994). TN-82
5. "Spin squeezing applied to frequency standards," J. J. Bollinger, D. J. Wineland, W. M. Itano, and D. J. Heinzen, *Proc. Fifth Symp. Freq. Standards and Metrology, Woods Hole, MA, Oct. 1995* (World Scientific). TN-104
6. "Demonstration of a fundamental quantum logic gate," C. Monroe, D. M. Meekhof, B. E. King, W. M. Itano, and D. J. Wineland, *Phys. Rev. Lett.* 75, 4714-4717 (1995). TN-112

INTERFERENCE

1. "Young's interference experiment with light scattered from two atoms," U. Eichmann, J. C. Bergquist, J. J. Bollinger, J. M. Gilligan, W. M. Itano, D. J. Wineland, and M. G. Raizen, *Phys. Rev. Lett.* 70, 2359-2362 (1993). TN-116
2. "Light scattered from two atoms," W. M. Itano, U. Eichmann, J. C. Bergquist, J. J. Bollinger, J. M. Gilligan, M. G. Raizen, and D. J. Wineland, *Proc. Lasers '93, Lake Tahoe, NV, edited by V. J. Corcoran and T. A. Goldman* (STS Press, McLean, VA, 1994), pp. 412-419. TN-120

NON-NEUTRAL PLASMAS AND SINGLE ELECTRON STUDIES

1. "Electrostatic modes of ion-trap plasmas," J. J. Bollinger, D. J. Heinzen, F. L. Moore, W. M. Itano, D. J. Wineland, and D. H. E. Dubin, *Phys. Rev. A* 48, 525-545 (1993). TN-128
2. "Electrostatic modes as a diagnostic in Penning-trap experiments," C. S. Weimer, J. J. Bollinger, F. L. Moore, and D. J. Wineland, *Phys. Rev. A* 49, 3842-3853 (1994). TN-149

- | | | |
|----|--|--------|
| 3. | "Long-range order in laser-cooled, atomic-ion Wigner crystals observed by Bragg scattering," J. N. Tan, J. J. Bollinger, B. Jelenković, and D. J. Wineland, <i>Phys. Rev. Lett.</i> <u>75</u> , 4198-4201 (1995). | TN-161 |
| 4. | "Observation of long-range order in trapped ion plasmas by Bragg scattering," J. N. Tan, J. J. Bollinger, B. Jelenković, W. M. Itano, and D. J. Wineland, <i>Proc., Intl. Conf. on the Physics of Strongly Coupled Plasmas</i> , Binz, Germany, Sept. 11-15, 1995, (World Scientific). | TN-165 |
| 5. | "Laser-cooled positron source," D. J. Wineland, C. S. Weimer, and J. J. Bollinger, <i>Proc., Anti-Hydrogen workshop</i> , Munich, July 30-31, 1992, ed. by J. Eades, in <i>Hyperfine Interactions</i> <u>76</u> , 115-125 (1993). | TN-175 |
| 6. | "High-order multipole excitation of a bound electron," C. S. Weimer, F. L. Moore, and D. J. Wineland, <i>Phys. Rev. Lett.</i> <u>70</u> , 2553-2556 (1993). | TN-186 |

APPARATUS

- | | | |
|----|--|--------|
| 1. | "Coaxial-resonator driven rf (Paul) trap for strong confinement," S. R. Jefferts, C. Monroe, E. W. Bell, and D. J. Wineland, <i>Phys. Rev. A</i> <u>51</u> , 3112-3116 (1995). | TN-190 |
|----|--|--------|

ADDITIONAL PUBLICATIONS

The following publications were published or prepared during the period between May 1992 and January 1996, but are not included in this technical note.

1. "Experimental results on normal modes in cold, pure ion plasmas," J. J. Bollinger, D. J. Heinzen, F. L. Moore, C. S. Weimer, W. M. Itano, and D. J. Wineland, in *Strongly Coupled Plasma Physics*, ed. by Van Horn and Ichimaru (University of Rochester Press, Rochester, NY, 1993), pp. 393-398.
2. "Quantum measurements of trapped ions," W. M. Itano, J. C. Bergquist, J. J. Bollinger, J. M. Gilligan, D. J. Heinzen, F. L. Moore, M. G. Raizen, and D. J. Wineland, Proc., Intl. Symp. on Quantum Physics and the Universe, Waseda Univ., Tokyo, Japan, Aug. 19-22, 1992, ed. by M. Namiki, K. Maeda, and I. Ohba, *Vistas in Astronomy* 37, 169-183 (1993).
3. "Precise spectroscopy for fundamental physics," W. M. Itano, J. C. Bergquist, J. J. Bollinger, J. M. Gilligan, D. J. Heinzen, F. L. Moore, M. G. Raizen, and D. J. Wineland, *Hyperfine Interactions* 78, 211-220 (1993).
4. "Non-neutral ion plasmas and crystals, laser cooling, and atomic clocks," J. J. Bollinger, D. J. Wineland, and D. H. E. Dubin, *Phys. Plasmas* 1, 1403-1414 (1994).
5. "Interference in the resonance fluorescence of two trapped atoms," U. Eichmann, J. C. Bergquist, J. J. Bollinger, J. M. Gilligan, W. M. Itano, M. G. Raizen, and D. J. Wineland, *Laser Spectroscopy*, Proc., XIth Intl. Conf., ed. by L. Bloomfield, T. Gallagher, and D. J. Larson (AIP Conf. Proc. 290, New York, NY, 1994), pp. 43-48.
6. "Paul trap for optical frequency standards," S. R. Jefferts, C. Monroe, A. S. Barton, and D. J. Wineland, *IEEE Trans. Instrum. Meas.* 44, 148-150 (1995).
7. "Progress on a cryogenic linear trap for $^{199}\text{Hg}^+$ ions," M. E. Poitzsch, J. C. Bergquist, W. M. Itano, and D. J. Wineland, Proc., 1994 IEEE Intl. Frequency Control Symp., pp. 744-746, June 1994.
8. "Nonneutral ion plasmas and crystals in Penning traps," J. J. Bollinger, J. N. Tan, W. M. Itano, D. J. Wineland, and D. H. E. Dubin, Proc. Nobel Symp. on Trapped Charged Particles and Related Fundamental Physics, Lysekil, Sweden, August 1994, *Physica Scripta* T59, 352-359 (1995).
9. "Cooling methods in ion traps," W. M. Itano, J. C. Bergquist, J. J. Bollinger, and D. J. Wineland, *ibid*, pp. 106-120.
10. "Quantum effects in measurements on trapped ions," D. J. Wineland, J. C. Bergquist, J. J. Bollinger, and W. M. Itano, *ibid*, pp. 286-293.

11. "Quantum mechanics with one, two, and many atoms," W. M. Itano, J. C. Bergquist, J. J. Bollinger, and D. J. Wineland, in *Group Theoretical Methods in Physics*, Proc., XX Intl. Colloquium (Yamada Conference XL, "Quantum mechanics with one, two, and many atoms,"), Toyonaka, Japan, 1994, ed. by A. Arima, T. Eguchi, and N. Nakanishi (World Scientific, Singapore, 1995), pp. 10-18.
12. "Laser-cooled trapped-ion experiments at NIST," J. N. Tan, J. J. Bollinger, A. S. Barton, and D. J. Wineland, in *Non-neutral Plasma Physics II*, ed. by J. Fajans and D. H. E. Dubin, AIP Conf. Proc. 331 (AIP Press, New York, NY, 1995), pp. 215-228.
13. "A cryogenic linear ion trap for $^{199}\text{Hg}^+$ frequency standards," J. Miller, M. E. Poitzsch, F. C. Cruz, D. J. Berkeland, J. C. Bergquist, W. M. Itano, and D. J. Wineland, Proc., 1995 IEEE Intl. Frequency Control Symp., June 1995, pp. 110-112.
14. "Quantum mechanically correlated states and atomic clocks," C. Monroe, D. M. Meekhof, B. E. King, W. M. Itano, J. J. Bollinger, and D. J. Wineland, Proc. 1995 Moriond Workshop (Editions Frontieres, Gif-sur-Yvette, France, 1996).
15. "Experiments at NIST with trapped ions: 3-D zero-point cooling, quantum gates, Bragg scattering, and atomic clocks," C. Monroe, A.S. Barton, J.C. Bergquist, D. J. Berkeland, J.J. Bollinger, F. Cruz, W.M. Itano, S.R. Jefferts, B.M. Jelenković, B.E. King, D.M. Meekhof, J.D. Miller, M.E. Poitzsch, J.N. Tan, and D.J. Wineland, Proc., 12th Intl. Conf. on Laser Spectroscopy, Capri, Italy, June 1995 (World Scientific), to be published.
16. "Minimizing time dilation in Penning trap ion clocks," J. N. Tan, J. J. Bollinger, W. M. Itano, and D. J. Wineland, Proc. 5th Symp. on Frequency Standards and Metrology, Woods Hole, MA, Oct. 1995 (World Scientific) to be published.
17. "Primary atomic frequency standards: New developments," R. E. Drullinger, S. L. Rolston, and W. M. Itano, in *Review of Radio Science*, in press.
18. "CW second harmonic generation with elliptical Gaussian beams," A. Steinbach, M. Rauner, F. C. Cruz, and J. C. Bergquist, Opt. Commun., in press.
19. "Generation of non-classical motional states of a trapped atom," D. M. Meekhof, C. Monroe, B. King, W. M. Itano, and D. J. Wineland, Phys. Rev. Lett., in press.
20. "A 'Schrödinger Cat' superposition state of an atom," C. Monroe, D. M. Meekhof, B. E. King, and D. J. Wineland, submitted to Science.
21. "Optimal frequency measurements with maximally correlated states," J. J. Bollinger, W. M. Itano, D. J. Wineland, and D. J. Heinzen, submitted to Phys. Rev. Lett.

Laser Stabilization to a Single Ion.

J. C. BERGQUIST, W. M. ITANO and D. J. WINELAND

*Time and Frequency Division, National Institute of Standards and Technology
Boulder, CO 80303*

I. – Spectrally narrow Optical Oscillators.

I.1. – Frequency references.

An unperturbed optical resonance in an atom or molecule provides a good absolute frequency reference, but practically there are limitations. The signal-to-noise ratio is limited by the number of atoms in the interrogation region and by saturation of the resonance. If the probe laser is spectrally broad, then the measured atomic line is broadened, which degrades the stability. Furthermore, atoms recognize interactions and collisions with neighboring atoms, usually with shifts to the internal energy level structure. The motion of the atoms also produces Doppler shifts and broadening. A single laser-cooled atom removes many of these problems but only with a severe penalty in the signal-to-noise ratio [1]. Even so, by detecting each transition in the single atom, it should be possible to stabilize the frequency of a laser oscillating in the visible to better than $10^{-15} \tau^{-1/2}$ with an accuracy approaching 10^{-18} [2], if the laser were sufficiently stable (or spectrally narrow) for times that are comparable to the interrogation time of the transition in the atom.

A two-step approach might then be appropriate; spectrally narrow the laser by some scheme that offers good short- to medium-term stability (*e.g.*, 1 ms to 10 s), then stabilize the frequency of the laser for longer times to a narrow resonance in a single atom. The reference for the short- to medium-term stabilization of the laser not only needs good stability in this time frame, but also low phase and frequency noise. If a Fabry-Perot cavity is used as the frequency discriminator, then the response of the frequency discriminator can be nearly linear as a function of power and the signal-to-noise ratio can be high [3]. Frequency shifts and fluctuations arise due to thermal distortion in the mirror coatings caused by absorption of light in a small volume in the dielectric stack and due to photochemical processes at the surfaces of the coatings. Also, practical

limits are reached at powers that saturate the detector or at powers (circulating in the cavity) that cause radiation pressure noise, but the signal-to-noise ratio from a cavity can be many orders of magnitude larger than that obtained with atoms. Although there are other types of optical frequency references, the most widely used is the Fabry-Perot interferometer, principally because the frequency excursions to error-voltage can be extremely large in a high-finesse cavity. We will spend time in the next few sections discussing some of the details and limits of a suitably stable reference cavity, and then turn our attention to the single atom.

I.2. – Reference cavity limitations.

We can begin with a brief look at the demands that a spectral purity of 1 Hz places on the physical stability of the reference cavity. If the cavity has a length of 30 cm and the optical wavelength is 500 nm, then the optical-path length between the mirrors must not change by more than 10^{-15} m, the approximate size of the nucleus of any of the constituent atoms in the dielectric coatings. Researchers who study parity-nonconserving interactions in atomic systems sometimes use the analogy that a human hair added to the radius of the Earth is equivalent to the distortion in an atom caused by the parity-nonconserving part of the Hamiltonian. By the same token, if the spacer for an optical cavity were the Earth, a human hair added to the diameter would cause a frequency shift of about 300 Hz! In the first part of this section, we investigate some of the fundamental limits to the attainment of an average spacing between two mirrors that is stable to better than $1 \cdot 10^{-15}$ and to the achievement of a laser that is spectrally narrowed to better than 1 Hz. We will also address some of the limitations imposed by various environmental factors. We will see that, although fundamental limits come from quantum mechanics and thermodynamics, important practical limitations come from mechanics and gravitational coupling to the noisy terrestrial environment. In particular, at low Fourier frequencies (< 100 Hz), seismic noise and pendulum motion dominate the noise budget.

At the quantum level, the measurement of the length of the cavity to which the laser is locked brings about the inevitable competition between the measurement precision and the perturbation of the measurement to the system. The measurement precision can be improved by a factor of $1/\sqrt{N}$ by increasing the number N of (signal) photons in the measurement interval, whereas the shot noise of the radiation pressure on the mirrors increases as \sqrt{N} . The optimum flux of signal photons, or input power (assuming 100% of the light is coupled into the cavity on resonance and that the detection efficiency is unity), is given when both effects are equal in magnitude [4]. For the laser interferometers used in gravity wave detection, the mirrors are suspended as pendulums and the optimum power is calculated for frequencies $\omega/2\pi$ well above the resonance frequency $\omega_0/2\pi$ of the pendulum support. As a function of frequency,

this limit length uncertainty is given by [5]

$$(1) \quad \Delta x \approx (4\hbar\Delta f/m)^{1/2}/\omega,$$

where m is the mass of suspended mirrors and Δf is the measurement bandwidth. Interestingly, this is the same measurement precision allowed by the standard quantum limit [4-7]. In our case the resonator is composed of a single bar, or spacer, to which the mirrors are rigidly attached. The resonator is then suspended, often by small-diameter wires, inside a temperature-regulated, evacuated housing. The resonator bar can also be treated as a harmonic system, but now the frequency of the lowest mechanical resonance frequency $\omega_0/2\pi$ is typically greater than a few kHz. The noise spectrum of length fluctuations that is of particular importance to us is at Fourier frequencies that are below the lowest resonance frequency of the bar. At frequencies lower than $\omega_0/2\pi$ and for optimum power, the measurement precision limit is independent of Fourier frequency

$$(2) \quad \Delta x \approx (4\hbar\Delta f/m)^{1/2}/\omega_0.$$

For $\omega_0/2\pi = 10$ kHz, a cavity finesse of 100 000 at $\lambda = 500$ nm and a near optimum input power of about 3 W, this limit corresponds to a fractional length uncertainty of less than $(5 \cdot 10^{-22} \text{ m}/\sqrt{\text{Hz}})(\Delta f)^{1/2}$ for a typical bar mass of 4 kg. Thus, with as little as 100 μW incident on the cavity, the quantum fluctuations in the radiation pressure acting on the mirrors are negligible, yet there is sufficient signal-to-noise ratio that the frequency of a laser can be made to track the resonance of the cavity to well below 1 Hz [8] (if only limited by the shot noise of the detected signal).

The technical fluctuations in the laser light that is coupled into the cavity must also be considered. If the finesse is 100 000 and the corresponding power enhancement as high as 30 000, then 100 μW of input power translates into 3 W of *circulating* power when the laser is resonant with the cavity. This in turn gives a force W on each mirror of about $2 \cdot 10^{-8}$ N. If the mirrors are treated as clamped disks of thickness t , the deflection of each mirror, δ , is given by [9]

$$(3) \quad \delta = 3Wr^2(1 - \rho^2)/4\pi Et^3,$$

where the light force is assumed to act uniformly over a concentric area much less than the area of the mirror. The radius r of the mirror is measured from the center to the clamped edge, ρ is Poisson's ratio and E is Young's modulus of elasticity. For a mirror substrate with a material composition similar to fused silica, ρ is about 0.17 and E is about $7 \cdot 10^{10}$ N/m². If t is 5 mm and r is 10 mm, then the deflection at the center of the mirror is about $1.7 \cdot 10^{-16}$ m for a radiation mode size (w_0) of 200 μm . For a cavity that is 30 cm long, the corresponding fractional length change ($2\delta/L$) is about $1 \cdot 10^{-15}$, or about 0.5 Hz. The dimen-

sions and physical properties of the resonator used in this example are typical. Cavities have been constructed that have been shorter, that have used thinner mirrors, and that have coupled in more light; all of these conspire to degrade the frequency stability through fluctuations of the intracavity light intensity. In our example, if 1 mW of power is used to stabilize the laser to the cavity, then the amplitude of the circulating light must be constant to about 10% to achieve a laser stability better than 1 Hz. The radiation pressure also works to stretch the entire bar. The strain, or fractional length change, induced by a force acting normal to the end of a cylindrical bar of cross-sectional area A is given by [9]

$$(4) \quad \Delta L/L = F/AE .$$

The fractional length change for 3 W of circulating power is about $2.5 \cdot 10^{-17}$. This is smaller than the elastic distortion of our typical mirror, and even power fluctuations as large as 10% would cause only millihertz frequency fluctuations through this term. The clear indication is that the fluctuations in the circulating power must be controlled if the laser frequency is to be stabilized to much better than 1 Hz. Cavity power fluctuations are caused by intensity fluctuations of the laser light external to the cavity and by variations in the amount of light that is coupled into the cavity. The latter fluctuations are caused, for example, by any motion of the resonator with respect to the input beam.

Another problem is the local heating of the dielectric mirror coating from the light circulating in the cavity. With high-finesse low-loss mirror coatings, one might assume that this would not be an important concern. However, as we have seen, even with as little as $100 \mu\text{W}$ of power coupled into the cavity that has a finesse of 100 000, the circulating power inside the cavity can exceed 3 W. If the absorption losses are as little as a few p.p.m., $(5 \div 10) \mu\text{W}$ are absorbed in the coating. Most of this power is absorbed in the first few layers of the dielectric stack where the light intensity is the highest. When the light amplitude fluctuates, there is a transient response followed by relaxation to a steady-state condition. For a radiation mode size of $200 \mu\text{m}$, we have measured a $2 \text{ Hz}/\mu\text{W}$ shift of the cavity resonance to higher frequencies with increased power. The magnitude has been measured to be as much as 20 Hz per μW change in the power of the input coupled light [10]. Both the thermal distortion of the mirror and the light pressure problem could be reduced by adjusting the mirror radii and the cavity length so that the mode size is larger at the mirrors (for example, by using a near-spherical resonator).

The thermal noise in the bar or spacer must also be considered. We can think of this as the weak coupling of the fundamental mode of the spacer to its environment, *e.g.*, the residual background gas, the wire suspension, radiation from the walls of the vacuum vessel, etc. If the bar is thermalized to this background or thermal bath at some physical temperature, T , then the weak coupling to the thermal bath causes the mode's amplitude to execute a random walk in the do-

main $|\Delta x| \leq \chi_{\text{r.m.s.}} \cdot \chi_{\text{r.m.s.}}$ is the average deviation of one end of the spacer from the equilibrium position assuming the other end is fixed. The magnitude of this deviation can be found by equating the energy in the harmonic motion of the fundamental mode to $k_{\text{B}}T$. After rearranging, this gives

$$(5) \quad \chi_{\text{r.m.s.}} = \{2k_{\text{B}}T/M_{\text{eff}}\omega_0^2\}^{1/2},$$

where k_{B} is Boltzmann's constant and M_{eff} is the effective mass of the spacer. The fluctuation-dissipation theorem states that the time scale on which this random walk produces changes of order $\chi_{\text{r.m.s.}}$ is the same as the time scale given by the decay time of the fundamental mode [11]. The decay time τ_0 is related to the quality factor of the fundamental mode by $\tau_0 = 2Q/\omega_0$. Q is inversely proportional to the fractional energy loss per cycle. For times τ shorter than τ_0 , the mean-square change in the mode's amplitude is $\chi_{\text{r.m.s.}}$ reduced by the ratio τ/τ_0 , $\Delta x = \chi_{\text{r.m.s.}} \tau/\tau_0$ [12]. Physically, this expresses the fact that a harmonic oscillator is a tuned system that responds to noise and other perturbations in a narrow range of frequencies. So, while the noise is proportional to temperature, the fluctuating forces cannot appreciably change the mode amplitude in times short compared to the decay time.

To reach an appreciation of the size of the length fluctuations due to thermal noise, we can calculate the frequency of the lowest mode of the spacer and solve for $\chi_{\text{r.m.s.}}$. Alternatively, since M_{eff} is only estimated, we can equate the work necessary to stretch or compress a cylindrical bar by $\chi_{\text{r.m.s.}}$ to the energy $k_{\text{B}}T$. The force necessary to elastically stretch a bar by a small amount x is given by eq. (4),

$$(6) \quad F = EAx/L.$$

$F dx$ is the incremental work done by this force in going from x to $x + dx$. Integrating from $x = 0$ to $x = \chi_{\text{r.m.s.}}$, the work done is

$$(7) \quad W = EA(\chi_{\text{r.m.s.}})^2/2L.$$

When this is equated to $k_{\text{B}}T$, $\chi_{\text{r.m.s.}}$ is simply related to the temperature of the spacer and to its physical properties,

$$(8) \quad \chi_{\text{r.m.s.}} = \{2Lk_{\text{B}}T/EA\}^{1/2}.$$

Recall that, for a spacer made from a material comparable in its properties to fused silica, E is about 10^{11} N/m². If the spacer is 30 cm long and 10 cm in diameter, then $\chi_{\text{r.m.s.}} \approx 1.8 \cdot 10^{-15}$ m at a thermal-bath temperature of 300 K. The frequency of a laser in the mid-optical locked to this cavity would move by about 3 Hz for a length change of this magnitude. However, this excursion occurs dominantly at the vibrational frequency of the lowest fundamental (mechanical) mode of the spacer. For a fused-silica spacer of this size, the resonance frequency of its lowest mode is about 10 kHz. Hence, there is little power in the

thermally induced sidebands at ± 10 kHz since the modulation index is so small [13] ($\approx 3 \cdot 10^{-4}$). It is worth noting that the resonant Q in a fused-silica bar at room temperature is only about 10^5 [14]. Therefore, the decay time for the lowest mode is about 10 s, and, unlike our colleagues looking for gravity waves with high- Q resonant-bar detectors, we are sensitive to the full change in the mode amplitude on time scales of critical interest to us. However, a few hertz at 10 kHz driven by the Brownian motion of the cavity is not a limitation to the frequency stability nor spectral purity of a 1 Hz laser.

The temperature sensitivity of low-expansion materials suitable for spacers can be better than 10^{-8} /K, which implies μ K control at the cavity in order to achieve stabilities of a few hertz. However, if the cavity is suspended in a thermally massive, evacuated chamber, then the thermal coupling to the environment is primarily radiative. The time constant can exceed a day. Therefore, if the temperature fluctuations of the walls of the vacuum vessel never exceed 10 mK, then the frequency fluctuation rate of the laser will be less than 1 Hz/s, independent of the time rate of change of the wall temperature.

Pressure fluctuations in the gas between the mirrors produce density variations which in turn cause refractive-index changes. This causes an effective optical-length change to the cavity, nL , where n is the index of refraction for air. Near room temperature, the index of refraction of dry air is linearly related to its pressure, P , by

$$(9) \quad n - 1 \approx 3 \cdot 10^{-9} P,$$

where P is in Pa ($133 \text{ Pa} = 1 \text{ Torr}$). Thus, even if the cavity is evacuated to 10^{-5} Pa, the absolute shift in the cavity resonance for optical frequencies near $\lambda \approx 500 \text{ nm}$ is about 15 Hz (from that of 0 Pa). 10% fluctuations in this pressure cause frequency excursions of the laser of approximately 1.5 Hz. The air pressure at 10^{-5} Pa also causes a strain in the bar but the length compression is negligible. The pressure at 10^{-5} Pa is less than 10^{-5} N/m^2 , which produces an axial strain in the spacer of about $1 \cdot 10^{-16}$. The fractional length change is not fully this magnitude since the pressure-induced stress in the axial direction is somewhat compensated by the radial stress. Consequently, in a reasonably stiff spacer, fluctuations in the cavity length due to fluctuations in the pressure are dominated by index-of-refraction changes.

Additional limitations to the stability of a laser locked to a Fabry-Perot resonator come from technical problems such as optical feedback, intensity fluctuations, beam pointing stability, etc. [15], but seismic noise or ambient vibrations that cause changes in the cavity length are the most important practical problems limiting the frequency stability for times longer than a few ms. Generally, there are two distinct effects: high-frequency vibrations, which may excite fundamental mechanical resonances of the bar, and low-frequency vibrations, which tend to produce nonresonant distortions of the bar. The first effect typi-

cally occurs at frequencies in the range of (100 ÷ 1000) Hz and often can be effectively eliminated, for example, by mounting the system on alternating layers of shock-absorbing material and passive masses, such as thin rubber and cinder block. Low-frequency vibrations ((0.1 ÷ 100) Hz), which are typically driven by ground noise and building vibrations, are much harder to eliminate. Some sophisticated vibration isolation systems, both active and passive, have been developed to reduce noise in this frequency interval[16]. While an active vibration isolation system may ultimately be necessary for sufficient attenuation of seismic noise to reach laser spectral purity below 1 Hz, we, for the moment, isolate only with passive systems. The simplest method of passive vibration isolation consists of mounting the device to be isolated on a resilient support, such as a pendulum or spring. A pendulum isolates in the horizontal plane, using gravity as its spring constant (note that this spring can be nearly lossless). A spring can isolate horizontally and vertically simultaneously. It is relatively simple to show that the attenuation in the amplitude of motion between the support and the bar increases as ω^2 for motion at frequencies higher than the resonance frequency ω_0 ($\omega_0^2 = k/m$, spring; $\omega_0^2 = g/l$, pendulum). Damping must be included to limit the amplitude of motion, a_1 , at resonance. The response of a damped system is

$$(10) \quad a_1 = a_2(1 + i\Gamma\omega)/\{1 - (\omega/\omega_0)^2 + i\Gamma\omega\},$$

where a_1 is the amplitude of the motion at the bar, a_2 is the amplitude of motion of the support at frequency ω , and Γ is the coefficient of damping. The amplitude a_1 is complex (phase shifted) and everywhere bounded. In practice the choice of damping is a compromise between low resonant amplitude and sufficient high-frequency isolation. There are more complex passive systems that offer better high-frequency isolation while at the same time reduce the resonance peaking to a factor of 2 or less[16]. Calculations of the vibration isolation produced by various mechanical suspensions have been driven by the work done on gravity wave detectors; a good treatment is that of Veitch[17].

The most important function of the isolation system is to reduce fractional length changes of the reference cavity to below (ideally, well below) $1 \cdot 10^{-15}$. If the cavity is suspended with its axis horizontal by wires that act as vertically stiff pendulums, then it has been demonstrated that the isolation from horizontal vibrations in the direction of the cavity axis can be adequate to attain a stability approaching 1 Hz[18]. However, a suspended bar is subjected to a distributed load resulting from the pull of gravity, which produces considerable stress to the support structure and to the bar. In addition, the bar is not perfectly rigid and must distort at some level under its weight and this causes additional stress. All these stresses can produce sudden acoustical emission[19] at the rate of up to several per second and at frequencies that may or may not coincide with the eigenfrequencies of the bar. Also, since the wires are essentially

stiff to vertical vibrations, these perturbations can be coupled into the bar. If, though, the wires were connected to the nodal points of the bar, then the external force would be unable to excite that mode (or modes) through that nodal position. Unfortunately, there are many bending modes and vibrational modes with disparate nodal positions, so, although it is possible to reduce some of the cavity sensitivity to vertical perturbations, single suspension points are not sufficient to eliminate excitation of all modes. Further improvement can be achieved if the cavity is isolated vertically as well. We now turn our attention to some of the experimental studies pursued over the past few years in the ion storage group at NIST.

I.3. – Experimental results: cavity comparisons.

In some of our studies, a direct heterodyne comparison of two independently frequency-stabilized light beams was made. The linewidths and frequency stabilities were analyzed in various ways. The beat note was recorded in an r.f. or microwave spectrum analyzer, thereby directly displaying the combined linewidth of the two sources. The signal-to-noise ratio was improved and the long-term relative frequency drift was studied by averaging many successive scans of the beat note. It was also possible to use two spectrum analyzers in tandem to identify the specific frequency noise components that contribute to the laser linewidth. This was particularly useful toward unraveling the noise sources that cause fluctuations to the length of the cavities. For instance, if the seismic noise was independently studied with a seismometer, a correspondence between the seismic-noise terms and the dominant contributors to the laser linewidth could be made. If the length fluctuations of the two cavities were similar in frequency and amplitude, but otherwise independent, the linewidth of either frequency-stabilized system is smaller than the recorded beat note by $\sqrt{2}$. If the effective length stability of one cavity had been worse than that of the other, the measured linewidth would have been dominated by the frequency fluctuations of the laser locked to the noisier cavity.

Either the transmitted light beam or the reflected beam that interferes with the light re-emerging from the cavity can be used to stabilize the frequency of the laser. In our experiments, we used the beam reflected from the cavity. The error signal can be derived either near zero frequency or at some higher frequency. Since technical-noise terms are present at low frequencies, it is better to modulate and detect at a frequency at which the signal-to-noise ratio is limited by the shot noise in the detected light beam. This is the Pound-Drever-Hall reflected-sideband technique that has been treated in detail elsewhere [8,20]. Attention to the optical layout and to the electronic-noise terms is critical to achieving a spectral linewidth that is smaller than a few hertz. This also has been discussed in papers by HOUGH *et al.* [21] and by SALOMON *et al.* [15]. By several separate measurements, the electrical problems in our work were deter-

mined to be unimportant to the attainment of a laser linewidth below 1 Hz; the dominant contribution to the laser linewidth were mechanical (and perhaps optical) perturbations that caused length changes in the reference cavity.

The frequency-stabilized light beams were derived from a home-built ring dye laser oscillating at 563 nm. The wavelength of the laser was chosen because its frequency would eventually be doubled into the ultraviolet to probe a narrow transition in $^{199}\text{Hg}^+$. Historically, the dye laser was locked in a two-step process. The laser was pre-stabilized to the order of a few hundred Hz by locking the laser to a lower-finesse (about 800) cavity. The cavity resonance was probed by the reflected-sideband technique using a modulation frequency of about 10 MHz. Rapid frequency fluctuations of the laser were removed by a fast (bandwidth > 2 MHz) servo driving an intracavity E/O modulator, and the lower-frequency fluctuations were corrected by a second-order servo-loop driving an intracavity PZT-mounted mirror. The frequency-stabilized light was then transmitted through optical fibers to the high-finesse cavities. Since the laser linewidth was less than 1 kHz, a smaller-bandwidth (100 kHz), lower-noise servo could be used to strip the remaining noise from the laser beams. Again, the reflected-sideband technique was used to probe the resonance of the high-finesse cavities. In the second stage, the frequency-correcting element was an acousto-optic modulator through which the laser beam was singly or doubly passed. The frequency corrections were simply written onto the acousto-optically shifted beam by the servo. Long-term corrections were fed back to the low-finesse cavity to maintain frequency alignment of the laser with one of the high-finesse cavities. The laser power was also stabilized by adjusting the r.f. power applied to the acousto-optic modulator. The overall intensity regulation was better than 0.1%, but this was applied to the beam before it entered the cavity. From the arguments made in sect. I.2, intensity variations in the light circulating in the cavity cause length fluctuations by light pressure changes and by heat variations in the mirror coatings. Therefore, although we have not done so yet, it may be better to stabilize the intensity of the light circulating in the resonator by using the light transmitted from the cavity. This should give a first-order insensitivity of the frequency of the laser to power fluctuations caused by relative motion between the cavity and the injected light beam.

The cavities were constructed from a cylindrical, Zerodur [22] rod that was cut and rough ground to a diameter of about 10 cm and a length of about 27 cm. A 1 cm round hole was bored along the axis of the spacers, and a smaller one was bored through the center of the rod midway from the ends and normal to its axis. The smaller bore permitted evacuation of the space between the mirrors. The length of the cavities and the mirror radii of curvature were chosen so that the cavities were highly nondegenerate for the spatially transverse modes. In particular, the frequency of the TEM_{01} and TEM_{10} modes are separated from the lowest-order TEM_{00} mode by approximately 30% of the free spectral range.

Even at the 12th transverse order, the frequencies are still separated from the lowest-order fundamental mode (modulo $c/2L$) by several percent of the free spectral range. This gives good immunity to any line pulling if any light power is coupled into the higher-order modes. Even so, great care is taken to mode match into the cavities. Note that this high immunity to line pulling would be somewhat compromised by going toward a near spherical resonator as suggested in sect. I.2.

Each cavity is suspended by two thin (250 μm) molybdenum wires inside a thick-walled (19.1 mm) aluminum vacuum vessel that has an inner diameter of 26.7 cm. The wires are placed as slings under either end of the spacer, about 1/5 the cavity length from each end, in an attempt to support at the nodal positions for the lowest-order bending mode. The ends of each wire are attached to the inner wall of the vacuum vessel by small clamps. Each wire either travelled vertically upward from either side of the spacer to the wall («U» shaped), or opened slightly away from the bar («V» shaped). This allowed free movement of the cavity along the direction of its axis and restricted, but not rigidly, the motion perpendicular to the axis. Damping of the pendulum motion was weak and dominantly into the table and its padding through the aluminum housing. The aluminum vessels are thermally insulated and temperature regulated to the order of a few mK. The temperature coefficient of the spacers is approximately $6 \cdot 10^{-9} \text{ K}^{-1}$ at $T = 300 \text{ K}$. The thermal time constant from the walls of the evacuated aluminum housing to the spacer is on the order of one day, giving adequate isolation to small temperature fluctuations at the vessel walls. Since the variations in the wall temperature were controlled to less than 10 mK for any time period, the maximum rate of change in the temperature of the bar did not exceed 100 pK/s. This corresponds to a frequency fluctuation rate of about 0.3 Hz/s and a maximum frequency change of about 50 kHz. A pressure of $1 \cdot 10^{-6} \text{ Pa}$ ($8 \cdot 10^{-9} \text{ Torr}$) is maintained in each vacuum vessel by an ion pump that is rigidly attached to the vessel. This is adequate to give frequency fluctuations of less than 1 Hz for pressure fluctuations of 10%.

The length of the longer rod corresponds to a free spectral range of 622 MHz and the shorter rod has a free spectral range of 562 MHz. The mirrors are highly polished Zerodur substrates that are coated to give high finesse and good efficiency and then optically contacted to the polished ends of the spacer. The finesses of the cavities are about 60 000 and 90 000, respectively, and, for both cavities, the transmission on resonance exceeded 30%. The high finesse F , or the long optical storage time, translates into a narrow fringe whose HWHM is given by $c/2LF$. Consequently, the ratio of error voltages to frequency excursions can be very high, even for short cavities. Shorter cavities have been constructed from ULE [22] that have measured finesses that exceed 130 000 (and, recently, finesses exceeding 10^6 have been reported [23]). The frequencies of the mechanical resonances of these shorter, stiffer bars will be about a factor of 3 higher than those of the Zerodur bars. As long as the frequencies of the me-

chanical vibrations are high enough, a narrow optical resonance can be probed with high resolution by the unperturbed carrier of the laser spectrum.

The aluminum vacuum vessels rested on Viton [22] rubber strips attached to v-blocks made of aluminum. The v-blocks were secured to a rigid acrylic plastic plate. Each reference cavity system was mounted on a separate optical table that (initially) consisted of surface plates that were deadened by damping their internal vibrations into sand. The sandbox sat on soft rubber pads and cinder blocks in one case and on low-pressure inner tubes and cinder block legs in the second. Noise vibrations from the floor and on the table tops were monitored with moving-coil seismometers that had a sensitivity of $629 \text{ V} \cdot \text{s/m}$ from approximately $(1 \div 100) \text{ Hz}$. Measurements of the floor motion in our laboratory revealed bright resonances at 14.6 Hz, 18.9 Hz and 29.2 Hz on top of a broad pedestal from about 1 to 40 Hz. The average amplitude of the resonant motion was greater than 10^{-6} m/s and the pedestal peak was about 10^{-7} m/s . Isolation from mechanical vibrations began at frequencies above about 5 Hz for both table tops. By 100 Hz the isolation from floor noise for either table had improved by a factor of 40 or better.

For heterodyning, a small fraction of the frequency-stabilized light from each cavity was combined on a beam splitter and detected with a fast diode. The heterodyned signal was amplified and analyzed with two spectrum analyzers used in series. This allowed us to look directly at the beat note and also Fourier-analyze the noise terms that contributed to its linewidth. The first analyzer could be used to observe the beat signal, or as a frequency discriminator. As a frequency discriminator, the scan was stopped and the analyzer was used as a tunable r.f. filter/receiver with a variable bandwidth. The center frequency of the analyzer was then shifted so that the heterodyned signal lay at the half-power point of the response curve. The bandwidth was adjusted so that the frequency excursions of the beat signal were much less than the bandwidth. This produced a one-to-one map of frequency excursions-to-voltage excursions whose Fourier power spectrum could be analyzed in the second low-frequency ($(0 \div 100) \text{ kHz}$) spectrum analyzer. The noise power spectrum in the second analyzer helped to reveal the nature and origin of the vibrational noise that contributes to the linewidth of the stabilized lasers.

The width of the heterodyne signal between the two stabilized lasers was less than 50 Hz. The noise power spectrum disclosed that low-frequency fluctuations in the range from near zero to 30 Hz dominated this linewidth. The vibrational-noise spectrum measured by the seismometers on the table tops matched the largest noise components of the beat note. The frequencies of the pendulum motion of the suspended cavities were about 1.4 Hz and 1.48 Hz which gave FM at these frequencies. There were also bright features in the laser power spectra that came from the floor motion at 14.6 Hz, 18.9 Hz and 29.2 Hz. The modulation indices of the latter three noise components were about one, so they all had enough power to contribute to the beat note linewidth. When the pendulum mo-

tions of the bars were quiet, their FM contributed little to the laser linewidths. However, the integral of the nearly featureless noise power spectrum from about 0 Hz to 10 Hz contributed about 15 Hz to the combined spectral purity of the lasers. Some, if not all, of this noise was mechanical, but it was not clear how it coupled to the suspended cavity. To help elucidate the connection, we drove one of the table tops in either the horizontal or vertical direction with a small loudspeaker connected to an audio signal generator. The motion of the speaker diaphragm was coupled to the table by a rod glued to the diaphragm and gently loaded against the table. The table could be driven at frequencies from a few hertz to about 100 Hz with enough power to be 40 dB above background noise. When the loudspeaker drove the table in the horizontal plane in a direction parallel to the axis of the cavity, the isolation of the suspended cavity was sufficiently good that the beat signal showed little evidence of the perturbation even at the high drive levels. However, when the drive was applied vertically at a level barely perceptible above the vertical background noise, the heterodyne signal showed added noise power at the drive frequency. The stiff support in the vertical direction strongly coupled vertical motion into effective cavity length changes. The sensitivity of the Fabry-Perot cavity to vertical motion was orders of magnitude higher than for horizontal motion parallel to the

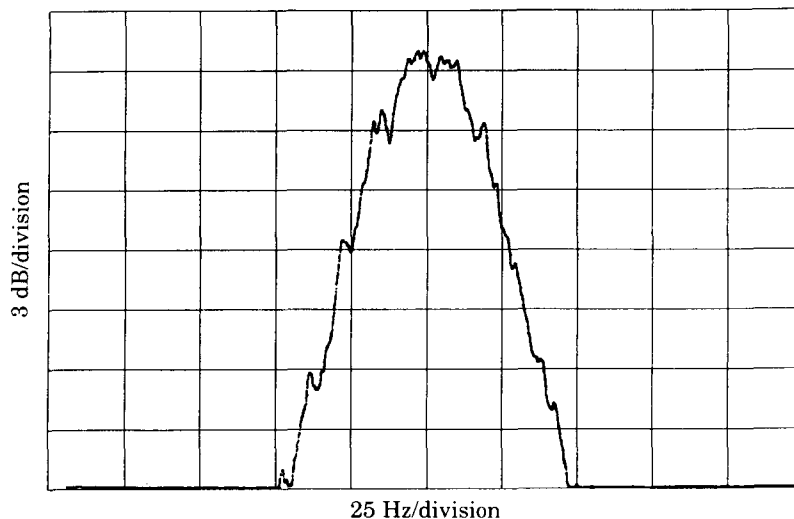


Fig. 1. - Spectrum of the beat frequency between the two independent, cavity-stabilized lasers discussed in the text. The resolution bandwidth is 30 Hz. Total integration time for these data is about 70 s (the relative linear drift between the two cavities is removed by mixing the beat note with the frequency from a synthesizer that is swept in time). The partially resolved sidebands at 14.6 Hz are due to a resonant floor vibration. The apparent linewidth is about 30 Hz; the linewidth of the better-stabilized laser is at least $\sqrt{2}$ narrower.

cavity axis. (For practical reasons, we did not drive the table in the horizontal plane in a direction perpendicular to the cavity axis.)

In order to improve the vertical isolation, one table was suspended just above the floor with latex-rubber tubing attached to the ceiling. The resonance frequencies for both the vertical motion and the horizontal pendulum motion of the suspended table were near 0.33 Hz. These were damped to the floor with two small dabs of grease, but the damping did not significantly change the isolation afforded by the latex tubing at higher frequencies. The isolation from vibrational noise above 1 Hz was more than an order of magnitude better than that of the quietest sandbox table. This was partially reflected in the linewidth of the heterodyne signal between the laser radiation stabilized to the cavity supported on this table and the laser radiation stabilized to the cavity supported on the best sandbox table; it dropped from about 50 Hz to less than 30 Hz. In fig. 1 the spectrum of the beat frequency is shown. Zerodur is known to temporally contract with a time constant of years[8,24]. The creep rate for both cavities corresponds to a linear frequency drift of $(3 \div 5)$ Hz/s, but the rates are not identical. The linear, relative cavity drift is removed by mixing the beat frequency with the frequency from a synthesizer that was swept in time. The spectrum of fig. 1 represents an integration time of 70 s. The noise vibrational sidebands at 14.6 Hz are partially resolved. Note that the linewidth of the best stabilized laser is at least $\sqrt{2}$ narrower. The Fourier noise power spectrum from 0 to 10 Hz is shown in fig. 2. The beat note linewidth obtained by integrating the power spectrum is about 15 Hz. We suspect that the laser stabilized to the cavity on the sandbox table is the dominant contributor to the width of the heterodyne signal since the vibrational noise measured on this table is greater. Perhaps the linewidth of the laser stabilized to the cavity on

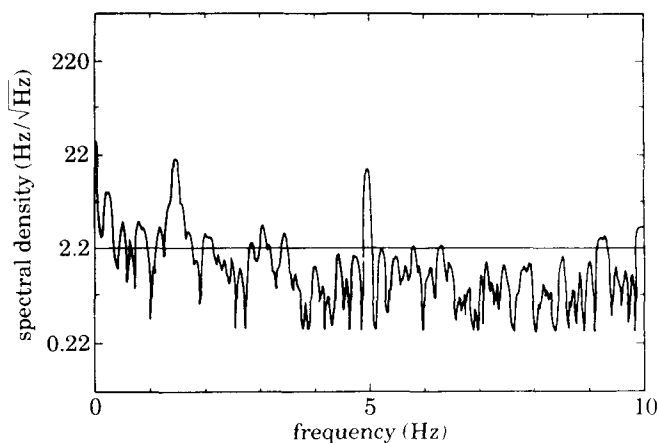


Fig. 2. - Fourier noise power spectrum of the laser heterodyne signal (shown in fig. 1) from 0 to 10 Hz.

the table suspended by the latex tubing is below 1 Hz. We are working to verify this and to build better cavities.

II. – Single-atom Spectroscopy.

II.1. – Single-ion results.

The ion trapping and laser cooling relevant to our experiments have been described elsewhere [25,26]. A ^{199}Hg atom is ionized and trapped in the harmonic pseudopotential well created by an r.f. potential applied between the electrodes of a miniature Paul trap. The separation between the endcap electrodes ($2z_0$) is about $650\ \mu\text{m}$. The frequency of the r.f. potential is about 21 MHz. Its amplitude can be varied up to 1.2 kV; at the maximum r.f. amplitude, the quadratic pseudopotential is characterized by a secular frequency of nearly 4 MHz. The ion is laser-cooled to a few millikelvin by a few microwatt of radiation from two 194 nm sources. One source drives transitions from the $5d^{10}6s\ ^2S_{1/2}(F=1)$ to the $5d^{10}6p\ ^2P_{1/2}(F=0)$ level (see fig. 3). This is essen-

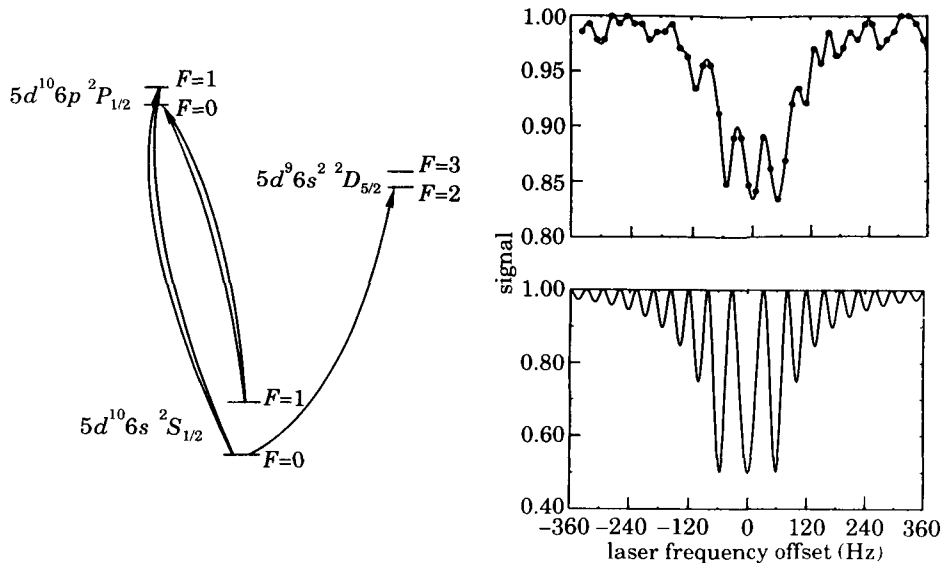


Fig. 3. – On the left is a simplified energy level diagram for $^{199}\text{Hg}^+$ at zero field. Shown in the upper figure on the right is the power-broadened lineshape obtained by scanning through the Doppler-free resonance of the $^2S_{1/2}(F=0, m_F=0)$ - $^2D_{5/2}(F=2, m_F=0)$ transition in a single laser-cooled $^{199}\text{Hg}^+$ ion. A 563 nm laser that is stabilized to a high-finesse reference cavity, which in turn is long-term stabilized to the ion, is frequency-doubled and stepped through the resonance for 138 consecutive sweeps. The step size is 15 Hz at 563 nm (30 Hz at 282 nm). The lower right figure shows the lineshape calculated for conditions similar to the experimental conditions for the upper figure, except that the ion is assumed to have zero temperature and the laser is assumed to have zero linewidth.

tially a two-level system suitable for laser cooling, except for weak off-resonance pumping into the ${}^2S_{1/2}(F=0)$ state. The second 194 nm source, tuned to the ${}^2S_{1/2}(F=0)$ to ${}^2P_{1/2}(F=1)$ transition, returns the ion to the ground-state $F=1$ hyperfine level. The frequency separation between the two radiation sources is equal to the sum of the ground- and excited-state hyperfine splittings (about 47 GHz). The two 194 nm beams propagate collinearly and irradiate the ion at an angle of 55° with respect to the symmetry (z) axis of the trap. In this way, all motional degrees of freedom are cooled to near the Doppler-cooling limit of 1.7 mK. 194 nm fluorescence from the ion, collected in a solid angle of about $5 \cdot 10^{-3} 4\pi$ sr, is detected with an efficiency of 10% to give a peak count rate on resonance of about 25 000/s. The complication of laser cooling with two lasers is brought about by the hyperfine structure of ${}^{199}\text{Hg}^+$. Only an isotope with nonzero nuclear spin can have first-order, field-independent transitions, which give great immunity to magnetic-field fluctuations. In ${}^{199}\text{Hg}^+$, the nuclear spin is $1/2$. Near $B=0$, the narrow $5d^{10}6s\ {}^2S_{1/2}$ - $5d^96s^2\ {}^2D_{5/2}$ transition at 282 nm is first-order field-independent. The decay rate of the metastable ${}^2D_{5/2}$ state corresponds to an optical linewidth of less than 2 Hz—certainly, a suitably challenging test for the stabilized dye laser.

The 282 nm radiation is obtained by frequency doubling the radiation from the dye laser that is stabilized to the Fabry-Perot cavity on the sandbox table. (The cavity comparisons were done subsequent to the single-ion studies and we had not yet suspended a table with latex tubing.) Prior to being frequency-doubled, the 563 nm radiation (beam 1) is passed through an acousto-optic modulator (A/O-1) so that its frequency can be tuned through the S - D resonance. We also used A/O-1 to suppress the linear drift of the cavity and the frequency fluctuations caused by relative motion between the cavity and the ion trap (which are supported on different tables separated by 3 m). These Doppler effects can be removed in a fashion similar to that used by VESSOT to remove Doppler frequency shifts between a ground-based microwave source and a rocket-borne microwave oscillator [27]. Another acousto-optic modulator (A/O-2) is placed in an auxiliary laser beam (beam 2) near the ion trap. The frequency of beam 2 need not be stabilized. A/O-2 generates a frequency-shifted beam (beam 3) that is sent to the cavity table and returned on a path very close (< 2 cm) to that followed by beam 1. The light paths need not be overlapping in order to reach a frequency stability of 1 Hz. Beam 3 is recombined with its carrier to produce a beat note at the r.f. frequency of A/O-2. However, because the shifted beam traveled over to the cavity and back to the trap, the frequency fluctuations caused by relative motion between the tables and atmospheric turbulence are impressed on the beat note. Dividing the beat frequency by 2 gives the one-way path noise information carried at half the radiofrequency of A/O-2. If this frequency is summed with the right quadrature to the frequency that sweeps the stabilized laser through the S - D resonance, then path noise is eliminated. This is equivalent to bringing the cavity and trapped ion together. Step-

ping the frequency of the stabilized laser through the S - D resonance and removing the linear cavity drift are accomplished with an r.f. drive frequency to A/O-1 obtained by summing the output of two synthesizers. The frequency of one synthesizer sweeps opposite to the cavity drift and the frequency of the second synthesizer is stepped back and forth, sweeping the frequency of the stabilized laser through the narrow atomic resonance.

The 282 nm radiation and the two-frequency 194 nm source are turned on and off sequentially using shutters and the acousto-optic modulator. This prevents any broadening of the narrow S - D transition due to the 194 nm radiation. Electron shelving [25,28] is used to detect each transition made to the metastable D state as a function of the frequency of the 282 nm laser. At the beginning of each cycle, both 194 nm lasers irradiate the ion. The fluorescence counts in a 10 ms period must exceed a minimum threshold (typically 20 counts) before the interrogation sequence can continue. The 194 nm beams irradiate the ion for sequential 10 ms periods until the threshold is met. The 194 nm radiation tuned to the ${}^2S_{1/2}(F=0)$ - ${}^2P_{1/2}(F=1)$ transition is chopped off for 5 ms. During this time, the 194 nm radiation tuned to the ${}^2S_{1/2}(F=1)$ - ${}^2P_{1/2}(F=0)$ transition optically pumps the ion into the ${}^2S_{1/2}(F=0)$ ground state. Then this 194 source is turned off. One millisecond later, the 282 nm radiation, tuned to a frequency resonant or nearly resonant with the ${}^2S_{1/2}(F=0, m_F=0)$ - ${}^2D_{5/2}(F=2, m_F=0)$ transition, irradiates the ion for an interrogation period that is varied up to 25 ms. At the end of this period, the 282 nm radiation was turned off and both 194 nm sources were turned on. Another 10 ms detection period was used to determine whether a transition to the D state had been made (fluorescence counts > threshold, no; fluorescence counts < threshold, yes). The result was recorded as a 1 or 0 (no or yes) and averaged with the previous results at this frequency. Then the frequency of the 282 nm radiation was stepped and the measurement cycle repeated.

Since the frequency drift of the 282 nm laser depended not only on the reference cavity contraction rate, but also on small pressure and temperature changes, on laser power variations, and so on (as discussed in sect. I.2), we locked the frequency of the laser to the narrow S - D transition to remove long-term frequency drifts. To do this, we modified the measurement cycle to include a locking cycle. We began each measurement cycle by stepping the frequency of the 282 nm radiation to near the half maximum on each side of the resonance N times (N varied from 8 to 32). At each step, we probed for 5 ms and then looked for any transition with the electron-shelving technique. We averaged the N results from each side of the resonance line, took the difference and corrected the frequency of the synthesizer used to compensate the cavity drift. The gain of this lock needed to be properly adjusted to avoid adding frequency noise to the laser. In this way, variations in the frequency of the 282 nm laser for time periods exceeding a few seconds were reduced.

In fig. 3, we show the spectrum obtained by scanning in this drift-free way

through the Doppler-free resonance of the ${}^2S_{1/2}(F=0, m_F=0)$ - ${}^2D_{5/2}(F=2, m_F=0)$ transition. The lineshape shown is the result of 138 consecutive scans, each of which included a locking cycle. The probe period was 15 ms, and the step size was 15 Hz at 563 nm (30 Hz at 282 nm). The resonance shows a clearly resolved triplet with the linewidth of each component less than 40 Hz (< 80 Hz at 282 nm). We first thought that the triplet structure might be due to 60 Hz modulation of the frequency of the 563 nm laser either due to grounding problems, line pickup or inadequate servo gain. However, when the radiation from two independently stabilized laser beams was heterodyned together, the 60 Hz modulation index was far too small to account for the sideband structure observed on the S - D resonance. In addition, the frequency separation of the peaks is nearer to 50 Hz, not to 60 Hz. We now think that, most likely, the triplet structure is caused by Rabi power broadening. The 282 nm radiation is focussed to a spot size of about $25\ \mu\text{m}$; therefore, on resonance, fewer than 10^6 photons/s (< 1 pW) will saturate the transition. Below, the data is a theoretical lineshape calculated for an ion at rest, for no broadening due to collisions or laser bandwidth, for a pulse length of 15 ms and for sufficient power at resonance to give a 3.5π pulse (which roughly corresponds to the power used).

Qualitatively, the figures compare well. The fluctuations from measurement cycle to measurement cycle in the quantum occupation number of the ion in the harmonic well of the trap cause variations in the transition probability of the ion. This, and the finite laser linewidth, likely cause the general broadening and weakening of the signal. Current efforts are devoted to measuring the narrow S - D transition using the laser stabilized to the cavity on the suspended table. A cryogenic, linear r.f. Paul trap has been constructed and will soon be tested. With this trap, it should be possible to laser-cool many ions and to store them without attrition for days. The increased numbers of trapped ions will give a better signal-to-noise ratio (thereby better stability), but it will still be possible to have a small second-order Doppler shift. We also plan to investigate the lineshape and the effects of power broadening in more detail in future experiments.

* * *

The authors gratefully acknowledge the contributions of the colleagues who participated in the work reported here: F. DIEDRICH, F. ELSNER and M. RAIZEN. We also acknowledge the support of the Office of Naval Research.

REFERENCES

- [1] D. J. WINELAND, W. M. ITANO, J. C. BERGQUIST and F. L. WELLS: in *Proceedings of the 35th Annual Symposium on Frequency Control, Philadelphia, Pa., May 1981* (copies available from Electronic Industries Assoc., 2001 Eye St., Washington, DC, 20006), p. 602.

- [2] D. J. WINELAND, J. C. BERGQUIST, J. J. BOLLINGER, W. M. ITANO, D. J. HEINZEN, S. L. GILBERT, C. H. MANNEY and M. G. RAIZEN: *IEEE Trans. Ultrason., Ferroelectr. Frequency Control*, **37**, 515 (1990).
- [3] MIAO ZHU and J. L. HALL: *J. Opt. Soc. Am. B.*, **10**, 802 (1993).
- [4] C. M. CAVES: *Phys. Rev. Lett.*, **45**, 75 (1980).
- [5] W. A. EDELSTEIN, J. HOUGH, J. R. PUGH and W. MARTIN: *J. Phys. E*, **11**, 710 (1980).
- [6] C. M. CAVES: *Phys. Rev. Lett.*, **54**, 2465 (1985).
- [7] R. LOUDON: *Phys. Rev. Lett.*, **47**, 815 (1981).
- [8] D. HILS and J. L. HALL: in *Frequency Standards and Metrology*, edited by A. DEMARCHI (Springer-Verlag, Berlin, 1989), p. 162.
- [9] R. J. REARK and W. C. YOUNG: in *Formulas for Stress and Strain* (McGraw-Hill, New York, N.Y., 1975).
- [10] N. SAMPRAS, Stanford University: private communication.
- [11] H. B. CALLEN and R. F. GREENE: *Phys. Rev.*, **86**, 702 (1952); H. B. CALLEN and T. A. WELTON: *Phys. Rev.*, **83**, 34 (1951).
- [12] G. W. GIBBONS and S. W. HAWKING: *Phys. Rev. D*, **4**, 2191 (1971).
- [13] P. F. PANTER: *Modulation, Noise and Spectral Analysis* (McGraw-Hill, New York, N.Y., 1965).
- [14] V. B. BRAGINSKY, V. P. MITROFANOV and V. I. PANOV: *Systems with Small Dissipation* (University of Chicago Press, Chicago, Ill., 1985).
- [15] CH. SALOMON, D. HILS and J. L. HALL: *J. Opt. Soc. Am. B*, **5**, 1576 (1988).
- [16] D. L. PLATUS: *SPIE Proceedings*, **1619**, 44 (1991); P. R. SAULSON: *Gravitational Astronomy; Instrument Design and Astrophysical Prospects*, edited by D. E. McCLELLAND and H.-A. BACHOR (World Scientific, Singapore, 1991), p. 248.
- [17] P. J. VEITCH: *Rev. Sci. Instrum.*, **62**, 140 (1991).
- [18] J. C. BERGQUIST, W. M. ITANO, F. ELSNER, M. G. RAIZEN and D. J. WINELAND: in *Light Induced Kinetic Effects on Atoms, Ions, and Molecules*, edited by L. MOI, S. GOZZINI, C. GABBANINI, E. ARIMONDO and F. STRUMIA (ETS Editrice, Pisa, 1991), p. 291.
- [19] F. LARSEN: *Acoustic Emission* (IFI/Plenum, New York, N.Y., 1979).
- [20] R. W. P. DREVER, J. L. HALL, F. V. KOWALSKI, J. HOUGH, G. M. FORD, A. J. MUNLEY and H. WARD: *Appl. Phys. B*, **31**, 97 (1983).
- [21] J. HOUGH, D. HILS, M. D. RAYMAN, L.-S. MA, L. HOLLBERG and J. L. HALL: *Appl. Phys. B*, **33**, 179 (1984).
- [22] Mention of a commercial product is for technical communication only.
- [23] G. REMPE, R. J. THOMPSON, H. J. KIMBLE and R. LALEZARI: *Opt. Lett.*, **17**, 363 (1992).
- [24] F. BAYER-HELMS, H. DARNEDDE and G. EXNER: *Metrologia*, **21**, 49 (1985).
- [25] J. C. BERGQUIST, W. M. ITANO and D. J. WINELAND: *Phys. Rev. A*, **36**, 428 (1987).
- [26] J. C. BERGQUIST, D. J. WINELAND, W. M. ITANO, H. HEMMATI, H.-U. DANIEL and G. LEUCHS: *Phys. Rev. Lett.*, **55**, 1567 (1985).
- [27] R. F. C. VESSOT, M. E. LEVINE, E. M. MATTISON, E. L. BLOMBERG, T. E. HOFFMAN, G. U. NYSTROM, B. F. FARREL, R. DECHER, P. B. EBY, C. R. BAUGHER, J. W. WATTS, D. L. TEUBER and F. D. WILLS: *Phys. Rev. Lett.*, **45**, 2081 (1980).
- [28] H. DEHMELT: *Bull. Am. Phys. Soc.*, **20**, 60 (1975); *J. Phys. (Paris) Colloq.*, **42**, C8-299 (1981).

Ionic crystals in a linear Paul trap

M. G. Raizen,* J. M. Gilligan, J. C. Bergquist, W. M. Itano, and D. J. Wineland

Time and Frequency Division, National Institute of Standards and Technology, Boulder, Colorado 80303

(Received 31 October 1991)

We describe a configuration for a linear Paul rf ion trap. This trap can store a long string of ions with a small second-order Doppler shift, comparable to that achieved with a single ion in a quadrupole Paul trap. Crystallized strings of trapped ions, as well as more complicated structures, have been observed in the trap. We report an observation of the 40.5-GHz ground-state hyperfine interval of $^{199}\text{Hg}^+$ by microwave-optical double-resonance spectroscopy and discuss prospects for a microwave frequency standard based on a trapped string of ions.

PACS number(s): 32.80.Pj, 32.30.Bv, 95.55.Wk, 36.40.+d

I. INTRODUCTION

Experiments with trapped and laser-cooled ions have been motivated by the possibility for high-accuracy spectroscopy, improved frequency standards, and experiments in fundamental physics. For a large range of spectroscopic experiments, the goal for ion confinement is the Lamb-Dicke regime, in which the extent of the motion of each ion is much less than the wavelength of an atomic transition. For an optical transition this requirement is severe. In a quadrupole rf Paul trap, the total kinetic energy of a single trapped ion can be on the order of the secular kinetic energy, and confinement of a single laser-cooled ion to the Lamb-Dicke regime for an optical transition has been verified spectroscopically in Ba^+ [1,2] and Hg^+ [3]. Laser cooling can significantly reduce the second-order Doppler shift due to the ion motion, which can otherwise limit the accuracy of a spectroscopic measurement. As an example, for a single $^{199}\text{Hg}^+$ ion laser-cooled to the Doppler limit [4], the fractional second-order Doppler shift is

$$\langle \Delta\nu/\nu_0 \rangle = -2.3 \times 10^{-18}$$

(Ref. [5]).

In many experiments it is advantageous or even necessary to work with a larger number of ions. However, in a quadrupole rf Paul trap, two or more ions are pushed by their mutual Coulomb repulsion from the center of the trap to regions where the rf field is stronger. This leads to increased amplitude of the micromotion [6–8], limits the achievable confinement, and may inhibit laser cooling [7,8]. One way to circumvent this problem is to design a trap in which the rf field vanishes along a line instead of at a single point. This goal has led to the development of the linear trap.

The linear-trap design descends from a “racetrack” configuration rf quadrupole trap first used by Drees and Paul for the short-term confinement of an electron-ion plasma [9] and later used by Church to trap atomic ions for longer times [10]. The racetrack trap resembles a quadrupole mass filter bent into a closed path. Charged particles are confined to trajectories along the closed path

formed by the electrodes. Dehmelt first suggested using a string of ions in a linear trap to suppress the second-order Doppler shift [11]. In addition to confining the ions radially, it is desirable to fix the axial positions of the ions. In racetrack traps, axial localization can arise from patch effects on the trap electrodes, which pin ions in one region of the trap. Coulomb repulsion among the ions then localizes the remaining ions. The traps described here and in Ref. [12] provide axial confinement with a purposely applied static electric field. This allows the trap to confine the ions more strongly to their axial positions than racetrack traps do and gives more control over the axial positions. The static field weakens the radial confinement, as will be discussed below. Also, racetrack traps can confine both positively and negatively charged particles simultaneously, while traps such as ours, which use static confining potentials, cannot.

Prestage, Dick, and Maleki have trapped a cloud of $^{199}\text{Hg}^+$ ions elongated along the axis of a linear trap and have demonstrated a $^{199}\text{Hg}^+$ microwave frequency standard with excellent frequency stability [12]. Crystallized strings of laser-cooled $^{24}\text{Mg}^+$ ions have been observed in a racetrack-type trap at the Max Planck Institute for Quantum Optics [13]. We have constructed a linear rf trap and observed simple crystallized linear structures of up to 33 $^{199}\text{Hg}^+$ ions [14]. By varying the strength of the axial confining potential, we have also observed more complex structures.

In Sec. II we discuss the theory of the linear trap and provide details of our trap. We then present images of trapped crystallized structures of ions and compare these observations with the results of numerical simulations. We next describe an observation of the 40.5-GHz ground-state hyperfine transition using microwave-optical double-resonance spectroscopy with a trapped string of $^{199}\text{Hg}^+$ ions and discuss the potential for a microwave frequency standard based on this transition. We conclude with a discussion of future experiments and prospects.

II. THEORY AND DESIGN OF THE LINEAR TRAP

The starting point in the discussion of our linear trap is the quadrupole mass analyzer [15,16]. This device con-

sists of four parallel rods. Typically, each rod has circular cross section in the plane perpendicular to the axis of the trap, as shown in Fig. 1. A time-varying rf potential $V_0 \cos \Omega t$ is applied to two opposing rods. The remaining two rods are held at rf ground. The rf electric fields are transverse to the axis of the mass analyzer. The time-varying potential near the axis can be approximated by

$$V = \frac{V_0}{2} \left[1 + \frac{x^2 - y^2}{R^2} \right] \cos \Omega t, \quad (1)$$

where R is the distance from the axis to the surface of the electrodes. For sufficiently high drive frequency Ω , a particle of mass m and charge q moves in an effective pseudopotential

$$\Phi = \frac{qV_0^2}{4m\Omega^2 R^4} (x^2 + y^2) = \frac{m}{2q} \omega_r^2 (x^2 + y^2), \quad (2)$$

where

$$\omega_r = qV_0 / (\sqrt{2}m\Omega R^2) \quad (3)$$

is the angular frequency of oscillations in the radial direction [12,15,16].

To reduce the anharmonicity of our trap, we chose the rods to have radius $R' = 1.03R$. The anharmonicity is minimized with a ratio of 1.146 [17], but is not dramatically worse for our design. A numerical multipole expansion of the field for the geometry of our trap shows that near the axis the harmonic term in the pseudopotential is 1% smaller than that predicted by Eq. (2). The total contribution of anharmonic terms in the pseudopotential, up to order $(r/R)^{10}$, is less than 0.1% of the quadratic term for $(r/R) < 0.2$, where r is the distance from the trap axis. While electrodes with hyperbolic cross sections would give a more nearly harmonic pseudopotential, the use of circular rods facilitates construction and is a good compromise since we are primarily interested in confining the ions near the axis. Such a geometry has found wide use as a mass analyzer, but it cannot function as a trap

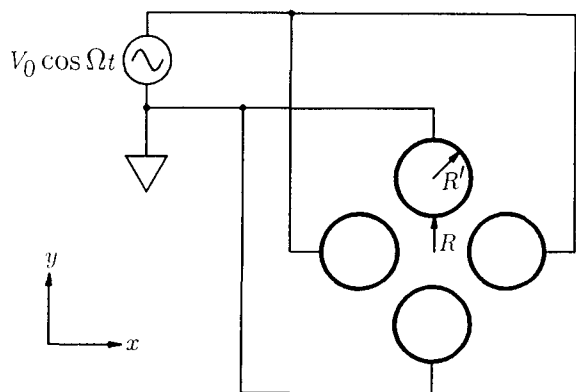


FIG. 1. Cross section of a linear quadrupole trap. An alternating rf voltage $V_0 \cos \Omega t$ is applied to a pair of diagonally opposite rods. The other pair of rods is maintained at rf ground. In the actual trap, the radius R' of the rods is 0.794 mm, 1.03 times the distance R (0.769 mm) from the trap axis to the surface of the rods.

since particles can move freely along the axis.

To confine the ions axially, a static potential can be applied from opposing sides along the axis, creating a region in the center in which particles can be trapped. Figure 2 shows how this is accomplished in our trap. Each of the circular trap rods is divided into two sections of unequal length. The static potential of the longer "central" sections is maintained at ground and a static bias voltage U_0 is applied to the shorter "end" sections. The segmented design divides the trap into three regions along the axis: two end regions where the end segments of two rods overlap the central segments of the other two and a central region where all four central segments overlap. As a function of axial position, the static potential has a minimum in the central region of the trap. The static potential thus provides axial confinement, but is expected to add far greater anharmonicity to the trap potential than does the use of circular rods.

A schematic diagram of the actual trap is shown in Fig. 3. Four circular rods, 12.6 mm long and 1.588 mm in diameter, are aligned with their axes parallel at a radial distance of 1.563 mm from a common axis (the z axis). Each rod is made of two segments of beryllium copper: an end segment 5 mm long and a central segment 7.5 mm long. The central region of the trap, where the four central segments overlap, is 2.5 mm long. The two segments are electrically isolated from each other using spacers of alumina and machinable ceramic, as shown in Fig. 4. This configuration allows independent static potentials to be applied to the segments of the rods. The insulating spacers are hidden from the outside of the rods, as shown in Fig. 4, to avoid perturbations caused by surface charge on the insulators. The ends of the rods are held in two machinable ceramic fixtures (not shown), which are themselves held together by four outer support rods (also not shown). The fixtures were coated with titanium, except where the trap electrodes are held, and grounded in

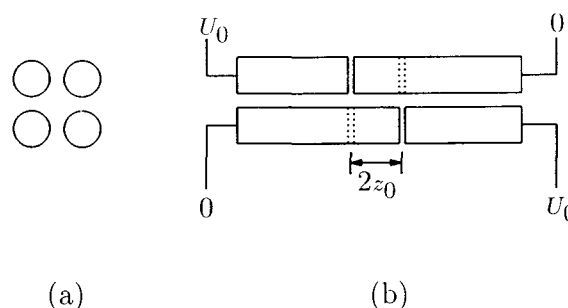


FIG. 2. (a) End view and (b) side view of the linear trap, showing how the axial confining potential is applied. For simplicity, the rf potentials are not indicated on this figure. Each trap rod is divided into two sections that are rf common and held at different static potentials. The dashed lines show the divisions between the sections of the rear rods (which are hidden behind the front ones). The short segments of the rods are held at a positive static potential U_0 and the long segments at static ground, as indicated for the front rods. With this arrangement, we create an axially confining potential for positive ions in the region where the four longer segments overlap. In our trap, this region has length $2z_0 = 2.5$ mm

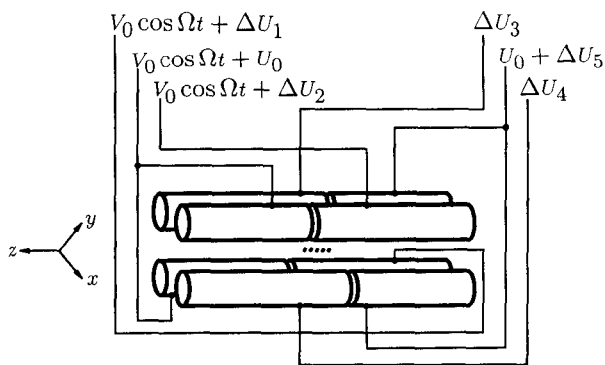


FIG. 3. Linear-trap configuration. An rf voltage $V_0 \cos \Omega t$ is applied to diagonally opposite electrodes as shown. The segments of each rod are rf common so that each central segment can be biased at a different static potential ΔU , yet remain at the same rf potential. The end segments of the electrodes are 5 mm long, much longer than the 0.769-mm radial distance from the axis of the trap to surface of the rods, so the rf electric fields in the center section of the trap are nearly parallel to the xy plane. The region in the center of the trap in which the four central segments of the electrodes overlap is 2.5 mm long. To trap positive ions along the z axis, the four central segments are held near static ground potential and a positive static potential U_0 is placed on the end segments. Small potentials $\Delta U_1 - \Delta U_4$ can be applied to the central segments to compensate for contact and patch potentials on the electrodes. The axial position of the ions can be varied by applying a bias ΔU_5 to one set of end segments. The ions are detected by an imaging photomultiplier tube that looks along an axis normal to the z axis and 45° to the x and y axes.

order to minimize effects due to charging of exposed insulators.

An rf potential is applied to two opposing rods, while the two other rods are kept at rf ground. The two segments that make up each rod are rf common. The end segment of each rod is biased at a static voltage $U_0 > 0$,

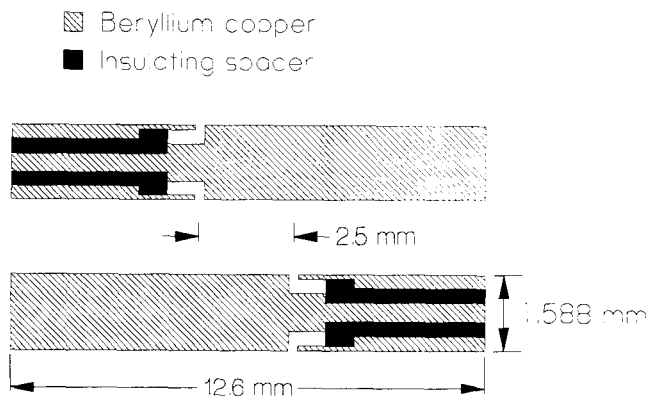


FIG. 4. Section through two trap rods (the front rods in Fig. 2). The end segment of each trap rod is a sleeve that fits over an insulating spacer, which in turn fits over an extension of the central segment. The insulating spacer is completely hidden from the outside of the rod to prevent surface charge on the insulators from perturbing the trap potential.

and the central segment is nominally held at zero. This arrangement confines positive ions within the central region of the trap. To compensate for contact and patch potentials on the trap electrodes, there are provisions for applying small static bias potentials ($\Delta U_1 - \Delta U_4$ in Fig. 3) to the central segments of the individual rods and to one pair of end segments (ΔU_5).

The rf voltage is supplied by a helical resonator, which acts as a resonant transformer with a 40:1 turns ratio. To allow the different segments of the rods to have different static potentials while remaining at the same rf potential, the secondary winding of the helical resonator is a trifilar coil, whose three filaments supply the voltages $V_0 \cos \Omega t + \Delta U_1$, $V_0 \cos \Omega t + U_0$, and $V_0 \cos \Omega t + \Delta U_2$, as shown in Fig. 3. The rf-grounded rods are capacitively coupled to one another. The resonator produces up to about 700 V amplitude at its 12.7 MHz resonant frequency when driven with about 5W. The high-voltage output is monitored with a capacitive voltage divider, which has been calibrated with 10% accuracy.

Because there is so little symmetry to the trap, describing the static potential in detail would require a full three-dimensional numerical solution. However, the region of interest is near the midpoint of the trap axis, a saddle point of the static potential. In this region the static potential can be approximated by the harmonic potential

$$\begin{aligned} \phi_s &= \frac{\kappa U_0}{z_0^2} \left[z^2 - \frac{1}{2}(x^2 + y^2) \right] \\ &= \frac{m}{2q} \omega_z^2 \left[z^2 - \frac{1}{2}(x^2 + y^2) \right], \end{aligned} \quad (4)$$

where z_0 is half the length of the central region of the trap ($z_0 = 1.25$ mm for our trap), κ is a geometric factor ($\kappa \approx 0.31$ for our trap; see below), and

$$\omega_z = (2\kappa q U_0 / m z_0^2)^{1/2} \quad (5)$$

is the angular frequency of axial oscillations in the trap. The factor κ depends on the geometry of the trap, and hence will vary with z_0 , so the secular frequency does not scale simply as $1/z_0$. The pseudopotential well in the radial direction is weakened by the addition of the static potential and is given by

$$\begin{aligned} \phi_r &= \frac{m}{2q} (\omega_r^2 - \frac{1}{2}\omega_z^2) (x^2 + y^2) \\ &= \frac{m}{2q} (\omega_r')^2 (x^2 + y^2), \end{aligned} \quad (6)$$

where

$$\omega_r' = (\omega_r^2 - \frac{1}{2}\omega_z^2)^{1/2} \quad (7)$$

is the angular frequency of radial oscillations in the presence of the static potential.

The radial size of the trap was chosen to allow confinement of Hg^+ ions near the Lamb-Dicke regime for a 194-nm optical transition. We define the Lamb-Dicke regime by the criterion that the rms motion of each ion be less than $\lambda/2\pi$, where λ is the wavelength of

the transition. Lamb-Dicke confinement in the radial direction is expected for a 12.7-MHz rf drive with an amplitude V_0 of 1.1 kV applied to the trap rods, assuming that the ions have been cooled to the 1.7-mK Doppler limit (this limit applies when motion along each axis is cooled equally [4]). Axial confinement is typically achieved with a static voltage U_0 of 1 V or less. Extrapolating from measured axial secular frequencies, we expect that a static potential of about 400 V would confine the axial motion of a single ion to the Lamb-Dicke regime at the Doppler limit of laser cooling.

III. ION CRYSTALS IN THE LINEAR TRAP

The trap is located in a vacuum chamber maintained at a base pressure of about 10^{-8} Pa (1 Pa \approx 7.5 mTorr) by a sputter ion pump. To load $^{199}\text{Hg}^+$ ions into the trap, the pump is turned off and neutral ^{199}Hg vapor (isotopic purity 91%) is bled into the vacuum chamber to give a pressure of approximately 10^{-6} Pa. Neutral atoms in the trap are ionized by electron bombardment from a field emission point. After the trap is loaded, the pump is turned on to return the chamber to near its base pressure. The ions are laser-cooled using the $6s\ ^2S_{1/2} \rightarrow 6p\ ^2P_{1/2}$ transition [3]. A few microwatts of 194-nm laser radiation is sufficient to cool the ions.

Because optical pumping between hyperfine levels of the $^{199}\text{Hg}^+$ ion can inhibit laser cooling, two lasers at 194 nm are required. Figure 5 shows the hyperfine levels for the $^2S_{1/2}$ and $^2P_{1/2}$ states of $^{199}\text{Hg}^+$ in the absence of a magnetic field. The ions are cooled and detected using a laser (laser 1 in Fig. 5) that is tuned slightly below resonance on the

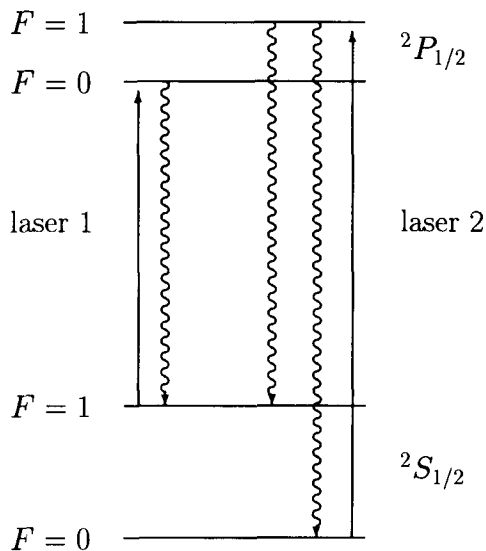


FIG. 5. Energy-level structure for the $6s\ ^2S_{1/2}$ ground state and $6p\ ^2P_{1/2}$ state of $^{199}\text{Hg}^+$ near zero magnetic field. The $^2S_{1/2}(F=0) - (F=1)$ hyperfine splitting is 40.5 GHz, and the $^2P_{1/2}(F=0) - (F=1)$ hyperfine splitting is 6.9 GHz. The intervals are not drawn to scale. Lasers 1 and 2 are used for cooling, optical pumping, and detection, as described in the text.

$$^2S_{1/2}(F=1) \rightarrow ^2P_{1/2}(F=0)$$

transition. This is a “cycling transition,” since selection rules require that the ions in the $^2P_{1/2}(F=0)$ level decay only to the $^2S_{1/2}(F=1)$ level. Ions are detected by collecting photons scattered as the ions cycle on this transition. Laser 1 can also weakly excite the

$$^2S_{1/2}(F=1) \rightarrow ^2P_{1/2}(F=1)$$

transition (the laser frequency is detuned 6.9 GHz from this resonance, whose natural linewidth is $\gamma/2\pi = 70$ MHz). From the $^2P_{1/2}(F=1)$ level, the ions can decay to the $^2S_{1/2}(F=0)$ level. This decay path acts to optically pump the ions into the $^2S_{1/2}(F=0)$ level, and ions in this level are not cooled by laser 1. To prevent optical pumping into the $^2S_{1/2}(F=0)$ level, a second laser (laser 2 in Fig. 5) is used to repump ions from the $^2S_{1/2}(F=0)$ level into the $^2S_{1/2}(F=1)$ level via the $^2P_{1/2}(F=1)$ state. Laser 2 is offset about 47.4 GHz to the blue of laser 1, putting its frequency near the

$$^2S_{1/2}(F=0) \rightarrow ^2P_{1/2}(F=1)$$

resonance. In addition to the above considerations, it is necessary to prevent pumping into the $^2S_{1/2}(F=1, m_F = \pm 1)$ levels. To this end, we apply a magnetic field of approximately 5×10^{-4} T (5G) at about 45° to the electric-field vector of the laser radiation.

The laser is directed through the trap at an angle of approximately 9° from the trap axis in order to cool both radial and axial motion. At this angle, the theoretical Doppler limit of laser cooling is about 1.1 mK for the axial motion and 24 mK for the radial motion [4]. Fluorescence is collected by a fast lens system that produces an image, magnified 22 times, on the front surface of an imaging photomultiplier tube. The spatial resolution of the lens and detector system, defined as the full width at half maximum of the image of a single localized ion, corresponds to $6\ \mu\text{m}$ at the center of the trap. The imaging system looks along an axis normal to the trap axis and at 45° to the x and y axes. At the Doppler limit of laser cooling described above, the rms secular motion along the z axis is calculated to be $1.4\ \mu\text{m}$ for $\omega_z/2\pi = 25$ kHz, the smallest secular frequency used in these experiments, so the extent of the secular motion of the ions is less than the spatial resolution of the detector. As the secular frequency is increased, the ions are pushed closer together along the trap axis. For sufficiently high secular frequencies, the ion spacing will decrease below the $6\text{-}\mu\text{m}$ spatial resolution of the imaging system and we will be unable to resolve the individual ions. With two ions in the trap, this should occur at a secular frequency of about $\omega_z/2\pi = 400$ kHz.

The temperature of the ions was not measured spectroscopically [3], but we can place an upper bound on the temperature by noting that the images of the ions were about $6\ \mu\text{m}$ full width at half-maximum. We think that this width is due largely to the spatial resolution of the imaging system, but even if the width were entirely due to motion of the ions, we would have $z_{\text{rms}} \approx 3\ \mu\text{m}$, from which $T_z \approx 5$ mK for $\omega_z = 25$ kHz. If the sizes of the im-

ages of the ions were primarily due to thermal motion, the images would be elliptical, since the secular frequencies in the radial and axial directions are different. The lack of eccentricity in the images supports our supposition that the widths are due to the imaging system and, hence, that the axial temperature is significantly less than 5 mK for $\omega_z = 25$ kHz.

The secular frequencies of the ions are measured by applying a drive to the trap electrodes and observing a drop in the fluorescence as the drive sweeps through resonance [18]. The drop in fluorescence when the amplitude of the secular motion increases is due to the combined effects of the ion's motion taking it out of the laser beam and of Doppler shifts detuning the ion resonance. These measurements permit a quantitative comparison between the observed ion configurations and numerical simulations. The secular frequencies were measured at several different rf and static voltages and showed the expected functional dependence on the voltages. The measured values for the axial secular frequency ω_z were proportional to the square root of the static voltage. The constant κ in Eq. (5) was determined from the measured secular frequencies to be 0.31 with an uncertainty of about 10%. The unperturbed radial secular frequency ω_r was determined from the measured secular frequencies ω_r' and ω_z using Eq. (7). The values for ω_r were proportional to the rf voltage and were consistently $17\% \pm 10\%$ lower than predicted by Eq. (3), where the uncertainty is dominated by a systematic error in measuring the rf voltage applied to the trap. For very small axial voltages (less than about 100 mV), the effects of local static fields, due to surface charge or patch potentials on the electrodes, make it difficult to characterize the axial potential.

By varying the neutral Hg background pressure and the duration and intensity of the electron bombardment when loading the trap, we can capture different numbers of $^{199}\text{Hg}^+$ ions. We have observed single ions and crystalline structures of up to 33 ions, as well as much larger clouds that did not crystallize. The simplest crystalline configuration of ions is a linear string, which is obtained when $\omega_r' \gg \omega_z$. We have observed crystallized linear strings of 2 to 33 ions.

Figure 6 shows images of linear crystals containing 15 and 33 ions. The number of ions we can observe in such crystals is limited by our ability to image the entire string while resolving the individual ions. Large strings, such as the string in Fig. 6(b), are longer than the approximately 200- μm -long region in which the laser intersects the trap axis, and it is not possible to illuminate the whole string at once. To obtain this picture, it was necessary to sweep the position of the laser beam back and forth to illuminate the whole string. A more powerful laser could illuminate a larger area with sufficient intensity to observe the ions easily. Alternatively, more ions could be confined within the illuminated region by increasing ω_z , but the imaging optics cannot resolve ions less than about 6 μm apart, so this approach would require improved imaging optics. We have formed crystallized strings with enough ions that when the spacing between the ions was sufficient for the imaging system to resolve them, the strings were longer than the field of view of the imaging

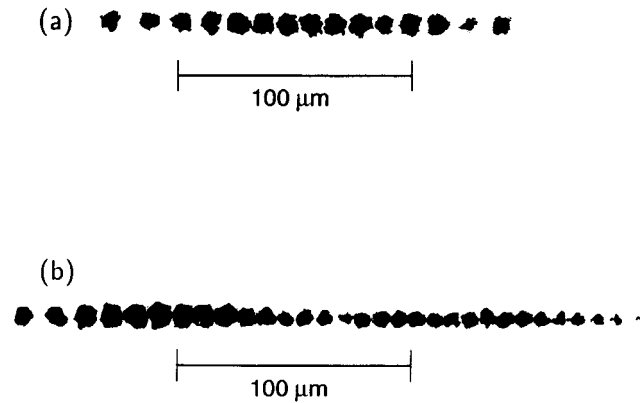


FIG. 6. (a) A picture of a linear crystal of 15 ions. (b) A picture of a linear crystal of 33 ions. This string was longer than the region of the trap axis illuminated by the cooling laser. To obtain an image of the entire string, it was necessary to sweep the laser beam back and forth.

system (about 300 μm). The fact that only part of the string was illuminated by the cooling laser did not seem to inhibit cooling and crystallization, although when much larger clouds of ions were trapped, crystallization was not observed. A limitation to forming extremely long strings may be our inability to compensate for the effects of local perturbations to the static potential due to patch fields or surface charge. In the present trap, static potentials can be independently applied to three of the four trapping rods to compensate for such perturbations. This technique works well for short strings, but as the length of the string approaches the radial dimension of the trap (about 750 μm), the patch fields may vary over the length of the string. In this case, we expect the static compensation to be less effective.

Figure 7(a) shows the measured positions of eight ions in a string and the positions calculated by a numerical simulation. The simulation, performed with no adjustable parameters, determines equilibrium positions for the ions by minimizing the potential energy of a given number of particles in harmonic radial and axial wells, with Coulomb repulsion between the particles. The secular frequencies used for the simulation were determined by scaling previously measured secular frequencies by the static and rf voltages applied to the trap. The linear configurations of ions are quite insensitive to the radial secular frequency, because the ions are confined to the axis of the trap.

The ions can be pushed into planar or three-dimensional configurations by increasing ω_z relative to ω_r' . The simplest structure beyond a linear string is a planar zigzag. Figure 8 shows such a structure composed of 11 ions (10 $^{199}\text{Hg}^+$ ions and 1 impurity ion, which did not fluoresce). We think that the impurity ion is another isotope of mercury, which would be consistent with the 91% isotopic purity of the mercury vapor used to load the trap. This structure was obtained by lowering the rf voltage on the trap. Figure 7(b) compares the measured positions of the ions to the predictions of a calculation. To obtain agreement between the zigzag configuration

and a numerical simulation with 11 $^{199}\text{Hg}^+$ ions, it was necessary to introduce into the calculations an *ad hoc* asymmetry of about 20% between the secular frequencies in the x and y directions. This azimuthal asymmetry forces the ions to lie in a plane; without it, the calculation predicts a quasihelical structure that disagrees significantly with the observed ion positions. The axial secular frequency ω_z and the smaller radial secular frequency ω'_y were determined by scaling previously measured secular frequencies by the voltages present on the trap when this crystal was observed. The larger radial secular frequency ω'_x was set to $1.2\omega'_y$.

The source of the azimuthal asymmetry in the potential well is not known. One possible cause is unequal contact or patch potentials on the trap rods. Another possible cause is the azimuthal asymmetry of the static trapping field. At the geometric center of the trap the static field should be the same in the x and y directions. However, the position of the ions along the axis was not necessarily at the center and varied from load to load. We suspect that this was due to surface charge deposited during loading. When the ions are not at the midpoint of the trap axis, there is a quadrupole component to the radial static field, which breaks the azimuthal symmetry of the

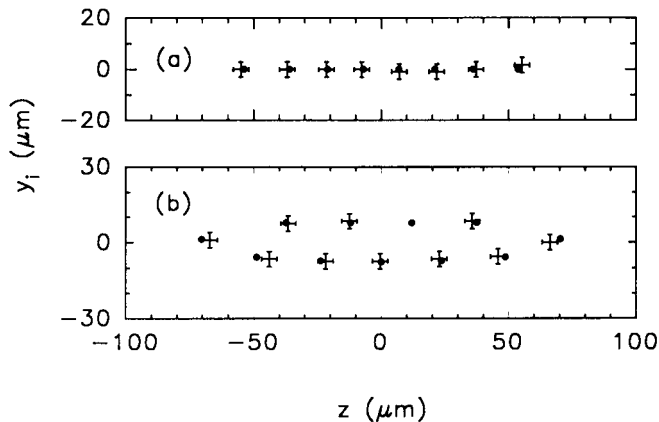


FIG. 7. Observed positions of ions in the trap (crosses) and positions predicted by a numerical simulation (circles). The arms of the crosses extend to the half-maximum intensity points of the images (about $4\ \mu\text{m}$ radius). The coordinates are as in Fig. 3: z represents the displacement along the trap axis and y_i represents the projection of the radial displacement onto the image plane. (a) A linear crystal of 8 ions. The secular frequencies used for the calculation are $\omega'_x/2\pi=435\ \text{kHz}$ and $\omega_z/2\pi=41.7\ \text{kHz}$. These frequencies were determined by scaling secular frequencies measured under different conditions by the voltages present on the trap when this image was acquired. (b) A nonlinear crystal of 11 ions. One site in the crystal was occupied by an impurity, which did not fluoresce. An asymmetry between the x and y directions was introduced *ad hoc* to make the results of the calculation agree with the data. This asymmetry makes $\omega'_x=1.2\omega'_y$ and confines the structure to the yz plane. The secular frequencies used for the calculation are $\omega'_x/2\pi=92.4\ \text{kHz}$, $\omega'_y/2\pi=77\ \text{kHz}$, and $\omega_z/2\pi=31\ \text{kHz}$. The frequencies ω'_y and ω_z were determined by scaling frequencies measured under different conditions by the voltages present on the trap when this image was acquired.

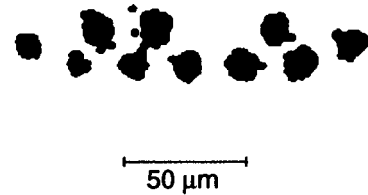


FIG. 8. A picture of a crystal of 11 ions in a zigzag configuration. The crystal consists of 10 $^{199}\text{Hg}^+$ ions and 1 impurity ion, which did not fluoresce. This is the same crystal shown in Fig. 7 (b).

effective radial potential given by Eq. (6). In the case of Fig. 7(b), the axial secular frequency is approximately 40% of the mean radial secular frequency, and it seems plausible that the quadrupole asymmetry could produce the observed planar structure. However, further work is required to characterize the asymmetry more completely.

The observed crystalline structures are closely related to the structures predicted for cold ions in storage rings [19]. With many ions and small ω'_r , we have observed complex crystallized structures which appear to be non-planar and require further study. To conduct a systematic and quantitative study of two- and three-dimensional crystallized structures, we will have to eliminate the azimuthal asymmetry from our trap or characterize it more completely.

IV. MICROWAVE-OPTICAL DOUBLE RESONANCE

A string of cold ions is of great interest for high-resolution spectroscopy and improved frequency standards. With imaging techniques, each ion can be treated as an independent atomic clock. Using Dehmelt's "electron shelving" technique, we should be able to detect the clock transition with 100% efficiency in each ion [1,3,20,21]. This would make the signal nearly immune to fluctuations arising from, for example, fluctuations in the laser intensity.

Consider a clock that uses the Ramsey separated-field method in the time domain to interrogate the clock transition at angular frequency ω_0 . The clock transition is excited by two phase-coherent pulses of radiation, each of duration ΔT_R , separated by a time T_R ($\Delta T_R \ll T_R$). By probing the clock transition on each side of the Ramsey peak, we can obtain an error signal to correct the average frequency of an oscillator to match the atomic resonance ω_0 [16,22]. The fractional frequency stability of such a locked oscillator, as characterized by the two-sample Allan variance [23], is

$$\sigma_y(\tau) = (\tau N T_R \omega_0^2)^{-1/2}, \quad (8)$$

where τ is the averaging time ($\tau > T_R$) and N is the number of atoms. Thus, it is advantageous to use large N , ω_0 , T_R , and τ . The trap environment can make long interrogation times T_R possible ($T_R=550\ \text{s}$ has been achieved with $^9\text{Be}^+$ ions in a Penning trap [22]).

To achieve high accuracy, we must minimize and account for external perturbations due to electric, magnet-

ic, and gravitational fields. These include ion-trap and ion-ion interactions, collisions with neutral background atoms, external magnetic and electric fields, and gravitational red shifts [5,6,11,24,25]. For a microwave transition in a cold string of $^{199}\text{Hg}^+$ ions, it should be possible to reduce these effects to the point where the uncertainty in the transition frequency is dominated by the uncertainty in the second-order Doppler shift. When the secular motion is cooled to the Doppler limit, the fractional second-order Doppler shift can be as low as -2×10^{-18} [16]. This limit can be realized if the ions lie exactly along the axis of the trap, where the rf trapping fields approach zero. In this case, the kinetic energy in the rf micromotion is about equal to that in the secular motion, and the two make approximately equal contributions to the second-order Doppler shift. If contact or patch potentials on the trap electrodes push the ions away from the region of minimum rf field, the kinetic energy in the micromotion, and hence the second-order Doppler shift, can be significantly greater. Thus, in a clock based on this trap, it will be necessary to adjust the static shimming potentials $\Delta U_1 - \Delta U_4$ on the trap rods to compensate for contact and patch potentials.

This potential for very high accuracy has led us to investigate the possibility of a microwave frequency standard based on the 40.5-GHz ground-state hyperfine splitting of $^{199}\text{Hg}^+$ with a trapped and laser-cooled string of ions. This transition is, to first order, independent of magnetic field at zero field. For a Ramsey interrogation time of $T_R = 100$ s and $\omega_0/2\pi = 40.5$ GHz, the frequency stability of a clock "ensemble" of $N = 50$ ions would be

$$\sigma_y(\tau) = 5.5 \times 10^{-14} \tau^{-1/2},$$

where τ is expressed in seconds.

As a first step toward this goal, we have recently observed the 40.5-GHz ground-state hyperfine transition of a string of $^{199}\text{Hg}^+$ ions by microwave-optical double resonance. In this preliminary observation the total fluorescence of the entire string of ions was detected. Fluctuations in the fluorescence from the ion cloud due to amplitude and frequency noise in the cooling and detection laser were too large for us to detect transitions with 100% efficiency. To describe the measurement sequence, we rely on the discussion of laser cooling and optical pumping given in Sec. III and on the level diagram shown in Fig. 5. To prevent optical pumping into the $^2S_{1/2}(F=1, m_F = \pm 1)$ levels of the ground state, it was necessary to apply a magnetic field while the cooling lasers were on. However, we also wanted to observe the microwave transition in near-zero magnetic field, so we used two sets of Helmholtz coils. One set was used to nearly cancel the ambient magnetic field in the trap. No magnetic shielding was used. The residual field near the trap was measured to be approximately 1.6×10^{-5} T (0.16 G). A second set of coils produced the field used to prevent optical pumping when laser 1 was on. The current in the second set of coils was switched off and on to switch the field between 1.6×10^{-5} T and approximately 5×10^{-4} T, respectively. The sequence of the experiment is the following.

(a) Initially, lasers 1 and 2 and both sets of Helmholtz coils are on. This allows the ions to be laser-cooled.

(b) Laser 2 is turned off and the ions are optically pumped by laser 1 into the $F=0$ ground state.

(c) Both lasers are turned off. The second set of Helmholtz coils is switched off, reducing the magnetic field to approximately 1.6×10^{-5} T. The

$$^2S_{1/2}(F=0) \rightarrow ^2S_{1/2}(F=1)$$

ground-state hyperfine transition is driven using the Ramsey method with two microwave pulses, each of duration ΔT_R and separated by a time T_R . The pulse duration ΔT_R is adjusted to be close to the value that gives a $\pi/2$ pulse at the resonant frequency. At the microwave intensities used here, this was obtained for $\Delta T_R = 0.13$ s.

(d) the second set of Helmholtz coils is switched back on, laser 1 is turned on, and the number of photons counted by the detector during a gate time is recorded. Only those ions that made the microwave transition are in the ($F=1$) hyperfine level of the ground state, so only those ions fluoresce. With laser 2 off, these ions are eventually optically pumped into the ($F=0$) level and cease fluorescing. The gate time is chosen to be shorter than the optical pumping time. In these experiments, gate times of 30–40 ms were used (at the laser intensity used here, the time constant for optical pumping was about 50 ms).

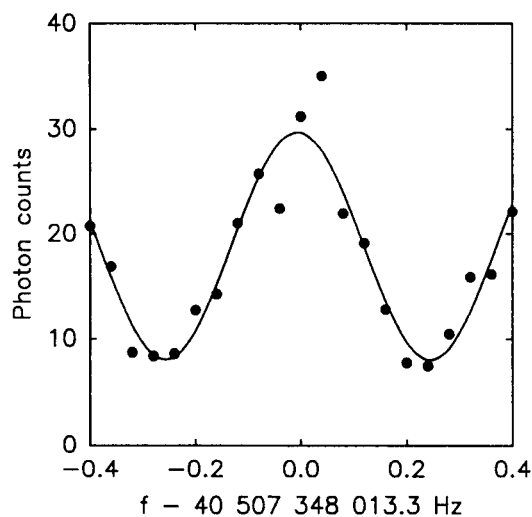


FIG. 9. Microwave-optical double-resonance spectrum of the

$$^2S_{1/2}(F=0) \rightarrow ^2S_{1/2}(F=1)$$

ground-state hyperfine transition in $^{199}\text{Hg}^+$ at 40.5 GHz. This figure shows the central peak of a Ramsey resonance, obtained using the measurement sequence described in the text, with a linear string of eight ions in the trap. The circles represent the measured fluorescence, and the solid line is a cosine function fit to the data. For this measurement $T_R = 1.8$ s, $\Delta T_R = 0.130$ s, and each point is the average of 27 measurements. Including time for cooling, pumping, and detection, each measurement cycle takes about 3 s.

At the end of this sequence, the frequency of the microwave source is stepped, and the sequence is repeated. The results of many scans of the microwave frequency are averaged together. Several sets of data were acquired, with T_R ranging from 0.32 to 1.8 s. The result of one observation, using a string of eight ions, is shown in Fig. 9. The linewidth, determined by a least-squares fit of a cosine function to the data, is 251 ± 6 mHz, giving a fractional resolution of 6.2×10^{-12} , and showing good agreement with the 254-mHz theoretical linewidth for the 0.13-s pulse duration and 1.8-s free precession time used in this measurement. Because we did not take advantage of the nearly 100% detection efficiency that would be possible if we counted the fluorescence from each ion individually, the signal-to-noise ratio is limited by fluctuations in the ion fluorescence caused by intensity and frequency noise in laser 1. With this amount of noise, the difference between a pure cosine and the central lobe of a Ramsey profile is insignificant. The amount of technical noise from laser 1 also means that the stability figure given by Eq. (8) is not applicable.

V. FUTURE PROSPECTS

Future experiments will measure the fluorescence from each ion individually. It should be possible to detect the microwave transition with 100% efficiency if the fluorescence detection efficiency is high enough that when laser 1 is turned on, many photons are detected from each ion in the ($F=1$) level before it is optically pumped into the ($F=0$) level. If laser 1 is detuned by half a linewidth from the

$${}^2S_{1/2}(F=1) \rightarrow {}^2P_{1/2}(F=0)$$

transition, the number of photons scattered by an ion in the ${}^2S_{1/2}(F=1)$ level before it is pumped into the ($F=0$) level is approximately the square of the ratio of 6.9 GHz [the detuning of laser 1 from the

$${}^2S_{1/2}(F=1) \rightarrow {}^2P_{1/2}(F=1)$$

transition] to 35 MHz (half the radiative linewidth). This gives about 4×10^4 photons. Therefore, the detection efficiency must be significantly greater than the inverse of this number, 2.5×10^{-5} . If this condition is met, it should be possible to detect the microwave transitions with nearly 100% efficiency. By observing the rate of quantum jumps by a single ion in the trap, we determined the rate at which the ion fluoresced [26], and by comparing this rate to the count rate from the detector, we measured the overall detection efficiency of our present apparatus to be about 1×10^{-4} , which is marginally acceptable.

To reach the very high accuracy which should be possible with such a clock, it will be advantageous to use longer interrogation times. To reduce the effects of collisions with neutral background gas atoms and molecules during long interrogation intervals, we plan to use cryogenic pumping. Although in our preliminary measurements the fluorescence was collected from the entire string, it should be possible to treat each ion as an independent clock, since our imaging system resolves the individual ions in the string. Beyond the applications to high-accuracy spectroscopy, the possibility of confining a string of ions so that each is in the Lamb-Dicke regime should permit experiments in fundamental physics, such as studies of interference, cavity QED, and collective behavior.

ACKNOWLEDGMENTS

We thank Sarah Gilbert and Fred Moore for helpful comments on this paper. This work was supported by the U.S. Office of Naval Research and the U.S. Air Force Office of Scientific Research.

*Present address: Department of Physics, University of Texas at Austin, Austin, TX 78712.

- [1] G. Janik, W. Nagourney, and H. Dehmelt, *J. Opt. Soc. Am. B* **2**, 1251 (1985); W. Nagourney, N. Yu, and H. Dehmelt, *Opt. Commun.* **79**, 176 (1990).
- [2] I. Siemers, M. Schubert, R. Blatt, W. Neuhauser, and P. Toschek (unpublished).
- [3] J. C. Bergquist, W. M. Itano, and D. J. Wineland, *Phys. Rev. A* **36**, 428 (1987); F. Diedrich, J. C. Bergquist, W. M. Itano, and D. J. Wineland, *Phys. Rev. Lett.* **62**, 403 (1989).
- [4] See, for example, W. M. Itano and D. J. Wineland, *Phys. Rev. A* **25**, 35 (1982); D. J. Wineland and W. M. Itano, *Phys. Today* **40** (6), 34 (1987).
- [5] D. J. Wineland, W. M. Itano, J. C. Bergquist, and R. G. Hulet, *Phys. Rev. A* **36**, 2220 (1987); D. J. Wineland, W. M. Itano, J. C. Bergquist, J. J. Bollinger, F. Diedrich, and S. Gilbert, in *Frequency Standards and Metrology*, Proceedings of the Fourth Symposium, Ancona, Italy, 1988, edited by A. DeMarchi (Springer, Berlin, 1989), pp. 71–77.
- [6] D. J. Wineland, in *Precision Measurement and Fundamental Constants II*, edited by B. N. Taylor and W. D. Phillips, Natl. Bur. Stand. (U.S.) Spec. Publ. No. 617 (U.S. GPO, Washington, DC, 1984), p. 83.
- [7] R. G. DeVoe, J. Hoffnagle, and R. G. Brewer, *Phys. Rev. A* **39**, 4362 (1989).
- [8] R. Blümel, C. Kappler, W. Quint, and H. Walther, *Phys. Rev. A* **40**, 808 (1989).
- [9] J. Drees and W. Paul, *Z. Phys.* **180**, 340 (1964).
- [10] D. A. Church, *J. Appl. Phys.* **40**, 3127 (1969).
- [11] H. G. Dehmelt, in *Frequency Standards and Metrology* (Ref. [5]), p. 286.
- [12] J. D. Prestage, G. J. Dick, and L. Maleki, *J. Appl. Phys.* **66**, 1013 (1989); *IEEE Trans. Instrum. Meas.* **40**, 132 (1991).
- [13] H. Walther, in *Proceedings of the Workshop on Light Induced Kinetic Effects on Atoms, Ions, and Molecules*, edited by L. Moi *et al.* (ETS Editrice, Pisa, Italy, 1991), p.

- 261; G. Birkl, S. Kassner, W. Quint, and H. Walther (private communication).
- [14] M. G. Raizen, J. C. Bergquist, W. M. Itano, and D. J. Wineland, in *Quantum Electronics Laser Science*, 1991 Technical Digest Series (Optical Society of America, Washington, DC, 1991), Vol. 11, p. 170; M. G. Raizen, J. M. Gilligan, J. C. Bergquist, W. M. Itano, and D. J. Wineland, *J. Mod. Opt.* (to be published).
- [15] W. Paul, H. P. Reinhard, and U. von Zahn, *Z. Phys.* **152**, 143 (1958).
- [16] D. J. Wineland, J. C. Bergquist, J. J. Bollinger, W. M. Itano, D. J. Heinzen, S. L. Gilbert, C. H. Manney, and M. G. Raizen, *IEEE Trans. Ultrason. Ferroelectr. Freq. Control* **37**, 515 (1990).
- [17] D. R. Denison, *J. Vac. Sci. Technol.* **8**, 266 (1971).
- [18] D. J. Wineland, J. J. Bollinger, and W. M. Itano, *Phys. Rev. Lett.* **50**, 628 (1983).
- [19] R. W. Hasse and J. P. Schiffer, *Ann. Phys. (N.Y.)* **203**, 419 (1990); R. W. Hasse and J. P. Schiffer, in *Proceedings of the Workshop on Crystalline Ion Beams*, Wertheim, Germany [Gesellschaft für Schwerionenforschung Report No. GSI-89-10, 1989 (unpublished)]; D. Habs, *ibid.*
- [20] W. Nagourney, J. Sandberg, and H. Dehmelt, *Phys. Rev. Lett.* **56**, 2797 (1986).
- [21] T. Sauter, W. Neuhauser, R. Blatt, and P. E. Toschek, *Phys. Rev. Lett.* **57**, 1696 (1986); T. Sauter, R. Blatt, W. Neuhauser, and P. E. Toschek, *Opt. Commun.* **60**, 287 (1986).
- [22] J. J. Bollinger, D. J. Heinzen, W. M. Itano, S. L. Gilbert, and D. J. Wineland, *IEEE Trans. Instrum. Meas.* **40**, 126 (1991).
- [23] J. A. Barnes *et al.*, *IEEE Trans. Instrum. Meas.* **IM-20**, 105 (1971).
- [24] W. M. Itano, L. L. Lewis, and D. J. Wineland, *Phys. Rev. A* **25**, 1233 (1982).
- [25] D. J. Wineland, W. M. Itano, J. C. Bergquist, J. J. Bollinger, and J. D. Prestage, *Ann. Phys. (Paris)* **10**, 737 (1985).
- [26] W. M. Itano, J. C. Bergquist, R. G. Hulet, and D. J. Wineland, *Phys. Rev. Lett.* **59**, 2732 (1987).

Cryogenic linear ion trap for accurate spectroscopy

M. E. Poitzsch,^{a)} J. C. Bergquist, W. M. Itano, and D. J. Wineland
Time and Frequency Division, National Institute of Standards and Technology,
Boulder, Colorado 80303

(Received 15 May 1995; accepted for publication 11 October 1995)

We have observed linear “crystals” of up to tens of laser-cooled $^{199}\text{Hg}^+$ ions in a linear rf ion trap. The trap operates at liquid-He temperature and is designed for use as a prototype 40.5 GHz frequency standard with high accuracy and stability. © 1996 American Institute of Physics. [S0034-6748(96)05001-1]

I. INTRODUCTION

The 40.5 GHz ground-state hyperfine transition of the $^{199}\text{Hg}^+$ ion provides the basis for a high-performance microwave frequency standard.¹⁻⁵ Our work on $^{199}\text{Hg}^+$ has been devoted to obtaining a system that will provide high accuracy as well as high stability.⁵ To help achieve this goal, we have incorporated laser cooling to suppress the second-order Doppler shift.

In this paper, we report preliminary results using a rf ion trap in a cryogenic (~ 4 K) environment. This should yield high vacuum, thereby reduce ion loss and frequency shifts due to background gas collisions, should provide the basis for superconducting magnetic shielding, and will suppress shifts due to blackbody radiation.⁶

Figure 1 shows the energy levels of interest in the $^{199}\text{Hg}^+$ ion. The $^2S_{1/2}(F=1, M=0)$ to $^2S_{1/2}(F=0, M=0)$ ground-state hyperfine splitting is ~ 40.5 GHz. It has no first-order Zeeman shift near zero field and is used as the clock transition.¹⁻⁵ The upper-state $^2P_{1/2}(F=1)$ to $^2P_{1/2}(F=0)$ hyperfine splitting is ~ 7 GHz. Laser cooling and fluorescence detection are accomplished using the 194 nm electric dipole cycling transition from the ground $^2S_{1/2}(F=1)$ state to the excited $^2P_{1/2}(F=0)$ state.^{5,7} The natural linewidth of this strongly allowed transition is 70 MHz, which is more than an order of magnitude larger than the width of the 194 nm laser used for cooling and detection. To prevent optical pumping of the ion into the $F=0$ ground-state sublevel by off-resonant driving of the $^2S_{1/2}(F=1)$ to $^2P_{1/2}(F=1)$ transition and subsequent decay, a second (collinear) laser at 194 nm is present during the laser cooling and tuned about 47.4 GHz to the blue of the main cooling laser.

Previously, a rf-trap $^{199}\text{Hg}^+$ ion frequency standard (using helium buffer gas cooling) was shown to have high frequency stability.³ It contained $N \approx 2 \times 10^6$ ions and had a fractional second-order Doppler shift of approximately -2×10^{-12} . More recently, a short-term fractional frequency instability of $< 7 \times 10^{-14} \tau^{-1/2}$ has been demonstrated in a linear rf trap (also using helium buffer gas cooling), which operated with $N \approx 2.5 \times 10^6$ ions, and a fractional second-order Doppler shift of approximately -4×10^{-13} was inferred.⁴ In comparison, the fractional second-order Doppler shift of a single $^{199}\text{Hg}^+$ ion laser cooled to the Doppler limit is about -2×10^{-18} (see Ref. 8). The fractional frequency

shift of the 40.5 GHz clock transition with magnetic field is $0.24B^2$, where B is expressed in teslas. Thus, a $^{199}\text{Hg}^+$ ion confined in an ion trap at near-zero magnetic field and laser cooled to the Doppler limit should constitute a highly accurate 40.5 GHz microwave frequency standard. To improve the signal-to-noise ratio (and hence the fractional frequency stability), it will, however, be desirable to have many $^{199}\text{Hg}^+$ ions, all with equally low Doppler shifts.

II. LINEAR RF ION TRAP

The linear rf quadrupole trap, which uses four rf rods for radial confinement and a static axial potential for longitudinal confinement, was developed as a way of confining multiple ions with low Doppler shifts due to rf micromotion.^{4,5,9-11} In this scheme, the four rods are configured as in a rf mass analyzer, with a zero-field node along the center line instead of at a single point as in a spherical Paul quadrupole rf trap.¹² Axial confinement is achieved by applying static potentials at the ends of the trap, using positively biased rings, pins, or split sections in the trap rods. Figure 2 shows the linear rf trap used in the present cryogenic experiment. The four rf rods are $R'=0.20$ mm in radius, centered on a radius of $R+R'=0.64$ mm from the trap axis (about half the size of our previous linear rf trap⁵). Axial confinement is achieved by positively biasing rings (electrodes C and R in Fig. 2), separated by 4 mm, at either end of the four-rod quadrupole.

Two (diagonally opposite) rf rods of the trap are driven with a rf potential $V_0 \cos(\Omega t)$, while the other two rf rods are maintained at rf ground. Near the trap axis, the time-varying potential is approximately a saddle-point potential in x and y ,

$$V(x, y) \approx \frac{V_0}{2} \left(1 + \frac{x^2 - y^2}{R^2} \right) \cos(\Omega t), \quad (1)$$

where x and y are the transverse coordinates. The centers of the two rf-driven rods intersect the x axis, one at $-(R+R')$ and the other at $R+R'$. The approximation assumes that the rods of circular cross section give the same potential as rods whose surfaces are equipotentials of Eq. (1). If the drive frequency Ω is high enough (that is, much higher than the ion's radial secular oscillation frequency), the ion of mass m and charge q will experience an approximately harmonic pseudopotential that confines in both x and y :

^{a)}Present address: Schlumberger-Anadrill, Sugar Land, TX 77778.

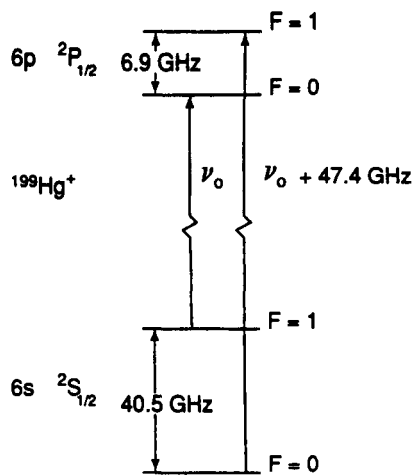


FIG. 1. Diagram of the hyperfine energy levels of the $^{199}\text{Hg}^+$ ground $6s^2S_{1/2}$ state and the $6p^2P_{1/2}$ state. Here ν_0 corresponds to a wavelength of 194.2 nm. The 40.5 GHz ground-state hyperfine transition is intended for use as a reference for a frequency standard.

$$\Phi(x, y) \approx \frac{m}{2q} \omega_r^2 (x^2 + y^2), \quad (2)$$

where ω_r is the radial angular oscillation frequency (secular frequency), which is given by

$$\omega_r = \frac{qV_0}{\sqrt{2m\Omega R^2}}. \quad (3)$$

Axial confinement (along z) results from biasing the rings at either end of the trap with a positive potential U_0 . Near the center of the trap, an ion experiences the static saddle-point potential

$$\phi_s(x, y, z) \approx \frac{m}{2q} \omega_z^2 [z^2 - \frac{1}{2}(x^2 + y^2)], \quad (4)$$

where the axial angular oscillation frequency ω_z is given by

$$\omega_z = \left(\frac{2\kappa q U_0}{mz_0^2} \right)^{1/2}. \quad (5)$$

The separation of the rings is $2z_0 = 4.0$ mm, and κ is a geometrical factor that is ~ 0.004 in this trap (as determined from measurements of ω_z). As Eq. (4) indicates, the radial pseudopotential Φ is weakened by the addition of the static axial potential. Thus, the effective radial angular oscillation frequency is

$$\omega_r' = (\omega_r^2 - \omega_z^2/2)^{1/2}. \quad (6)$$

Under typical operating conditions in this trap, we expect $\omega_r'/2\pi \approx 350$ kHz and $\omega_z/2\pi \approx 25$ kHz, assuming $\Omega/2\pi = 13$ MHz, $V_0 = 100$ V, and $U_0 = 25$ V.

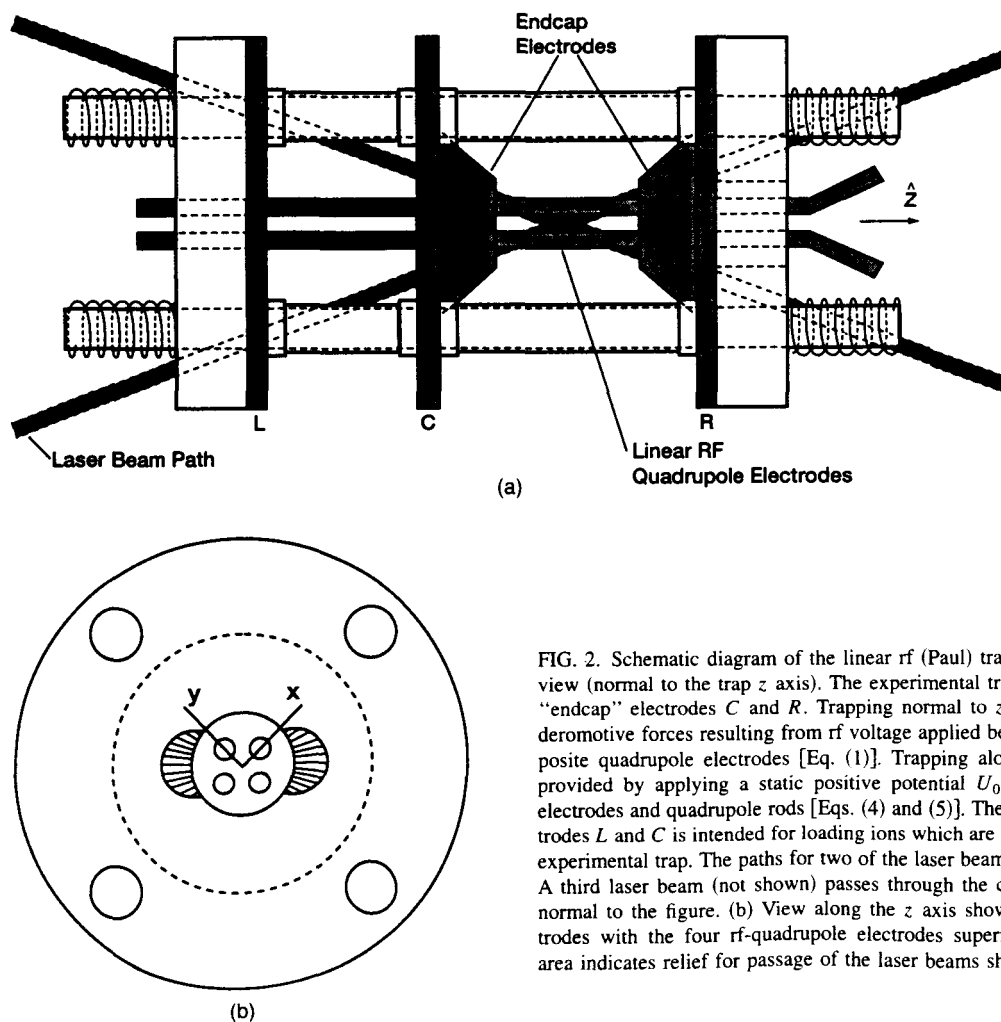


FIG. 2. Schematic diagram of the linear rf (Paul) trap electrodes. (a) Side view (normal to the trap z axis). The experimental trap is located between "endcap" electrodes C and R . Trapping normal to z is provided by ponderomotive forces resulting from rf voltage applied between diagonally opposite quadrupole electrodes [Eq. (1)]. Trapping along the z direction is provided by applying a static positive potential U_0 between the endcap electrodes and quadrupole rods [Eqs. (4) and (5)]. The region between electrodes L and C is intended for loading ions which are then transferred to the experimental trap. The paths for two of the laser beams are shown in black. A third laser beam (not shown) passes through the center of the trap and normal to the figure. (b) View along the z axis showing the endcap electrodes with the four rf-quadrupole electrodes superimposed. The shaded area indicates relief for passage of the laser beams shown in (a).

As shown in Fig. 2, the trap's axial-confinement "ring" electrodes are in fact, bored-out conical disks of beryllium copper, appropriately drilled to allow laser access to the trap center. The four rf rods are beryllium-copper wires. The dimensions of the quadrupole rods were chosen to allow $f/1$ light collection from the center of the trap. Also, the choice of the small R dimension makes the trap radially unstable, due to the Mathieu instability, for unwanted contaminant ions (created during the loading procedure) with $\omega_r > \Omega/2$ or, equivalently

$$m \leq 10.6u \times \left(\frac{V_0}{100 \text{ V}} \right), \quad (7)$$

where u is the atomic mass unit. The four outer support rods for the trap structure are alumina (Al_2O_3) rods sheathed in thin beryllium-copper tubing of an outer diameter of 1.28 mm. These support rods can each receive independent biasing potentials to "shim" the ions back onto the trap's geometrical center line, in the event that patch charges on the rod electrodes should cause the trap's geometrical and dc electrical centers to not coincide. (Without this compensation, the ions could experience large rf electric fields and undergo substantial rf micromotion.) The ceramic insulating endpieces that define the positions of the trap rods are high-purity alumina slabs 2.0 mm in thickness, with appropriately placed laser beam access holes.

Figure 2(a) shows that the electrodes form two linear traps in tandem. The leftmost trap, between electrodes L and C , is intended for capturing ions in the initial loading process. Ions would then be pushed through electrode C into the experimental trap (between electrodes C and R). This design was implemented with the idea of gaining immunity from contact potentials or electric charge buildup on the electrodes near where the ions were loaded.

Appropriately placed mirrors allow laser cooling to be performed along any one of three noncoplanar directions at the center of the trap, as illustrated in Fig. 2(a): in the plane of the page at $\pm 20^\circ$ to the trap's z axis or normal to the plane of the page (using a small mirror located directly below the trap). We require only one of the beams shown in Fig. 2(a) for cooling, optical pumping, and detection. The three beam paths are required for probing the velocity distribution in three dimensions. The kinetic temperatures achievable in these cooling geometries are derived using Ref. 13. The temperatures at the Doppler-cooling limit with either of the $\pm 20^\circ$ beams correspond to $T_{\text{radial}} \approx 5.6$ mK and $T_{\text{axial}} \approx 1.2$ mK, under the assumption that the radiation is emitted isotropically. These temperatures imply a fractional second-order Doppler shift of the 40.5 GHz hyperfine transition frequency that is approximately -5.5×10^{-18} .

Previously, a slightly larger linear rf trap, in which the rods were segmented in such a way that dc potential differences could be applied to the different segments, was used, thus providing axial confinement.⁵ In that apparatus, operating at room temperature and at a pressure of about 10^{-8} Pa, several tens of $^{199}\text{Hg}^+$ ions were crystallized at fixed positions in a single row along the trap's nodal center line. Such a geometry is optimal for the present frequency standard application, since the ions can be imaged independently for

improved signal-to-noise ratio, and all have approximately the same low second-order Doppler shift as a single ion in a quadrupole trap. The major limitation of this previous apparatus was the background gas pressure in the vacuum chamber, which was high enough that ions would be lost in several minutes due to chemical reactions. For a frequency standard application, it is desirable to be able to interrogate a particular ensemble of ions, located at relatively fixed positions, for periods of many hours, several days, or longer. Also, even at 10^{-8} Pa, shifts of the transition frequency with changes in the background gas pressure could limit the accuracy.¹⁴

III. CRYOGENIC LINEAR RF ION TRAP

Our solution to the background gas pressure problem is to maintain the trap and vacuum vessel at liquid-He temperature (~ 4 K). At this low temperature, most gases cryopump to the walls of the chamber, giving a very low background pressure. In a similar sealed vacuum can, lowered to 4 K, Gabrielse *et al.*¹⁵ report background pressures below 10^{-14} Pa. Thus by lowering the pressure by several orders of magnitude, we should be able to store trapped ions for at least several days, interrogate them with Ramsey free-precession times as long as tens or hundreds of seconds, and eliminate or greatly reduce pressure shifts of the 40.5 GHz clock frequency. In addition, the 4 K temperature should allow us to operate a superconducting shield around the ion trap region to help in shielding changes in the magnetic field.

We have constructed and have made initial tests of a prototype apparatus based on these concepts. The trap described in Sec. II and related components are mounted in an In-sealed OFHC copper vacuum can (see Fig. 3), inside a nested liquid-He/liquid- N_2 Dewar, heat sunk to the outside bottom of the liquid-He reservoir and surrounded by radiation shields at 4 and 77 K. Figure 4 shows a schematic view of the small vacuum can mounted inside its nested liquid-He/liquid- N_2 Dewar, which has a liquid-He hold time of about four days. Optical access to the trap region is through windows around the base of the Dewar, aligned with baffled holes in the radiation shields and windows in the sides of the can. The laser beams are introduced into the vacuum apparatus through In-sealed fused silica windows.¹⁶ Electrical and microwave access is through heat-sunk cabling leading down from connectors on the Dewar's top vacuum flange. The cables are routed along the liquid- N_2 and liquid-He reservoirs, into the radiation-shielded 4 K space around the experimental vacuum can, to cryogenic vacuum feedthroughs on the sides of the can. The 13 MHz rf drive for the trap (see below) and the dc currents for the field coils surrounding the trap are routed down the neck of the Dewar, through the liquid-He, and into the can by cryogenic feedthroughs in its top plate (which is also the bottom plate for the liquid-He reservoir). The superconducting shield consists of a $5 \mu\text{m}$ coating of lead, electroplated onto the inside of the copper vacuum vessel.

The rf potential V_0 is applied to the trap electrodes by a resonant step-up transformer. In the frequency range of interest here, the most convenient type of resonator consists of a helical "secondary" coil that is effectively $\lambda/4$ in length in-

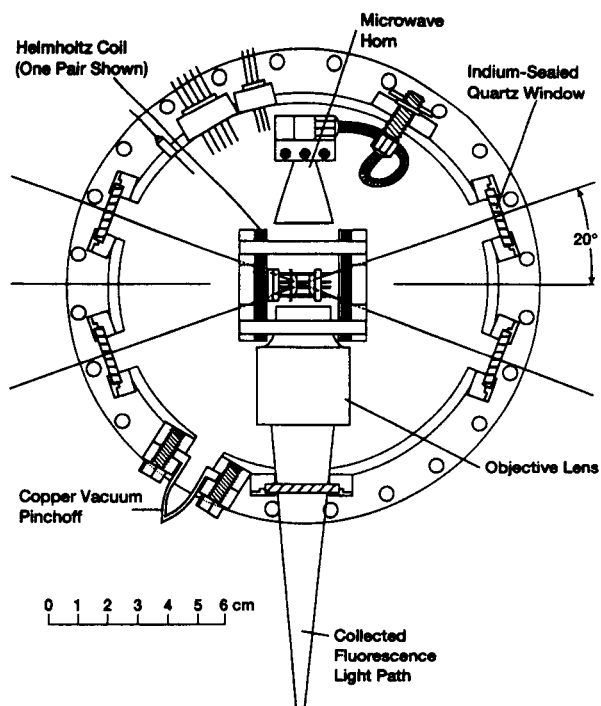


FIG. 3. Top view of pillbox vacuum assembly. The trap is shown at the center of the diagram in the same orientation as Fig. 2(a). Two of the laser beam paths are shown at 20° with respect to the trap z axis. The top of this pillbox assembly forms the bottom of the liquid-He reservoir shown in Fig. 4.

side a shielding cylindrical can,¹⁷ with an inductive-coupling input "primary" loop at the end of the input coaxial line. In our cryogenic apparatus, it is desirable to dissipate as little rf power as possible into the liquid helium. Thus, we constructed a superconducting lead helical resonator with $Q \approx 3000$ when attached to the trap apparatus. The losses are mainly in the connecting leads and not in the resonator. (The resonator by itself had an unloaded Q in excess of 200 000.) It was determined that 4 mW of rf at 13 MHz produced an amplitude $V_0 \approx 150$ V at the trap rods. The superconducting resonator sits at the bottom of the Dewar reservoir, immersed in liquid He, with the high-potential end of its secondary coil attached to a copper cryogenic feedthrough leading through the top plate of the experimental vacuum chamber and connected to the two rf-driven rods of the trap. The input coupling loop is a small off-axis coil, attached to a stainless-steel coaxial cable leading out through the top of the Dewar through an O-ring compression seal. This coaxial cable can be rotated from outside the Dewar so as to orient the coupling loop properly for optimized power coupling into the resonator.

The trap is surrounded by orthogonal pairs of small coils, each consisting of 350–600 turns of 0.076 mm diam Nb wire, in order to produce the desired magnetic field components *inside* the superconducting shield. The coils allow arbitrary x , y , and z components of magnetic induction to be produced at the trap center with efficiencies of 5–10 $\mu\text{T}/\text{mA}$ (in each coil).

To ensure 100%-efficient "electron shelving" detection, we need to collect a large fraction of the ions'

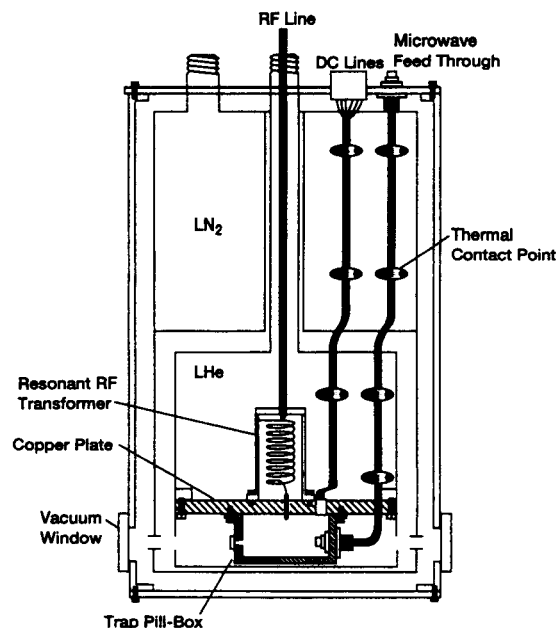


FIG. 4. Side view of cryostat assembly (not to scale). The pillbox containing the trap and related hardware is bolted to a copper plate which forms the bottom of the liquid-He reservoir. The resonant rf transformer is shown on top of this copper plate. The high-voltage output lead is connected to a vacuum feedthrough which is then connected to the trap quadrupole electrodes inside the trap pillbox.

fluorescence.^{7,18} For this reason, the imaging objective lens has a large numerical aperture. Also, it is advantageous to be able to resolve the fluorescence of the individual ions so as to be able to detect them independently using different portions of the photocathode of the imaging UV detector. The lens used in the experiment therefore also has resolving power at 194 nm sufficient to resolve point objects separated by less than 4 μm . The field of view over which the lens can image with aberrations insignificant at this level is about 250 μm . The f number is $f/1$, with the lens's front surface sitting 8.1 mm away from the center of the trap. In order for the lens to be capable of surviving temperature cycles over a range of about 370 K ("bakeout" temperature during vacuum processing) to 4 K (operational temperature in the experiment), the housing for the five-element lens was constructed of the same UV-grade fused silica as the elements themselves, and the assembly was performed without any bonding agent or cushioning material.

Loading the trap with $^{199}\text{Hg}^+$ ions is accomplished by decomposing a sample of isotopically enriched (92%) ^{199}HgO powder in a small ceramic oven tube wound with heater wire, located below the trap. A fraction of the diffuse beam of ^{199}Hg atoms is ionized at the center of the trap by electrons emitted by a field-emitter point. When a sample of ions has been captured, the oven and electron beam are turned off, and the vacuum chamber returns to a uniform 4 K temperature from whatever local warming has occurred.

We first tried loading ions between electrodes L and C [see Fig. 2(a)] and transferring them to the experimental trap. This was unsuccessful. If the ions were loaded between electrodes L and C , we were unable to push them through electrode C into the experimental trap by biasing electrode L

FIG. 5. A linear crystal of laser-cooled $^{199}\text{Hg}^+$ ions, illuminated by 194 nm radiation. The gaps are due to the presence of other ions, possibly other mercury isotopes, which do not fluoresce at the same wavelength as $^{199}\text{Hg}^+$. The spacing between adjacent ions is $\sim 10\ \mu\text{m}$.

with a positive potential with respect to electrode *C* (up to about 250 V). This result may have been caused by shielding from the quadrupole rf electrodes and by the non-negligible thickness of the central conical electrode. Subsequent to these experiments, the HgO source and electron source were moved near the experimental trap and the ions were created and captured directly into this trap.

We load and optically resolve individual cold ions, coalesced into linear crystals with interion spacings of 10–30 μm . We have seen crystals ranging in number from one to several tens of ions, very similar in appearance to those reported in Ref. 5. An example is shown in Fig. 5. With laser cooling, these crystals are stable over periods of at least 10 h. One rough measure of the background gas pressure is the rate at which trapped “impurity” ions (which show up as readily identifiable nonfluorescing spots in the crystal) exchange places with their $^{199}\text{Hg}^+$ ion neighbors. In the room-temperature apparatus at 10^{-8} Pa, these interchanges occurred every few minutes, but they do not occur over periods of several hours or more in our cryogenic vacuum.

We have observed all three ground-state hyperfine microwave transitions ($\Delta M = 0, \pm 1$) by the method discussed in Refs. 5 and 7.

IV. PROSPECTS

We plan to study the microwave transitions in detail after making technical improvements to the magnetic shielding, the nulling of the residual rf micromotion, and the microwave local oscillator frequency synthesis. The scheme for operating this apparatus as a microwave clock will initially be that described for the room-temperature experiment.⁵ The ions will be imaged onto separate portions of the detector’s photocathode and detected individually as an ensemble of independent atomic clocks. Dehmelt’s technique of electron shelving can be used to detect the clock transition in each ion with nearly 100% efficiency.^{7,18} Under these assumptions, the fractional frequency stability is given by⁸

$$\sigma_y(\tau) = \frac{1}{\omega_0 \sqrt{N T_R \tau}}, \quad (8)$$

where $\omega_0/2\pi = 40.5$ GHz, N is the number of ions in the linear crystal ensemble, T_R is the free-precession time between the two phase-coherent rf pulses (in Ramsey’s interrogation scheme), and $\tau > T_R$ is the averaging time. Assuming a 100 s Ramsey interrogation time, the short-term fractional frequency stability of an ensemble of 30 ions would be $\sim 7 \times 10^{-14} \tau^{-1/2}$, and longer free-precession times with larger samples of ions seem possible. The fractional second-order Doppler shift to the frequency should be no greater than a few parts in 10^{18} with ions on the trap’s nodal center line, cooled to the Doppler limit. The second-order Zeeman shift, as a fraction of 40.5 GHz, is equal to $0.24B^2$, where B

is in teslas. Control of this shift may require conventional external magnetic shielding as well as the internal superconducting magnetic shield surrounding the trap. With sufficiently cold ions and small field fluctuations, a fractional inaccuracy of $< 1 \times 10^{-16}$ of the clock frequency appears attainable.

In addition, this apparatus contains features (the superconducting coil pairs) that should allow us to investigate new effects based on motional Zeeman coherences. These include a novel cooling scheme (proposed by Harde¹⁹) using optical pumping in conjunction with a motional magnetic coupling between the spin orientation and the harmonic oscillator state of the ions in the trap potential, as well as a scheme for “squeezing” the total ensemble spin,²⁰ which could improve the signal-to-noise ratio in frequency standards where the dominant noise contribution is projection noise.⁷

ACKNOWLEDGMENTS

We thank John Miller for making improvements in the light-collection optics used to acquire the image shown in Fig. 5. We thank Dale Thoele, Doug Gallagher, Richard McLaughlin, and David Kelley for their fine technical support in the construction of the apparatus as well as Donald McDonald and Ronald Ono for their advice on cryogenic matters. We thank John Miller and Joseph Tan for reading the manuscript. This work was supported by the U. S. Office of Naval Research.

¹F. G. Major and G. Werth, *Phys. Rev. Lett.* **30**, 1155 (1973).

²M. D. McGuire, R. Petsch, and G. Werth, *Phys. Rev. A* **17**, 1999 (1978).

³L. S. Cutler, R. P. Giffard, P. J. Wheeler, and G. M. R. Winkler, in *Proceedings of the 41st Annual Frequency Control Symposium, Philadelphia, 1987* (IEEE, Piscataway, NJ, 1987), pp. 12–19.

⁴R. L. Tjoelker, J. D. Prestage, G. J. Dick, and L. Maleki, in *Proceedings of the 1993 IEEE International Frequency Control Symposium, Salt Lake City, UT, 1993* (IEEE, Piscataway, NJ, 1993), pp. 132–138.

⁵M. G. Raizen, J. M. Gilligan, J. C. Bergquist, W. M. Itano, and D. J. Wineland, *Phys. Rev. A* **45**, 6493 (1992).

⁶W. M. Itano, L. L. Lewis, and D. J. Wineland, *Phys. Rev. A* **25**, 1233 (1982).

⁷W. M. Itano, J. C. Bergquist, J. J. Bollinger, J. M. Gilligan, D. J. Heinzen, F. L. Moore, M. G. Raizen, and D. J. Wineland, *Phys. Rev. A* **47**, 3554 (1993).

⁸D. J. Wineland, J. C. Bergquist, J. J. Bollinger, W. M. Itano, D. J. Heinzen, S. L. Gilbert, C. H. Manney, and M. G. Raizen, *IEEE Trans. Ultrason. Ferroelectr. Freq. Control* **37**, 515 (1990).

⁹P. T. H. Fisk, M. A. Lawn, and C. Coles, *Appl. Phys. B* **57**, 287 (1993).

¹⁰J. D. Prestage, G. J. Dick, and L. Maleki, *J. Appl. Phys.* **66**, 1013 (1989).

¹¹H. G. Dehmelt, in *Frequency Standards and Metrology, Proceedings of the 4th Symposium, Ancona, Italy, 1988*, edited by A. DeMarchi (Springer-Verlag, Berlin, 1989), p. 286.

¹²W. Paul, O. Osberghaus, and E. Fischer, *Berichte des Wirtschaftsministeriums Nordrhein-Westfalen*, Nr. 415 (1958).

¹³W. M. Itano and D. J. Wineland, *Phys. Rev. A* **25**, 35 (1982).

¹⁴D. J. Wineland, J. C. Bergquist, J. J. Bollinger, W. M. Itano, F. L. Moore, J. M. Gilligan, M. G. Raizen, D. J. Heinzen, C. S. Weimer, and C. H. Manney, in *Laser Manipulation of Atoms and Ions, Proceedings of the International School of Physics “Enrico Fermi,” Course CXVIII, Varenna*,

Italy, edited by E. Arimondo, W. D. Phillips, and F. Strumia (North-Holland, Amsterdam, 1992), pp. 553–567.

¹⁵G. Gabrielse, X. Fei, W. Jhe, L. A. Orozco, J. Tan, R. L. Tjoelker, J. Haas, H. Kalinowsky, T. A. Trainor, and W. Kells, *Am. Inst. Phys. Conf. Ser.* **233**, 549 (1991).

¹⁶C. C. Lim, *Rev. Sci. Instrum.* **57**, 108 (1986).

¹⁷W. W. Macalpine and R. O. Schildknecht, *Proc. IRE* **47**, 2099 (1959).

¹⁸H. G. Dehmelt, *IEEE Trans. Instrum. Meas.* **IM-31**, 83 (1982).

¹⁹H. Harde, in *International Conference on Quantum Electronics Technical Digest, Series 1990* (Optical Society of America, Washington, DC, 1990), Vol. 8, p. 278.

²⁰D. J. Wineland, J. J. Bollinger, W. M. Itano, F. L. Moore, and D. J. Heinzen, *Phys. Rev. A* **46**, R6797 (1992); D. J. Wineland, J. J. Bollinger, W. M. Itano, and D. J. Heinzen, *ibid.* **50**, 67 (1994).

Minimizing the Time-Dilation Shift in Penning Trap Atomic Clocks

Joseph N. Tan, J. J. Bollinger, and D. J. Wineland

Abstract—If environmental perturbations are made negligible, the time-dilation shift is expected to give one of the largest systematic uncertainties in a stored ion clock. In general, this shift increases with the number of trapped ions. Fluctuations in the time dilation shift therefore could limit the frequency stability of an ion clock. We show that in a Penning trap, relativistic time dilation can be minimized if the laser-cooled ions are prepared in a special spheroidal state. In addition, a modest stabilization of the spheroid near the minimum-shift configuration can significantly reduce fluctuations in the time dilation. The results obtained for a single-species ion clock also provide a good approximation for a sympathetically cooled system.

I. INTRODUCTION

ONE of the goals of the Time and Frequency Division at NIST-Boulder is to realize an ion frequency standard with absolute uncertainty better than 1 part in 10^{15} . In recent years, experiments at NIST with ${}^9\text{Be}^+$ ions stored in a Penning trap have demonstrated that an RF oscillator can be steered by a nuclear spin-flip “clock” transition (~ 303 MHz) with $\sigma_y(\tau) \approx 3 \times 10^{-12}/\sqrt{\tau}$ fractional frequency stability [1]–[4]. If collisional shifts [3], [4] are negligible, the expected performance of a stored ion clock using the Ramsey method [5] of interrogation is limited by the “projection-noise” [6] frequency instability

$$\sigma_y(\tau) = \frac{1}{2\pi\nu_o\sqrt{NT_R\tau}} \quad (1)$$

and the uncertainty in the time-dilation shift (second-order Doppler shift)

$$\frac{\Delta\nu}{\nu_o} = -\frac{1}{2} \frac{\langle v^2 \rangle}{c^2}. \quad (2)$$

The frequency stability (1), depends on the clock transition frequency ν_o , the number of ions N , the Ramsey interrogation period T_R , and the averaging time $\tau \gg T_R$. The possibility of using “squeezed” atomic states to obtain higher frequency stability than (1) is being explored [7]. The time-dilation shift, (2), depends on the average squared velocity $\langle v^2 \rangle$ of the ions. A systematic error of 5×10^{-15} due to time dilation has been determined for a stored ${}^9\text{Be}^+$ ion clock [1]–[4]. In this paper, we give a detailed treatment of the time-dilation effects in Penning traps to identify the important factors for optimized performance [8].

Manuscript received July 1, 1994; revised October 15, 1994. This work was supported in part by the Office of Naval Research.

The authors are with Time and Frequency Division, NIST, Boulder, CO 80303 USA.

IEEE Log Number 9408707.

II. LASER-COOLED, SINGLE-SPECIES ION CLOCK

The simplest stored-ion clock consists of one trapped ion, with charge q and mass M . In an ideal Penning trap, the ion is confined by a pure quadrupole electrostatic potential superimposed on a uniform magnetic field. The motions of the trapped ion consist of a harmonic oscillation (angular frequency ω_z) along the trap’s symmetry axis, a high-frequency cyclotron orbit (ω'_c) about the magnetic field, and a low-frequency magnetron orbit ($\omega_m = \omega_z^2/2\omega'_c$) about the trap z -axis that generates a $qv \times \mathbf{B}$ force for radial confinement [9]. A suitable internal transition (e.g., between hyperfine levels) which is field-independent at a particular field B_o , can be used in a frequency standard. If the ion motions are cooled (or heated in the case of the magnetron orbit) to their ground states, the time-dilation shift in the selected “clock transition” is very small. The potentially high accuracy obtainable with a single ion ($N = 1$), however, exacts a cost in low signal-to-noise ratio and long averaging times.

The signal-to-noise ratio and frequency stability can be improved significantly by using large numbers of ions—see (1). However, the time-dilation shift also increases with the number of ions. This is because, in general, a larger ion “cloud” extends farther from the trap axis, and because, for stable trapping, an ion cloud or plasma [10], [11] must rotate (spin) about the trap’s symmetry axis (taken as z -axis). This rotation frequency ω_r lies in the range

$$\omega_m < \omega_r < \omega'_c \quad (3)$$

where $\omega'_c = \omega_c - \omega_m$, and ω_c is the cyclotron frequency $\omega_c = qB_o/M$. The accompanying thermal motions of the ions can be reduced greatly by Doppler laser cooling (typically to < 1 K, with a cooling limit of ~ 1 mK for ${}^9\text{Be}^+$). We can assume that the time dilation due to thermal motions is negligible, and hereon study the $T = 0$ K limit. In a nearly ideal Penning trap [9], the laser-cooled ions form a uniform density spheroid bounded by

$$\left(\frac{x}{r_s}\right)^2 + \left(\frac{y}{r_s}\right)^2 + \left(\frac{z}{z_s}\right)^2 = 1 \quad (4)$$

with an aspect ratio $\alpha \equiv z_s/r_s$ which varies in a known way with the rotation frequency ω_r [10], [11]. When the $qv \times \mathbf{B}$ radial restoring force is weak ($\omega_r \rightarrow \omega_m$) or when the centrifugal force is very strong ($\omega_r \rightarrow \omega'_c$), the spheroid is stretched into a thin circular disk ($\alpha \rightarrow 0$). Hence, near the upper and lower bounds of ω_r , the magnitude of the time-dilation shift ($\Delta\nu/\nu_o = -\omega_r^2 r_s^2/5c^2$) for the thin disk of ions

is very large. We now show that the magnitude of the time-dilation shift goes to a minimum at a particular (low) value of ω_r which brings the ions closer to the trap axis.

For a single ion species, the time-dilation shift due to the plasma rotation may be written as

$$\frac{\Delta\nu}{\nu_o} = -S_1 X^2 Y^2. \quad (5)$$

We use a dimensionless spheroid radius $X = r_s/b$ scaled by the radius b of a fictitious sphere enclosing N ions with the minimum cold fluid ($T = 0$ K) density $n_E = \epsilon_o M \omega_z^2 / q^2$. This mass-independent radius b may be written as $b = \sqrt[3]{3N\tilde{r}c^2/\omega_z^2}$ where $\tilde{r} \equiv q^2/(4\pi\epsilon_o M c^2)$. The dimensionless rotation frequency Y is given by $Y = (\omega_r/\omega_m)(\omega_c/\omega'_c)$. The scaling factor $S_1 > 0$ is defined by

$$S_1 \equiv \frac{1}{20} \left[\frac{\omega_z}{\omega_c} \right]^2 \left[3N \frac{\omega_z \tilde{r}}{c} \right]^{2/3}. \quad (6)$$

The radius and rotation frequency of the spheroidal ion cloud are related through the conditions [11, (2.1) and (2.6)] required for rotational equilibrium. For our purpose, these conditions are recast in the form

$$\frac{1}{X^3 \alpha} = Y - \frac{1}{2} \left(\frac{\omega_z}{\omega_c} \right)^2 Y^2, \quad (7)$$

$$X^3 \alpha (\alpha^2 - 1) = Q_1^0 \left(\frac{\alpha}{\sqrt{\alpha^2 - 1}} \right) \quad (8)$$

where $Q_1^0(\chi)$ is an associated Legendre polynomial of the second kind in χ . The first of these coupled equations, (7) is derived by taking the divergence of the Lorentz force law and eliminating the electric field with Gauss' law. It has a centrifugal term $\propto Y^2$ in a frame corotating with the ions. In the cold fluid model, (8) represents the solution to Maxwell's equations for a uniformly charged spheroid rotating in an ideal Penning trap. It uses the electrostatic approximation, wherein fields generated by the ion motions are negligible. Interaction with image charges induced in the trap electrodes is also negligible since the ions are assumed to be distributed in a central volume much smaller than the trap size [10], [11].

The dependence of the time-dilation shift on system parameters comes almost entirely from the mass-independent scaling factors S_1 , ω_m , and b because (7) depends weakly on $(\omega_z/\omega_c)^2$ for small values of ω_z/ω_c , as illustrated in Fig. 1. Convergence is particularly rapid for low rotation frequencies (i.e., Y of order unity). In the limit $\omega_z/\omega_c \rightarrow 0$, the product $X^2 Y^2$ yields a universal curve. This universal ($\omega_z/\omega_c \rightarrow 0$) limit is of experimental interest since it gives the smallest time-dilation shift and provides a good approximation for the experimental regime $\omega_z/\omega_c \lesssim 0.1$. For convenience, subsequent discussions employ this limit. The minimum shift occurs at $X = X_o \simeq 1.06$ (see Fig. 1) and is attained by preparing the ions in a spheroid with aspect ratio $\alpha = z_s/r_s \simeq 0.460$ rotating at $\omega_r \simeq 1.82\omega_m(\omega_c/\omega'_c) \simeq 1.82\omega_m$. To the extent that this limit is a good approximation, the optimal shape of the spheroid is independent of system parameters, and the fractional frequency

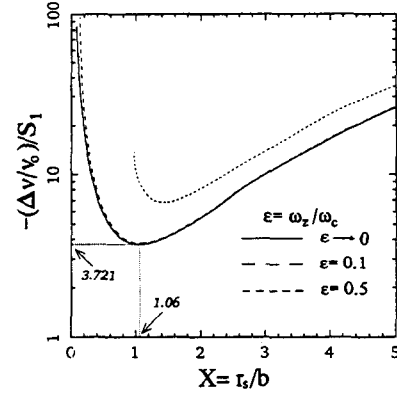


Fig. 1. Time-dilation shift versus spheroid radius, for various values of $\epsilon \equiv \omega_z/\omega_c$. Solid curve gives the universal limit as $\epsilon \rightarrow 0$.

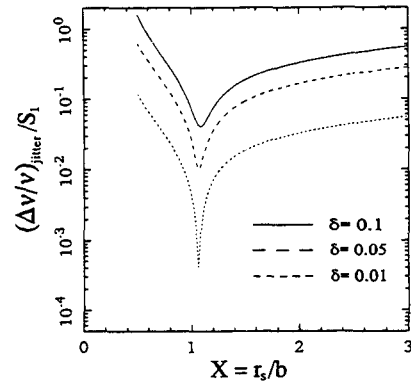


Fig. 2. Root-mean-squared frequency jitter in a single-species ion clock as a function of mean spheroid radius X , for various values of the Gaussian standard deviation δ in the radius fluctuations.

shift near the minimum is

$$\frac{\Delta\nu}{\nu_o} \simeq -S_1 \left[3.721 + 3.4 \left(\frac{\Delta r_s}{r_{so}} \right)^2 \right]. \quad (9)$$

This is expressed in terms of the deviation Δr_s from the optimal spheroid radius $r_{so} = 1.06 b$ because the spheroid radius is typically monitored in real-time with an imaging device and thus provides an observable for locking schemes to stabilize the spheroid. By stabilizing the spheroid radius near the optimal value r_{so} , it should be possible to reduce the jitter in the time-dilation shift. If the spheroid radius fluctuates about X with Gaussian standard deviation δ , the frequency jitters by

$$\left\langle \left(\frac{\Delta\nu}{\nu} \right)^2 \right\rangle_{jitter} = \int_{-\infty}^{+\infty} dX' \frac{1}{\delta\sqrt{2\pi}} \exp \left[-\frac{(X' - X)^2}{2\delta^2} \right] \cdot \left[\frac{\nu(X') - \langle \nu \rangle}{\nu_o} \right]^2. \quad (10)$$

As shown in Fig. 2, near the minimum-shift configuration, even a modest stabilization of $\delta \lesssim 0.1$ (i.e., $(\Delta r_s)_{rms}/r_{so} \lesssim 0.1$) can reduce the frequency jitter to less than 1% of the time-dilation shift, i.e., $\Delta\nu_{rms}/\nu \lesssim 4 \times 10^{-2} S_1$.

In the $\omega_z/\omega_c \rightarrow 0$ limit, the minimum time-dilation shift ($\Delta\nu_{min}/\nu_o \simeq -3.721 S_1$) is independent of the ion mass. Thus, ions with clock transitions which are field-independent at high magnetic fields are desirable since the scaling factor S_1

TABLE I
EXPECTED PERFORMANCE FOR A SINGLE-SPECIES ION CLOCK WITH $N = 10^6$,
 $T_R = 100$ s, $\alpha = 0.46$, AND $r_{so} = 4.2$ mm. EQUATION (1) IS USED TO
EVALUATE σ_y . VALUES OF ν_o AND B_o ARE TAKEN FROM [12], [13]

Ion	ν_o (GHz)	B_o (T)	ω_z/ω_c	$\sigma_y(1\text{ s})$ $\times 10^{15}$	minimum $\Delta\nu/\nu_o$ $\times 10^{15}$
$^9\text{Be}^+$	0.303016	0.8194	0.0989	53	-241
$^{25}\text{Mg}^+$	0.291996	1.2398	0.1089	55	-105
$^{67}\text{Zn}^+$	$\simeq 1$	$\simeq 8.0$	0.0276	16	-2.5
$^{199}\text{Hg}^+$	20.9	43.9	0.0087	0.76	-0.084
$^{201}\text{Hg}^+$	7.73	3.91	0.0979	2.1	-11

is inversely proportional to the square of the magnetic field. The expected performance for several systems with $N = 10^6$, $T_R = 100$ s, and fixed spheroid dimensions ($\alpha = 0.46$, $r_{so} = 4.2$ mm) is given in Table I. The gain in frequency stability with large numbers of ions will allow measurements of the time-dilation shift in reasonably short integration time. Since $S_1 \propto V_o^{4/3}$ (V_o is the trapping voltage), it should be possible, by measuring the minimally shifted clock frequency for various V_o , to extrapolate down to the $V_o = 0$ limit for the unshifted clock frequency to an accuracy limited by $\sigma_y(\tau)$. The slope of the extrapolation would provide an independent determination of the number of ions.

III. SYMPATHETICALLY COOLED ION CLOCK

In a frequency standard, it is desirable to interrogate the clock transition without the perturbations (a.c. Stark shifts) caused by the cooling laser. If the heating by the environment is sufficiently weak, then the cooling laser can be turned off during the interrogation cycles. However, when the interrogation time is rather long or heating is significant, continuous cooling of the clock ions is required. This cooling can be provided by using a second, simultaneously-stored laser-cooled ion species, which sympathetically cools the clock ions through the Coulomb coupling between species [14]–[16]. When the second ion species, the “coolant” ions, have smaller charge-to-mass ratio than the clock ions, the two species of ions centrifugally separate [14]–[16] with the coolant ions occupying an annular region surrounding a central core of clock ions. Ramsey interrogation times as long as $T_R \simeq 550$ s have been attained using laser-cooled $^{24}\text{Mg}^+$ ions to sympathetically cool $^9\text{Be}^+$ clock ions [3], [4]. Moreover, the time-dilation shift is smaller for sympathetically cooled clocks since the clock ions are distributed closer to the axis than in a single-species configuration.

For low rotation frequency and $\omega_z/\omega_c \ll 1$, the surface enclosing the two species may be approximated by the spheroidal surface for a single species. This is because, for a single species in this limit, the centrifugal term in (7) becomes negligible and the ion distribution becomes independent of ion

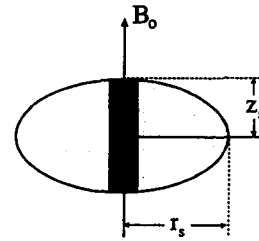


Fig. 3. Cross-sectional diagram of a two-species ion plasma for an ion clock. Coolant ions occupy the annular region surrounding the clock ions (shown darker) in the cylindrical core.

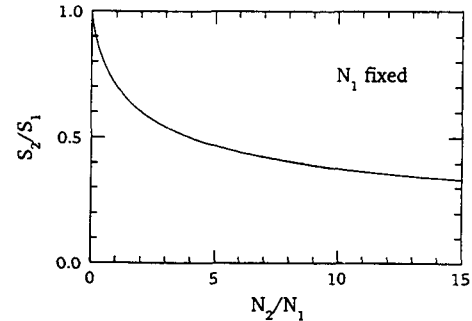


Fig. 4. Ratio of the time-dilation shift in a sympathetically cooled clock to that in a single-species clock. The number of clock ions is fixed.

mass to order $(\omega_z/\omega_c)^2$. Therefore, if a cylindrical core is removed from a minimum-shift configuration and is substituted by an equal number of clock ions, as illustrated in Fig. 3, the spheroidal boundary is well preserved. Neglecting the small gap [14]–[16] between the two species, (5) and (9) derived for the time-dilation shift in a single species, are still applicable to the cylindrical core of clock ions provided the scaling factor S_1 is replaced by

$$S_2 \equiv S'_1 \Lambda \quad (11)$$

where S'_1 is S_1 evaluated assuming $N = N_1 + N_2$ (N_1 is the number of clock ions and N_2 is the number of coolant ions) and Λ is defined by

$$\Lambda \equiv 1 - \frac{3 N_2}{2 N_1} \left[1 - \left(\frac{N_2}{N_1 + N_2} \right)^{2/3} \right]. \quad (12)$$

Fig. 4 plots S_2/S_1 as a function of N_2/N_1 , comparing the time-dilation shift in a two-species clock to that in a single-species clock with the same number of clock ions N_1 . In the regime $N_2/N_1 \gg 1$, we have $S_2/S_1 \simeq (5/6) \sqrt[3]{N_1/N_2}$. For a typical $N_2/N_1 \sim 10$, the time-dilation shift is about 60% smaller than in a single-species clock.

The design and realization of an ion frequency standard, of course, must take into account other considerations [12]. For instance, preliminary studies showed that the $^9\text{Be}^+$ hyperfine clock transition (303 MHz) has an unexpectedly large pressure shift $\{(-1.7 \pm 0.4) \times 10^{-5} \text{ Pa}^{-1} \text{ for CH}_4\}$ [3], [4]. For some ions, a cryogenic environment may be required to suppress this effect. Significant improvement in both frequency stability and accuracy also requires the ability to trap and laser-cool large numbers of ions, as well as to characterize and control the ion distribution for minimizing the time-dilation shift. Experiments

are underway in a new Penning trap [17] designed for these and other studies.

ACKNOWLEDGMENT

The authors thank A. Barton and S. Gilbert for carefully reading the manuscript.

REFERENCES

- [1] J. J. Bollinger, J. D. Prestage, W. M. Itano, and D. J. Wineland, "Laser-cooled-atomic frequency standard," *Phys. Rev. Lett.*, vol. 54, pp. 1000–1003, 1985.
- [2] J. J. Bollinger, D. J. Heinzen, W. M. Itano, S. L. Gilbert, and D. J. Wineland, "Test of the linearity of quantum mechanics by rf spectroscopy of the $^9\text{Be}^+$ ground state," *Phys. Rev. Lett.*, vol. 63, pp. 1031–1034, 1989.
- [3] ———, "A 303-MHz frequency standard based on trapped Be^+ ions," *IEEE Trans. Instrum. Meas.*, vol. 40, pp. 126–128, Apr. 1991.
- [4] D. J. Wineland, *et al.*, "Recent experiments on trapped ions at the National Institute of Standards and Technology," in E. Arimondo, W. D. Phillips, and F. Strumia, Ed. *Laser Manipulation of Atoms and Ions*. New York: North-Holland, 1992, pp. 553–567.
- [5] N. F. Ramsey, *Molecular Beams*. London: Oxford Univ. Press, 1956, p. 124.
- [6] W. M. Itano, J. C. Bergquist, J. J. Bollinger, J. M. Gilligan, D. J. Heinzen *et al.*, "Quantum projection noise: Population fluctuations in two-level systems," *Phys. Rev. A*, vol. 47, pp. 3554–3570, 1993.
- [7] D. J. Wineland, J. J. Bollinger, W. M. Itano, and D. J. Heinzen, "Squeezed atomic states and projection noise in spectroscopy," *Phys. Rev. A*, vol. 50, pp. 67–88, 1994.
- [8] J. N. Tan, J. J. Bollinger, and D. J. Wineland, "Experiments with large numbers of laser-cooled, trapped ions," *Bull. APS*, vol. 39, p. 1218, 1994.
- [9] L. S. Brown and G. Gabrielse, "Geonium theory: Physics of an electron or ion in a Penning trap," *Rev. Mod. Phys.*, vol. 58, no. 1, pp. 233–311, 1986.
- [10] L. R. Brewer, J. D. Prestage, J. J. Bollinger, W. M. Itano, D. J. Larson, and D. J. Wineland, "Static properties of a non-neutral $^9\text{Be}^+$ -ion plasma," *Phys. Rev. A*, vol. 38, pp. 859–873, 1988.
- [11] J. J. Bollinger, D. J. Heinzen, F. L. Moore, W. M. Itano, D. J. Wineland, and D. H. E. Dubin, "Electrostatic modes of ion-trap plasmas," *Phys. Rev. A*, vol. 48, pp. 525–545, 1993.
- [12] D. J. Wineland, J. C. Bergquist, J. J. Bollinger, W. M. Itano, D. J. Heinzen *et al.*, "Progress at NIST toward absolute frequency standards using stored ions," *IEEE Trans. Ultr. Fer. Freq. Control*, vol. 37, no. 6, pp. 515–523, 1990.
- [13] W. M. Itano and D. J. Wineland, "Frequency and time standards utilizing laser-cooled ions," *Bull. APS*, vol. 24, p. 1185, 1979; "Precision measurement of the ground-state hyperfine constant of $^{25}\text{Mg}^+$," *Phys. Rev. A*, vol. 24, p. 1364, 1981.
- [14] D. J. Larson, J. C. Bergquist, J. J. Bollinger, W. M. Itano, and D. J. Wineland, "Sympathetic cooling of trapped ions: A laser-cooled two-species nonneutral ion plasma," *Phys. Rev. Lett.*, vol. 57, pp. 70–74, 1986.
- [15] T. M. O'Neil, "Centrifugal separation of a multispecies pure ion plasma," *Phys. Fluids*, vol. 24, pp. 1447–1451, 1981.
- [16] J. J. Bollinger, *et al.*, "Ion trapping techniques: Laser cooling and sympathetic cooling," in E. H. Ottewitte and W. Kells, Ed., *Intense Positron Beams*. Singapore: World Scientific, 1988, pp. 63–73.
- [17] J. N. Tan, J. J. Bollinger, and D. J. Wineland, "A new Penning trap for laser-cooling large ion numbers," *Bull. APS*, vol. 38, p. 1972, 1993.

HIGH-MAGNETIC-FIELD CORRECTIONS TO CESIUM HYPERFINE STRUCTURE *

WAYNE M. ITANO

*Time and Frequency Division, National Institute of Standards and Technology,
Boulder, Colorado 80303, USA*

Corrections to the Breit-Rabi formula for the ground state of ^{133}Cs are calculated. For a recently proposed high-magnetic-field frequency standard, the corrections amount to a few parts in 10^{12} .

De Marchi has proposed a cesium atomic-beam frequency standard based on the ($M_F = -1$, $\Delta M_F = 0$) transition, at the magnetic field ($B \approx 82$ mT) where the derivative of the frequency with respect to B is zero,¹ and has carried out preliminary experiments.² In order for this to be a *primary* frequency standard, it is necessary to relate the measured frequency to that of the zero-field transition frequency ν_0 , which defines the SI unit of time. The Breit-Rabi formula predicts the frequency to be $\sqrt{15/16}\nu_0 = 8\,900\,727\,438.257$ Hz.¹ For higher accuracy, additional terms must be taken into account.

Three corrections to the Breit-Rabi formula have been measured for the ground-state hyperfine structure of rubidium by Larson and coworkers.³⁻⁵ These are the dipole diamagnetic shift, the quadrupole diamagnetic shift, and the hyperfine-assisted Zeeman shift. These terms have not yet been measured for cesium.

The dipole diamagnetic shift results from a cross term between the contact hyperfine interaction and the atomic diamagnetic interaction in second-order perturbation theory. This leads to a shift, proportional to B^2 , in the dipole hyperfine constant A . I evaluated the perturbation sum over states, including the continuum, by solving an inhomogeneous differential equation for the perturbed wavefunction. I used an empirical potential for the valence electron derived by Klapisch.⁶ The result is $\delta A/A = 5.46 \times 10^{-10} B^2$, where B is expressed in teslas. This leads to an increase in the ($M_F = -1$) field-independent transition frequency of 33 mHz. Previous calculations have been reported by Bender⁷ and by Ray *et al.*⁸ In order to check the method, I used Klapisch's potential to calculate $\delta A/A$ for rubidium. The result is 10% below the experimental value. I estimate an accuracy of around 20% for the present calculation in cesium.

The quadrupole diamagnetic shift results from a cross term between the nuclear quadrupole hyperfine interaction and the electronic diamagnetic interaction in second-order perturbation theory. The interaction is diagonal in M_I and M_J . The perturbation sum over states is the same one that appears in the calculation of the quadrupole shielding factor γ_∞ .⁴ Using the value $\gamma_\infty(\text{Cs}^+) = -86.8$,⁹ I obtain the result

$$\langle M_I, M_J | H_{\text{QD}} | M_I, M_J \rangle = -4.6 \times 10^{-5} B^2 \frac{[3M_I^2 - I(I+1)]}{I(2I-1)}. \quad (1)$$

The result is in hertz if B is expressed in teslas. A similar calculation for rubidium yields a coefficient in good agreement with experiment.⁴ For cesium, the estimate of the coefficient

*Work of the US government. Not subject to US copyright.

for the shift is probably accurate within around 30%. However, for the special case of the ($M_F = -1$) field-independent transition, the shift vanishes. The two states involved in the transition are $(|-1/2, -1/2\rangle \pm |-3/2, 1/2\rangle)/\sqrt{2}$, in the $|M_I, M_J\rangle$ basis, where $+$ refers to the higher-energy state and $-$ to the lower-energy state. Hence, the states are shifted by the same amount, since they have the same M_I -content.

The hyperfine-assisted Zeeman shift was explained by Fortson as a third-order perturbation, in which the contact hyperfine interaction acts twice and the electronic Zeeman interaction acts once.¹⁰ Fortson gave diagonal matrix elements in the $|M_I, M_J\rangle$ basis. For the ($M_F = -1$) field-independent transition, it is necessary to extend Fortson's calculation to include off-diagonal matrix elements. In the $|(IJ)F, M_F\rangle$ basis, the nonzero matrix elements for ^{133}Cs are

$$\langle 3, M_F | H_{\text{HAZ}} | 4, M_F \rangle = 4h\beta B \sqrt{16 - M_F^2}. \quad (2)$$

Fortson used quantum-defect theory to make a semi-empirical estimate for β in rubidium; it agreed with experiment within 10%. The same method, applied to cesium, yields $\beta = 88$ mHz/T. For the ($M_F = -1$) field-independent transition, the shift at $B = 82$ mT is $-2\sqrt{15}\beta B = -56$ mHz. This estimate of the shift is probably accurate within around 30%.

To achieve a theoretical error of 10^{-14} in the total frequency, which is the projected accuracy of the high-field frequency standard,¹ the larger shifts must be known within less than 1%. This could possibly be done by *ab initio* calculations or by experiments carried out at much higher magnetic field, similar to those of Larson and coworkers in rubidium.

Acknowledgments

This work was supported by the Office of Naval Research and the Army Research Office.

References

1. A. De Marchi, in *Proc. 7th European Frequency and Time Forum*, Neuchâtel, Switzerland, 1993, p. 541.
2. G. Costanzo, E. Rubiola, A. De Marchi, in *Proc. 9th European Frequency and Time Forum*, Besançon, France 1995 (in press).
3. N. P. Economou, S. J. Lipson, and D. J. Larson, *Phys. Rev. Lett.* **38**, 1394 (1977).
4. S. J. Lipson, G. D. Fletcher, and D. J. Larson, *Phys. Rev. Lett.* **57**, 567 (1986).
5. G. D. Fletcher, S. J. Lipson, and D. J. Larson, *Phys. Rev. Lett.* **58**, 2535 (1987).
6. M. Klapisch, *C. R. Acad. Sci. Paris* **265**, 914 (1967).
7. P. L. Bender, in *Quantum Electronics, Proceedings of the Third International Congress, Paris*, ed. P. Grivet and N. Bloembergen (Columbia Univ. Press, New York, 1964), p. 263.
8. S. N. Ray, M. Vajed-Samii, and T. P. Das, *Bull. Am. Phys. Soc.* **24**, 477 (1979).
9. H. M. Foley, R. M. Sternheimer, and D. Tycko, *Phys. Rev.* **93**, 734 (1954).
10. N. Fortson, *Phys. Rev. Lett.* **59**, 988 (1987).

APPLICATION OF LASER-COOLED IONS TO FREQUENCY STANDARDS AND METROLOGY*

D. J. Wineland, J. C. Bergquist, D. Berkeland, J. J. Bollinger, F. C. Cruz,
W. M. Itano, B. M. Jelenković, B. E. King, D. M. Meekhof,
J. D. Miller, C. Monroe, M. Rauner, and J. N. Tan
*National Institute of Standards and Technology, Time and Frequency Division
Boulder, CO, 80303
E-mail: dwineland@nist.gov*

ABSTRACT

With the first experiments on laser cooling, it was realized that a principal application of the technique would be to reduce Doppler shifts in frequency standards. Laser cooling is still thought to be essential to achieve uncertainty significantly smaller than 1 part in 10^{14} ; however, a number of other problems must be solved to achieve this goal with stored atomic ions. For both RF/microwave and optical frequency standards based on trapped ions, some of these problems are discussed. Laser cooling of trapped ions also appears to be important for other reasons in metrology. For example, for frequency standards, cooling to the zero-point of motion should enable the creation of quantum mechanically correlated states for improved signal-to-noise ratio in spectroscopy, or provide accurate measurement of Stark shifts. Cooling to the zero-point of motion also enables the creation of nonclassical states of motion or correlated states which may be applicable to sensitive detection, quantum computation, or to test quantum measurement principles. Techniques to achieve laser cooling to the zero-point of motion are briefly described.

1. Introduction

The first laser cooling experiments^{1,2} were accomplished on trapped ions in 1978. It was apparent then that one important application for laser cooling would be the reduction of the time-dilation (2nd-order-Doppler) shift in frequency standards. In fact by 1980, temperatures achieved from laser cooling on ions were low enough that the corresponding time-dilation shift was significantly below 1 part in 10^{16} . This is illustrated in Fig. 1, where we plot time-dilation shifts (shown as a fraction of the transition frequency) corresponding to temperatures reported in some laser cooling experiments. Since these shifts are significantly smaller than the smallest reported inaccuracies for atomic clocks, we can ask why the overall accuracies reported do not approach these numbers.

One source of the discrepancy is that, for trapped ions, laser cooling affects only the thermal or random modes of motion. However, ion motion in both Paul and Penning traps³⁻⁵ in part consists of unavoidable coherent motion; this motion can result in large ion velocities and accompanying Doppler shifts. In a Penning trap, a cloud of ions must rotate about the symmetry axis of the trap. The velocity associated with this rotation gives rise to a $\underline{v} \times \underline{B}$ Lorentz force which provides trapping normal to the symmetry axis. For large clouds, the velocity in this rotation motion can be significantly larger than the thermal velocity in the axial and cyclotron motions (which can be laser-cooled), thereby limiting the degree to which the time-dilation shift can

* Contribution of the U.S. Government; not subject to U.S. copyright.

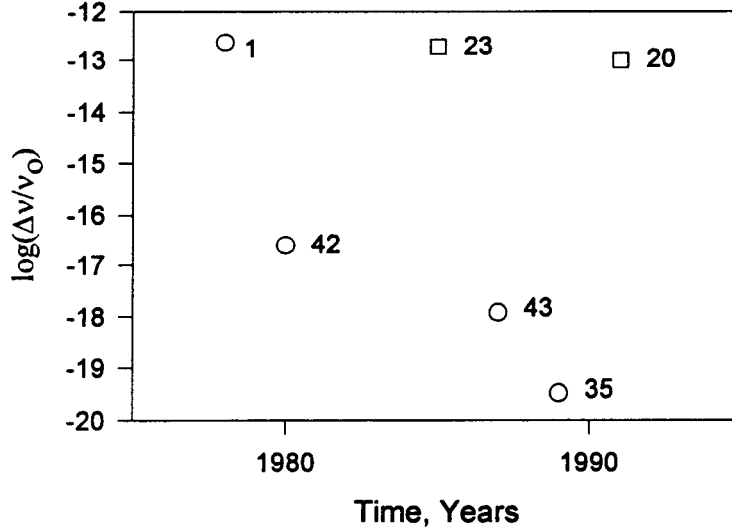


Fig. 1. The circles show magnitudes of calculated (fractional) time-dilation shifts $|\Delta\nu_{D2}/\nu_0|$ based on reported temperatures achieved in selected trapped-ion, laser cooling experiments. These calculations omit the contributions from the coherent modes of motion (see text). The squares show (fractional) uncertainties in trapped-ion, laser-cooled atomic frequency standard experiments in which overall errors were estimated. The numbers beside the symbols indicate the corresponding reference numbers.

be suppressed.⁶ In a Paul trap, ions are forced to oscillate at the driving field frequency (the micromotion). Since the driving fields are spatially inhomogeneous, the force on an ion, averaged over one cycle of the driving field, gives rise to trapping (the ponderomotive force). For ions near the outside of a large ion cloud this force must be large to balance the Coulomb repulsion from the ions near the center of the trap. This implies that the velocity of this coherently driven motion is large; it is often much larger⁶ than the velocity of the ions associated with their "secular" motion in the ponderomotive well (which can be laser-cooled).

In 1973, Dehmelt suggested storing a single ion in a Paul trap.⁷ This system has the advantage that the kinetic energy in the ion micromotion is approximately equal to the kinetic energy in the secular motion. Therefore, if the secular motion is laser-cooled, the time-dilation shift from secular motion and micromotion can be very small. On the other hand, a single-ion frequency standard may not give sufficient short-term frequency stability. For N ions, the frequency stability (two-sample Allan variance) is limited to^{6,8}

$$\sigma_y(\tau) = \frac{1}{\omega_0 \sqrt{NT\tau}}, \quad (1)$$

where ω_0 is the clock transition frequency, T is the transition interrogation time (the Ramsey method is assumed, where the time of the two Ramsey pulses is much less than the free-precession period T), τ is the averaging time, and we assume 100% detection efficiency. For a single-ion clock using RF or microwave transitions, this may imply a long averaging time to reach a measurement precision better than one part in 10^{14} . For example, for an ion with $\nu_0 = \omega_0/2\pi = 10$ GHz, and T = 10 s,

Eq. (1) implies $\sigma_y(\tau) \approx 5.0 \times 10^{-12} \tau^{-1/2}$. Therefore, in general, for both Penning and Paul trap RF/microwave frequency standards, where we desire large N to make $\sigma_y(\tau)$ sufficiently small, we require methods to minimize the velocity in the coherent modes of motion. Some strategies are discussed below.

If the velocity in the coherent motion can be suppressed sufficiently, Doppler cooling⁹ will suffice (at least for the next generation of frequency standards) to provide small enough time-dilation shifts for frequency standards. If we neglect the velocity in the coherent modes of motion, minimum temperatures achieved from Doppler cooling give rise to a time-dilation shift of $\Delta\nu_{D2}/\nu_0 = -3.3 \times 10^{-18} (\gamma/2\pi)/M$ where $\gamma/2\pi$ is the laser-cooling transition linewidth in megahertz and M is the ion mass in relative atomic mass units. For example, for $^{199}\text{Hg}^+$ ions ($\gamma/2\pi \approx 70$ MHz, $M = 199$ u), we could expect $\Delta\nu_{D2}/\nu_0 = -1.2 \times 10^{-18}$.

However, there now appear to be other reasons for achieving better laser cooling - in particular for reaching the zero-point energy state of motion. New applications are emerging for this extreme form of laser cooling, both for frequency standards and other forms of metrology. Some of these applications and methods to reach the zero-point energy through laser cooling are discussed below. Reference 10 provides a more comprehensive review of cooling methods in ion traps.

2. Reduction of the coherent motion (micromotion) in a Paul trap

One way to suppress the velocity in the micromotion and still achieve a large number of ions for good signal-to-noise ratio is to use an elongated "linear" trap geometry. In this type of trap, shown schematically in Fig. 2, the RF electric fields vanish along the axis of the trap. Therefore, if ions are confined near the trap axis in an elongated ion cloud geometry, the micromotion can be suppressed. This idea was first developed and used by Prestage et al.¹¹ In part, because of the relatively small time-dilation shift, excellent stabilities have been achieved in clocks where the ions' secular motion in a linear trap is cooled by buffer gas (see the contributions at this conference by Tjoelker et al. and Fisk et al.).

Dehmelt suggested applying this idea to frequency standards in its limiting form,¹² that is, where a single string of ions is confined to the trap axis like "beads on a string." Here, as for a single ion in a spherical quadrupole trap, the velocity of micromotion can be approximately the same as for the secular motion. With laser cooling, the time-dilation shifts can therefore be very small. At NIST, this idea is being pursued for application to a frequency standard of high accuracy. Strings of laser cooled $^{199}\text{Hg}^+$ ions have been obtained in a room temperature apparatus¹³ and in a cryogenic (4 K) apparatus¹⁴ whose good vacuum suppresses collisional frequency shifts and ion loss from chemical reactions. The bottom part of Fig. 2 shows an image of a string of laser cooled $^{199}\text{Hg}^+$ ions taken in this cryogenic apparatus. The Munich group has also achieved strings of laser-cooled (Mg^+) ions in a race-track-type trap¹⁵; this type of apparatus could also be used for frequency standard applications.

Another approach to suppress micromotion is to use arrays of conventional (spherical quadrupole) ion traps.^{16,17} Here, single laser-cooled ions could be stored in each trap thereby ensuring small time-dilation shifts. Important technical problems appear to be the loading, addressing, and detecting of the individual ions.

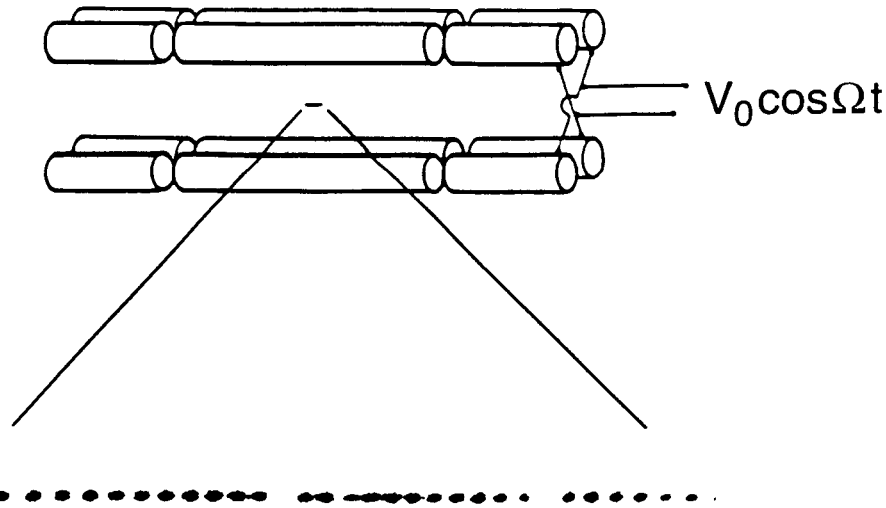


Fig. 2. The upper part of the figure shows a schematic diagram of the electrode configuration for a linear Paul-RF trap.¹³ Typical parameters for trapping $^{199}\text{Hg}^+$ ions are: rod-electrode separation of approximately 1 mm, $V_0 \approx 400$ V, and $\Omega/2\pi \approx 10$ MHz. The lower part of the figure shows an image of a string of $^{199}\text{Hg}^+$ ions, illuminated with 194 nm radiation, taken with a UV-sensitive, photon counting imaging tube. The spacing between adjacent ions is approximately 10 μm . The "gaps" in the string are occupied by impurity ions, most likely other isotopes of Hg^+ , which do not fluoresce because the frequencies of their resonant transitions do not coincide with the 194 nm $^2S_{1/2} \rightarrow ^2P_{1/2}$ transition of $^{199}\text{Hg}^+$.

3. Reduction of the coherent (rotation) motion in a Penning trap

Following the example of the linear or racetrack Paul traps, the coherent motion in a Penning trap could be suppressed by storing ions near the axis of the trap - ideally as a single string along the axis. A more modest approach might be the following. For a cloud of laser-cooled ions in a Penning trap, as the radius of the cloud is varied, the time-dilation shift goes through a minimum (see Ref. 18 and Tan, et al., this conference). Therefore if the cloud of ions is stabilized at this extremum point, the time-dilation shift and its fluctuations can be made very small.

Any configuration of ions in a Penning trap is in an unstable equilibrium (as opposed to a sample of ions in a Paul trap). Therefore, once created, the configuration would not be preserved if, for example, collisions are present. Torques from laser scattering could restore the configuration but at the expense of possible perturbing effects from the cooling laser.

4. Sympathetic laser cooling

One solution to the problems associated with Penning trap cloud stability is sympathetic laser cooling.¹⁹ As an example, in the laser-cooled frequency standard experiment reported in Ref. 20, a $^9\text{Be}^+$ ion sample was cooled sympathetically, through Coulomb coupling, by a simultaneously stored, surrounding cloud of Mg^+ ions which were directly laser-cooled. This method has the advantage that the laser cooling (and laser torques) can be applied continuously to the Mg^+ ions, thereby maintaining the geometry and temperature of the $^9\text{Be}^+$ ions. Because the frequency of

the Mg^+ optical cooling transition is significantly different than the optical transitions in $^9\text{Be}^+$, the $^9\text{Be}^+$ ions are not appreciably perturbed by the Mg^+ cooling laser beam. It should be possible to apply this technique to sympathetically cool a string of ions in a Penning trap or a cloud that is configured to give the minimum time-dilation shift.¹⁸

Sympathetic cooling might also be employed to advantage in a (linear) Paul trap. When long Ramsey interrogation times T are desired, the ions may heat from, for example, RF heating. However, in a long string of ions, cooling could be applied to ions on one end which then cool the "clock" ions sympathetically. In principle, the "cooling ions" could be of the same species if the string is long enough or, if the string is bent around a (light-baffled) corner or, if the clock ions are shielded by a coupling electrode²¹ to minimize the perturbing effects of scattered light from the cooling ions.

5. Laser-cooled, trapped-ion, optical frequency standards

Most researchers agree that, in the future, the most accurate and stable clocks will be made using optical or higher frequency transitions. From Eq. (1), if the clock transition frequency is high enough, then a single ion would give good short term stability. For example for the $^2S_{1/2} \rightarrow ^2D_{5/2}$ 282 nm transition in $^{199}\text{Hg}^+$, assuming $N = 1$, $T = 0.01$ s (the radiative lifetime of the $^2D_{5/2}$ level is approximately 0.1 s), Eq. (1) implies $\sigma_y(\tau) \approx 1.5 \times 10^{-15} \tau^{-1/2}$. As discussed above, the time-dilation shift could be very small. In addition, shorter interrogation times will mitigate the effects of various sources of ion heating, since clock cycles could be alternated with relatively frequent laser cooling. Work on optical frequency standards is represented by several groups at this conference; see, for example, the stored-ion contributions by Barwood, et al., Fermigier, et al., Gill, et al., Knoop, et al., Madej, et al., Nagourney, et al., Peik, et al., and Tamm and Engelke.

Currently, laser local oscillators are not as stable as desired. A representation of the state of the art for trapped-ion optical frequency standards is given in Ref. 22, where a laser with frequency bandwidth of less than 25 Hz (for 60 s averaging times) was locked to the 282 nm quadrupole transition in a single laser-cooled $^{199}\text{Hg}^+$ ion.

Finally, an additional technical difficulty for all optical frequency standards is that of comparing laser local oscillators to other oscillators (particularly oscillators at low frequency). Several approaches are discussed in these proceedings.

6. Present and future laser-cooled ion frequency standards

So far, there has been only one report of an ion-based, laser-cooled atomic frequency standard whose accuracy has been evaluated. In this experiment, laser-cooled $^9\text{Be}^+$ ions in Penning trap were used.²³ A second evaluation²⁰ of this system uncovered an unexpected background gas pressure shift. This shift was apparently caused, in part, by background methane gas, which has a strong perturbing effect on $^9\text{Be}^+$ ion hyperfine structure.²⁴ (Interestingly, methane does not have nearly as large a perturbing effect in the $^{171}\text{Yb}^+$ experiments reported by Bauch and Tamm at this conference.) At present, the inaccuracy of the laser-cooled $^9\text{Be}^+$ ion clock is limited to about one part in 10^{13} from this pressure shift.²⁰

Further work is required to minimize possible pressure shifts and a number of other typical systematic effects (for example, magnetic field shifts) present in all

frequency standards. However, we can be optimistic that frequency standards based on laser-cooled ions will eventually have inaccuracies considerably smaller than 1 part in 10^{14} , perhaps as small as 1 part in 10^{18} or less.^{6,25,26}

7. Applications of trapped ions which are laser-cooled to the zero-point of motion

Although Doppler cooling should yield sufficiently small time-dilation shifts for frequency standards, there now appear to be other reasons for achieving better laser cooling. At very low kinetic energies, the quantum nature of the motion becomes apparent; this quantized motion, particularly the zero-point state, can be used for various purposes.

For example, when inaccuracies of optical clocks become smaller than one part in 10^{15} , Stark shifts may become significant.²⁷ As Dehmelt has pointed out²⁵, the intercombination transitions in group IIIA ions are superior in this regard, although for various technical reasons, optical quadrupole $S \rightarrow D$ transitions in other ions can be easier to implement. The quadratic Stark shifts on these latter transitions depend on the kinetic energy of the ions. Since the secular motion is quantized, the quadratic Stark shift from the secular motion becomes quantized. This could be used to identify the zero-point energy states of the ion²⁷ or, conversely, the Stark shift could be calibrated from its discrete spectrum caused by quantized motion.

Another possible frequency standard application of zero-point cooling is to improve the quantum-limited signal-to-noise ratio in the detection process (see Ref. 28 and Bollinger, et al., this conference). If spectroscopy is performed on atoms which are first prepared in particular quantum mechanically correlated, or entangled, states, the frequency stability would be given by $\sigma_y(\tau) = 1/(\omega_0 N(T\tau)^{1/2})$ rather than that given by Eq. (1). In this case, the time to reach a desired measurement precision would be reduced in proportion to $1/N$.

Outside the realm of frequency standards, there may be other metrological applications of ions which are laser-cooled to the zero-point of motion. Cirac and Zoller have recently suggested a very interesting scheme to perform quantum computation using an array of ions confined in a linear trap.²⁹ Quantum computers have received attention lately because of their ability to crack the most common form of public-key encryption. The first quantum logic gates using prepared input "qubits" have now been realized using trapped ions which are first cooled to the zero-point energy.³⁰ A second possible application might be to the generation of multiparticle "EPR"-type correlated states which would be interesting from the standpoint of quantum measurement theory.³¹ Finally, if a single ion or single mode of oscillation is cooled to the zero-point state, it is possible to generate nonclassical states of motion such as squeezed states^{21,28,32,33} (see also Blatt et al., this conference). Such states may be useful for sensitive detection, for example, mass spectroscopy at the quantum level²¹. In all of these applications, efficient cooling to the zero-point of motion is a crucial prerequisite.

8. Methods for zero-point laser cooling

With the use of Doppler cooling,⁹ minimum energies for a bound atom in one dimension are approximately equal to $\hbar\gamma/2$, where $2\pi\hbar$ is Planck's constant and γ is the natural linewidth of the cooling transition. For an atom bound in a harmonic well

with "vibrational" frequency ω_v , this energy can be expressed as $\hbar\omega_v(\langle n_v \rangle + 1/2)$ where n_v is the harmonic oscillator quantum number. Since Doppler cooling is valid in the regime where $\gamma \gg \omega_v$, limiting kinetic energies for Doppler cooling necessarily imply $\langle n_v \rangle \gg 1$.

When $\omega_v \gg \gamma$, cooling can be achieved in the "resolved sideband" regime.³⁴ Consider a two-level atom characterized by resonant transition frequency ω_0 and radiative linewidth γ . If a laser beam (frequency ω_L) is incident along the direction of the atomic motion, the absorption spectrum is composed of a "carrier" at frequency ω_0 and resolved frequency-modulation sidebands spaced by ω_v which are generated from the Doppler effect. Cooling occurs if the laser is tuned to a lower sideband, for example, at $\omega_L = \omega_0 - \omega_v$. In this case, photons of energy $\hbar(\omega_0 - \omega_v)$ are absorbed and spontaneously emitted photons of average energy $\hbar\omega_0$ return the atom to its ground internal state (assuming that $\hbar\omega_v$ is much greater than the photon recoil energy). Therefore, the atom's kinetic energy is reduced by $\hbar\omega_v$ per scattering event. Cooling proceeds until the atom's mean vibrational quantum number in the harmonic well is given by^{2,9} $\langle n_v \rangle_{\min} \approx (\gamma/2\omega_v)^2 \ll 1$. Two experiments on single ions have reported laser cooling to the zero-point of motion.^{35,36} In Ref. 36, resolved-sideband stimulated Raman transitions replaced single photon transitions; cooling to the zero-point of motion was achieved 98% of the time in 1-D and 92% of the time in 3-D. Before correlated states between ions can be obtained, zero-point cooling must be extended to certain modes (such as the center-of-mass oscillation) on collections of $N (\geq 2)$ ions.

Dramatic advances in laser cooling of neutral atoms were made with the introduction of polarization-gradient and Sisyphus cooling.³⁷ Because of this success, it was interesting to investigate whether or not these methods would yield $\langle n_v \rangle \approx 0$ for bound atoms. Theoretical investigations have shown that particular applications of Sisyphus cooling or polarization-gradient cooling^{38,39,40} to trapped atoms appear to give cooling near $\langle n \rangle \approx 1$, but not $\langle n \rangle \rightarrow 0$. More recently, it has been suggested that ions in the $n = 0$ state could be selected from a distribution by null detection.⁴¹ Other discussions of laser cooling appear in the contributions to this conference by Knoop et al., Sugiyama and Yoda, and Alekseev and Krylova.

9. Summary

Laser cooling, which can suppress time-dilation shifts, appears to be essential to achieve high accuracy in atomic frequency standards. However, before the benefits of laser cooling can be realized with trapped ions, the velocity in the coherent or nonthermal modes of motion must be suppressed. We have discussed several approaches which address this problem. It also appears that laser cooling may have other benefits in metrology. We have pointed out the application of zero-point laser cooling to the generation of correlated states for improved signal-to-noise ratio in spectroscopy, fundamental quantum measurements and quantum computation.

10. Acknowledgements

We gratefully acknowledge the support of the U.S. Office of Naval Research and the U.S. Army Research Office. We thank D. Howe, D. Lee, J. Kitching, and M. Young for helpful comments on the manuscript.

11. References:

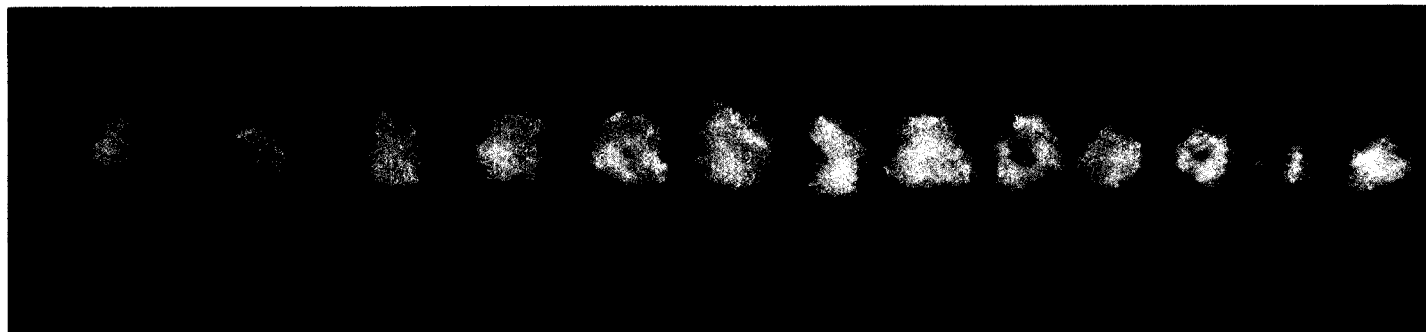
1. D.J. Wineland, R.E. Drullinger, and F.L. Walls, Phys. Rev. Lett. 40, 1639 (1978).
2. Neuhauser, M. Hohenstatt, P. Toschek, and H. Dehmelt, Phys. Rev. Lett. 41, 233 (1978).
3. H.G. Dehmelt, Adv. At. Mol. Phys. 3, 53 (1967) and 5, 109 (1969).
4. D.J. Wineland, Wayne M. Itano, and R.S. VanDyck, Jr., Adv. At. Mol. Phys. 19, 135 (1983).
5. R. C. Thompson, Adv. At. Mol. Phys. 31, 253 (1993).
6. D. J. Wineland, J. C. Bergquist, J. J. Bollinger, W. M. Itano, D. J. Heinzen, S. L. Gilbert, C. H. Manney, and M. G. Raizen, IEEE Trans. on Ultrasonics, Ferroelectrics, and Frequency Control 37, 515 (1990).
7. H.G. Dehmelt, Bull. Am. Phys. Soc. 18, 1521 (1973).
8. W. M. Itano, J. C. Bergquist, J. J. Bollinger, J. M. Gilligan, D. J. Heinzen, F. L. Moore, M. G. Raizen, and D. J. Wineland, Phys. Rev. A47, 3554 (1993).
9. see, for example: D.J. Wineland and W.M. Itano, Physics Today, vol. 40, no. 6, p. 34 (1987).
10. W. M. Itano, J. C. Bergquist, J. J. Bollinger, and D. J. Wineland, Proceedings of the Nobel Symposium on Trapped Charged Particles and Related Fundamental Physics, Lysekil, Sweden, August, '94, to be published in Physica Scripta.
11. J. Prestage, G. J. Dick and L. Maleki, J. Applied Physics, 66, 1013 (1989); J. D. Prestage, G. J. Dick, and L. Maleki, IEEE Trans. Instrum. and Meas. 40, 132 (1991).
12. H. G. Dehmelt, in *Frequency Standards and Metrology*, Proc. 4th Symposium, ed. by A. DeMarchi, Ancona, Italy (Springer-Verlag, Berlin, Heidelberg, 1989) p. 286.
13. M. G. Raizen, J. M. Gilligan, J. C. Bergquist, W. M. Itano, and D. J. Wineland, Phys. Rev. A45, 6493 (1992).
14. M. E. Poitzsch, J. C. Bergquist, W. M. Itano, and D. J. Wineland, Proc. 1994 IEEE International Frequency Control Symposium, p. 744, June, 1994; J. Miller, M. E. Poitzsch, F. C. Cruz, D. J. Berkeland, J. C. Bergquist, W. M. Itano. and D. J. Wineland, 1995 IEEE International Frequency Control Symposium, June, 1995.
15. G. Birkl, S. Kassner, and H. Walther, Nature 357, 310 (1992).
16. F. Major, J. Phys. Lett. 38, L221 (1977).
17. R. Brewer, R. G. DeVoe, and R. Kallenbach, Phys. Rev. A46, R6781 (1992).
18. J. N. Tan, J. J. Bollinger, and D. J. Wineland, Proc. Conf. Prec. Electromagnetic Meas., Boulder, CO, June, 1994; IEEE Transactions on Instrumentation and Measurement 44, 144 (1995).
19. D.J. Larson, J.C. Bergquist, J.J. Bollinger, W.M. Itano, and D.J. Wineland, Phys. Rev. Lett. 57, 70 (1986).
20. J. J. Bollinger, D. J. Heinzen, W. M. Itano, S. L. Gilbert, and D. J. Wineland, IEEE Trans. on Instrum. and Measurement 40, 126 (1991).
21. D. J. Heinzen and D. J. Wineland, Phys. Rev. A42, 2977 (1990).
22. J. C. Bergquist, W. M. Itano, and D. J. Wineland, in *Frontiers in Laser Spectroscopy*, proc. International School of Physics << Enrico Fermi >>, Course

- CXX, ed. by T. W. Hänsch and M. Inguscio, (North Holland, Amsterdam, 1994), pp. 359 - 376.
23. J. J. Bollinger, J.D. Prestage, W.M. Itano, and D.J. Wineland, *Phys. Rev. Lett.* **54**, 1000-1003 (1985).
 24. D. J. Wineland, J. C. Bergquist, J. J. Bollinger, W. M. Itano, F. L. Moore, J. M. Gilligan, M. G. Raizen, D. J. Heinzen, C. S. Weimer, and C. H. Manney, in *Laser Manipulation of Atoms and Ions*, ed. by E. Arimondo, W. D. Phillips, and F. Strumia (North-Holland, Amsterdam, 1992), pp. 553-567.
 25. H. Dehmelt, in *Frequency Standards and Metrology*, Proc. 4th Symposium, ed. by A. DeMarchi, Ancona, Italy (Springer-Verlag, Berlin, Heidelberg) p.15.
 26. D.J. Wineland, W.M. Itano, J.C. Bergquist and R.G. Hulet, *Phys. Rev.* **A36**, 2220 (1987).
 27. N. Yu, X. Zhao, H. Dehmelt, and W. Nagourney, *Phys. Rev.* **A50**, 2738 (1994).
 28. D. J. Wineland, J. J. Bollinger, W. M. Itano, and D. J. Heinzen, *Phys. Rev.* **A50**, 67 (1994).
 29. J. I. Cirac and P. Zoller, *Phys. Rev. Lett.* **74**, 4091 (1995).
 30. C. Monroe, D. M. Meekhof, B. E. King, W. M. Itano, and D. J. Wineland, *Phys. Rev. Lett.* **75**, 4714-4717 (1995).
 31. D. M. Greenberger, M. A. Horne, and A. Zeilinger, *Phys. Today* **46**(8), 22 (1993).
 32. J. I. Cirac, A. S. Parkins, R. Blatt, and P. Zoller, *Phys. Rev. Lett.* **70**, 556 (1993); J. I. Cirac, R. Blatt, A. S. Parkins, and P. Zoller, *Phys. Rev. Lett.* **70**, 762 (1993).
 33. D. M. Meekhof, C. Monroe, B. King, W. M. Itano, D. J. Wineland, submitted.
 34. D. J. Wineland and H. G. Dehmelt, *Bull. Am. Phys. Soc.* **20**, 637 (1975).
 35. F. Diedrich, J.C. Bergquist, W. M. Itano, and D.J. Wineland, *Phys. Rev. Lett.* **62**, 403 (1989).
 36. C. Monroe, D. M. Meekhof, B. E. King, S. R. Jefferts, W. M. Itano, D. J. Wineland, and P. Gould, *Phys. Rev. Lett.* **75**, 4011-4104 (1995).
 37. see, for example, C. Cohen-Tannoudji and W. D. Phillips, *Phys. Today* **43**(10), 33 (1990).
 38. D. J. Wineland, J. Dalibard, and C. Cohen-Tannoudji, *J. Opt. Soc. Am.* **B9**, 32 (1992).
 39. J. I. Cirac, R. Blatt, A. S. Parkins, and P. Zoller, *Phys. Rev.* **A48**, 1434 (1993).
 40. S. M. Yoo and J. Javanainen, *Phys. Rev.* **A48**, R30 (1993); J. Javanainen and S. M. Yoo, *Phys. Rev.* **A48**, 3776 (1993).
 41. J. Eschner, B. Appasamy, and P. E. Toschek, *Phys. Rev. Lett.* **74**, 2435 (1995).
 42. W. Neuhauser, M. Hohenstatt, P. E. Toschek, and H. Dehmelt, *Phys. Rev.* **A22**, 1137 (1980).
 43. J.C. Bergquist, W.M. Itano and D.J. Wineland, *Phys. Rev.* **A36**, 428 (1987).

Accurate Measurement of Time

Increasingly accurate clocks—now losing no more than a second over millions of years—are leading to such advances as refined tests of relativity and improved navigation systems

by Wayne M. Itano and Norman F. Ramsey



Few people complain about the accuracy of modern clocks, even if they appear to run more quickly than the harried among us would like. The common and inexpensive quartz-crystal watches lose or gain about a second a week—making them more than sufficient for everyday living. Even a spring-wound watch can get us to the church on time. More rigorous applications, such as communications with interplanetary spacecraft or the tracking of ships and airplanes from satellites, rely on atomic clocks, which lose no more than a second over one million years.

WAYNE M. ITANO and NORMAN F. RAMSEY have collaborated many times before writing this article: Itano earned his Ph.D. at Harvard University under the direction of Ramsey. Itano, a physicist at the Time and Frequency Division of the National Institute of Standards and Technology in Boulder, Colo., concentrates on the laser trapping and cooling of ions and conducts novel experiments in quantum mechanics. He is also an amateur paleontologist and fossil collector. Ramsey, a professor of physics at Harvard, earned his Ph.D. from Columbia University. He has also received degrees from the University of Oxford and the University of Cambridge, as well as several honorary degrees. A recipient of numerous awards and prizes, Ramsey achieved the highest honor in 1989, when he shared the Nobel Prize in Physics for his work on the separated oscillatory field method and on the atomic hydrogen maser.

There might not seem to be much room for the improvement of clocks or even a need for more accurate ones. Yet many applications in science and technology demand all the precision that the best clocks can muster, and sometimes more. For instance, some pulsars (stars that emit electromagnetic radiation in periodic bursts) may in certain respects be more stable than current clocks. Such objects may not be accurately timed. Meticulous tests of relativity and other fundamental concepts may need even more accurate clocks. Such clocks will probably become available. New technologies, relying on the trapping and cooling of atoms and ions, offer every reason to believe that clocks can be 1,000 times more precise than existing ones. If history is any guide, these future clocks may show that what is thought to be constant and immutable may on finer scales be dynamic and changing. The sundials, water clocks and pendulum clocks of the past, for example, were sufficiently accurate to divide the day into hours, minutes and seconds, but they could not detect the variations in the earth's rotation and revolution.

A clock's accuracy depends on the regularity of some kind of periodic motion. A grandfather clock relies on the sweeping oscillation of its pendulum. The arm is coupled to a device called an escapement, which strikes the teeth of a gear in such a way that the gear moves in only one direc-

tion. This gear, usually through a series of additional gears, transfers the motion to the hands of the clock. Efforts to improve clocks are directed for the most part toward finding systems in which the oscillations are highly stable.

The three most important gauges of frequency standards are stability, reproducibility and accuracy. Stability is a measure of how well the frequency remains constant. It depends on the length of an observed interval. The change in frequency of a given standard might be a mere one part per 100 billion from one second to the next, but it may be larger—say, one part per 10 billion—from one year to the next. Reproducibility refers to the ability of independent devices of the same design to produce the same value. Accuracy is a measure of the degree to which the clock replicates a defined interval of time, such as one second.

Until the early 20th century, the most accurate clocks were based on the regularity of pendulum motions. Galileo had noted this property of the pendulum after he observed how the period of oscillation was approximately independent of the amplitude. In other words, a pendulum completes one cycle in about the same amount of time, no matter how big each sweep is. Pendulum clocks became possible only after the mid-1600s, when the Dutch scientist Christiaan Huygens invented an escapement to keep the pendulum swinging. Later chronometers used the oscillations of balance wheels attached



TRAPPED MERCURY IONS, separated by about 10 microns, fluoresce under illumination by ultraviolet light (*photograph*). The ions are held by oscillating electric fields generated by electrodes (*cutaway diagram*). Static electric potentials (*not shown*) prevent the ions from escaping through the ends of the trap. Strings of trapped ions may lead to new timing devices more stable than conventional atomic clocks.

to springs. These devices had the advantage of being portable.

Considerable ingenuity went into improving the precision of pendulum and balance-wheel clocks. Clockmakers would compensate for temperature changes by combining materials with different rates of thermal expansion. A more radical approach came in the 1920s, when William H. Shortt, a British engineer, devised a clock in which a "slave pendulum" was synchronized to a "free pendulum." The free pendulum oscillates in a low-pressure environment and does not have to operate any clock mechanism. Instead it actuates an electrical switch that helps to keep the slave pendulum synchronized. As a result, the period of the Shortt clock is extremely stable. These clocks had an error of a few seconds in a year (about one part per 10 million) and became the reference used in laboratories.

The next major advance in timekeeping was based on the development of quartz-crystal electronic oscillators. The frequency of such devices depends on the period of the elastic vibration of a carefully cut quartz crystal. The vibrations are electronically maintained through a property of such crystals called piezoelectricity. A mechanical strain on the crystal produces a low electric voltage; inversely, a voltage induces a small strain.

The quartz vibrates at a frequency that depends on the shape and dimensions of the crystal. In some wristwatches, it is cut into the shape of a

tuning fork a few millimeters long. In other timepieces, it is a flat wafer. The quartz is connected to an electric circuit that produces an alternating current. The electrical feedback from the quartz causes the frequency of the circuit to match the frequency at which the crystal naturally vibrates (usually 32,768 hertz). The alternating current from the circuit goes to a frequency divider, a digital electronic device that generates one output pulse for a fixed number of input pulses. The divider also actuates either a mechanical or digital electronic display.

In the late 1920s Joseph W. Horton and Warren A. Marrison, then at Bell Laboratories, made the first clock based on a quartz-crystal oscillator. In the 1940s quartz-crystal clocks replaced Shortt pendulum clocks as primary laboratory standards. These clocks were stable to about 0.1 millisecond per day (about one part per billion). Relatively inexpensive, quartz clocks continue to be extensively used. The timekeeping elements of common quartz watches and clocks are simplified and miniaturized versions of quartz frequency standards. Quartz wristwatches became common once the ability emerged to cut the quartz into thin, tuning-fork shapes reliably and to manufacture miniature, low-power digital electronic components.

Yet quartz-crystal clocks prove inadequate for many scientific applications, such as tests of relativity. According to Albert Einstein's calculations, gravity distorts both space and time. The differ-

ence in gravitational potential causes time to pass more quickly high in the atmosphere than it does on the surface. The difference is slight. Time runs about 30 millionths of a second per year faster at the top of Mount Everest than it does at sea level. Only atomic frequency standards achieve the requisite precision.

The quantized energy levels in atoms and molecules provide the physical basis for atomic frequency standards. The laws of quantum mechanics dictate that the energies of a bound system, such as an atom, have certain discrete values. An electromagnetic field can boost an atom from one energy level to a higher one. The process can also work in reverse. If the atom is in a high energy level, it can drop to a lower level by emitting electromagnetic energy.

The maximum amount of energy is absorbed or emitted at a definite frequency—the resonance frequency, or the difference between the two energy levels divided by Planck's constant. This value is sometimes called the Bohr frequency. Such frequencies make ideal time standards because they are extremely stable. Time can be kept by observing the frequencies at which electromagnetic energy is emitted or absorbed by the atoms. In essence, the atom serves as the master pendulum whose oscillations are counted to mark the passage of time.

Although we have described general quantum properties, the effects exploit-

ed in atomic clocks are slightly more complicated. In most atomic clocks the energy that atoms absorb or release actually results from transitions between so-called hyperfine energy levels. These levels exist because of an intrinsic property of particles known as the magnetic moment. Electrons and the nuclei of most atoms spin about their axes as if they were tops. In addition, they are magnetized, like compass needles oriented along their axes of rotation. These axes can have different orientations with respect to one another, and the energies of the orientations may differ.



These positions correspond to the hyperfine levels. The nomenclature comes about because the levels were first observed in spectroscopy as small splittings of spectral lines.

On paper, standards based on atomic processes are ideal. In practice, perfection is elusive. Atoms do not absorb or emit energy precisely at the resonance frequency. Some energy is spread over a small interval surrounding the frequency—a smearing of frequencies, so to speak. All else being equal, the precision to which the resonance frequency can be measured is inversely proportional to this smearing. The greater the spread, the less precise the measurement. The spread is often expressed in terms of the quality factor, or Q , which is equal to the resonance frequency divided by the frequency spread. In many cases, the higher the resonance frequency, the higher the Q . Furthermore, smearing is often inversely proportional to the time the atom is in the apparatus. In those situations, the Q of the resonance, and hence the precision of the measurement, increases as the measuring time increases.

The motions of the atoms also introduce uncertainty by causing apparent shifts in the resonance frequencies. Such changes appear because of the Doppler effect. The phenomenon can be divided into first- and second-order shifts if the atoms are moving much slower than the speed of light. The first-order Doppler shift is an apparent change in the frequency of the applied electromagnetic wave as seen by a moving atom. The amount of the shift is proportional to the velocity of the atom. If the atom moves in the same direction as the wave does, the shift is to a lower frequency. If the atom's motion is opposed to that of the wave, the shift is to a higher frequency. If the directions are perpendicular, the first-order shift is zero.

The second-order Doppler shift comes about as a consequence of time dilation. According to relativity, time slows down for objects in motion; a moving atom "sees" a slightly different frequency than does a stationary counterpart. The effect on the resonance frequency is usually much smaller than the first-order shift. The second-order shift is proportional to the square of the atomic velocity and does not depend on the relative directions of the atom-

MASTER PENDULUM of this 1920s Short clock oscillates in an evacuated enclosure. It actuates an electrical switch to synchronize a slave pendulum, which drives the clock mechanism.

ic motion and the electromagnetic wave.

Several other factors affect the quality of the information. Atoms in the system may collide with one another; the impacts add noise to the signal. The surrounding environment can perturb the resonance frequencies. Defects in the electronic equipment, stray electromagnetic fields and the ever present thermal radiation all introduce errors. Therefore, a good atomic frequency standard not only must establish a steady, periodic signal but also must minimize these potential errors.

One of the earliest and now widely used methods to sidestep many of these difficulties is called atomic beam resonance, pioneered by I. I. Rabi and his colleagues at Columbia University in the 1930s. The atoms emerge from a small chamber, exit through a narrow aperture and then travel as a beam. The entire instrument can be shielded from stray magnetic and electric fields and insulated from external sources of heat. Perhaps more important, collisions of atoms are virtually eliminated, because the entire device is housed in a long, evacuated chamber. The pressure in the chamber is so low that the atoms are unlikely to strike anything before reaching the other end.

In simplified form, atomic beam resonance involves three steps. The first is to select only those atoms in the appropriate energy level. This selection is accomplished by using a specially shaped magnetic field, which acts as a kind of filter. It allows atoms in one energy level to pass and blocks all others by bending the beam. Only atoms in the correct energy level are bent the correct amount to reach and pass through the aperture that serves as the entrance to the cavity.

The second and crucial step is to send the selected atoms into another energy level. The task is accomplished by passing the atoms through an oscillating microwave field inside a cavity. The atoms will go to another energy level only if the frequency of the applied oscillating microwaves matches their Bohr frequency.

The third step is to detect those atoms that have changed energy levels. At this point, the beam of atoms passes through another magnetic field filter, which allows only atoms in the correct energy level to strike a detector that records the atoms as current flow. An abundance of such atoms will exist if the frequency of the applied oscillating microwaves precisely matches their natural frequency. If the frequency of the applied microwave field is off the mark, fewer atoms change their energy

levels, and so fewer will strike the detector. One knows, therefore, that the applied microwaves match the natural frequency of the atoms if the number of atoms striking the detector is maximal. An electronic feedback mechanism, called a servo loop, keeps this value constant. If it finds that the current from the detector is falling off, it changes the frequency of the applied field until the current reaches a maximum again.

By keeping the current from the detector at a maximum, the servo loop maintains the frequency of the applied microwave field at the natural frequency of the atoms. To measure time, one couples the applied field to a frequency divider, which generates timing pulses. By analogy, the atoms represent the quartz crystal in a watch or the master pendulum in a Shortt clock. The applied microwave field is the oscillating circuit or the slave pendulum, which actually drives the clock mechanism.

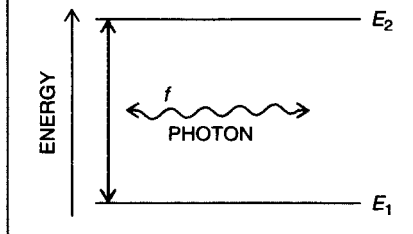
Minor variations of the atomic beam standard exist. For example, in some devices the atoms that undergo a change in energy level are made to miss, rather than strike, the detector. Not much difference in accuracy exists, however. Rather all the versions to some extent represent trade-offs in terms of size, cost and complexity.

A more important modification of the atomic beam came in 1949, when one of us (Ramsey) invented the so-called separated oscillatory field method. Instead of irradiating the atoms with a single applied field, this technique relies on two fields, separated by some distance along the beam path. Applying the oscillating field in two steps has many benefits, including a narrowing of the resonance and the elimination of the first-order Doppler shift. Jerrold R. Zacharias of the Massachusetts Institute of Technology and Louis Essen and John V. L. Parry of the National Physical Laboratory in Teddington, England, adapted this method to working frequency standards in the mid-1950s.

Currently the separated oscillatory field method provides the most reproducible clocks. The best ones are located at a few national laboratories, although smaller and less accurate versions are commercially available. The clocks rely on cesium, which has several advantages over other elements. It has a relatively high resonance frequency—about 9,192 megahertz—and low resonance width, which lead to an excellent Q . Cesium can also be detected readily and efficiently; all that is needed is a hot metal filament. When a cesium atom strikes the filament, it ionizes and becomes observable as electric current.

Resonance Frequency

Atomic frequency standards depend on the quantization of the internal energies of atoms or molecules. A pair of such energy levels, shown here as levels E_1 and E_2 , is associated with an atomic resonance. The resonance frequency f , at which it absorbs or emits electromagnetic radiation, is $f = (E_2 - E_1)/h$, where h is Planck's constant. The radiation, however, is not precisely f but instead is spread over a range near f , called Δf . The precision to which f can be measured is proportional to the quality factor, Q , defined by $Q = f/\Delta f$. The higher the Q , the more stable the clock.



The Q s of these standards are about 100 million, exceeding the Q of quartz wristwatches by a factor of several thousand. The greatest reproducibilities are about a part per 10^{14} . The best cesium frequency standards are so much more reproducible than the rate of rotation and revolution of the earth that in 1967 the second was defined as 9,192,631,770 periods of the resonance frequency of the cesium 133 atom.

One of the most promising improvements in cesium atomic-beam standards is the use of optical pumping to select the atomic states. Beginning in the 1950s optical-pumping techniques were developed by Francis Bitter of M.I.T., Alfred Kastler and Jean Brossel of the École Normale Supérieure and others. In this method, light, rather than a magnetic field, selects atoms in the desired states. Before the atoms are subjected to the microwave field, radiation from a laser is used to drive (or pump) the atoms from one energy level into another. In fact, one can control the number of atoms in energy levels by tuning the frequency of the light.

After the atoms have been irradiated by the microwave field, they pass through a second light beam. Only atoms occupying the correct energy level absorb this light, which they quickly re-

emit. A light-sensitive detector records the reemissions and converts them into a measurable current. As in atomic beam resonance that relies on magnetic selection, one knows that the applied microwave field matches the natural frequency of the atoms if the current from the detector is at a maximum.

Using light instead of magnets has many advantages. Perhaps the most crucial is that, with the right optical-pumping techniques, all the atoms in the beam can be put into the desired energy level. Magnetic selection merely filters out those that are in the other energy levels. Hence, the signal strength from optical pumping is much higher than it is from magnetic selection. Researchers at various laboratories are developing optically pumped cesium atomic-beam clocks. One such clock, at the National Institute of Standards and Technology (NIST) in Boulder, Colo., has recently become the primary frequency standard for the U.S. Designated NIST-7, it has an expected error of one second in about one million years, making it many times more stable than its predecessor.

There is an optically pumped atomic clock that is available commercially. Such a clock is based on the 6,835-megahertz, hyperfine resonance of rubidium 87. Rather than moving through the apparatus as a beam, the rubidium atoms are contained in a glass cell. The cell also houses a mixture of gases that prevents the rubidium atoms from colliding with the cell walls. A discharge lamp containing rubidium vapor, rather than a laser, irradiates the atoms. A photovoltaic sensor on the opposite side of the cell detects changes in the amount of light absorbed by the atoms. The atoms are prepared, the microwaves applied and the light detected in one cell. As a result, rubidium clocks can be made to fit in a cube about 10 centimeters on a side. In contrast, cesium beam clocks can extend from about 50 centimeters to more than five meters. Rubidium clocks are also much less expensive than are cesium ones.

The drawback is that the rubidium devices are generally less accurate and less reproducible. The Q of rubidium standards is about 10 million, a factor of 10 less than the cesium beam's quality factor; their reproducibility is only about a part per 10^{10} . Shifts in the resonance frequency mostly account for the poor reproducibility. The frequent collisions of the rubidium atoms with other gas molecules cause the shifts. But the rubidium standards' short-term stabilities are good—in fact, better than those of some cesium atomic beams.

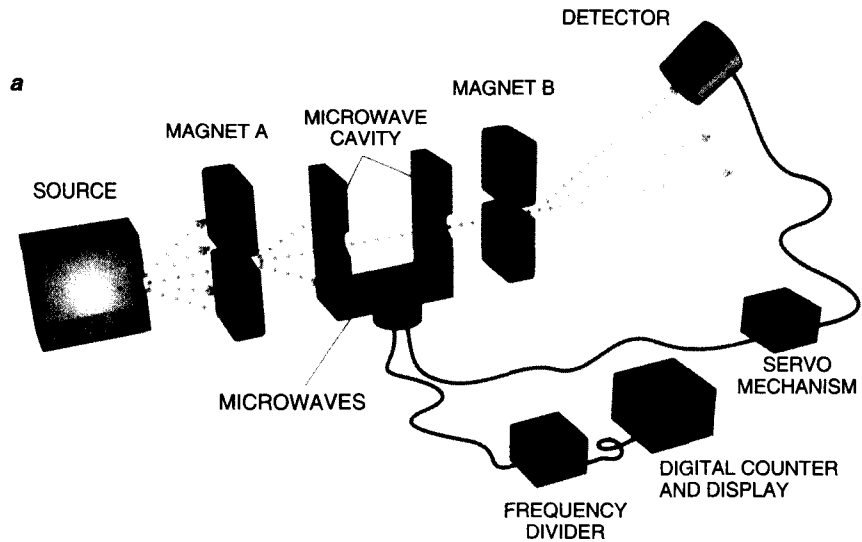
The atomic clocks described thus far work in a rather roundabout way—by

detecting a change in some signal, such as the number of atoms striking a detector, as the frequency of the applied oscillatory field shifts. One way to make use of the radiation emitted by the atoms more directly relies on the principle of the maser (an acronym for microwave amplification by stimulated emission of radiation). In 1953 Charles H. Townes and his associates at Columbia invented the first maser, which was based on ammonia. Beginning in 1960, Ramsey, Daniel Kleppner, now at M.I.T., H. Mark Goldenberg, then at Harvard University, and Robert F. C. Vessot, now at the Harvard-Smithsonian Center for Astrophysics, developed the atomic hydrogen maser, the only type that has been used extensively as an atomic clock.

In this instrument, a radio frequency discharge first splits hydrogen molecules held in a high-pressure bottle into their constituent atoms. The atoms emerge from a small opening in the bottle, forming a beam. Those in the higher energy level are focused by magnetic fields and enter a specially coated storage bulb surrounded by a tuned, resonant cavity.

In the bulb, some of these atoms will drop to a lower energy level, releasing photons of microwave frequency. The photons will stimulate other atoms to fall to a lower energy level, which in turn releases additional microwave photons. In this manner, a self-sustaining microwave field builds up in the bulb—thus the name “maser.” The tuned cavity around the bulb helps to redirect photons back into the system to maintain the stimulated emission process. The maser oscillation persists as long as the hydrogen is fed into the system.

A loop of wire in the cavity can detect the oscillation. The microwave field in-



ATOMIC-BEAM frequency standards provide the most accurate, long-term timekeeping. Conventional atomic clocks rely on magnets (a). Atoms in the correct energy level are deflected by magnet A through the microwave cavity. Microwave fields oscillating at the resonance frequency of the atoms drive some of them into a second energy level. These atoms are deflected by magnet B so as to strike a detector. The servo mechanism monitors the detector and maintains the frequency of the applied microwaves at the resonance frequency. To keep time, some of the microwaves are

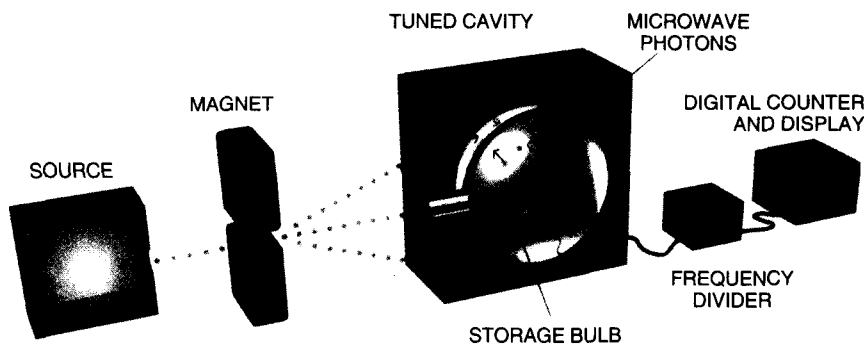
duced a current in the wire, which leads out of the cavity to a series of circuits. The circuits convert the induced current to a lower frequency signal suitable for generating timing pulses.

The resonance frequency in the hydrogen maser is about 1,420 megahertz, which is much lower than the resonance frequency of cesium. But because the hydrogen atoms reside in the bulb much longer than cesium atoms do in a beam, the maser's resonance width is much narrower. Consequently, the Q of a hydrogen maser standard is about 10^9 , exceeding the Q of the cesium atomic clock by an order of magnitude. In addition, a hydrogen maser has the

highest stability of any frequency standard, better than one part per 10^{15} .

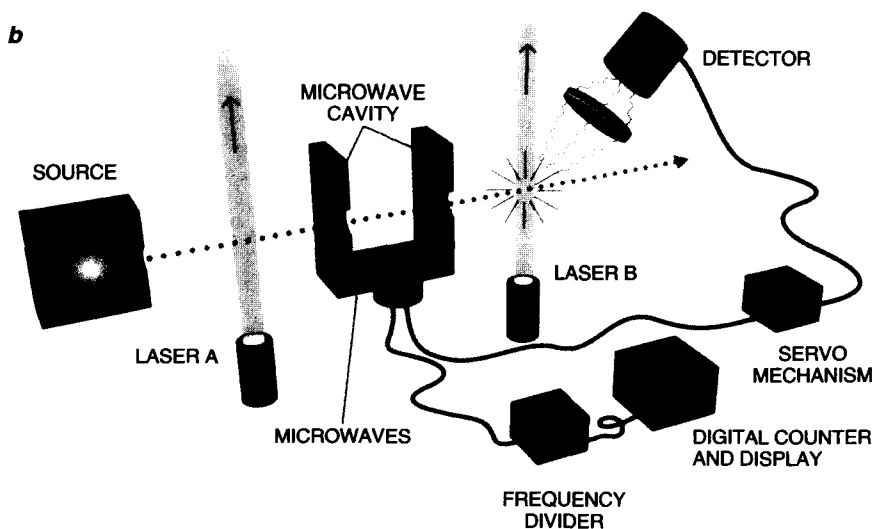
Unfortunately, the maser's superior attributes last just for a few days. Beyond that, its performance falls below that of cesium beams. The stability decreases because of changes in the cavity's resonant frequency. Collisions between the atoms and the bulb shift the frequency by about one part per 10^{11} .

One way to overcome the problem is to operate the hydrogen maser at low temperatures. This condition allows more atoms to be stored (thus resulting in a stronger signal) and reduces electronic noise. Coating the inside of the bulb with superfluid liquid helium also enhances performance. This substance acts as a good surface against which the hydrogen atoms can bounce. More effective magnets, better coating substances and servo loop techniques that keep the cavity resonance centered on the atomic resonance are other approaches now being taken to improve maser stability.

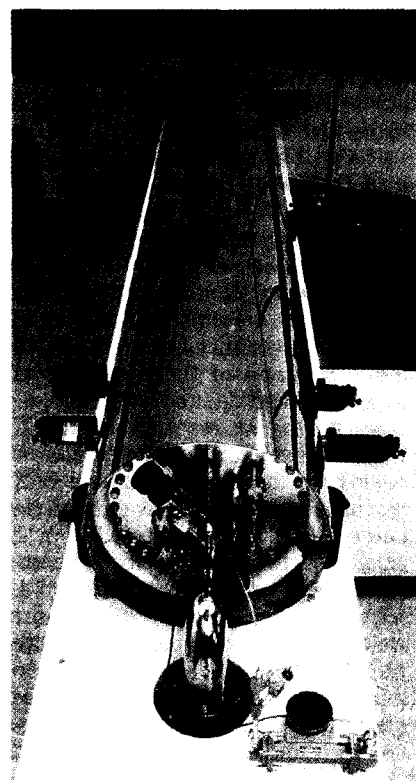


ATOMIC HYDROGEN MASER relies on a self-sustaining microwave field to serve as a frequency standard. Hydrogen atoms in the correct energy level are deflected by a magnet into a storage bulb. Some atoms will drop to a lower level, releasing a microwave photon. The photon stimulates other atoms to drop to a lower level, which produces more photons. The process quickly builds up a microwave field in the bulb. The field induces an alternating current in a wire placed in the cavity. The tuned cavity helps to redirect the photons back into the bulb to maintain the process.

Although the cesium atomic-beam frequency standard is the most accurate, long-term standard we have, several breakthroughs have indicated that it is possible to fabricate even more precise clocks. One of the most promising depends on the resonance frequency of trapped, electrically charged ions. Trapped ions can be suspended in a vacuum so that they are almost perfectly isolated from disturbing influences. The ions themselves stay well separated from one another



directed to a device that divides the frequency into usable timing pulses. Optically pumped standards (b) use light rather than magnets to select atoms. Laser A pumps the atoms into the right energy level, preparing them to be excited by the microwaves. Only atoms placed in the correct energy level by the microwaves absorb light from laser B. They quickly reemit that energy, which is sensed by a photodetector. An optically pumped clock using cesium atoms at the National Institute of Standards and Technology, called NIST-7, now keeps time for the U.S. (photograph).



because they have the same electric charge. Hence, they do not suffer collisions with other particles or with the walls of the chamber. Ions can be trapped for long periods, sometimes for days.

Two different types of traps are used. In a Penning trap, a combination of static, nonuniform electric fields and a static, uniform magnetic field holds the ions. In a radio frequency trap (often called a Paul trap), an oscillating, nonuniform electric field does the job. Each type of trap has its own characteristic shortcoming. The strong magnetic fields of Penning traps can alter the resonance frequency. The electric field in Paul traps can create heating effects that cause Doppler shifts. The kind of trap chosen depends on its suitability for a particular experimental setup.

Workers at Hewlett-Packard, the Jet Propulsion Laboratory in Pasadena, Calif., and elsewhere have fabricated experimental standard devices using Paul traps. The particles trapped were mercury 199 ions. This ion was selected because it has the highest hyperfine frequency—40.5 gigahertz—of all the atoms that are appropriate for the trapping technique. A few million such ions are caught between the electric fields generated by electrodes. Then the ions are optically pumped by ultraviolet radiation from a lamp. Subsequent operation resembles that of the optically pumped standards, but the maximum Q s of trapped-ion standards exceed 10^{12} . This value is 10,000 times

greater than that for current cesium beam clocks. Their short-term stabilities are also extremely good, although they do not yet reach those of hydrogen masers. The second-order Doppler shift limits the reproducibility to about one part per 10^{13} .

The Doppler shifts can be greatly reduced by laser cooling. In 1975 David J. Wineland, now at NIST, Hans G. Dehmelt of the University of Washington, Theodor W. Hänsch, now at the University of Munich, and Arthur L. Schawlow of Stanford University first proposed such a technique. In essence, a beam of laser light is used to reduce the velocities of the ions. Particles directed against the laser beam absorb some of the laser photon's momentum. As a result, the particles slow down. To compensate for the Doppler shifting as the particle moves against the laser, one tunes the beam to a frequency slightly lower than that produced by a strongly allowed resonance transition.

Many laboratories are developing frequency standards based on laser-cooled ions in traps. A standard based on beryllium 9 ions, laser-cooled in a Penning trap, has been constructed. Its reproducibility is about one part per 10^{13} , limited as it is by collisions of the ions with neutral molecules. Improvements in the quality of the vacuum should significantly increase the reproducibility because the uncertainty of the second-order Doppler shift is only about five parts per 10^{15} .

During the past few years, there have

been spectacular developments in trapping and cooling neutral atoms, which had been more difficult to achieve than trapping ions. Particularly effective laser cooling results from the use of three pairs of oppositely directed laser-cooling beams along three mutually perpendicular paths. A moving atom is then slowed down in whatever direction it moves. This effect gives rise to the designation "optical molasses." Several investigators have contributed to this breakthrough, including William D. Phillips of NIST in Gaithersburg, Md., Claude Cohen-Tannoudji and Jean Dalibard of the École Normale Supérieure and Steven Chu of Stanford [see "Laser Trapping of Neutral Particles," by Steven Chu; SCIENTIFIC AMERICAN, February 1992].

Neutral-atom traps can store higher densities of atoms than can ion traps, because ions, being electrically charged, are kept apart by their mutual repulsion. Other things being equal, a larger number of atoms results in a higher signal-to-noise ratio.

The main hurdle in using neutral atoms as frequency standards is that the resonances of atoms in a trap are strongly affected by the laser fields. A device called the atomic fountain surmounts the difficulty. The traps capture and cool a sample of atoms that are then given a lift upward so that they move into a region free of laser light. The atoms then fall back down under the influence of gravity. On the way up

and again on the way down, the atoms pass through an oscillatory field. In this way, resonance transitions are induced, just as they are in the separated oscillatory field beam apparatus.

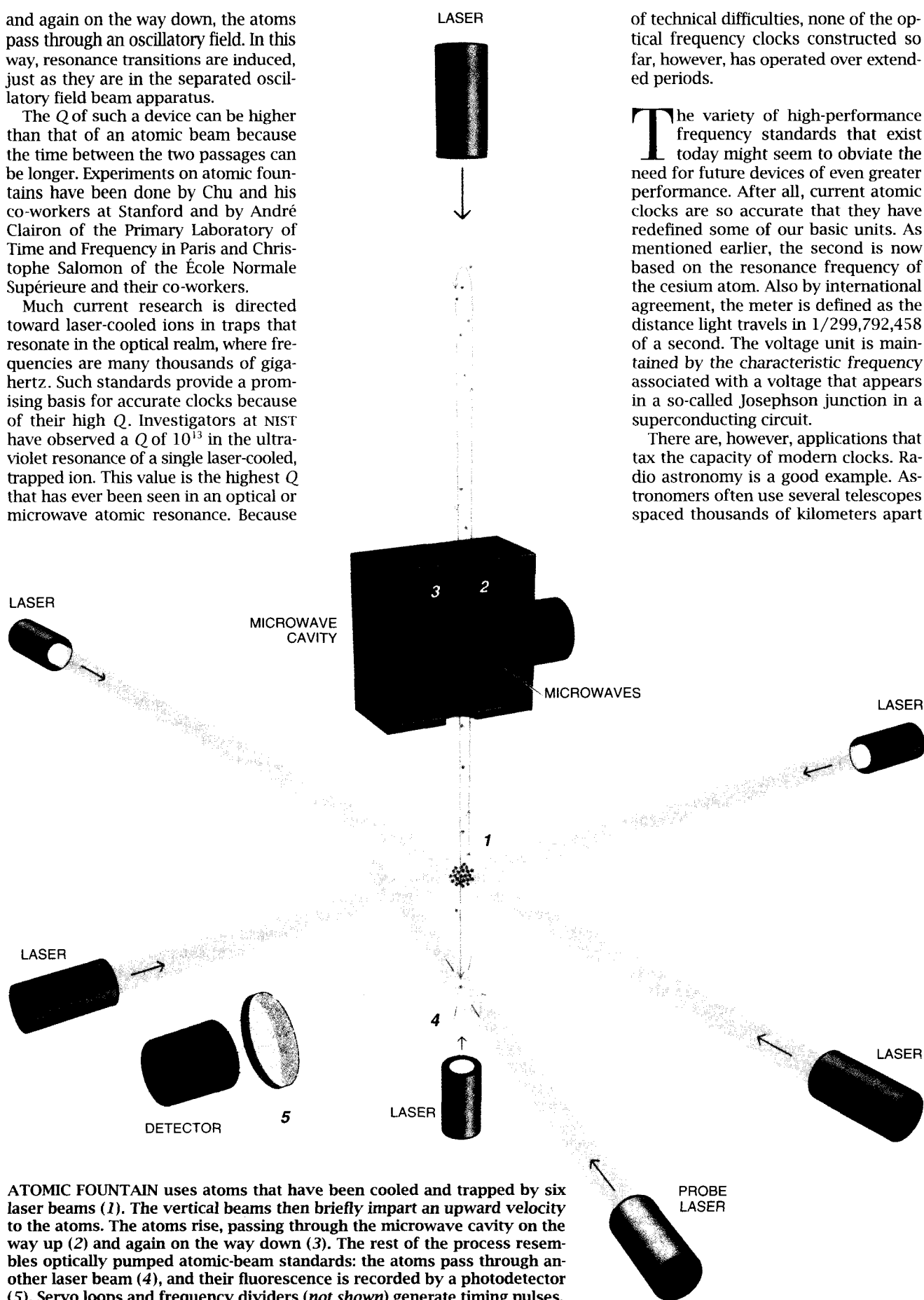
The Q of such a device can be higher than that of an atomic beam because the time between the two passages can be longer. Experiments on atomic fountains have been done by Chu and his co-workers at Stanford and by André Clairon of the Primary Laboratory of Time and Frequency in Paris and Christophe Salomon of the École Normale Supérieure and their co-workers.

Much current research is directed toward laser-cooled ions in traps that resonate in the optical realm, where frequencies are many thousands of gigahertz. Such standards provide a promising basis for accurate clocks because of their high Q . Investigators at NIST have observed a Q of 10^{13} in the ultraviolet resonance of a single laser-cooled, trapped ion. This value is the highest Q that has ever been seen in an optical or microwave atomic resonance. Because

of technical difficulties, none of the optical frequency clocks constructed so far, however, has operated over extended periods.

The variety of high-performance frequency standards that exist today might seem to obviate the need for future devices of even greater performance. After all, current atomic clocks are so accurate that they have redefined some of our basic units. As mentioned earlier, the second is now based on the resonance frequency of the cesium atom. Also by international agreement, the meter is defined as the distance light travels in $1/299,792,458$ of a second. The voltage unit is maintained by the characteristic frequency associated with a voltage that appears in a so-called Josephson junction in a superconducting circuit.

There are, however, applications that tax the capacity of modern clocks. Radio astronomy is a good example. Astronomers often use several telescopes spaced thousands of kilometers apart



ATOMIC FOUNTAIN uses atoms that have been cooled and trapped by six laser beams (1). The vertical beams then briefly impart an upward velocity to the atoms. The atoms rise, passing through the microwave cavity on the way up (2) and again on the way down (3). The rest of the process resembles optically pumped atomic-beam standards: the atoms pass through another laser beam (4), and their fluorescence is recorded by a photodetector (5). Servo loops and frequency dividers (not shown) generate timing pulses.

to study a stellar object, a technique that dramatically increases the resolution [see "Radio Astronomy by Very-Long-Baseline Interferometry," by Anthony C. S. Redhead; SCIENTIFIC AMERICAN, June 1982]. Two radio telescopes spaced 10,000 kilometers apart have an effective angular resolution more than one million times better than either telescope alone. But to combine the data from each telescope appropriately, investigators need to know precisely when each telescope received the signal. Present-day hydrogen masers have the stability required for such observations. More stable clocks may be needed for space-borne radio telescopes.

Highly stable clocks are essential for the best tests of relativity. Timing measurements of millisecond pulsars, some of which are as stable as the best atomic clocks, offer evidence for gravity waves. In 1978 Joseph H. Taylor, Jr., and his associates at Princeton University found that the period of a binary-pulsar system has been slowly varying by just the amount that would be expected for the loss of energy by gravitational radiation, as predicted by general relativity. Greater precision can be achieved if measurements are taken over many years, so clocks with better long-term stability would be useful.

In other tests of relativity, Vessot and his colleagues confirmed the predicted increase in clock rates at high altitudes. They sent on board a rocket a hydrogen maser and measured the small, relativistic clock shift to within an accuracy of 0.007 percent at an altitude of 10,000 kilometers. Highly stable clocks have also been used by Irwin I. Shapiro, now at the Harvard-Smithsonian Center for Astrophysics, to observe the relativistic delay of a light signal passing by the sun.

Ultraprecise timekeeping has more practical applications as well—most notably, for navigation. The location of *Voyager 2* as it sped by Neptune was determined by its distance from each of three widely separated radar telescopes. Each of these distances in turn was obtained from accurate measurements of the eight hours it took for light to travel from each telescope to the spacecraft and return.

Navigation is, of course, also important on the earth. One of the latest applications of precise clocks is the satellite-based assemblage called the Global Positioning System, or GPS. This system relies on atomic clocks on board orbiting satellites. The GPS enables anyone with a suitable radio receiver and computer to determine his or her position to approximately 10 meters and the correct time to better than 10^{-7} second.



Coordinating Time Scales

In the article, we discuss the measurement of an interval of time, such as a second or a minute. This process requires only a good clock. But to be able to state that an event happened at a particular time, say, 22 seconds after 12:31 p.m. on July 5, 1993, requires synchronization with a clock that is, by mutual agreement, the standard. The world's "standard clock" exists on paper as an average of the best clocks in the world. The International Bureau of Weights and Measures in Sèvres, France, is responsible for coordinating international time. This coordinated time scale is called International Atomic Time, or TAI.

Many users require a time scale that keeps pace with the rotation of the earth. That is, averaged over a year, the sun should be at its zenith in Greenwich, England, at noon. The day as determined by the apparent position of the sun is irregular but on the average longer than the 24 hours as defined by TAI. To compensate, another time scale, called Coordinated Universal Time, or UTC, is specified by occasionally adding or subtracting a whole number of seconds from TAI. These seconds, or leap seconds, are inserted or deleted, usually on December 31 or June 30, to keep UTC within 0.9 second of the time as defined by the rotation of the earth. The record of leap seconds must be consulted to determine the exact interval between two stated times.

Two observers monitoring the same satellite can synchronize their clocks to within a few nanoseconds.

It is expected that the GPS will have widespread practical applications, such as pinpointing the positions of ships, airplanes and even private automobiles. The GPS was used during the 1991 Persian Gulf War to enable troops to determine their positions on the desert. Commercial receivers can be purchased for less than \$1,000, although these civilian versions are limited to an accu-

racy of about 100 meters because of deliberate scrambling of the signals transmitted from the satellites. A full complement of 24 satellites would give 24-hour, worldwide coverage. The system is nearly complete.

These and other applications show the importance of time and frequency standards. The anticipated improvements in standards will increase the effectiveness of the current uses and open the way for new functions. Only time will tell what these uses will be.

FURTHER READING

FROM SUNDIALS TO ATOMIC CLOCKS: UNDERSTANDING TIME AND FREQUENCY. J. Jespersen and J. Fitz-Randolph. Dover, 1982.

HISTORY OF ATOMIC CLOCKS. N. F. Ramsey in *Journal of Research of the National Bureau of Standards*, Vol. 88, No. 5,

pages 301-320; September/October 1983. PRECISE MEASUREMENT OF TIME. N. F. Ramsey in *American Scientist*, Vol. 76, No. 1, pages 42-49; January/February 1988.

TIME AND FREQUENCY. Special issue of *Proceedings of the IEEE*, Vol. 79, No. 7; July 1991.

Resolved-Sideband Raman Cooling of a Bound Atom to the 3D Zero-Point Energy

C. Monroe, D. M. Meekhof, B. E. King, S. R. Jefferts, W. M. Itano, and D. J. Wineland

Time and Frequency Division, National Institute of Standards and Technology, Boulder, Colorado 80303

P. Gould

Department of Physics, University of Connecticut, Storrs, Connecticut 06269

(Received 19 December 1994)

We report laser cooling of a single ${}^9\text{Be}^+$ ion held in a rf (Paul) ion trap to where it occupies the quantum-mechanical ground state of motion. With the use of resolved-sideband stimulated Raman cooling, the zero point of motion is achieved 98% of the time in 1D and 92% of the time in 3D. Cooling to the zero-point energy appears to be a crucial prerequisite for future experiments such as the realization of simple quantum logic gates applicable to quantum computation.

PACS numbers: 32.80.Pj, 42.50.Vk, 42.65.Dr

Dramatic progress in the field of atomic laser cooling has provided cooling of free or weakly bound atoms to temperatures near the Doppler cooling limit [1], near the photon recoil limit [2], and, more recently, below the photon recoil limit [3,4]. For a tightly bound atom, a more natural energy scale is given by the quantized vibrational level n , where the energy is $E = \hbar\omega_v(n + \frac{1}{2})$ for an atom confined in a harmonic potential of frequency ω_v . In this case, the fundamental cooling limit is the $n = 0$ zero-point energy of the binding potential. In this Letter, we demonstrate a new technique for laser cooling a trapped atom to the 3D zero-point energy.

Attainment of the 3D ground state is significant for two primary reasons: (i) it appears to be a goal of intrinsic interest as it is the fundamental limit of cooling for a bound atom and approaches the ideal of an isolated particle at rest and (ii) it will be important in future planned experiments. For example, once the ion is cooled to the $n = 0$ state, it should be possible to realize the Jaynes-Cummings interaction [5] in the regime of strong coupling and generate other nonclassical states of motion such as squeezed states [6–8]. If the collective motion of two or more trapped ions can be cooled to the zero point, it may be possible to transfer correlation from the external motional state to the internal spin state of the ions. Generating “EPR”-like atomic spin states would not only be interesting from the point of view of quantum measurements [9], but may also allow a reduction of quantum noise in spectroscopy [6,7]. Zero-point cooling combined with long coherence times may make it possible to construct a quantum computer [10]. Cirac and Zoller have proposed a quantum computer based on a system of trapped ions, in which information is stored in the spin and motional states of the ions [11]. The fundamental switching action in this implementation of a quantum computer is a coherent exchange between the spin state of an individual ion and a collective vibrational state of all the ions. Cooling to the zero-point energy and realizing the Jaynes-Cummings coupling is critical to this scheme.

We cool a single beryllium ion bound in a rf (Paul) ion trap to near the zero-point energy using resolved-sideband laser cooling with stimulated Raman transitions along the lines suggested in Ref. [6]. The idea of resolved-sideband laser cooling with a single-photon transition is as follows [12]. Consider a two-level atom characterized by resonant transition frequency ω_0 and radiative linewidth γ . We assume the atom is confined by a 1D harmonic well of vibration frequency $\omega_v \gg \gamma$. If a laser beam (frequency ω_L) is incident along the direction of the atomic motion, the absorption spectrum is composed of a “carrier” at frequency ω_0 and resolved frequency-modulation sidebands spaced by ω_v , which are generated from the Doppler effect. Cooling occurs if the laser is tuned to a lower sideband, for example, at $\omega_L = \omega_0 - \omega_v$. In this case, photons of energy $\hbar(\omega_0 - \omega_v)$ are absorbed and spontaneously emitted photons of average energy $\hbar\omega_0$ return the atom to its initial internal state thereby reducing the atom’s kinetic energy by $\hbar\omega_v$ per scattering event (assuming $\hbar\omega_v$ is much greater than the photon recoil energy). Cooling proceeds until the atom’s mean vibrational quantum number in the harmonic well is given by $\langle n \rangle_{\min} \approx (\gamma/2\omega_v)^2 \ll 1$ [1,13]. The interaction with the laser is significantly reduced once in the $n = 0$ state; thus the zero-point state satisfies the *operational definition* of a dark state [14] for γ/ω_v sufficiently small. Resolved-sideband cooling in 2D was previously achieved on a ${}^{198}\text{Hg}^+$ ion using a narrow single-photon optical quadrupole transition [15].

For laser cooling with stimulated Raman transitions [4,6,16,17], the single-photon transition is replaced by a stimulated Raman transition between metastable levels (e.g., hyperfine or Zeeman electronic ground states), and spontaneous Raman transitions irreversibly recycle the internal state of the atom. Stimulated Raman cooling offers the important practical advantages that the cooling linewidth can be varied experimentally, and the effective laser linewidth can be made very narrow by the use of optical frequency modulators. These features of stimu-

lated Raman cooling have already been used to achieve very low temperatures for free or weakly bound neutral atoms in the unresolved-sideband limit [4]. Since narrow single-photon transitions are not required, the resolved-sideband Raman cooling technique described here can be generalized to many ion species and may also be applied to strongly bound neutral atoms held in dipole traps [18] and optical lattices [19].

The experiment is conducted as follows. We first achieve $\langle n_\nu \rangle \approx 1$ in 3D ($\nu = x, y, z$) by performing Doppler cooling on an allowed electric dipole transition (γ large) and making the trap strong enough that $\omega_\nu \approx \gamma$. This Doppler “precooling” places the ion into the Lamb-Dicke regime ($\Delta x \ll \lambda/2\pi$, where Δx is the rms spread of the ion position and λ is the wavelength of the dipole transition). We reduce $\langle n_\nu \rangle$ further in 3D by employing a second stage of cooling on narrower Raman transitions between hyperfine ground states ($\gamma_{\text{Ram}} \ll \omega_\nu$). Finally we extract $\langle n_\nu \rangle$ by measuring the asymmetry of the resolved motional sidebands in the Raman absorption spectrum [15].

A single ${}^9\text{Be}^+$ ion is stored in a coaxial-resonator-based rf (Paul) ion trap ($r_0 \approx 170 \mu\text{m}$, $z_0 \approx 130 \mu\text{m}$) described in Ref. [20]. A potential $V_0 \cos(\Omega_0 t)$ is applied to the ring ($V_0 \approx 600 \text{ V}$, $\Omega_0/2\pi \approx 231 \text{ MHz}$), yielding ${}^9\text{Be}^+$ pseudopotential oscillation frequencies of $(\omega_x, \omega_y, \omega_z)/2\pi \approx (11.2, 18.2, 29.8) \text{ MHz}$ along the principal axes of the trap [21]. Once a ${}^9\text{Be}^+$ ion is loaded in the trap, its lifetime is about 6 h (background pressure $< 10^{-8} \text{ Pa}$).

The geometry and polarizations of the various laser beams as well as the relevant energy levels in ${}^9\text{Be}^+$ are summarized in Fig. 1. The quantization axis is defined by an applied magnetic field $|\mathbf{B}| \approx 0.18 \text{ mT}$. Laser radiation (beam $D2$, σ^+ polarized) detuned slightly to the red of the ${}^2S_{1/2}(F=2) \rightarrow {}^2P_{3/2}$ transitions ($\lambda \approx 313 \text{ nm}$, $\gamma/2\pi \approx 19.4 \text{ MHz}$, ${}^2P_{3/2}$ hyperfine structure $\approx 1 \text{ MHz}$) is directed at oblique angles to all the principal axes of the trap, providing Doppler precooling in all trap dimensions. A second 313 nm source (beam $D1$, σ^+ polarized) tuned to the ${}^2S_{1/2}(F=1) \rightarrow {}^2P_{3/2}$ transition prevents optical pumping to the $F=1$ ground state. A pair of Raman beams is also directed into the trap (beams $R1$ and $R2$) to drive a much narrower transition between the ${}^2S_{1/2} |F=2\rangle$ and $|F=1\rangle$ hyperfine ground states of ${}^9\text{Be}^+$ through the virtual ${}^2P_{1/2}$ state. The Raman beams are detuned $\approx 12 \text{ GHz}$ to the red of the ${}^2S_{1/2} \rightarrow {}^2P_{1/2}$ transition with a difference frequency very near the ${}^2S_{1/2}$ hyperfine splitting of $\omega_0/2\pi \approx 1.250 \text{ GHz}$. A third 313 nm source (beam $D3$, σ^+ polarized) is tuned to the ${}^2S_{1/2}(F=2) \rightarrow {}^2P_{1/2}(F=2)$ transition and depletes the $|F, m_F\rangle = |2, 1\rangle$ ground state. Beams $D1$, $D2$, and $D3$ are derived from two frequency-doubled dye lasers, producing 5–10 μW of power in each beam, enough to saturate the ion near resonance. Beams $R1$ and $R2$ are derived from a third frequency-doubled dye laser, providing a few mW of power in each

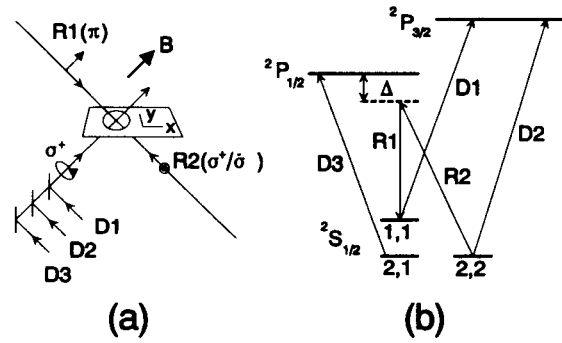


FIG. 1. (a) Laser beam geometry. The trap ring electrode (in the x - y plane) is shown rotated 45° into the page (the endcap electrodes along the z axis are not shown; see Ref. [20]). A magnetic field \mathbf{B} defines a quantization axis along $\hat{x}/\sqrt{2} + \hat{y}/2 + \hat{z}/2$, and laser beam polarizations are indicated. Fluorescence light is collected along the direction perpendicular to the page. (b) Relevant ${}^9\text{Be}^+$ energy levels (not to scale), indicated by F, m_F , quantum numbers in the ${}^2S_{1/2}$ ground state (2P fine-structure splitting is $\approx 197 \text{ GHz}$, ${}^2S_{1/2}$ hyperfine splitting is $\omega_0/2\pi \approx 1.250 \text{ GHz}$, and the ${}^2P_{3/2}$ hyperfine and Zeeman structure is not resolved). All optical transitions are near $\lambda = 313 \text{ nm}$. $D1$ and $D2$: Doppler precooling and detection beams; $D3$: $|2, 1\rangle$ depletion beam; $R1$ and $R2$: Raman beams. The detuning of $R1$ and $R2$ from the ${}^2S_{1/2} \rightarrow {}^2P_{1/2}$ transition is $\Delta/2\pi \approx 12 \text{ GHz}$.

beam. The difference frequency of the Raman beams is tunable over the range 1200–1300 MHz with the use of a double-pass acousto-optic modulator (AOM). The counterpropagating Raman beams are also at oblique angles to the trap’s principal axes and are therefore sensitive to motion in all dimensions. All beams are shuttered with AOMs. The 313 nm fluorescence from the trapped ion is imaged through $f/2$ optics onto a position-sensitive photomultiplier tube, resulting in a photon count rate as high as $\approx 10 \text{ kHz}$ (quantum efficiency $\approx 2 \times 10^{-4}$). The background count rate is $\approx 100 \text{ Hz}$.

Doppler precooling, Raman cooling, and measurement of the Raman absorption spectrum are accomplished by following the sequence outlined in Table I. After precooling (beams $D1$, $D2$, and $D3$), the ion is prepared in the ${}^2S_{1/2}|2, 2\rangle$ electronic ground state by turning off beam $D2$. The relative tuning of the Raman beams is set to a first lower (red) sideband near $\omega_0 - \omega_\nu$, driving a stimulated Raman transition from the $|2, 2\rangle |n_\nu\rangle$ state to the $|1, 1\rangle |n_\nu - 1\rangle$ state. The ion is then recycled with nearly resonant beams $D1$ and $D3$, inducing spontaneous Raman transitions predominantly to the $|2, 2\rangle |n_\nu - 1\rangle$ state. This cycling of stimulated and spontaneous Raman transitions (steps 3 and 4 of Table I) is repeated as desired on any or all of the three dimensions. The relative tuning of the Raman beams is then set near $\omega_0 + \delta_{\text{pr}}$, and a stimulated Raman “probe” transition is driven between the states, where $\Delta n_\nu = 0, \pm 1$. The probability of driving the probe transition is then measured by

driving a stimulated Raman “exchange π pulse” from $|2, 2\rangle|n_v\rangle \leftrightarrow |1, 1\rangle|n_v\rangle$, followed by driving the cycling $^2S_{1/2}|2, 2\rangle \rightarrow ^2P_{3/2}|3, 3\rangle$ transition with beam $D2$ and gating and collecting the fluorescence. (The exchange π pulse in step 6 of the table reduces the fluorescence noise when $\langle n_v \rangle \approx 0$.) The ion scatters thousands of photons on the cycling transition before decaying into the $|1, 1\rangle$ electronic state due to imperfect circular polarization of beam $D2$, resulting in a net quantum efficiency near 1. As this sequence is repeated at ≈ 4 kHz, δ_{pr} is slowly swept, yielding the Raman absorption spectrum.

The Raman carrier represents the transition $|2, 2\rangle|n_v\rangle \leftrightarrow |1, 1\rangle|n_v\rangle$ and occurs at $\delta_{pr} \equiv 0$ (compensating for stable Zeeman and ac Stark shifts of ≈ 2 MHz). In the Lamb-Dicke regime, the carrier feature has strength $I_c = \sin^2(\Omega \tau_{pr})$, where $\Omega = g_1 g_2 / \Delta$ is the carrier Rabi flopping frequency, τ_{pr} is the exposure time of the atom to the probe Raman beams, g_1 and g_2 are the resonant Rabi frequencies of Raman beams $R1$ and $R2$, and Δ is the detuning of the Raman beams from the excited state (we assume $\Delta \gg \gamma, g_1, g_2$) [6]. In each dimension, blue and red sidebands occurring at $\delta_{pr} = \pm \omega_v$ represent the transitions $|2, 2\rangle|n_v\rangle \leftrightarrow |1, 1\rangle|n_v \pm 1\rangle$. The strengths of the blue and red sidebands in the Lamb-Dicke regime are given by $I_v^{\text{blue}} = \langle \sin^2[\Omega \tau_{pr} \eta_v (n_v + 1)^{1/2}] \rangle$ and $I_v^{\text{red}} = \langle \sin^2[\Omega \tau_{pr} \eta_v n_v^{1/2}] \rangle$, where the average is performed over the distribution of n_v . The Lamb-Dicke parameters are given by $\eta_v = \delta k_v r_v = (0.21, 0.12, 0.09)$, where $\delta k_v = 2k_v$ is the component of the difference in the counterpropagating Raman beam wave vectors in the v th dimension, and $r_v = (\hbar/2m\omega_v)^{1/2}$ is the spread of the $n_v = 0$ wave function. The sideband Rabi flopping frequencies $\Omega \eta_v$ are typically a few hundred kilohertz, thus the absorption features are well resolved and spontaneous emission during all stimulated Raman processes is negligible.

A Raman absorption spectrum of the first blue and red sidebands of the x direction ($\delta_{pr} = \pm \omega_x$) is shown in Fig. 2 (solid points) for Doppler precooling only (omitting steps 3 and 4 in Table I). Similar features appear at $\delta_{pr} = \pm \omega_y$ and $\pm \omega_z$. If n_v is thermally distributed, then it is straightforward to show that $I_v^{\text{red}}/I_v^{\text{blue}} = \langle n_v \rangle / (1 + \langle n_v \rangle)$, independent of $\Omega \tau_{pr} \eta_v$. By recording several spectra varying τ_{pr} , we find the ratio of red to blue sideband strength remains approximately constant, indicating a nearly thermal distribution of n_v . (We ensure that Ω is the same on the blue and red sidebands.) We measure $\langle n_v \rangle$ for a variety of red detunings of Doppler precooling beams $D1$ and $D2$ and obtain values as low as $\langle n_v \rangle \approx (0.47, 0.30, 0.18)$ in the three dimensions at a detuning of about -30 MHz (we estimate $\approx 10\%$ uncertainties in the measurements). At other detunings, we measure values as high as $\langle n_v \rangle \approx 7$. These values and their behavior with detuning are consistent with the theoretical limit of Doppler cooling [17].

Figure 2 includes a Raman absorption spectrum following additional sideband Raman cooling (hollow points). Five Raman cooling cycles in the x dimensions are em-

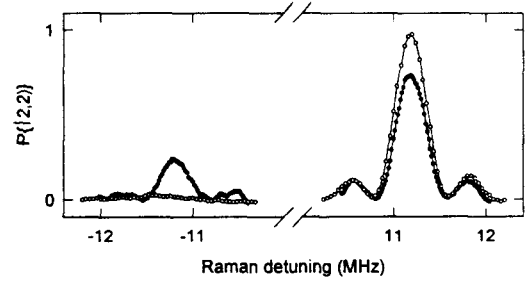


FIG. 2. Raman absorption spectrum of a single $^9\text{Be}^+$ ion after Doppler precooling (solid points) and after five cycles of additional resolved sideband stimulated Raman cooling on the x dimension (hollow points). The observed count rate is normalized to the probability $P\{|2, 2\rangle\}$ of the ion being in the $|2, 2\rangle$ state. The first blue and red sidebands of the x dimension are shown at $\delta_{pr}/2\pi \approx \pm 11.2$ MHz. Similar sidebands are found near ± 18.2 MHz (y dimension) and at ± 29.8 MHz (z dimension). For precooling, the asymmetry in the sidebands indicates a thermal average vibrational occupation number of $\langle n_x \rangle \approx 0.47(5)$. For Raman cooling, the reduction of the red sideband and growth of the blue sideband implies further Raman cooling in the x dimension to $\langle n_x \rangle \approx 0.014(10)$. The widths of the features are consistent with the $2.5 \mu\text{s}$ Raman probe time. Each point represents an average of 400 measurements, corresponding to ≈ 5 min of integration time for the entire data set. The lines connect the data points.

ployed (steps 3 and 4 of Table I with $\omega_v = \omega_x$). The exposure time τ_{Ram} of the last Raman pulse is set so that $\Omega \tau_{\text{Ram}} \eta_x = \pi/2$ or $\tau_{\text{Ram}} \approx 2.5 \mu\text{s}$, corresponding to nearly a π pulse from the $n_x = 1$ state to the $n_x = 0$ state. The durations of the earlier pulses are set shorter to optimize the cooling. The recycle time between each stimulated Raman transition is about $7 \mu\text{s}$, ample time for the ion to scatter the expected average of ≈ 3 photons from beams $D1$ and $D3$ and ultimately get recycled to the $|2, 2\rangle$ state. The suppression of the red sideband (and growth of the blue sideband) indicates the extent of the additional cooling, from $\langle n_x \rangle \approx 0.47$ to $\langle n_x \rangle \approx 0.014(10)$ (the $n_x = 0$ state is occupied $\approx 98\%$ of the time). We observe no further cooling by increasing the number of Raman cooling cycles beyond about five and see little sensitivity to the details of the Raman cooling pulse durations. As discussed above, we verify that the distribution of n_v is nearly thermal after Raman cooling. We achieve resolved-sideband Raman cooling in 3D by sequentially driving on all three red sidebands. Five cycles of cooling are applied to each dimension (order $xyzxyz\dots$) by alternating the tuning of the Raman cooling beams between the three red sidebands. From the measured asymmetry of each pair of sidebands, we infer 3D Raman cooling to $\langle n_v \rangle \approx (0.033, 0.022, 0.029)$, or the $n_x = n_y = n_z = 0$ 3D ground state being occupied $\approx 92\%$ of the time.

The limit of Raman cooling is determined by heating from off-resonant stimulated-Raman transitions [expected to result in a limit of $\langle n_x \rangle_{\text{St Ram}} \approx (g_1 g_2)^2 / (\omega_v \Delta)^2 \approx$

TABLE I. Timing sequence for Doppler precooled, resolved-sideband stimulated Raman cooling and Raman detection of $\langle n_v \rangle$. As the sequence is repeated through steps 1–7, δ_{pr} is slowly swept across absorption features. Raman cooling steps (3 and 4) are repeated as desired within the sequence.

Step	Duration (μs)	Beams D1, D3 D2 R1, R2	Raman tuning	Function
1	≈ 50	On On	Off ...	Doppler precooled
2	≈ 7	On Off	Off ...	Prepare in $ 2, 2\rangle$ state
3	1–3	Off Off	On $\omega_0 - \omega_v$	Stimulated Raman transition $ 2, 2\rangle n_v\rangle \rightarrow 1, 1\rangle n_v - 1\rangle$
4	≈ 7	On Off	Off ...	Spontaneous Raman recycle $ 1, 1\rangle n_v - 1\rangle \rightarrow 2, 2\rangle n_v - 1\rangle$
5	1–3	Off Off	On $\omega_0 + \delta_{pr}$	Probe $\langle n_v \rangle$ with stimulated Raman transitions $ 2, 2\rangle n_v\rangle \rightarrow 1, 1\rangle n'_v\rangle$
6	≈ 1	Off Off	On ω_0	Exchange π pulse: $ 2, 2\rangle n_v\rangle \leftrightarrow 1, 1\rangle n_v\rangle$
7	≈ 200	Off On	Off ...	Detect transition in step 5: cycle on $ 2, 2\rangle \rightarrow 3, 3\rangle$; collect fluorescence

10^{-3}] and heating from off-resonant spontaneous emission from the Raman beams [a limit of $\langle n_x \rangle_{\text{Sp Ram}} \approx (g_1 g_2 / \Delta^2) \eta_x \gamma \tau_{\text{Ram}} \approx 10^{-3}$]. We believe the minimum measured value of $\langle n_x \rangle \approx 0.02$ may be due to anomalous heating of the ion, which we measure to be $\partial \langle n \rangle / \partial t \approx +1/\text{msec}$ by inserting various amounts of time between cooling probing. We are currently investigating the source of this heating.

This work is supported by the Office of Naval Research and the Army Research Office. We acknowledge considerable contributions from J. C. Bergquist. We thank N. R. Newbury, J. D. Miller, and M. Young for comments on the manuscript.

- [1] D. J. Wineland and W. M. Itano, *Phys. Today* **40**, No. 6, 34 (1987).
- [2] C. Cohen-Tannoudji and W. D. Phillips, *Phys. Today* **43**, No. 10, 33 (1990).
- [3] A. Aspect, E. Arimondo, R. Kaiser, N. Vansteenkiste, and C. Cohen-Tannoudji, *Phys. Rev. Lett.* **61**, 826 (1988); J. Lawall, F. Bardou, B. Saubamea, M. Leduc, A. Aspect, and C. Cohen-Tannoudji, *Phys. Rev. Lett.* **73**, 1915 (1994).
- [4] M. Kasevich and S. Chu, *Phys. Rev. Lett.* **69**, 1741 (1992); H. Lee, C. Adams, N. Davidson, B. Young, M. Weitz, M. Kasevich, and S. Chu, in *Atomic Physics XIV*, edited by D. J. Wineland, C. E. Wieman, and S. J. Smith (AIP Press, New York, 1995), p. 258.
- [5] E. T. Jaynes and C. W. Cummings, *Proc. IEEE* **51**, 89 (1963).
- [6] D. J. Heinzen and D. J. Wineland, *Phys. Rev. A* **42**, 2977 (1990).
- [7] D. J. Wineland, J. J. Bollinger, W. M. Itano, and D. J. Heinzen, *Phys. Rev. A* **50**, 67 (1994).
- [8] J. I. Cirac, A. S. Parkins, R. Blatt, and P. Zoller, *Phys. Rev. Lett.* **70**, 556 (1993); J. I. Cirac, R. Blatt, A. S. Parkins, and P. Zoller, *Phys. Rev. Lett.* **70**, 762 (1993).
- [9] D. M. Greenberger, M. A. Horne, and A. Zeilinger, *Phys. Today* **46**, No. 8, 22 (1993).
- [10] A. Ekert, in *Atomic Physics XIV*, edited by D. J. Wineland, C. E. Wieman, and S. J. Smith (AIP Press, New York,

1995), p. 450, and references therein.

- [11] J. I. Cirac and P. Zoller, *Phys. Rev. Lett.* **74**, 4091 (1995).
- [12] D. J. Wineland and H. Dehmelt, *Bull. Am. Phys. Soc.* **20**, 637 (1975).
- [13] W. Neuhauser, M. Hohenstatt, P. Toschek, and H. Dehmelt, *Phys. Rev. Lett.* **41**, 233 (1978).
- [14] R. Dum, P. Marte, T. Pellizzari, and P. Zoller, *Phys. Rev. Lett.* **73**, 2829 (1994).
- [15] F. Diedrich, J. C. Bergquist, W. M. Itano, and D. J. Wineland, *Phys. Rev. Lett.* **62**, 403 (1989).
- [16] P. E. Toschek, *Phys. (Paris)* **10**, 761 (1985); H. Dehmelt, G. Janik, and W. Nagourney, *Bull. Am. Phys. Soc.* **30**, 111 (1985); B. Appasamy, I. Siemers, Y. Stalgies, J. Eschner, R. Blatt, W. Neuhauser, and P. E. Toschek, *Appl. Phys. B* **60**, 473 (1995).
- [17] M. Lindberg and J. Javanainen, *J. Opt. Soc. Am. B* **3**, 1008 (1986).
- [18] S. Chu, J. E. Bjorkholm, A. Ashkin, and A. Cable, *Phys. Rev. Lett.* **57**, 314 (1986); W. D. Phillips, in *Laser Manipulation of Atoms and Ions*, Proceedings of the International School of Physics "Enrico Fermi," Varenna, 1991, edited by E. Arimondo and W. D. Phillips (North-Holland, Amsterdam, 1992), p. 325; J. D. Miller, R. A. Cline, and D. J. Heinzen, *Phys. Rev. A* **47**, R4567 (1993).
- [19] P. Verkerk, B. Lounis, C. Salomon, and C. Cohen-Tannoudji, *Phys. Rev. Lett.* **68**, 3861 (1992); P. Jessen, C. Gerz, P. Lett, W. Phillips, S. Rolston, R. Spreuw, and C. Westbrook, *Phys. Rev. Lett.* **69**, 49 (1992); A. Hemmerich and T. Hänsch, *Phys. Rev. Lett.* **70**, 410 (1993).
- [20] S. R. Jefferts, C. Monroe, E. Bell, and D. J. Wineland, *Phys. Rev. A* **51**, 3112 (1995).
- [21] The drive frequency $\Omega_0 \approx 231$ MHz is much larger than the pseudopotential vibration frequencies ω_v , so the contribution of the driven "micromotion" at Ω_0 to the overall amplitude of the ion motion is very small. This includes the micromotion induced from static background fields, which are minimized with compensation electrodes (see Ref. [20]). Moreover the small FM micromotion sidebands at $\pm\Omega_0$ are well resolved ($\Omega_0 \gg \gamma$) and far from the region of interest in the absorption spectrum. Thus the trap can be accurately approximated as a simple harmonic oscillator with frequencies ω_v .

Quantum projection noise: Population fluctuations in two-level systems

W. M. Itano, J. C. Bergquist, J. J. Bollinger, J. M. Gilligan, D. J. Heinzen,* F. L. Moore,*
M. G. Raizen,* and D. J. Wineland

Time and Frequency Division, National Institute of Standards and Technology, Boulder, Colorado 80303

(Received 9 December 1992)

Measurements of internal energy states of atomic ions confined in traps can be used to illustrate fundamental properties of quantum systems, because long relaxation times and observation times are available. In the experiments described here, a single ion or a few identical ions were prepared in well-defined superpositions of two internal energy eigenstates. The populations of the energy levels were then measured. For an individual ion, the outcome of the measurement is uncertain, unless the amplitude for one of the two eigenstates is zero, and is completely uncertain when the magnitudes of the two amplitudes are equal. In one experiment, a single $^{199}\text{Hg}^+$ ion, confined in a linear rf trap, was prepared in various superpositions of two hyperfine states. In another experiment, groups of $^9\text{Be}^+$ ions, ranging in size from about 5 to about 400 ions, were confined in a Penning trap and prepared in various superposition states. The measured population fluctuations were greater when the state amplitudes were equal than when one of the amplitudes was nearly zero, in agreement with the predictions of quantum mechanics. These fluctuations, which we call quantum projection noise, are the fundamental source of noise for population measurements with a fixed number of atoms. These fluctuations are of practical importance, since they contribute to the errors of atomic frequency standards.

PACS number(s): 03.65.Bz, 32.80.Pj, 32.30.Bv

I. INTRODUCTION

Quantum mechanics is not a deterministic theory, even though the time development of the quantum-state vector is governed by the Schrödinger equation, which *is* deterministic. That is, quantum mechanics does not, in general, predict the result of an experiment. Rather, it provides a prescription for predicting the *probability* of observing a given result. The relationship of the quantum-state vector to the physical system that it describes is central to the interpretation of quantum mechanics. There are at least two distinct interpretations of the quantum state [1].

According to the Copenhagen interpretation, the state vector provides a complete description of an individual system (a single atom, for example). This is not the only definition of the Copenhagen interpretation, but it is the one that we adopt here. According to this interpretation, the state vector of a system develops in time according to the Schrödinger equation until a measurement causes it to be projected into an eigenstate of the dynamical variable that is being measured. The assumption that the state vector "collapses" in this manner is considered unattractive by some, because of its *ad hoc* nature.

According to another interpretation, sometimes called the statistical-ensemble interpretation, the state vector is merely a mathematical construct which describes an ensemble of similarly prepared systems [2-4]. One common misconception is that this interpretation is not capable of describing an experiment on a single atom. In this case, the state vector describes a *conceptual ensemble* (a Gibbs ensemble) of similarly prepared atoms. The single atom in the experiment is a member of that ensemble. Exper-

mentally, an ensemble is generated by repeatedly preparing the state of the atom and then making a measurement. The state vector, in this interpretation, is analogous to a statistical distribution function of the kind that appears in classical statistical mechanics. The difference is that, in quantum mechanics, there is no underlying microscopic theory which can predict the behavior of a single system, even in principle. The statistical-ensemble interpretation has the virtue of avoiding the necessity of "reducing" or "collapsing" the state vector.

In spite of occasional claims to the contrary [5], it appears that the Copenhagen and statistical-ensemble interpretations do not differ in their predictions of experiments *when properly applied* [6]. In practice, either interpretation may motivate a particular calculation. For example, some problems in quantum optics have been solved by simulating the behavior of the wave function of a single atom, explicitly including the reduction of the wave function at random times [7-10]. Such methods follow naturally from the Copenhagen interpretation (which is not to say that the practitioners of these methods would necessarily advocate the Copenhagen interpretation as *opposed* to the statistical-ensemble interpretation). On the other hand, the conventional method of solving the density-matrix equations follows naturally from the statistical-ensemble interpretation. The results of averaging many wave-function simulations are the same as those of solving the density-matrix equations. The experiments described here can be interpreted within either framework.

Perhaps the simplest example of the indeterminism of quantum mechanics is the behavior of a two-level system prepared in a superposition $|\psi\rangle = c_A|A\rangle + c_B|B\rangle$ of the two states $|A\rangle$ and $|B\rangle$ and subjected to a measure-

ment. The measurement yields one indication or “pointer reading” for a system in $|A\rangle$ and another for a system in $|B\rangle$. Except when either c_A or c_B is zero, the outcome of the measurement cannot be predicted with certainty. Provided that the state vector is properly normalized ($|c_A|^2 + |c_B|^2 = 1$), $|c_A|^2 \equiv p_A$, and $|c_B|^2 \equiv p_B$ are the probabilities of finding the system in $|A\rangle$ or $|B\rangle$. The indeterminacy is present no matter how accurately the state has been prepared. It is an inherent feature of quantum mechanics. We will call this source of measurement fluctuations “quantum projection noise,” since it can be interpreted as arising from the random projection of the state vector into one of the states compatible with the measurement process.

In some experiments we have a sample of N identical systems that are effectively independent. If we carry out the same kind of state preparation and measurement as that just described for a single system, then we should get the same result as by repeating the experiment N times. That is, the sum over all N atoms of the measured quantity should have the same mean and fluctuations as the sum of N independent measurements on one system.

The internal states of a set of N ions in an ion trap constitute a system of this type. The ions are well separated from each other by their mutual Coulomb repulsion, so, to a very good approximation, the state of one ion has no effect on that of another ion. If all of the ions are subjected to the same optical and radiofrequency fields, they can all be described by the same state vector for their internal degrees of freedom. In an ion trap, unlike an atomic beam, for example, we can repeatedly prepare and observe the *same* set of N atoms.

To illustrate the main ideas, we will first describe a simplified version of the experiment. The actual experiments, carried out with single $^{199}\text{Hg}^+$ ions in a linear rf trap and with numbers of $^9\text{Be}^+$ ions ranging from about 5 to 400 in a Penning trap, will be explained in detail in later sections.

Consider a single atom, or several identical atoms, with three energy levels $|A\rangle$, $|B\rangle$, and $|C\rangle$ (see Fig. 1). The

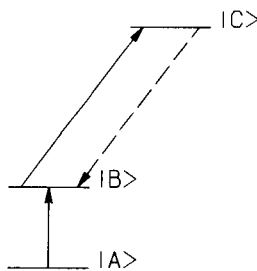


FIG. 1. A simplified energy-level diagram of an atom of the type used in the experiments. The atom or atoms are prepared in a superposition of $|A\rangle$ and $|B\rangle$ by a combination of laser optical pumping and rf excitation. The state is measured by applying laser radiation resonant with the $|B\rangle \rightarrow |C\rangle$ transition. If the atom is in $|A\rangle$, it does not absorb any photons from the laser beam and remains in $|A\rangle$. If the atom is in $|B\rangle$, the laser radiation drives it to $|C\rangle$. The atom then decays back to $|B\rangle$ and emits a photon. It can then be excited to $|C\rangle$ again.

lower two levels $|A\rangle$ and $|B\rangle$ are stable. They are separated by a radiofrequency photon energy. Level $|C\rangle$ decays, by emission of an optical photon, to $|B\rangle$ only. The state vector is prepared in a superposition of $|A\rangle$ and $|B\rangle$ by first preparing it in $|A\rangle$ and then applying an rf pulse near the $|A\rangle \rightarrow |B\rangle$ transition frequency. Any desired superposition of $|A\rangle$ and $|B\rangle$ can be obtained by controlling the frequency, amplitude, and duration of the rf pulse. The number of atoms in $|B\rangle$ is then measured. The measurement is made by applying a laser beam that is resonant with the transition from $|B\rangle$ to $|C\rangle$ and detecting the photons emitted in the decay from $|C\rangle$ to $|B\rangle$. If an atom is found in $|B\rangle$ when the laser pulse is applied, it is excited to $|C\rangle$. It quickly decays to $|B\rangle$ and emits a photon. It can then be excited back to $|C\rangle$ by the laser and emits another photon. Thus, an atom in $|B\rangle$ emits a series of many photons, while an atom in $|A\rangle$ emits none. The rate at which photons are emitted by the entire sample of atoms is proportional to the number of atoms in $|B\rangle$ when the laser beam is applied. If there is only one atom in the sample volume, the detection is particularly simple: If some photons are emitted, the atom was in $|B\rangle$; otherwise it was in $|A\rangle$. Quantum-amplification detection of this type, sometimes called electron shelving, was first proposed by Dehmelt [11] and, to the best of our knowledge, was first used by Wineland *et al.* [12].

In the preceding discussion, we assumed that each atom either emits a burst of photons or does not. According to the Copenhagen interpretation, the wave function of each atom is a superposition of $|A\rangle$ and $|B\rangle$ before the measurement and collapses to one state or the other when the detection laser beam is applied. According to the statistical-ensemble interpretation, the atom is found to be in $|A\rangle$ or $|B\rangle$ when the measurement is made, with probabilities p_A and p_B , respectively. There is no point in asking which state the atom was in just before the measurement, since this is not a question that can be answered by the experiment.

Quantum projection noise in the measured populations of states prepared in superpositions may be of some practical interest. This point was discussed previously, in the context of atomic frequency standards, by Wineland *et al.* in Appendix A of Ref. [13]. In some atomic frequency standards, such as cesium atomic beams, a signal which is proportional to the population of a particular quantum state is measured as a function of the frequency of an applied rf field. The signal is a maximum (or a minimum, depending on the detection method used) when the frequency matches the transition frequency ω_0 between two atomic states and decreases when the frequency increases or decreases from this value (see Fig. 2). The frequency ω of an oscillator is matched to the resonance frequency ω_0 by measuring the signal at two frequencies $\omega - \Delta\omega$ and $\omega + \Delta\omega$ and making a correction to ω by an amount proportional to the difference between the two signals. In the example shown in Fig. 2, the signal at $\omega + \Delta\omega$ is less than the signal at $\omega - \Delta\omega$, which indicates that ω must be decreased in order to match ω_0 . If the noise is independent of the position on the resonance line shape, measurements at the points of maximum slope would give the greatest sensitivity for determining ω_0 . However, the

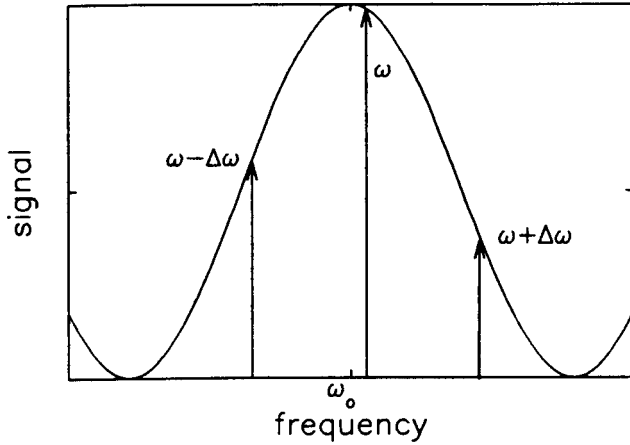


FIG. 2. A graph of the mean detected signal as a function of the frequency of the applied field for a resonance like that used in an atomic clock. The signal is proportional to the population of a particular energy level after the field has been applied. The maximum signal occurs at frequency ω_0 . If the line shape is symmetric, ω_0 can be determined by measuring the signal at two different frequencies $\omega - \Delta\omega$ and $\omega + \Delta\omega$ and varying ω until the signal intensities are equal. The frequency ω determined in this way is an estimate of ω_0 .

noise will in general vary with the signal level, due to quantum projection noise and also to other causes. Assume we have the extreme case where the only noise is quantum projection noise, where the maximum and the minima of the line shape correspond to pure energy eigenstates $|A\rangle$ and $|B\rangle$, and where the half-intensity points

correspond to equal superpositions of $|A\rangle$ and $|B\rangle$. In that case, it is not so obvious what the optimum value of $\Delta\omega$ should be. The noise goes to zero at the maxima and minima of the line shape, where the sensitivity to frequency deviations also goes to zero. The noise is the greatest at the half-intensity points, which, for a typical line shape, is where the frequency sensitivity is approximately the greatest. It will be shown later that the precision with which the line center can be determined is independent of $\Delta\omega$, if the line shape has a cosinusoidal form, often a good approximation when Ramsey's separated-oscillatory-field resonance method [14] is used.

II. THEORY

A. Single atom

Suppose a single system, such as a single atom, is prepared in a well-defined superposition of two stable or metastable states $|A\rangle$ and $|B\rangle$, which have energies $\hbar\omega_A$ and $\hbar\omega_B$. This could be done by preparing the atom in $|A\rangle$, by optical pumping, for example, and then applying a nearly resonant rf field of well-controlled frequency, amplitude, and duration. Suppose that the system is in $|A\rangle$ at time $t = 0$. We then apply an oscillatory perturbation V which has matrix elements:

$$\langle A|V|A\rangle = \langle B|V|B\rangle = 0, \quad (2.1)$$

$$\langle A|V|B\rangle = \langle B|V|A\rangle^* = \hbar b e^{i\omega t}. \quad (2.2)$$

The state at a later time $t > 0$ is [14]

$$|\psi(t)\rangle = c_A(t)|A\rangle + c_B(t)|B\rangle \quad (2.3)$$

$$= \left[i \frac{(\omega_0 - \omega)}{\Omega} \sin\left(\frac{\Omega t}{2}\right) + \cos\left(\frac{\Omega t}{2}\right) \right] \exp\left[\frac{i}{2}(\omega - \omega_A - \omega_B)t\right] |A\rangle \\ - i \frac{2b}{\Omega} \sin\left(\frac{\Omega t}{2}\right) \exp\left[-\frac{i}{2}(\omega - \omega_A - \omega_B)t\right] |B\rangle, \quad (2.4)$$

where

$$\omega_0 \equiv \omega_B - \omega_A, \quad (2.5)$$

$$\Omega \equiv \sqrt{(\omega_0 - \omega)^2 + (2b)^2}. \quad (2.6)$$

In deriving Eq. (2.4), we assumed that V does not induce transitions to states other than $|A\rangle$ and $|B\rangle$ and that spontaneous decay can be neglected. Also, all other perturbations, such as those due to collisions, are assumed to be negligible. For the levels studied experimentally in this work, which are hyperfine Zeeman sublevels of ground electronic states of atoms, spontaneous decay can be neglected. Such states decay primarily by magnetic dipole radiation. The rate for magnetic dipole decay from a higher sublevel $|e\rangle$ to a lower level $|g\rangle$ is

$$\gamma(e \rightarrow g) = \frac{4\omega_{eg}^3}{3\hbar c^3} |\langle e|\mu|g\rangle|^2, \quad (2.7)$$

where $\hbar\omega_{eg}$ is the energy difference between $|e\rangle$ and $|g\rangle$ and μ is the magnetic dipole operator. For typical values of the parameters for transitions between hyperfine-Zeeman sublevels, the mean lifetime for spontaneous decay is many years. For example, if $\omega_{eg} = 2\pi \times 30$ GHz and $|\langle e|\mu|g\rangle| = \mu_B$, where μ_B is the Bohr magneton, then the decay rate given by Eq. (2.7) is $2.7 \times 10^{-11} \text{ s}^{-1}$; that is, the lifetime is 1200 years.

In order to prepare a state with a given value of $p_B \equiv |c_B(t)|^2$, we can adjust b , ω , and the time t during which V is applied. For example, if $\omega = \omega_0$, then

$$p_B = \sin^2\left(\frac{\Omega t}{2}\right) = \sin^2(bt). \quad (2.8)$$

Any value of p_B from 0 to 1 can be obtained by adjusting the value of the product bt . Alternatively, it may be more convenient to vary ω , keeping b and t fixed at values so

that $bt = \pi$. (This is what is done in order to observe the resonance line shape, for example.) This induces a complete inversion ($p_B = 1$) at exact resonance ($\omega = \omega_0$). Any value of p_B down to 0 can be obtained by varying ω between ω_0 and $\omega_0 - 2\pi\sqrt{3}/t$ or between ω_0 and $\omega_0 + 2\pi\sqrt{3}/t$.

Ramsey's method of separated oscillatory fields [14] is another way of creating a given value of p_B . In this method, the perturbation is applied in two phase-coherent pulses of duration τ with a delay T between them. If the strength of the perturbation b is adjusted so that $b\tau = \pi/2$, then $p_B \equiv |c_B(T + 2\tau)|^2$ can be made to take any value between 0 and 1 by varying ω . If, in addition, $\tau \ll T$ and $|\omega - \omega_0|\tau \ll 1$, the probability p_B to be in $|B\rangle$ at time $T + 2\tau$ is

$$p_B \approx \frac{1}{2}\{1 + \cos[(\omega - \omega_0)T]\}. \quad (2.9)$$

An expression valid for arbitrary values of the parameters has been given by Ramsey [14].

It is useful to define a vector operator \mathbf{r} on the subspace spanned by $|A\rangle$ and $|B\rangle$. The components of \mathbf{r} are defined as

$$\begin{aligned} r_1 &\equiv \frac{1}{2}(|A\rangle\langle B| + |B\rangle\langle A|), \\ r_2 &\equiv \frac{i}{2}(|A\rangle\langle B| - |B\rangle\langle A|), \\ r_3 &\equiv \frac{1}{2}(|B\rangle\langle B| - |A\rangle\langle A|). \end{aligned} \quad (2.10)$$

The operator \mathbf{r} is equivalent to a spin- $\frac{1}{2}$ angular momentum operator, since it operates on a two-dimensional complex vector space and since the commutators satisfy the same algebra:

$$[r_i, r_j] = i\epsilon_{ijk}r_k, \quad (2.11)$$

where ϵ_{ijk} is the Levi-Civita symbol. For a general pure state of the form of Eq. (2.3), the expectation values of these operators are

$$\begin{aligned} \langle r_1 \rangle &= \frac{1}{2}(c_A^*c_B + c_B^*c_A) = \frac{1}{2}\sin\theta\cos\phi, \\ \langle r_2 \rangle &= \frac{i}{2}(c_A^*c_B - c_B^*c_A) = \frac{1}{2}\sin\theta\sin\phi, \\ \langle r_3 \rangle &= \frac{1}{2}(|c_B|^2 - |c_A|^2) = \frac{1}{2}\cos\theta, \end{aligned} \quad (2.12)$$

where we have used the notation $\langle r_1 \rangle \equiv \langle \psi|r_1|\psi \rangle$, etc. The expectation values can be represented geometrically by a three-dimensional vector $\langle \mathbf{r} \rangle$ of length $\frac{1}{2}$. The spherical polar angles (θ, ϕ) define the orientation of $\langle \mathbf{r} \rangle$. As pointed out by Feynman, Vernon, and Hellwarth [15], this representation is sometimes useful because of the way in which the evolution of the quantum state can be visualized as a rotation of a vector. The quantities $\{2\langle r_1 \rangle, 2\langle r_2 \rangle, 2\langle r_3 \rangle\}$ are equivalent to the quantities $\{r_1, r_2, r_3\}$ defined by Feynman, Vernon, and Hellwarth. The reason for using the definition of \mathbf{r} given by Eq. (2.10), rather than one differing by a factor of 2, is that \mathbf{r} then corresponds precisely to a spin- $\frac{1}{2}$ angular momentum operator. The vector representation can be generalized to deal with mixed states (statistical ensembles of pure states), but that will not be necessary here. The third component of \mathbf{r} is proportional to the internal energy operator. The

eigenstates of r_3 with eigenvalues $m = -\frac{1}{2}$ and $m = +\frac{1}{2}$ correspond to $|A\rangle$ and $|B\rangle$, respectively.

The variance of the measurement of the state ($|A\rangle$ or $|B\rangle$) of a single atom is particularly simple to calculate. We define a projection operator $P_B \equiv |B\rangle\langle B|$. The expectation value of P_B is $|c_B|^2 \equiv p_B$, the probability of a measurement finding the atom in $|B\rangle$. The variance of the measurement is

$$\begin{aligned} (\Delta P_B)^2 &\equiv \langle (P_B - \langle P_B \rangle)^2 \rangle \\ &= \langle P_B^2 - 2\langle P_B \rangle P_B + \langle P_B \rangle^2 \rangle \end{aligned} \quad (2.13)$$

$$= \langle P_B^2 \rangle - \langle P_B \rangle^2 = \langle P_B \rangle - \langle P_B \rangle^2 \quad (2.14)$$

$$= \langle P_B \rangle(1 - \langle P_B \rangle) = p_B(1 - p_B). \quad (2.15)$$

In Eq. (2.14), we have used the fact that

$$P_B^2 = (|B\rangle\langle B|)(|B\rangle\langle B|) = |B\rangle\langle B| = P_B. \quad (2.16)$$

Equation (2.15) shows that the uncertainty is zero when p_B is 0 or 1 and has its maximum value when $p_B = \frac{1}{2}$.

B. N atoms

If cooperative effects can be neglected over the time of the experiments, we may consider the atoms to be independent. For the systems used in the experiments, the decay rate of an individual atom is extremely small. It is possible for a suitably prepared collection of N atoms to exhibit a maximum spontaneous-decay rate per atom of about N times the usual rate given by Eq. (2.7), due to cooperative effects [16]. Even if the rate is enhanced by a factor of N , though, it can still be ignored for the small values of N that were used in these experiments.

One natural way to calculate the fluctuations of the measured populations is to consider the N atoms to be independent and to combine the probabilities according to the binomial distribution [17]. Let N_A and N_B be the numbers of atoms found to be in $|A\rangle$ and $|B\rangle$, respectively ($N_A + N_B = N$). Then, according to this model, the probability of measuring a given value of N_B is

$$P(N_B, N, p_B) = \frac{N!}{N_B!(N - N_B)!} (p_B)^{N_B} (1 - p_B)^{(N - N_B)}, \quad (2.17)$$

where $p_B \equiv |c_B|^2$ is the probability for a single atom to be in $|B\rangle$ and $(1 - p_B) = p_A \equiv |c_A|^2$ is the probability to be in $|A\rangle$. The variance of the binomial distribution is [17]

$$\sigma^2 = Np_B(1 - p_B). \quad (2.18)$$

The variance is zero when $p_B = 0$ or $p_B = 1$ and has its maximum value of $N/4$ when $p_B = \frac{1}{2}$. For $N = 1$, Eq. (2.18) agrees with Eq. (2.15). Figure 3 shows plots of probability distributions calculated from Eq. (2.17), for $N = 20$ and $p_B = 0, 0.1, \dots, 1$.

In general, it would be better to use a formalism that treats the N atoms as a combined quantum system. This should give a correct description both when cooperative

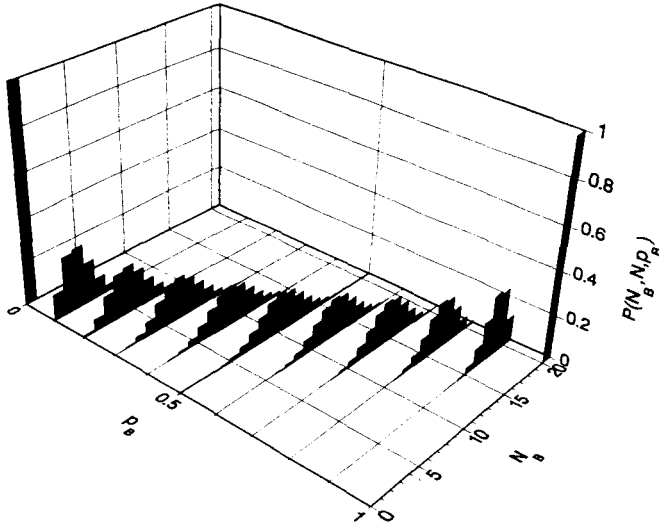


FIG. 3. A plot of the probability distributions of N_B , the number of atoms in $|B\rangle$, for $p_B = 0, 0.1, \dots, 1$. The total number of atoms N is 20. As p_B increases from 0, the distribution broadens and reaches its maximum variance at $p_B = 0.5$. As p_B increases beyond 0.5 the distribution narrows, eventually becoming a spike at $N_B = 20$ for $p_B = 1$.

effects are important and when they are negligible. Each two-level atom can be described by a spin- $\frac{1}{2}$ operator \mathbf{r}_i , defined as in Eq. (2.10), where $i = 1, \dots, N$ labels the atom. The eigenstates of r_{i3} with eigenvalues $m_i = -\frac{1}{2}$ or $+\frac{1}{2}$ correspond, respectively, to the $|A\rangle$ and $|B\rangle$ states of the i th atom, which we denote by $|A_i\rangle$ and $|B_i\rangle$. One basis for the 2^N -dimensional Hilbert space of N atoms is provided by the direct-product states of the form

$$|m_1, m_2, \dots, m_N\rangle \equiv \prod_{i=1}^N |m_i\rangle. \quad (2.19)$$

A collective-angular-momentum operator for the N atoms can be defined by

$$\mathbf{R} \equiv \sum_{i=1}^N \mathbf{r}_i. \quad (2.20)$$

It is implicitly assumed that each term in the summation is multiplied by the identity operators for all of the other atoms. Another basis for N atoms is given by states of the form $|g, R, M\rangle$, which are linear combinations of the product states defined by Eq. (2.19) [16]. Here, $R(R+1)$ is the eigenvalue of \mathbf{R}^2 , M is the eigenvalue of R_3 , and g is an index that may be required to provide a complete

set of labels. The eigenvalue M is related to the variables previously defined by

$$M = \frac{1}{2}(N_B - N_A), \quad (2.21)$$

$$N_B = \frac{1}{2}N + M. \quad (2.22)$$

Thus, fluctuations in M correspond directly to fluctuations in N_B , although M and N_B differ by a constant.

The state in which all of the atoms are in $|A\rangle$ has $R = \frac{1}{2}N$ and $M = -\frac{1}{2}N$ and is nondegenerate. This state is denoted by

$$|R = \frac{1}{2}N, M = -\frac{1}{2}N\rangle \equiv \prod_{i=1}^N |m_i = -\frac{1}{2}\rangle \equiv \prod_{i=1}^N |A_i\rangle. \quad (2.23)$$

We assume the atoms are far enough apart that they do not overlap spatially, so that symmetrization or antisymmetrization of the total wave function is unnecessary. Suppose that we apply the same perturbation to all of the atoms, so that the state of the i th atom goes to $c_A|A_i\rangle + c_B|B_i\rangle$ for each i . That is, the new state is

$$\prod_{i=1}^N (c_A|A_i\rangle + c_B|B_i\rangle). \quad (2.24)$$

We can visualize this as a rotation of the collective state vector from the negative R_3 axis ($\theta = \pi$) to new values of θ and ϕ given in terms of c_A and c_B by Eq. (2.12). Equivalently, it can be described as a rotation of the coordinate system by $\pi - \theta$ about the original R_2 axis, followed by a rotation of $-\phi$ about the new R_3 axis. The properties of states of this kind were discussed by Arecchi *et al.* [18], who called them atomic coherent states. They also called them Bloch states, because they resemble the spin states studied in nuclear magnetic resonance. The new state given by Eq. (2.24) is a linear combination of the states $|R = \frac{1}{2}N, M\rangle$, for $M = -\frac{1}{2}N, -\frac{1}{2}N + 1, \dots, \frac{1}{2}N$, since it is generated from Eq. (2.23) by a rotation. This state is

$$|R = \frac{1}{2}N, \theta, \phi\rangle = \sum_{M=-N/2}^{M=N/2} D_{M-N/2}^{(N/2)}(0, \pi - \theta, -\phi) \times |R = \frac{1}{2}N, M\rangle, \quad (2.25)$$

where $D_{M-N/2}^{(N/2)}$ is a matrix element of the rotation operator as defined in Eq. (4.1.10) of Ref. [19]. If the system is prepared in the state given by Eq. (2.25), the probability of measuring a given value of M is the absolute square of the coefficient of $|R = \frac{1}{2}N, M\rangle$, which is

$$P_{\text{Bloch}}(M, N, \theta) \equiv |D_{M-N/2}^{(N/2)}(0, \pi - \theta, -\phi)|^2 \quad (2.26)$$

$$= \left[a_{M-N/2}^{(N/2)}(\pi - \theta) \right]^2 \quad (2.27)$$

$$= \left[a_{M-N/2}^{(N/2)}(\theta) \right]^2 \quad (2.28)$$

$$= \frac{N!}{(\frac{1}{2}N + M)!(\frac{1}{2}N - M)!} \left(\cos \frac{\theta}{2} \right)^{N+2M} \left(\sin \frac{\theta}{2} \right)^{N-2M} \quad (2.29)$$

$$= \frac{N!}{N_B!(N-N_B)!} \left(\cos^2 \frac{\theta}{2} \right)^{N_B} \left(\sin^2 \frac{\theta}{2} \right)^{(N-N_B)} \quad (2.30)$$

$$= \frac{N!}{N_B!(N-N_B)!} \left[\frac{1}{2}(1 + \cos \theta) \right]^{N_B} \left[\frac{1}{2}(1 - \cos \theta) \right]^{(N-N_B)} \quad (2.31)$$

$$= \frac{N!}{N_B!(N-N_B)!} (p_B)^{N_B} (1-p_B)^{(N-N_B)}. \quad (2.32)$$

The final result is the same as Eq. (2.17), which was obtained by another method. Arecchi *et al.* obtained an equivalent result from the algebraic properties of the angular momentum operators, without explicitly making use of the rotation-operator matrix elements [18]. The quantity $d_{M-N/2}^{(N/2)}$ in Eq. (2.27) is defined in Eq. (4.1.12) of Ref. [19]. Equation (2.28) follows from Eq. (2.27) by making use of Eqs. (4.2.4)–(4.2.6) of Ref. [19]. The explicit form for $d_{M-N/2}^{(N/2)}(\theta)$ given in Eq. (2.29) is from Eq. (4.1.27) of Ref. [19]. Equation (2.30) results from using Eq. (2.22) to express M in terms of N_B and N , and Eq. (2.31) follows by making use of trigonometric identities. The final expression [Eq. (2.32)] results from using Eq. (2.12) to express $\cos \theta$ in terms of $p_B \equiv |c_B|^2$.

The variance of the measured value of M can be calculated by the standard formula

$$\langle \Delta R_3 \rangle^2 = \langle R_3^2 \rangle - \langle R_3 \rangle^2. \quad (2.33)$$

For a state with the form of Eq. (2.24), in which the c_{A_i} 's and c_{B_i} 's are the same for all i , $\langle R_3 \rangle$ and $\langle R_3^2 \rangle$ can be easily be evaluated:

$$\langle R_3 \rangle = \frac{N}{2}(p_B - p_A), \quad (2.34)$$

and

$$\langle R_3^2 \rangle = \left\langle \left(\sum_{i=1}^N r_{i3} \right)^2 \right\rangle \quad (2.35)$$

$$= \sum_{i=1}^N \sum_{j=1}^N \langle r_{i3} r_{j3} \rangle \quad (2.36)$$

$$= \sum_{i=1}^N \langle r_{i3}^2 \rangle + \sum_{\substack{i,j \\ i \neq j}} \langle r_{i3} r_{j3} \rangle \quad (2.37)$$

$$= \frac{N}{4} + \frac{N(N-1)}{4} (p_B - p_A)^2. \quad (2.38)$$

In obtaining Eq. (2.38), we used the fact that the first sum in Eq. (2.37) contains N terms, all equal to

$$\begin{aligned} & (c_{A_1}^* \langle A_1 | + c_{B_1}^* \langle B_1 |) r_{i3}^2 (c_{A_1} | A_1 \rangle + c_{B_1} | B_1 \rangle) \\ &= \frac{|c_{A_1}|^2}{4} + \frac{|c_{B_1}|^2}{4} = \frac{1}{4}, \end{aligned} \quad (2.39)$$

and the second sum contains $N(N-1)$ terms, all equal to

$$\begin{aligned} & (c_{A_1}^* \langle A_1 | + c_{B_1}^* \langle B_1 |) (c_{A_2}^* \langle A_2 | + c_{B_2}^* \langle B_2 |) r_{13} r_{23} \\ & \times (c_{A_1} | A_1 \rangle + c_{B_1} | B_1 \rangle) (c_{A_2} | A_2 \rangle + c_{B_2} | B_2 \rangle) \\ &= \left(\frac{|c_{B_1}|^2}{2} - \frac{|c_{A_1}|^2}{2} \right) \left(\frac{|c_{B_2}|^2}{2} - \frac{|c_{A_2}|^2}{2} \right) \\ &= \frac{1}{4} (p_B - p_A)^2. \end{aligned} \quad (2.40)$$

Substituting the values of $\langle R_3 \rangle$ and $\langle R_3^2 \rangle$ from Eqs. (2.34) and (2.38) into Eq. (2.33), we obtain

$$\begin{aligned} \langle \Delta R_3 \rangle^2 &= \frac{N}{4} + \frac{N(N-1)}{4} (p_B - p_A)^2 - \frac{N^2}{4} (p_B - p_A)^2 \\ &= \frac{N}{4} [1 - (p_B - p_A)^2] \\ &= \frac{N}{4} \{1 - [p_B - (1-p_B)]^2\} \\ &= N p_B (1-p_B). \end{aligned} \quad (2.41)$$

This result agrees with Eq. (2.18), which was based on the properties of the binomial distribution. Equation (2.41) was derived for the special case of an uncorrelated N -atom system in which all of the atoms have the same state vector. For more general states, in which the state vectors of different atoms are correlated with each other, it may be possible for the variance to be either larger or smaller than this value [20–23].

The error of an atomic frequency standard depends on the ratio of the noise in the signal to the frequency derivative of the signal. Aside from an additive constant, the signal of an idealized frequency standard with N atoms is proportional to $\langle R_3 \rangle$. The quantum projection noise is proportional to $\sqrt{\langle \Delta R_3 \rangle^2}$. If the Ramsey method is used, so that p_B is given by Eq. (2.9), the ratio of the quantum projection noise to the frequency derivative is independent of the frequency ω at which the measurement is made:

$$\sqrt{\langle \Delta R_3 \rangle^2} = \frac{1}{2} \sqrt{N} \sin[(\omega - \omega_0)T], \quad (2.42)$$

$$\frac{\partial \langle R_3 \rangle}{\partial \omega} = \frac{1}{2} N T \sin[(\omega - \omega_0)T], \quad (2.43)$$

$$\frac{\sqrt{\langle \Delta R_3 \rangle^2}}{\partial \langle R_3 \rangle / \partial \omega} = \frac{1}{T \sqrt{N}}. \quad (2.44)$$

The error is proportional to $1/\sqrt{N}$, which is sometimes called the shot-noise limit. If noise from other sources is significant, the ratio is not constant, and it is best to

measure the signal near the points of maximum slope. If the Ramsey method is not used, the exact trade-off of Eq. (2.44) does not hold, but the situation is not greatly different.

A simple graphical representation of a Bloch state can be used to provide an estimate of $(\Delta R_3)^2$ which agrees qualitatively with the result of Eq. (2.41). We can represent the Bloch state $|R = \frac{1}{2}N, M = -\frac{1}{2}N\rangle \equiv |R = \frac{1}{2}N, \theta = \pi\rangle$ by the set of all vectors of length

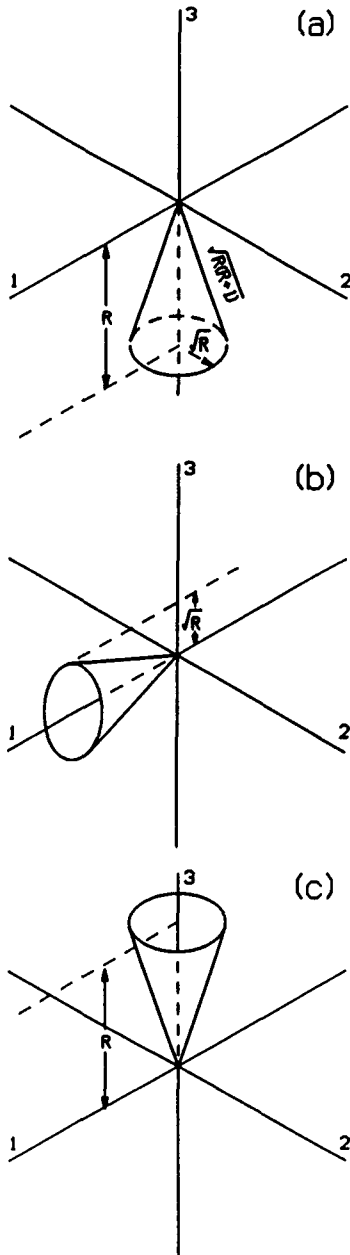


FIG. 4. Graphical representations of Bloch states (a) $|R = \frac{1}{2}N, M = -\frac{1}{2}N\rangle \equiv |R = \frac{1}{2}N, \theta = \pi\rangle$, (b) $|R = \frac{1}{2}N, \theta = \frac{\pi}{2}, \phi = 0\rangle$, and (c) $|R = \frac{1}{2}N, \theta = 0\rangle$. The uncertainty in the number of atoms in $|B\rangle$ (or $|A\rangle$) is represented by the spread in the third (R_3) component for the points on the circle surrounding the base of the cone. The uncertainty goes to zero for (a) and (c) and has its largest value for (b).

$\sqrt{R(R+1)}$ having their third (R_3) component equal to $-R$. This set forms a cone whose base has a radius equal to \sqrt{R} , as shown in Fig. 4(a). The fact that $(\Delta R_3)^2 = 0$ for this state is represented by the fact that all of the points on the circle surrounding the base of the cone have the same third component. The Bloch state $|R = \frac{1}{2}N, \theta = \frac{1}{2}\pi, \phi = 0\rangle$ is represented by Fig. 4(b). The points on the base of the cone have third components which vary over a range of $\pm\sqrt{R}$, while the rms deviation is approximately $\sqrt{R/2}$. Thus, we obtain the estimate $(\Delta R_3)^2 \approx R/2$. For a Bloch state with an arbitrary value of θ , we can use the same method to make the estimate

$$(\Delta R_3)^2 \approx \frac{R}{2} \sin^2 \theta = N p_B (1 - p_B). \quad (2.45)$$

This agrees with the actual value, which is given by Eq. (2.41). The Bloch state $|R = \frac{1}{2}N, \theta = 0\rangle$ is represented by Fig. 4(c). For this state, $(\Delta R_3)^2 = 0$.

III. SINGLE-ATOM EXPERIMENT

Quantum-state preparation and detection experiments were carried out with $^{199}\text{Hg}^+$ ions confined in a linear rf trap. Detailed observations were made of single ions, although some experiments were also carried out with several simultaneously trapped ions.

A. $^{199}\text{Hg}^+$ energy levels

Figure 5 shows the energy levels of $^{199}\text{Hg}^+$ which were important for the experiments. The ground electronic state has the configuration $5d^{10}6s^2S_{1/2}$. The first electric dipole transition, at 194 nm, is to the $5d^{10}6p^2P_{1/2}$ state. The metastable $5d^96s^2D_{3/2}$ and $5d^96s^2D_{5/2}$ states (not shown in Fig. 5) lie below the $^2P_{1/2}$ state. The ^{199}Hg nucleus has spin $\frac{1}{2}$, so both the $^2S_{1/2}$ and the $^2P_{1/2}$ states are split by hyperfine interactions into states with total angular momentum $F = 0$ and $F = 1$. For both the $^2S_{1/2}$ and $^2P_{1/2}$ states, the $F = 1$ hyperfine state is higher in energy than the $F = 0$ hyperfine state. The $^2S_{1/2}$ hyperfine split-

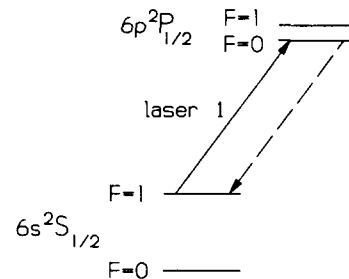


FIG. 5. Energy levels of $^{199}\text{Hg}^+$. The transition between the $^2S_{1/2}$ and $^2P_{1/2}$ states is at 194 nm. The hyperfine splittings in the $^2S_{1/2}$ and $^2P_{1/2}$ states are 40.5 and 6.9 GHz, respectively. The $^2S_{1/2}$ ($F = 1$) state is detected by exciting the $^2S_{1/2}$ ($F = 1$) \rightarrow $^2P_{1/2}$ ($F = 0$) transition with laser 1.

ting has been measured by microwave resonance methods to be 40.507 347 996 9(3) GHz [24]. The $^2P_{1/2}$ hyperfine splitting has been measured by Fabry-Pérot interferometry to be 6.955(90) GHz [25]. The natural linewidth of the $^2P_{1/2}$ state is about 70 MHz [26,27].

B. Apparatus

The $^{199}\text{Hg}^+$ ions were confined in a linear rf trap that consisted of four parallel cylindrical electrodes of radius 0.794 mm arranged symmetrically around a central axis [28]. The distance from the central axis to the inner surface of each electrode was 0.769 mm. The rf potentials on any two adjacent electrodes were 180° out of phase. The amplitude of the rf potential difference between two adjacent electrodes was about 500 V, and its frequency was 12.7 MHz. The electric fields produced by these electrodes created a force which pushed the ions to the central axis. The electrodes were divided into sections, to which static electric potentials of 1 V or less were applied to keep the ions from escaping along the axis.

Ions were produced by electron-impact ionization of neutral atoms inside the trap volume. A sample of ^{199}Hg of isotopic purity 91% was used. Typically, the pressure was about 10^{-7} Pa (1 Pa \approx 7.5 mTorr), except when the ions were being created, when it was raised to a higher level. The ions were confined to a region of a few hundred micrometers extent around the center of the trap. After being laser cooled, an individual ion was localized in position to about $1\ \mu\text{m}$ or less.

Narrow-band cw radiation at 194 nm was required for laser cooling and optical detection of the $^{199}\text{Hg}^+$ ions. This was generated by a combination of second-harmonic generation and sum-frequency mixing, starting with cw lasers [29]. About $5\ \mu\text{W}$ of 194-nm radiation were available. In order to laser cool and continuously observe the ions, 194-nm radiation near both the $^2S_{1/2}(F=1) \rightarrow ^2P_{1/2}(F=0)$ and the $^2S_{1/2}(F=0) \rightarrow ^2P_{1/2}(F=1)$ transition wavelengths was required [28]. We call these two sources laser 1 and laser 2. Otherwise, with only laser 1 or laser 2 on, the ions were optically pumped to a hyperfine state which could not absorb the 194-nm radiation. Also, in order to prevent trapping of the ions in Zeeman sublevels of the $^2S_{1/2}(F=1)$ state, we had to apply a magnetic field of approximately 5×10^{-4} T at an angle of approximately 45° with respect to the electric field vector of the radiation from laser 1 (see Appendix). The magnitude and orientation of the magnetic field were controlled by several pairs of Helmholtz coils. The 194-nm beams were directed through the trap at an angle of 9° with respect to the trap axis, so that both the axial and radial degrees of freedom were laser cooled. For this geometry, the theoretical Doppler cooling limit was 1.1 mK for the axial motion and 24 mK for the radial motion [30].

Some of the 194-nm radiation emitted by the ions perpendicular to the trap axis was focused by a multi-element lens onto a two-dimensional imaging photon-counting tube. The probability of a photon emitted by an ion being detected was about 10^{-4} . Individual ions could

be resolved with this apparatus. Some images showing several clearly resolved ions have been published previously [28]. The electronics could be adjusted so that the photons from any rectangular region of the image, for example, a region including only one ion, could be counted separately. To a good approximation, the ions in the trap do not interact and are independent.

A stable source of 40.5-GHz radiation was required for exciting the $^2S_{1/2}(F=0) \rightarrow (F=1)$ hyperfine transition. The output of a 10.125-GHz frequency synthesizer was amplified and then frequency multiplied by four. The output of the frequency multiplier was directed at the ions with a horn antenna.

The data from the photon-counting tube were recorded by a computer. The computer also controlled the light shutters, a microwave switch, the frequency of the microwave frequency synthesizer, and the magnitude and orientation of the magnetic field.

C. State preparation and detection

Optical pumping can be used to prepare the ions in either the ($F=1$) or the ($F=0$) hyperfine level of the $^2S_{1/2}$ ground state. In order to prepare them in the ($F=1$) state, both laser 1 and laser 2 are left on. If an ion in the ground ($F=1$) state is excited to the $^2P_{1/2}(F=0)$ state, it is forbidden by electric dipole selection rules from decaying to the ground ($F=0$) state, so it must return to the ($F=1$) state. There is a weak transition rate from the ground ($F=1$) state to the ground ($F=0$) state, via the $^2P_{1/2}(F=1)$ state. This rate is approximately 3×10^{-5} times the rate of leaving the ground ($F=1$) state and returning to the same state, via the $^2P_{1/2}(F=0)$ state, since laser 1 is far from resonance with the $^2S_{1/2}(F=1) \rightarrow ^2P_{1/2}(F=1)$ transition. If an ion does make a transition to the ground ($F=0$) state, laser 2 quickly drives it back to the $^2P_{1/2}(F=1)$ state, which decays, with probability $\frac{2}{3}$, to the ground ($F=1$) state. If laser 1 and laser 2 are both blocked at the same time, the ion will be in the ground ($F=1$) state with high probability, after a few multiples of the $^2P_{1/2}$ state lifetime (2.3 ns). This method does not select out a particular M_F Zeeman sublevel of the ground ($F=1$) state. If desired, a single M_F state could be selected by switching the polarization of laser 1 (to right or left circular polarization with propagation along the magnetic field for $M_F = \pm 1$ or linear polarization perpendicular to the magnetic field for $M_F = 0$). However, this was not done in this work.

An ion can be prepared in the $^2S_{1/2}(F=0)$ hyperfine level by blocking laser 2 while leaving laser 1 unblocked. For a typical intensity of laser 1, the ion is pumped to the ground ($F=0$) state in about 10 ms. In contrast to the previous method, the ion is prepared in a single M_F state. Laser 1 can also pump an ion from the ground ($F=0$) state to the ground ($F=1$) state. However, the rate for ($F=0$) \rightarrow ($F=1$) is less than that for ($F=1$) \rightarrow ($F=0$), mainly because laser 1 is farther from resonance for this process. In the steady state, the probability of being in the ($F=0$) state is about 94% (see Appendix). A

possible way to improve the state selection, for a single ion, is to observe the 194-nm photons emitted and to block laser 1 when the fluorescence drops to zero.

There is a probability of about 10^{-7} that an ion in the $^2P_{1/2}$ state will decay to the $^2D_{3/2}$ metastable state rather than to the $^2S_{1/2}$ state [27]. The $^2D_{3/2}$ state has a lifetime of 9.2 ms and decays, with about equal probability, to the $^2S_{1/2}$ state or to the metastable $^2D_{5/2}$ state, which has a lifetime of 86 ms [27,31]. This process is a potential problem for the state-selection methods, since the metastable states decay randomly to both ground hyperfine states. The effect was kept small by reducing the intensity of laser 1 so that the transition rate to the $^2D_{3/2}$ state was less than about 1 s^{-1} .

After the ion was prepared in the ground ($F = 0$) state, any desired superposition with the ground ($F = 1, M_F = 0$) state could be created by applying rf fields of well-controlled frequency, amplitude, and duration. These two states were used, because the magnetic shift of the transition frequency is quadratic, rather than linear, in the field. Thus, the transition frequency was stable enough to create the superposition states consistently.

State detection was carried out by counting the 194-nm photons emitted by the ions for a period, typically 15 ms, with laser 1 unblocked and laser 2 blocked. The mean number of photons detected was proportional to the number of ions in the ($F = 1$) state. However, the number is subject to statistical fluctuations, since the detection is essentially a Poissonian process. Also, laser intensity fluctuations lead to fluctuations in the overall counting rate.

Quantitative studies were made with only a single ion. In this case, the ion was presumed to be in the ($F = 1$) state if the number of photons detected was greater than a given threshold value and in the ($F = 0$) state if it was not. This threshold was set empirically, and was usually either 0 or 1. There was some possibility of error with this detection method. Dark counts from the phototube or photons scattered from some surface and then detected could lead to a false ($F = 1$) signal. Also, since the mean number of photons detected from an ($F = 1$) ion was small (about 5 in 15 ms), it was possible that not enough of them would be observed, thus leading to a false ($F = 0$) signal. If the detection efficiency could be improved, both of these problems could be reduced by using a higher threshold number of photons to distinguish between ($F = 1$) and ($F = 0$).

D. Results

The ability to prepare an ion in either the ($F = 0$) or ($F = 1$) ground hyperfine state is shown in Fig. 6. Each vertical line denotes the detection of a single photon at a particular time. The detection electronics were adjusted so that photons from only a single ion were detected. Before recording the data shown in Fig. 6(a), the ion was prepared in the ground ($F = 1$) state by leaving both laser 1 and laser 2 unblocked for about 0.1 s and then blocking them both. After a short delay, laser 1 was unblocked, and for 0.1 s, the photons were counted.

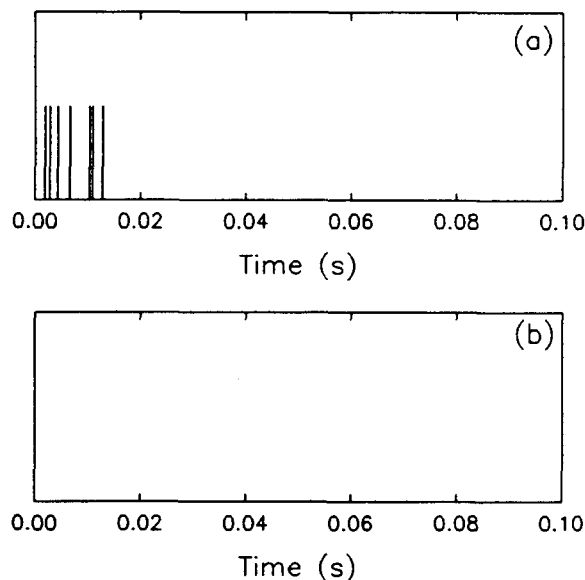


FIG. 6. Typical record of the detected photons from a single $^{199}\text{Hg}^+$ ion prepared in the ground (a) ($F = 1$) state and (b) ($F = 0$) state. The horizontal axis represents the time after laser 1, the detection laser, is unblocked. Each vertical line represents the detection of a single photon. In (a), eight photons were detected (two photons were too close in time to resolve on the graph). In (b), no photons were detected.

Their detection times were recorded with a resolution of $100\ \mu\text{s}$. In the example shown in Fig. 6(a), eight photons were recorded, but two of them were too nearly simultaneous to be resolved on the graph. Before recording the data shown in Fig. 6(b), the ion was prepared in the ground ($F = 0$) state by leaving laser 1 unblocked and laser 2 blocked for 0.05 s. Laser 1 was then blocked. After a short delay, laser 1 was unblocked again, and the computer was set to record photons, as for Fig. 6(a). None was recorded, so, with high probability, the ion was in the ($F = 0$) state.

Figure 7 shows the results of 100 successive single-ion state preparation and detection cycles of the type shown in Fig. 6. Preparation of the ($F = 1$) state [Fig. 7(a)] was alternated with that of the ($F = 0$) state [Fig. 7(b)], so that slow drifts in parameters such as the laser intensity would affect both plots in the same way. Each point represents the mean photon-count rate during a given 0.5-ms period after laser 1 was unblocked. The data from the first 1.5 ms, which was the time required for the light shutter to open fully, are not shown. The solid curve in Fig. 7(a) is a least-squares fit of the data to a decreasing exponential plus a constant base line. The fitted time constant of the exponential is $8.66 \pm 0.41\text{ ms}$. The fitted amplitude of the exponential is $769 \pm 22\text{ counts/s}$. The fitted base line is $47.3 \pm 4.3\text{ counts/s}$. The solid line in Fig. 7(b) corresponds to 47.3 counts/s , the base line determined from Fig. 7(a). This value does not differ significantly from the mean of all of the points in Fig. 7(b), which is 50.05 counts/s . The background count rate due to all sources other than photons emitted by the ion was measured by detuning laser 1 far from resonance. This

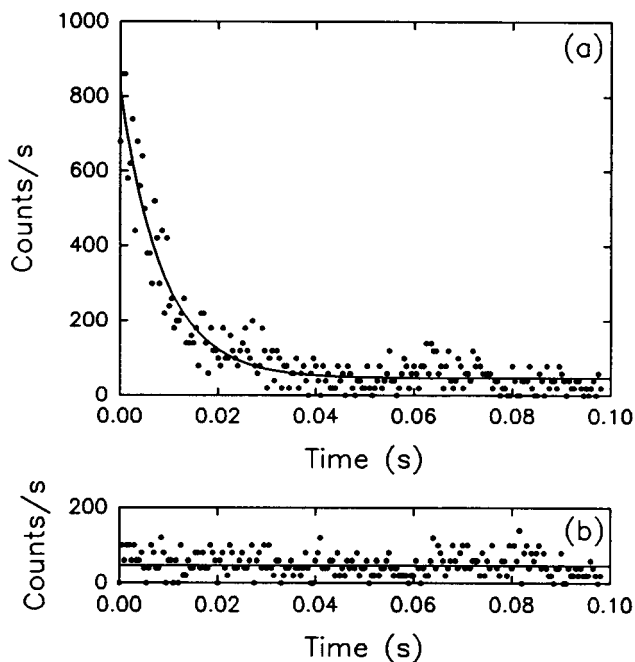


FIG. 7. Plot of the mean photon count rate as a function of the time after unblocking laser 1 for (a) a single ion prepared in the ($F = 1$) state and (b) the same ion prepared in the ($F = 0$) state. These plots were generated from 100 measurements like those in Fig. 6. The solid curve in (a) is a least-squares fit of the data to a decreasing exponential plus a baseline. The solid line in (b) is the base line determined from (a). The origin of the time axis is 1.5 ms after the laser 1 shutter is activated. After 1.5 ms this shutter is fully open.

rate was 4 ± 2 counts/s, so the actual base line for light scattered from the ion was 43 ± 5 counts/s. The ratio of the base line to the sum of the base line and the amplitude of the exponential is 0.053 ± 0.006 . This represents the steady-state probability that an ion is in the ground ($F = 1$) state when laser 1 alone is applied. This compares well with a calculated value of approximately 0.06 (see Appendix).

The Rabi resonance line shape shown in Fig. 8 was measured by repeatedly preparing the ($F = 0$) state, applying a microwave pulse at a given frequency, and determining whether the ion was in ($F = 0$) or ($F = 1$). At each frequency, 19 measurements were made, and the results were averaged [$(F = 0)$ corresponding to 0 and ($F = 1$) to 1]. For this run, the sequence of operations for each measurement was as follows.

(1) Both laser 1 and laser 2 were left on for 200 ms to laser cool the ion. The magnetic field was set to about 5×10^{-4} T to avoid optical pumping.

(2) The fluorescence from the ion was measured for 5 ms. This step was repeated if the number of photons counted was 50 or less. This was done to avoid proceeding while the ion was trapped in one of the metastable D states.

(3) Laser 2 was blocked to allow the ion to be pumped to the ground ($F = 0$) state. The fluorescence was measured for 10 ms. If any photons were detected during this

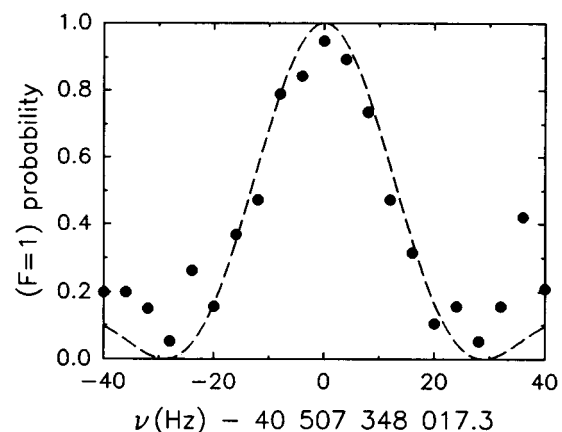


FIG. 8. Microwave resonance of a single ion. Each dot represents the average of 19 measurements. The curve is a calculated Rabi line shape. The calculation does not take into account the imperfect state preparation.

period, another 10-ms measurement was made. This was to ensure that the ion was in the ground ($F = 0$) state before proceeding.

(4) Laser 1 was blocked, and the magnetic field was decreased to approximately 5×10^{-5} T in order to reduce the effect of magnetic field fluctuations on the resonance frequency. A 30-ms rf pulse near the 40.5-GHz resonance was applied. The magnetic field was then increased to its previous value.

(5) Laser 1 was unblocked, and the fluorescence was measured for 15 ms. If 0 or 1 photons were detected, the ion was assumed to be in ($F = 0$). If more photons were detected, it was assumed to be in ($F = 1$).

The dashed line is a theoretical Rabi line shape for optimum power and a 30-ms rf pulse duration, calculated from Eq. (2.4). The deviation between the data and the calculation is most obvious at the minima of the line shape. The deviations result from the combined effects of imperfect ($F = 0$) state preparation and imperfect state detection. The combination of these effects results in a signal that goes from about 0.1 to 0.95 instead of from 0 to 1. The frequency instability of the microwave source is known, from separate measurements, to be small enough as to have a negligible effect on the line shape [28].

We can also compute the variance of the signal at various positions on the resonance curve. At the point corresponding to the maximum signal, it is 0.053. At the two points corresponding approximately to the half-maximum points, it is 0.26. At the two points corresponding to the minimum signal on both sides of the resonance, it is 0.051.

We have published a microwave resonance curve in which the total fluorescence from several ions was measured [28]. Such a signal is more sensitive to noise from the intensity fluctuations of the 194-nm sources, background scattered light, and other sources. In order to reduce this noise, it should be possible to count the photons from each ion separately, in order to clearly discriminate between ions in the ground ($F = 0$) and ($F = 1$) states,

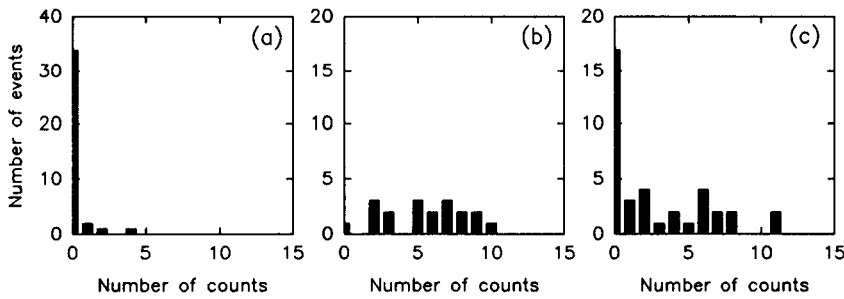


FIG. 9. Photon count distributions for a single $^{199}\text{Hg}^+$ ion prepared in (a) the $(F=0, M_F=0)$ state, (b) the $(F=1, M_F=0)$ state, and (c) an equal superposition of these two states. The bars represent the number of cases in which a given number of fluorescence photons was detected when the detection laser was applied. The number of measurements was 38 for (a), 19 for (b), and 38 for (c).

as was done here with a single ion.

Figure 9 shows the distributions of the numbers of photons detected at various points on the resonance curve of Fig. 8. Figure 9(a) shows the distribution at the points corresponding to the minima on both sides of the resonance. In most cases, no photons were observed. However, in a few cases one or more photons were observed, presumably due to a combination of background scattered light and imperfect state preparation. Figure 9(b) shows the distribution at the maximum of the resonance. There is a broad distribution of numbers of photons detected, with a mean of about 5.5. In one measurement, no photons were measured. This may have been due to imperfect state preparation or to the possibility that no photons were detected, even though some were emitted. Figure 9(c) shows the distribution at the two half-maximum points on the resonance. The distribution is a superposition of those at the maximum and the minima. This bimodal distribution is the signature of the quantum projection noise for the single-atom case. That is, for a superposition state with equal amplitudes of the two components, the measurement finds the ion randomly in one state or the other.

IV. *N*-ATOM EXPERIMENT

N-atom quantum-state preparation and detection experiments were carried out with $^9\text{Be}^+$ ions in a Penning trap. The Penning trap was used, rather than the rf trap, because the number of atoms that could be stably trapped could be varied from a few to several thousand. However, loading and detecting single ions was difficult with this apparatus.

A. $^9\text{Be}^+$ energy levels

Figure 10 shows the energy levels of $^9\text{Be}^+$ which were important for the experiments. The ground electronic state has the configuration $2s\ ^2S_{1/2}$. The ^9Be nucleus has spin $\frac{3}{2}$, so the ground state has eight hyperfine Zeeman sublevels. In a high magnetic field, as is present in the Penning trap, the energy eigenstates are approximate eigenstates of I_z and J_z , the z components of the nuclear and electronic angular momenta. The static magnetic-field direction defines the z axis. These eigenstates will be referred to by their main components in the $|M_I, M_J\rangle$ basis. For brevity, they will also be referred to by num-

bers 1–8, as shown in Fig. 10, which correspond, in order of decreasing energy, to $|-\frac{3}{2}, +\frac{1}{2}\rangle$, $|-\frac{1}{2}, +\frac{1}{2}\rangle$, $|+\frac{1}{2}, +\frac{1}{2}\rangle$, $|+\frac{3}{2}, +\frac{1}{2}\rangle$, $|+\frac{3}{2}, -\frac{1}{2}\rangle$, $|+\frac{1}{2}, -\frac{1}{2}\rangle$, $|-\frac{1}{2}, -\frac{1}{2}\rangle$, and $|-\frac{3}{2}, -\frac{1}{2}\rangle$. The 313-nm transition to the $2p\ ^2P_{3/2}$ electronic state was used for state selection and detection.

B. Apparatus

The experimental apparatus and techniques have been described previously [32–35]. The Penning trap was made of cylindrical electrodes, to which static electric potentials were applied. It was inserted into the bore of a superconducting solenoid magnet, which generated a uniform magnetic field B_0 of approximately 0.82 T. The combination of the electrostatic potentials and uniform magnetic field trapped the ions in three dimensions. The pressure in the trap was approximately 10^{-8} Pa. The ions were created by electron-impact ionization of neutral atoms.

The state preparation experiments required that the 313-nm light be blocked for some periods in order to avoid

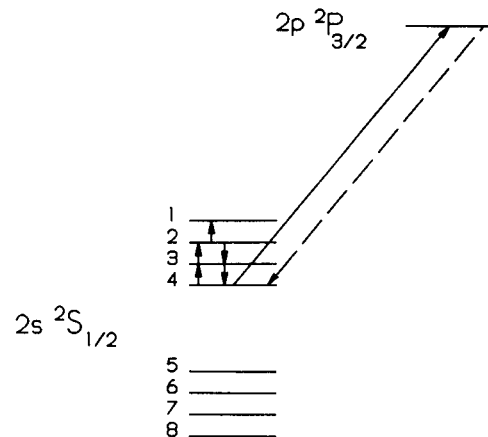


FIG. 10. Level diagram for $^9\text{Be}^+$. The ground-state Zeeman hyperfine states are labeled by numbers 1–8. Their quantum numbers are given in the text. Laser radiation at 313 nm optically pumps most of the ions into state 4. These atoms are then transferred to state 3 and then to state 2 by rf π pulses. Other rf pulses then create a superposition of states 1 and 2. Atoms which remain in state 2 are transferred back to state 4. The laser radiation is applied again, and the number of atoms in state 4 is determined from the fluorescence intensity in the first second after the laser radiation is reapplied.

perturbations of the energy levels. In order to keep the ${}^9\text{Be}^+$ ion plasma from heating and increasing its spatial extent when the 313-nm light was not available for laser cooling, approximately 1000 ${}^{26}\text{Mg}^+$ ions were trapped and laser cooled at the same time. This cooled the ${}^9\text{Be}^+$ ions by long-range Coulomb collisions [36]. The 280-nm $3s^2S_{1/2} \rightarrow 3p^2P_{3/2}$ transition was used for laser cooling the ${}^{26}\text{Mg}^+$ ions.

The 313-nm and 280-nm beams required for state selection and detection of the ${}^9\text{Be}^+$ ions and for laser cooling the ${}^{26}\text{Mg}^+$ were generated by frequency doubling the outputs of cw dye lasers in nonlinear crystals. Fluorescence from the ions was focused by a multielement lens onto the photocathode of an imaging photon-counting tube. The overall detection efficiency was approximately 2×10^{-4} . To generate the rf magnetic fields required for the state preparation and detection, the amplified output of a frequency synthesizer was coupled into a wire loop antenna. The light shutters, rf switches, and frequency synthesizer were controlled by a computer, which also recorded the photon counts.

C. Ion-number measurement

In the ${}^{199}\text{Hg}^+$ experiments, the number of ions could be determined directly from the image. This could not be done for the ${}^9\text{Be}^+$ ions in the Penning trap, since they rotate rapidly around the z axis. Therefore, the number was determined indirectly. Calculations based on a charged fluid model relate the density of the ion plasma to its shape, for given external fields [36–38]. The shapes and sizes of the nonneutral, ion plasmas were determined by moving the laser beam and observing the imaged fluorescence. The product of the density and volume yielded the number of ions with an uncertainty estimated to be about 30%.

D. State preparation and detection

In the ${}^9\text{Be}^+$ experiments, coherent superpositions of two internal states (states 1 and 2) were created and then subjected to measurements. These states were chosen because, for a value of B_0 near 0.8194 T, the first derivative of the transition frequency with respect to B_0 goes to zero. The resulting insensitivity to magnetic-field fluctuations makes it easier to generate coherent superposition states reproducibly.

The state preparation began by subjecting the ions to 313-nm radiation, polarized perpendicular to the magnetic field, for approximately 15 s. The frequency of the 313-nm radiation was slightly below the $2s^2S_{1/2} (M_I = +\frac{3}{2}, M_J = +\frac{1}{2}) \rightarrow 2p^2P_{3/2} (M_J = +\frac{3}{2}, M_I = +\frac{3}{2})$ transition frequency. This is a cycling transition, since electric dipole selection rules require that the ion return to the ground-state sublevel that it started from. Spontaneous Raman transitions induced by the 313-nm radiation established a steady state in which approximately $\frac{16}{17}$ of the ions were in state 4 and the remaining $\frac{1}{17}$ were in state

5. This optical pumping has been discussed previously [12,39] and studied experimentally [40]. There are fluctuations about these average values, since any given ion is continually making transitions between states. The ions could have been completely optically pumped into state 4 by circularly polarized light propagating along the z axis, but this was not convenient experimentally.

The 313-nm beam was blocked to stop the optical pumping and to prevent perturbations to the ${}^9\text{Be}^+$ energy levels. Next, the ions in state 4 were transferred to state 3 and then to state 2 by 0.2 s resonant rf pulses. These were π pulses; that is, the products of the rf magnetic fields and the pulse durations were adjusted so that $bt = \pi$ in Eq. (2.8). The frequencies were 320 712 280 Hz for the $(4 \rightarrow 3)$ transition and 311 493 688 Hz for the $(3 \rightarrow 2)$ transition. The Ramsey method was then used to create various superpositions of states 1 and 2. The two Ramsey rf pulses were 0.5 s long and were separated by 5 s; the frequency was 303 016 377.265 Hz.

Then a measurement was made of the number of ions in state 2. First, the ions in state 2 were transferred to state 3 and then to state 4 by applying the π pulses in the opposite order. Then the 313-nm beam was unblocked, and the fluorescence photons were counted for 1 s.

The ions which were left in state 5 at the time that the 313-nm beam was blocked (about $\frac{1}{17}$ of the total number) contributed to the fluorescence signal. This is so, because the time constant for exchanging population between states 4 and 5 by spontaneous Raman transitions was about 0.1 s, which was much less than the 1-s observation time. The time constant for ions in state 1 to be optically pumped to states 4 and 5 was approximately 10 s. Therefore, the number of ions pumped from state 1 back to states 4 and 5 could be neglected.

E. Results

Ion plasmas containing numbers of ${}^9\text{Be}^+$ ions ranging from a few to a few hundred were studied. Figures 11(a)–11(d) show the results from plasmas containing approximately 5, 21, 72, and 385 ions. The rf power for the $(2 \rightarrow 1)$ Ramsey resonance was adjusted so as to give a minimum fluorescence signal at the line center. Measurements were made at rf frequencies corresponding to the transition maximum (minimum fluorescence), the first upper and lower transition minima (maximum fluorescence), and the points halfway between the transition maximum and the upper and lower transition minima. The measured signal is the number of photons detected in the first second after the laser is unblocked. This is

$$S = B + K(N_4 + N_5), \quad (4.1)$$

where B is the background signal, N_4 and N_5 are the numbers of ions in states 4 and 5, and K is a constant which must be calibrated for a given set of conditions. At the line center, the signal is $B + (KN/17)$, where N is the total number of ${}^9\text{Be}^+$ ions, while at the points of maximum fluorescence, it is $B + KN$. For the $N = 5, 21, 72,$ and 385 data shown in Figs. 11(a)–11(d), $K = 87.3$,

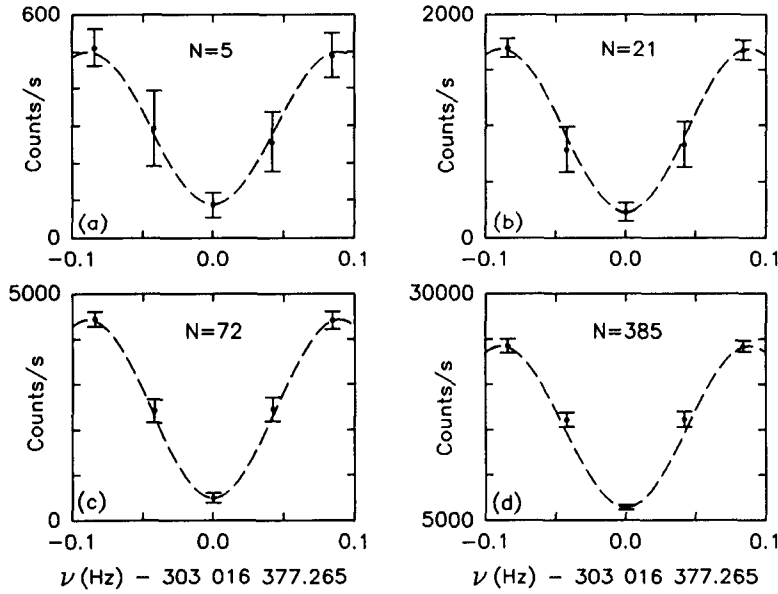


FIG. 11. Plots of the fluorescence detected from ${}^9\text{Be}^+$ ions confined in a Penning trap as a function of the frequency of the applied rf radiation for (a) 5 ions, (b) 21 ions, (c) 72 ions, and (d) 385 ions. The dots are the experimental mean signals, and the error bars show the experimental standard deviations. On the sides of the resonances, the standard deviations are mainly due to quantum projection noise. The dashed lines show the calculated line shapes, fitted to the experimental minimum and maxima.

73.9, 58.0, and 48.6 counts/ion, respectively. The fact that $K \gg 1$ for all of these cases means that quantum projection noise should be more important than photon shot noise, except when the vanishing of one of the state amplitudes causes the quantum projection noise to go to zero. This is a good example of electron-shelving detection. In Figs. 11(a)–11(d), the dots are the experimental mean signals:

$$\bar{S} \equiv \frac{1}{n} \sum_{i=1}^n S_i, \quad (4.2)$$

where S_1, S_2, \dots, S_n is the sequence of n measurements made under the same conditions. The error bars correspond to $\pm\sigma$, where σ was calculated from

$$\sigma^2 = \frac{1}{2(n-1)} \sum_{i=1}^{n-1} (S_{i+1} - S_i)^2. \quad (4.3)$$

Equation (4.3) was used, rather than the usual formula,

$$\sigma^2 = \frac{1}{n-1} \sum_{i=1}^n (S_i - \bar{S})^2, \quad (4.4)$$

for the standard deviation, because it is less sensitive to slow drifts of the signal, such as those caused by variations in the laser intensity or other experimental parameters [41].

Table I summarizes the data shown graphically in Figs. 11(a)–11(d). For each value of N , the data from the point of minimum fluorescence is labeled “dip,” the data from the two points of maximum fluorescence are combined and labeled “peaks,” and the data from the two points halfway between the minimum and the maxima are combined and labeled “sides.”

Four contributions to σ^2 are listed in Table I: σ_{proj}^2 ,

σ_{pump}^2 , σ_{shot}^2 , and σ_{tech}^2 . They are assumed to be independent, so they are added in quadrature to yield σ_{calc}^2 :

$$\sigma_{\text{calc}}^2 \equiv \sigma_{\text{proj}}^2 + \sigma_{\text{pump}}^2 + \sigma_{\text{shot}}^2 + \sigma_{\text{tech}}^2. \quad (4.5)$$

The quantum projection noise σ_{proj} is approximately zero at the peaks and at the dip and is $\frac{1}{2}(\frac{16}{17}N)^{1/2}K$ on the sides [see Eq. (2.41)]. The factor of $\frac{16}{17}$ appears in this expression because, on the average, $\frac{1}{17}$ of the ions are left in state 5 by the optical pumping that precedes the rf pulses. The fluctuations in the number of ions left in state 5 are the source of σ_{pump} . This has the greatest effect at the dip, where the only contribution to the fluorescence is from the ions in state 5. At the dip,

$$\sigma_{\text{pump}} = [N(\frac{1}{17})(\frac{16}{17})]^{1/2} K = \frac{4}{17}\sqrt{NK}. \quad (4.6)$$

This is derived from the expression for the variance of a binomial distribution [see Eq. (2.18)]. At the peaks, σ_{pump} is approximately zero, because all of the ions are either in state 4 or state 5 and contribute to the signal. At the sides, σ_{pump} is half as large as at the dip. The shot noise σ_{shot} is equal to $(\bar{S})^{1/2}$ and results from Poisson statistics in the photon detection.

All other contributions to σ , such as those due to intensity fluctuations of the laser, are called technical noise σ_{tech} . Laser-intensity fluctuations will lead to a contribution to σ_{tech} proportional to S . Fluctuations in the shape and temperature of the ion plasma may make a large contribution to σ_{tech} , approximately proportional to S . Such fluctuations have been observed in other laser-cooled ion plasmas in Penning traps [42,43], but are not well understood. Small fluctuations in the frequency of the microwave source, or in the resonance frequency of the ions, would cause an increase in σ_{tech} on the sides of the line shape but not at the dips or peaks. However, from auxiliary measurements, including the observation

TABLE I. Mean signals \bar{S} and variances σ^2 for $N = 5, 21, 72,$ and 385 ${}^9\text{Be}^+$ ions. The terms “dip,” “peaks,” and “sides” refer to the points of minimum fluorescence, the points of maximum fluorescence, and the points halfway between the minima and the maxima, respectively. The number of measurements is n . The measured variance is σ_{expt}^2 . The calculated variance σ_{calc}^2 is equal to $\sigma_{\text{proj}}^2 + \sigma_{\text{pump}}^2 + \sigma_{\text{shot}}^2 + \sigma_{\text{tech}}^2$. The value of σ_{expt}^2 at the peaks was used to empirically determine σ_{tech}^2 . Hence σ_{calc}^2 is not listed at the peaks, since it is necessarily equal to σ_{expt}^2 . However, the agreement between σ_{expt} and σ_{calc} at the sides and at the dip is a test of the theory. The units for the variances are 10^3 counts^2 .

N	Position	n	\bar{S} (counts)	σ_{expt}^2	σ_{proj}^2	σ_{calc}^2 (10^3 counts^2)			
						σ_{pump}^2	σ_{shot}^2	σ_{tech}^2	σ_{calc}^2
5	dip	19	89	1.0	≈ 0	2.1	0.1	0.1	2.3
5	sides	38	275	6.6	9.0	0.5	0.3	0.7	10.5
5	peaks	38	500	2.8	≈ 0	≈ 0	0.5	2.3	
21	dip	30	232	5.5	≈ 0	6.3	0.2	0.1	6.6
21	sides	60	810	37.8	27.0	1.6	0.8	1.3	30.7
21	peaks	60	1693	7.6	≈ 0	≈ 0	1.7	5.9	
72	dip	30	498	11.5	≈ 0	13.4	0.5	0.3	14.2
72	sides	60	2432	61.0	57.0	3.4	2.4	6.3	69.1
72	peaks	60	4429	25.2	≈ 0	≈ 0	4.4	20.8	
385	dip	30	6642	69	≈ 0	50	7	26	83
385	sides	60	16108	600	214	13	16	151	394
385	peaks	60	24253	367	≈ 0	≈ 0	24	343	

of lineshapes as narrow as $900 \mu\text{Hz}$ [34], we determined that this potential source of noise was negligible. Since known contributions to σ_{tech} are roughly proportional to S , σ_{tech} was determined empirically from σ_{expt} at the peaks, where the only other contribution to σ is σ_{shot} , which is small. For $N = 5, 21, 72,$ and 385 , $\sigma_{\text{tech}}/\bar{S}$ at the peaks was 9.6%, 4.5%, 3.2%, and 2.4%, respectively. The values of σ_{tech} at the sides and the dips were estimated by assuming that, for a given set of experimental conditions, σ_{tech} was proportional to \bar{S} .

The entries on Table I show that different types of noise dominate at each of the three positions on the line: σ_{proj}^2 on the sides, σ_{pump}^2 at the dip, and σ_{tech}^2 at the peaks. Shot noise is not a large contribution for any of the cases shown in Table I. Considering the uncertainties in the experimental parameters, particularly in N , the agreement between σ_{expt}^2 and σ_{calc}^2 is quite good. Figure 12 shows that the noise on the sides of the lines is mainly attributable to quantum projection noise. The quantity plotted is $\sigma/\Delta S$ and is defined as

$$\frac{\sigma}{\Delta S} \equiv \frac{\sigma_{\text{expt}}(\text{sides})}{\bar{S}(\text{peaks}) - \bar{S}(\text{dip})}. \quad (4.7)$$

The dashed line is the theoretical prediction for quantum projection noise alone:

$$\frac{\sigma_{\text{proj}}}{\Delta S} = \frac{\sqrt{17}}{8\sqrt{N}} \approx \frac{0.515}{\sqrt{N}}. \quad (4.8)$$

The deviation of the experiment from theory for large N is presumably due to technical noise. As noted previously, $\sigma_{\text{tech}}/\bar{S}$ decreases as N increases, apparently because the ion plasma becomes more stable in shape and

temperature. However, it should not continue to decrease indefinitely with N , since the contribution from laser intensity fluctuations, for example, should approach a constant value for large N . Hence $\sigma/\Delta S$ should approach a constant value for large N rather than continuing to decrease as $1/\sqrt{N}$. For $N = 10\,000$, $\sigma_{\text{proj}}/\bar{S}$ is approximately 1% on the sides, while we might, from the present results, expect $\sigma_{\text{tech}}/\bar{S}$ to be about 2%. This is consistent with previous experimental results from a frequency

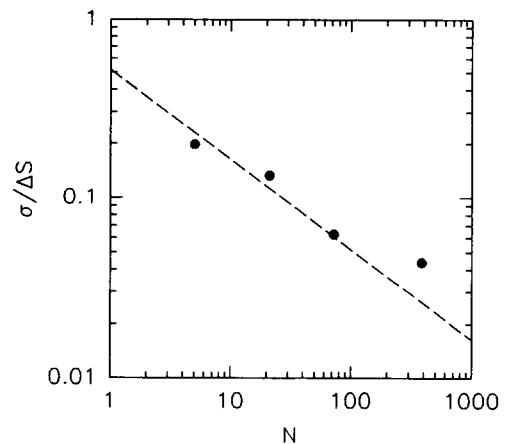


FIG. 12. Plot of the normalized standard deviations as a function of N , the number of ${}^9\text{Be}^+$ ions. The quantity $\sigma/\Delta S$ is the ratio of the experimental standard deviation on the sides of the resonance to the difference in the signal between the peaks and the dip. The dashed line is the theoretical prediction for the contribution from quantum projection noise alone.

standard based on 5000–10 000 ${}^9\text{Be}^+$ ions [34]. However, there is no fundamental reason that the technical noise cannot be greatly reduced.

V. CONCLUSION

We have prepared one or many ions in well-defined superpositions of two states and then measured the population of one of these states. The population measurements display quantum fluctuations which are greatest when the amplitudes of the two states are equal. In the case of a single ion, where photon scattering is used to distinguish between the two states, the fluctuations take the form of random switching between two distinguishable conditions — the observation of zero photons (or background) or of some photons. There is good agreement between the observations and theoretical predictions for both one and many ions.

Population fluctuations of the type observed here (quantum projection noise) are present and could be observed in other kinds of experiments, for example, those using atomic or neutron beams. Quantum projection noise might be observed in neutron interferometry [44]. In this case, the two neutron beams which emerge from the interferometer correspond to the two energy states $|A\rangle$ and $|B\rangle$. Introducing a phase shift in one arm of the interferometer allows one to create coherent superposition states. Rauch *et al.* [44] show counting-rate histograms for phase shifts corresponding to the maximum and minimum counting rates in one beam. However, they do not show the histograms for a phase shift halfway between a maximum and a minimum, which might show an increased variance due to quantum projection noise.

In the preceding discussions, the single-atom and N -atom experiments were treated from different perspectives. This was because of the different experimental methods which were used for the ${}^{199}\text{Hg}^+$ and ${}^9\text{Be}^+$. How-

ever, if the N atoms are uncorrelated, there is not a fundamental difference between the two cases. We could simulate the results of an N -atom measurement by making N successive measurements on a single atom and summing the results.

In many experiments, quantum projection noise would be obscured by other forms of noise, such as fluctuations in the beam intensity or the statistics of the detection process. In the experiments described here, trapping nearly eliminates fluctuations in the number of atoms, and the electron-shelving detection method nearly eliminates statistical fluctuations in the detection, thereby making quantum projection noise the dominant source of noise. In spectroscopic measurements on fixed numbers of atoms, where transitions are detected by monitoring changes in population, this is the fundamental noise limit.

ACKNOWLEDGMENTS

We acknowledge financial support from the Office of Naval Research. We thank Jean Dalibard for pointing out the simple calculation of the variance for one atom [Eq. (2.15)].

APPENDIX: OPTICAL PUMPING IN ${}^{199}\text{Hg}^+$

For low enough laser intensities, optical pumping among the Zeeman hyperfine sublevels of the ground state of ${}^{199}\text{Hg}^+$ can be described by population rate equations. The following set of equations applies to the populations of the Zeeman hyperfine sublevels of the $6s\ {}^2S_{1/2}$ and $6p\ {}^2P_{1/2}$ states, when a linearly polarized optical field of the form $\mathbf{E}(\mathbf{r}, t) = \hat{\mathbf{e}}E_0 \cos(\mathbf{k} \cdot \mathbf{r} - \omega_k t)$, nearly resonant with the ${}^2S_{1/2}(F=1) \rightarrow {}^2P_{1/2}(F=0)$ transition, is applied:

$$\frac{dP_0}{dt} = - \left(\frac{\gamma/2}{\Delta_S + \Delta_P} \right)^2 R_0 P_0 + \frac{\gamma}{3} (P_5 + P_6 + P_7), \quad (\text{A1})$$

$$\frac{dP_1}{dt} = -\frac{1}{2} \sin^2 \theta R_0 L(\Delta) P_1 - \frac{1}{2} (1 + \cos^2 \theta) \left(\frac{\gamma/2}{\Delta_P} \right)^2 R_0 P_1 + \frac{\gamma}{3} (P_4 + P_5 + P_6), \quad (\text{A2})$$

$$\frac{dP_2}{dt} = -\cos^2 \theta R_0 L(\Delta) P_2 - \sin^2 \theta \left(\frac{\gamma/2}{\Delta_P} \right)^2 R_0 P_2 + \frac{\gamma}{3} (P_4 + P_5 + P_7), \quad (\text{A3})$$

$$\frac{dP_3}{dt} = -\frac{1}{2} \sin^2 \theta R_0 L(\Delta) P_3 - \frac{1}{2} (1 + \cos^2 \theta) \left(\frac{\gamma/2}{\Delta_P} \right)^2 R_0 P_3 + \frac{\gamma}{3} (P_4 + P_6 + P_7), \quad (\text{A4})$$

$$\frac{dP_4}{dt} = \frac{1}{2} \sin^2 \theta R_0 L(\Delta) (P_1 + P_3) + \cos^2 \theta R_0 L(\Delta) P_2 - \gamma P_4, \quad (\text{A5})$$

$$\frac{dP_5}{dt} = \frac{1}{2} \sin^2 \theta \left(\frac{\gamma/2}{\Delta_S + \Delta_P} \right)^2 R_0 P_0 + \cos^2 \theta \left(\frac{\gamma/2}{\Delta_P} \right)^2 R_0 P_1 + \frac{1}{2} \sin^2 \theta \left(\frac{\gamma/2}{\Delta_P} \right)^2 R_0 P_2 - \gamma P_5, \quad (\text{A6})$$

$$\frac{dP_6}{dt} = \cos^2 \theta \left(\frac{\gamma/2}{\Delta_S + \Delta_P} \right)^2 R_0 P_0 + \frac{1}{2} \sin^2 \theta \left(\frac{\gamma/2}{\Delta_P} \right)^2 R_0 (P_1 + P_3) - \gamma P_6, \quad (\text{A7})$$

$$\frac{dP_7}{dt} = \frac{1}{2} \sin^2 \theta \left(\frac{\gamma/2}{\Delta_S + \Delta_P} \right)^2 R_0 P_0 + \frac{1}{2} \sin^2 \theta \left(\frac{\gamma/2}{\Delta_P} \right)^2 R_0 P_2 + \cos^2 \theta \left(\frac{\gamma/2}{\Delta_P} \right)^2 R_0 P_3 - \gamma P_7. \quad (\text{A8})$$

Figure 13 shows the correspondence between the numerical state labels used in Eqs. (A1)–(A8) and the quantum numbers. The labels 0–3 correspond to the $6s^2S_{1/2}$ ($F = 0, M_F = 0$), ($F = 1, M_F = -1$), ($F = 1, M_F = 0$), and ($F = 1, M_F = 1$) states, respectively. The labels 4–7 correspond to the $6p^2P_{1/2}$ ($F = 0, M_F = 0$), ($F = 1, M_F = -1$), ($F = 1, M_F = 0$), and ($F = 1, M_F = 1$) states, respectively. The quantity γ is the natural decay rate of the $^2P_{1/2}$ state, $\hbar\Delta_S$ and $\hbar\Delta_P$ are the $^2S_{1/2}$ and $^2P_{1/2}$ hyperfine energy splittings, and θ is the angle between the z axis, defined by the magnetic field, and $\hat{\epsilon}$. The quantity R_0 , which has dimensions of inverse time, is

$$R_0 \equiv \frac{|E_0(6p^2P_{1/2} \parallel D^{(1)} \parallel 6s^2S_{1/2})|^2}{6\gamma\hbar^2}, \quad (\text{A9})$$

where $(6p^2P_{1/2} \parallel D^{(1)} \parallel 6s^2S_{1/2})$ is a reduced matrix element of the electric-dipole-moment operator, defined according to the conventions of Edmonds [19]. The quantity $L(\Delta)$ is a Lorentzian resonance line shape, defined by

$$L(\Delta) \equiv \frac{(\gamma/2)^2}{\Delta^2 + (\gamma/2)^2}, \quad (\text{A10})$$

where $\Delta \equiv \omega_k - \omega_0$ is the laser detuning from the $^2S_{1/2}(F = 1) \rightarrow ^2P_{1/2}(F = 0)$ resonance frequency ω_0 . We consider the low-intensity limit, defined by $R_0L(\Delta) \ll \gamma$. A typical experimental value for $R_0L(\Delta)$ was 10^7 s^{-1} , while γ is $4.3 \times 10^8 \text{ s}^{-1}$. The Zeeman shifts are not included in Δ , because they are assumed to be small compared to γ . For a typical magnetic field of $5 \times 10^{-4} \text{ T}$, states 1 and 3 are separated from state 2 by $\pm 7 \text{ MHz}$, while γ , in the same units, is 70 MHz .

When a second laser near the $^2S_{1/2}(F = 0) \rightarrow ^2P_{1/2}(F = 1)$ resonance is present, the atom spends nearly all of its time in the $^2S_{1/2}(F = 1)$ and $^2P_{1/2}(F = 0)$ states. The following reduced set of rate equations then describes the system:

$$\frac{dP_1}{dt} = -\frac{1}{2}(\sin^2 \theta)R_0L(\Delta)P_1 + \frac{1}{3}\gamma P_4, \quad (\text{A11})$$

$$\frac{dP_2}{dt} = -(\cos^2 \theta)R_0L(\Delta)P_2 + \frac{1}{3}\gamma P_4, \quad (\text{A12})$$

$$\frac{dP_3}{dt} = -\frac{1}{2}(\sin^2 \theta)R_0L(\Delta)P_3 + \frac{1}{3}\gamma P_4, \quad (\text{A13})$$

$$\begin{aligned} \frac{dP_4}{dt} &= \frac{1}{2}(\sin^2 \theta)R_0L(\Delta)(P_1 + P_3) \\ &+ (\cos^2 \theta)R_0L(\Delta)P_2 - \gamma P_4. \end{aligned} \quad (\text{A14})$$

The mean populations of the states are obtained by setting the time derivatives in Eqs. (A11)–(A14) to zero. The mean populations are

$$P_1 \approx \frac{2 \cos^2 \theta}{1 + 3 \cos^2 \theta}, \quad (\text{A15})$$

$$P_2 \approx \frac{\sin^2 \theta}{1 + 3 \cos^2 \theta}, \quad (\text{A16})$$

$$P_3 \approx \frac{2 \cos^2 \theta}{1 + 3 \cos^2 \theta}, \quad (\text{A17})$$

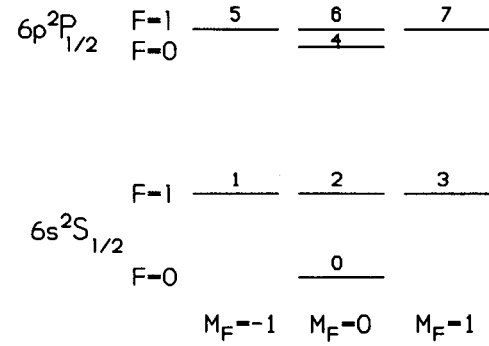


FIG. 13. Hyperfine Zeeman sublevels of the $6s^2S_{1/2}$ and $6p^2P_{1/2}$ states of $^{199}\text{Hg}^+$. The labels 0–7 for the sublevels are used in the discussion of optical pumping in the Appendix.

$$P_4 \approx \frac{3 \sin^2 \theta \cos^2 \theta}{1 + 3 \cos^2 \theta} \left[\frac{R_0L(\Delta)}{\gamma} \right] \ll 1. \quad (\text{A18})$$

The dependence of P_4 on θ is of interest, because the number of fluorescence photons emitted per ion is γP_4 . From Eqs. (A18)–(A15), it can be seen that the fluorescence goes to zero for $\theta = 0$ or π , when the population is pumped into states 1 and 2. The fluorescence also goes to zero for $\theta = \pi/2$, when the population is pumped into state 2. The fluorescence has its maximum value for $\cos \theta = 3^{-1/2}$ ($\theta \approx 54.7^\circ$), when states 1, 2, and 3 are equally populated.

Another quantity of interest is the mean population of the $^2S_{1/2}(F = 1)$ state when only one laser beam is present. This quantity is equal to $P_1 + P_2 + P_3$ and can be determined from the steady-state solutions to Eqs. (A1)–(A8). In the low-intensity limit,

$$\frac{P_1 + P_2 + P_3}{P_0} \approx \left(\frac{\Delta_P}{\Delta_S + \Delta_P} \right)^2 \left[\frac{2(1 + 3 \cos^2 \theta)}{1 + 3 \cos^4 \theta} \right]. \quad (\text{A19})$$

The quantity inside the square brackets varies from 2 to 3, depending on θ . It reaches its maximum value for $\cos \theta = 3^{-1/2}$, the same value for which Eq. (A18) predicts the maximum fluorescence when both lasers are present. Since θ was set empirically so as to maximize the fluorescence, it was probably close to this value in the experiment. From Eq. (A19), and using $P_0 + P_1 + P_2 + P_3 \approx 1$, we find that $P_1 + P_2 + P_3$ lies between 0.041 and 0.06. This compares well with the experimental value of 0.053 ± 0.06 determined from the data shown in Fig. 7.

In order for the rate-equation approach to be valid, the laser intensity must not be too large. A density-matrix calculation including the coherences between states 1, 2, 3, and 4 shows that if the magnetic field is not large enough compared to the optical electric field, the atom is optically pumped into a nonfluorescing superposition state [45]. While the density-matrix approach is valid over a larger range of parameters, the rate-equation approach is used here because it is simpler and is still a good approximation for the low laser intensities which were used in the experiment.

- * Present address: Department of Physics, University of Texas, Austin, TX 78712.
- [1] L. E. Ballentine, *Am. J. Phys.* **55**, 785 (1987).
 - [2] L. E. Ballentine, *Rev. Mod. Phys.* **42**, 358 (1970).
 - [3] A. Peres, *Am. J. Phys.* **54**, 688 (1986).
 - [4] D. Home and M. A. B. Whitaker, *Phys. Rep.* **210**, 223 (1992).
 - [5] M. Pavičić, in *Problems in Quantum Physics II, Gdansk, 1989*, edited by J. Mizerski *et al.* (World Scientific, Singapore, 1990), pp. 440–452.
 - [6] D. Home and M. A. B. Whitaker, *Phys. Lett. A* **160**, 325 (1991).
 - [7] J. Dalibard, Y. Castin, and K. Mølmer, *Phys. Rev. Lett.* **68**, 580 (1992).
 - [8] H. J. Carmichael, R. J. Brecha, and P. R. Rice, *Opt. Commun.* **82**, 73 (1991).
 - [9] G. C. Hegerfeldt and T. S. Wilsner, in *Quantum Systems—Foundations and Symmetries: Proceedings of the Second International Wigner Symposium, Goslar, 1991*, edited by W. Scherer, H. D. Doebner, and F. Schroeck, Jr. (World Scientific, Singapore, 1992).
 - [10] R. Dum, P. Zoller, and H. Ritsch, *Phys. Rev. A* **45**, 4879 (1992).
 - [11] H. G. Dehmelt, *Bull. Am. Phys. Soc.* **20**, 60 (1975).
 - [12] D. J. Wineland, J. C. Bergquist, W. M. Itano, and R. E. Drullinger, *Opt. Lett.* **5**, 245 (1980).
 - [13] D. J. Wineland, W. M. Itano, J. C. Bergquist, and F. L. Walls, in *Proceedings of the 35th Annual Frequency Control Symposium, Philadelphia, 1981*, NTIS Doc. No. AD-A110870 (Electronic Industries Association, Washington, DC, 1981), pp. 602–611 [reprinted in *Trapped Ions and Laser Cooling*, edited by D. J. Wineland, W. M. Itano, J. C. Bergquist, and J. J. Bollinger, *Natl. Bur. Stand. (U.S.) Technical Note 1086* (U.S. GPO, Washington, DC, 1985), pp. TN-47–TN-56].
 - [14] N. F. Ramsey, *Molecular Beams* (Oxford University Press, London, 1956).
 - [15] R. P. Feynman, F. L. Vernon, Jr., and R. W. Hellwarth, *J. Appl. Phys.* **28**, 49 (1957).
 - [16] R. H. Dicke, *Phys. Rev.* **93**, 99 (1954).
 - [17] P. R. Bevington, *Data Reduction and Error Analysis for the Physical Sciences* (McGraw-Hill, New York, 1969).
 - [18] F. T. Arecchi, E. Courten, R. Gilmore, and H. Thomas, *Phys. Rev. A* **6**, 2211 (1972).
 - [19] A. R. Edmonds, *Angular Momentum in Quantum Mechanics* (Princeton University Press, Princeton, NJ, 1974).
 - [20] B. Yurke, *Phys. Rev. Lett.* **56**, 1515 (1986); B. Yurke, S. L. McCall, and J. R. Klauder, *Phys. Rev. A* **33**, 4033 (1986).
 - [21] M. Kitagawa and M. Ueda, *Phys. Rev. Lett.* **67**, 1852 (1991); in *Noise in Physical Systems and 1/f Fluctuations*, Proceedings of the International Conference, Kyoto, Japan, 1991, edited by T. Musha, S. Sato, and M. Yamamoto (IOS, Burke, VA, 1992), p. 355.
 - [22] G. S. Agarwal and R. R. Puri, *Phys. Rev. A* **41**, 3782 (1990).
 - [23] D. J. Wineland, J. J. Bollinger, W. M. Itano, F. L. Moore, and D. J. Heinzen, *Phys. Rev. A* **46**, 6797 (1992).
 - [24] L. S. Cutler, R. P. Giffard, and M. D. McGuire, in *Proceedings of the 13th Annual Precise Time and Time Interval Applications and Planning Meeting*, edited by L. J. Rueger, NASA Conf. Publ. 2220 (NASA, Washington, DC, 1982), pp. 563–578.
 - [25] Y. Guern, A. Bideau-Méhu, R. Abjean, and A. Johannin-Gilles, *Phys. Scr.* **14**, 273 (1977).
 - [26] P. Eriksen and O. Poulsen, *J. Quant. Spectrosc. Radiat. Transfer* **23**, 599 (1980).
 - [27] W. M. Itano, J. C. Bergquist, R. G. Hulet, and D. J. Wineland, *Phys. Rev. Lett.* **59**, 2732 (1987).
 - [28] M. G. Raizen, J. M. Gilligan, J. C. Bergquist, W. M. Itano, and D. J. Wineland, *J. Mod. Opt.* **39**, 233 (1992); *Phys. Rev. A* **45**, 6493 (1992).
 - [29] H. Hemmati, J. C. Bergquist, and W. M. Itano, *Opt. Lett.* **8**, 73 (1983).
 - [30] See, for example, W. M. Itano and D. J. Wineland, *Phys. Rev. A* **25**, 35 (1982); D. J. Wineland and W. M. Itano, *Phys. Today* **40** (6), 34 (1987).
 - [31] A. G. Calamai and C. E. Johnson, *Phys. Rev. A* **42**, 5425 (1990).
 - [32] J. J. Bollinger, D. J. Heinzen, W. M. Itano, S. L. Gilbert, and D. J. Wineland, *Phys. Rev. Lett.* **63**, 1031 (1989).
 - [33] S. L. Gilbert, J. J. Bollinger, and D. J. Wineland, *Phys. Rev. Lett.* **60**, 2022 (1988).
 - [34] J. J. Bollinger, D. J. Heinzen, W. M. Itano, S. L. Gilbert, and D. J. Wineland, *IEEE Trans. Instrum. Meas.* **40**, 126 (1991).
 - [35] W. M. Itano, D. J. Heinzen, J. J. Bollinger, and D. J. Wineland, *Phys. Rev. A* **41**, 2295 (1990).
 - [36] D. J. Larson, J. C. Bergquist, J. J. Bollinger, W. M. Itano, and D. J. Wineland, *Phys. Rev. Lett.* **57**, 70 (1986).
 - [37] D. J. Wineland, J. J. Bollinger, W. M. Itano, and J. D. Prestage, *J. Opt. Soc. Am. B* **2**, 1721 (1985).
 - [38] L. R. Brewer, J. D. Prestage, J. J. Bollinger, W. M. Itano, D. J. Larson, and D. J. Wineland, *Phys. Rev. A* **38**, 859 (1988).
 - [39] R. G. Hulet and D. J. Wineland, *Phys. Rev. A* **36**, 2758 (1987).
 - [40] R. G. Hulet, D. J. Wineland, J. C. Bergquist, and W. M. Itano, *Phys. Rev. A* **37**, 4544 (1988).
 - [41] H. Mark and J. Workman, *Statistics in Spectroscopy* (Academic, San Diego, 1991), pp. 57–68.
 - [42] R. C. Thompson, G. P. Barwood, and P. Gill, *Appl. Phys. B* **46**, 87 (1988).
 - [43] W. M. Itano, L. R. Brewer, D. J. Larson, J. J. Bollinger, S. L. Gilbert, and D. J. Wineland, in *Frequency Standards and Metrology*, Proceedings of the Fourth Symposium, Ancona, Italy, edited by A. De Marchi (Springer-Verlag, Berlin, 1989), p. 447.
 - [44] H. Rauch, J. Summhammer, M. Zawisky, and E. Jericha, *Phys. Rev. A* **42**, 3726 (1990).
 - [45] W. M. Itano (unpublished calculations).

Spin squeezing and reduced quantum noise in spectroscopy

D. J. Wineland, J. J. Bollinger, W. M. Itano, and F. L. Moore

Time and Frequency Division, National Institute of Standards and Technology, Boulder, Colorado 80303

D. J. Heinzen

Physics Department, University of Texas, Austin, Texas 78712

(Received 25 March 1992)

We investigate the quantum-mechanical noise in spectroscopic experiments on ensembles of N two-level (or spin- $\frac{1}{2}$) systems where transitions are detected by measuring changes in state population. By preparing correlated states, here called squeezed spin states, we can increase the signal-to-noise ratio in spectroscopy (by approximately $N^{1/2}$ in certain cases) over that found in experiments using uncorrelated states. Possible experimental demonstrations of this enhancement are discussed.

PACS number(s): 42.50.Lc, 03.65.Bz, 42.50.Dv

Squeezed states of the electromagnetic field have received much attention for over a decade [1] and have now been applied to fundamental metrology such as the reduction of noise in optical interferometers below the standard quantum limit [2]. Related to this are theoretical investigations of noise reduction in fermion interferometers with correlated input states [3,4]. In this paper we investigate an application of squeezing to the reduction of quantum-mechanical noise in spectroscopic experiments on ensembles of two-level systems. We also suggest how this squeezing might be realized in an experiment.

We will be specifically interested in experiments where transitions are detected by measuring the changes in population of one of the two levels. This is to be contrasted with experiments which detect the radiation transmitted through an absorber; these experiments benefit from squeezed radiation [5]. We first show that preparation of correlated input states (squeezed spin states) improves, in a fundamental way, the signal-to-noise ratio (SNR) in any spectroscopic experiment which is limited by the quantum-mechanical uncertainty in the measurement of the level populations. We then discuss, as an example, a possible experimental realization of this improvement using laser-cooled stored ions, where the SNR is currently limited by quantum fluctuations in measured populations [6].

Since the dynamics of a two-level system interacting with radiation are the same as the dynamics of a spin- $\frac{1}{2}$ particle in a magnetic field [7] we will discuss only the latter case. We begin by assuming an ensemble of N spin $S = \frac{1}{2}$ systems each with magnetic moment $\mu = \mu_0 \mathbf{S}$ and whose direct dipole-dipole interaction can be neglected. Each spin interacts with an externally applied magnetic field $B_0 \hat{z}$ ($B_0 = \text{const}$) through the Hamiltonian $H_0 = -\mu \cdot (B_0 \hat{z}) = \hbar \omega_0 S_z$ where ω_0 is the precession frequency of each spin about the \hat{z} axis. We assume N is fixed and the relaxation negligible [6]. Suppose all the spins are initially prepared at time $t=0$ in the $|-\frac{1}{2}\rangle$ state. In this case, the spin wave function for the ensemble can be represented by the Dicke state $|J, M = -J\rangle$ where $\mathbf{J} = \sum_i \mathbf{S}_i$ (\mathbf{S}_i is the spin of the i th particle), $J = N/2$, and $M = \langle J_z \rangle$ [8]. For this state, $\Delta J_x(t=0) = \Delta J_y(0)$

$= (J/2)^{1/2}$ and $\Delta J_z(0) = 0$, where ΔA is the square root of the variance of operator A , $(\Delta A)^2 \equiv \langle A^2 \rangle - \langle A \rangle^2$. In Fig. 1(a), the lower cone shows, pictorially, a more general initial state with $\langle \mathbf{J} \rangle = \langle J_z \rangle \hat{z}$, $\langle J_z \rangle < 0$, and $\Delta J_y < \Delta J_x$ in a reference frame which corotates about the \hat{z} axis with the spin precession frequency ω_0 . In this rotating frame, the field B_0 transforms to zero and the state remains stationary [9].

We perform spectroscopy (here, essentially nuclear magnetic or electron spin resonance) using the Ramsey method of separated oscillatory fields [9]. Description in terms of the Ramsey method leads to mathematical simplification, but the improvement of SNR is quite general. The Ramsey method consists of applying an oscillat-

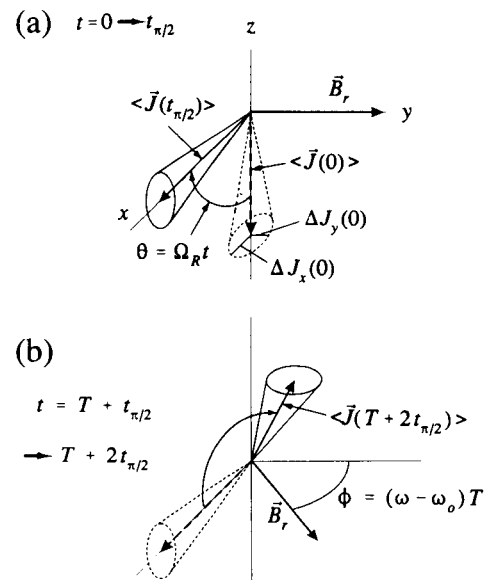


FIG. 1. Pictorial representation of the Ramsey method of spectroscopy in a frame corotating with the spin precession frequency. In (a), the lower cone represents the initial spin state for the Ramsey spectroscopy described in the text. After application of the second $\pi/2$ pulse [upper cone in (b)], we detect the number of spins in the $|+\frac{1}{2}\rangle$ state.

ing classical field $\hat{y}B_1(t)\cos(\omega t)$ where $\omega \approx \omega_0$. This field can be decomposed into two fields which rotate about the \hat{z} axis; one of these fields \mathbf{B}_r ($|\mathbf{B}_r| = B_1/2$) rotates in the same direction as the spin precession and the other can usually be neglected as is assumed here [9]. We will assume that B_1 is nonzero and constant with value B_{10} from time $t=0$ to $t=t_{\pi/2}$ such that $\Omega_R t_{\pi/2} = \pi/2$ and $|\omega - \omega_0|t_{\pi/2} \ll 1$, where $\Omega_R \equiv \mu_0 B_{10}/(2\hbar)$ is the Rabi frequency. At $t=0$ in the rotating frame, \mathbf{B}_r lies along the y axis as shown in Fig. 1(a). The lower cone of Fig. 1(a) rotates about \mathbf{B}_r and preserves its size and shape so that after time $t_{\pi/2}$, the cone lies along the x axis. At $t=t_{\pi/2}$, B_1 is reduced to zero and the cone remains stationary along x . After a time $T (\gg t_{\pi/2})$, B_1 is made equal to B_{10} again for a time $t_{\pi/2}$. If $\omega \neq \omega_0$, \mathbf{B}_r is now at an angle $\phi = (\omega - \omega_0)T$ with respect to its original direction and the cone precesses about \mathbf{B}_r as shown in Fig. 1(b). At time $t_f \equiv T + 2t_{\pi/2}$, the number of particles in the $|+\frac{1}{2}\rangle$ state is measured. The expected number of particles $\langle N_+ \rangle$ in the $|+\frac{1}{2}\rangle$ state, where $N_+ = J + J_z$, is given by the Ramsey resonance curve

$$\langle N_+ \rangle = J - \langle J_z(0) \rangle \cos(\omega - \omega_0)T. \quad (1)$$

The discussions of correlated-particle interferometer experiments [3,4] parallel the description of the Ramsey method.

With N constant we eliminate noise due to fluctuations in N as found in an atomic beam experiment. However, successive measurements of N_+ for a particular value of $\omega - \omega_0$ fluctuate by ΔN_+ due to fluctuations in the number of spins measured to be in the $|+\frac{1}{2}\rangle$ state. This produces apparent fluctuations in the center frequency of the Ramsey curve, given by $|\Delta\omega| \equiv \Delta N_+ / |\partial \langle N_+ \rangle / \partial \omega| = \Delta J_z(t_f) / |\partial \langle J_z(t_f) \rangle / \partial \omega|$. It is these fluctuations we desire to make small. If the initial state is the $|J, -J\rangle$ Dicke state, we find $|\Delta\omega|_{DS} = 1/TN^{1/2}$. The somewhat surprising independence of $|\Delta\omega|_{DS}$ on ω occurs because the quantum noise is proportional to the slope of $\langle N_+ \rangle$. In the presence of added noise it is advantageous to operate at frequencies ω where $|\partial \langle N_+ \rangle / \partial \omega|$ is maximized in which case $\langle N_+ \rangle = J = N/2$. This condition on ω is assumed in the remaining discussion. The frequency noise $|\Delta\omega|_{DS}$ has been observed in experiments on trapped ions [6]. By use of suitably prepared "squeezed" initial spin states, which show correlations between the individual spin- $\frac{1}{2}$ particles, it should be possible to achieve $|\Delta\omega| < |\Delta\omega|_{DS}$. Hence, we define squeezing in Ramsey spectroscopy as $\xi_R < 1$ where

$$\xi_R \equiv |\Delta\omega| / |\Delta\omega|_{DS} = [2J]^{1/2} \Delta J_y(0) / |\langle J_z(0) \rangle|. \quad (2)$$

Spin squeezing has been defined in other ways. From the commutation relations for angular momentum, the corresponding uncertainty relation can be given by $\Delta J_x \Delta J_y \geq |\langle J_z \rangle|/2$ and the expressions which follow from cyclic permutations. From this expression, it is natural to define squeezed states [10] as those where $\Delta J_i / |\langle J_j \rangle| / 2^{1/2} < 1$ for some $i \neq j \in \{x, y, z\}$. This squeezing is present in Bloch states [8], which are obtained by rotating the $|J, \pm J\rangle$ Dicke states [10]. For example, during the first Ramsey pulse [Fig. 1(a)], $\Delta J_x / |\langle J_z \rangle| / 2^{1/2} = (\cos\theta)^{1/2}$

≤ 1 . However, these rotated $|J, \pm J\rangle$ Dicke states have $\xi_R = 1$ and do not improve the spectroscopy we describe here. Spin squeezing might also be defined as follows [4]: Let ΔJ_{\perp} denote the smallest uncertainty of a spin component perpendicular to mean spin vector $\langle \mathbf{J} \rangle$. The spin is squeezed if $\xi_{\text{spin}} < 1$ where

$$\xi_{\text{spin}} \equiv \Delta J_{\perp} / |\langle \mathbf{J} \rangle| / 2^{1/2}. \quad (3)$$

For the Bloch states, $\xi_{\text{spin}} = 1$. A squeezed spin state with $\xi_{\text{spin}} < 1$ can be rotated so that $\langle \mathbf{J} \rangle = \langle J_z \rangle \hat{z}$ and $\Delta J_{\perp} = \Delta J_y$ and can then be used in Ramsey spectroscopy with $\xi_R = (J / |\langle \mathbf{J} \rangle|)^{1/2} \xi_{\text{spin}}$.

We now examine possible methods to prepare the initial squeezed spin state. For a single particle ($J = \frac{1}{2}$), $\xi_{\text{spin}}, \xi_R \geq 1$. For $J \geq 1$, states with $\xi_{\text{spin}}, \xi_R \leq 1$ can be prepared using an interaction proportional to the square of angular momentum operators [4]. Because we were unable to find a physical interaction of this type for our problem, we have investigated an interaction of the form $-\mu_0 J_x z B' \cos(\omega_m t_p)$. Here, B' has units of a field gradient ($\partial B_x / \partial z$), $z = z_0(a^\dagger + a)$ is the quantum-mechanical amplitude of a harmonic oscillator of frequency ω_z , z_0 is its zero-point amplitude [$z_0 = \Delta z$ (coherent state)], a^\dagger and a are raising and lowering operators, t_p is the time during the preparation period, and we assume $\omega_z \neq \omega_0$. For a suitable choice of ω_m , this interaction gives rise to a resonant coupling between \mathbf{J} and z . In the interaction picture and in the rotating-wave approximation it has the form

$$H_1 = -\hbar \Omega (J_+ a + J_- a^\dagger), \quad (4a)$$

for $\omega_m = \omega_0 - \omega_z$ and

$$H_2 = -\hbar \Omega (J_+ a^\dagger + J_- a), \quad (4b)$$

for $\omega_m = \omega_0 + \omega_z$ where $J_+ \equiv J_x + iJ_y$, $J_- = (J_+)^\dagger$, and $\Omega \equiv \mu_0 B' z_0 / 4\hbar$.

The Heisenberg equations of motion for a and J_- can be solved analytically for Eqs. (4) when $dJ_z/dt_p = 0$. If the initial spin state is the $|J, -J\rangle$ Dicke state, this amounts to the small-angle approximation $J_z = -\mathbf{J} \cdot \mathbf{I}$ where \mathbf{I} is the identity operator [11]. For the interaction H_1 , we find

$$\xi_{\text{spin}}^2 = \xi_R^2 = \cos^2 \Omega_N t_p + \xi_z^2(t_p=0) \sin^2 \Omega_N t_p, \quad (5)$$

where $\Omega_N^2 \equiv N \Omega^2$ and $\xi_z(t_p=0) \equiv \Delta z(t_p=0) / \Delta z$ (coherent state) is the initial squeezing of the harmonic oscillator. Therefore if $\xi_z(t_p=0) < 1$, this squeezing is transferred to the spins (in a time $\pi/2\Omega_N$) like wave-function exchange between coupled harmonic oscillators [12]. Because of the limited validity of the small-angle approximation, we have numerically evaluated Schrödinger's equation to compute ξ_{spin} and ξ_R for two special cases shown in Figs. 2 and 3 assuming an initial $|J, -J\rangle$ Dicke state. For our implementation of squeezing [Eqs. (4)], these figures show the improvement in SNR which can be obtained over the quantum limit obtained with uncorrelated input states.

This squeezing can, in principle, be generated by the interaction of an ensemble of atoms with a single-mode cavity field [1,11,13]. It can be viewed as the complement of

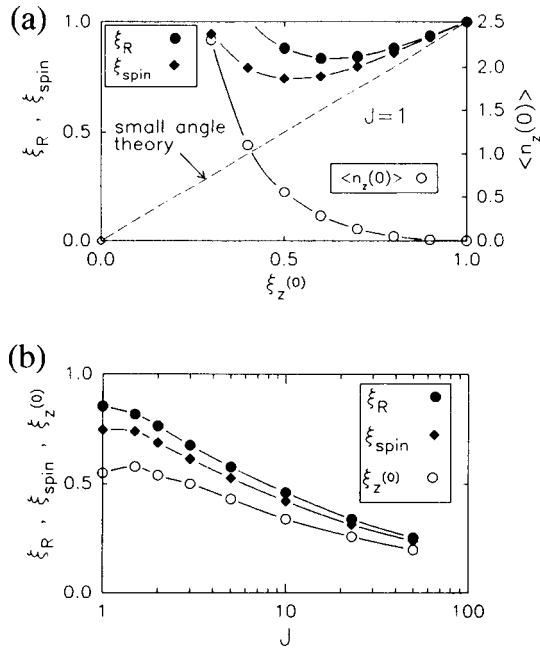


FIG. 2. Squeezed spin state preparation assuming the interaction of Eq. (4a) and assuming the harmonic oscillator is initially in the squeezed vacuum state where $\langle z(t_p=0) \rangle = \langle \dot{z}(t_p=0) \rangle = 0$, $\xi_z(t_p=0) < 1$. In (a), we plot the first minima (as a function of preparation time t_p) of ξ_{spin} , and the resulting value of ξ_R , and the corresponding value of $\langle n_z(t_p=0) \rangle$ ($\equiv \langle a^\dagger(0)a(0) \rangle$) vs $\xi_z(t_p=0)$ for the case $J=1$. As expected, the small-angle theory is valid for $\xi_z(t_p=0) \rightarrow 1$, ($\langle n_z(0) \rangle \rightarrow 0$). In (b), we show the first minimum values (as a function of preparation time t_p) of ξ_{spin} which have also been minimized with respect to $\xi_z(t_p=0)$, the resulting value of ξ_R , and the corresponding values of $\xi_z(t_p=0)$ vs J .

the squeezing of a single-mode radiation field by coupling to an ensemble of spins [11,13]. It might also be generated in an ensemble of trapped ions where the harmonic oscillator corresponds to the center-of-mass (c.m.) oscillation in a particular (z) direction. For simplicity, we consider N ions trapped along the axis of a linear rf trap [14]. The two-level system is the Zeeman doublet for an unpaired electron on each ion. B' is a gradient field $\partial B_x/\partial z$ generated by current $I_y \hat{y}$ in two wires (which could double as trap electrodes) situated as the positions $z = \pm z_T$ relative to the ions. We assume the Coulomb interaction between the ions is large enough that the frequencies of the ions' internal modes are significantly different from ω_z . The c.m. mode is first laser cooled to the zero-point state [15]. A "squeezed vacuum" state of the c.m. mode (appropriate for Fig. 2) could be obtained by suddenly changing the ions' well depth or driving the z oscillation parametrically at $2\omega_z$ [12]. A coherent state of nonzero amplitude (appropriate for Fig. 3) could be created by suddenly changing the center position of the well or driving the zero-point state with a classical resonant excitation [12]. When μ_0 is equal to two Bohr magnetons, we find $\Omega/2\pi \approx 2I_y z_T^{-2} \times (M\omega_z/2\pi)^{-1/2}$ where I_y , z_T , M , and $\omega_z/2\pi$ are expressed in amperes, centimeters, atomic mass units, and megahertz, respectively. For $I_y = 0.1$ A, $z_T = 0.01$ cm, $M = 24$ u ($^{24}\text{Mg}^+$), and $\omega_z/2\pi = 1$ MHz, we

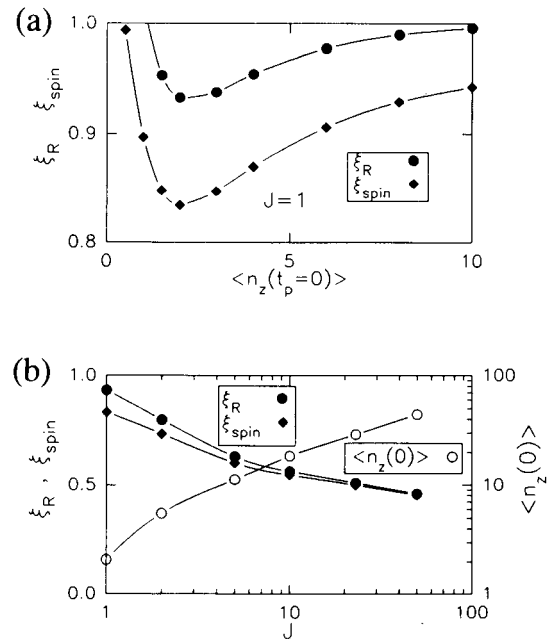


FIG. 3. Squeezed spin state preparation assuming the interaction of Eq. (4b) and assuming the harmonic oscillator is initially prepared in a coherent state [$\xi_z(t_p=0) = 1$] with $\langle z(t_p=0) \rangle \neq 0$ and $\langle \dot{z}(t_p=0) \rangle = 0$. In (a) we show the first minima of ξ_{spin} (as a function of t_p), and the resulting values of ξ_R vs $\langle n_z(t_p=0) \rangle$ for $J=1$. In (b), we show the first minimum values (as a function of preparation time t_p) of ξ_{spin} which have also been minimized with respect to $\langle n_z(t_p=0) \rangle$, the resulting values of ξ_R , and the corresponding values of $\langle n_z(t_p=0) \rangle$ vs J . We find the first minima of ξ_{spin} (as a function of t_p) occur after $\langle J_z \rangle$ has reached its maximum value and the spin vector is moving back toward the negative z axis. In this case the squeezed state must be rotated back to the negative z axis before applying the Ramsey fields.

find $\Omega/2\pi \approx 400$ Hz. The interesting cooling method proposed by Harde [16] uses the same parametric coupling described here. For Ramsey spectroscopy, the relative phase between the squeezing and Ramsey fields must be reproducible from measurement to measurement.

When N is even, there exist correlated states where $\xi_R = (N/2 + 1)^{-1/2}$ (see also Ref. [3]) in which case the uncertainty in the measurement of ω_0 will be approximately proportional to N^{-1} rather than the usual $N^{-1/2}$. For example, for $N=2$ ($J=1$), the $|J=1, M=0\rangle$ Dicke state is maximally squeezed ($\langle J \rangle = 0$ for this state, but $\xi_R \rightarrow 2^{-1/2}$ as $|\langle J \rangle| \rightarrow 0$). It can be used in Ramsey spectroscopy by detecting J_z^2 rather than J_z [17]. For this state the correlations between spins is clear. If one spin is measured to be in the $+\frac{1}{2}$ ($-\frac{1}{2}$) state, the other spin will be found in the $-\frac{1}{2}$ ($+\frac{1}{2}$) state. Starting from the $|n_z=0\rangle|J=1, M=-1\rangle$ state, we can prepare this squeezed state by making ω_z anharmonic to break the degeneracy of the $\delta n_z = 1$ transitions. With a classical field we drive to the $|1\rangle|1, -1\rangle$ state and then turn the anharmonicity off. We then apply the interaction of Eq. (4a) to drive to the $|0\rangle|1, 0\rangle$ squeezed state.

In summary, it should be possible to improve the signal-to-noise ratio in spectroscopic experiments which

detect the changes of state population over the case where uncorrelated particles are used. It might also be possible to demonstrate spin squeezing in individual atoms or ions with $J \geq 1$ such as in the Zeeman sublevels of a particular hyperfine state [17]. The relatively large value of Ω suggests that cavity-QED problems in the strong-coupling (weak relaxation) regime might be studied in the ion system. The correlated states described here could be used in Bell's inequality experiments. A possibility is the creation of multiparticle correlated states which strongly violate

Bell's inequality [18]. The individual particle states could be detected with nearly 100% efficiency [6].

We gratefully acknowledge the support of ONR. We thank M. Kitagawa for sending us copies of the work of Ref. [4]. D.J.H. acknowledges support from the Sloan Foundation. We also thank J. Bergquist, J. Kimble, M. Poitzsch, C. Weimer, and B. Yurke for comments on the manuscript.

-
- [1] See for example the feature issue edited by H. J. Kimble and D. F. Walls, *J. Opt. Soc. Am. B* **4**, 1450 (1987); special issue edited by R. Loudon and P. L. Knight, *J. Mod. Opt.* **34**, Nos. 6/7 (1987); H. J. Kimble, in *Fundamental Systems in Quantum Optics*, edited by J. Dalibard, J. M. Raimond, and J. Zinn-Justin (Elsevier, New York, 1991).
- [2] M. Xiao, L.-A. Wu, and H. J. Kimble, *Phys. Rev. Lett.* **59**, 278 (1987); P. Grangier, R. E. Slusher, B. Yurke, and A. LaPorta, *ibid.* **59**, 2153 (1987).
- [3] B. Yurke, *Phys. Rev. Lett.* **56**, 1515 (1986); B. Yurke, S. L. McCall, and J. R. Klauder, *Phys. Rev. A* **33**, 4033 (1986).
- [4] M. Kitagawa and M. Ueda, *Phys. Rev. Lett.* **67**, 1852 (1991); in *Noise in Physical Systems and 1/f Fluctuations*, edited by T. Musha, S. Sato, and M. Yamamoto (Ohmsha, Ltd., Tokyo, 1991), p. 355; and (unpublished).
- [5] C. K. Hong, S. R. Friberg, and L. Mandel, *Appl. Opt.* **24**, 3877 (1985); B. Yurke and E. A. Whittaker, *Opt. Lett.* **12**, 236 (1987); A. Heidmann, R. J. Horowicz, S. Reynaud, E. Giacobino, C. Fabre, and G. Camy, *Phys. Rev. Lett.* **59**, 2555 (1987); M. Xiao, L.-A. Wu, and H. J. Kimble, *Opt. Lett.* **13**, 476 (1988); C. D. Nabors and R. M. Shelby, *Phys. Rev. A* **42**, 556 (1990); P. R. Tapster, S. F. Seward, and J. G. Rarity, *ibid.* **44**, 3266 (1991).
- [6] W. M. Itano *et al.* (unpublished).
- [7] R. P. Feynman, F. L. Vernon Jr., and R. W. Hellwarth, *J. Appl. Phys.* **28**, 49 (1957).
- [8] See for example, F. T. Arecchi, E. Courtens, R. Gilmore, and H. Thomas, *Phys. Rev. A* **6**, 2211 (1972).
- [9] N. F. Ramsey, *Molecular Beams* (Oxford, London, 1963), p. 124.
- [10] D. F. Walls and P. Zoller, *Phys. Rev. Lett.* **47**, 709 (1981); K. Wodkiewicz and J. Eberly, *J. Opt. Soc. Am. B* **2**, 458 (1985); J. D. Macomber and R. Lynch, *J. Chem. Phys.* **83**, 6514 (1985).
- [11] See, for example, S. Haroche and J. M. Raimond, *Adv. At. Mol. Phys.* **20**, 347 (1985); S. Haroche, M. Brune, and J. M. Raimond, in *Atomic Physics 12*, edited by J. C. Zorn and R. R. Lewis (AIP, New York, 1991), p. 204; G. Rempe, M. O. Scully, and H. Walther, *ibid.*, p. 219.
- [12] D. J. Heinzen and D. J. Wineland, *Phys. Rev. A* **42**, 2977 (1990).
- [13] A. Heidmann, J. M. Raimond, and S. Reynaud, *Phys. Rev. Lett.* **54**, 326 (1985); S. M. Barnett and M.-A. Dupertuis, *J. Opt. Soc. Am. B* **4**, 505 (1987); M.-A. Dupertuis, S. M. Barnett, and S. Stenholm, *ibid.* **4**, 1124 (1987); M. G. Raizen, L. A. Orozco, M. Xiao, T. L. Boyd, and H. J. Kimble, *Phys. Rev. Lett.* **59**, 198 (1987).
- [14] M. G. Raizen *et al.*, *Phys. Rev. A* **45**, 6493 (1992).
- [15] F. Diedrich, J. C. Bergquist, W. M. Itano, and D. J. Wineland, *Phys. Rev. Lett.* **62**, 403 (1989).
- [16] H. Harde, in *International Conference on Quantum Electronics Technical Digest*, Series 1990, Vol. 8 (Optical Society of America, Washington, DC, 1990), p. 278.
- [17] K. Abdullah, C. Carlberg, E. D. Commins, H. Gould, and S. B. Ross, *Phys. Rev. Lett.* **65**, 2347 (1990).
- [18] D. M. Greenberger, M. Horne, and A. Zeilinger, in *Bell's Theorem, Quantum Theory, and Conceptions of the Universe*, edited by M. Kafatos (Kluwer Academic, Dordrecht, The Netherlands, 1989), p. 69.

Squeezed atomic states and projection noise in spectroscopy

D. J. Wineland, J. J. Bollinger, and W. M. Itano

Time and Frequency Division, National Institute of Standards and Technology, Boulder, Colorado 80303

D. J. Heinzen

Physics Department, University of Texas, Austin, Texas 78712

(Received 11 January 1994)

We investigate the properties of angular-momentum states which yield high sensitivity to rotation. We discuss the application of these “squeezed-spin” or correlated-particle states to spectroscopy. Transitions in an ensemble of N two-level (or, equivalently, spin- $\frac{1}{2}$) particles are assumed to be detected by observing changes in the state populations of the particles (population spectroscopy). When the particles’ states are detected with 100% efficiency, the fundamental limiting noise is projection noise, the noise associated with the quantum fluctuations in the measured populations. If the particles are first prepared in particular quantum-mechanically correlated states, we find that the signal-to-noise ratio can be improved over the case of initially uncorrelated particles. We have investigated spectroscopy for a particular case of Ramsey’s separated oscillatory method where the radiation pulse lengths are short compared to the time between pulses. We introduce a squeezing parameter ξ_R which is the ratio of the statistical uncertainty in the determination of the resonance frequency when using correlated states vs that when using uncorrelated states. More generally, this squeezing parameter quantifies the sensitivity of an angular-momentum state to rotation. Other squeezing parameters which are relevant for use in other contexts can be defined. We discuss certain states which exhibit squeezing parameters $\xi_R \approx N^{-1/2}$. We investigate possible experimental schemes for generation of squeezed-spin states which might be applied to the spectroscopy of trapped atomic ions. We find that applying a Jaynes-Cummings-type coupling between the ensemble of two-level systems and a suitably prepared harmonic oscillator results in correlated states with $\xi_R < 1$.

PACS number(s): 03.65.Bz, 32.80.Pj, 06.30.Ft

I. INTRODUCTION

Intriguing features of quantum-mechanically correlated particles have become well known through the celebrated gedanken experiment of Einstein, Podolsky, and Rosen (EPR) [1]. The most important of these have been demonstrated in “EPR-type” experiments which use correlated photons [2,3]. Optical fields have also provided the basis for numerous studies devoted to nonclassical harmonic-oscillator states such as squeezed states [4–7]. Demonstrated applications of squeezed optical states include the improvement of the signal-to-noise ratio in interferometers [8,9] and absorption spectroscopy [10]. By contrast, analogous studies of correlated or squeezed states of material particles are much less common, although they may lead to interesting new phenomena and applications.

First, it should be possible to generate squeezed states of harmonic oscillators which are not associated with the electromagnetic field. For example, as a result of the investigations devoted to the detection of gravitational waves with macroscopic antennas [11,12], it should be possible to generate squeezing in a material harmonic oscillator. In atomic physics, it has recently become possible to generate quantized states of motion for trapped atoms [13–16]. Therefore, it may also be possible to generate states of squeezed position or momentum for these atomic particles [15,17–21]. In addition, interest-

ing studies have been devoted to the (phase) correlations between the different internal states within the same atomic particle (as opposed to correlations between different atomic particles). As a recent example, attention has been focused on atomic states which yield dispersion without absorption and “lasing without inversion” [22].

In this paper, we examine methods for the generation of quantum-mechanical correlations between the internal states of different atomic particles and investigate the use of these correlated atoms in spectroscopy. For example, consider atoms which have two internal levels with corresponding wave functions denoted $|1\rangle$ and $|2\rangle$. For the case of two such atoms, a and b , we will be interested in finding ways to generate correlated or “entangled” states of the form

$$\psi = [2 \cosh(2\theta)]^{-1/2} \times (e^{-\theta} |2\rangle_a |2\rangle_b + e^{i\phi} e^{\theta} |1\rangle_a |1\rangle_b), \quad (1)$$

where the subscripts refer to the atoms. (Here, the entanglement of the particle wave functions is evident because the total wave function cannot be written as the product of wave functions of the separate atoms). These states (for $\theta \rightarrow 0$, $\phi \rightarrow \pi$) are the correlated two-particle states discussed in Bohm’s version of the Einstein, Podolsky, and Rosen experiment [23]. We will be interested in finding ways to generate these states and the analogous

correlated states for much larger numbers of particles.

If we make the connection between spin- $\frac{1}{2}$ particles and two-level systems [24], such states can also be called “squeezed-spin” states, where squeezing is defined in analogy to the squeezing for the electromagnetic field. Various aspects of spin squeezing have been considered previously [25–38]. For example, in the work of Ref. [26], the relationship between squeezing in a two-level system and squeezing of the radiation which is emitted by the two-level system is discussed. Reference [33] considers the generation of correlated or squeezed-spin states, in ensembles of two-level systems, by broadband squeezed vacuum radiation. The use of correlated states in interferometers has been discussed in Refs. [30] and [35]; these states correspond formally to the squeezing of angular-momentum operators.

We have found it useful to investigate spin squeezing in the context of spectroscopy. Part of the reason for this is that we were led to consider it as a natural outgrowth of our experiments on the spectroscopy of stored atomic ions [39,40]. Also, the squeezed-spin states that are useful in one physical context or application are not necessarily the ones of interest in another. For example, the form of spin squeezing discussed in Refs. [25–28,33] does not, as we describe below, appear to be relevant for the spectroscopy we describe here. However, the method of spectroscopy we assume is formally equivalent to the description of particle interferometry discussed earlier [30,35]. Therefore, the same form of squeezed states is of interest in both contexts even though the states describe quite different physical systems and will require different interactions to be produced. The states of interest in spectroscopy and interferometry can be put in a more general context. In any system which can be represented by a net angular momentum \mathbf{J} , the states we are interested in are those which give the highest angular resolution of $\langle \mathbf{J} \rangle$ about a particular axis.

In our experiments on stored ions [39], we detect atomic transitions by observing changes in atomic state population. Typically, we first localize an ensemble of N identical atoms in a trap, where N remains fixed throughout the experiments. We initially prepare each of the atoms in the same internal eigenstate, which we take to be state $|1\rangle$. We then apply (classical) radiation, which we will call the clock radiation, to the atoms. The clock radiation has a frequency that drives the atoms from state $|1\rangle$ to another state, designated state $|2\rangle$. After application of this radiation, an atom is, in general, in a coherent superposition state $c_1|1\rangle + c_2|2\rangle$, where $|c_1|^2 + |c_2|^2 = 1$. We assume that relaxation of states 1 and 2 is negligible; this is usually a good approximation for stored atomic ions. We then detect the number of atoms in state $|1\rangle$ (or $|2\rangle$). In the detection process, we will find the atom to be in either state 1 or state 2; that is, the measurement can be thought of as projecting the atom into one of these states [40]. If we perform this preparation, irradiation, and detection many times, on average, we will detect $N_1 = |c_1|^2 N$ atoms to be in state 1. However, unless $|c_1| = 1$ or 0, the number of atoms found in state 1 will fluctuate from measurement to measurement. We call these fluctuations “projection noise” [40]. They are given

by

$$\Delta N_1 = [N|c_1|^2(1 - |c_1|^2)]^{1/2}.$$

Recently, we have reduced all other sources of noise in the experiments so that the signal-to-noise ratio is limited by projection noise [40]. In those experiments, ΔN_1 was given by the expression above. The ability to see the projection noise clearly was enabled by detecting a fixed number of atomic ions with high efficiency.

Projection noise is the fundamental limiting noise in spectroscopic experiments which detect transitions by monitoring changes in population on a fixed number of particles. In Ref. [38], we have investigated, theoretically, ways to increase the signal-to-noise ratio over what has been observed in Ref. [40], that is, when all of the atoms are initially prepared in the same internal eigenstate. This can be accomplished if we can initially prepare the atoms in particular correlated states.

The generation and detection of correlated atomic particle states by the methods described below is interesting because it would allow the investigation of squeezed states outside the domain of the electromagnetic field. Also, the increase in signal-to-noise ratio possible in spectroscopy with correlated states may be of practical interest. A dramatic example is the following: In atomic clocks which use uncorrelated atoms and are limited by projection noise, the signal-to-noise ratio is equal to $K(N\tau)^{1/2}$, where N is the number of atoms, τ is the total measurement time, and K is a constant. However, if the atoms are initially prepared in particular correlated states, the signal-to-noise ratio would be equal to $KN\tau^{1/2}$. Therefore an atomic clock using 10^{10} correlated atoms would yield the same precision in 1 s as an atomic clock using 10^{10} uncorrelated atoms taking 300 years. On a less ambitious scale, the attainment of modest squeezing should also be of practical significance. This is particularly true in measurements on atomic clocks where precision measurements take many days, weeks, or even years of averaging time. Therefore, for example, even if a squeezing of only $\xi_R = \frac{1}{2}$ is obtained (ξ_R defined in Sec. V A), a four-day measurement of a certain precision is reduced to a one-day measurement.

The purpose of the present paper is to extend the discussion of Ref. [38]. As in that paper, we will be interested in two things: (1) identifying states which reduce projection noise in the context of spectroscopy, and (2) how these states might be generated in an experiment. We will concentrate on squeezing in systems of trapped atoms because it is relevant to our experimental work and might be where such effects will first be demonstrated. However, the results are quite general, and the increase in signal-to-noise ratio will, in principle, apply to spectroscopy on any ensemble of two-level systems.

In Sec. II, we discuss the signal-to-noise ratio, or transition-frequency measurement uncertainty, in spectroscopic experiments which detect transitions by observing changes in level populations. As is often done, we use the analogy between spectroscopy on two-level systems and spectroscopy on spin- $\frac{1}{2}$ systems. This analogy will lead to a useful pictorial representation of the noise and

will make obvious what is desired of the squeezed-spin states. In Sec. III, we apply this analysis to a special case of spectroscopy which uses Ramsey's method of separated oscillatory fields [41]. Here, we discuss the connection between Ramsey's method and interferometry. In Sec. IV, we examine the signal-to-noise ratio when the particles are initially prepared in particular uncorrelated pure states. This is essentially a summary of the results of Ref. [40]. In Sec. V, we show that some correlated particle states can be used in spectroscopy to increase the signal-to-noise ratio over that found in experiments which use uncorrelated particles. We define a squeezing parameter ξ_R which is relevant for these experiments and also show that ξ_R expresses the measurement sensitivity of an angular-momentum state to rotations. In Sec. VI, we discuss alternate definitions of spin squeezing. In Secs. VII and VIII, we investigate possible ways to generate the correlated states useful for spectroscopy. The difficulty will be in finding a practical scheme; we discuss some possibilities in Sec. VIII. Although the discussion will apply to an arbitrary number N of correlated particles, in many cases we will find it useful to illustrate various aspects of the squeezing for two particles.

II. POPULATION SPECTROSCOPY

We are interested in the spectroscopy of an ensemble of N identical two-level particles. We assume that transitions are detected by observing changes in the populations of the two levels after application of classical radiation. It will be convenient to use the fact that the dynamics of an individual two-level system interacting with radiation is the same as the dynamics of a spin- $\frac{1}{2}$ particle in a magnetic field [24]. This spin representation provides a simple pictorial way to follow the evolution of operators (or quantum states) under the influence of radiation. For an ensemble of particles, the spin representation also provides a simple way to visualize the noise in the measurement of populations, which will make obvious what is desired of the correlated states discussed in Sec. V.

Therefore, we begin by assuming that we have an ensemble of N identical particles, where N is fixed. Each particle has spin \mathbf{S} where $S = \frac{1}{2}$. Associated with each spin is a magnetic moment $\boldsymbol{\mu} = \mu_0 \mathbf{S}$. We assume that the particles are far enough apart that they do not overlap spatially, so that antisymmetrization (or symmetrization for integral-spin two-level particles) of the total wave function is unnecessary. We will also assume the particles are far enough apart that the direct dipole-dipole coupling or other direct interactions between particles can be neglected. Relaxation is assumed to be negligible. These are good approximations for many spectroscopic experiments on trapped atomic ions where the storage time is long, the background gas pressure is low, and the Coulomb repulsion between ions typically restricts particle separations to greater than $1 \mu\text{m}$.

We apply a uniform external magnetic field $B_0 \hat{\mathbf{z}}$ to the ensemble of spins, so the Hamiltonian for each particle is given by

$$H_0 = -\boldsymbol{\mu} \cdot \mathbf{B}_0 = \hbar \omega_0 S_z, \quad (2)$$

where $\omega_0 \equiv -\mu_0 B_0 / \hbar$. The eigenstates of this Hamiltonian are the $|m\rangle = |+\frac{1}{2}\rangle$ and $|-\frac{1}{2}\rangle$ states where $S_z |m\rangle = m |m\rangle$. The Heisenberg equation for \mathbf{S} is

$$\partial \mathbf{S} / \partial t = \omega_0 \times \mathbf{S}, \quad (3)$$

where $\omega_0 \equiv \omega_0 \hat{\mathbf{z}}$. If the particles are electrons, $\mu_0 = g_J \mu_B$ where $g_J (\approx -2)$ is the electron g factor and μ_B is the Bohr magneton. In this case, $\omega_0 > 0$ and \mathbf{S} precesses in the $+\phi$ direction defined by Eq. (3). The upper and lower energy levels of this two-level system correspond to the $|+\frac{1}{2}\rangle$ and $|-\frac{1}{2}\rangle$ states, respectively.

In spectroscopy, we are interested in experimentally measuring ω_0 . In our spin- $\frac{1}{2}$ model, the spectroscopy is essentially equivalent to NMR (nuclear magnetic resonance) on a spin- $\frac{1}{2}$ nucleus or ESR (electron spin resonance). In general, we might be interested in the case where the particles are first prepared in a mixed state. In this case, we would employ a density matrix treatment to describe the evolution of the system. However, since we will be concerned with maximizing the signal-to-noise ratio, we will assume that the particles are initially prepared in pure states with an average value of \mathbf{S} which, for most of our discussion, we take to be aligned along the $\hat{\mathbf{z}}$ axis and denote $\langle S_z \rangle$. ($\langle A \rangle$ denotes the mean value of operator A .) We then apply (classical) radiation, which we call the spectroscopic or "clock" radiation, at a frequency ω (near ω_0), which changes $\langle S_z \rangle$. The measurement apparatus is configured to detect this change in $\langle S_z \rangle$. We assume the amplitude and duration of the radiation is adjusted so that $\langle S_z \rangle$ reverses sign when $\omega = \omega_0$.

An alternative method of performing spectroscopy is to observe the radiation transmitted through the sample of particles. If the intensity of the radiation is chosen appropriately, the maximum change in the transmitted intensity corresponds to the condition $\omega = \omega_0$. In some cases, for example, when N is large and the clock radiation weak, the fluctuations of the detected radiation (which limit the signal-to-noise ratio) are dominated by the fundamental quantum fluctuations of this radiation. In these experiments, the signal-to-noise ratio can be improved by using squeezed radiation [10, 42–46]. Here, we have assumed that the radiation used for the spectroscopy is classical: that is, it is in a coherent state, and the number of photons in the radiation source is large enough that the quantum fluctuations in this radiation can be neglected. We assume all sources of technical noise (for example, fluctuations in the amplitude of the clock radiation caused by an unstable power supply) are also negligible. Since N is assumed constant, fluctuations in N , such as those which occur in an atomic-beam experiment, are absent.

In the measurement of S_z , we assume that each particle is projected into either the $|+\frac{1}{2}\rangle$ or $|-\frac{1}{2}\rangle$ eigenstate [40]. We will assume that we can detect which state the particle is measured to be in with 100% efficiency. With these assumptions, the noise in the measurements of S_z (for the same value of ω) from measurement to measurement is due to fluctuations in finding particles in either the $|+\frac{1}{2}\rangle$ or $|-\frac{1}{2}\rangle$ eigenstate.

It will be useful to use a formalism which treats the N particles as a combined quantum system. This has the advantage that, for one choice of basis states, it will provide a simple way to visualize the measurement noise when the particles are either uncorrelated or correlated. One possible choice of basis states is the set of direct-product states

$$|m_1, m_2, \dots, m_N\rangle \equiv \prod_{i=1}^N |m_i\rangle, \quad (4)$$

where $|m_i\rangle$ is an eigenstate for the i th particle. However, we will use another common representation in which we define a collective angular-momentum operator

$$\mathbf{J} = \sum_{i=1}^N \mathbf{S}_i, \quad (5)$$

where \mathbf{S}_i is the spin operator for the i th particle. The set of basis states we use are of the familiar form $|J, M\rangle$, which are linear combinations of the states in Eq. (4) [47,48]. For these states, $\mathbf{J}^2|J, M\rangle = J(J+1)|J, M\rangle$ and $J_z|J, M\rangle = M|J, M\rangle$.

Heisenberg picture

In the presence of the field \mathbf{B}_0 , Eqs. (3) and (5) yield the Heisenberg equation for \mathbf{J} (see Fig. 1):

$$\partial\mathbf{J}/\partial t = \omega_0 \times \mathbf{J}. \quad (6)$$

The clock radiation is assumed to be a classical field, which rotates about the z axis, of the form

$$\mathbf{B}_1 = B_1 \left[\hat{\mathbf{x}} \cos(\omega t + \theta) + \frac{\omega_0}{|\omega_0|} \hat{\mathbf{y}} \sin(\omega t + \theta) \right], \quad (7)$$

where $\omega \simeq \omega_0$ and the factor $\omega_0/|\omega_0|$ insures that \mathbf{B}_1 rotates in the same sense as ω_0 . In general, B_1 is also a function of time. We assume that B_1 is switched rapidly

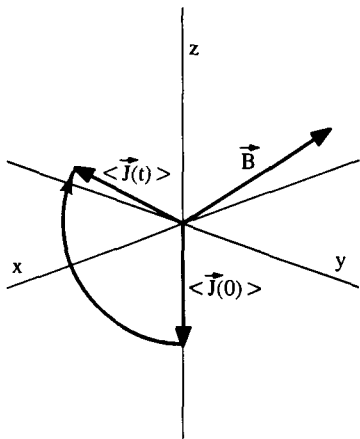


FIG. 1. Pictorial representation of the precession of the angular momentum \mathbf{J} about an applied magnetic field \mathbf{B} . The angular momentum is assumed to have a net magnetic moment $\boldsymbol{\mu} = \mu_0 \mathbf{J}$, where $\mu_0 > 0$ for the figure. The figure represents the motion of $\langle \mathbf{J} \rangle$ or the operator \mathbf{J} in the Heisenberg representation [Eq. (6)].

between 0 and some constant value. In practice, the clock radiation may be an oscillating (magnetic) field which is perpendicular to \mathbf{B}_0 . This oscillating magnetic field can be decomposed into two rotating fields: one which rotates at frequency ω [given by Eq. (7)], and the other rotating in the opposite sense. Usually the effects of the oppositely rotating field can be neglected [41] (rotating-wave approximation); we assume this to be the case here.

To solve for the system evolution, it will be convenient to transform to a frame which rotates at frequency ω [41,49]. In this frame of reference, the angular momentum \mathbf{J}_r will interact with the effective field

$$\mathbf{B} = \hat{\mathbf{z}} B_r + B_1 (\hat{\mathbf{x}} \cos\theta + \hat{\mathbf{y}} \sin\theta),$$

where

$$B_r \equiv B_0 + \hbar\omega/\mu_0 = B_0(\omega_0 - \omega)/\omega_0.$$

Without loss of generality, we will assume $\theta = \pi/2$, in which case

$$\mathbf{B} = \hat{\mathbf{z}} B_r + \hat{\mathbf{y}} B_1. \quad (8)$$

In this rotating frame, the Hamiltonian is given by

$$H_r = -\mu_0 \mathbf{J} \cdot \mathbf{B} \equiv \hbar\omega' \cdot \mathbf{J}, \quad (9)$$

where $\omega' \equiv \omega_r \hat{\mathbf{z}} + \omega_1 \hat{\mathbf{y}}$, $\omega_r \equiv -\mu_0 B_r / \hbar = \omega_0 - \omega$, $\omega_1 \equiv -\mu_0 B_1 / \hbar$, and \mathbf{J} is now the angular momentum in the rotating frame. We have omitted an explicit subscript or superscript on \mathbf{J} since only J_z will be measured and J_z is the same in both frames. The Heisenberg equation for \mathbf{J} in the rotating frame is

$$\partial\mathbf{J}/\partial t = \omega' \times \mathbf{J}. \quad (10)$$

In Fig. 1 we represent, pictorially, the time evolution of \mathbf{J} (or $\langle \mathbf{J} \rangle$) when $\mu_0, \omega_0 - \omega > 0$, $|\omega_0 - \omega| \simeq |\omega_1|$, and $\langle \mathbf{J}(t=0) \rangle = -\hat{\mathbf{z}} |\langle J_z(0) \rangle|$.

As discussed by Ramsey [41], we could now transform to a second frame which rotates about \mathbf{B} at a frequency $-\mu_0 B / \hbar$. In this frame, the effective magnetic field is 0 and therefore wave functions (in the Schrödinger picture) or operators (in the Heisenberg picture) remain constant. In this case, the system evolution is obtained by applying the appropriate rotation operators to the initial (laboratory) wave function or operators. In this paper, we will describe the system evolution in the first rotating frame corresponding to Eq. (10).

We will assume that, after application of the clock radiation, the detector measures the number of particles N_+ in the $|\frac{1}{2}\rangle$ state. In the Heisenberg picture, this is given by the operator

$$N_+(t_f) = J_z(t_f) + \mathbf{J}I, \quad (11)$$

where I is the identity operator and t_f is the "final" time corresponding to the time just after the clock radiation is applied. For a particular value of ω , we denote a single measurement of N_+ by $(N_+)_1$, and the average of M measurements of N_+ by $(N_+)_M$. By making measurements of $(N_+(t_f))_M$ for various values of ω , we obtain a resonance curve as a function of ω . To find ω_n , we could

fit this resonance curve to a particular function. The uncertainty in the determination of ω_0 would result from the noise in our measurements of $(N_+(t_f))_M$ at each value of ω .

In many cases of experimental interest, we can assume the resonance curve is symmetric about ω_0 ; this is true for the spin- $\frac{1}{2}$ example discussed here when $\langle \mathbf{J}(t=0) \rangle = -\hat{z} |\langle J_z(0) \rangle|$. In this case, rather than fitting to the entire resonance curve, it will, in general, be advantageous to measure N_+ at particular values of ω which minimize the uncertainty in the apparent position (as a function of ω) of the curve. For a particular value of ω , the deviation of the apparent position of the curve from the true curve $\langle N_+ \rangle$ is given by

$$\delta\omega_M = [(N_+)_{M-} - \langle N_+ \rangle] / (\partial \langle N_+ \rangle / \partial \omega), \quad (12)$$

where the subscript M on $\delta\omega$ denotes the results for M measurements. The magnitude of the rms fluctuations of $\delta\omega$ for repeated measurements of $(N_+)_{M_1}$ at a particular value of ω is given by

$$\begin{aligned} |\Delta\omega| &= \Delta N_+(t_f) / |\partial \langle N_+ \rangle / \partial \omega| \\ &= \Delta J_z(t_f) / |\partial \langle J_z(t_f) \rangle / \partial \omega|, \end{aligned} \quad (13)$$

where, as usual, for operator A , ΔA is the square root of the variance, $(\Delta A)^2 \equiv \langle A^2 \rangle - \langle A \rangle^2$. If we make M measurements at a particular value of ω , the uncertainty in the value of ω_0 is reduced to $|\Delta\omega|_M = |\Delta\omega| (M)^{-1/2}$. Given N and t_f , our task in spectroscopy is to minimize $|\Delta\omega|$. Equivalently, since the signal-to-noise ratio can be defined as being proportional to $|\Delta\omega|^{-1}$, we therefore want to maximize signal-to-noise ratio.

If the exact form of the resonance curve were known, it would be necessary to measure the curve at only one frequency to determine the best value of ω_0 . This is impractical since, for example, the height of the resonance curve ($\propto |\langle J_z(0) \rangle|$) depends on the exact value of B_1 and this may not be precisely determined. However, when the resonance curve is symmetric about ω_0 , this difficulty is overcome, experimentally, by measuring two points on the resonance curve, at frequencies $\omega_A > \omega_0$ and $\omega_B < \omega_0$ where $\omega_A - \omega_0 \simeq \omega_0 - \omega_B$. If $\langle N_+(\omega = \omega_A) \rangle = \langle N_+(\omega = \omega_B) \rangle$, then $(\omega_A + \omega_B)/2 = \omega_0$. In practice, we approximate this condition with a servo mechanism [50].

III. POPULATION SPECTROSCOPY USING THE RAMSEY METHOD

In order to illustrate the basic ideas behind the improvement in signal-to-noise ratio using correlated states, we will examine $|\Delta\omega|$ for a special case of the resonance method due to Ramsey [41]. This is an important case to analyze because, experimentally, for a given time t_f in

which to apply the clock radiation, the narrowest linewidths are obtained with this method. The Ramsey method [41] breaks the resonance period ($t=0 \rightarrow t_f$) into three parts. In the special case discussed here, during the first part of the resonance period, B_1 is nonzero and constant with value B_{10} from time $t=0$ to $t=t_{\pi/2}$ such that $\Omega_R t_{\pi/2} = \pi/2$ and $\Omega_R \gg |\omega - \omega_0|$, where $\Omega_R \equiv \mu_0 B_{10} / \hbar$ is usually called the Rabi frequency. At time $t_{\pi/2}$, B_1 is reduced to zero. After an additional time T , B_1 is again made equal to B_{10} for a time $t_{\pi/2}$ and then reduced to zero. We will assume that B_1 is switched between zero and B_{10} in a time much less than $t_{\pi/2}$ in which case $t_f = 2t_{\pi/2} + T$. We make the further assumption that $T \gg t_{\pi/2}$.

With these assumptions, and assuming $\langle \mathbf{J}(0) \rangle = -\hat{z} |\langle J_z(0) \rangle|$, during the first part of the Ramsey period, that is, during the first "Ramsey pulse," $\mathbf{B} = B_1 \hat{z} + B_{10} \hat{y} \simeq B_{10} \hat{y}$. In the rotating frame, from Eq. (10), \mathbf{J} (or $\langle \mathbf{J} \rangle$) precesses around the \hat{y} axis until it lies along the \hat{x} axis at which point B_1 is reduced to 0 [Fig. 2(a)]. From time $t=t_{\pi/2}$ to $t_{\pi/2} + T$, \mathbf{J} precesses around $\mathbf{B} = B_1 \hat{z}$ so that $\mathbf{J}(t_{\pi/2} + T)$ lies at an angle $(\omega_0 - \omega)T$ with respect to \hat{x} but still in the x - y plane [Fig. 2(b)]. In the third part of the Ramsey period, from time $t_{\pi/2} + T$ to $2t_{\pi/2} + T = t_f$, \mathbf{J} again precesses around $B_{10} \hat{y}$ so that at time t_f it lies in the y - z plane [Fig. 2(c)]. At this point, N_+ or, equivalently, J_z is measured [Eq. (11)]. We have

$$\langle N_+(t_f) \rangle = J - \langle J_z(0) \rangle \cos(\omega_0 - \omega)T, \quad (14)$$

which is the Ramsey resonance curve for $T \gg t_{\pi/2}$ [51]. In general, we can choose $B_{10} = \pm(n + \frac{1}{2})\pi\hbar / (\mu_0 t_{\pi/2})$ ($n=0, 1, 2, 3, \dots$) with the same result [52]. Other choices of B_{10} will result in smaller values of $|\partial \langle J_z(t_f) \rangle / \partial \omega|$. For brevity we will assume $n=0$.

Application of the Ramsey fields corresponds, in the Heisenberg picture in the rotating frame, to the transformations

$$J_x(t_f) = -J_x(0), \quad (15)$$

$$J_y(t_f) = J_z(0) \sin\omega_r T + J_y(0) \cos\omega_r T, \quad (16)$$

and

$$J_z(t_f) = -J_z(0) \cos\omega_r T + J_y(0) \sin\omega_r T, \quad (17)$$

where $\omega_r \equiv \omega_0 - \omega$. Therefore, in general, from Eqs. (11) and (15)-(17),

$$\begin{aligned} \langle N_+(t_f) \rangle &= J - \langle J_z(0) \rangle \cos\omega_r T + \langle J_y(0) \rangle \sin\omega_r T \\ &= J - [\langle J_z(0) \rangle^2 + \langle J_y(0) \rangle^2]^{1/2} \\ &\quad \times \cos\{\omega_r T + \tan^{-1}[\langle J_y(0) \rangle / \langle J_z(0) \rangle]\} \end{aligned} \quad (18)$$

and

$$\begin{aligned} |\Delta\omega|^2 &= \{ \Delta J_z(0)^2 \cos^2\omega_r T + \Delta J_y(0)^2 \sin^2\omega_r T \\ &\quad + [\langle J_y(0) \rangle \langle J_z(0) \rangle - \frac{1}{2} \langle J_z(0) J_y(0) + J_y(0) J_z(0) \rangle] \sin 2\omega_r T \} [T (\langle J_z(0) \rangle \sin\omega_r T + \langle J_y(0) \rangle \cos\omega_r T)]^{-2}. \end{aligned} \quad (19)$$

We see from Eq. (18) that the resonance curve is not symmetric about ω_0 unless $\langle J_y(0) \rangle = 0$. Even when $\langle J_y(0) \rangle = 0$, for initial states where

$$\langle J_z(0)J_y(0) + J_y(0)J_z(0) \rangle \neq 0,$$

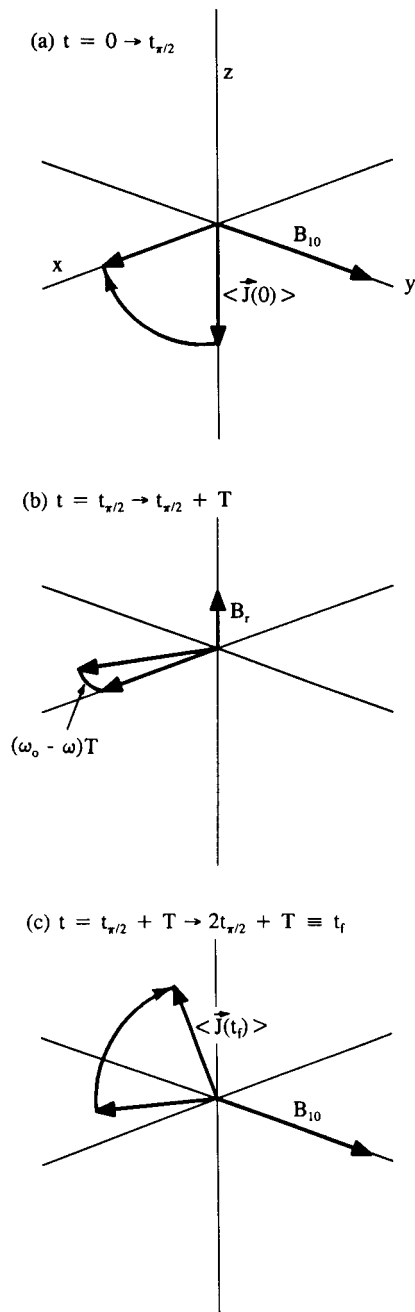


FIG. 2. Pictorial representation of the three parts of the Ramsey separated-field method. The figures apply to a frame which rotates with the applied time-varying field given by Eq. (7) of the text. Part (a) shows the precession of \mathbf{J} during the first " $\pi/2$ pulse." In (b), \mathbf{J} precesses about the residual field \mathbf{B}_r . In (c), \mathbf{J} rotates into the y - z plane under the application of the second $\pi/2$ pulse. We assume $|\mathbf{B}_r| \ll |\mathbf{B}_1|$ and $t_{\pi/2} \ll T$, so the total "interrogation time" $t_f = t_{\pi/2} + T + t_{\pi/2} \approx T$. After the second $\pi/2$ pulse, $J_z(t_f)$ is measured; this yields the signal used in spectroscopy [Eqs. (11) and (14)].

the quantum noise on the Ramsey curve $\Delta N_+(t_f)$ [$=\Delta J_z(t_f)$] is not symmetric about ω_0 . This is not necessarily a problem for finding the best value of ω_0 since the contribution to the noise in a measurement of $N_+(\omega_A) - N_+(\omega_B)$ from this term drops out. If we assume

$$\langle J_z(0)J_y(0) + J_y(0)J_z(0) \rangle = \langle J_y(0) \rangle = 0,$$

then

$$|\Delta\omega|^2 = \frac{\Delta J_z(0)^2 \cos^2 \omega_r T + \Delta J_y(0)^2 \sin^2 \omega_r T}{T^2 \langle J_z(0) \rangle^2 \sin^2 \omega_r T}. \quad (20)$$

In practice, some additional noise will be present in the measurement of N_+ . Assuming that this noise is uncorrelated with the projection noise and with ω , the noise $\Delta N_+(t_f)$ in the measurement of N_+ must be replaced by $[\Delta N_+(t_f)^2 + \Delta N_{\text{add}}^2]^{1/2}$, where ΔN_{add} is the rms value of the added noise. From Eq. (13), Eq. (20) becomes

$$|\Delta\omega|^2 = \frac{\Delta J_z(0)^2 \cos^2 \omega_r T + \Delta J_y(0)^2 \sin^2 \omega_r T + \Delta N_{\text{add}}^2}{T^2 \langle J_z(0) \rangle^2 \sin^2 \omega_r T}. \quad (21)$$

Equation (21) shows that with $\Delta J_z(0) \neq 0$ and/or $\Delta N_{\text{add}} \neq 0$, $|\Delta\omega|$ is minimized for the choices $\omega_0 - \omega = \pm(n + \frac{1}{2})\pi/T$ ($n=0, 1, 2, 3, \dots$) [53].

Independent of the values of $\Delta J_z(0)$ and ΔN_{add} , $|\Delta\omega|$ is minimized for $n=0$ or equivalently for $\omega_0 - \omega = \pm\pi/(2T)$. These values of $\omega_0 - \omega$ will be assumed throughout the remainder of the paper except where noted. In other words, we will measure the resonance curve at frequencies $\omega_A = \omega + \pi/(2T)$ and $\omega_B = \omega - \pi/(2T)$ where $|\omega - \omega_0|$ is assumed to be much less than $\pi/(2T)$. In terms of Eq. (14), this means that we measure N_+ at two frequencies corresponding to the half-intensity points on the central lobe of the Ramsey resonance curve. With this assumption on ω_A and ω_B , $|\Delta\omega|$ is independent of $\langle J_z(0)J_y(0) + J_y(0)J_z(0) \rangle$ and $\langle J_y(0) \rangle$.

In the remainder, we will assume $\Delta N_{\text{add}} \ll \Delta J_y(0)$, in which case we end up with a simple expression for $|\Delta\omega|$ [38]:

$$|\Delta\omega| = \Delta J_y(0) / [T |\langle J_z(0) \rangle|]. \quad (22)$$

We can represent $\Delta N_+(t_f)$ [$=\Delta J_z(t_f)$] pictorially. More generally, we can represent ΔJ_x , ΔJ_y , and ΔJ_z by an "error spheroid" (or error ellipsoid) [28] which lies at the end of the vector \mathbf{J} and whose dimensions are given by ΔJ_x , ΔJ_y , and ΔJ_z . This is shown schematically in Fig. 3 for the case $\langle \mathbf{J} \rangle = -|\langle \mathbf{J} \rangle| \hat{\mathbf{z}}$. (In Refs. [29], [36], [38], and [40], ΔJ_x and ΔJ_y are represented as semimajor axes of an ellipse placed at the end of, and perpendicular to, $\langle \mathbf{J} \rangle$.) The pictorial representation shown in Fig. 3 will be useful for the method of spectroscopy described above, but is somewhat limited. For example, certain states with $\langle \mathbf{J} \rangle = -|\langle \mathbf{J} \rangle| \hat{\mathbf{z}}$ and $\langle J_z J_y + J_y J_z \rangle \neq 0$ might have, in a (primed) coordinate system rotated with respect to the spheroid shown in Fig. 3, a value of $\Delta J'_z < \Delta J_x, \Delta J_y, \Delta J_z$. This state might be more appropriately represented with an error spheroid which is tilted

with respect to the one shown in Fig. 3. Also, when $\langle \mathbf{J} \rangle = -|\langle \mathbf{J} \rangle| \hat{z}$, and $|\langle \mathbf{J} \rangle| \neq J$, the distribution of measured values of J_z is not symmetric about $\langle J_z(0) \rangle$. Therefore the error spheroid should be distorted along z . A more accurate representation is given by plotting the probability distributions for $N_+(t_f)$ which are, in general, asymmetric about $\langle N_+(t_f) \rangle$ (see, for example, Fig. 3 of Ref. [40]). Other pictorial methods can be used to describe the probability distribution for measurements of N_+ or \mathbf{J} . For example, Ref. [37] provides a way of visualizing correlated or squeezed-spin states through the use of Wigner functions for angular momentum.

Since we have chosen $\omega_0 - \omega = \pm\pi/(2T)$, the evolution of the error spheroid at various times during the Ramsey period has a simple representation, as shown in Fig. 4. Since the three parts of the Ramsey period correspond to $\pi/2$ rotations about $B_{10}\hat{y}$, $B_r\hat{z}$, and $B_{10}\hat{y}$, respectively, the evolution of the variances is particularly easy to follow. In Fig. 4(d), we plot $\langle N_+(t_f) \rangle$ as a function of ω

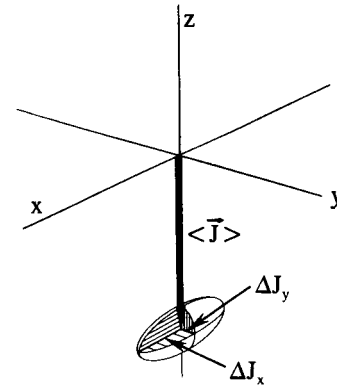
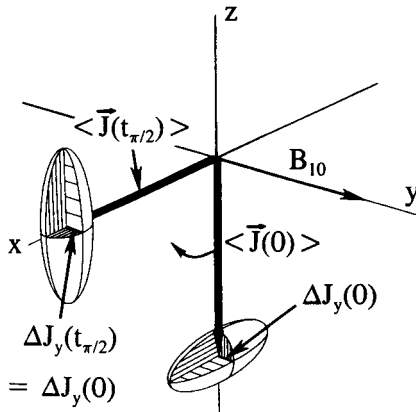
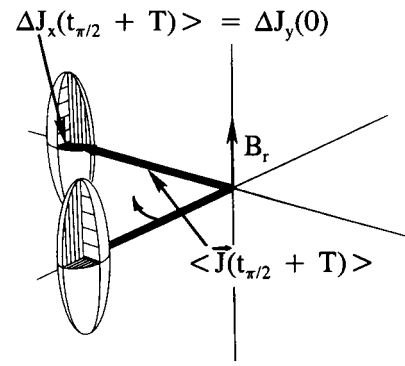


FIG. 3. Pictorial representation of the fluctuations in the measured values of J_x , J_y , and J_z . In this figure $\langle \mathbf{J} \rangle$ is taken to point along the negative z axis. The dimensions of the axes of the spheroid are ΔJ_x , ΔJ_y , and ΔJ_z where $\Delta J_i^2 \equiv \langle J_i^2 \rangle - \langle J_i \rangle^2$ and $i = x, y, z$.

(a) $t = 0 \rightarrow t_{\pi/2}$



(b) $t = t_{\pi/2} \rightarrow t_{\pi/2} + T$



(c) $t = t_{\pi/2} + T \rightarrow 2t_{\pi/2} + T \equiv t_f$

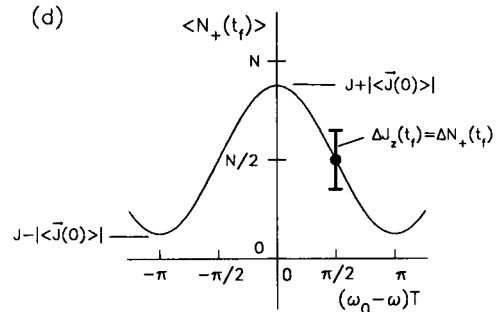
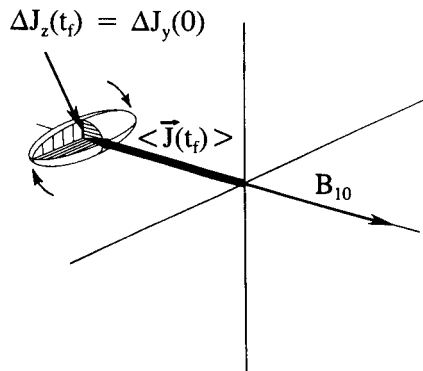


FIG. 4. Pictorial representation of the evolution of $\langle \mathbf{J} \rangle$ and the fluctuations at various parts of the Ramsey method for the condition $\omega_0 - \omega = \pi/2T$. From these figures we see that the fluctuations in $N_+(t_f)$ are given by $\Delta J_z(t_f)$ or $\Delta J_y(0)$. In part (d) of the figure, we show the point on the Ramsey curve corresponding to $\omega_0 - \omega = \pi/2T$. ΔN_+ represents the rms fluctuations for repeated measurements of N_+ for $\omega_0 - \omega = \pi/2T$. For part (d), we have assumed that the initial state is such that $\langle \mathbf{J} \rangle$ is aligned with the negative z axis but $|\langle \mathbf{J} \rangle| < J$.

[Eq. (14)], the particular point on the resonance curve corresponding to $\omega_0 - \omega = \pi/(2T)$, and the corresponding value of the uncertainty in the measurement $\Delta N_+(t_f) = \Delta J_z(t_f) = \Delta J_y(0)$.

A. Schrödinger picture

In some cases, it will be useful to represent the system dynamics in the Schrödinger picture. As before, we assume we are in the rotating frame in which \mathbf{B}_1 is station-

$$U(t_f, 0) = \frac{1}{2} \begin{pmatrix} (\cos\omega_r T - 1) & -i\sqrt{2} \sin\omega_r T & (\cos\omega_r T + 1) \\ i\sqrt{2} \sin\omega_r T & -2 \cos\omega_r T & i\sqrt{2} \sin\omega_r T \\ (\cos\omega_r T + 1) & -i\sqrt{2} \sin\omega_r T & (\cos\omega_r T - 1) \end{pmatrix}, \quad (24)$$

where we use the notation

$$\psi = a|1, 1\rangle + b|1, 0\rangle + c|1, -1\rangle \equiv \begin{pmatrix} a \\ b \\ c \end{pmatrix}. \quad (25)$$

B. Comparison of Ramsey spectroscopy to interferometry

Yurke and co-workers [29–31] and others [55] have discussed the connection between a linear lossless passive device with two input and output ports and the SU(2) symmetry group. They construct abstract operators [56] $J_x = (a_1^\dagger a_2 + a_2^\dagger a_1)/2$, $J_y = -i(a_1^\dagger a_2 - a_2^\dagger a_1)/2$, $J_z = \frac{1}{2}(a_1^\dagger a_1 - a_2^\dagger a_2)$, and $N = (a_1^\dagger a_1 + a_2^\dagger a_2)$, where a_i^\dagger and a_i ($i=1,2$) are the creation and annihilation operators for particles (bosons or fermions) entering ports 1 or 2 of the device. For example, the system might be photons injected into a Mach-Zehnder interferometer. These abstract operators J_i ($i=x,y,z$) have the same mathematical properties as the angular-momentum operators and therefore the interferometer can be described in terms of this abstract spin space. N corresponds to the total number of particles entering both ports of the interferometer. Beam splitters and differential phase shifters between the two arms of the interferometer behave like rotations of the net spin operator. If we compare our case to this formalism for interferometers, the Ramsey spectroscopy we discuss is formally equivalent to a Mach-Zehnder interferometer where the two $\pi/2$ Ramsey pulses are identified with 50-50 beam splitters in the interferometer, and the phase shift incurred between the spin precession and the applied field in Ramsey spectroscopy corresponds to the differential phase shift between the interferometer arms. If we define the phase sensitivity in Ramsey spectroscopy as $\Delta\phi_R \equiv \Delta\omega T$, then the sensitivity of the Ramsey method is equivalent to the phase sensitivity of a Mach-Zehnder interferometer [see Eq. (13) of this paper and Eq. (3.16) of Ref. [29]]. Because of this connection, we wish to create the same form of correlated input states as desired for interferometers.

ary [Eq. (8)]. In this frame, operators will now be assumed to be time independent, and the wave function evolves according to

$$\Psi(t) = U(t, 0)\Psi(0), \quad (23)$$

where the evolution operator U is the solution to the equation $i\hbar dU/dt = H_r U$ [54].

In the case of two particles ($J=1$), for example, following the application of the Ramsey fields, we have

IV. SPECTROSCOPY OF UNCORRELATED PARTICLES

In this section, we consider the particles to be initially uncorrelated and independent. This case is treated in detail in Ref. [40]. Because the particles are assumed to be uncorrelated, the initial wave function can be written as a direct product

$$\psi(0) = \prod_{i=1}^N \psi_i(0), \quad (26)$$

where $\psi_i(0)$ is the initial wave function for particle i .

By optical pumping techniques we can prepare atoms in energy eigenstates. Therefore, in our spin- $\frac{1}{2}$ model, we will be particularly interested in the case where all of the particles are initially prepared in, for example, the $\psi_i(0) = |-\frac{1}{2}\rangle$ state. In this case, the initial state is represented by the wave function

$$\psi(0) = |J=N/2, M=-N/2\rangle = \prod_{i=1}^N |-\frac{1}{2}\rangle_i, \quad (27)$$

which is a particular Dicke state [47]. For this state, $\langle J_z(0) \rangle = -J$, $\Delta J_z(0) = 0$, $\Delta J_x(0) = \Delta J_y(0) = (J/2)^{1/2}$, and

$$\langle N_+(t_f) \rangle = \frac{1}{2}N[1 + \cos(\omega - \omega_0)T].$$

Equation (20) is identical to Eq. (22) for all values of ω_r since $\Delta J_z(0) = 0$. In this case, the best value of ω_0 can be determined independent of where we measure on the resonance curve. This somewhat surprising result occurs because the quantum noise $\Delta N_+(t_f)$ is proportional to the signal slope $\partial\langle N_+ \rangle/\partial\omega$ for all values of ω . Therefore, from Eq. (13), $|\Delta\omega|$ is independent of our choice of ω . The noise is equal to zero on the peaks and valleys of the Ramsey resonance curve because, there, we detect eigenstates of J_z [Fig. 5(a)]. Unfortunately, the sensitivity to frequency shifts is also equal to 0 on the peaks and valleys since the slope of the Ramsey curve is equal to 0. As discussed in the last section, if ΔN_{add} is not negligible, we

minimize $|\Delta\omega|$ if we operate at frequencies $\omega_0 - \omega = \pm(n + \frac{1}{2})\pi/T$ ($n=0, 1, 2, 3, \dots$), and, for simplicity, we have restricted ourselves to $\omega_0 - \omega = \pm\frac{1}{2}\pi/T$.

It is instructive to consider the evolution of the wave

$$\begin{aligned}\psi(t_f) &= \frac{1}{2}(\cos\omega_r T + 1)|1, 1\rangle + \frac{i}{\sqrt{2}}\sin\omega_r T|1, 0\rangle + \frac{1}{2}(\cos\omega_r T - 1)|1, -1\rangle \\ &= (\cos\omega_r T/2|+\rangle_1 + i\sin\omega_r T/2|-\rangle_1)(\cos\omega_r T/2|+\rangle_2 + i\sin\omega_r T/2|-\rangle_2) \\ &= [U_1(t_f, 0)|-\rangle_1][U_2(t_f, 0)|-\rangle_2] = \psi_1(t_f)\psi_2(t_f),\end{aligned}\quad (28)$$

where, for simplicity, we write $|+\frac{1}{2}\rangle = |+\rangle$ and $|-\frac{1}{2}\rangle = |-\rangle$. The evolution operator for particle j satisfies $i\hbar dU_j/dt = H_r U_j$ and $\psi_j(t_f)$ is the wave function of particle j after being acted upon by the Ramsey fields. Therefore, the final wave function is the product of the final wave functions of the individual particles. The particles remain uncorrelated (or unentangled) after application of the Ramsey fields. This is true for the application of any form of the (classical) clock radiation and for any number of particles since the initial wave function is given by Eq. (26) and $U(t_f) = \prod U_j(t_f)$.

This case (when all particles are initially prepared in eigenstates) serves as a benchmark and has been realized experimentally. In Ref. [40], we reported spectroscopic experiments on ${}^9\text{Be}^+$ and ${}^{199}\text{Hg}^+$ ions where the signal-to-noise ratio was limited by the projection noise ΔN_+ in the measurements. In these experiments, the ions were prepared in eigenstates corresponding to the initial Dicke state given by Eq. (27) in our spin- $\frac{1}{2}$ model. For this case $|\Delta\omega|$ is given by Eq. (22), which we denote

$$|\Delta\omega|_{\text{DS}} \equiv \frac{1}{T(2J)^{1/2}} = \frac{1}{TN^{1/2}}. \quad (29)$$

This value of $|\Delta\omega|$ is the minimum that can be obtained using uncorrelated states in the Ramsey spectroscopy described above. It is limited by the fundamental quantum fluctuations in the measurement. This limitation on $|\Delta\omega|$ observed in the experiments led us to consider the possibility of using correlated states for spectroscopy where even smaller values of $|\Delta\omega|$ might be obtained.

V. SPECTROSCOPY OF CORRELATED PARTICLES

A. Squeezing parameter for spectroscopy

Before we examine specific states which can reduce $|\Delta\omega|$ below $|\Delta\omega|_{\text{DS}}$, we introduce a parameter which indicates the level of improvement. As described in the last section, $|\Delta\omega|_{\text{DS}}$ provides a useful benchmark. Therefore we will define a ‘‘squeezing’’ parameter

$$\begin{aligned}\xi_R &\equiv |\Delta\omega|/|\Delta\omega|_{\text{DS}} = (2J)^{1/2}\Delta J_z(t_f)/|\langle J_y(t_f) \rangle| \\ &= (2J)^{1/2}\Delta J_y(0)/|\langle J_z(0) \rangle|,\end{aligned}\quad (30)$$

where $|\Delta\omega|$, $\Delta J_z(t_f)$, $\langle J_y(t_f) \rangle$, $\Delta J_y(0)$, and $\langle J_z(0) \rangle$ refer to the new states to be considered and the subscript R denotes that this is the relevant squeezing parameter for the particular form of the Ramsey method of spectroscopy

in the Schrödinger picture. For example, for $J=1$, our initial wave function is $|1, -1\rangle$ [$a=b=0$, $c=1$ in Eq. (25)]. After application of the Ramsey fields we have from Eq. (24)

considered. The goal of the paper is to examine ways to make ξ_R less than 1 and as small as possible.

More generally, consider a state with arbitrary $\langle \mathbf{J} \rangle$. Let $\hat{\mathbf{e}}$ denote a direction perpendicular to $\langle \mathbf{J} \rangle$ ($\langle \mathbf{J} \rangle \cdot \hat{\mathbf{e}} = 0$) such that $\Delta(\mathbf{J} \cdot \hat{\mathbf{e}})$ is a minimum. This state can always be rotated (by, for example, application of a classical field)

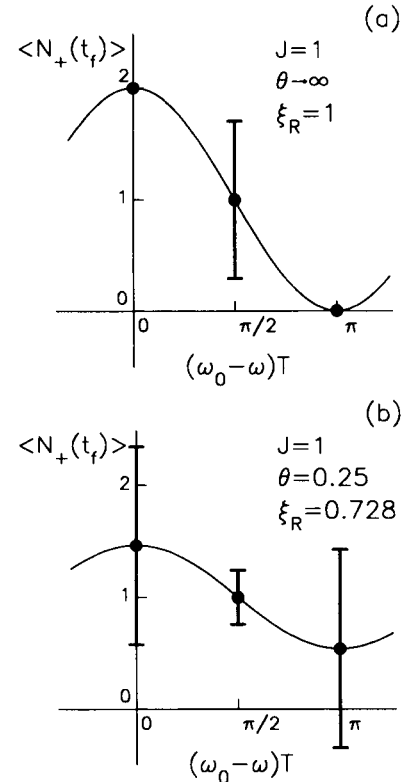


FIG. 5. Plot of $\langle N_+(t_f) \rangle$ and $\Delta N_+(t_f)$ for three values of ω corresponding to $\omega_0 - \omega = 0, \pi/2T$, and π/T , for $N=2$ ($J=1$). For both (a) and (b), $\psi(0) = (e^{-\theta}|1, 1\rangle + e^{\theta}|1, -1\rangle) / [2 \cosh(2\theta)]^{1/2}$. In (a), we assume $\theta \rightarrow \infty$, that is, the initial state is the $|1, -1\rangle$ Dicke state. For $\omega_0 - \omega = 0$ and π/T , the noise $\Delta N_+(t_f) = 0$ since the corresponding final states $\psi(t_f) = |1, 1\rangle$ and $|1, -1\rangle$ are eigenstates. However, the sensitivity to frequency fluctuations $\partial \langle N_+(t_f) \rangle / \partial \omega$ also goes to zero at these frequencies, so the signal-to-noise ratio is not improved. In general, for $\psi(0) = |J, -J\rangle$ (or $|J, J\rangle$), the error $\Delta\omega$ in our determination of ω_0 [Eqs. (13) and (22)] is independent of ω . In (b), $\theta = 0.25$. This state leads to a reduced value of $\Delta\omega$ for $\omega_0 - \omega = \pi/2T$ ($\xi_R = 0.728$). However, for $|\omega_0 - \omega| \approx 0$ and π/T , $\Delta\omega$ increases substantially over case (a).

so that $\hat{\mathbf{e}}$ and $\langle \mathbf{J} \rangle$ point along the $\hat{\mathbf{y}}$ and negative $\hat{\mathbf{z}}$ axes, respectively. This state can then be used in Ramsey spectroscopy with ξ_R given by Eq. (30). If we define $\Delta J_{\perp} \equiv \Delta(\mathbf{J} \cdot \hat{\mathbf{e}})$, a more general definition of ξ_R is given by

$$\xi_R = (2J)^{1/2} \Delta J_{\perp} / |\langle \mathbf{J} \rangle|. \quad (31)$$

B. Squeezing parameter to indicate sensitivity to rotation

We may view the squeezing parameter ξ_R as having a more general geometrical interpretation which indicates the degree to which we can sense rotations of angular momentum states. This generalization can then be applied to specific cases such as interferometry [29] or spectroscopy [38]. To see this, first consider a state which has $\langle \mathbf{J} \rangle = -\hat{\mathbf{z}} |\langle J_z \rangle|$ (Fig. 3). Suppose we are interested in measuring a small rotation of \mathbf{J} about the x axis by the angle θ . A way to do this is to measure J_y . We define θ through the relation $\langle J_y \rangle = \sin\theta |\langle \mathbf{J} \rangle|$. The mean-squared noise in θ is given by $(\Delta\theta)^2 = (\Delta J_y)^2 / (\partial \langle J_y \rangle / \partial \theta)^2$. Therefore the precision of the angle measurement is given by $\Delta\theta = \Delta J_y / (\cos\theta |\langle \mathbf{J} \rangle|)$, which is minimized for $\theta = \pm n\pi$ ($n=0, 1, 2, \dots$). More generally, for a state with arbitrary $\langle \mathbf{J} \rangle$, consider rotations $\phi(\hat{\boldsymbol{\eta}})$ of $\langle \mathbf{J} \rangle$ about an axis $\hat{\boldsymbol{\eta}}$ where $\langle \mathbf{J} \rangle \cdot \hat{\boldsymbol{\eta}} = 0$. We can measure these rotations by measuring $J_{\perp} \equiv \hat{\boldsymbol{\alpha}} \cdot \mathbf{J}$ where $\hat{\boldsymbol{\alpha}} \cdot \langle \mathbf{J} \rangle = \hat{\boldsymbol{\alpha}} \cdot \hat{\boldsymbol{\eta}} = 0$. In this case the uncertainty in our measurement of $\phi(\hat{\boldsymbol{\eta}})$ is given by

$$\Delta\phi = \Delta J_{\perp} / |\langle \mathbf{J} \rangle|. \quad (32)$$

If we compare this angle uncertainty to the value $\Delta\phi_{\text{DS}}$ obtained using the Bloch states (states obtained from the $|J, -J\rangle$ Dicke states by a rotation [48]), we can define a squeezing parameter indicating sensitivity to rotation as $\Delta\phi / \Delta\phi_{\text{DS}}$. We have

$$\Delta\phi / \Delta\phi_{\text{DS}} \equiv (2J)^{1/2} \Delta J_{\perp} / |\langle \mathbf{J} \rangle| = \xi_R. \quad (33)$$

Therefore the subscript R can also be used to signify rotation and ξ_R the improved sensitivity to rotations using squeezed-spin states.

From this definition of squeezing, we gain a pictorial representation of what is desired in this kind of squeezed-spin state. Referring to Fig. 3 and Eq. (30), (31), or (33), we desire a state where $|\langle \mathbf{J} \rangle|$ is as long as possible and the error spheroid is compressed as much as possible in a direction perpendicular to $\langle \mathbf{J} \rangle$ [along $\hat{\mathbf{y}}$ in Fig. 3(a)], but, at the same time, minimizing $\Delta J_{\perp} / |\langle \mathbf{J} \rangle|$. As discussed in Sec. V C and in Refs. [30] and [34], some states show the best squeezing when $|\langle \mathbf{J} \rangle| \rightarrow 0$. The pictorial representation of such a state is a spheroid nearly centered on the origin with $\Delta J_y(0) \ll \Delta J_x(0), \Delta J_z(0)$.

C. A simple example (squeezed states for $N=2$)

Consider two particles which are initially prepared in the state

$$\psi(0) = [2 \cosh(2\theta)]^{-1/2} \times (e^{-\theta} |+\rangle_1 |+\rangle_2 + e^{\theta} |-\rangle_1 |-\rangle_2). \quad (34)$$

This is a correlated or entangled state of particles 1 and 2 since the wave function cannot be written as a direct product (except for $\theta \rightarrow \pm\infty$). Many properties of this kind of state have been considered by Rashid [25], who investigated states of the form

$$\Psi'(J, M, \theta) = C_N \exp(-\theta J_z) \exp(-i\pi J_x / 2) |J, M\rangle,$$

where C_N is a normalization constant. The state in Eq. (34) is, to an overall phase factor, the Rashid state $\Psi'(1, 0, \theta)$. It has also been considered in Ref. [32] in the context of the radiation emitted by the two particles. It would be produced by coupling the two particles to a broadband squeezed vacuum [33]. This state has the properties that $\langle J_x(0) \rangle = \langle J_y(0) \rangle = 0$, $\langle J_z(0) \rangle = -\tanh 2\theta$, $\Delta J_x^2(0) = \frac{1}{2}(1 + \text{sech} 2\theta)$, $\Delta J_y^2(0) = \frac{1}{2}(1 - \text{sech} 2\theta)$, $\Delta J_z(0) = \text{sech} 2\theta$, and $\xi_R = \text{sech} \theta [(\cosh 2\theta) / 2]^{1/2}$. This state also satisfies the condition $\Delta J_x(0) \Delta J_y(0) = \frac{1}{2} |\langle J_z(0) \rangle|$ and is therefore a minimum-uncertainty state [25]. When θ is large, $\psi(0) \simeq |1, -1\rangle$ and $\xi_R \simeq 1$; this is just the initial state considered in the example in Sec. IV. When θ is small, $\xi_R \simeq (1 + \theta^2/2) / 2^{1/2}$. Therefore, as $\theta \rightarrow 0$, $\xi_R \rightarrow 1/\sqrt{2} = 1/\sqrt{N}$. We can also show that, for $J=1$, the state of Eq. (34) is the state which minimizes ξ_R .

In Fig. 5, we plot the Ramsey resonance curve ($\langle N_+(t_f) \rangle$ vs ω) when using this initial state for two cases, $\theta \rightarrow \infty$ ($\xi_R = 1$) and $\theta = 0.25$ ($\xi_R = 0.728$). We also plot the fluctuations $\Delta N_+(t_f)$ for values of ω given by $(\omega_0 - \omega)T = 0, \pi/2$, and π . For $(\omega_0 - \omega)T = 0$ and π , we see that plotting $\Delta N_+(t_f)$ is some what misleading because, for example, values of $N_+(t_f)$ outside the range of 0-2 are not allowed. However, at the primary values of interest, $(\omega_0 - \omega)T = \pm\pi/2$, $\Delta N_+(t_f)$ gives a reasonable representation of the fluctuations between measurements.

From Fig. 5(b), the key point is that, although the amplitude of the Ramsey curve becomes smaller, the noise at the probe frequencies $(\omega_0 - \omega)T = \pm\pi/2$ becomes smaller more rapidly. Therefore the signal-to-noise ratio ($\propto |\Delta\omega|^{-1}$) is increased at these frequencies. It is also clear that the signal-to-noise ratio approaches 0 near the peaks and valleys of the curve; hence it is important to probe near the half-intensity points.

A physical explanation for the noise reduction is as follows. In the Schrödinger picture, for $\theta \rightarrow 0$, the final wave function (to an overall phase factor) is given from Eqs. (24) and (34) as

$$\psi(t_f) \simeq |1, 0\rangle = (|+\rangle_1 |-\rangle_2 + |-\rangle_1 |+\rangle_2) / \sqrt{2}.$$

This state has the property that, if J_z is measured for either particle 1 or 2, we find $\langle J_z \rangle = 0$; that is, it is equally likely to find the particle in the $|+\rangle$ or the $|-\rangle$ state. On the other hand, when we measure J_z sequentially for each particle, we find opposite values of J_z for each particle. For example, if when measuring particle 1 we find it to be in the $|+\rangle_1$ state, then $\psi(t_f)$ has been projected into the $|+\rangle_1 |-\rangle_2$ state. Therefore, when J_z is measured for particle 2, we find it to be in the $|-\rangle_2$ state. This property of correlated states is at the heart of the correlations observed in two-particle EPR experiments

[1,23]. The correlations exist even if the particles do not interact.

Letting $\theta \rightarrow 0$ in Eq. (34) clearly shows the correlations between particles but gives rise to practical problems since the signal ($\propto |\langle J_z(0) \rangle| = \tanh 2\theta$) also approaches 0. More generally, for $\theta \rightarrow 0$, $\langle J \rangle \rightarrow 0$ and the signal goes to zero for any form of the (classical) resonance radiation, since any excitation, Ramsey or otherwise, is equivalent to a rotation. Therefore, for example, in the presence of added noise, we want to choose a value of θ which minimizes $|\Delta\omega|$ given by Eq. (21).

D. Squeezed states for other values of N

We first consider $N=1$ ($J=\frac{1}{2}$). We would not expect a way to make $\xi_R < 1$ because there is only one particle and the issue of correlations does not arise. For $J=\frac{1}{2}$, the most general initial pure state can be written in the form

$$\psi(0) = \cos\theta/2e^{-i\phi/2}|+\rangle + \sin\theta/2e^{i\phi/2}|-\rangle$$

in which case $\xi_R = (1 + \tan^2\theta \cos^2\phi)^{1/2} \geq 1$.

For $N > 2$, states which give rise to minimum values of ξ_R are not immediately apparent. For example, for $N=3$, as the parameters of the wave function are varied, local minima can be found. Using a minimization program we find locally minimum states

$$\psi(0) \approx 0.935|\frac{3}{2}, \frac{3}{2}\rangle + 0.354|\frac{3}{2}, -\frac{1}{2}\rangle$$

and $\psi(0) = \Psi'(\frac{3}{2}, \frac{1}{2}, 0)$, the Rashid state for $\theta \rightarrow 0$. These states give locally minimum values of ξ_R with values $\xi_R \approx 0.76$ and 0.66 , respectively. Neither of these states has $\xi_R = 1/\sqrt{N} = 0.577$.

Finding states which minimize ξ_R becomes more complicated for larger N . Nevertheless, we can guess at states which approximate $\xi_R = 1/\sqrt{N}$. When N is odd, consider the relatively simple *final* states (considered previously by Yurke [30] for interferometers)

$$\psi(t_f) = \frac{1}{\sqrt{2}}(|J, \frac{1}{2}\rangle + |J, -\frac{1}{2}\rangle) \quad (N \text{ odd}). \quad (35)$$

The appropriate initial states can be obtained through rotations (for example for reversing the order of the Ramsey pulses). These states have the property that $\xi_R = (1/\sqrt{N})[2/(1+1/N)]$. When N is even consider the *final* states

$$\begin{aligned} \psi(t_f) = & \frac{1}{\sqrt{2}} \sin\alpha |J, 1\rangle + i \cos\alpha |J, 0\rangle \\ & - \frac{1}{\sqrt{2}} \sin\alpha |J, -1\rangle \quad (N \text{ even}). \end{aligned} \quad (36)$$

For these states, $\xi_R = (1+N/2)^{-1/2}/\cos\alpha$. For $N=2$, this state is equivalent to the Rashid state of Eq. (34). We see that ξ_R is minimized for $\alpha \rightarrow 0$, but as noted in Sec. VC, the amplitude of the Ramsey curve also goes to zero as $\alpha \rightarrow 0$. Agarwal and Puri [34] have shown that the states of Rashid [25]

$$\Psi'(J, M, \theta) = C_N \exp(-\theta J_z) \exp(-i\pi J_x/2) |J, M\rangle$$

can be used in Ramsey spectroscopy and give minimum

values of $\xi_R = [1 + (J^2 - M^2)/J]^{-1/2}$ for $\theta \rightarrow 0$. Therefore, for N even, $\xi_R = (1+N/2)^{-1/2}$ with $M=0$. For N odd, $\xi_R = [1 + (N^2 - 1)/2N]^{-1/2}$ with $M = \pm \frac{1}{2}$. This gives a value of ξ_R somewhat smaller than the states of Eq. (35).

E. Minimum value of ξ_R

Although the particular Rashid states considered by Agarwal and Puri [34] give the best value of squeezing of the states considered above, it is useful to consider the minimum possible value of ξ_R . We find that $\xi_R \geq N^{-1/2}$ from the inequalities

$$\begin{aligned} \xi_R &= (2J)^{1/2} \Delta J_y / |\langle J_z \rangle| \\ &\geq (J/2)^{1/2} / \Delta J_x \geq (2J)^{-1/2} = N^{-1/2}. \end{aligned} \quad (37)$$

The first inequality follows from the uncertainty principle applied to angular momentum, $\Delta J_y \geq |\langle J_z \rangle| / 2\Delta J_x$ (see Sec. VIA). The second inequality follows from $\Delta J_x \leq J$. This last relation can be seen by noting that, if we quantize the angular momentum along the x direction, it is straightforward to show that the states with the largest value of ΔJ_x are of the form

$$\psi_x = 2^{-1/2}(|J, J\rangle_x + e^{i\phi}|J, -J\rangle_x),$$

in which case $\Delta J_x = J$. In the states considered above, the only state which shows this maximum degree of squeezing is the $J=1$ state considered in Eq. (34).

VI. ALTERNATE DEFINITIONS OF SPIN SQUEEZING

A. Squeezing parameter based on angular-momentum commutation relations

Different definitions of spin squeezing can be used depending on the context in which squeezing is considered. From the commutation relations for angular momentum, the uncertainty relations between different components of the angular momentum are given by

$$\Delta J_x \Delta J_y \geq |\langle J_z \rangle| / 2 \quad (38)$$

and the expressions which follow from cyclic permutations of indices. From these uncertainty relations, it is natural to define squeezed-spin states as states where $\Delta^2 J_i < |\langle J_j \rangle| / 2$ for $i \neq j$. Hence a squeezing parameter for this "natural" definition of squeezing might be written as

$$\xi_n = \Delta J_i / |\langle J_j \rangle|^{1/2}, \quad i \neq j \in (x, y, z). \quad (39)$$

Squeezing in the context of this definition is discussed in Refs. [26–28] and [33]. For example, Walls and Zoller [26] illustrate the relation between spin squeezing defined in this way and the squeezing in resonance fluorescence light from two-level atoms. This squeezing is exhibited by Bloch states which are states derived from the $|J, -J\rangle$ Dicke states by a rotation. We can see this using Eq. (10). During the first Ramsey pulse where $\omega' \approx \omega_1 \hat{y}$ (corresponding to a rotation about \hat{y}), the angular-momentum operators transform according to

$$J_z(t) = J_z(0)\cos\omega_1 t - J_x(0)\sin\omega_1 t$$

and

$$J_x(t) = J_x(0)\cos\omega_1 t + J_z(0)\sin\omega_1 t .$$

Therefore, if we define squeezing as $\xi_n \equiv \Delta J_x / |\langle J_z \rangle / 2|^{1/2}$, we find $\xi_n(t) = \cos^{1/2}\omega_1 t \leq 1$ when $\psi(0) = |J, -J\rangle$.

B. Squeezing parameter to indicate the degree of correlation

As pointed out by Kitagawa and Ueda [36] the definition of squeezing discussed in Sec. VIA does not necessarily reflect the correlations between particles. For example, the Bloch states remain uncorrelated under rotation [cf. Eq. (28)] even though they show $\xi_n < 1$. Kitagawa and Ueda therefore regard the spin to be squeezed only if the variance of one spin component J_\perp normal to the mean spin vector is smaller than the variance for a Bloch state ($= J/2$) [36]. In this view, a spin-squeezing parameter might be defined as

$$\xi_S = \Delta J_\perp / (J/2)^{1/2} , \quad (40)$$

where the \perp subscript refers to an axis perpendicular to $\langle \mathbf{J} \rangle$ where the minimum value of ΔJ is obtained. A squeezed-spin state ($\xi_S < 1$) can be rotated so that $\langle \mathbf{J} \rangle = \langle J_z \rangle \hat{z}$ and $\Delta J_\perp = \Delta J_y$ and could be used in Ramsey spectroscopy (or interferometry) with $\xi_R = (J / |\langle J_z \rangle|) \xi_S$. In Ref. [38], we used a somewhat different definition of ξ_S which we called ξ_{spin} .

VII. GENERATION OF SQUEEZED-SPIN STATES

As discussed in the last section, states for which $\xi_n < 1$ can be generated by rotations of the $|J, \pm J\rangle$ Dicke states. Since $\xi_R = \xi_S = 1$ for these states, we do not consider them further. The specific correlated or squeezed states considered in Refs. [29–31] and in Eqs. (35) and (36) above were constructed to emphasize the benefits of spin squeezing in the context of various experiments, but generators for these states were not given.

Rashid [25] investigated the class of angular-momentum states which satisfy the equality in Eq. (38). These minimum-uncertainty or “intelligent” states can be formed from the $|J, M\rangle$ Dicke states by the transformation of the form

$$\Psi'(J, M, \theta) = C_N \exp(-\theta J_z) \exp(-i\pi J_x / 2) |J, M\rangle ,$$

where C_N is a normalization constant. These kinds of states show $\xi_R \approx N^{-1/2}$ for $\theta \rightarrow 0$ as discussed in Sec. VD. Agarwal and Puri have shown [33] that the $\Psi'(J, 0, \theta)$ Rashid states for integral J can be created by the interaction of an ensemble of two-level or spin- $\frac{1}{2}$ particles with broadband squeezed vacuum radiation.

Barnett and Dupertuis [32] considered the correlated states between pairs of particles (1 and 2) generated by a Hamiltonian of the form $H = i(g^* J_{1+} J_{2+} - g J_{1-} J_{2-})$, where $J_+ = J_x + iJ_y$ and $J_- = J_x - iJ_y$ are the usual raising and lowering operators. Kitagawa and Ueda [35,36] considered the squeezed-spin states, for arbitrary N , gen-

erated by interaction of the spins through nonlinear Hamiltonians of the form $H = \hbar\chi J_z^2$ and $H = \hbar\chi(J_+^2 - J_-^2)/2i$. Both of these interactions lead to useful squeezing. They have shown that the Coulomb interaction between electrons in the two arms of an electron interferometer corresponds to a Hamiltonian of the form $H = \hbar\chi J_z^2$ and might be used to generate the squeezed states in that system.

A. Coupling to a harmonic oscillator

In Ref. [38], we considered the spin squeezing produced when an ensemble of two-level particles was coupled to a (single) harmonic oscillator. One reason we considered this coupling was the prior theoretical demonstration of the complementary effect—harmonic-oscillator squeezing through the same coupling to two-level systems [57] (see also Ref. [21]). The hope was that, for certain initial conditions, the same type of system might produce spin squeezing. As discussed below, it may be possible to realize coupling to a suitable harmonic oscillator, whereas we have not thought of a practical way to realize the couplings discussed by Kitagawa and Ueda [35,36] for ensembles of two-level atoms.

Therefore, in the laboratory frame, the Hamiltonian we consider is given by

$$\begin{aligned} H &= \hbar\omega_0 J_z + \hbar\omega_z (a^\dagger a + \frac{1}{2}) + H_I , \\ H_I &= -2\hbar\Omega (a^\dagger + a)(J_+ + J_-) \cos\omega_m t , \end{aligned} \quad (41)$$

where the first term is given by Eqs. (2) and (5), a^\dagger and a are the creation and annihilation operators for the harmonic oscillator of frequency ω_z and amplitude $z = z_0(a + a^\dagger)$, and Ω represents the strength of the coupling, which we assume, in general, is sinusoidally modulated at frequency ω_m . It will be useful to transform to the interaction picture where, for $\Omega = 0$, the operators (or wave functions) are constant in time. In this interaction picture, the new operators are given by $\tilde{a} = a \exp(i\omega_z t)$, $\tilde{J}_- = J_- \exp(i\omega_0 t)$, and the adjoint expressions. The operators \tilde{J} are the operators in the rotating frame introduced in the subsection of Sec. II. In this interaction picture, the Hamiltonian representing the coupling becomes

$$\begin{aligned} H_I &= -2\hbar\Omega \cos\omega_m t [a^\dagger J_+ e^{i(\omega_z + \omega_0)t} + a J_- e^{-i(\omega_z + \omega_0)t} \\ &\quad + a^\dagger J_- e^{i(\omega_z - \omega_0)t} \\ &\quad + a J_+ e^{i(\omega_0 - \omega_z)t}] , \end{aligned} \quad (42)$$

where, for convenience, we have dropped the tilde symbols (\sim). Resonant interactions occur for two values of ω_m . For $\omega_z \neq \omega_0$ and $\omega_m = \pm(\omega_0 - \omega_z)$, the Hamiltonian is

$$H_I = -\hbar\Omega (a J_+ + a^\dagger J_-) , \quad (43)$$

plus high-frequency terms which we neglect (rotating-wave approximation). This is the Hamiltonian of the Jaynes-Cummings model [58] which is of considerable interest in quantum optics. For $\omega_z \neq \omega_0$ and $\omega_m = \pm(\omega_0 + \omega_z)$, the Hamiltonian is

$$H_2 = -\hbar\Omega(a^\dagger J_+ + aJ_-), \quad (44)$$

plus high-frequency terms which we neglect. When $\omega_0 = \omega_z$, Ω should be replaced by 2Ω in the expressions for H_1 and H_2 . For brevity, we will assume $\omega_z \neq \omega_0$. H_1 and H_2 are essentially equivalent since H_1 becomes H_2 if we switch the roles of the $|+\frac{1}{2}\rangle$ and $|-\frac{1}{2}\rangle$ states for each particle.

We now consider the preparation of the spins into correlated states through the interactions H_1 or H_2 . The states which are prepared this way could then be used in Ramsey spectroscopy. For simplicity of notation, we will consider this preparation phase to start at $t=0$. However, this time should not be confused with the time when the first Ramsey pulse is applied.

B. Approximate solution

One way squeezing can be imparted to the spins is by first squeezing the harmonic oscillator and transferring this squeezing to the spins through H_1 [38]. To get a feeling for how this works without making the problem mathematically complicated, consider the following special case. The spin is assumed to be initially prepared in the $|J, -J\rangle$ Dicke state and the harmonic oscillator is prepared in a squeezed vacuum state characterized by $\langle z(t=0) \rangle = \langle \dot{z}(0) \rangle = 0$ and $\Delta z(0) < \Delta z(\text{coherent state}) = z_0$. We can characterize the squeezing of the harmonic oscillator by the parameters $\xi_z(t) \equiv \Delta z(t)/z_0$ or $\xi_v(t) \equiv \Delta \dot{z}(t)/(\omega_z z_0)$. The condition $\xi_z < 1$ indicates amplitude squeezing and $\xi_v < 1$ indicates velocity or momentum squeezing. When H_1 applies, the Heisenberg equations of motion are

$$da/dt = i\Omega J_-, \quad dJ_-/dt = -2i\Omega a J_z, \quad (45)$$

and the adjoint expressions. We now make the assumption that the initial mean number of quanta $\langle n(0) \rangle \equiv \langle a^\dagger(0)a(0) \rangle$ in the harmonic oscillator is small enough and/or N is large enough that the value of $\langle J_z \rangle$ does not change appreciably during the time H_1 is applied. In this case, we make the approximation $J_z(t) = -JI$, where I is the identity operator. With this approximation, the Heisenberg equations of motion can be solved analytically to give

$$J_-(t) = J_-(0)\cos\Omega_N t + iN(\Omega/\Omega_N)a(0)\sin\Omega_N t, \quad (46)$$

$$a(t) = a(0)\cos\Omega_N t + iJ_-(0)N^{-1/2}\sin\Omega_N t, \quad (47)$$

and the adjoint expressions, where $\Omega_N^2 \equiv N\Omega^2$. From these equations, we find

$$\xi_R^2(t) = \xi_S^2(t) = \cos^2\Omega_N t + \xi_z^2(0)\sin^2\Omega_N t, \quad (48)$$

$$\xi_{R,x}^2(t) = \cos^2\Omega_N t + \xi_v^2(0)\sin^2\Omega_N t, \quad (49)$$

$$\xi_z^2(t) = \xi_z^2(0)\cos^2\Omega_N t + \sin^2\Omega_N t, \quad (50)$$

and

$$\xi_v^2(t) = \xi_v^2(0)\cos^2\Omega_N t + \sin^2\Omega_N t. \quad (51)$$

In Eq. (49), we make the definition $\xi_{R,x} \equiv (2J)^{1/2}\Delta J_x/|\langle J_z \rangle|$. If a state with $\xi_{R,x} < 1$ is produced, it could be used in Ramsey spectroscopy by first rotating the state by $\pi/2$ about the z axis so that $\xi_{R,x} \rightarrow \xi_{R,y} \equiv \xi_R$. From Eqs. (48) and (49), we can create squeezed-spin states by first squeezing the harmonic oscillator ($\xi_z(0) < 1$ or $\xi_v(0) < 1$) and transferring the squeezing to the spins. Correspondingly, from Eqs. (50) and (51) we see that the squeezing is "drained away" from the harmonic oscillators as it is transferred to the spins. In this small-angle approximation, squeezing is transferred to the spins like wavefunction exchange between harmonic oscillators [18]. The squeezing is sinusoidally transferred back and forth between the harmonic oscillator and the spins; however, in a more precise treatment, where we no longer assume $\langle J_z \rangle$ to be constant, this will no longer be true. We find the same expressions for $\xi_R(t)$, $\xi_{R,x}(t)$, $\xi_z(t)$, and $\xi_v(t)$ when $\omega_m = \pm(\omega_0 + \omega_z)$ (H_2 applies), $\psi(0) = |J, +J\rangle$, and if we make the small-angle approximation $J_z = +JI$.

For H_1 , if we instead assume $\psi(0) = |J, +J\rangle$ and make the small-angle approximation $J_z(t) = +JI$, we find

$$\xi_R^2(t) = 1 + [\xi_z^2(0) + 1]\sinh^2\Omega_N t, \quad (52)$$

$$\xi_{R,x}^2(t) = 1 + [\xi_v^2(0) + 1]\sinh^2\Omega_N t, \quad (53)$$

$$\xi_z^2(t) = \xi_z^2(0) + [1 + \xi_z^2(0)]\sinh^2\Omega_N t, \quad (54)$$

$$\xi_v^2(t) = \xi_v^2(0) + [1 + \xi_v^2(0)]\sinh^2\Omega_N t. \quad (55)$$

The same expressions are found for H_2 if we assume $\psi(0) = |J, -J\rangle$ and make the small-angle approximation $J_z(t) = -JI$. In these cases, for short times, no squeezing is transferred to the spins and the harmonic-oscillator squeezing degrades.

C. Numerical solution

Because of the limited validity of the small-angle approximation, we have integrated Schrödinger's equation for H_1 and H_2 for some special cases. We write the wave function for the combined harmonic-oscillator-spin ensemble as

$$\Psi_c(t) = \sum_{n,M} C_{n,M}(t)|n\rangle|M\rangle, \quad (56)$$

where $|n\rangle$ are the harmonic-oscillator eigenstates and we use the shorthand notation $|M\rangle = |J, M\rangle$ since J is a constant of the motion for H_1 and H_2 . From Schrödinger's equation, we find for H_1

$$dC_{n,M}/dx = i(n+1)^{1/2}[j(j+1) - M(M-1)]^{1/2}C_{n+1, M-1} + in^{1/2}[j(j+1) - M(M+1)]^{1/2}C_{n-1, M+1}, \quad (57)$$

where $x \equiv \Omega t$. We have integrated this equation and the corresponding one for H_2 using a fourth-order Runge-Kutta method [59]. For the initial wave function, we assume the atoms and harmonic oscillator are uncorrelated so that the wave function can be written as a direct product

$$\Psi_c(0) = \left[\sum_n c_n(0) |n\rangle \right] \psi(0), \quad (58)$$

where $c_n(0)$ are the initial harmonic-oscillator wavefunction coefficients [60] and we will assume $\psi(0) = |J, -J\rangle$ or $|J, +J\rangle$. Of course, we must truncate the basis of harmonic-oscillator states; an adequate number of states is determined by increasing the basis until the result remains unchanged.

For $J=1$, we also solved Schrödinger's equation for

H_1 and H_2 with a different numerical approach. For $J=1$, the Hamiltonians H_1 or H_2 can be written as blocks of 3×3 matrices on the diagonal and zeros elsewhere. Explicitly, H_1 only couples states where $n+M$ is a constant and H_2 only couples the states $|n-1\rangle|-1\rangle$, $|n\rangle|0\rangle$, and $|n+1\rangle|+1\rangle$. The 3×3 matrices corresponding to the Hamiltonian of the coupled states were diagonalized and the wave function for the combined harmonic-oscillator-spin ensemble written as a sum over the eigenstates. The time evolution of the wave function

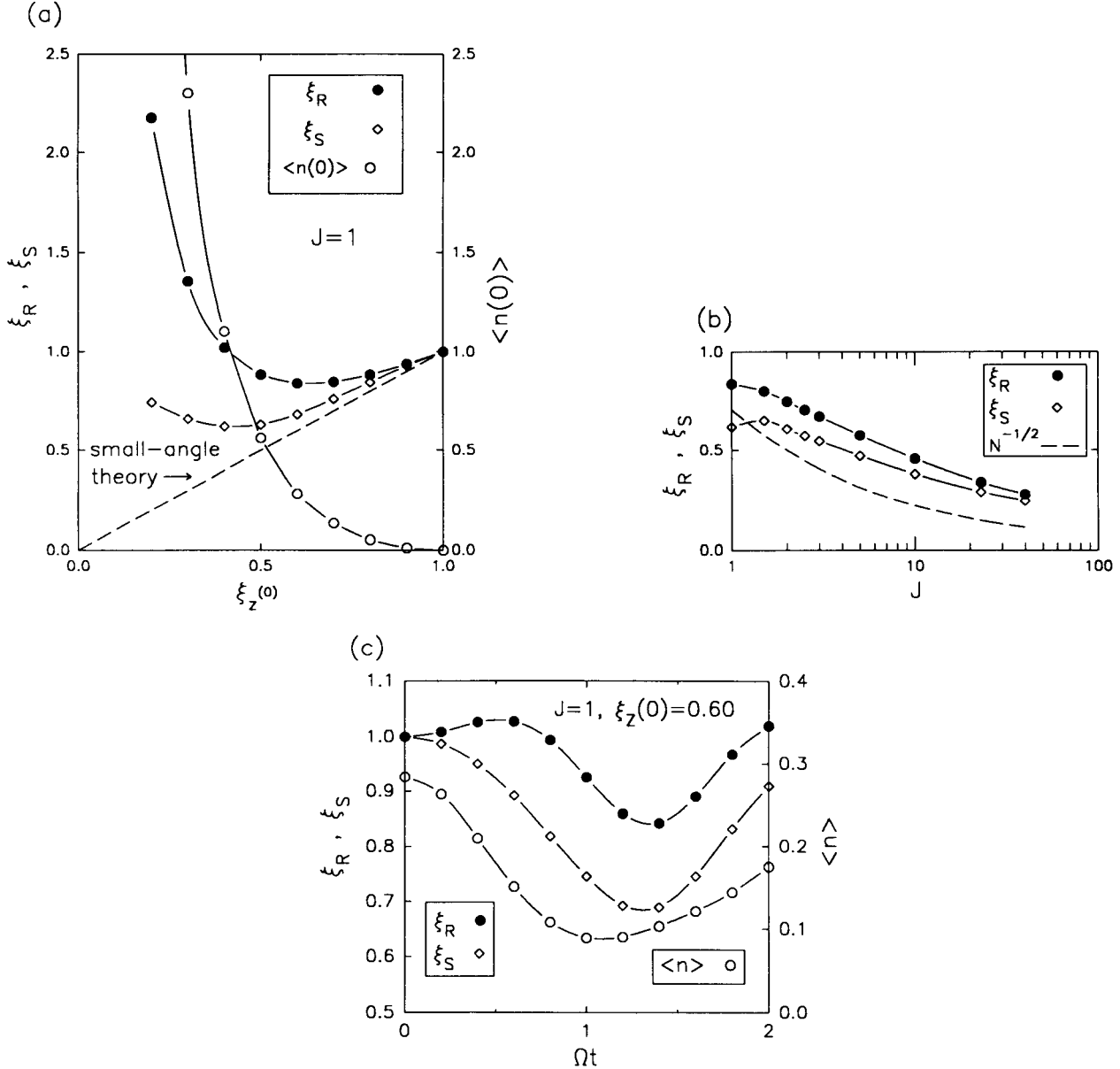


FIG. 6. Plots of ξ_R [Eq. (30)] and ξ_S [Eq. (40)] assuming the squeezed-spin states are prepared by coupling a single harmonic oscillator to the spins via the interaction H_1 [Eq. (43)]. We assume $\psi(0) = |J, -J\rangle$ and the harmonic oscillator to be initially prepared in the squeezed vacuum state where $\langle z(0) \rangle = \langle \dot{z}(0) \rangle = 0$ and $\xi_z(0) < 1$. In (a), $J=1$. We plot the values of the first minima of ξ_R and ξ_S as a function of time after H_1 is turned on [refer to (c)] vs the initial value of $\xi_z(0)$. We also plot the value of $\langle n(0) \rangle \equiv \langle a^\dagger a \rangle$ vs $\xi_z(0)$. In addition, we plot the prediction of the small-angle theory, $\xi_R = \xi_S = \xi_z(0)$, as a dashed line. As expected, the small-angle theory is valid only for very small values of $\xi_z(0)$ (or $\langle n \rangle$). In (b), we plot the first minimum values of ξ_R and ξ_S less than 1, after H_1 is turned on, vs J . For each point, $\xi_z(0)$ has been adjusted to give the smallest value of ξ_R and ξ_S . In (c), we plot ξ_R , ξ_S , and $\langle n \rangle$ as a function of time for $J=1$, and $\xi_z(0)=0.60$. At $\Omega t \approx 1.35$, ξ_R reaches its minimum value of ≈ 0.84 .

is then obtained from the time evolution of the eigenstates. With this method a larger number of harmonic-oscillator states could be included in the calculation. We obtained results that agreed with the numerical approach described above. This method can be generalized for $J > 1$ with the complication that $(2J + 1) \times (2J + 1)$ matrices would need to be diagonalized.

In Fig. 6, we plot ξ_R and ξ_S for H_1 assuming $\psi(0) = |J, -J\rangle$ and assuming the oscillator is initially in an amplitude-squeezed vacuum state where $\langle z(0) \rangle = \langle \dot{z}(0) \rangle = 0$ and $\xi_z(0) < 1$. This figure indicates the limited validity of the small-angle approximation, which is shown as a dashed line. We see that there are states for which $\xi_s < 1$ while $\xi_R > 1$. This emphasizes the need to define squeezing in the context of a particular problem. From Fig. 6(a), we also see that the minimum values of ξ_S and ξ_R are obtained for different initial values of $\xi_z(0)$. In Fig. 6(c) we plot the evolution of ξ_R , ξ_S , and $\langle n \rangle$ as functions of time for $J = 1$ and $\xi_z(0) = 0.60$. Initially, ξ_R becomes greater than 1 but eventually reaches a minimum value of 0.840 corresponding to that shown in Fig. 6(a).

In Fig. 7, we plot $\xi_{R,x}$ and ξ_S for H_2 assuming $\psi(0) = |J, -J\rangle$ and assuming the oscillator is initially in a coherent state where $\langle z(0) \rangle \neq 0$, $\langle \dot{z}(0) \rangle = 0$, and $\xi_z(0) = \xi_v(0) = 1$. Before using the resulting states in Ramsey spectroscopy, we want to first rotate $\langle J \rangle$ so that it points along the negative z axis and then rotate the state about the z axis by $\pi/2$ so that the squeezing in the x direction is transferred to the y direction ($\xi_{R,x} \rightarrow \xi_{R,y} \equiv \xi_R$). The harmonic oscillator, in combination with H_2 , drives the spin $\langle J \rangle$ to lie in the y - z plane. This is indicated in Fig. 7(c) where we plot, for $J = 1$, $\xi_{R,x}$, $\xi_{S,x}$, and $\langle n \rangle$ vs time and $\langle J(t) \rangle$ as viewed in the $-\hat{x}$ direction, assuming the value of $\langle n(0) \rangle$ which minimizes $\xi_{R,x}$. Spin squeezing along these lines may be of practical interest since we require the initial harmonic-oscillator state to be only a coherent state, not a squeezed state.

A squeezed state of the harmonic oscillator can be generated by parametric pumping of the oscillator at frequency $2\omega_z$. In the laboratory frame this pumping interaction can be represented by

$$H_p(\text{lab}) = -2\hbar\Omega_p(a + a^\dagger)^2 \sin 2\omega_z t \propto z^2 \sin 2\omega_z t.$$

If we add this interaction to H_1 , the total Hamiltonian in the interaction frame becomes

$$H_3 = -\hbar\Omega(aJ_+ + a^\dagger J_-) + i\hbar\Omega_p(a^2 - (a^\dagger)^2), \quad (59)$$

plus high-frequency terms which we neglect. In general, we could let Ω_p vary in time. The case considered in Fig. 6 is equivalent to having Ω_p nonzero and large for a very short time after $t = 0$ and then allowing the system to evolve under the influence of H_1 . In Fig. 8, we consider a special case where Ω_p and Ω are constant in time and applied together. We show a plot of ξ_R and ξ_S vs time for $J = 1$, $\psi(0) = |1, -1\rangle$, the harmonic oscillator initially in the vacuum state [$\langle z(0) \rangle = \langle \dot{z}(0) \rangle = 0$, and $\xi_z(0) = \xi_v(0) = 1$], and $\Omega_p/\Omega = 0.23$. This value of Ω_p/Ω yields a (local) minimum in ξ_R for these initial conditions.

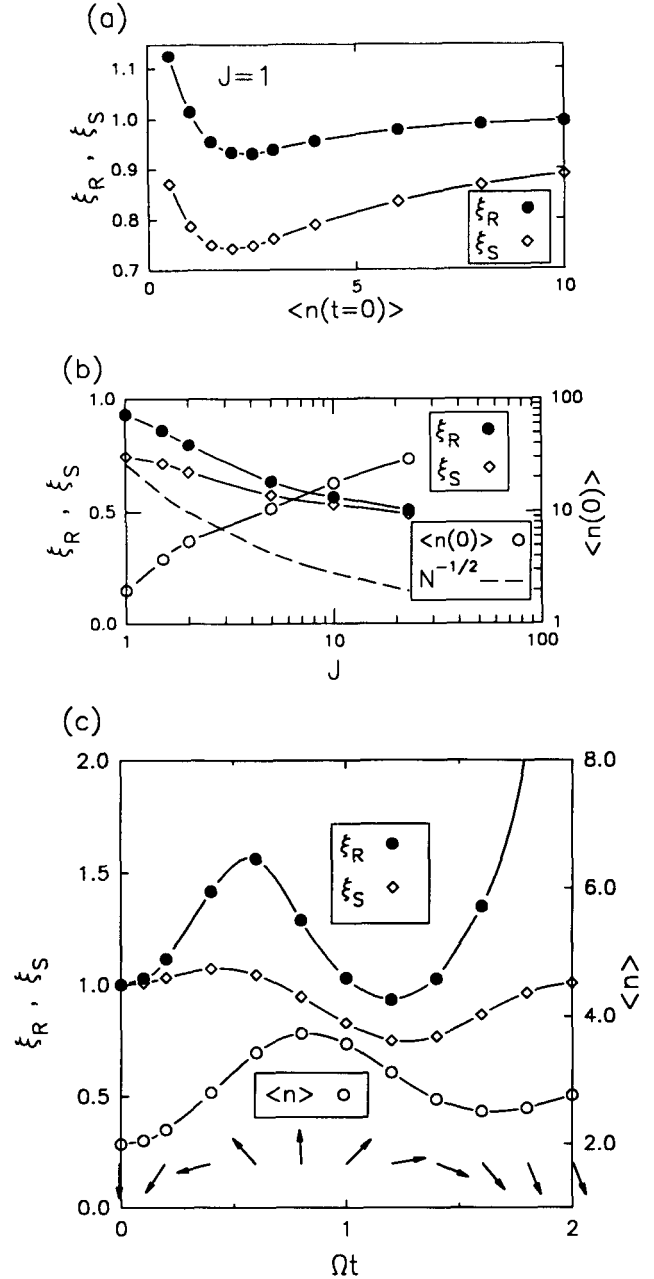


FIG. 7. Plots of $\xi_{R,x}$ [or ξ_R , Eq. (31)] and ξ_S [Eq. (40)] assuming the squeezed-spin states are prepared by coupling a harmonic oscillator to the spins via the interaction H_2 [Eq. (44)]. We assume $\psi(0) = |J, -J\rangle$ and the harmonic oscillator is initially prepared in a coherent state where $\langle z(0) \rangle \neq 0$, $\langle \dot{z}(0) \rangle = 0$, and $\xi_z(0) = \xi_v(0) = 1$. In (a), $J = 1$. We plot the values of the first minima of ξ_R and ξ_S , as a function of time after H_2 is turned on [refer to (c)] vs $\langle n(0) \rangle$. In (b), we plot the values of the first minima of ξ_R and ξ_S less than 1 after H_2 is turned on vs J . For each point, $\langle z(0) \rangle$ has been adjusted to give the smallest value of ξ_R and ξ_S . The harmonic oscillator, in combination with H_2 , drives the spin $\langle J \rangle$ to lie in the y - z plane. Before using the resulting states in Ramsey spectroscopy, we want to first rotate $\langle J \rangle$ so that it points along the negative z axis and then rotate the state about the z axis by $\pi/2$ so that the squeezing in the x direction is transferred to the y direction ($\xi_{R,x} \rightarrow \xi_{R,y} \equiv \xi_R$). In (c), we plot, for $J = 1$, $\xi_{R,x}$, $\xi_{S,x}$, and $\langle n \rangle$ vs time and $\langle J(t) \rangle$, shown as an arrow, as viewed in the $-\hat{x}$ direction, assuming the value of $\langle n(0) \rangle$ which minimizes $\xi_{R,x}$.

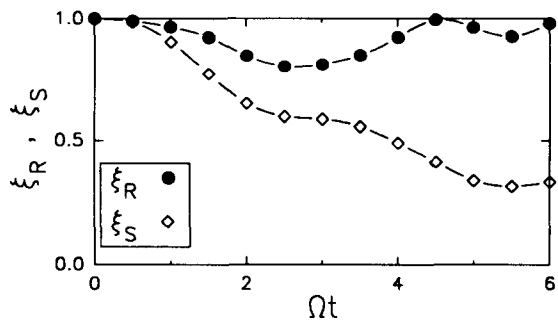


FIG. 8. For $J=1$, we plot ξ_R [Eq. (31)] and ξ_S [Eq. (40)] vs time assuming the squeezed-spin state is prepared by coupling a parametrically pumped harmonic oscillator to the spins via the interaction H_3 [Eq. (59)]. We assume $\psi(0)=|1, -1\rangle$ and the harmonic oscillator is initially prepared in the vacuum state. The curves use the value $\Omega_p/\Omega=0.23$ which minimizes (locally) the value of ξ_R at $\Omega t \approx 2.5$. At certain times, the values of both ξ_R and ξ_S are reduced below those found in Fig. 6(a).

The values of both ξ_R and ξ_S are less than in the case of Fig. 6(a).

VIII. POSSIBLE EXPERIMENTAL METHODS

As shown by Agarwal and Puri [33,34], a way to produce good squeezing is to couple the spins to a broadband squeezed vacuum. However, this may be difficult in practice, because all spatial modes of the field must be squeezed [61]. These modes are then properly phased only at a particular spatial location and the atoms must all be localized about this point to within a small fraction of a wavelength. For optical transitions with stored ions this is difficult because the Coulomb repulsion typically results in ion-ion separations of more than $1 \mu\text{m}$. Neutral atoms could be confined with spacings less than λ , but then the direct dipole-dipole coupling must be included. An alternative strategy might be to confine the atoms in a cavity that is driven by a squeezed vacuum field [61].

From the previous section, another way to produce spin squeezing is to first prepare a harmonic oscillator in a squeezed or coherent state and then couple the oscillator to the spins through a Jaynes-Cummings-type interaction [Eqs. (43) or (44)]. Using the extensive work on “cavity QED” as a guide, this could be accomplished by the interaction of an ensemble of atoms with a suitably prepared electromagnetic field of a single cavity mode [4–7, 62–64]. In these types of experiments, the presence of thermal noise and/or cavity and atomic relaxation would reduce the degree of spin squeezing that could be achieved. Although we can expect these problems to be overcome in the future, it may be useful to consider alternate systems. Our experiments have led us to consider coupling of the internal levels of atoms to a different harmonic oscillator—that associated with the oscillation of atoms in a trap. In this paper, we will concentrate on the use of trapped atomic ions, but many of the considerations apply to trapped neutral atoms as well.

A. Trapped-atomic-ion oscillator

The interest in a trapped-ion oscillator is due to its potential immunity from relaxation and thermal noise excitation. To a good approximation, a single ion confined in an ion trap [65,66] can be modeled as a charged harmonic oscillator. For an ensemble of ions localized near the center of the trap this model is also valid for the center-of-mass (c.m.) motion of the ensemble [66]. In what follows, we will assume all internal mode frequencies are shifted away from the c.m. frequency by the ions’ Coulomb interaction. The c.m. charged harmonic oscillator is subject to radiative decay and heating from the environment. It can be considered to be confined in a cavity formed by the trap electrodes. Typically, the wavelength of the harmonic-oscillator radiation (corresponding to oscillation frequencies of a few megahertz or less) is much larger than the dimensions of the trap electrodes. A useful representation of this situation is to model the c.m. motion of the harmonically bound ion (in one direction) as a series LC circuit which is shunted by the capacitance of the trap electrodes as shown in Fig. 9 [66]. The resistance r is due to losses in the electrodes and conductors which connect the electrodes. The equivalent inductance of the ions is given [66] by $l \approx md^2/N(Zq)^2$ where m is the ion mass, d the characteristic internal dimension of the ion-trap electrodes, N the ion number, Zq the charge of a single ion (q = charge of the proton), and we neglect geometrical factors on the order of 1. The resistance r both damps and imparts thermal energy to the ions with time constant l/r . To characterize the damping and thermal heating, we calculate the time t^* for heating the ion’s c.m. motion from the $n=0$ to the $n=1$ state,

$$t^* = l\hbar\omega_z / (rk_B T) \approx 2.9(\omega_z/2\pi)d^2 M(u) / (NrTZ^2), \quad (60)$$

where k_B is Boltzmann’s constant, T the temperature of

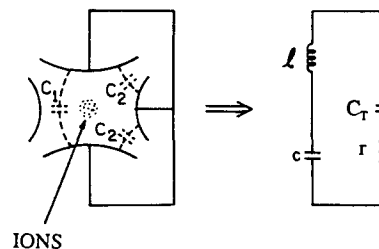


FIG. 9. Equivalent circuit representation of one component (z) of the trapped ions’ center-of-mass motion coupled to the surrounding trap electrodes (from Ref. [66]). We have $l \approx md^2/N(Zq)^2$ where m is the ion mass, d the characteristic internal dimension of the ion-trap electrodes, N the ion number, Zq the charge of a single ion (q = charge of proton), and we neglect geometrical factors on the order of unity. The resistance r is due to losses in the electrodes and conductors which connect the electrodes. The equivalent capacitance of the ion, $c = 1/\omega_z^2 l$, is typically much less than C_T which is usually on the order of a few picofarads. As discussed in the text, damping and thermal heating from r can be neglected in many cases.

resistor r , ω_z is the oscillation frequency, and the ion mass M is expressed in atomic mass units. For $\omega_z/2\pi=3$ MHz, $d=2$ mm, $M=100$ u, $N=2$, $r=0.1\Omega$, $T=300$ K, and $Z=1$, we obtain $t^*\simeq 58$ s. In this case, and in general when $\hbar\omega_z \ll k_B T$, the decay time from $n=1$ to $n=0$ is much longer. In the experiment reported in Ref. [13], ($\omega_z/2\pi\simeq 5$ MHz, $d\simeq 0.7$ mm, $M\simeq 200$ u, $N=1$, $T\simeq 300$ K, and $Z=1$), t^* was measured to be 0.17 s even though no care was taken to make r small or to reduce external sources of noise. If we can make Ω large enough ($\gg 1/t^*$), it should be possible to avoid the effects of damping and thermal heating on the ion harmonic oscillator.

Similarly, it should be possible to avoid radiative relaxation in the two-level system. This is particularly true if the levels are separated by rf or microwave frequencies where radiative decay rates can be extremely small [41]. Even at optical frequencies, many forbidden transitions have radiative decay times on the order of seconds or longer and may be viable as candidates for spin squeezing.

B. Squeezed or coherent states of ion motion

A single trapped ion can be laser cooled to its quantum ground state of motion [13]. It should also be possible to extend this technique to cool the c.m. motion of an ensemble of ions to the ground state. In analogy with methods used in quantum optics, a squeezed vacuum state of the c.m. mode (appropriate for Fig. 6) could be obtained from the ground state by suddenly changing the ion's well depth or parametrically modulating the well depth at $2\omega_z$ as indicated by the second term in Eq. (59) [17,18]. A coherent state of nonzero amplitude (appropriate for Fig. 7) could be obtained from the vacuum state by suddenly shifting the center position of the ions' well, or by driving the oscillator with a classical resonant excitation [17,18].

Cirac *et al.* [19] have shown that the ion could be laser cooled and squeezed at the same time by superimposing the nodes of two standing-wave laser beams at the mean position of the ions and tuning the laser frequencies to the first lower and upper sidebands of the two-level transition frequency, that is, to $\omega_0 - \omega_z$ and $\omega_0 + \omega_z$. Independently of the way the harmonic-oscillator state is produced, the phase of the oscillator and/or squeezing must be referenced to the phase of the clock radiation in a predictable and reproducible way.

C. Possible realizations of the Jaynes-Cummings-model coupling

After the harmonic-oscillator state is prepared, squeezing could be imparted to the spins (or two-level systems) by application of the Jaynes-Cummings interaction given by Eqs. (43) or (44). This form of coupling has already been realized to couple the spin and cyclotron motion of a single electron in the classic g -2 experiments of Dehmelt and his collaborators [67]. In Ref. [38], we considered one possible realization of the Jaynes-Cummings model for atoms. We considered N ions having an un-

paired outer electron which are trapped along the axis of a linear rf trap [68] where, here, we take the axis of the trap to be in the y direction. The ions are subjected to a homogeneous magnetic field which quantizes the spins according to Eq. (2). We then superimpose an inhomogeneous field gradient $B' = \partial B_x / \partial z$ whose value, averaged over the ions' orbits, is zero. However, as the ions oscillate, they experience a motional oscillating magnetic field which tends to flip the spin and reduce or increase the ions' c.m. harmonic oscillator as in Eq. (43) for H_1 [69]. The B' field could be generated by a current $I\hat{y}$ in two wires (which could double as trap electrodes) situated at the positions $z = \pm z_T$ relative to the ions. We find $\Omega/2\pi \simeq 2I_y z_T^{-2} (M\omega_z/2\pi)^{-1/2}$, where I_y , z_T , M , and $\omega_z/2\pi$ are expressed in ampères, centimeters, atomic mass units, and megahertz, respectively. For $I_y = 0.1$ A, $z_T = 0.01$ cm, $M = 24$ u ($^{24}\text{Mg}^+$), and $\omega_z/2\pi = 1$ MHz, we find $\Omega/2\pi \simeq 400$ Hz.

Blockley, Walls, and Risken [70] have shown that the Jaynes-Cummings model is realized for a harmonically bound atom or ion which interacts with a traveling-wave laser tuned near the transition frequency of the atom. They assume the atom is confined to the Lamb-Dicke limit and the resulting coupling strength is much smaller than the oscillator frequency [$\Omega \ll \omega_z$ in our Eq. (41)]. If the laser is tuned to the first upper or lower motional sideband of the atomic transition, and spontaneous emission from the excited state can be neglected, Rabi oscillations occur between ground and excited states accompanied by oscillations between adjacent harmonic-oscillator states. Cirac *et al.* [71] have shown that the Jaynes-Cummings model is realized for the harmonic motion of a two-level ion confined to the Lamb-Dicke limit whose mean position is located at the node of a standing-wave laser field tuned near the ion's transition frequency. In both cases, if a suitably narrow optical level (one with weak relaxation) can be used, one might hope to impart squeezing to optical levels. These schemes could, in principle, also be applied to transitions of much lower frequency (infrared or microwave frequencies). The coupling Ω would be reduced for the same value of ω_z (reduced Lamb-Dicke parameter) but the radiative decay could be expected to be considerably reduced.

References [72–74] and [18] have theoretically considered the use of stimulated Raman transitions to achieve laser cooling of trapped ions to the zero-point energy. (Stimulated Raman transitions have recently been used to cool free atoms to a kinetic energy less than that corresponding to the recoil of one photon [75].) The systems used to achieve this cooling can also be used to realize the Jaynes-Cummings model. Under certain conditions, stimulated Raman transitions produce a Rabi oscillation [18] which can be described by an effective Jaynes-Cummings interaction. For convenience, we use the notation of Ref. [18].

Reference [18] considered stimulated Raman laser cooling to proceed by repeated applications of a sequential, two-step process. Figure 10 illustrates the first step of this process, where we have restricted our attention to harmonic motion (of frequency ω_z) along one direction taken to be the \hat{z} direction. The eigenstates of the system

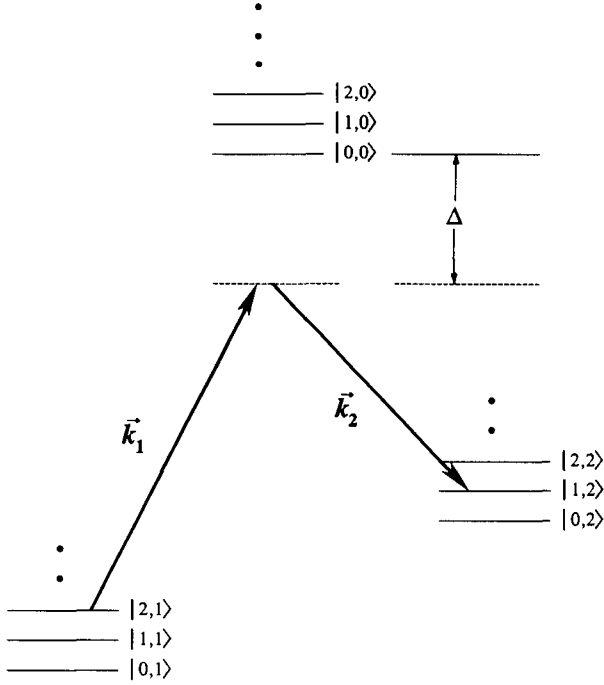


FIG. 10. Schematic representation of the energy levels for stimulated Raman transitions between internal (electronic) levels 1 and 2 of the trapped ion. The states are designated by the notation $|n, j\rangle$ where n denotes the ion harmonic-oscillator level and $j=0, 1, 2$ denotes the electronic state. \mathbf{k}_1 and \mathbf{k}_2 are the wave vectors for the traveling-wave fields which couple electronic level 0 to levels 1 and 2. We assume $\Delta \gg \omega_z$. In the figure, we schematically show the $|2, 1\rangle \leftrightarrow |1, 2\rangle$ stimulated Raman transition. Under the assumptions discussed in the text, the stimulated Raman transitions are equivalent to a Jaynes-Cummings-type coupling between electronic levels 1 and 2 and the harmonic (center-of-mass) motion of the ions.

are denoted by $|n, q\rangle = |n\rangle |q\rangle_e$ where n is the occupation number of the harmonic motion and $q=0, 1, 2$ denotes a particular electronic level. Decay from levels $|1\rangle_e$ and $|2\rangle_e$ is assumed to be negligible; level $|0\rangle_e$ decays at rate γ . The ions are irradiated by two laser beams with classical field amplitudes $\bar{E}_j = \text{Re}\{\mathbf{E}_{0j} \exp[i(\mathbf{k}_j \cdot \mathbf{r} - \omega_j t)]\}$ ($j=1, 2$) which couple level $|0\rangle_e$ to levels $|1\rangle_e$ and $|2\rangle_e$ with Rabi frequencies $g_{j0} \equiv |\boldsymbol{\mu}_{j0} \cdot \mathbf{E}_{0j}|/2\hbar$ where $\boldsymbol{\mu}_{0j}$ is the dipole matrix element between states $|0\rangle_e$ and $|j\rangle_e$. The frequencies of the beams are assumed to be equal to $\omega_1 = \omega_{01} - \Delta - \omega_z + \delta$ and $\omega_2 = \omega_{02} - \Delta$ where ω_{0j} is the transition frequency between states $|n, 0\rangle$ and $|n, j\rangle$. We assume $\omega_{01}, \omega_{02} \gg \Delta \gg \omega_z \gg \delta$. The ions are initially prepared in the electronic state $|1\rangle_e$. When the ions are confined to the Lamb-Dicke limit (amplitude of motion $\ll 1/k_{jz}$ where $k_{jz} \equiv \mathbf{k}_j \cdot \hat{\mathbf{z}}$), a reduction in the harmonic-oscillator energy by $\hbar\omega_z$ occurs by stimulated Raman transitions $|n, 1\rangle \rightarrow |n, 0\rangle \rightarrow |n-1, 2\rangle$ and $|n, 1\rangle \rightarrow |n-1, 0\rangle \rightarrow |n-1, 2\rangle$ which reduce n by 1. In the second step of the cooling process, a laser tuned near ω_{02} causes spontaneous Raman transitions from level $|2\rangle_e$ back to $|1\rangle_e$. In the Lamb-Dicke limit, transitions of the form $|n-1, 2\rangle \rightarrow |n-1, 0\rangle \rightarrow |n-1, 1\rangle$ are dominant in this second step. Therefore, after the two steps

of the cooling process, $\langle n \rangle$ is reduced by 1. After repeated applications of this two-step process, the ions are eventually cooled until $\langle n \rangle \ll 1$ [18].

The first step of the cooling process realizes a Jaynes-Cummings coupling between the ions' harmonic oscillator and the internal levels $|1\rangle_e$ and $|2\rangle_e$. If we ensure the condition $\Delta \gg \pi\gamma/(2|\delta k_z|z_0 n^{1/2})$, where $\delta k_z \equiv k_{2z} - k_{1z}$, then the ions undergo stimulated Raman transitions with negligible probability of spontaneous decay from level $|0\rangle_e$ [18]. Under these conditions, the first step of the cooling process is adequately described by amplitude equations derived from Schrödinger equation. If we write the wave function for the system as

$$\Psi(t) = \sum_n \sum_{q=0}^2 a_{n,q} e^{-i\omega_{n,q} t} |n, q\rangle, \quad (61)$$

then Schrödinger's equation leads to the amplitude equations [18]

$$da_{n,q}/dt = -\frac{i}{\hbar} \sum_{n'} \sum_{q'=0}^2 a_{n',q'} e^{i\omega_{n',q'} t} V_{n,q,n',q'}, \quad (62)$$

where $\hbar\omega_{n,q,n',q'}$ is the energy of state $|n, q\rangle$ minus the energy of state $|n', q'\rangle$ and $V_{n,q,n',q'}$ is the matrix element of the perturbation $-\boldsymbol{\mu} \cdot (\mathbf{E}_1 + \mathbf{E}_2)$ between states $|n, q\rangle$ and $|n', q'\rangle$. If

$$|\omega_{10} - \omega_{20}| \gg \Delta \gg \gamma, g_{10}, g_{20}, \omega_z,$$

we can adiabatically eliminate the excited states from the equations. With the additional assumption that $\omega_z \gg g_j^2/\Delta$, and neglecting terms in the equations of motion that vary with frequency ω_z or higher, we arrive at the amplitude equations

$$da_{n,1}/dt = i\Delta_{S1} a_{n,1} - \Omega^* n^{1/2} e^{i\delta t} a_{n-1,2} \quad (63)$$

and

$$da_{n-1,2}/dt = i\Delta_{S2} a_{n-1,2} + \Omega^* n^{1/2} e^{-i\delta t} a_{n,1}, \quad (64)$$

where $\Omega^* \equiv g_{10} g_{20} \delta k_z z_0 / \Delta$, $\Delta_{S1} = g_{10}^2 / \Delta$, and $\Delta_{S2} = g_{20}^2 / \Delta$. The first terms in these equations are due to the ac Stark shifts of levels $|1\rangle_e$ and $|2\rangle_e$ by lasers 1 and 2, respectively. If $\Delta \gg |\omega_{10} - \omega_{20}|$, we have $\Delta_{S1} = (g_{10}^2 + g_{12}^2) / \Delta$, and $\Delta_{S2} = (g_{20}^2 + g_{21}^2) / \Delta$, where $g_{12} \equiv |\boldsymbol{\mu}_{10} \cdot \mathbf{E}_{02}|/2\hbar$ and $g_{21} \equiv |\boldsymbol{\mu}_{20} \cdot \mathbf{E}_{01}|/2\hbar$. We can now make the transformations $a_{n,1} = iA_{n,1} \exp(i\Delta_{S1} t)$ and $a_{n,2} = A_{n,2} \exp(i\Delta_{S2} t)$. If we let $\delta = \Delta_{S1} - \Delta_{S2}$, the equations of motion become

$$dA_{n,1}/dt = i\Omega^* n^{1/2} A_{n-1,2} \quad (65)$$

and

$$dA_{n-1,2}/dt = i\Omega^* n^{1/2} A_{n,1}. \quad (66)$$

The choice of δ is that which compensates for the differential ac Stark shifts in levels $|1\rangle_e$ and $|2\rangle_e$ and makes $\omega_1 - \omega_2$ resonant with the first lower motional sideband of the stimulated Raman transition. These equations are identical to Eqs. (57) (for $J = \frac{1}{2}$) if we make the identification $A_{n,1} \leftrightarrow C_{n-1/2}$ and $A_{n,2} \leftrightarrow C_{n+1/2}$; that is, if we identify the $|1\rangle_e$ and $|2\rangle_e$ states of Fig. 10 with the

$|-\rangle$ and $|+\rangle$ states of the spin- $\frac{1}{2}$ model. Hence, when spontaneous Raman transitions can be neglected, the system of Fig. 10 gives rise to the Jaynes-Cummings model coupling between the two-level system consisting of states $|1\rangle_e$ and $|2\rangle_e$, and the z c.m. harmonic motion of the ions. This causes Rabi oscillations between states $|n, 1\rangle$ and $|n-1, 2\rangle$ at frequency $\Omega^* n^{1/2}$.

To indicate possible experimental parameters, we consider the ${}^2S_{1/2}(F=1) \rightarrow {}^2P_{1/2} \rightarrow {}^2S_{1/2}(F=2)$ stimulated Raman transition in ${}^9\text{Be}^+$ ($\lambda=313$ nm, $\omega_{20}-\omega_{10}=1.25$ GHz). If we assume $|\delta k_z|=|k_z|$, $\omega_z/2\pi=5$ MHz, $g_{10}=g_{20}=750$ MHz, $\Delta/2\pi=20$ GHz, we find $|\delta k_{z,z_0}| \simeq 0.21$, $\Omega^*/2\pi \simeq 150$ kHz, and the probability of spontaneous emission from the excited state during the time for complete transfer from the $F=1$ to $F=2$ ground state [18] to be approximately 0.01. If we assume that $\mu_{10}=\mu_{20}=q(0.5 \times 10^{-8}$ cm) where q is the electron charge and that the ions are at the center of Gaussian laser beams with waist $w_0=20$ μm , then we require approximately 325 μW in each beam.

Realizations of the Jaynes-Cummings model using optical transitions are potentially interesting because the coupling frequencies Ω may be much higher than that provided by inhomogeneous magnetic fields acting on electron spins. In addition, lasers may allow spin squeezing to be applied to atomic levels which are of more interest for atomic clocks, such as hyperfine and optical transitions.

IX. SUMMARY AND DISCUSSION

In this paper, we have discussed the application of correlated particle states, or squeezed-spin states, to spectroscopy. Spin squeezing in other contexts has been discussed elsewhere [25–37]. This work extends that of a previous paper which introduced some of the ideas [38]. Transitions are assumed to be excited by classical radiation and detected by observing changes in the state populations of the particles (population spectroscopy). In this case, the fundamental limiting noise is projection noise [40], the noise associated with the quantum fluctuations in the measurement of populations. We find that the signal-to-noise ratio can be improved over the case of initially uncorrelated particles if the particles are first prepared in particular quantum-mechanically correlated or squeezed-spin states. We have considered a particular case of Ramsey's separated-oscillatory-field method of spectroscopy [41] since it gives the narrowest linewidth for a given interaction time. We introduce a squeezing parameter ξ_R which is the ratio of the uncertainty in the determination of the resonance frequency when using correlated states vs that when using uncorrelated states. This squeezing parameter has more general applicability, in that it gives a measure of the sensitivity of angular-momentum states to rotation. Since one description of interferometers is formally equivalent to Ramsey spectroscopy, the squeezing parameter might also be used in that context. Other squeezing parameters which are relevant in other contexts can be defined. We discussed certain states which exhibit a squeezing $\xi_R \simeq N^{-1/2}$. Because of our experimental background in the spectroscopy

of stored atomic ions, we have investigated possible experimental schemes which might yield $\xi_R < 1$ in this system.

The investigation and demonstration of squeezed-spin states is interesting for various reasons. These studies extend the realm of squeezing beyond the electromagnetic field. The ideas apply, in principle, to particle interferometry [29–31, 35, 36] and spectroscopy. From the practical side, since some trapped-ion spectroscopy experiments are currently limited by projection noise [40], the use of squeezed-spin states would yield more precise measurements. As a byproduct of these investigations we have discussed some schemes where it might be possible to realize the Jaynes-Cummings model [58] by coupling atomic internal levels to harmonic particle motion. In practice, this might allow the study of this fundamental quantum system and related cavity-QED experiments in the regime of weak relaxation and high detection efficiency. Also, it may be possible to generate correlated states which would be useful in multiparticle EPR experiments [2, 38].

In spectroscopy, if we assume that the state preparation and detection time are small compared to the Ramsey interrogation time T , and if the measurement noise is limited by projection noise, the measurement uncertainty of the particle's transition frequency ω_0 , expressed fractionally, is [76]

$$\frac{\Delta\omega}{\omega_0} = \frac{\xi_R}{\omega_0(\tau NT)^{1/2}}, \quad (67)$$

where $\tau \gg T$ is the total measurement time and ξ_R accounts for the use of correlated states. In a particular application, if we require a certain fractional frequency-measurement precision and if N and T are fixed, then the time τ required to reach this measurement precision is proportional to ξ_R^2 . The reduction in measurement time due to $\xi_R < 1$ would be particularly important in many applications using atomic clocks, where, to reach the highest measurement precision, the frequency is averaged over very long times, perhaps years. For states with $\xi_R = N^{-1/2}$, the required measurement time would be reduced by N .

We emphasize the importance of setting and maintaining the phase relationship between the fields which prepare the squeezed-spin states and the Ramsey fields. In the case where the squeezed-spin state is prepared by coupling to a harmonic oscillator, we must maintain the correct phase relationship between the oscillation of the harmonic oscillator, the coupling Ω at frequency ω_m , and the Ramsey fields. When we start from a squeezed-vacuum state of the harmonic oscillator, slight phase errors will increase the value of ξ_R that is obtained, but should not affect the accuracy of the measurement since the correlated state that is created should have $\langle J_y(0) \rangle = 0$ [see Eq. (18)]. However, in the case where the squeezed-spin state is created from a coherent harmonic oscillator, it may be difficult to ensure that $\langle J_y(0) \rangle = 0$. The resulting offset in the Ramsey curve would affect the accuracy (that is, it would give a systematic offset in our determination of ω_0), but if the offset

can be maintained constant it will not affect the relative measurement precision attained.

After the particles are put in squeezed-spin states, the correlations exist even though the particles do not interact. During the application of the squeezing Hamiltonian, the particles interact through their mutual coupling to the quantized harmonic oscillator(s). After this preparation stage, the particles do not interact even though the correlations remain. When the final particle states are measured, these correlations between particles are manifested even though, as in the classic EPR experiment, the particles have no way of “communicating” between one another.

In Sec. V C, we noted that it may be necessary to work with states that are not maximally squeezed since, when ξ_R reaches its minimum value, the signal also approaches 0 [for example, $\theta \rightarrow 0$ in Eq. (34)]. However, we can recover the advantages of squeezing without losing the signal by using a different measurement strategy. We can accomplish this by measuring higher moments of J_z . As an example, we consider measuring J_z^2 rather than J_z (or N_+) [38,77]. We illustrate the idea for $N=2$ ($J=1$). Let $\psi(0)=|1,0\rangle$. Using Eq. (24) we obtain

$$\langle J_z^2(t_f) \rangle = \sin^2 \omega_r T \quad (68)$$

and

$$\Delta(J_z^2(t_f)) = \frac{1}{2} \sin 2\omega_r T. \quad (69)$$

As a function of ω (or ω_r), $\langle J_z^2(t_f) \rangle$ oscillates twice as fast as $\langle J_z(t_f) \rangle$ [in Eq. (14)]. In analogy with Eq. (13), the frequency imprecision for a single measurement is given by

$$|\Delta\omega| = \Delta(J_z^2(t_f)) / |\partial \langle J_z^2(t_f) \rangle / \partial \omega| = 1/2T, \quad (70)$$

which is independent of ω . Therefore, effectively, $\xi_R = 1/\sqrt{2}$ ($=1/\sqrt{N}$) is obtained. For states of higher J , the maximum sensitivity may be given by measuring higher moments or combinations of higher moments.

Although we are most interested in states which exhibit quantum correlations between different particles, some of the interesting features and spectroscopic advantages of squeezed states can be studied in a different model system. In particular, consider an individual atom with $J > \frac{1}{2}$. As a concrete example assume $J=1$, as in the $^2S_{1/2}$ ($F=1$) ground hyperfine state of $^{199}\text{Hg}^+$. Suppose we are interested in measuring the Zeeman transition frequency for $\Delta M_F = \pm 1$ transitions when the ion is placed in a weak magnetic field. By weak, we mean a field where the Zeeman energy is much smaller than the ground-state hyperfine frequency, so the Zeeman sublevels are split equally. Suppose the ion is prepared in the $|F=1, M=0\rangle$ state. This state is equivalent to the squeezed

state of Eq. (34) for $\theta \rightarrow 0$. We then apply radiation which drives the ion from the $|1,0\rangle$ state to the $|1,1\rangle$ and $|1,-1\rangle$ states. We can measure J_z^2 , after application of the Zeeman radiation, by measuring the probability that the ion is detected to be in the $|1,0\rangle$ state by methods similar to those of Refs. [40] and [68]. As outlined in the last paragraph, this effectively gives $\xi_R = 2^{-1/2}$. One possible application of spin squeezing within a Zeeman level is for improved signal-to-noise ratio in electric-dipole-moment (EDM) experiments [77].

Several issues need further investigation. For example, we have not proved that, for a given measurement time T , the minimum value of $\Delta\omega$ is obtained for the particular method of spectroscopy we have assumed. Even for this method, other states may more closely approach the lower limit of $\xi_R = N^{-1/2}$ than the particular Rashid states investigated by Agarwal and Puri [34]. In considering the parametrically pumped oscillator [Eq. (59)], we have not optimized the squeezing for initial conditions or form of $\Omega_p(t)$. In considering the application of H_1 (or H_2), we have not considered all possible initial conditions, interaction times, or forms of $\Omega(t)$.

In all that we have discussed, we have assumed wave functions constructed with $|J, M\rangle$ basis states where $J=N/2$. This is because, prior to preparation of the spin-squeezed states, we assume initial states of the form $|J=N/2, M\rangle$, and the generators for the squeezed states preserve J . For completeness, we should consider similar basis states with $J < N/2$. Since, in general, ξ_R is larger for smaller values of J , we suspect that the smallest values of ξ_R are obtained for states with $J=N/2$.

In the spectroscopy we have described, we have assumed that, once the initial states are prepared, transitions are driven by classical fields. It will be interesting to investigate the signal-to-noise ratio when the spectroscopy is performed with quantized fields. In this case, we could consider both the case where transitions are detected by observing changes in state population and when they are detected by looking at changes in the transmitted or scattered radiation.

From the experimental side, we are hopeful that simpler practical ways can be found to generate spin squeezing than the schemes we have discussed. Nevertheless, even if states with only modest squeezing could be produced they would be very important in spectroscopy and perhaps other applications.

ACKNOWLEDGMENTS

We gratefully acknowledge the support of ONR. We thank G. S. Agarwal for sending a prepublication copy of Ref. [34]. We thank C. Monroe, J. Tan, M. Young, and P. Zoller for critical comments on the manuscript.

[1] A. Einstein, B. Podolsky, and N. Rosen, Phys. Rev. **47**, 777 (1935).

[2] For a recent review, see D. M. Greenberger, M. A. Horne, and A. Zeilinger, Phys. Today **46** (8), 22 (1993), and references therein.

[3] We note the EPR experiment using protons reported by M. Lamehi-Rachti and W. Mittig, Phys. Rev. D **14**, 2543 (1976), and the recently proposed experiment using correlated Hg atoms: E. Fry, in *Lasers '92*, Proceedings of the International Conference, Houston, TX, edited by C. P.

- Wang (STS, McLean, VA, 1993), p. 621. See also the earlier review by J. F. Clauser and A. Shimony, *Rep. Prog. Phys.* **41**, 1881 (1978).
- [4] *J. Opt. Soc. Am. B* **4**, 1450–1741 (1987), special issue on squeezed states of the electromagnetic field, edited by H. J. Kimble and D. F. Walls.
- [5] *J. Mod. Opt.* **34**, 709–1020 (1987), special issue on squeezed light, edited by R. Loudon and P. L. Knight.
- [6] H. J. Kimble, in *Fundamental Systems in Quantum Optics*, Proceedings of the Les Houches Summer School of Theoretical Physics, Session LIII, Les Houches, France, 1990, edited by J. Dalibard, J. M. Raimond, and J. Zinn-Justin (Elsevier, Amsterdam, 1992), p. 545.
- [7] S. Reynaud, A. Heidmann, E. Giacobino, and C. Fabre, in *Progress in Optics*, edited by E. Wolf (North-Holland, Amsterdam, 1992), Vol. 30, pp. 3–85.
- [8] M. Xiao, L. A. Wu, and H. J. Kimble, *Phys. Rev. Lett.* **59**, 278 (1987).
- [9] P. Grangier, R. E. Slusher, B. Yurke, and A. LaPorta, *Phys. Rev. Lett.* **59**, 2153 (1987).
- [10] E. S. Polzik, J. Carri, and H. J. Kimble, *Phys. Rev. Lett.* **68**, 3020 (1992).
- [11] C. M. Caves, K. S. Thorne, R. W. P. Drever, V. D. Sandberg, and M. Zimmermann, *Rev. Mod. Phys.* **52**, 341 (1980).
- [12] V. B. Braginsky, Y. I. Vorontsov, and K. S. Thorne, *Science* **209**, 547 (1980).
- [13] F. Diedrich, J. C. Bergquist, W. M. Itano, and D. J. Wineland, *Phys. Rev. Lett.* **62**, 403 (1989).
- [14] P. Verkerk, B. Lounis, C. Salomon, C. Cohen-Tannoudji, J.-Y. Courtois, and G. Grynberg, *Phys. Rev. Lett.* **68**, 3861 (1992).
- [15] P. S. Jessen, C. Gerz, P. D. Lett, W. D. Phillips, S. L. Rolston, R. J. C. Spreeuw, and C. I. Westbrook, *Phys. Rev. Lett.* **69**, 49 (1992).
- [16] A. Hemmerich and T. W. Hänsch, *Phys. Rev. Lett.* **70**, 410 (1993).
- [17] J. C. Bergquist, F. Diedrich, W. M. Itano, and D. J. Wineland, in *Laser Spectroscopy IX*, edited by M. S. Feld, J. E. Thomas, and A. Mooradian (Academic, San Diego, 1989), p. 274.
- [18] D. J. Heinzen and D. J. Wineland, *Phys. Rev. A* **42**, 2977 (1990).
- [19] J. I. Cirac, A. S. Parkins, R. Blatt, and P. Zoller, *Phys. Rev. Lett.* **70**, 556 (1993).
- [20] B. Baseia, R. Vyas, and V. S. Bagnato, *Quantum Opt.* **5**, 155 (1993).
- [21] H. Zeng and F. Lin, *Phys. Rev. A* **48**, 2393 (1993).
- [22] S. E. Harris, *Phys. Rev. Lett.* **62**, 1033 (1989); E. S. Fry, X. Li, D. Nikonov, G. G. Padmabandu, M. O. Scully, A. V. Smith, F. K. Tittel, C. Wang, S. R. Wilkinson, and S.-Y. Zhu, *ibid.* **70**, 3253 (1993); W. E. van der Veer, R. J. J. van Diest, A. Dönszelmann, and H. B. van Linden van den Heuvell, *ibid.* **70**, 3243 (1993), and references therein.
- [23] D. Bohm, *Quantum Theory* (Prentice-Hall, Englewood Cliffs, NJ, 1951), p. 611.
- [24] R. P. Feynman, F. L. Vernon, Jr., and R. W. Hellwarth, *J. Appl. Phys.* **28**, 49 (1957).
- [25] M. A. Rashid, *J. Math. Phys.* **19**, 1391 (1978); **19**, 1397 (1978).
- [26] D. F. Walls and P. Zoller, *Phys. Rev. Lett.* **47**, 709 (1981).
- [27] K. Wodkiewicz and J. Eberly, *J. Opt. Soc. Am. B* **2**, 458 (1985); P. K. Aravind, *ibid.* **5**, 1545 (1988).
- [28] J. D. Macomber and R. Lynch, *J. Chem. Phys.* **83**, 6514 (1985).
- [29] B. Yurke, S. L. McCall, and J. R. Klauder, *Phys. Rev. A* **33**, 4033 (1986).
- [30] B. Yurke, *Phys. Rev. Lett.* **56**, 1515 (1986).
- [31] B. Yurke and E. A. Whittaker, *Opt. Lett.* **12**, 236 (1987).
- [32] S. M. Barnett and M.-A. Dupertuis, *J. Opt. Soc. Am. B* **4**, 505 (1987).
- [33] G. S. Agarwal and R. R. Puri, *Phys. Rev. A* **41**, 3782 (1990).
- [34] G. S. Agarwal and R. R. Puri, *Phys. Rev. A* (to be published).
- [35] M. Kitagawa and M. Ueda, *Phys. Rev. Lett.* **67**, 1852 (1991); in *Noise in Physical Systems and 1/f Fluctuations*, edited by T. Musha, S. Sato, and M. Yamamoto (Ohmsha, Tokyo, 1991), p. 355.
- [36] M. Kitagawa and M. Ueda, *Phys. Rev. A* **47**, 5138 (1993).
- [37] G. S. Agarwal, J. P. Dowling, and W. P. Schleich, in *Proceedings of the Second Workshop on Squeezed States and Uncertainty Relations, Moscow, 1992*, edited by Y. S. Kim and V. I. Man'ko (NASA, Goddard Spaceflight Center, in press).
- [38] D. J. Wineland, J. J. Bollinger, W. M. Itano, F. L. Moore, and D. J. Heinzen, *Phys. Rev. A* **46**, R6797 (1992).
- [39] *Trapped Ions and Laser Cooling III*, edited by J. C. Bergquist, J. J. Bollinger, W. M. Itano, and D. J. Wineland, Natl. Inst. Stand. Technol. (U.S.) Tech. Note No. 1353 (U.S. GPO, Washington, DC, 1992).
- [40] W. M. Itano, J. C. Bergquist, J. J. Bollinger, J. M. Gilligan, D. J. Heinzen, F. L. Moore, M. G. Raizen, and D. J. Wineland, *Phys. Rev. A* **47**, 3554 (1993).
- [41] N. F. Ramsey, *Molecular Beams* (Oxford University, London, 1963).
- [42] C. K. Hong, S. R. Friberg, and L. Mandel, *Appl. Opt.* **24**, 3877 (1985).
- [43] A. Heidmann, R. J. Horowicz, S. Reynaud, E. Giacobino, C. Fabre, and G. Camy, *Phys. Rev. Lett.* **59**, 2555 (1987).
- [44] M. Xiao, L.-A. Wu, and H. J. Kimble, *Opt. Lett.* **13**, 476 (1988).
- [45] C. D. Nabors and R. M. Shelby, *Phys. Rev. A* **42**, 556 (1990).
- [46] P. R. Tapster, S. F. Seward, and J. G. Rarity, *Phys. Rev. A* **44**, 3266 (1991).
- [47] R. H. Dicke, *Phys. Rev.* **93**, 99 (1954).
- [48] F. T. Arecchi, E. Courtens, R. Gilmore, and H. Thomas, *Phys. Rev. A* **6**, 2211 (1972).
- [49] In Ref. [38], we transformed to a frame rotating at ω_0 .
- [50] J. J. Bollinger, J. D. Prestage, W. M. Itano, and D. J. Wineland, *Phys. Rev. Lett.* **54**, 1000 (1985); J. J. Bollinger, D. J. Heinzen, W. M. Itano, S. L. Gilbert, and D. J. Wineland, *ibid.* **63**, 1031 (1989).
- [51] From the form of Eq. (14), it is only possible to determine ω_0 modulo $2\pi/(lT)$ where l is an integer. Experimentally, the “central lobe” of the Ramsey pattern is identified by varying T and observing which lobe is stationary, or using the Rabi resonance method (B_1 constant from $t=0$ to t_f) which gives a (lower-resolution) resonance curve peaked at ω_0 .
- [52] A choice of $n > 0$ can be experimentally useful to test for any systematic effects associated with the power of the clock radiation.
- [53] For a choice of $n > 0$, it is possible to investigate experimentally a class of systematic effects, such as the presence of a systematic term of the form $K_s(\omega - \omega_0)$ (K_s a constant) which adds to the signal $\langle N_+(t_f) \rangle$ given in Eq. (14).

- This "background slope" effect can be accounted for by determining ω_0 for various values of n , which effectively measures K_+ .
- [54] A. Messiah, *Quantum Mechanics* (Wiley, New York, 1961).
- [55] R. A. Campos, B. E. A. Saleh, and M. C. Teich, *Phys. Rev. A* **40**, 1371 (1989).
- [56] These operators have also been considered earlier by J. Schwinger in a reformulated theory of angular momentum. See J. Schwinger, in *Quantum Theory of Angular Momentum*, edited by L. C. Biedenharn and H. van Dam (Academic, New York, 1965).
- [57] A. Heidmann, J. M. Raimond, and S. Reynaud, *Phys. Rev. Lett.* **54**, 326 (1985).
- [58] E. T. Jaynes and F. W. Cummings, *Proc. IEEE* **51**, 89 (1963).
- [59] W. H. Press, B. P. Flannery, S. A. Teukolsky, and W. T. Vetterling, *Numerical Recipes* (Cambridge University, New York, 1986), p. 547.
- [60] See, for example, R. W. Henry and S. C. Glotzer, *Am. J. Phys.* **56**, 318 (1988).
- [61] C. W. Gardiner, *Phys. Rev. Lett.* **56**, 1917 (1986); A. S. Parkins and C. W. Gardiner, *Phys. Rev. A* **40**, 3796 (1989).
- [62] S. Haroche and J. M. Raimond, *Adv. At. Mol. Phys.* **20**, 347 (1985).
- [63] S. Haroche, M. Brune, and J. M. Raimond, in *Atomic Physics 12*, edited by J. C. Zorn and R. R. Lewis (AIP, New York, 1991), p. 204; S. Haroche, in *Fundamental Systems in Quantum Optics* (Ref. [6]), p. 767.
- [64] G. Rempe, M. O. Scully, and H. Walther, in *Atomic Physics 12* (Ref. [63]), p. 219.
- [65] H. G. Dehmelt, *Adv. At. Mol. Phys.* **3**, 53 (1967); **5**, 109 (1969).
- [66] D. J. Wineland and H. G. Dehmelt, *J. Appl. Phys.* **46**, 919 (1975).
- [67] H. Dehmelt, *Science* **247**, 539 (1990).
- [68] M. G. Raizen, J. M. Gilligan, J. C. Bergquist, W. M. Itano, and D. J. Wineland, *Phys. Rev. A* **45**, 6493 (1992).
- [69] This coupling was previously considered in a cooling scheme discussed by H. Harde, in *International Conference on Quantum Electronics Technical Digest Series 1990* (Optical Society of America, Washington, DC, 1990), Vol. 8, p. 278.
- [70] C. A. Blockley, D. F. Walls, and H. Risken, *Europhys. Lett.* **17**, 509 (1992).
- [71] J. I. Cirac, R. Blatt, A. S. Parkins, and P. Zoller, *Phys. Rev. Lett.* **70**, 762 (1993).
- [72] H. Dehmelt, G. Janik, and W. Nagourney, *Bull. Am. Phys. Soc.* **30**, 111 (1985).
- [73] M. Lindberg and J. Javanainen, *J. Opt. Soc. Am. B* **3**, 1008 (1986).
- [74] P. E. Toschek and W. Neuhauser, *J. Opt. Soc. Am. B* **6**, 2220 (1989).
- [75] M. Kasevich and S. Chu, *Phys. Rev. Lett.* **69**, 1741 (1992).
- [76] D. J. Wineland, W. M. Itano, J. C. Bergquist, J. J. Bollinger, S. L. Gilbert, and F. Diedrich, in *Frequency Standards and Metrology*, Proceedings of the Fourth Symposium on Frequency Standards and Metrology, Ancona, Italy, 1988, edited by A. De Marchi (Springer-Verlag, Berlin, Heidelberg, 1989), p. 71.
- [77] This measurement scheme has been used in other experiments. See, for example, K. Abdullah, C. Carlberg, E. D. Commins, H. Gould, and S. B. Ross, *Phys. Rev. Lett.* **65**, 2347 (1990). The noise in that experiment, however, was not dominated by projection noise.

SPIN SQUEEZING APPLIED TO FREQUENCY STANDARDS*

J.J. Bollinger, D.J. Wineland, and Wayne M. Itano
Time and Frequency Div., NIST, 325 Broadway, Boulder, CO 80303
E-mail: jjb@enh.nist.gov

and

D.J. Heinzen
Physics Dept., University of Texas, Austin, TX 78712

ABSTRACT

In experiments on N atoms initially prepared in uncorrelated states, the precision of a transition frequency measurement (limited only by the quantum fluctuations in the measurement) improves as $N^{-1/2}$. We show that the precision of a frequency measurement can improve as N^{-1} , if the atoms are prepared in particular quantum mechanically correlated states. These correlated states can be interpreted as squeezed spin states in analogy with the squeezing that has been discussed with reference to the electromagnetic field. We discuss states which provide the maximum possible precision in a transition frequency measurement and briefly describe possible methods for generating correlated states.

1. Spin Squeezing and Ramsey Spectroscopy

In this manuscript we consider the spectroscopy of N two-level atoms, where transitions are driven by classical radiation and detected by measuring changes in the state populations. We assume that the relaxation of the atomic states can be neglected. The use of correlated states to improve the signal-to-noise ratio in this type of spectroscopy has been discussed recently under the subject of spin squeezing.¹⁻³ In particular, Refs. 1 and 2 discuss spin squeezing for the Ramsey technique of separated oscillatory fields (SOF). After reviewing this discussion below, we discuss in Sec. 2 the best squeezed spin states for $N=2$ atoms. In Sec. 3 we give a state that can be used in Ramsey spectroscopy to provide a frequency imprecision of $(NT)^{-1}$ where T is the time of a single measurement. From a time-energy uncertainty relation, we show that this is the best precision possible. Finally in the last section we briefly describe possible methods for generating correlated or squeezed spin states of ions in a trap.

Let $|e\rangle$ denote the excited state of a two-level atom and $|g\rangle$ the ground state, and consider the case where N atoms are uncorrelated and each atom is initially prepared in its ground state $|g\rangle$. Because any two-level system interacting with classical radiation

*Work of the US government; not subject to US copyright.

is equivalent to a spin- $1/2$ magnetic dipole in a magnetic field,⁴ the initial state of the composite system for this case is equivalent to the $|J=N/2, M_J=-N/2\rangle$ state of a $J=N/2$ spin. This initial ($t=0$) state has $\langle J_z \rangle_0 = -N/2$, $\langle J_x \rangle_0 = \langle J_y \rangle_0 = 0$, and $\Delta J_x(0) = \Delta J_y(0) = N^{1/2}/2$. (Here $\langle A \rangle_t$ denotes the expectation value of an operator A at time t and $\Delta A(t) = \langle \Delta A^2 \rangle_t^{1/2}$, where $\Delta A^2 = A^2 - \langle A \rangle^2$.) The Hamiltonian for the equivalent spin system is $H = -\bar{\mu} \cdot \bar{B}$ where $\bar{\mu} = \mu_0 \bar{J}$ is the magnetic moment of the composite system and \bar{B} is the applied field. Here $\bar{B} = B_0 \hat{z} + \bar{B}_1$, where B_0 is a time independent field set by the frequency of the transition ($\omega_0 = -\mu_0 B_0 / \hbar$, where we assume $\mu_0 < 0$), and \bar{B}_1 is an applied oscillating field used to perform spectroscopy on the atoms. We assume \bar{B}_1 is perpendicular to, and is rotating about the z axis according to $\bar{B}_1 = B_1 [-\hat{x} \sin \omega t + \hat{y} \cos \omega t]$. In the Ramsey SOF technique,⁵ B_1 is applied (that is, nonzero) for two periods of length $t_{\pi/2} = \pi / (2\Omega_R)$ where $\Omega_R = |\mu_0 B_1| / \hbar$ is the Rabi frequency, separated by a period of length T during which $B_1 = 0$. Throughout this manuscript we assume $\Omega_R \gg |\omega_0 - \omega|$ and $T \gg t_{\pi/2}$ which results in a simple expression for the Ramsey lineshape. In a frame of reference rotating with \bar{B}_1 , the first pulse rotates the spin vector about \bar{B}_1 (the y axis in the rotating frame) by 90° . The spin vector then precesses about the z axis during the field free period, acquiring an angle $(\omega_0 - \omega)T$ relative to the x axis in the rotating frame. This angle could be read out by measuring, for example, J_x in the rotating frame. Experimentally this is done by the second $\pi/2$ pulse, which rotates the spin vector by 90° about the \bar{B}_1 axis, and then measuring the number of atoms in $|e\rangle$, or equivalently J_z . We obtain

$$\langle J_z \rangle_{t_f} = (N/2) \cos(\omega_0 - \omega)T \quad (1)$$

where $t_f = 2t_{\pi/2} + T$.

Measurements of J_z along with Eq. (1) can be used to estimate the frequency ω_0 . Because of the statistical nature of quantum mechanics, the number of particles which make a transition to $|e\rangle$ from measurement to measurement will fluctuate by $\Delta J_z(t_f)$.⁶ This produces an uncertainty in the estimate of ω_0 of $|\Delta\omega| = \Delta J_z(t_f) / |\partial \langle J_z \rangle_{t_f} / \partial \omega|$. We obtain

$$|\Delta\omega| = \Delta J_y(0) / [T |\langle J_z \rangle_0|] = N^{-1/2} T^{-1} \quad (2)$$

independent of ω . (Experimental measurements are usually made with $\omega \sim \omega_0 \pm \pi / (2T)$ where Eq. (1) has its steepest slope. This minimizes the effect of any added technical noise.) The fundamental noise limit of Eq. (2) has been achieved with small numbers of ions in a trap.⁶ Qualitatively, the dependence of $|\Delta\omega|$ on $\Delta J_y(0)$ in Eq. (2) can be understood from the picture that the Ramsey SOF technique measures the accumulated angle $(\omega_0 - \omega)T$ of a spin in the x - y plane which is precessing about the z axis. In particular, spectroscopy with the Ramsey SOF technique is equivalent to determining the rotation of a spin state (after the first $\pi/2$ pulse) about the z axis. The precision of this

measurement is limited by the uncertainty of the spin normal to the mean spin vector and in the x-y plane, which here is $\Delta J_y(0)$. The idea of spin squeezing is to start with a state $\langle \vec{J} \rangle = \hat{z} \langle J_z \rangle_0$ such that $\Delta J_y(0) < N^{1/2}/2$. Such a state can be used to improve the frequency resolution in Ramsey spectroscopy if the squeezing parameter $\xi_R \equiv (2J)^{1/2} \Delta J_y(0) / |\langle J_z \rangle_0| < 1$.⁷ The parameter ξ_R is a measure of the improvement in Ramsey spectroscopy over the case where the initial state consists of uncorrelated atoms. States with $\xi_R < 1$ are in general entangled; they cannot be written as a product of individual atomic wave functions. These states are multiparticle versions of the correlated two-particle states discussed in the Einstein-Podolsky-Rosen experiments. Spin squeezing has also been discussed in the context of interferometry.⁸⁻¹¹ The discussion there parallels the discussion here because there is a one-to-one correspondence between the Ramsey SOF technique and a Mach-Zehnder interferometer.

2. Two-Atom Squeezed States

For simplicity, consider $N=2$ ($J=1$) and let the mean spin vector be parallel to the z-axis, $\langle \vec{J} \rangle = \langle J_z \rangle \hat{z}$. In this case it is straightforward to show that the state with the best squeezing (lowest value of ξ_R) is

$$|\psi_M\rangle = (2\cosh(2\theta))^{-1/2} \{ e^{-\theta} |J=1, m_J=1\rangle + e^{\theta} |1, -1\rangle \}, \quad (3)$$

where θ is determined by $\langle J_z \rangle = -\tanh(2\theta)$. As discussed above, except for the $\theta \rightarrow \pm \infty$ limits, this is a correlated state of the two atoms; it cannot be written as the product of individual atomic states. In addition, $\Delta J_y^2 = 1/2(1 - \text{sech}(2\theta))$, $\Delta J_x^2 = 1/2(1 + \text{sech}(2\theta))$, and $\xi_R = \sqrt{2\text{sech}\theta} / (\cosh(2\theta))^{1/2}$. The smallest (that is, best) values of ξ_R are obtained for small θ . As $\theta \rightarrow 0$, $\xi_R \rightarrow 1/\sqrt{2}$. However, as $\theta \rightarrow 0$, the mean spin vector $\langle \vec{J} \rangle = \langle J_z \rangle \hat{z}$ and the SOF signal also approach 0. The next section indicates how this problem can be solved by detecting an operator different than J_z .

3. Optimal Frequency Measurements

Some squeezed states for $N > 2$ are discussed in Refs. 2 and 3. Reference 3 shows that certain "intelligent" states, discussed in detail by Rashid,¹² provide a squeezing $\xi_R \rightarrow \sqrt{2N^{-1/2}}$ as $N \rightarrow \infty$. By detecting an operator different than J_z , we can find a state with a squeezing $\xi_R = N^{-1/2}$. In order to motivate the choice of this state, recall that the angle $(\omega_0 - \omega)T$ which is measured in the Ramsey method is, in the rotating frame, just the phase factor $e^{-i(\omega_0 - \omega)T}$ that the excited state $|e\rangle$ acquires relative to the ground state $|g\rangle$ during the free precession period T . Consequently it may be possible to improve the precision of Ramsey spectroscopy by making a coherent superposition (after the first $\pi/2$ pulse) of two energy eigenstates whose energies differ by more than $\hbar(\omega_0 - \omega)$. For N

two-level atoms the eigenstates $|N/2, -N/2\rangle$ and $|N/2, N/2\rangle$ provide the largest energy difference, with an accumulated phase difference of $N(\omega_0 - \omega)T$ over the free precession period. It appears that the state

$$|\psi_M\rangle = \{ |N/2, N/2\rangle + |N/2, -N/2\rangle \} / \sqrt{2} \quad (4)$$

may therefore provide a frequency imprecision of $(NT)^{-1}$, which is $N^{1/2}$ smaller than that provided by N independent atoms. However, because $\langle \psi_M | \vec{J} | \psi_M \rangle = 0$, some operator other than J_z with higher-order tensor components must be detected.

Consider the operator $\tilde{O} = \prod_{i=1}^N \sigma_{z_i}$ which is a product of the z-component Pauli spin matrices for the atoms. For $J=N/2$ this operator is diagonal in the $|J, M_J\rangle$ basis with eigenvalues $(-1)^{J-M_J}$. (This follows by expressing $|J, M_J\rangle$ as a sum over all states which are products of individual spin up or spin down states with $J-M_J$ spins down.) Quantum jump detection can be used to measure \tilde{O} (or J_z) without added noise.⁶ The result of measuring x atoms in the spin up state is assigned the value $(-1)^{N-x}$. Suppose at the end of the first $\pi/2$ pulse the state $|\psi_M\rangle$ is created. After the second $\pi/2$ pulse we detect $\langle \tilde{O} \rangle_{t_f} \equiv \langle \psi_f | \tilde{O} | \psi_f \rangle$ where

$$|\psi_f\rangle = e^{-i\frac{\pi}{2}J_z} e^{-i(\omega_0 - \omega)TJ_z} |\psi_M\rangle. \quad (5)$$

Explicit computation gives $\langle \tilde{O} \rangle_{t_f} = (-1)^N \cos[N(\omega_0 - \omega)T]$ and, because $\tilde{O}^2 = 1$, $\langle \Delta \tilde{O}^2 \rangle_{t_f} = \sin^2[N(\omega_0 - \omega)T]$. By detecting the operator \tilde{O} , we can therefore use the state $|\psi_M\rangle$ in spectroscopy with a frequency imprecision

$$|\Delta\omega| = \Delta \tilde{O}(t_f) / |\partial \langle \tilde{O} \rangle_{t_f} / \partial \omega| = (NT)^{-1} \quad (6)$$

independent of ω .

The Ramsey method measures ω_0 by measuring the phase $\omega_0 T$ (we now use the laboratory frame of reference) which state $|e\rangle$ acquires relative to $|g\rangle$ during the free precession period; that is, ω_0 is measured by observing the free time evolution of the system. With the state $|\psi_M\rangle$ a frequency imprecision of $(NT)^{-1}$ is obtained. We show that this is in fact the best precision that can be obtained on N identical two-level atoms undergoing free time evolution. This follows from an application of the time-energy uncertainty principle

$$\delta t^2 \langle \Delta H^2 \rangle \geq \hbar^2 / 4, \quad (7)$$

where $\langle \Delta H^2 \rangle$ is the variance of the Hamiltonian and δt^2 is the variance in estimating time, derived from measurements of an operator of the system. (In many texts δt is interpreted

as a characteristic evolution time of the system and Eq. (7) then relates the uncertainty in the system's energy to this characteristic evolution time. However δt can also be interpreted as the uncertainty in determining time from measurements of an operator of the system. For example, measurements of an operator A can be used to determine time with an uncertainty $\Delta A/|d\langle A \rangle/dt|$. See Ref. 13 for a simple proof of the time-uncertainty relation and Refs. 14-16 for a more rigorous discussion.) For the system of N identical two-level particles, Eq. (7) can be expressed in terms of dimensionless quantities

$$\delta\phi^2 \langle \Delta h^2 \rangle \geq 1/4 \quad (8)$$

where $\phi = \omega_0 t$ and

$$h = \sum_{i=1}^N \left\{ \frac{1}{2} |e\rangle_{ii} \langle e| - \frac{1}{2} |g\rangle_{ii} \langle g| \right\}. \quad (9)$$

We are here considering the full 2^N -dimensional Hilbert space and not just the $J=N/2$ subspace discussed earlier. We can establish an upper limit $\langle \Delta h^2 \rangle \leq N^2/4$ from $\langle \Delta h^2 \rangle = \langle h^2 \rangle - \langle h \rangle^2 \leq \langle h^2 \rangle$ and $\langle h^2 \rangle \leq N^2/4$. The last inequality follows because the maximum eigenvalue of h^2 is $N^2/4$. From these inequalities and Eq. (8) we have

$$\delta\phi^2 \geq \frac{1}{4 \langle \Delta h^2 \rangle} \geq \frac{1}{N^2}. \quad (10)$$

For a free time evolution of duration T , Eq. (10) implies that

$$\delta\omega_0 \geq \frac{1}{NT}, \quad (11)$$

where $\delta\omega_0$ is the uncertainty in determining ω_0 from measurements at the end of the evolution period. Therefore the optimum precision in measuring ω_0 can be obtained using Ramsey spectroscopy with $|\psi_M\rangle$ and detecting the operator \tilde{O} as described above.

We can apply the above results to particle interferometry. In particular, for a Mach-Zehnder interferometer employing n input particles for each measurement, the desired state corresponding to Eq. (4) (that is, the state after the first beam splitter) is $|\psi\rangle = \{ |n\rangle_a |0\rangle_b + |0\rangle_a |n\rangle_b \} / \sqrt{2}$ where a and b denote the two modes after the first beam splitter.^{8,9} In this case, the operator \tilde{O} can be detected by measuring the number of particles $n(b')$ detected in the b' output mode of the second beam splitter. The result of such a measurement is assigned the value $(-1)^{n(b')}$. Equation (6) implies that the phase sensitivity of the interferometer is given by $\Delta\phi = n^{-1}$, and Eq. (11) shows that this is the maximum sensitivity possible.

4. Methods for Making Squeezed States

In this section we briefly discuss several ideas for making squeezed spin states with ions in a trap. (There are also ideas for making squeezed spin states with neutral atoms. One possibility replaces the center-of-mass mode of the ion cloud discussed below with an electromagnetic cavity mode.¹⁷⁾ Ion traps provide an isolated environment for the internal energy states of trapped ions. At first sight, this isolation appears to make correlating the internal states of the trapped ions difficult. However, with cooling, the translational states of the trapped ions can be strongly interacting. (For example, with laser cooling, ions in a linear rf trap freeze into a 1-D string.^{18,19)} In the schemes discussed so far for generating correlated states of trapped ions, the internal states of the ions are coupled to a particular (shared) motional degree of freedom. In Refs. 1 and 2, quasi-static inhomogeneous fields and stimulated Raman transitions were discussed as possible methods for coupling ground state hyperfine levels of an ion with the center-of-mass (COM) mode of a trapped ion cloud. The ions were assumed to be prepared in either one of the $|N/2, \pm N/2\rangle$ states and all ions were assumed to see the same coupling with the COM mode. (For the stimulated Raman interaction, this will be satisfied if the laser beam waists and confocal parameters are large compared to the ion cloud.) In this case, in the interaction picture and the rotating wave approximation, the interaction H_1 between the internal states and the COM mode can take the form of a Jaynes-Cummings-type interaction

$$H_1 = -\hbar\Omega(J_+a + J_-a^\dagger) \quad (12)$$

where a^\dagger (a) is the raising (lowering) operator for the COM mode, J_+ (J_-) is the raising (lowering) operator for the $J=N/2$ ladder of atomic states, and Ω is the strength of the interaction. Two different schemes were investigated. In one, the COM mode is initially assumed to be a coherent state and in the other a squeezed state. The interaction of Eq. (12) was then applied for a specific time and the resulting squeezing of the spins calculated. In general, this method results in a mixed state of the ions' internal states and the COM mode, and a squeezing less than the optimal value discussed in the last section. By preparing appropriate (probably nonclassical) states of the COM mode, we may be able to prepare to prepare the state $|\psi_M\rangle$. For example, with $N=2$ the coupling in Eq. (12) can be used to evolve the $|n=1\rangle|J=1, M_J=-1\rangle$ state into the $|n=0\rangle|J=1, M_J=0\rangle$ state. For $N=2$, the internal state differs from $|\psi_M\rangle$ by a rotation.

More recently, Cirac and Zoller²⁰ have discussed the use of a string of N ions in a linear rf trap for quantum computation and described a method for preparing general quantum states of this system. Their method is similar to that discussed in the previous paragraph but differs in that it uses a well focussed laser beam to couple the internal states of *individual* ions with a mode of the ion string. The mode is initially prepared

in $|n=0\rangle$. The laser beam is then used to address an individual ion and correlate, or entangle, the internal state of the ion with the mode. The laser beam can then be used to address a different ion and change the correlation between the ion and the mode to a correlation between two different ions. Reference 20 lays out the steps needed to prepare the state $|\psi_M\rangle$. Here we discuss the simple case of $N=2$. We assume lasers can be focussed and used to drive transitions on an individual ion without perturbing the other ion. (If $|g\rangle$ and $|e\rangle$ are hyperfine levels of an atomic ground state, lasers can be used to drive a stimulated Raman transition between the states.²¹) Suppose that the 2 ions are prepared in the initial state $|g\rangle_1|g\rangle_2|n=0\rangle$ where the indices refer to the internal states of ions 1 and 2 and $|n=0\rangle$ is the $n=0$ state of a mode of the 2-ion string. First a $\pi/2$ -pulse on the blue sideband of ion 1 takes the $|g\rangle_1|g\rangle_2|n=0\rangle$ state into the $|g\rangle_2\{|g\rangle_1|n=0\rangle+|e\rangle_1|n=1\rangle\}/\sqrt{2}$ state. This is then followed by a π pulse on the red sideband of ion 2. This leaves the $|g\rangle_1|g\rangle_2|n=0\rangle$ state unperturbed, but takes the $|e\rangle_1|g\rangle_2|n=1\rangle$ state into the $|e\rangle_1|e\rangle_2|n=0\rangle$ state. In this manner $|\psi_M\rangle$ can be prepared for $N=2$.

5. Acknowledgements

We gratefully acknowledge the support of the Office of Naval Research and the Army Research Office. We thank Joseph Tan, John Kitching, and Matt Young for their comments on the manuscript.

6. References

1. D.J. Wineland, J.J. Bollinger, W.M. Itano, F.L. Moore, and D.J. Heinzen, *Phys. Rev. A* **46** (1992) R6797.
2. D.J. Wineland, J.J. Bollinger, W.M. Itano, and D. J. Heinzen, *Phys. Rev. A* **50** (1994) 67.
3. G.S. Agarwal and R.R. Puri, *Phys. Rev. A* **49** (1994) 4968.
4. R.P. Feynman, F.L. Vernon Jr., and R.W. Hellwarth, *J. Appl. Phys.* **28** (1957) 49.
5. N.F. Ramsey, *Molecular Beams* (Oxford, London, 1963), p. 124.
6. W.M. Itano, J.C. Bergquist, J.J. Bollinger, J.M. Gilligan, D.J. Heinzen, F.L. Moore, M.G. Raizen, and D.J. Wineland, *Phys. Rev. A* **47** (1993) 3554.
7. As discussed in Refs. 1 and 2, to achieve the full benefit of a squeezed state, the oscillating field in the $\pi/2$ pulses must have the correct phase relative to the squeezed state.
8. B. Yurke, S.L. McCall, and J.R. Klauder, *Phys. Rev. A* **33** (1986) 4033.
9. B. Yurke, *Phys. Rev. Lett.* **56** (1986) 1515.

10. M. Kitagawa and M. Ueda, *Phys. Rev. Lett.* **67** (1991) 1852.
11. M. Kitagawa and M. Ueda, *Phys. Rev.* **A47** (1993) 5138.
12. M.A. Rashid, *J. Math. Phys.* **19** (1978) 1391; **19** (1978) 1397.
13. A. Messiah, *Quantum Mechanics*, Vol. I (North-Holland, Amsterdam, 1961) pp. 319-320.
14. C.W. Helstrom, *Quantum Detection and Estimation Theory* (Academic, New York, 1976), Chaps. VIII.2.c and VIII.4.c.
15. A.S. Holevo, *Probabilistic and Statistical Aspects of Quantum Theory* (North-Holland, Amsterdam, 1982), Chaps. III.2, III.8, IV.7, and VI.3.
16. S.L. Braunstein and C.M. Caves, *Phys. Rev. Lett.* **72** (1994) 3439.
17. H.J. Kimble, to appear in *Laser Spectroscopy XII*, edited by M. Ignuscio, (World Scientific); M. Brune, F. Schmidt-Kaler, J. Dreyer, A. Maali, and J.M. Raimond, to appear in *Laser Spectroscopy XII*, edited by M. Ignuscio, (World Scientific).
18. M.G. Raizen, J.M. Gilligan, J.C. Bergquist, W.M. Itano, and D.J. Wineland, *Phys. Rev.* **A45** (1992) 6493.
19. G. Birkl, S. Kassner, and H. Walther, *Nature* **357** (1992) 310.
20. J.I. Cirac and P. Zoller, *Phys. Rev. Lett.* **74** (1995) 4091.
21. C. Monroe, D.M. Meekhof, B.E. King, S.R. Jefferts, W.M. Itano, and D.J. Wineland, "Resolved-sideband Raman cooling of a bound atom to the zero-point energy," to be published in *Phys. Rev. Lett.*.

Demonstration of a Fundamental Quantum Logic Gate

C. Monroe, D. M. Meekhof, B. E. King, W. M. Itano, and D. J. Wineland

National Institute of Standards and Technology, Boulder, Colorado 80303

(Received 14 July 1995)

We demonstrate the operation of a two-bit "controlled-NOT" quantum logic gate, which, in conjunction with simple single-bit operations, forms a universal quantum logic gate for quantum computation. The two quantum bits are stored in the internal and external degrees of freedom of a single trapped atom, which is first laser cooled to the zero-point energy. Decoherence effects are identified for the operation, and the possibility of extending the system to more qubits appears promising.

PACS numbers: 89.80.+h, 03.65.-w, 32.80.Pj

We report the first demonstration of a fundamental quantum logic gate that operates on prepared quantum states. Following the scheme proposed by Cirac and Zoller [1], we demonstrate a controlled-NOT gate on a pair of quantum bits (qubits). The two qubits comprise two internal (hyperfine) states and two external (quantized motional harmonic oscillator) states of a single trapped atom. Although this minimal system consists of only two qubits, it illustrates the basic operations necessary for, and the problems associated with, constructing a large scale quantum computer.

The distinctive feature of a quantum computer is its ability to store and process superpositions of numbers [2]. This potential for parallel computing has led to the discovery that certain problems are more efficiently solved on a quantum computer than on a classical computer [3]. The most dramatic example is an algorithm presented by Shor [4] showing that a quantum computer should be able to factor large numbers very efficiently. This appears to be of considerable interest, since the security of many data encryption schemes [5] relies on the inability of classical computers to factor large numbers.

A quantum computer hosts a register of qubits, each of which behaves as quantum mechanical two-level systems and can store arbitrary superposition states of 0 and 1. It has been shown that any computation on a register of qubits can be broken up into a series of two-bit operations [6], for example, a series of two-bit "controlled-NOT" (CN) quantum logic gates, accompanied by simple rotations on single qubits [7,8]. The CN gate transforms the state of two qubits ϵ_1 and ϵ_2 from $|\epsilon_1\rangle|\epsilon_2\rangle$ to $|\epsilon_1\rangle|\epsilon_1 \oplus \epsilon_2\rangle$, where the \oplus operation is addition modulo 2. Reminiscent of the classical exclusive-OR (XOR) gate, the CN gate represents a computation at the most fundamental level: the "target" qubit $|\epsilon_2\rangle$ is flipped depending on the state of the "control" qubit $|\epsilon_1\rangle$.

Experimental realization of a quantum computer requires isolated quantum systems that act as the qubits, and the presence of controlled unitary interactions between the qubits that allow construction of the CN gate. As pointed out by many authors [6,9,10], if the qubits are not sufficiently isolated from outside influences, decoherences can destroy the quantum interferences that form the computation. Several proposed experimental schemes for quantum

computers and CN gates involving a dipole-dipole interaction between quantum dots or atomic nuclei [6,7,11,12] may suffer from decoherence efforts. The light shifts on atoms located inside electromagnetic cavities have been shown to be large enough [13,14] that one could construct a quantum gate where a single photon prepared in the cavity acts as the control qubit [7,15] for the atomic state. However, extension to large quantum registers may be difficult. Cirac and Zoller [1] have proposed a very attractive quantum computer architecture based on laser-cooled trapped ions in which the qubits are associated with internal states of the ions, and information is transferred between qubits through a shared motional degree of freedom. The highlights of their proposal are that (i) decoherence can be small, (ii) extension to large registers is relatively straightforward, and (iii) the qubit readout can have nearly unit efficiency.

In our implementation of a quantum CN logic gate, the target qubit $|S\rangle$ is spanned by two $^2S_{1/2}$ hyperfine ground states of a single $^9\text{Be}^+$ ion (the $|f=2, m_F=2\rangle$ and $|f=1, m_F=1\rangle$ states, abbreviated by the equivalent spin-1/2 states $|\downarrow\rangle$ and $|\uparrow\rangle$) separated in frequency by $\omega_0/2\pi \approx 1.250$ GHz. The control qubit $|n\rangle$ is spanned by the first two quantized harmonic oscillator states of the trapped ion ($|0\rangle$ and $|1\rangle$), separated in frequency by the vibrational frequency $\omega_x/2\pi \approx 11$ MHz of the harmonically trapped ion. Figure 1 displays the relevant $^9\text{Be}^+$ energy levels. Manipulation between the four basis eigenstates spanning the two-qubit register ($|n\rangle|S\rangle = |0\rangle|\downarrow\rangle, |0\rangle|\uparrow\rangle, |1\rangle|\downarrow\rangle, |1\rangle|\uparrow\rangle$) is achieved by applying a pair of off-resonant laser beams to the ion, which drives stimulated Raman transitions between basis states. When the difference frequency δ of the beams is set near $\delta = \omega_0$ (the carrier), transitions are coherently driven between internal states $|S\rangle$ while preserving $|n\rangle$. Likewise, for $\delta = \omega_0 - \omega_x$ (the red sideband), transitions are coherently driven between $|1\rangle|\downarrow\rangle$ and $|0\rangle|\uparrow\rangle$, and for $\delta = \omega_0 + \omega_x$ (the blue sideband), transitions are coherently driven between $|0\rangle|\downarrow\rangle$ and $|1\rangle|\uparrow\rangle$. Note that when δ is tuned to either sideband, the stimulated Raman transitions entangle $|S\rangle$ with $|n\rangle$, a crucial part of the trapped-ion quantum CN gate.

We realize the controlled-NOT gate by sequentially applying three pulses of the Raman beams to the ion

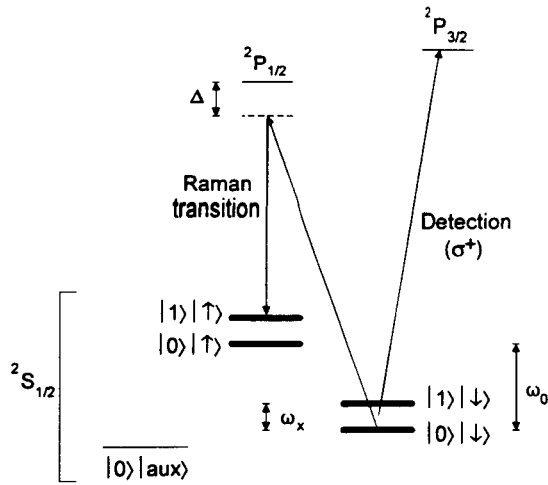


FIG. 1. ${}^9\text{Be}^+$ energy levels. The levels indicated with thick lines form the basis of the quantum register: internal levels are $|S\rangle = |\downarrow\rangle$ and $|\uparrow\rangle$ (${}^2S_{1/2}|F=2, m_F=2\rangle$ and ${}^2S_{1/2}|F=1, m_F=1\rangle$ levels, respectively, separated by $\omega_0/2\pi \approx 1.250$ GHz), and $|\text{aux}\rangle = {}^2S_{1/2}|F=2, m_F=0\rangle$ (separated from $|\downarrow\rangle$ by ≈ 2.5 MHz); external vibrational levels are $|n\rangle = |0\rangle$ and $|1\rangle$ (separated by $\omega_x/2\pi \approx 11.2$ MHz). Stimulated Raman transitions between ${}^2S_{1/2}$ hyperfine states are driven through the virtual ${}^2P_{1/2}$ level ($\Delta \approx 50$ GHz) with a pair of ≈ 313 nm laser beams. Measurement of S is accomplished by driving the cycling $|\downarrow\rangle \rightarrow {}^2P_{3/2}|F=3, m_F=3\rangle$ transition with σ^+ -polarized light and detecting the resulting ion fluorescence.

according to the following format:

- A $\pi/2$ pulse is applied on the carrier transition. The effect is described by the operator $V^{1/2}(\pi/2)$ in the notation of Ref. [1].
- A 2π pulse is applied on the blue sideband transition between $|\uparrow\rangle$ and an auxiliary atomic level $|\text{aux}\rangle$ (see Fig. 1).
- A $\pi/2$ pulse is applied on the carrier transition, with a π phase shift relative to (a), leading to the operator $V^{1/2}(-\pi/2)$ of Ref. [1].

The $\pi/2$ pulses in steps (a) and (c) cause the spin $|S\rangle$ to undergo $+1/4$ and $-1/4$ of a complete Rabi cycle, respectively, while leaving $|n\rangle$ unchanged. The auxiliary transition in step (b) simply reverses the sign of any component of the register in the $|1\rangle|\uparrow\rangle$ state by inducing a complete Rabi cycle from $|1\rangle|\uparrow\rangle \rightarrow |0\rangle|\text{aux}\rangle \rightarrow -|1\rangle|\uparrow\rangle$. The auxiliary level $|\text{aux}\rangle$ is the ${}^2S_{1/2}|F=2, m_F=0\rangle$ ground state, split from the $|\downarrow\rangle$ state by virtue of a Zeeman shift of ≈ 2.5 MHz resulting from a 0.18 mT applied magnetic field (see Fig. 1). Any component of the quantum register in the $|n\rangle = |0\rangle$ state is unaffected by the blue sideband transition of step (b), and the effects of the two Ramsey $\pi/2$ pulses cancel. On the other hand, any component of the quantum register in the $|1\rangle|\uparrow\rangle$ state acquires a sign change in step (b), and the two Ramsey pulses add constructively, effectively “flipping” the target qubit by π radians. The truth table of the CN operation

is as follows:

Input state	Output state
$ 0\rangle \downarrow\rangle$	$\rightarrow 0\rangle \downarrow\rangle$
$ 0\rangle \uparrow\rangle$	$\rightarrow 0\rangle \uparrow\rangle$
$ 1\rangle \downarrow\rangle$	$\rightarrow 1\rangle \uparrow\rangle$
$ 1\rangle \uparrow\rangle$	$\rightarrow 1\rangle \downarrow\rangle$.

(2)

The experiment apparatus is described elsewhere [16,17]. A single ${}^9\text{Be}^+$ ion is stored in a coaxial-resonator rf-ion trap [17], which provides pseudopotential oscillation frequencies of $(\omega_x, \omega_y, \omega_z)/2\pi \approx (11.2, 18.2, 29.8)$ MHz along the principal axes of the trap. We cool the ion so that the $n_x = 0$ vibrational ground state is occupied $\approx 95\%$ of the time by employing resolved-sideband stimulated Raman cooling in the x dimension, exactly as in Ref. [16]. The two Raman beams each contain ≈ 1 mW of power at ≈ 313 nm and are detuned ≈ 50 GHz red of the ${}^2P_{1/2}$ excited state. The Raman beams are applied to the ion in directions such that their wave-vector difference $\delta\mathbf{k}$ points nearly along the x axis of the trap; thus the Raman transitions are highly insensitive to motion in the other two dimensions. The Lamb-Dicke parameter is $\eta_x = \delta k x_0 \approx 0.2$, where $x_0 \approx 7$ nm is the spread of the $n_x = 0$ wave function. The carrier ($|n\rangle|\downarrow\rangle \rightarrow |n\rangle|\uparrow\rangle$) Rabi frequency is $\Omega_0/2\pi \approx 140$ kHz, the red ($|1\rangle|\downarrow\rangle \rightarrow |0\rangle|\uparrow\rangle$) and blue ($|0\rangle|\downarrow\rangle \rightarrow |1\rangle|\uparrow\rangle$) sideband Rabi frequencies are $\eta_x \Omega_0/2\pi \approx 30$ kHz, and the auxiliary transition ($|1\rangle|\uparrow\rangle \rightarrow |0\rangle|\downarrow\rangle$) Rabi frequency is $\eta_x \Omega_{\text{aux}}/2\pi \approx 12$ kHz. The difference frequency of the Raman beams is tunable from 1200 to 1300 MHz with the use of a double pass acousto-optic modulator (AOM), and the Raman pulse durations are controlled with additional switching AOMs. Since the Raman beams are generated from a single laser and an AOM, broadening of the Raman transitions due to a finite laser linewidth is negligible [18].

Following Raman cooling to the $|0\rangle|\downarrow\rangle$ state, but before application of the CN operation, we apply appropriately tuned and timed Raman pulses to the ion, which can prepare an arbitrary state of the two-qubit register. For instance, to prepare a $|1\rangle|\downarrow\rangle$ eigenstate, we apply a π pulse on the blue sideband followed by a π pulse on the carrier ($|0\rangle|\downarrow\rangle \rightarrow |1\rangle|\uparrow\rangle \rightarrow |1\rangle|\downarrow\rangle$). We perform two measurements to detect the population of the register after an arbitrary sequence of operations. First, we measure the probability $P\{S=\downarrow\}$ that the target qubit $|S\rangle$ is in the $|\downarrow\rangle$ state by collecting the ion fluorescence when σ^+ -polarized laser radiation is applied resonant with the cycling $|\downarrow\rangle \rightarrow {}^2P_{3/2}|F=3, m_F=3\rangle$ transition (radiative linewidth $\gamma/2\pi \approx 19.4$ MHz at $\lambda \approx 313$ nm; see Fig. 1). Since this radiation does not appreciably couple to the $|\uparrow\rangle$ state (relative excitation probability: $\approx 5 \times 10^{-5}$), the fluorescence reading is proportional to $P\{S=\downarrow\}$. For $S=\downarrow$, we collect on average ≈ 1 photon per measurement cycle [16]. Once S is measured, we

perform a second independent measurement that provides the probability $P\{n = 1\}$ that the control bit $|n\rangle$ is in the $|1\rangle$ state: After the same operation sequence is repeated, an appropriate Raman pulse is added just prior to the detection of S . This “detection preparation” pulse maps $|n\rangle$ onto $|S\rangle$. For instance, if we first measure S to be \downarrow , we repeat the experiment with the addition of a “ π pulse” on the red sideband. Subsequent detection of S resulting in the presence (absence) of fluorescence indicates that $n = 0$ (1). Likewise, if we first measure S to be \uparrow , we repeat the experiment with the addition of a “ π pulse” on the blue sideband. Subsequent detection of S resulting in the presence (absence) of fluorescence indicates that $n = 1$ (0).

In the above measurement scheme, we do not obtain phase information about the quantum state of the register and therefore do not measure the complete transformation matrix associated with the CN operation. The phase information could be obtained by performing additional operations (similar to those described above) prior to the measurement of S . Here, we demonstrate the key features of the CN gate by (i) verifying that the populations of the register follow the truth table given in (2), and (ii) demonstrating the conditional quantum dynamics associated with the CN operation.

To verify the CN truth table, we separately prepare each of the four eigenstates spanning the register ($|n\rangle|S\rangle = |0\rangle|\downarrow\rangle, |0\rangle|\uparrow\rangle, |1\rangle|\downarrow\rangle, |1\rangle|\uparrow\rangle$), then apply the CN operation given in (1). We measure the resulting register population as described above after operation of the CN gate, as shown in Fig. 2. When the control qubit is prepared in the $|n\rangle = |0\rangle$ state, the measurements show that the gate preserves S with high probability, whereas when the initial control qubit is prepared in the $|n\rangle = |1\rangle$ state, the CN gate flips the value of S with high probability. In contrast, the gate preserves the population n of the control qubit $|n\rangle$ with high probability, verifying that the register populations follow the CN truth table expressed in (2). The fact that the measured probabilities are not exactly zero or one is primarily due to imperfect laser-cooling, imperfect state preparation and detection preparation, and decoherence effects.

To illustrate the conditional dynamics of a quantum logic gate, we desire to perform a unitary transformation on one physical system conditioned upon the quantum state of another subsystem [19]. To see this in the present experiment, it is useful to view steps (a) and (c) of the CN operations given in (1) as Ramsey radiation pulses [20], which drive the $|n\rangle|\downarrow\rangle \rightarrow |n\rangle|\uparrow\rangle$ transition—with the addition of the perturbation (b) inserted between the pulses. If we now vary the frequency of the Ramsey pulses, we obtain the typical sinusoidal Ramsey interference pattern indicative of the coherent evolution between states $|S\rangle = |\downarrow\rangle$ and $|\uparrow\rangle$. However, the final population S depends on the status of the control qubit $|n\rangle$. This is illustrated in Fig. 3 where we plot the measured probability $P\{S = \downarrow\}$ as a function of detuning of the Ram-

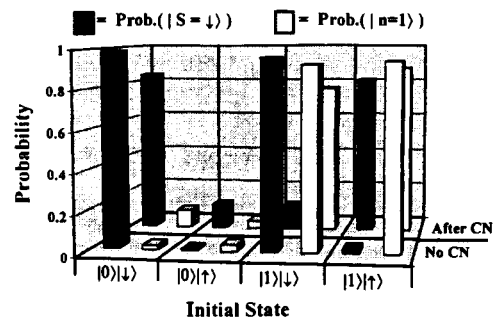


FIG. 2. Controlled-NOT (CN) truth table measurements for eigenstates. The two horizontal rows give measured final values of n and S with and without operation of the CN gate, expressed in terms of the probabilities $P\{n = 1\}$ and $P\{S = \downarrow\}$. The measurements are grouped according to the initial prepared eigenstate of the quantum register ($|0\rangle|\downarrow\rangle, |0\rangle|\uparrow\rangle, |1\rangle|\downarrow\rangle, |1\rangle|\uparrow\rangle$). Even without CN operations, the probabilities are not exactly 0 or 1 due to imperfect laser-cooling, state preparation and detection preparation, and decoherence effects. However, with high probability, the CN operation preserves the value of the control qubit n , and flips the value of the target qubit S only if $n = 1$.

sey pulses. For initial state $|0\rangle|\downarrow\rangle$, we obtain the normal Ramsey spectrum since step (b) is inactive. For initial state $|1\rangle|\downarrow\rangle$, the Ramsey spectrum is inverted indicating the conditional control (by quantum bit $|n\rangle$) of the dynamics of the Ramsey pulses. Appropriate Ramsey curves are also obtained for initial states $|0\rangle|\uparrow\rangle$ and $|1\rangle|\uparrow\rangle$.

The switching speed of the CN gate is approximately 20 kHz, limited mainly by the auxiliary 2π pulse in step (b) given in (1). This rate could be increased with more Raman beam laser power, although a fundamental limit in switching speed appears to be the frequency separation of the control qubit vibrational energy levels, which can be as high as 50 MHz in our experiment [17].

We measure a decoherence rate of a few kHz in the experiment, adequate for a single CN gate operating at a speed of ≈ 20 kHz, but certainly not acceptable for a more extended computation. We identify several sources responsible for decoherence, including instabilities in the laser beam power and the relative position of the ion with respect to the beams, fluctuating external magnetic fields (which can modulate the qubit phases), and instabilities in the rf-ion trap drive frequency and voltage amplitude. Substantial reduction of these sources of decoherence can be expected. Other sources of decoherence that may become important in the future include external heating and dissipation of the ion motion [16,21], and spontaneous emission caused by off-resonant transitions. We note that decoherence rates of under 0.001 Hz have been achieved for internal-state ion qubits [22].

The single-ion quantum register in the experiment comprises only two qubits and is therefore not useful for computation. However, if the techniques described here are applied to a collection of many ions cooled to the $n = 0$ state of collective motion, it should be possible to imple-

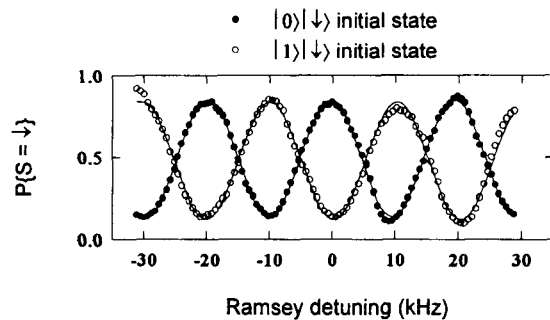


FIG. 3. Ramsey spectra of the controlled-NOT (CN) gate. The detuning of the Ramsey $\pi/2$ pulses of the CN gate [steps (a) and (c)] is swept, and S is measured, expressed in terms of the probability $P\{S = \downarrow\}$. The solid points correspond to initial preparation in the $|n\rangle|S\rangle = |0\rangle|\downarrow\rangle$ state, and the hollow points correspond to preparation in the $|n\rangle|S\rangle = |1\rangle|\downarrow\rangle$ state. The resulting patterns are shifted in phase by π rad. This flipping of $|S\rangle$ depending on the state of the control qubit indicates the conditional dynamics of the gate. Similar curves are obtained when the $|n\rangle|S\rangle = |0\rangle|\uparrow\rangle$ and $|1\rangle|\uparrow\rangle$ states are prepared. The lines are fits by a sinusoid, and the width of the Ramsey fringes is consistent with the ≈ 50 μ sec duration of the CN operation.

ment computations on larger quantum registers. For example, the CN gate between two ions (m and n) might be realized by mapping the internal state of the m th ion onto the collective vibrational state of all ions, applying the single-ion CN operation demonstrated in this work to the n th ion, then returning the vibrational state back to the internal state of the m th ion. (This mapping may be achieved by simply driving a π pulse on the red or blue sideband of the m th ion.) This approach is equivalent to the scheme proposed by Cirac and Zoller [1,23]. An arbitrary computation may then be broken into a number of such operations on different pairs of ions, accompanied by single qubit rotations on each ion (carrier transitions) [6–8].

We are currently devoting effort into the multiplexing of the register to many ions. Several technical issues remain to be explored in this scaling, including laser-cooling efficiency, the coupling of internal vibrational modes due to trap imperfections, and the unique addressing of each ion with laser beams. Although we can trap and cool a few ions in the current apparatus, other geometries such as the linear rf-ion trap [24] or an array of ion traps each confining a single ion [25] might be considered.

This work is supported by the U.S. Office of Naval Research and the U.S. Army Research Office. We acknowledge useful contributions from J.C. Bergquist and J.J. Bollinger. We thank Robert Peterson, Dana Berkeland, and Chris Myatt for helpful suggestions on the manuscript.

- [1] J.I. Cirac and P. Zoller, Phys. Rev. Lett. **74**, 4091 (1995).
- [2] R.P. Feynman, Int. J. Theor. Phys. **21**, 467 (1982); Opt. News **11**, 11 (1985).
- [3] D. Deutsch, Proc. R. Soc. London A **425**, 73 (1989); D. Deutsch and R. Jozsa, Proc. R. Soc. London A **439**, 554 (1992).
- [4] P. Shor, in Proceedings of the 35th Annual Symposium on the Foundations of Computer Science (IEEE Computer Society Press, New York, 1994), p. 124.
- [5] R.L. Rivest, A. Shamir, and L. Adelman, Comm. ACM, **28**, 120 (1978).
- [6] D.P. DiVincenzo, Phys. Rev. A **51**, 1015 (1995).
- [7] A. Barenco, D. Deutsch, A. Ekert, and R. Jozsa, Phys. Rev. Lett. **74**, 4083 (1995).
- [8] A. Barenco, C.H. Bennett, R. Cleve, D.P. DiVincenzo, N. Margolus, P. Shor, T. Sleator, J. Smolin, and H. Weinfurter, Phys. Rev. A **52**, 3457 (1995).
- [9] R. Landauer, in Proceedings of the Drexel-4 Symposium on Quantum Nonintegrability-Quantum Classical Correspondence, edited by D.H. Feng and B-L. Hu (International Press, Boston, to be published).
- [10] W.G. Unruh, Phys. Rev. A **51**, 992 (1995).
- [11] K. Obermeyer, W.G. Teich, and G. Mahler, Phys. Rev. B **37**, 8111 (1988).
- [12] S. Lloyd, Science **261**, 1569 (1993).
- [13] M. Brune, P. Nussenzweig, F. Schmidt-Kaler, F. Bernardot, A. Maali, J.M. Raimond, and S. Haroche, Phys. Rev. Lett. **72**, 3339 (1994); M. Brune, F. Schmidt-Kaler, J. Deyer, A. Maali, and J.M. Raimond, "Laser Spectroscopy XII," edited by M. Inguscio (World Scientific, Singapore, to be published).
- [14] H.J. Kimble, in "Laser Spectroscopy XIII" Ref. [13].
- [15] T. Sleator and H. Weinfurter, Phys. Rev. Lett. **74**, 4087 (1995).
- [16] C. Monroe, D.M. Meekhof, B.E. King, S.R. Jefferts, W.M. Itano, D.J. Wineland, and P. Gould, Phys. Rev. Lett. **75**, 4011 (1995).
- [17] S.R. Jefferts, C. Monroe, E.W. Bell, and D.J. Wineland, Phys. Rev. A **51**, 3112 (1995).
- [18] J.E. Thomas, P.R. Hemmer, S. Ezekiel, C.C. Leiby, R.H. Picard, and C.R. Willis, Phys. Rev. Lett. **48**, 867 (1982).
- [19] A. Ekert and R. Jozsa, Rev. Mod. Phys. (to be published).
- [20] N.F. Ramsey, *Molecular Beams* (Oxford University Press, London, 1956).
- [21] F. Diedrich, J.C. Bergquist, W.M. Itano, and D.J. Wineland, Phys. Rev. Lett. **62**, 403 (1989).
- [22] J.J. Bollinger, D.J. Heinzen, W.M. Itano, S.L. Gilbert, and D.J. Wineland, IEEE Trans. Instrum. Meas. **40**, 126 (1991).
- [23] The controlled-NOT operator proposed in Ref. [1] is $V_n^{1/2}(\pi/2)U_m^{1,0}U_n^{2,1}U_m^{1,0}V_n^{1/2}(-\pi/2)$, adopting their notation. This is equivalent to the controlled-NOT operator proposed here between ions m and n , $U_m^{1,0}V_n^{1/2}(\pi/2)U_n^{2,1}V_n^{1/2}(-\pi/2)U_m^{1,0}$, since V_n and U_m commute.
- [24] M.G. Raizen, J.M. Gilligan, J.C. Bergquist, W.M. Itano, and D.J. Wineland, Phys. Rev. A **45**, 6493 (1992).
- [25] F. Major, J. Phys. (Paris) Lett. **38**, L221 (1977); R. Brewer, R.G. DeVoe, and R. Kallenbach, Phys. Rev. A **46**, R6781 (1992).

PHYSICAL REVIEW LETTERS

VOLUME 70

19 APRIL 1993

NUMBER 16

Young's Interference Experiment with Light Scattered from Two Atoms

U. Eichmann,^(a) J. C. Bergquist, J. J. Bollinger, J. M. Gilligan, W. M. Itano,
and D. J. Wineland

National Institute of Standards and Technology, Boulder, Colorado 80303

M. G. Raizen

Department of Physics, University of Texas, Austin, Texas 78712

(Received 18 December 1992)

We report the first observation of interference effects in the light scattered from two trapped atoms. The visibility of the fringes can be explained in the framework of Bragg scattering by a harmonic crystal and simple “which path” considerations of the scattered photons. If the light scattered by the atoms is detected in a polarization-sensitive way, then it is possible to selectively demonstrate either the particle nature or the wave nature of the scattered light.

PACS numbers: 03.65.Bz, 32.50.+d, 32.80.Pj, 42.50.-p

Young's two-slit experiment [1], in the context of wave-particle duality, is often regarded as a paradigm for quantum phenomena. To some it “has in it the heart of quantum mechanics. In reality it contains the only mystery” [2]. In this Letter we report, for the first time, a version of Young's experiment where we detect the interference of weak laser light scattered from two localized atoms which act as two slits. The visibility of the interference fringes has a simple interpretation in terms of Bragg scattering and “which way” arguments based on the changes of the atoms' internal states.

Interference of light scattered from atoms has received recent attention because it has provided information on the degree of localization of laser-cooled neutral atoms in optical wells [3, 4]. Optical interference has also been observed in the time-resolved atomic fluorescence following the photodissociation of a molecule [5]. Although fixed numbers of atomic ions have been localized in ion traps [6–9], interference has not been previously reported due, in part, to inadequate localization. In the experiments described here, we observe interference of light scattered from two $^{198}\text{Hg}^+$ ions localized in a linear Paul trap [10].

The experiment is shown schematically in Fig. 1. Using established procedures, we trapped two $^{198}\text{Hg}^+$ ions along the axis of a linear trap [10]. The ions were ir-

radiated by a linearly polarized, traveling wave laser beam tuned below the resonance frequency of the $^{198}\text{Hg}^+$ $6s\ ^2S_{1/2}-6p\ ^2P_{1/2}$ transition at 194 nm. The beam serves two functions in the experiment. It reduces the ions' kinetic energy by preferentially imparting photon momentum to them in a direction that opposes their motion (Doppler laser cooling) [11]. The low temperatures strongly localize the ions in our trap. The beam also

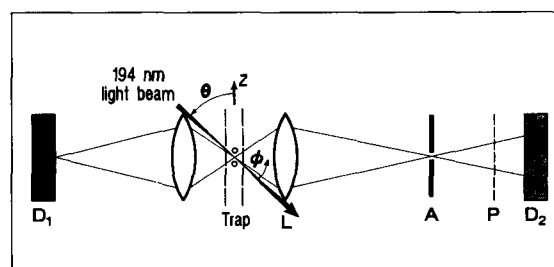


FIG. 1. Schematic diagram of the experiment. Scattered light from two ions (represented by small circles near the center of the trap) was imaged onto detector D_2 via the collecting lens L , aperture A , and an optional polarizer P . The polarizer was a UV-absorbing glass plate oriented at Brewster's angle (see text). Detector D_1 served as a monitor of ion number.

acts as the light source for the interference experiment. It was directed through the center of the trap at an angle $\theta=62^\circ$ with respect to the trap axis (z axis). The beam waist was about $50\ \mu\text{m}$ and the laser power could be varied to a maximum of about $50\ \mu\text{W}$. A $7.77\ \text{MHz}$ rf drive with an amplitude $V_0 \simeq 1\ \text{kV}$ confined the ions radially while a static voltage U_0 applied to both ends of the trap provided axial confinement. Scattered light was observed with two position-sensitive imaging detectors D_1 and D_2 (Fig. 1). On one side, a lens system produced a real image of the ions on detector D_1 [10]. This allowed for continuous monitoring to make sure that exactly two ions had been trapped. On the opposite side, detector D_2 was set up to measure the intensity of the light as a function of the scattering angle. This scattered light was collected with an $f/1$ lens and imaged with a magnification of 4.7 onto an aperture $300\ \mu\text{m}$ in diameter. The light that passed through the aperture was directed onto the position-sensitive photocathode of detector D_2 about $0.1\ \text{m}$ from the aperture. Although the interference fringes could, in principle, be detected using D_2 alone, the lens and aperture suppressed background stray light from reaching the detector. With this configuration, detector D_2 covered an in-plane detection angle $\phi = 10^\circ$ to 45° , where ϕ is defined with respect to the $194\ \text{nm}$ beam direction and the plane is defined by the traps z axis and the $194\ \text{nm}$ beam. The out-of-plane detection angle Φ ranged from -15° to 15° . The ion separation d could be adjusted by varying the axial voltage U_0 . The separation can be calculated with our trap parameters using the formula $d = 19.4U_0^{-1/3}$, where d is in μm and U_0 is in volts [8]. In the experiment, U_0 was varied between $10\ \text{V}$ and $200\ \text{V}$, which produced spacings from $9\ \mu\text{m}$ to $3.3\ \mu\text{m}$, respectively. At these separations, the dipole-dipole interaction between ions can be neglected.

Figure 2 shows examples of the experimental results with polarization-insensitive detection. The fringes were recorded at three different ion separations: $5.4\ \mu\text{m}$, $4.3\ \mu\text{m}$, and $3.7\ \mu\text{m}$. The fringe spacing increases with decreasing ion separation, as expected. Additionally, the fringe contrast is highest close to the forward scattering direction and deteriorates with increasing ϕ . At higher angles ϕ , the scattered light loses its coherence due to the residual ion motion.

We have performed calculations that quantitatively describe the fringe contrast and spacing. These calculations proceed along the same lines as those for Bragg scattering by a harmonic crystal [12] and use Fermi's "golden rule" to determine the scattering rate from an initial state to a final state. Since our detector does not differentiate between elastically and inelastically scattered light, both processes contribute to the detected interference signal. We have calculated the loss of contrast caused by the residual ion velocity at our ion temperatures and find it to be negligible. Also, loss of fringe contrast due to the resulting variations in the energy of the scattered light is

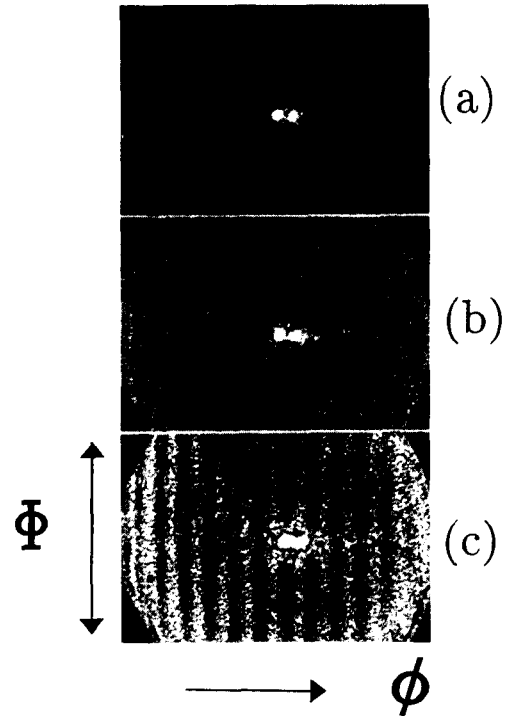


FIG. 2. Interference pattern for three different ion separations: (a) $5.4\ \mu\text{m}$, (b) $4.3\ \mu\text{m}$, and (c) $3.7\ \mu\text{m}$. The two white spots are caused by stray reflections of the laser beam.

negligible. We obtain the scattered light intensity as a function of momentum transfer $\hbar\mathbf{q} = \hbar(\mathbf{k}_{\text{out}} - \mathbf{k}_{\text{in}})$:

$$I(\mathbf{q}) = 2I_0(1 + \cos(q_z d) \exp\{-\langle[\mathbf{q} \cdot (\mathbf{u}_1 - \mathbf{u}_2)]^2\rangle/2\}), \quad (1)$$

where \mathbf{k}_{out} and \mathbf{k}_{in} are the scattered and incident photon wave vectors and I_0 represents the scattered intensity of a single ion (assumed to be equal for both ions). The brackets $\langle \rangle$ denote an ensemble average and \mathbf{u}_i denotes the displacement of the i th ion from its equilibrium position. We assume that the positions of the ions are characterized by a thermal distribution of the normal modes of the two ions in the trap. These modes are the stretch mode along the trap axis, two rocking or tilt modes normal to the trap axis, and the center-of-mass modes. Excitation of these modes during the scattering process gives rise to inelastic light scattering similar to phonon excitation processes in Bragg scattering by crystals. If we could measure only the elastically scattered contribution, it would have 100% fringe contrast independent of the momentum transfer, but the intensity would be weighted by an overall exponential factor (the Debye-Waller factor) as it is in the case of elastic Bragg scattering by crystals. The fringe contrast expressed by the exponential factor in Eq. (1) is due to the contribution of inelastic scattering processes in the interference of light scattered from two atoms. For two ions with fixed posi-

tions, Eq. (1) recalls the result obtained by Heitler in his classic treatment of resonance fluorescence [13] giving a fringe contrast equal to 1. The center-of-mass modes are absent from the exponential factor. These modes do not contribute to loss of fringe contrast, because they do not affect the relative phase of the scattered light.

We can calculate $\langle [\mathbf{q} \cdot (\mathbf{u}_1 - \mathbf{u}_2)]^2 \rangle$ from the residual kinetic energy (temperature) in the normal modes of the two ions given by $k_B T_j / 2 = m_j \omega_j^2 \langle X_j^2 \rangle / 2$, where k_B is the Boltzmann constant, j denotes the mode, m_j is the effective ion mass for mode j (for the stretch and tilt modes m_j equals one-half of the single ion mass), and $\langle X_j^2 \rangle$ is the mean squared amplitude of the modes. At the Doppler-cooling limit, the kinetic energy of the stretch mode is $\{1 + [3 \cos^2(\theta)]^{-1}\} \hbar \gamma / 8$ and the kinetic energy of the rocking mode is $\{1 + [3 \sin^2(\theta)]^{-1}\} \hbar \gamma / 8$ [11], where γ is the natural linewidth. Since the laser detuning and the degree of saturation were not precisely determined, we might expect somewhat higher kinetic energies. The frequencies of the normal modes are conveniently expressed in terms of the single-ion secular frequencies, which can be easily measured. We have $\omega_{\text{stretch}} = \sqrt{3} \omega_z$ and $\omega_{\text{tilt}} = (\omega_r'^2 - \omega_z^2)^{1/2}$, where the single-ion axial and radial secular frequencies at the maximum applied voltages were about $\omega_z / 2\pi = 1$ MHz and $\omega_r' / 2\pi = 1.5$ MHz, respectively.

To compare our data with theory, we normalized the interference data with respect to the detected fluorescence light of a single ion. This method compensates for net efficiency variations across the detector. Furthermore, we need to include a constant background intensity I_b . This background is partly due to stray light, partly due to incoherent fluorescence radiation (see below), and partly due to quantum jumps from the $6p \ ^2P_{1/2}$ state into the metastable level $5d^9 6s \ ^2D_{3/2}$ [14], which leave only one ion fluorescing. The background due to single-ion fluorescence caused by quantum jumps depends on the mean population of the $6p \ ^2P_{1/2}$ state and the lifetime of the metastable state.

We fitted Eq. (1) (including I_b) to the data and found excellent agreement for all measured interference patterns with a temperature of about twice the 1.7 mK Doppler-cooling limit. Radial confinement was about 30 nm, and the residual amplitude in the axial direction was about 60 nm to 300 nm, depending on U_0 . Figure 3 shows an example where $U_0 = 193$ V, corresponding to an ion separation of 3.4 μm .

Our experiment resembles the classic Young's two-slit arrangement with the slits replaced by the two atoms. In discussions of Young's type interference experiments, the position-momentum uncertainty relation is often used to show that it is impossible to determine through which slit the photon or particle passes without interacting with the photon or particle strongly enough to destroy the interference pattern. The position-momentum uncertainty relation need not be invoked; the destruction of the interference can arise due to correlation between the mea-

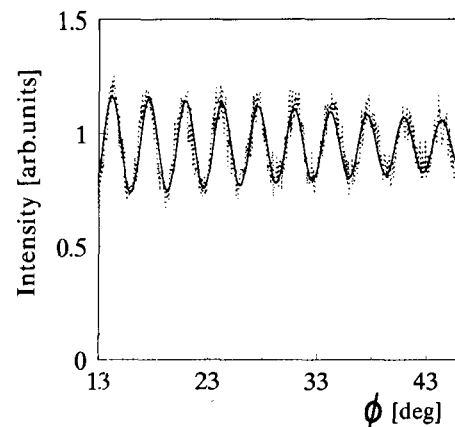


FIG. 3. Shown are the interference fringes for $d = 3.35 \mu\text{m}$ together with a fit to the data. For these data, the temperature of the ions was determined to be 1.5 times higher than the temperature at the Doppler-cooling limit.

surement apparatus and the measured system [15]. The present experiment offers the possibility to obtain "which path" information by exploiting the internal level structure of the atom. The $^{198}\text{Hg}^+$ ground state $6s \ ^2S_{1/2}$ and the excited state $6p \ ^2P_{1/2}$ are twofold degenerate with respect to the magnetic quantum number m_J . The effect of this level structure is that scattering linearly polarized light off the two ions can result in either π - or σ -polarized scattered light. Assume that only one photon is scattered at a time. In the case of π -polarized scattered light ($\Delta m_J = 0$ transition) the ions' final states are the same as the initial states. Which atom scattered the photon cannot be determined. Quantum mechanics therefore predicts that interference must be present in the light scattered from the two ions. On the other hand, observation of the σ -polarized scattered light ($|\Delta m_J| = 1$ transition) indicates that the final state of one atom differs from its initial state. This allows us, at least in principle, to distinguish the scattering atom from the "spectator" atom, and hence to determine which path the photon traveled. Consequently, there is no interference in the light scattered from the ions. In this context, the existence of interference fringes indicates wavelike behavior, while the absence of fringes, consistent with a single photon trajectory, which begins at the source, intersects one of the atoms, and continues to the detector, indicates a particlelike behavior. Thus, polarization-sensitive detection of the scattered photons can serve as a switch to extract either the wavelike or the particlelike character of the scattered photon. These two complementary pictures are essentially classical. Both types of behavior are contained in the quantum description. The interference then occurs between Feynman path amplitudes, and the presence or absence of fringes depends on whether or not there are two or one possible paths from the initial state to the final state.

Our simple "which path" considerations are confirmed

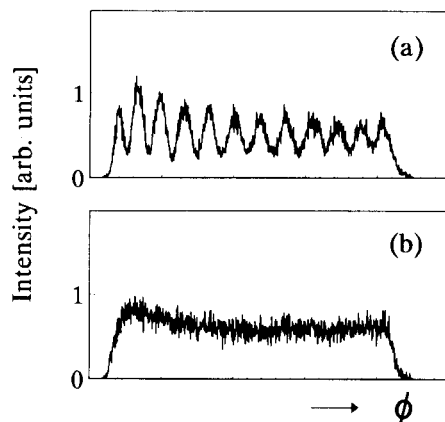


FIG. 4. Polarization-sensitive detection of the scattered light (unnormalized): (a) π -polarized scattered light, showing interference; (b) σ -polarized scattered light, showing no interference pattern as explained in the text.

by a detailed theoretical study of the coherence properties of the resonance fluorescence from a single atom with the same level structure as $^{198}\text{Hg}^+$ [16]. It reveals that for a weak, linearly polarized field, only the π -polarized scattered light is coherent, while the σ -polarized components are incoherent.

In our experiment, polarization-sensitive detection of the 194 nm scattered light was accomplished with a glass plate oriented at Brewster's angle. It was mounted between the aperture and the detector. Light linearly polarized normal to the plane of incidence of the Brewster plate was reflected toward the detector with about 15% efficiency. Light polarized in the plane of incidence was transmitted into the glass, where it was absorbed. Consequently, with the laser beam polarized normal to the plane of incidence, π -scattered light was detected. Conversely, when the laser beam was polarized in the plane of incidence, the π -scattered light was absorbed, and only σ -scattered light reached the detector. Figure 4 shows the results (unnormalized) of the polarization-sensitive detection. Figure 4(a) displays the interference pattern as expected for the case of π -scattered light. When σ -scattered light was detected, no interference pattern could be observed [Fig. 4(b)], in agreement with the quantum mechanical predictions.

In summary, we have reported the observation of interference fringes in the light scattered from two localized atoms driven by a weak laser field. The measured fringe pattern and contrast can be explained in the framework of Bragg scattering by a harmonic crystal. These results show that interference measurements provide another method to determine ion temperatures and separations in traps. By exploiting the atom's internal level structure, we showed, without invoking the position-momentum uncertainty relation, that the possibility of determining the path of the scattered photon destroyed the interference fringes.

Future prospects include measurements of the dependence of the fringe contrast on the saturation of the atomic transition, since the coherent component decreases in a predictable way as the light field intensity is increased [17]. We plan to study the interference pattern of more than two ions and have already been able to observe the interference pattern of three ions. Finally, heterodyne measurements could distinguish the different contributions of the elastic and inelastic scattering processes to the interference pattern.

We gratefully acknowledge the support of ONR. U.E. gratefully acknowledges financial support of the Deutsche Forschungsgemeinschaft. We thank M. E. Poitzsch and J. Tan for their suggestions on the manuscript.

- (a) Permanent address: Universität Freiburg, 7800 Freiburg, Germany.
- [1] See, e.g., *Great Experiments in Physics*, edited by M.H. Shamos (Henry Holt and Company, New York, 1959), p. 93.
 - [2] R. Feynman, R. Leighton, and M. Sands, *The Feynman Lectures on Physics* (Addison-Wesley, Reading, 1965), Vol. III, p. 1-1.
 - [3] P. Verkerk, B. Lounis, C. Salomon, C. Cohen-Tannoudji, J.-Y. Courtois, and G. Grynberg, *Phys. Rev. Lett.* **68**, 3861 (1992).
 - [4] P.S. Jessen, C. Gerz, P.D. Lett, W.D. Phillips, S.L. Rolston, R.J.C. Spreeuw, and C.I. Westbrook, *Phys. Rev. Lett.* **69**, 49 (1992).
 - [5] P. Grangier, A. Aspect, and J. Vigue, *Phys. Rev. Lett.* **54**, 418 (1985).
 - [6] W. Neuhauser, M. Hohenstatt, P.E. Toschek, and H. Dehmelt, *Phys. Rev. A* **22**, 1137 (1980); Th. Sauter, H. Gilhaus, I. Siemers, R. Blatt, W. Neuhauser, and P.E. Toschek, *Z. Phys. D* **10**, 153 (1988).
 - [7] F. Diedrich, E. Peik, J.M. Chen, W. Quint, and H. Walther, *Phys. Rev. Lett.* **59**, 2931 (1987).
 - [8] D.J. Wineland, J.C. Bergquist, W.M. Itano, J.J. Bollinger, and C.H. Manney, *Phys. Rev. Lett.* **59**, 2935 (1987).
 - [9] R.G. Brewer, J. Hoffnagle, R.G. DeVoe, L. Reyna, and W. Henshaw, *Nature (London)* **344**, 305 (1990).
 - [10] M.G. Raizen, J.M. Gilligan, J.C. Bergquist, W.M. Itano, and D.J. Wineland, *Phys. Rev. A* **45**, 6493 (1992). The trap asymmetry reported in this reference has been greatly reduced.
 - [11] W.M. Itano and D.J. Wineland, *Phys. Rev. A* **25**, 35 (1982).
 - [12] N.W. Ashcroft and N.D. Mermin, *Solid State Physics* (Saunders College, Philadelphia, 1976), Appendix N.
 - [13] W. Heitler, *The Quantum Theory of Radiation* (Dover, New York, 1984), p. 194.
 - [14] W.M. Itano, J.C. Bergquist, R.G. Hulet, and D.J. Wineland, *Phys. Rev. Lett.* **59**, 2732 (1987).
 - [15] M.O. Scully, B.-G. Englert, and H. Walther, *Nature (London)* **351**, 111 (1991).
 - [16] D. Polder and M. F. H. Schuurmans, *Phys. Rev. A* **14**, 1468 (1976).
 - [17] L. Mandel, *Phys. Rev. A* **28**, 929 (1983); C.K. Hong, Z.Y. Ou, and L. Mandel, *Phys. Rev. A* **37**, 3006 (1988).

LIGHT SCATTERED FROM TWO ATOMS*

W. M. Itano, U. Eichmann,** J. C. Bergquist, J. J. Bollinger,
J. M. Gilligan,† M. G. Raizen,†† and D. J. Wineland

National Institute of Standards and Technology
325 Broadway Street
Boulder, Colorado 80303

Abstract

We have observed interference fringes, like those in Young's classic experiment, in the laser light scattered from two trapped atoms. The interference fringes are present only in one polarization of the scattered light. The polarization dependence is related to the complementarity principle, which forbids the simultaneous observation of wave-like and particle-like aspects of light. The interference fringes are due to processes in which a single photon scatters from two atoms. We describe methods which might be used to observe other interference effects due to two photons scattering from two atoms.

Introduction

We have observed Young's interference fringes resulting from the light scattered from two atoms. In Young's original experiments, sunlight, passing through two slits, produced a pattern of closely-spaced fringes on another screen. Those observations established the wave nature of light and resulted in the first accurate determination of the wavelength of light.¹

Interference experiments of this form have played an important part in the conceptual development of quantum mechanics. Either matter (electrons, for example) or light can display interference (a wave-like property). However, if it is possible to infer which slit the matter or light passed through, thereby extracting a particle-like property, interference is not observed. Wave-particle duality is a particular example of a more general principle, the principle of complementarity, which states, "For each degree of freedom, the dynamical variables are a pair of complementary variables."² Variables are complementary if a precise determination of one implies an inability to predict the other. For example, the position and momentum of a particle are complementary variables, since, according to Heisenberg's uncertainty principle, the product of their uncertainties must be greater than $\hbar/2$. In our experiments, in contrast to various *gedanken* experiments, complementarity is enforced in a manner which does not require the position-momentum uncertainty relations.

Experimental Apparatus

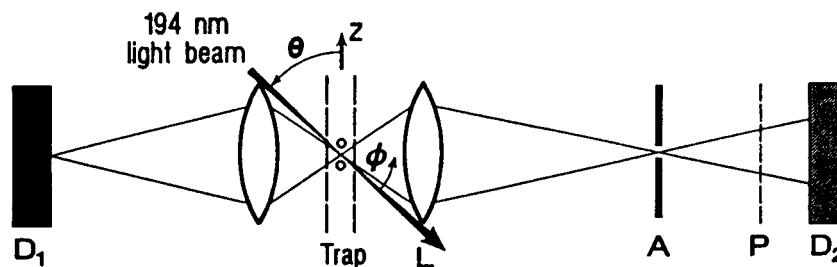


Figure 1: Diagram of the experimental apparatus.

Figure 1 shows the experimental apparatus, which has been described previously.³ A linear rf trap⁴ was used to confine $^{198}\text{Hg}^+$ ions. In $^{198}\text{Hg}^+$, the lowest-frequency electric-dipole transition is from the ground $6s^2S_{1/2}$ level to the $6p^2P_{1/2}$ level at 194 nm. The ions were laser-cooled to temperatures of a few millikelvins with a beam of linearly polarized,

*Work of the National Institute of Standards and Technology. Not subject to U.S. copyright.

**Present address: Max Born Institut, Berlin, Germany.

†Present address: Environmental Research Laboratory, National Oceanic and Atmospheric Administration, Boulder, Colorado.

††Present address: Department of Physics, University of Texas, Austin, Texas.

continuous-wave light. Cooling in the trap resulted in strong localization of the ions, which is essential for observation of interference fringes. The trap potentials were arranged so that a pair of ions would be oriented along the symmetry (z) axis of the trap. The laser beam intersected the ions at an angle θ of 62° with respect to the trap axis. Light emitted by the ions was focused by a lens L through an aperture A and then directed to the surface of an imaging detector D_2 . This detector was used to observe the fringes. The axis of the detection optics was in the plane defined by the laser beam and the trap axis. The in-plane detection angle ϕ varied from 15° to 45° with respect to the laser beam direction. The out-of-plane detection angle varied from -15° to $+15^\circ$. Optionally, a linear polarizer P was inserted before D_2 . Another lens system formed a real image of the ions on another imaging detector D_1 . This image was used to determine when there were precisely two ions in the trap.

One-Photon Two-Atom Scattering

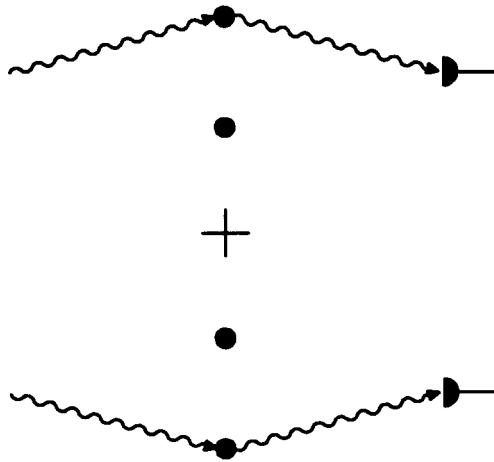


Figure 2: The two paths which contribute to the Young's interference fringes. The paths correspond to the photon being scattered by one atom or the other and then being detected.

Our version of Young's interference experiment, in which the two slits are replaced by two atoms, is an example of a case in which each photon interferes only with itself. (We call this second-order interference, i.e., second-order in the fields, in order to distinguish it from other forms of interference to be discussed later.) From the point of view of quantum mechanics, we expect interference whenever there are two or more possible paths from a given initial state to the same final state. The absolute square of the sum of the complex amplitudes assigned to these paths yields the probability for the final state. The two paths which yield the interference are represented by the two parts of Fig. 2. In each path, the photon, represented by the wavy arrow, is scattered by one of the two atoms, represented by circles, and reaches the detector, represented by the half circle. After the photon is detected, there is no way to tell which atom scattered it, i.e., which of the two paths the system took.

Interference fringes were obtained for ion separations varying from $9 \mu\text{m}$ to $3.3 \mu\text{m}$. The angular separation of the fringes increased as the distance between the ions was decreased. The fringe visibility was observed to decrease with increasing ϕ .

An example of interference data is shown in Fig. 3. The two ions were separated by $3.4 \mu\text{m}$. The angular separation of successive fringes is about 3° . The angle ϕ between the incident and scattered photon directions increases to the

right. The dependence of the fringe spacing on the ion separation and the variation in the fringe visibility with angle are contained in the following expression for the intensity I of the scattered light as a function of \vec{q} , where $\hbar\vec{q} = \hbar(\vec{k}_{\text{out}} - \vec{k}_{\text{in}})$, and \vec{k}_{in} and \vec{k}_{out} are the wavevectors of the incoming and outgoing photons:

$$I(\vec{q}) = 2I_0 \left[1 + \cos(q_z d) \exp \left\{ - \langle [\vec{q} \cdot (\vec{u}_1 - \vec{u}_2)]^2 \rangle / 2 \right\} \right]. \quad (1)$$

In this expression, I_0 is the intensity due to scattering by a single ion, d is the ion separation, and \vec{u}_1 and \vec{u}_2 are the displacements of the ions 1 and 2 from their equilibrium positions. The angular brackets denote an ensemble average. Equation (1) was derived by methods similar to those used for Bragg scattering by a harmonic crystal.^{3, 5} The fringe separation is contained in the factor $\cos(q_z d)$ and is therefore inversely proportional to d . The fringe visibility depends on the quantity $\langle [\vec{q} \cdot (\vec{u}_1 - \vec{u}_2)]^2 \rangle$. The visibility is greatest in the forward scattering direction, where $\vec{q} = 0$, and decreases with increasing scattering angle and with increasing ion temperature. The temperature of the ions has been determined from the rate of decrease in fringe visibility with angle and is approximately equal to the theoretically calculated value.³

The data shown in Fig. 3 were obtained with polarization-insensitive detection. When a linear polarizer was placed in front of the detector, the fringes were present only in the light having polarization in the plane defined by the polarization of the incident light and \vec{k}_{out} (π -polarization) and not in the light having the orthogonal polarization (σ -polarization). Figure 4 shows interference patterns observed in (a) π -polarized and (b) σ -polarized light. The π -polarization shows high fringe visibility, while the σ -polarization shows no fringes, only the slow variation with scattering angle of the detection sensitivity.

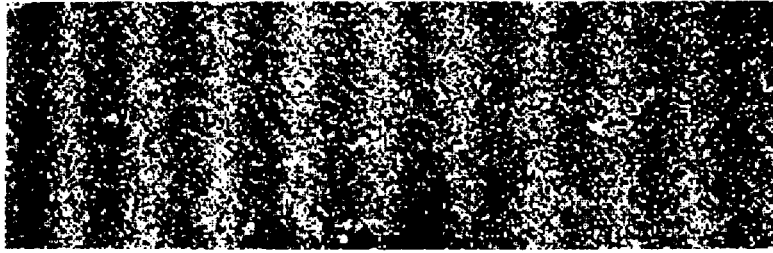


Figure 3: Interference fringes observed for an ion separation of $3.4 \mu\text{m}$. The deviation from the forward scattering direction increases to the right.

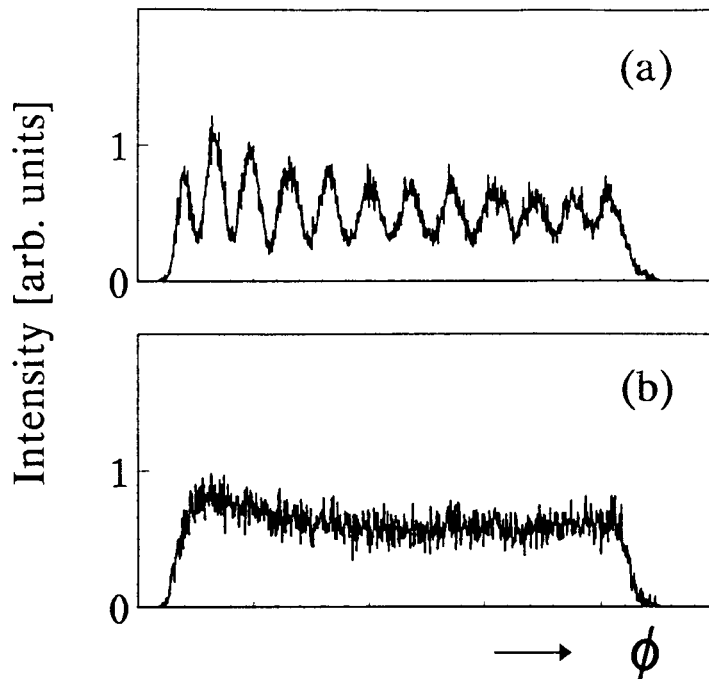


Figure 4: Intensity of the scattered light from two ions as a function of the scattering angle ϕ . (a) π -polarized light. (b) σ -polarized light. Only the π -polarized light shows interference fringes. The data are not normalized for the detection efficiency, which varies with ϕ .

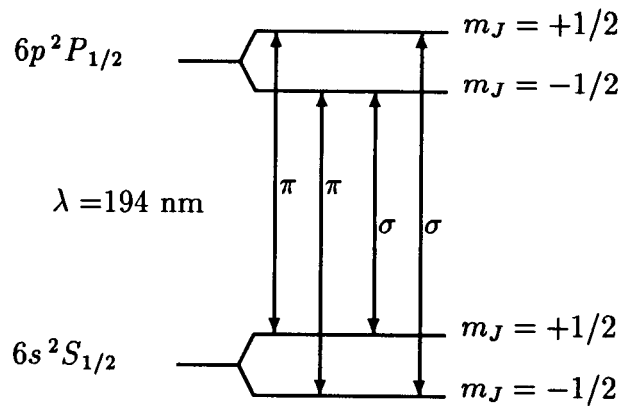


Figure 5: Zeeman sublevels involved in the 194 nm, $6s^2 S_{1/2}$ -to- $6p^2 P_{1/2}$ transition of $^{198}\text{Hg}^+$. The allowed π and σ transitions are labeled. The Zeeman splitting of the levels is exaggerated.

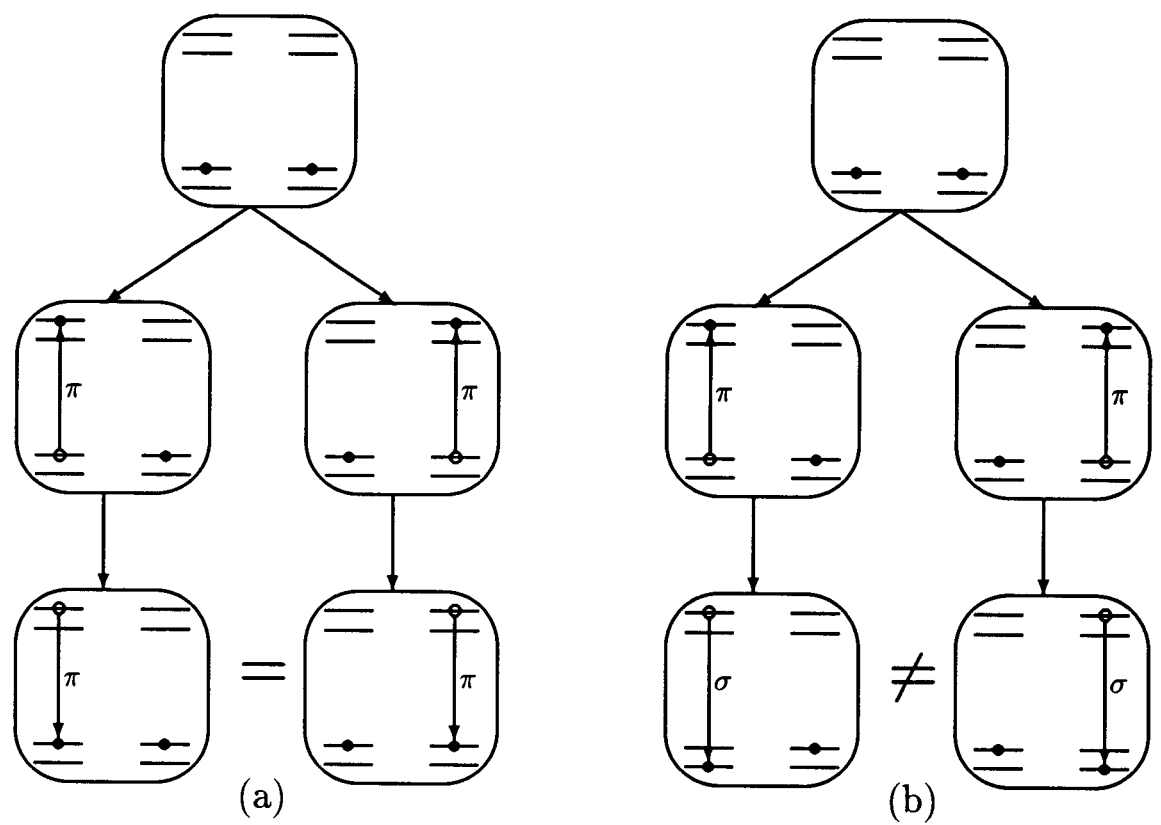


Figure 6: Each box represents the combined state of the two atoms. The ordering of energy levels is the same as in Fig. 5. In (a), a π -transition is made from the ground state to the excited state and is followed by a π -transition back to the ground state. There are two possible paths, both of which lead to the same final state, so that interference is possible. In (b), the π -transition from the ground to excited state is followed by a σ -transition back to the ground state. The two paths do not lead to the same final state, so there is no interference.

The source of the polarization dependence of the fringe visibility lies in the internal level structure of the $^{198}\text{Hg}^+$ ion and in basic principles of quantum mechanics. Figure 5 shows the magnetic sublevels involved in the $6s^2S_{1/2}$ -to- $6p^2P_{1/2}$ transition. The static magnetic field is small enough that we are free to define the quantization axis of the ions to be along the electric polarization vector of the incident light. If the static magnetic field is along some other direction, then the Zeeman sublevels defined according to the electric polarization vector are not stationary states. This does not change the analysis as long as the Zeeman precession frequency is much less than the inverse of the scattering time, which is approximately equal to the $6p^2P_{1/2}$ -state lifetime (2.3 ns). In the experiments described here, the magnetic field was small enough that this was always the case.

The π -transitions ($\Delta m_J = 0$) and σ -transitions ($\Delta m_J = \pm 1$) are labelled in Fig. 5. The incident laser light drives only π -transitions from the ground to the excited state. However, the decay from the excited state to the ground state can be either a π -transition or a σ -transition. If the decay is a π -transition, the atom returns to the same m_J sublevel it occupied before it absorbed a photon. Hence, it is not possible to tell, by examining the atoms, which one scattered the photon. On the other hand, if the decay is a σ -transition, the atom returns to a different m_J sublevel and it would be possible in principle to examine the atoms after the scattering and tell which one scattered the photon. In the context of the principle of complementarity, a particle-like property is present, and interference, a wave-like property, must vanish.

From a more modern point of view, we say that interference occurs when there is more than one transition amplitude connecting the initial and final states.⁶ Figure 6 illustrates this point of view. There are four possible initial states of the combined system of two atoms, since each atom can be in either of two m_J sublevels. We consider a particular initial state, in which both atoms are in the $m_J = +1/2$ sublevel. All four choices of initial states contribute to the interference fringes in the same way. In Fig. 6(a), a π -polarized photon is absorbed and a π -polarized photon is emitted. There are two paths for this process. Since they lead to the same final state, interference can occur. In Fig. 6(b), a π -polarized photon is absorbed and a σ -polarized photon is emitted. There are two paths for this process. However, they lead to different final states, so there is no interference.

Polder and Schuurmans⁷ calculated the spectrum of resonance fluorescence from a ($J = 1/2$)-to-($J = 1/2$) transition. They found that, for low intensities, the π -polarized scattered light is coherent with the incident light, while the σ -polarized scattered light is not. Thus, it is reasonable that the π -polarized light should show interference fringes while the σ -polarized light should not. The fringe visibility for the π -polarized light should decrease with intensity, since, as is the case for two-level atoms,^{8, 9} the ratio of incoherent scattering to coherent scattering increases with intensity. The intensity dependence of the visibility has not yet been examined experimentally.

Two-Photon Two-Atom Scattering

Next, we consider the interference process represented by Fig. 7. Two photons are scattered by two atoms and are each detected at different spatial positions. However, it is not possible to tell which atom scatters which photon, so there is interference between the two paths. This is a kind of fourth-order interference (i.e., fourth-order in the fields), which can persist even when there is no second-order interference. The interference effects that we have labeled fourth-order and second-order are called second-order and first-order, respectively, by others,⁹ since they are second-order and first-order in the intensities.

Interference by independent quantum sources has been discussed in detail by various authors.^{10, 11} If the sources are independent, there is no stationary interference pattern. However, both classical and quantum calculations predict intensity correlations between two detectors. In particular, if the sources are two single atoms, there will be a finite coincidence rate if the detectors are separated by n interference fringes ($n=0, 1, 2, \dots$) and no coincidences if the detectors are separated by $n + 1/2$ fringes.¹⁰ In this case, the quantum calculation predicts a fringe visibility of 1, while the corresponding classical calculation predicts a visibility less than or equal to 1/2. The difference arises from the fact that a single atom cannot emit two photons simultaneously. After emitting one photon, it must be excited to the upper state again before it can emit another. In the classical calculation, the simultaneous detection of two photons emitted by the same atom is allowed, and this gives rise to a background signal that reduces the fringe visibility. The observation of a fringe visibility greater than 1/2 for independently phased atoms would thus be an example of a quantum phenomenon having no classical analog.

Consider a simple case originally treated by Dicke.¹² Two two-level atoms are both in the excited state and are separated by much more than the wavelength of the light that they emit (see Fig. 8). This state can be written as $|e\rangle_1|e\rangle_2$, where e denotes the excited state of an atom and 1 and 2 label the two atoms. The first photon can be emitted in any direction consistent with the dipole radiation pattern of a single atom. The state of the atoms immediately after the first photon has been emitted can be symmetric, i.e., $(|e\rangle_1|g\rangle_2 + |g\rangle_1|e\rangle_2)/\sqrt{2}$, or antisymmetric, i.e., $(|e\rangle_1|g\rangle_2 - |g\rangle_1|e\rangle_2)/\sqrt{2}$, where g denotes the ground state of an atom. In general, the state can be a linear combination of these two cases.

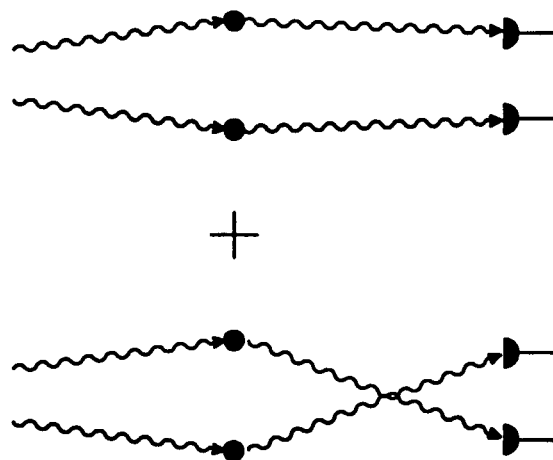
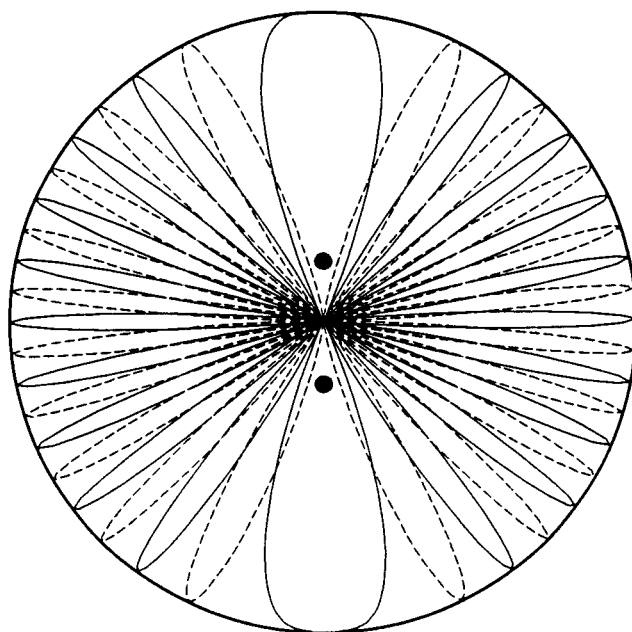


Figure 7: The two paths which contribute to fourth-order interference fringes. The paths correspond to each of the two photons being scattered by one of the two atoms and then being detected by one of the two detectors.



- Symmetric
- - - Antisymmetric
- Atoms

Figure 8: Radiation patterns for two atoms (indicated by circles) separated by 5 wavelengths and initially both in the excited state. The solid curve is for the case in which, after the emission of one photon, the atoms are in a symmetric state. The dashed curve is for the case in which they are in an antisymmetric state.

Like the radiation pattern of pair of classical dipoles, the probability distribution for the emission of the second photon is made up of many interference fringes. A pair of classical dipoles has a pattern which shifts according to their relative phases. Here, the pattern shifts according to the relative phases of the wavefunctions of the two atoms. Figure 8 shows an example, for a separation of five wavelengths. If the wavefunction is symmetric with respect to the two atoms, the radiation pattern is given by the solid curve. If it is antisymmetric, it is given by the dashed curve. If it is a linear combination of symmetric and antisymmetric wavefunctions, it is intermediate between the two curves.

The direction of the second photon is constrained by the direction of the first. It cannot be in a direction differing by $n + 1/2$ fringes and has the greatest probability of differing by n fringes. The emission of the first photon fixes the symmetry of the wavefunction and hence the probability distribution for the emission of the second photon. The symmetry must be such that the direction of the first photon is along a fringe (lobe) of the radiation pattern. It is important to remember that each photon is emitted by *both* atoms. If, after the emission of the first photon, a measurement is made to determine which of the atoms is in the excited state, the coherent superposition is totally destroyed, and the second photon can be emitted in any direction.

Consider the following modification of the experiment. Wait until the first photon is detected. Its direction of emission fixes the symmetry of the wavefunction. Then, before the second photon is emitted, change the separation between the atoms to a different value. In an ion trap, this can be done by changing the electric potentials on the electrodes. This changes the radiation pattern, adding or subtracting fringes. The second photon will be emitted into a fringe of the new radiation pattern. Thus, the second photon can be aimed toward certain directions and away from others by controlling the distance between the atoms.

Estimated Signals

Experimentally, a higher data-collection rate could be achieved by exciting the atoms continuously and using coincidence detection, rather than by sequentially exciting the atoms and then detecting the emitted photons. It should be possible to observe fourth-order interference with a slight modification of the present experimental apparatus. Two imaging detectors would be used, together with fast coincidence electronics. In order to avoid the intensity variations due to the second-order interference [as in Fig. 4(a)], only the σ -polarized light should be detected. For each coincidence, the position of both photons would be recorded.

Let R_{coinc} be the detected coincidence rate. Then,

$$R_{\text{coinc}} = 2(\eta R_{\text{scatt}})^2 \delta\tau, \quad (2)$$

where η is the fraction of scattered photons that are detected, R_{scatt} is the rate at which photons are scattered by one atom, and $\delta\tau$ is the coincidence time window. A reasonable value for η is 10^{-3} , assuming a detection solid angle of 1% and a detector quantum efficiency, including the polarizer efficiency, of 10%. If the incident light intensity is high enough to saturate the transition, R_{scatt} approaches $\gamma/2$, where γ is the decay rate of the upper state. The coincidence time window $\delta\tau$ should be less than the coherence time for the fourth-order interference, which is less than or approximately equal to γ^{-1} . If we let $\delta\tau \approx 0.25\gamma^{-1}$, then

$$R_{\text{coinc}} \approx 1.25 \times 10^{-7} \gamma. \quad (3)$$

For Hg^+ , where $\gamma \approx 4.3 \times 10^8 \text{ s}^{-1}$, $R_{\text{coinc}} \approx 54 \text{ s}^{-1}$. Thus, it should be possible to observe a fringe pattern with a few minutes of observation time.

Other ions might be better suited than Hg^+ for this experiment. For example, Mg^+ has a smaller mass, thus allowing better spatial localization, and a longer resonance wavelength, thus allowing the use of more efficient detectors and polarizers. On the other hand, it has a smaller value of γ than Hg^+ ($\gamma \approx 2.7 \times 10^8 \text{ s}^{-1}$).

It would also be of interest to observe the coincidences in the π -polarized light, particularly in the high-intensity limit. In this limit, the second-order interference disappears, but the fourth-order interference remains.⁹ The visibility of the fourth-order interference fringes is 1 for arbitrary intensity, but the time window during which it can be observed decreases with intensity.

Quantum Erasers

The term “quantum eraser” was used by Scully and Drühl¹³ to describe a *gedanken* experiment involving the observation of interference fringes in the light scattered by two atoms. Other forms of quantum erasers have been described.^{14, 15} The common element is that interference is destroyed when it is possible to tell, in principle, which path the system has taken, and is recovered when that information is erased or hidden. In Scully and Drühl’s original proposal, two atoms are excited by a laser pulse. In the case of two-level atoms, interference fringes are observed, as in the case of

π -polarized emission discussed in the previous Section. In the case of three-level atoms, interference is not observed when the light emission from the atoms is accompanied by a transition to a level different than the one occupied before the laser pulse. This is because it is possible to tell which atom scattered the photon, as in the previous case of σ -polarized emission. This information is erased by exciting the atoms to a fourth level, from which they decay back to the initial level. Fringes are recovered, but only in a coincidence measurement, which is in principle similar to the fourth-order interference experiment that we have proposed. The experiment can be operated in a “delayed choice” mode. That is, the interference fringes can be made to appear or not, depending on whether or not a shutter is operated, even though this is done after the photon is on its way to the detector.

The fourth-order interference experiment we have proposed is a kind of quantum eraser, though, in common with some other quantum erasers,^{14, 15} it lacks the “delayed-choice” feature. If we detect only the σ -polarized light, no interference fringes are detected in a non-coincidence experiment. In principle the states of the atoms could have been measured before and after the photon scattering, and it would be possible to tell which atom scattered the photon. In a coincidence detection, *both* atoms have scattered a photon and have changed their states. However, it is impossible to tell *which* atom scattered *which* photon. That is, it is impossible to tell which of the paths shown in Fig. 7 the system took. This is what makes it possible to observe interference fringes.

Conclusion

We have observed Young’s interference fringes in the light scattered from two localized atoms. The interference patterns can be used to infer the separation and temperature of the two atoms. The fact that the interference appears only for one polarization of the light has a simple explanation based on the fact that only paths leading to the same final state can interfere. Fourth-order interference effects might be observed by detecting coincidences in two photon detectors.

This work was supported by the Office of Naval Research.

References

- [1] In *Great Experiments in Physics*, edited by M. H. Shamos (Henry Holt and Company, New York, 1959), p. 93.
- [2] M. O. Scully, B.-G. Englert, and H. Walther, *Nature* **351**, 111 (1991).
- [3] U. Eichmann, J. C. Bergquist, J. J. Bollinger, J. M. Gilligan, W. M. Itano, D. J. Wineland, and M. G. Raizen, *Phys. Rev. Lett.* **70**, 2359 (1993).
- [4] M. G. Raizen, J. M. Gilligan, J. C. Bergquist, W. M. Itano, and D. J. Wineland, *Phys. Rev. A* **45**, 6493 (1992).
- [5] N. W. Ashcroft and N. D. Mermin, *Solid State Physics* (Saunders College, Philadelphia, 1976), Appendix N.
- [6] C. Cohen-Tannoudji, J. Dupont-Roc, and G. Grynberg, *Photons and Atoms* (Wiley, New York, 1989), pp. 204–215.
- [7] D. Polder and M. F. H. Schuurmans, *Phys. Rev. A* **14**, 1468 (1976).
- [8] B. R. Mollow, *Phys. Rev.* **188**, 1969 (1969).
- [9] Th. Richter, *Opt. Commun.* **80**, 285 (1991).
- [10] L. Mandel, *Phys. Rev. A* **28**, 929 (1983).
- [11] H. Paul, *Rev. Mod. Phys.* **58**, 209 (1986).
- [12] R. H. Dicke, in *Quantum Electronics*, proceedings of the Third International Conference, Paris, edited by P. Grivet and N. Bloembergen (Columbia University Press, New York, 1964) p. 35.
- [13] M. O. Scully and K. Drühl, *Phys. Rev. A* **25**, 2208 (1982).
- [14] P. G. Kwiat, A. M. Steinberg, and R. Y. Chiao, *Phys. Rev. A* **45**, 7729 (1992).
- [15] A. G. Zajonc, L. J. Wang, X. Y. Zou, and L. Mandel, *Nature* **353**, 507 (1991).

Electrostatic modes of ion-trap plasmas

J. J. Bollinger, D. J. Heinzen,* F. L. Moore,* Wayne M. Itano, and D. J. Wineland
Time and Frequency Division, National Institute of Standards and Technology, Boulder, Colorado 80303

Daniel H. E. Dubin

Department of Physics, University of California at San Diego, La Jolla, California 92093

(Received 4 January 1993)

The electrostatic modes of a non-neutral plasma confined in a Penning or Paul (rf) trap are discussed in the limit that the Debye length is small compared to the plasma dimensions and the plasma dimensions are small compared to the trap dimensions. In this limit the plasma shape is spheroidal and analytic solutions exist for all of the modes. The solutions for the modes of a Paul-trap plasma are a special case of the modes of a Penning-trap plasma. A simple derivation of some of the low-order quadrupole modes is given. Experimental measurements of these mode frequencies on plasmas of laser-cooled Be^+ ions in a Penning trap agree well with the calculations. A general discussion of the higher-order modes is given. The modes provide a nondestructive method for obtaining information on the plasma density and shape. In addition, they may provide a practical limit to the density and number of charged particles that can be stored in a Penning trap.

PACS number(s): 32.80.Pj, 32.90.+a, 52.25.Wz, 52.35.Fp

I. INTRODUCTION

Penning traps [1,2] typically use a uniform magnetic field superimposed along the axis of azimuthally symmetric electrodes to confine charged particles. Radial confinement is provided by the axial magnetic field and axial confinement is provided by electrostatic potentials applied to the trap electrodes (see Fig. 1). Paul (rf) traps [1] use an electrode structure similar to Penning traps, but there is no magnetic field, and a combination of rf and electrostatic potentials are applied to trap electrodes. Charged particles are confined by the inhomogeneous rf fields (the ponderomotive force) to a region of minimum rf field strength near the trap center. Penning and Paul traps are used in a number of studies on charged atomic particles such as mass spectroscopy [3–8], high-precision magnetic-moment measurements [1,9,10], high-resolution spectroscopy and frequency standards [1,11–14], charge-transfer studies [15], non-neutral-plasma studies [2,16–21], and antimatter storage [7,22–24]. In many of these experiments more than one charged atomic particle (a “cloud”) are stored in the trap and cooled to low temperatures. A cloud of charged particles in a Penning trap can be considered a plasma, in particular a non-neutral plasma, when the Debye length is less than the cloud dimensions. This paper discusses the electrostatic modes of these plasmas in the limit that the Debye length is much less than the plasma dimensions and when the plasma dimensions are small compared to the trap dimensions. As discussed below, the modes of a Paul-trap plasma are described by a special case of the Penning-trap plasma modes. Therefore in this paper we concentrate our discussion on the modes of Penning-trap plasmas and show how solutions for the modes of an rf-trap plasma follow from the Penning-trap results.

Measurement of the plasma mode frequencies may have applications for ion trap experiments. For example,

mass spectroscopy experiments done with a cloud or plasma of ions in a Penning trap can have systematic shifts associated with the distances of the ions from the trap center and the small anharmonicities of the trapping po-

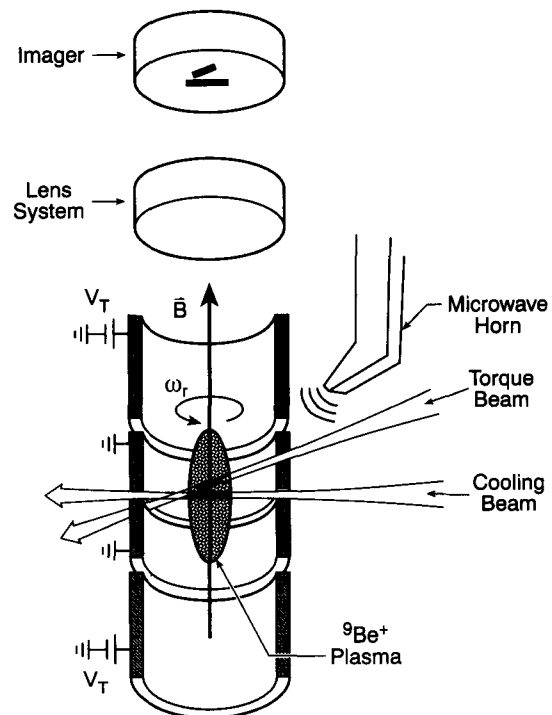


FIG. 1. Sketch of a Penning trap used to make mode measurements on a plasma of ${}^9\text{Be}^+$ ions. The size of the plasma is exaggerated. The trap electrodes (shown in cross section) are right circular cylinders with inner radius $\rho_0 = 1.27$ cm. They provide a quadratic potential near the trap center with $A_2 = 0.236$. Some other Penning traps use hyperboloids of revolution as trap electrodes. The laser beams, microwave horn, and imaging system are used in the measurement of the plasma modes as described in Sec. IV.

tential [6,25,26]. In high-resolution atomic spectroscopy of ions in a Penning trap, one of the largest systematic shifts is the second-order Doppler shift associated with the $\mathbf{E} \times \mathbf{B}$ rotation of the ions about the magnetic field axis of the trap [12]. The larger the radius of the plasma, the larger the second-order Doppler shift. A third application is illustrated by experiments which measure electron-ion recombination by passing an electron beam through a sample of ions trapped in a Penning trap [27]. In these studies, it would be desirable to have a direct knowledge of the geometrical overlap of the electron beam with the ion sample. In all of the above examples, the plasma shape and density, along with the number of trapped ions, determine the radial and axial positions of the ions and therefore the size of the required corrections. Similar considerations apply to experiments on ions in a Paul trap. In some cases the plasma shape and density can be determined with a laser [20,28]. When this or other techniques are not available, detection of the plasma modes, perhaps through induced image currents in the trap electrodes, could provide this information.

Recent experiments have trapped positron [23] and antiproton [7,24] plasmas in Penning traps. The current techniques for obtaining information about these plasmas involves ejecting the plasma from the trap. Detection of the plasma modes should provide a nondestructive diagnosis for obtaining information on the antimatter plasma density, temperature, and shape. A goal of the antimatter work is the high-density storage of large numbers of positrons and antiprotons for transport to different laboratories around the world. Field errors in the trapping potential can excite plasma modes and enhance radial transport. Excitation of the plasma modes may therefore set a practical limit on the density and number of antiparticles that can be stored in a Penning trap.

In addition to having potential applications to current experiments, the electrostatic modes of a Penning-trap plasma may also provide a tool for studying the dynamics of non-neutral and strongly coupled plasmas. A simple, analytic form has been obtained for all of the electrostatic modes of a low-temperature Penning-trap plasma [29]. This is the only finite length geometry for which exact mode eigenfrequencies and eigenfunctions have been calculated. Therefore the Penning trap may provide an interesting geometry for the study of plasma modes and their importance to the dynamical behavior of non-neutral plasmas. For example, it should be possible to study how errors in the trapping fields couple to the plasma modes and enhance radial transport [19]. Measurement of the damping of the modes should provide information on the plasma's viscosity. This measurement could presumably be done with a strongly correlated plasma over a range of magnetic field strengths where very little information is available.

In Sec. II we review the static properties of a cold, Penning-trap plasma in thermal equilibrium. We assume the trapped particle number $N \gg 1$. For sufficiently low temperature or small Debye length, the plasma has constant density. If the plasma dimensions are small compared to the trap electrode dimensions, then the confining

potential may be assumed to be quadratic and the effect of image charges neglected. In this case, the plasma has a spheroidal boundary with an aspect ratio determined by the plasma density and the axial restoring force of the trap. This is the starting point for describing and calculating the modal excitations of a plasma in thermal equilibrium. In Sec. III we describe a simple but exact calculation for some of the quadrupole modes of a spheroidal Penning-trap plasma. We show how these modes could be used to measure the density and shape of a Penning-trap plasma. Section IV compares the results of the quadrupole mode calculations with measurements [21] done on about 2000 laser-cooled ${}^9\text{Be}^+$ ions in a Penning trap. In that section we show how a zero-frequency quadrupole mode was excited by a misalignment of the magnetic field axis with respect to the electrostatic symmetry axis of the trap. Excitation of this mode tended to limit the plasma density. Section V discusses the higher-order modes of a Penning-trap plasma [29]. Modes that can be excited by static field errors are identified.

II. STATIC PROPERTIES

The Penning trap shown in Fig. 1 consists of four cylindrical electrodes. The outer cylinders are called the "end-cap" electrodes in analogy with the end caps of a hyperbolic Penning trap [1]. The inner cylinders are electrically shorted and together called the "ring" electrode. With a positive potential V_T applied to the end-cap electrodes with respect to the ring electrode, positively charged particles (ions) can be electrostatically confined in the direction of the trap axis. A static, uniform magnetic field $\mathbf{B} = B\hat{z}$ parallel to the trap's symmetry axis confines the ions in the radial direction. Near the center of the trap, where the ions are confined, the radial component of the trap electric field is directed outward. This field produces an $\mathbf{E} \times \mathbf{B}$ circular drift of the ions about the symmetry axis of the trap. As the ions rotate through the magnetic field, they experience a Lorentz force directed radially inward.

With sufficiently long confinement, the ions evolve to a state of thermal equilibrium characterized by a uniform "rigid" rotation of the ions at a frequency ω_r [18,28,30]. Specifically, the rotation frequency ω_r is independent of radius. In the limit of zero temperature, the plasma density n_0 and plasma frequency ω_p are constant in the plasma interior and drop abruptly to 0 at the plasma edge. The density depends on the rotation frequency according to (Système International units are used throughout)

$$n_0 = \frac{2\epsilon_0 m \omega_r (\Omega - \omega_r)}{q^2}, \quad (2.1)$$

where $\Omega = qB/m$ is the ion cyclotron frequency, q and m are the charge and mass of the ion, and ϵ_0 is the permittivity of the vacuum. The plasma frequency is therefore related to the rotation frequency through the equation

$$\omega_p^2 \equiv \frac{q^2 n_0}{\epsilon_0 m} = 2\omega_r (\Omega - \omega_r). \quad (2.2)$$

In this paper we use the convention that the symbols ω_r ,

and Ω denote positive quantities. However, for positive ions, the sense of the rotation and the sense of the cyclotron motion with respect to \mathbf{B} are actually negative. Specifically, when viewed from above the x - y plane, the ions move in clockwise orbits. For nonzero temperatures, the density drops to 0 at the plasma edge in a distance on the order of a Debye length λ_D [18,30], where

$$\lambda_D = \left[\frac{\epsilon_0 k T}{n_0 q^2} \right]^{1/2}, \quad (2.3)$$

k is Boltzmann's constant, and T is the ion temperature. For $\lambda_D \ll$ (plasma dimensions), the plasma therefore has a uniform density, given by Eq. (2.1), with sharp boundaries. For very low temperatures, there are correlations in the ion positions [20,31,32], and the ion density is not constant over length scales small compared to the interion spacing ($\sim n_0^{-1/3}$). However, as long as the interion spacing is small compared to the plasma dimensions (that is, as long as the number of ions $N \gg 1$) and small compared to the wavelength of the plasma modes, the plasma can be treated as a constant-density plasma even in the presence of spatial correlations.

The plasma boundary has a simple shape in the limit that the plasma dimensions are small compared to the trap dimensions [28,33]. Near its center, the electrostatic potential of the trap, relative to the potential at the trap center, can be written as

$$\phi_T(r, z) = \frac{m \omega_z^2}{4q} (2z^2 - r^2), \quad (2.4)$$

where r and z are cylindrical coordinates, and ω_z is the frequency at which a single trapped ion (or the center-of-mass of a cloud of ions) oscillates along the z axis. For the cylindrical trap of Fig. 1,

$$\omega_z = \left[\frac{4q V_T A_2}{m \rho_0^2} \right]^{1/2}, \quad (2.5)$$

where ρ_0 is the inner radius of the trap electrodes and A_2 is a dimensionless parameter that depends on the geometry of the trap design. For the trap of Fig. 1, $A_2 = 0.236$. In general, the total electrostatic potential is the sum of the trap potential, the space-charge potential of the ions, and a potential due to the induced image charges on the trap electrodes. If the plasma dimensions are much less than the trap dimensions, the trap potential over the region of the plasma is given by Eq. (2.4), and the effect of the induced image charges can be neglected. In this case the shape of the plasma boundary is a spheroid (an ellipsoid of revolution) as shown in Fig. 2 [28,33]. Let $2r_0$ and $2z_0$ denote the diameter and the axial extent of the plasma as shown in Fig. 2. The plasma aspect ratio $\alpha \equiv z_0/r_0$ is related [28] to the plasma frequency ω_p and the trap axial frequency ω_z by

$$\frac{\omega_z^2}{\omega_p^2} = Q_1^0 \left[\frac{\alpha}{(\alpha^2 - 1)^{1/2}} \right] / (\alpha^2 - 1), \quad (2.6)$$

where Q_l^m is the associated Legendre function of the second kind [34]. When the plasma is a prolate spheroid

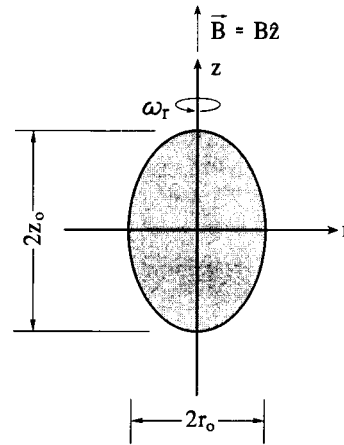


FIG. 2. Spheroidal shape of a Penning-trap plasma. This shape is obtained under the conditions of thermal equilibrium and $\lambda_D \ll$ (plasma dimensions) \ll (trap dimensions).

($\alpha > 1$), Eq. (2.6) can be written as

$$\frac{\omega_z^2}{\omega_p^2} = \frac{1}{\alpha^2 - 1} \left[\frac{u_p}{2} \ln \left(\frac{u_p + 1}{u_p - 1} \right) - 1 \right], \quad u_p \equiv \frac{\alpha}{(\alpha^2 - 1)^{1/2}}. \quad (2.7)$$

When the plasma is an oblate spheroid ($\alpha < 1$), Eq. (2.6) can be written as

$$\frac{\omega_z^2}{\omega_p^2} = \frac{1}{\alpha^2 - 1} \left[u_0 \tan^{-1} \left(\frac{1}{u_0} \right) - 1 \right], \quad u_0 \equiv \frac{\alpha}{(1 - \alpha^2)^{1/2}}. \quad (2.8)$$

Figure 3 shows a graph of ω_z^2/ω_p^2 versus the plasma aspect ratio α . Experimental measurements of ω_z , ω_p , and α discussed in Ref. [28] are in good agreement with the

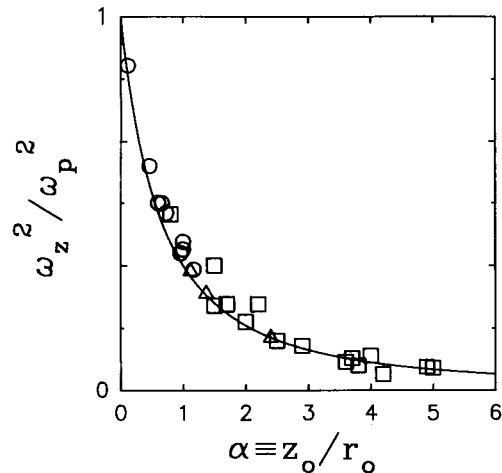


FIG. 3. Relationship between the plasma aspect ratio α and ω_z^2/ω_p^2 for spheroidal-shaped plasmas in a Penning trap. The solid line is a theoretical curve from Eq. (2.6) with no adjustable parameters. The experimental measurements, described in Ref. [28], were taken with two different traps at three different axial frequencies between $\omega_z/\Omega = 0.071$ and 0.121 .

theoretical calculation of Eq. (2.6).

In the next section the potential inside a uniformly charged spheroid (the space-charge potential of a cold Penning-trap plasma) will be used to calculate some of the quadrupole mode frequencies. For r, z inside the plasma, the space-charge potential ϕ_I can be written [28,33,35] as

$$\phi_I(r, z) = -\frac{m\omega_p^2}{6q} [a(\alpha)r^2 + b(\alpha)z^2], \quad (2.9)$$

where α is the plasma aspect ratio, ω_p is the plasma frequency given by Eq. (2.2), $b(\alpha) = 3Q_1^0(\alpha/(\alpha^2-1)^{1/2})/(\alpha^2-1)$, and Poisson's equation requires $2a(\alpha) + b(\alpha) = 3$. A spherical plasma has $a = b = 1$. At the limit $b = 3$, the aspect ratio $\alpha = 0$, and the plasma is an infinitely thin disk. (Because we require $z_0 \gg \lambda_D$, here infinitely thin means $z_0 \ll r_0$.) With $a = \frac{3}{2}$, the aspect ratio α is infinite, and the plasma is an infinitely long cylindrical column ($z_0 \gg r_0$). In Eq. (2.9) we choose the potential at the center of the spheroid to be 0. If the potential is chosen to be 0 at ∞ , then Eq. (2.9) neglects a term which depends on the plasma aspect ratio α but is independent of r and z .

It is instructive to consider the plasma equilibrium as a function of rotation frequency ω_r for fixed trapping conditions (fixed ω_z , Ω , and N). Constant density equilibria exist for $\omega_z < \Omega/\sqrt{2}$ and $\omega_m < \omega_r < \Omega - \omega_m$, where

$$\omega_m = \Omega/2 - (\Omega^2/4 - \omega_z^2/2)^{1/2} \quad (2.10)$$

is a single-ion magnetron frequency [1]. For ω_r slightly larger than ω_m , $\omega_z^2/\omega_p^2 \approx 1$, and the plasma is shaped like a pancake (an oblate spheroid). In the limit that $\omega_r \rightarrow \omega_m$, the plasma's aspect ratio $\alpha \rightarrow 0$, and the plasma's radius $r_0 \rightarrow \infty$. As ω_r increases, ω_z^2/ω_p^2 decreases and the plasma's aspect ratio α increases by decreasing r_0 and increasing z_0 . At $\omega_r = \Omega/2$ the plasma attains its maximum aspect ratio (smallest r_0 and largest z_0) and maximum density $n_B = \epsilon_0 m \Omega^2 / 2q^2$. The condition $\omega_r = \Omega/2$ is often called Brillouin flow [36]. In a frame of reference rotating with the plasma, the motion of an individual ion within the non-neutral plasma consists of circular gyrations (perturbed cyclotron orbits) at the frequency $\Omega - 2\omega_r$. At Brillouin flow, these gyrating orbits become free streaming (straight-line trajectories), and the plasma behaves in many ways like an unmagnetized plasma [36]. Therefore at $\omega_r = \Omega/2$, a Penning-trap plasma behaves dynamically like a plasma confined in an rf (Paul) trap (neglecting the rf micromotion). As ω_r increases beyond $\Omega/2$, the plasma's aspect ratio α and density n_0 decrease. Because n_0 is an even function of ω_r about $\omega_r = \Omega/2$ [see Eq. (2.1)], the plasma's aspect ratio, radius, and axial extent are even functions of ω_r about $\omega_r = \Omega/2$. Figure 4 shows a graph of the radius of a plasma of ${}^9\text{Be}^+$ ions as a function of rotation frequency. The plasma's rotation frequency and radius were measured with techniques described in Sec. IV. Good agreement was obtained between the observed and predicted dependence of the plasma's radius on rotation frequency.

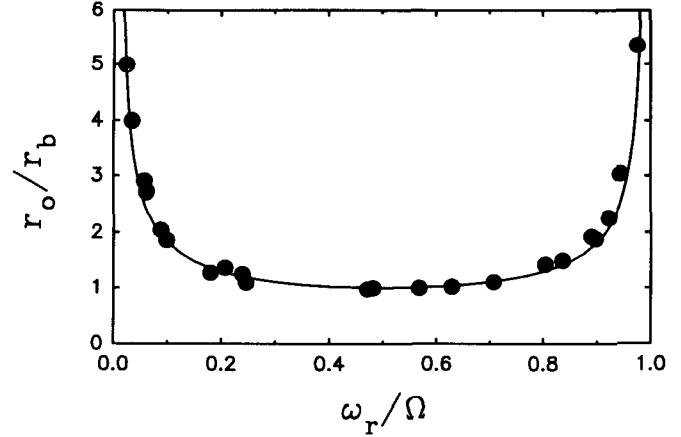


FIG. 4. Radius r_0 of a plasma of ≈ 2000 ${}^9\text{Be}^+$ ions as a function of rotation frequency ω_r . The radius is plotted in units of r_b , the plasma radius at the Brillouin limit, and the rotation frequency is plotted in units of the cyclotron frequency Ω . The solid line is a theoretical curve involving no adjustable parameters. The data were taken as described in Sec. IV with $\Omega/2\pi = 1.4$ MHz and $\omega_z/\Omega = 0.151$.

With the assumption of thermal equilibrium and $\max(\lambda_D, n_0^{-1/3}) \ll (\text{plasma dimensions}) \ll (\text{trap dimensions})$, a Penning-trap plasma has uniform density with a spheroidal boundary. Modal excitations on this equilibrium can be conveniently described with spheroidal coordinates by two integers (l, m) with $l \geq 1$ and $m \geq 0$ [29]. (Negative integral values of m are allowed, but do not give rise to new modes.) The index m denotes an azimuthal dependence $e^{im\phi}$ of the plasma mode potential. The index l describes the variation along a spheroidal surface (for example, the plasma boundary) in a direction perpendicular to $\hat{\phi}$. In this paper, Secs. III and IV give a simple, detailed discussion of some of the $l=2$ modes and Sec. V gives a general discussion of higher-order modes of a Penning-trap plasma. Excitation of an $l=2$ mode produces a quadrupole deformation of the plasma shape. The $l=1$ modes are the familiar center-of-mass modes. Here the ion plasma's shape remains unchanged, but the center-of-mass of the plasma executes one of the three motions of a single ion in a Penning trap. For example, the $(1,0)$ mode is the axial center-of-mass mode at frequency ω_z . There are two $(1,1)$ modes which correspond to the perturbed cyclotron and magnetron center-of-mass modes at frequencies $\Omega - \omega_m$ and ω_m . (In experiments on long columns of electrons where the induced image charges cannot be neglected, the analog of the magnetron center-of-mass mode is the $l=1$ diocotron mode [37,38].) These center-of-mass frequencies can, in general, be measured or calculated very precisely. Figure 3 gives the $(1,0)$ mode frequency or ω_z in units of the plasma frequency as a function of the plasma aspect ratio or shape. Because ω_p is typically unknown, a measurement of ω_z does not provide information on the plasma aspect ratio. However, measurement of an $l=2$ mode frequency along with the $(1,0)$ mode frequency will determine the plasma's aspect ratio and density.

III. QUADRUPOLE PLASMA MODES

In this section we calculate two different types of $l=2$ Penning-trap plasma modes. This is done by making a guess for the plasma eigenmode, then verifying that this guess is a mode of the plasma and calculating the eigenfrequency. In particular, we consider small axial and radial displacements of the ions from their equilibrium positions consistent with the assumed eigenmode. A self-consistent calculation of the axial and radial restoring forces gives two linear differential equations describing the motion of the axial and radial displacements. We then require that the eigenfrequencies from these two equations be equal.

A. (2,0) modes

We first consider an azimuthally symmetric quadrupole mode. We assume that in this mode the plasma always stays spheroidal, but the aspect ratio of the plasma oscillates in time as shown in Fig. 5. This mode turns out to be a (2,0) mode [29]. Let $\tilde{\rho} \equiv x + iy$ and z denote the equilibrium radial and axial position of an ion (or group of ions) in a plasma with an equilibrium density n_0 and aspect ratio α . The displacements from equilibrium

$$\begin{aligned} z &\rightarrow z[1 + \epsilon(t)], \\ \tilde{\rho} &\rightarrow \tilde{\rho}[1 + \tilde{\delta}(t)], \end{aligned} \quad (3.1)$$

parametrized by ϵ and $\tilde{\delta} \equiv \delta_R + i\delta_I$, give another spheroidal plasma but with a density and aspect ratio given by

$$\begin{aligned} n_0 &\rightarrow \frac{n_0}{(1 + \epsilon)|1 + \tilde{\delta}|^2}, \\ \alpha &\rightarrow \alpha \frac{1 + \epsilon}{|1 + \tilde{\delta}|}, \end{aligned} \quad (3.2)$$

where $|1 + \tilde{\delta}| = [(1 + \delta_R)^2 + \delta_I^2]^{1/2}$. Here ϵ , δ_R , and δ_I characterize axial, radial, and azimuthal displacements. For an eigenmode the axial and radial displacements should have the same time dependence. We assume

$$\frac{\epsilon(t)}{\delta_R(t)} = \eta, \quad (3.3)$$

where η , the mode parameter, is independent of time.

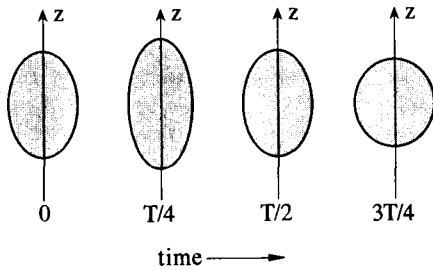


FIG. 5. Sketch of one cycle of the (2,0) mode at time intervals $T/4$ where $T = 2\pi/\omega_{20}$ is the period of the mode. The plasma always stays spheroidal with a uniform density, but the aspect ratio oscillates in time.

Equations (2.4) and (2.9) can be used to calculate the electric field at the displaced ion positions with the results that

$$\begin{aligned} \tilde{E}_\perp &= \frac{m\omega_p^2}{3q} \left[\frac{3\omega_z^2}{2\omega_p^2} + \frac{a[\alpha(1+\epsilon)|1+\tilde{\delta}|^{-1}]}{(1+\epsilon)|1+\tilde{\delta}|^2} \right] \tilde{\rho}(1+\tilde{\delta}) \\ &\equiv \frac{m\omega_p^2}{3q} A(\tilde{\delta}, \epsilon) \tilde{\rho}(1+\tilde{\delta}), \end{aligned} \quad (3.4)$$

$$\begin{aligned} E_z &= \frac{m\omega_p^2}{3q} \left[-\frac{3\omega_z^2}{\omega_p^2} + \frac{b[\alpha(1+\epsilon)|1+\tilde{\delta}|^{-1}]}{(1+\epsilon)|1+\tilde{\delta}|^2} \right] z(1+\epsilon) \\ &\equiv \frac{m\omega_p^2}{3q} B(\tilde{\delta}, \epsilon) z(1+\epsilon). \end{aligned} \quad (3.5)$$

Here \tilde{E}_\perp and E_z are the components of the electric field perpendicular and parallel to the z axis and ω_p is the equilibrium plasma frequency. The equations describing the radial and axial motions of the displaced ions are

$$\begin{aligned} \frac{d^2}{dt^2} \{ \tilde{\rho}(1+\tilde{\delta}) \} + i\Omega \frac{d}{dt} \{ \tilde{\rho}(1+\tilde{\delta}) \} \\ - \frac{\omega_p^2}{3} A(\tilde{\delta}, \epsilon) \tilde{\rho}(1+\tilde{\delta}) = 0, \end{aligned} \quad (3.6)$$

$$\frac{d^2}{dt^2} \{ z(1+\epsilon) \} - \frac{\omega_p^2}{3} B(\tilde{\delta}, \epsilon) z(1+\epsilon) = 0. \quad (3.7)$$

After transforming to a frame rotating at the equilibrium rotation frequency ω_r , and keeping terms no higher than first order in $\tilde{\delta}$ and ϵ , we obtain linear differential equations for $\tilde{\delta}$ and ϵ . The equations are

$$\frac{d^2}{dt^2} \tilde{\delta} + i(\Omega - 2\omega_r) \frac{d}{dt} \tilde{\delta} - \frac{\omega_p^2}{3} (\eta A_\epsilon + A_\delta) \delta_R = 0, \quad (3.8)$$

$$\frac{d^2}{dt^2} \epsilon - \frac{\omega_p^2}{3} \{ B_\epsilon + B_\delta / \eta \} \epsilon = 0. \quad (3.9)$$

Here $A_\delta \equiv \partial A(0,0)/\partial \delta_R$ and $A_\epsilon \equiv \partial A(0,0)/\partial \epsilon$, with similar definitions for B_ϵ and B_δ . There are no first-order δ_I terms in the expansion of A and B , because A and B are even functions of δ_I . The real and imaginary parts of Eq. (3.8) can be solved simultaneously. The solution is oscillatory with eigenfrequency ω_{20} given by

$$\omega_{20}^2 = (\Omega - 2\omega_r)^2 - \frac{\omega_p^2}{3} (\eta A_\epsilon + A_\delta). \quad (3.10)$$

The eigenfrequency of Eq. (3.9) is given by

$$\omega_{20}^2 = \frac{-\omega_p^2}{3} \{ B_\epsilon + B_\delta / \eta \}. \quad (3.11)$$

The requirement that the two eigenfrequencies be equal gives a quadratic equation for η . Substitution of the solutions for η back into either Eq. (3.10) or (3.11) gives the (2,0) mode frequency ω_{20} . After a number of algebraic manipulations we find

$$\left. \begin{aligned} 2(\omega_{20}^+)^2 \\ 2(\omega_{20}^-)^2 \end{aligned} \right\} = \Omega_u^2 + \omega_Q^2 \left[\begin{array}{c} + \\ - \end{array} \right] [(\Omega_u^2 - \omega_Q^2)^2 - 4\Omega_v^2(\omega_z^2 - \omega_Q^2/3)]^{1/2}. \quad (3.12)$$

Here $\Omega_v \equiv \Omega - 2\omega_r$ is the vortex frequency (the cyclotron frequency as seen in the rotating frame), $\Omega_u \equiv (\Omega_v^2 + \omega_p^2)^{1/2}$ is the upper hybrid frequency, and

$$\omega_Q^2 \equiv \omega_p^2 \frac{3\alpha}{(\alpha^2 - 1)^{3/2}} Q_2^0 \left[\frac{\alpha}{(\alpha^2 - 1)^{1/2}} \right]. \quad (3.13)$$

The lower-frequency mode [denoted by the negative sign in Eq. (3.12)] is called a plasma mode and is characterized by $\eta \leq 0$ and a mode frequency $\omega_{20}^- \leq \Omega/\sqrt{3}$. The higher-frequency mode [denoted by the positive sign in Eq. (3.12)] is called an upper hybrid mode and is characterized by $\eta \geq 0$ and a mode frequency $\omega_{20}^+ \geq \Omega/\sqrt{3}$. Plasma and upper hybrid modes are discussed in Sec. V. The frequency ω_Q is the (2,0) plasma mode frequency in the absence of a magnetic field (that is, $\Omega_v \rightarrow 0$ or a plasma confined by a uniform background of opposite charge). It is a mode frequency of a cold cloud of ions in an rf trap.

Most Penning-trap experiments are done with $\omega_z \ll \Omega$. For simplicity we therefore discuss the two modes of Eq. (3.12) for this experimentally interesting case. Figure 6 shows a graph of ω_{20}^+ and ω_{20}^- as a function of rotation frequency for $\omega_z/\Omega = 0.151$. In the limit of low rotation frequencies ($\omega_r \rightarrow \omega_m$) the plasma mode frequency approaches ω_p . At $\omega_r = \omega_m$, the mode frequency $\omega_{20}^- = \omega_p = \omega_z$. In this limit the mode parameter η for the plasma mode frequency is large in magnitude and negative. The plasma mode looks predominantly like an axial stretch mode with only small radial excursions which are

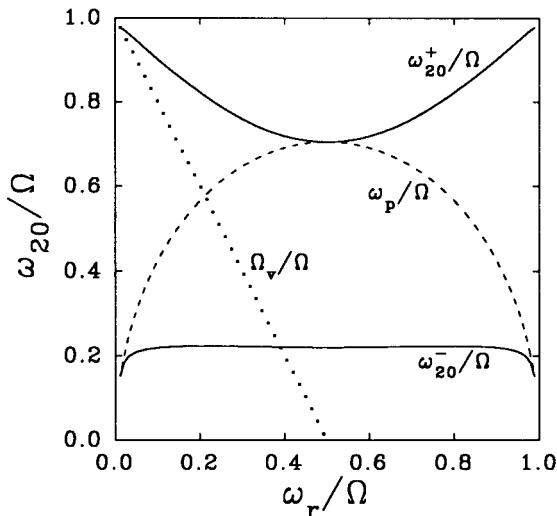


FIG. 6. Graph of the plasma ω_{20}^- and upper hybrid ω_{20}^+ mode frequencies [from Eq. (3.12)] as a function of rotation frequency ω_r for $\omega_z/\Omega = 0.151$. Also shown are the vortex frequency $\Omega_v = \Omega - 2\omega_r$ (dotted line) and the plasma frequency ω_p (dashed line) in units of the cyclotron frequency.

180° out of phase with the axial excursions. This is because for $\omega_r \simeq \omega_m \ll \Omega$ the magnetic field in the rotating frame ($\propto \Omega - 2\omega_r$) is large and constrains the radial excursions of the plasma. At the Brillouin limit ($\Omega_v = 0$) or in a cold plasma confined in an rf trap, the plasma mode frequency equals ω_Q and the mode parameter $\eta = -2$. This means the volume and therefore the density of the plasma stay constant during the excitation of this mode. At the Brillouin limit, the plasma mode therefore consists of incompressible deformations of the plasma shape (a surface mode). The (2,0) plasma mode of a spheroidal plasma is similar to an $m = 0$ plasma mode of a cylindrical plasma column with a wavelength equal to the plasma length [37,38].

The upper hybrid mode frequency approaches $\Omega_v = \Omega - 2\omega_r$ for low rotation frequencies and is equal to $\Omega - 2\omega_m$ at $\omega_r = \omega_m$. In this limit the mode parameter η for the upper hybrid mode is small and positive (radial excursions \gg axial excursions). For low rotation frequencies we can show that this mode looks like a coherent excitation of the perturbed cyclotron orbits of the ions. For two ions on opposite sides of the trap axis, the perturbed cyclotron orbits are 180° out of phase. At the Brillouin limit (or for ions confined in an rf trap), the upper hybrid mode is equal to $\omega_p = \Omega/\sqrt{2}$. Here $\eta = \alpha^{-2}$, which implies that the plasma oscillates (or “breathes”) from a small spheroid to a larger confocal spheroid and back again. The electric field outside the plasma does not change under such an oscillation. This can be called a bulk mode because it is confined to the plasma interior and is difficult to couple to with external fields. Both of the (2,0) modes are symmetric (even functions) about the Brillouin condition ($\omega_r = \Omega/2$), as can be seen in Fig. 6.

If either one of the (2,0) mode frequencies can be measured, it can be used together with the (1,0) mode frequency ω_z and the cyclotron frequency Ω to obtain the plasma rotation frequency ω_r . The plasma rotation frequency can then be used to determine the plasma’s density n_0 and aspect ratio α from Eqs. (2.1), (2.2), and (2.6). Figure 7(a) shows points of constant ω_{20}^+ (the upper hybrid frequency) and Fig. 7(b) shows points of constant ω_{20}^- (the plasma mode frequency) on graphs of rotation frequency versus the trap axial frequency. All frequencies are normalized by Ω . The axial frequency ω_z [equivalently the (1,0) mode frequency] depends only on the trap design and the potential difference between the trap end cap and ring electrodes. Typically it can be measured or calculated very precisely. Similarly the cyclotron frequency can be measured or calculated very precisely and the operating point for ω_z/Ω along the x axis of Fig. 7 precisely determined. A measurement of a (2,0) mode frequency can then be used with Fig. 7 to determine the rotation frequency. Figure 7(b) shows that the plasma mode frequency ω_{20}^- gives accurate information on ω_r/Ω mainly for slow rotation frequencies slightly greater than ω_m . However, the upper hybrid frequency gives accurate information on ω_r/Ω over a wide range of conditions, especially over the experimentally interesting range $\omega_z/\Omega \ll 1$. Section IV describes some (2,0) mode mea-

measurements on plasmas of ${}^9\text{Be}^+$ ions. The modes were excited by applying an oscillatory potential between the ring electrode and the trap end caps which was resonant with the mode frequencies.

Figure 7 assumes a spheroidal plasma with $\lambda_D, n_0^{-1/3} \ll$ (plasma dimensions) as discussed in Sec. II. However, even for finite temperatures, the (2,0) modes should provide useful information on the plasma rotation frequency. For example, in the limit that the ion space-charge fields can be neglected, the upper hybrid mode frequency is $\Omega - 2\omega_m$. The difference between $\Omega - 2\omega_m$ and the measured upper hybrid mode frequency is therefore a measure of the importance of the space-charge fields. Also, an oscillatory drive on the ring electrode at $\Omega - 2\omega_m$ can parametrically excite the perturbed cyclo-

tron motion of the plasma center of mass [the high-frequency (1,1) mode] whose frequency is $\Omega - \omega_m$ in the laboratory frame. This parametric excitation requires an initial, nonzero mode amplitude.

B. (2,1) modes

We now consider an azimuthally asymmetric quadrupole mode. As in the previous section, we let $\bar{\rho} \equiv x + iy$ and z denote the equilibrium radial and axial position of an ion (or group of ions) in a plasma with an equilibrium density n_0 and aspect ratio α . We guess that there is a mode described by displacements from equilibrium of the form

$$\begin{aligned} x &\rightarrow x + \delta z \cos(\omega_{21}^{\text{lab}} t), \\ y &\rightarrow y + \delta z \sin(\omega_{21}^{\text{lab}} t), \\ z &\rightarrow z + \epsilon [x \cos(\omega_{21}^{\text{lab}} t) + y \sin(\omega_{21}^{\text{lab}} t)]. \end{aligned} \quad (3.14)$$

As the subscripts in Eq. (3.14) indicate, this turns out to be a (2,1) mode. The superscript lab indicates that the description is in the laboratory frame of reference. [This labeling was not required with the azimuthally symmetric (2,0) mode because its frequency is the same in either the laboratory or rotating frame.] Equation (3.14) can be rewritten using complex notation as

$$\begin{aligned} \bar{\rho} &\rightarrow \bar{\rho} + \bar{\delta}(t)z, \\ z &\rightarrow z + \text{Re}\{\bar{\epsilon}(t)\bar{\rho}^*\}, \end{aligned} \quad (3.15)$$

where the time dependence is now included in $\bar{\delta}(t)$ and $\bar{\epsilon}(t)$, the asterisk denotes the complex conjugate, Re denotes the real part, and

$$\frac{\bar{\epsilon}(t)}{\bar{\delta}(t)} = \eta, \quad (3.16)$$

where the mode parameter η is independent of time and real. Equation (3.15) transforms a uniform density spheroid into a uniform density ellipsoid. The ellipsoid is rotated with respect to the original, equilibrium spheroid by an angle $|\bar{\gamma}|$, where, to first order in $\bar{\epsilon}$ and $\bar{\delta}$,

$$\bar{\gamma} = \frac{\bar{\delta}\alpha^2 + \bar{\epsilon}}{1 - \alpha^2}. \quad (3.17)$$

The modulus $|\bar{\gamma}|$ denotes the magnitude of the rotation angle. The phase of $\bar{\gamma}$ denotes the plane in which the rotation takes place. Specifically, the rotation occurs about the unit vector $(\text{Im}\bar{\gamma}/|\bar{\gamma}|, -\text{Re}\bar{\gamma}/|\bar{\gamma}|, 0)$ or, equivalently, the $\bar{\rho} = -i\bar{\gamma}$ axis. To first order in $\bar{\epsilon}$ and $\bar{\delta}$, the tilted ellipsoid is a spheroid with the same aspect ratio as the equilibrium spheroid. Therefore to calculate the electric field at the displaced ion positions to first order in $\bar{\epsilon}$ and $\bar{\delta}$, we have only to calculate the electric field inside the equilibrium spheroid rotated by an angle $|\bar{\gamma}|$ about the $\bar{\rho} = -i\bar{\gamma}$ axis. We obtain

$$\bar{E}_1 \simeq \frac{m\omega_p^2}{2q}(\bar{\rho} + \bar{\delta}z) + \frac{m\omega_p^2}{3q}(a-b)\bar{\gamma}z, \quad (3.18)$$

$$E_z \simeq \frac{m\omega_p^2}{2q}(a-b)\text{Re}\{\bar{\gamma}\bar{\rho}^*\}. \quad (3.19)$$

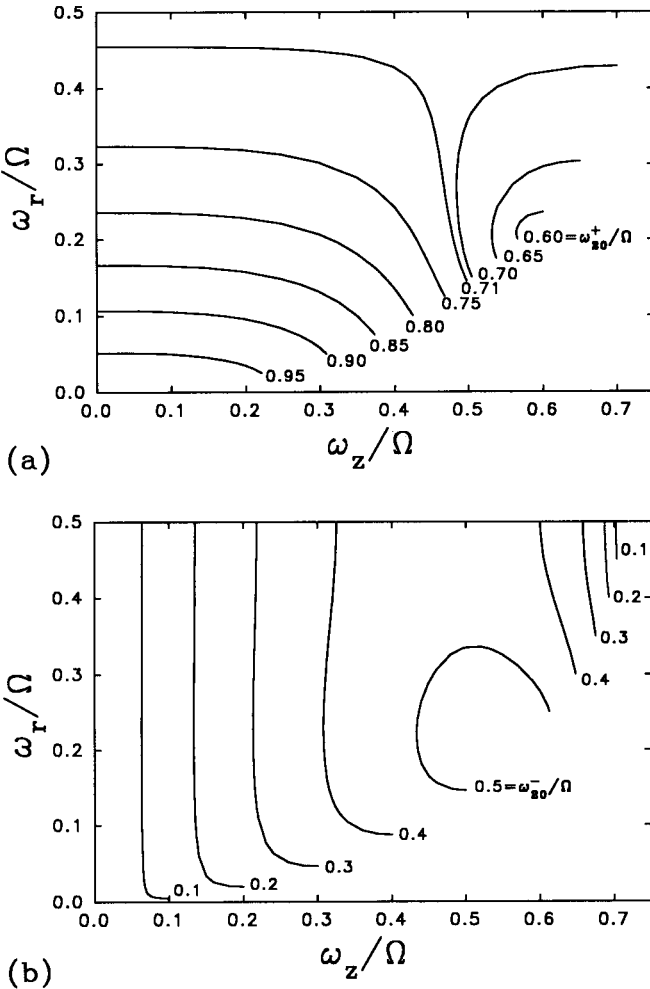


FIG. 7. Sensitivity of the (2,0) mode frequencies for determining the plasma rotation frequency. Points of constant (a) upper hybrid frequency ω_{20}^+ or (b) plasma mode frequency ω_{20}^- are plotted on a graph of rotation frequency ω_r vs the trap axial frequency ω_z (in units of the cyclotron frequency Ω). A measurement of ω_z , Ω , and ω_{20}^+ or ω_{20}^- can be used with these graphs to determine the rotation frequency. The ω_{20}^+ plots are symmetric about $\omega_r/\Omega = 0.5$. The boundary defined by the low- ω_r end of the curves denotes the condition $\omega_r = \omega_m$. Ion confinement requires $\omega_r \geq \omega_m$.

Here ω_p is the equilibrium plasma frequency and $a(\alpha)$ and $b(\alpha)$ are evaluated at the equilibrium aspect ratio α .

After transforming to a frame rotating at the equilibrium rotation frequency, the following differential equations are obtained for $\delta_r \equiv \exp\{i\omega_r t\}\delta$ and $\tilde{\epsilon}_r \equiv \exp\{i\omega_r t\}\tilde{\epsilon}$:

$$\frac{d^2}{dt^2}\delta_r + i\Omega_v \frac{d}{dt}\delta_r - \frac{\omega_p^2}{3}f(\alpha)(\alpha^2 + \eta)\delta_r = 0, \quad (3.20)$$

$$\frac{d^2}{dt^2}\tilde{\epsilon}_r - \frac{\omega_p^2}{3}f(\alpha)\left[\frac{\alpha^2}{\eta} + 1\right]\tilde{\epsilon}_r = 0. \quad (3.21)$$

Here

$$f(\alpha) \equiv [a(\alpha) - b(\alpha)] / (1 - \alpha^2) = \frac{3}{2}(1 - 3\omega_z^2/\omega_p^2) / (1 - \alpha^2).$$

With the convention that the time dependence of δ_r and $\tilde{\epsilon}_r$ is given by $\exp(i\omega_{21}t)$, Eqs. (3.20) and (3.21) give the following two equations for ω_{21} , the (2,1) mode eigenfrequency in the rotating frame. We obtain

$$-\omega_{21}^2 - \Omega_v \omega_{21} - \frac{\omega_p^2}{3}f(\alpha)(\alpha^2 + \eta) = 0, \quad (3.22)$$

$$-\omega_{21}^2 - \frac{\omega_p^2}{3}f(\alpha)\left[\frac{\alpha^2}{\eta} + 1\right] = 0. \quad (3.23)$$

When Eqs. (3.22) and (3.23) are solved simultaneously, a cubic equation for η is obtained,

$$\Omega_v^2 \eta + \frac{\omega_p^2}{3}f(\alpha)(\alpha^2 + \eta)(\eta - 1)^2 = 0. \quad (3.24)$$

Solutions for η from Eq. (3.24) can be plugged back into either Eq. (3.22) or (3.23) to obtain values of ω_{21} for three different (2,1) modes. The laboratory (2,1) mode frequency ω_{21}^{lab} is obtained from $\omega_{21}^{\text{lab}} = \omega_{21} - \omega_r$. With the convention used here, a positive ω_{21} (ω_{21}^{lab}) denotes a counterclockwise precession when viewed from above the x - y plane in the rotating (laboratory) frame. This agrees with the usual right-hand rule for the sign of an angular frequency.

Figure 8 shows a graph of the three different (2,1) mode frequencies (in the laboratory) versus rotation frequency for $\omega_z/\Omega = 0.151$. As discussed in the previous two paragraphs, all three modes correspond to a tilt of the equilibrium spheroid with respect to the z axis. This tilted spheroid then precesses about the trap symmetry axis at the frequency ω_{21}^{lab} as shown in Fig. 9. Because the density remains constant during the mode excitation, all three (2,1) modes are surface modes. The modes with the highest and lowest values of $|\omega_{21}^{\text{lab}}|$ are characterized by $\eta \geq 0$ (axial and radial excursions in phase). The third mode with intermediate frequency is characterized by $\eta \leq 0$ (axial and radial excursions 180° out of phase). For the mode with the highest value of $|\omega_{21}^{\text{lab}}|$ in Fig. 8, the tilted spheroid precesses rapidly at a frequency near Ω . For $\omega_r \approx \omega_m \ll \Omega$, the mode frequency approaches $\omega_{21}^{\text{lab}} \approx -(\Omega - \omega_r)$ and the mode parameter satisfies $\eta \ll 1$. Equations (3.15) and (3.16) show that the axial excursions are small compared to the radial excursions and the precession can be thought of as being due to a coherent (although asymmetric in z) excitation of individual ion cy-

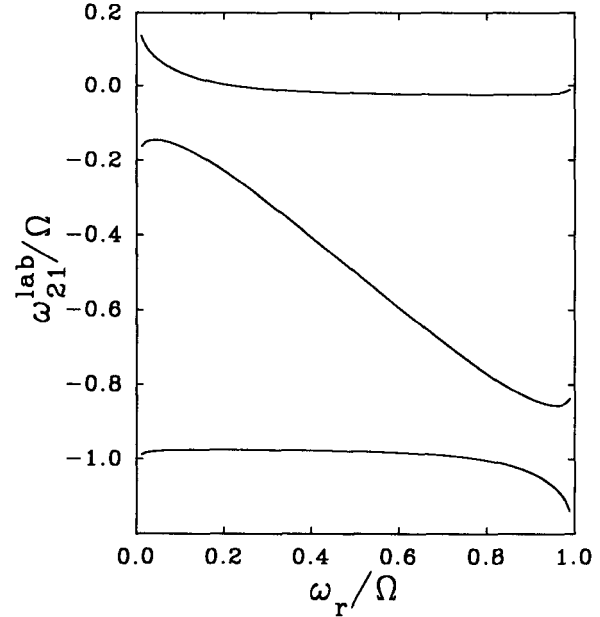


FIG. 8. Graph of the three (2,1) mode frequencies ω_{21}^{lab} as a function of the plasma rotation frequency ω_r , for $\omega_z/\Omega = 0.151$. The mode frequencies in the laboratory frame are plotted. The mode with the lowest value of $|\omega_{21}^{\text{lab}}|$ has a frequency equal to 0 for $\omega_r/\Omega = 0.219$.

clotron orbits. For low rotation frequencies, this mode is classified as an upper hybrid mode (see Sec. V). For the mode with the lowest $|\omega_{21}^{\text{lab}}|$ in Fig. 8, the tilted spheroid precesses at a low frequency. For $\omega_z \ll \Omega$ and $\omega_r \approx \omega_m \ll \Omega$, the mode parameter satisfies $\eta \gg 1$ and $\omega_{21}^{\text{lab}} \approx \omega_z - \omega_r$. Here this mode can be thought of as a coherent (and azimuthally asymmetric) excitation of the axial motion of individual ions. For low rotation frequencies, this mode is classified as a magnetized plasma mode (see Sec. V). At the Brillouin limit, the highest- and lowest-frequency modes both have $\eta = 1$, and their frequencies are equally spaced about $-\Omega/2$. Stated

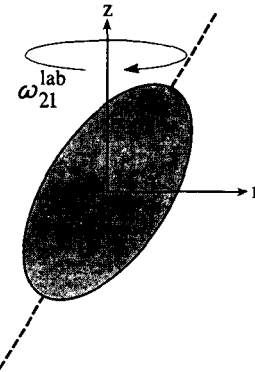


FIG. 9. Sketch of the (2,1) mode in the laboratory frame. The plasma spheroid is tilted with respect to the z axis and precesses about the z axis at ω_{21}^{lab} . In this figure the sense of the precession is positive. The picture in the rotating frame is the same except the precession occurs at the frequency $\omega_{21} = \omega_{21}^{\text{lab}} + \omega_r$.

differently, in the rotating frame the two modes have equal and opposite frequencies at the Brillouin limit. Near the Brillouin limit, these two modes are classified as evanescent modes (see Sec. V). The intermediate frequency mode has $\eta < 0$. For $\omega_z \ll \Omega$ and $\omega_r \approx \omega_m \ll \Omega$, the intermediate mode has $|\eta| \gg 1$ and $\omega_{21}^{\text{lab}} \approx -\omega_z - \omega_r$. Therefore this mode has an interpretation similar to the lowest-frequency mode. However, the behavior of this mode is quite different for $\omega_r \gg \omega_m$. At the Brillouin limit $\eta = -\alpha^2$, which means that the plasma shape does not change (that is, the plasma spheroid does not tilt), and this mode frequency in the rotating frame is 0. Therefore this mode vanishes at the Brillouin limit and is called a magnetized plasma mode (see Sec. V).

Figure 8 shows that the (2,1) mode with the lowest magnitude of frequency in the laboratory frame is 0 at $\omega_r/\Omega = 0.219$ for $\omega_z/\Omega = 0.151$. This zero-frequency mode can be excited by a static field error [19,21,39]. From the ion's point of view (the rotating frame) the static field error looks like a rotating field with a frequency ω_r . When $\omega_{21} = \omega_r$ or $\omega_{21}^{\text{lab}} = \omega_{21} - \omega_r = 0$ the (2,1) mode is excited. Section IV describes the excitation of the static (2,1) mode by a tilt of the electrode symmetry axis of the trap relative to the trap magnetic field axis. If the rotation frequency ω_r was increased from small values by an external torque, excitation of this mode tended to limit ω_r to values less than the rotation frequency where $\omega_{21}^{\text{lab}} = 0$.

In addition to the (2,0) and (2,1) modes, there are two (2,2) modes. The (2,2) modes are discussed with the other $l = m$ modes in Sec. V. In a (2,2) mode, the plasma forms an ellipsoid with unequal principal axes in the x - y plane. The ellipsoid rotates about the z axis at the (2,2) mode frequency. A measurement of one of the (2,1) or (2,2) mode frequencies can be used to determine the plasma rotation frequency and aspect ratio in the same manner as described for the (2,0) modes (see Fig. 7).

IV. EXPERIMENTAL RESULTS

In this section we compare experimental measurements of some quadrupole modes of a Penning-trap plasma with the calculations of Sec. III. Much of the experimental work has been described previously in Ref. [21]. Typically between 1000 and 5000 ${}^9\text{Be}^+$ ions were stored in a cylindrical Penning trap shown schematically in Fig. 1. Most of the experimental work was done with $B = 0.82$ T where $\Omega({}^9\text{Be}^+)/2\pi = 1400$ kHz. Some singly charged, heavier ions were created when the ${}^9\text{Be}^+$ ions were created or loaded into the trap. In addition, singly charged, heavier ions slowly formed after loading ${}^9\text{Be}^+$, presumably due to ion-molecule reactions involving the ${}^9\text{Be}^+$ ions. Their presence appeared to shift the observed mode frequencies. We could eliminate them from the trap by momentarily raising V_T so that $\omega_z/\Omega > 1/\sqrt{2}$ for the heavier ions, making them unstable. In practice we would raise V_T to satisfy $\omega_z/\Omega \approx 0.67$ for ${}^9\text{Be}^+$. We then obtained repeatable and consistent measurements for the mode frequencies.

Radiation pressure from a laser was used to cool the ${}^9\text{Be}^+$ plasma [20,21,28]. A 313-nm laser (power

$\approx 100 \mu\text{W}$) was tuned 10–50 MHz below the rest frequency ω_0 of the $2s\ ^2S_{1/2}(m_I = +\frac{3}{2}, m_J = +\frac{1}{2}) \rightarrow 2p\ ^2P_{3/2}(\frac{3}{2}, \frac{3}{2})$ transition in ${}^9\text{Be}^+$. In addition to cooling the ions, this laser optically pumped the ions into the $(\frac{3}{2}, \frac{1}{2})$ ground state [28]. The ions were detected by imaging the laser-induced ion fluorescence onto the photocathode of a photon-counting imaging tube (see Fig. 1). A real-time display of the image was used to monitor qualitatively the plasma's kinetic energy; a hot plasma had a more diffuse boundary and less ion fluorescence. With this simple diagnostic we were unable to distinguish between an increase in the random thermal energy of the ions and the excitation of a coherent modal motion of the plasma. The cooling laser was split into two beams. One beam (shown in Fig. 1) was directed perpendicularly to the z axis near the center of the trap. The second beam (not shown in Fig. 1) was used along with the first beam when the lowest ion temperatures were desired [20,21,28]. It was directed at a 51° angle with respect to the z axis. (The projection of this beam along the z axis cooled the ion's axial motion directly.) With laser cooling, the ${}^9\text{Be}^+$ ions quickly evolved into a near thermal equilibrium distribution and could be confined for many hours [28]. The temperature of the ions could be measured from the Doppler broadening of an optical transition [28]. Typical temperatures ranged from 5 to 200 mK. (Here temperature refers to the Maxwell-Boltzmann velocity distribution which occurs in thermal equilibrium in the rotating frame.)

The plasma density was determined from Eq. (2.1) by measuring the plasma rotation frequency. We measured the rotation frequency by driving the $(m_I = +\frac{3}{2}, m_J = +\frac{1}{2}) \rightarrow (+\frac{3}{2}, -\frac{1}{2})$ electron spin-flip transition at frequency ω_s in the $2s\ ^2S_{1/2}$ ${}^9\text{Be}^+$ ground state. The transition frequency ω_s is approximately equal to 22 GHz at $B = 0.82$ T. The transition was observed as a decrease in the ion fluorescence when the frequency of the applied microwave field is resonant with ω_s [40]. In addition, a decrease in the ion fluorescence was observed at the sideband frequencies $\omega_s \pm \omega_r$. This is because from the ion's point of view the phase and amplitude of the microwave field are modulated due to the rotation of the plasma. This produces sidebands in the microwave spectrum observed by the ions at $\omega_s \pm \omega_r$ [41]. Measurement of these sidebands enabled $\omega_r/2\pi$ to be determined to about 5 kHz. At $B = 0.82$ T, the ${}^9\text{Be}^+$ ion densities usually were measured to be greater than $10^7/\text{cm}^3$. This density with temperatures less than 200 mK results in Debye lengths less than $10 \mu\text{m}$. With 1000–5000 ions in the trap, the typical plasma dimensions were between 100 and 1000 μm , which is one or two orders of magnitude larger than λ_D . The radius of the cylindrical trap electrodes (1.27 cm) was another order of magnitude larger. Consequently the laser-cooled ${}^9\text{Be}^+$ plasmas satisfied the condition $\lambda_D \ll (\text{plasma dimensions}) \ll (\text{trap dimensions})$ and formed constant density, spheroidal plasmas. The axial frequency ω_z was measured by applying an oscillating potential to one of the end caps [42]. The cyclotron frequency Ω was calculated from the magnetic field. The magnetic field was determined accurately from measure-

ments of the electron spin-flip or nuclear spin-flip transition frequencies in the ${}^9\text{Be}^+$ ground state.

The angular momentum and therefore the rotation frequency ω_r of the ${}^9\text{Be}^+$ plasmas were controlled by a torque from the radiation pressure of a second, weak laser beam (power $\approx 2 \mu\text{W}$) whose frequency ω_T was tuned above the cooling transition frequency ω_0 . This torque beam (see Fig. 1) was directed perpendicularly to the z axis but displaced from the z axis through the side of the plasma which recedes from the laser beam due to the plasma rotation. This beam imparted to the plasma a torque which tended to increase the plasma rotation frequency ω_r . Initially the plasma was cooled by the cooling laser beam with the result that $\omega_r \ll \Omega$. The torque laser beam was then directed through the side of the plasma with a frequency ω_T tuned slightly below ω_0 . As ω_T was increased above ω_0 , ω_T became resonant with the frequency of the Doppler-shifted ions in the torque beam. This produced ion fluorescence and a torque on the plasma which increased the rotation frequency. As shown in Fig. 4, an increase in ω_r produced a decrease in the plasma radius r_0 for $\omega_r < \Omega/2$ and an increase in r_0 for $\omega_r > \Omega/2$. The plasma radius was measured with the imaging tube. Accurate measurements of the plasma's axial extent were more difficult to obtain. However, we could qualitatively check that the plasma obtained its maximum axial extent (and therefore maximum aspect ratio) at the Brillouin limit by scanning the position of one of the laser beams along the axial direction.

By appropriate tuning of the torque laser frequency and with some adjustment of the positions of the cooling and torque lasers, we could obtain a steady-state, equilibrium plasma with a rotation frequency anywhere in the allowed range from ω_m to $\Omega - \omega_m$. In addition to supplying a torque, the torque laser also supplied energy to the plasma when $\omega_T > \omega_0$ [43]. Equilibrium occurred when the energy input from the torque laser was removed by the cooling laser and when the laser beam torques and torques from static field asymmetries summed to 0. We were also able to increase ω_r to values greater than $\Omega/2$ by using just the cooling laser. An increase in the cooling laser frequency increased ω_r . In this case, however, the rotation frequency sensitively depended on the cooling laser frequency and a steady-state condition was more difficult to achieve.

We discovered [21] that as the plasma rotation frequency was increased, there was a range of rotation frequencies where the plasma acquired a diffuse boundary and a low level of ion fluorescence characteristic of a hot plasma. The range over which this apparent heating occurred depended sensitively on the alignment of the trap's symmetry axis with the magnetic field axis. Let θ_0 denote the angle between these two axes. If we assume that the trap is aligned when the apparent heating resonance is minimized, then we could adjust $\theta_0 < 0.01^\circ$ by searching for an alignment which gave no apparent heating. For $\theta_0 > 0.1^\circ$ the plasma rotation frequency could not be increased beyond the point at which heating first occurred. This heating resonance appeared to get stronger with an increase in the number of ions. We have

been able to identify this heating resonance as an excitation of a collective (2,1) plasma mode by the static field asymmetry associated with the misalignment of the trap symmetry axis with the magnetic field. Figure 10 shows the measured rotation frequencies where heating occurred with $\theta_0 \approx 0.02^\circ$ for different trap axial frequencies. Also shown (solid line) is the calculated rotation frequency at which $\omega_{21}^{\text{lab}} = 0$, that is, $\omega_r = \omega_{21}$ as calculated from Eqs. (3.22)–(3.24). Excellent agreement is obtained between the predicted and measured rotation frequencies where heating is observed.

We did not attempt to understand the source of energy in the heating resonance. However, two possibilities are listed below. A static asymmetry cannot change the total energy of the plasma, but it can convert potential to thermal energy by producing an expansion of the plasma. Because the ratio of potential to thermal energy is large in our plasmas, a small expansion can produce a large increase in the ion thermal energy. This energy source increases with the potential energy per ion of the plasma. For example, it increases with the ion number or plasma density. With the lasers operating continuously, the time-averaged plasma radius does not change. However, the plasma radius may fluctuate. For example, there could be a small plasma expansion between photon scattering events, balanced by a plasma contraction when a photon is scattered. Heat could be generated by expansion during plasma fluctuations. Another source of energy is the torque laser. The energy input from this laser could increase when the static (2,1) resonance is excited if there is an increase in the scatter rate from this laser.

If the density is increased from low values corresponding to $\omega_r \ll \Omega/2$, excitation of the static (2,1) mode may provide a practical limit to the density and number of charged particles that can be stored in a Penning trap. For large ion numbers or $\theta_0 > 0.1^\circ$ we were unable to obtain densities greater than $n_0(\omega_r = \omega_{21})$. For $\omega_z/\Omega > 0.53$, Fig. 10 shows that $\omega_r = \omega_{21}$ occurs for

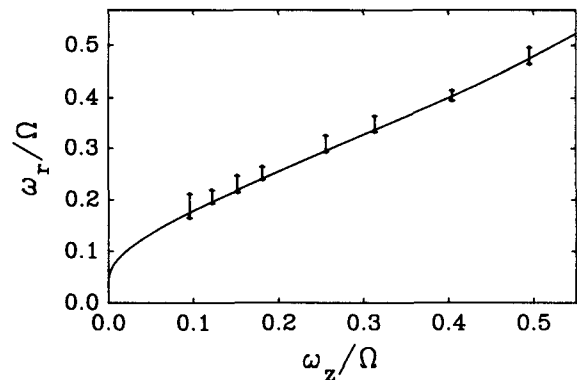


FIG. 10. Rotation frequency ω_r at which heating was observed as a function of the single-particle axial frequency ω_z . Both frequencies are expressed in units of the cyclotron frequency Ω . The experimental data were obtained with 1000–5000 ${}^9\text{Be}^+$ ions stored in the trap of Fig. 1. The solid line indicates the calculated rotation frequency ω_r at which $\omega_{21} = 0$. This is a universal curve involving no adjustable parameters.

$\omega_r/\Omega > 0.5$ and therefore the static (2,1) mode will not prevent reaching the Brillouin limit in this case. However, for a high magnetic field and a trap with large dimensions, the condition $\omega_z/\Omega > 0.53$ may be difficult to obtain because of practical limitations on the voltage that can be applied to the trap electrodes. In addition, $\omega_r/\Omega = 0.5$ with $\omega_z/\Omega = 0.53$ occurs for an aspect ratio $\alpha = 0.44$. For storage of a large number of charged particles, this would require a trap with a large radius. However, a large volume trap is more easily constructed by extending it axially while keeping the radius fixed [44]. For storage of large ion numbers, the plasma dimensions may not be small compared to the trap dimensions. This changes the calculation of the modes because the trap potential will not, in general, be quadratic and the image charges in the trap electrodes cannot be neglected. In spite of the difficulty of increasing ω_r (and the density) through the point where the heating resonance occurs, there is still the potential to “jump through” this condition by sudden switching of ω_z or creating the plasma with $\omega_r > |\omega_{21}|$.

Laser torques were also used to increase ω_r in ${}^9\text{Be}^+$ plasmas consisting of 40 000 ${}^9\text{Be}^+$ ions at $B = 6$ T. We were unable to remove possible contaminant ions at this high magnetic field because of the high voltages required on the trap electrodes. In addition, we did not have a microwave source (≈ 160 GHz at $B = 6$ T) to drive the ground-state electron spin-flip transition and measure the plasma rotation frequency. However, a rough measure of ω_r could be obtained from the plasma aspect ratio. We were able to obtain rotation frequencies $\omega_r > \Omega/2$. Figure 11 shows an image of a rapidly rotating Be^+ plasma with $\omega_r/2\pi \approx \Omega/2\pi = 10$ MHz. The propeller shape of the ion fluorescence is due to the fast rotation of the plasma. The ions get excited in the laser beam, but decay outside the laser beam because the 8.2-ns lifetime of the excited P state is longer than the typical transit time



FIG. 11. Image of the ion fluorescence of a rapidly rotating ${}^9\text{Be}^+$ plasma at $B = 6$ T with $\omega_r/2\pi \approx \Omega/2\pi = 10$ MHz. Fluorescence due to the perpendicular and diagonal cooling beams is observed. The plasma diameter in the $z = 0$ plane is approximately 1 mm. The ion kinetic energy due to rotation at the radial edge of the plasma is approximately 50 eV.

through the beam. The (2,1) heating resonance was much stronger and more sensitive to the magnetic field alignment at $B = 6$ T than in our work at 0.8 T. This may have been due to the larger number of trapped ions at $B = 6$ T. We also observed additional heating resonances at lower rotation frequencies than the (2,1) heating resonance. Section V discusses other static modes that are potential candidates for these additional heating resonances. We note that many of these resonances tend to limit the plasma density to even lower values than the static (2,1) resonance.

Density limits on trapped ion plasmas have also been reported in other Penning-trap experiments. In Ref. [45] the experimentally observed ion fluorescence in a Penning trap was interpreted in terms of limits to the ion density imposed by single-particle resonant transport [46]. In single-particle resonant transport, enhanced transport (and lower ion density) may occur when the axial bounce frequency of an individual ion is commensurate with the ion's rotation frequency. In this process an individual ion resonantly interacts with an external field error. This is different from transport due to the excitation of a zero-frequency mode where a collective plasma mode resonantly interacts with an external field error. In our work we observe no evidence for single-particle resonant transport as an important mechanism for limiting the ion density. An important difference between our work and that of Ref. [45] is the ion temperature. In our work the ions are sufficiently cold that the ion-ion collision time is short compared to the axial bounce time. The experimental measurements of Ref. [45] were done on relatively hot ion clouds (≈ 5000 K) where the ions may bounce faster than they collide. In addition, the Debye length in this work was likely comparable to or larger than the cloud dimensions. In this case the ion density is not constant, and calculation of the space-charge-shifted axial bounce frequency of an individual ion requires a model different from the cold thermal equilibrium discussed in Sec. II. The theoretical analysis of Ref. [45] would be more convincing with a self-consistent calculation of the space-charge shifts. Such a self-consistent calculation is described in Ref. [47]. When space charge is important, the potential variation in the axial direction is no longer harmonic, so the axial bounce frequency depends on the ion temperature and axial dimension of the ion cloud. Both of these dependencies are neglected in Ref. [45].

We also measured the (2,0) plasma and upper hybrid modes. These modes were excited by applying a sinusoidal potential between the two central and two outer electrodes in Fig. 1. They were detected by a change in the ion fluorescence when the frequency of the applied rf was resonant with the mode frequency. This change was presumably caused by a change in the ions' Doppler width and possibly by a change in the laser beam-plasma overlap. Measurements of the plasma mode frequency as a function of the plasma rotation frequency are shown in Fig. 12 for two different trap axial frequencies. The solid lines show the plasma mode frequency calculated from Eqs. (3.12), (3.13), and (2.6). Again, good agreement between the predicted and ob-

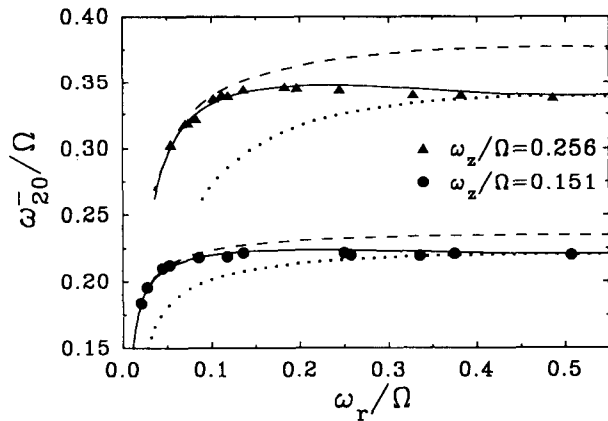


FIG. 12. Plasma mode frequency ω_{20}^- as a function of the rotation frequency ω_r for two different axial frequencies ω_z . All frequencies are expressed in units of the cyclotron frequency Ω . The circles and triangles give the experimental data. The solid lines give the cold-fluid model predictions for ω_{20}^- . The dashed and dotted lines give the high- and low-magnetic-field calculations for ω_{20}^- , respectively. The dotted line corresponds to the ω_{20}^- frequency for an rf-trap plasma with the same density and aspect ratio.

served modes is obtained with no adjustable parameters. Figure 12 shows two additional calculations. In the first, shown as dashed lines, the magnetic field is assumed to be effectively infinite; that is, the ions are not allowed to move radially, and the mode frequency is calculated assuming a simple axial stretch of the charged spheroid. The mode frequency in this case is calculated from Eq. (3.11) by setting the B_δ/η term equal to 0. In the second calculation, shown as dotted lines, the magnetic field is assumed to be effectively 0; that is, the curve shows ω_Q [see Eq. (3.13)]. From this figure, the (2,0) plasma mode behaves like a mode of a strongly magnetized plasma at low rotation frequencies and an unmagnetized plasma near the Brillouin limit. We attempted to excite the upper hybrid (2,0) mode with a drive frequency near the upper hybrid frequency. A resonance (a change in the ion fluorescence) was observed as the frequency of the applied rf was swept. The amplitude of the drive was decreased until the resonance signal was barely detectable. Figure 13 shows a plot of the measured resonance frequency along with a calculation of the upper hybrid (2,0) mode from Eqs. (3.12), (3.13), and (2.6). Agreement is good, indicating that the observed resonance was likely the excitation of the upper hybrid (2,0) mode. As discussed in Sec. V, our drive could also potentially excite an upper hybrid (4,0) mode. For the conditions of this experiment, the two mode frequencies would be difficult to distinguish. However, for sufficiently weak drive strength, the (2,0) mode should be excited more strongly than the (4,0) mode. We could not excite this upper hybrid mode near the Brillouin limit because, as discussed in Secs. III and V, the upper hybrid modes become difficult to couple to with external fields there.

The agreement obtained here with the zero-temperature calculations requires that $\lambda_D \ll (\text{plasma dimensions}) \ll (\text{trap dimensions})$. This condition is usual-

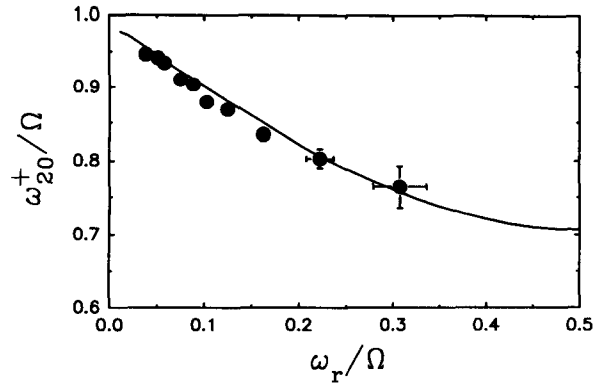


FIG. 13. Upper hybrid mode frequency ω_{20}^+ as a function of the rotation frequency ω_r for $\omega_z/\Omega = 0.151$. All frequencies are expressed in units of the cyclotron frequency Ω . The circles give the experimental data. The uncertainty for measurements done at low rotation frequencies is approximately the size of the circles. At high rotation frequencies the uncertainties increase because the mode becomes difficult to excite. The solid line gives the cold-fluid model predictions.

ly easy to satisfy with a laser-cooled ion plasma and, in fact, may not be difficult to satisfy with a cryogenic ($T = 4$ K) plasma. For example, a plasma with $n_0 \approx 10^7/\text{cm}^3$ at $T = 4$ K has a Debye length $\lambda_D = 44 \mu\text{m}$. Consequently if the dimensions of this plasma are greater than 1 mm, the inequality $\lambda_D \ll (\text{plasma dimensions})$ is satisfied. A plasma with $z_0 = r_0 \approx 1$ mm and $n_0 \approx 10^7/\text{cm}^3$ requires loading $4\pi r_0^3 n_0 / 3 = 4 \times 10^4$ charged particles within 1 mm of the trap axis. The charged particles must then be cooled and evolve into a thermal equilibrium state before the plasma radius expands [18,46] due to radial transport produced by trap asymmetries. For electrons this appears to be possible because at large magnetic fields ($B \approx 6$ T) the cyclotron radiation time is short (< 1 s) and the time over which the plasma spreads due to trap asymmetries can be long [16] (many hours). In addition, localized sources such as field emission points can be used to load many electrons close to the trap axis. For ions which cannot be laser cooled the inequality for a zero-temperature plasma may be more difficult to achieve. This is because radiative cooling times are typically longer. In addition, the radial transport in Penning traps due to trap asymmetries is likely faster for ions than electrons because of the larger ion mass. However, with care in loading the plasma, or with the development of a technique to reduce the plasma radius and increase the ion density, it should be possible to satisfy the conditions for a zero-temperature plasma with ions at 4 K. Ions in a Paul trap can be rapidly cooled to the temperature of a background buffer gas. In this case it should be possible to obtain a plasma where the Debye length is small compared to the plasma dimensions. Some experiments in Paul traps approximate this regime [47].

V. GENERAL LINEAR MODES

The quadratic oscillations discussed in Secs. III and IV are important special cases of an infinite set of linear nor-

mal modes. Although we have, up to now, emphasized the behavior of the quadratic modes, there are several reasons to consider the general modes here. First, although the general higher-order modes have not yet been experimentally measured, we will see that it should be possible to observe at least a few of them using the same experimental techniques as were described in Sec. IV. Second, a deeper understanding of the quadratic modes may follow from consideration of their place in the hierarchy of general oscillations. Finally, a simple exact analytic solution for all of these modes has been found [29].

In Sec. V A we briefly review some features of this general solution. We then discuss a simple form of the general dispersion relation for the modes which allows one to obtain numerical solutions of the mode frequencies using a polynomial-root-finding algorithm. We also consider some examples, including some of the modes which can be resonantly driven by applying an oscillating potential between the two end electrodes and the center electrodes. In Sec. V B, we focus on modes which can be resonantly driven by static field errors. We find that such resonances occur in profusion, becoming dense when the cloud rotation frequency is small compared to the cyclotron frequency.

A. Description of the normal modes

In order to obtain a general solution for the normal modes several assumptions must be made. We assume the cloud is near thermal equilibrium, and we assume the oscillations around this equilibrium are small so that we can linearize the equations of motion. The temperature is assumed to be sufficiently small that pressure effects on the fluid dynamics are negligible, and correlation effects are also neglected; these are good approximations provided that both the Debye length and interparticle spacing are small compared to both the size of the cloud and the wavelength of the mode. Electromagnetic effects are neglected (that is, $\nabla \times \mathbf{E} = \nabla \times \mathbf{H} = 0$ in Maxwell's equations) since the cloud is small and the mode frequency is relatively low, and the effect on the dynamics of image charges in the electrodes is neglected.

These approximations are identical to those used in the earlier sections and apply well to present experiments on small cold ion clouds. However, unlike in the previous analysis, we do not assume a particular form for the density perturbations. Rather, a general linear perturbation is employed. The dynamics are described in a frame rotating at the constant rotation frequency ω_r of the equilibrium plasma. In this frame the plasma is stationary and the density, fluid velocity, and the potential are perturbed from their equilibrium values:

$$n(\mathbf{x}, t) = n_0(\mathbf{x}) + \delta n(\mathbf{x}, t), \quad (5.1a)$$

$$\mathbf{v}(\mathbf{x}, t) = \mathbf{0} + \delta \mathbf{v}(\mathbf{x}, t), \quad (5.1b)$$

$$\phi(\mathbf{x}, t) = \phi_0(\mathbf{x}) + \psi(\mathbf{x}, t), \quad (5.1c)$$

where δn , $\delta \mathbf{v}$, and ψ are the perturbed density, fluid velocity, and potential, respectively. The equilibrium densi-

ty $n_0(\mathbf{x})$ is uniform within the plasma spheroid and zero outside, and ϕ_0 is the total equilibrium potential in a rotating frame, equal to [28]

$$\phi_0 = \phi_T + \phi_I + \frac{m\omega_r}{2q}(\Omega - \omega_r)r^2.$$

The first two terms in ϕ_0 are the external trap and space-charge potentials, given by Eqs. (2.4) and (2.9), respectively, and the last term is a pseudopotential due to rotation through the magnetic field.

We substitute Eqs. (5.1) into the cold-fluid equations [48] describing conservation of momentum and particle number, as well as into Poisson's equation. In the rotating frame, the cold-fluid equations have the same form as in an inertial frame (for example, the laboratory frame), except that the electrostatic potential is changed as indicated above and the cyclotron frequency is changed to the vortex frequency $\Omega_v = \Omega - 2\omega_r$. When equilibrium force balance is taken into account and the equations are linearized in the small perturbations, we obtain the linearized continuity, momentum, and Poisson equations of cold-fluid theory:

$$\frac{\partial \delta n}{\partial t} + \nabla \cdot (n_0 \delta \mathbf{v}) = 0, \quad (5.2a)$$

$$\frac{\partial \delta \mathbf{v}}{\partial t} + \frac{q}{m} \nabla \psi - \delta \mathbf{v} \times \Omega_v \hat{\mathbf{z}} = 0, \quad (5.2b)$$

$$\nabla^2 \psi = -\frac{q}{\epsilon_0} \delta n, \quad (5.2c)$$

where $\hat{\mathbf{z}}$ is a unit vector along the z axis. Equation (5.2b) and further equations implicitly assume $q > 0$. For $q < 0$, $\Omega_v \rightarrow -\Omega_v$. Using the assumption that the perturbed quantities have a time dependence of the form $e^{-i\omega t}$ in the rotating frame (so that ω is the mode frequency as seen in this frame), a differential equation for ψ follows from standard algebraic manipulations of Eqs. (5.2):

$$\nabla \cdot \epsilon \cdot \nabla \psi = 0, \quad (5.3a)$$

where ϵ is the cold-plasma dielectric tensor. In Cartesian coordinates

$$\epsilon = \begin{pmatrix} \epsilon_1 & -i\epsilon_2 & 0 \\ i\epsilon_2 & \epsilon_1 & 0 \\ 0 & 0 & \epsilon_3 \end{pmatrix}, \quad (5.3b)$$

where $\epsilon_1 \equiv 1 - \omega_p^2 / (\omega^2 - \Omega_v^2)$, $\epsilon_2 \equiv \Omega_v \omega_p^2 / [\omega(\omega^2 - \Omega_v^2)]$, and $\epsilon_3 \equiv 1 - \omega_p^2 / \omega^2$. Equation (5.3a) is just Maxwell's equation $\nabla \cdot \mathbf{D} = 0$ for a medium with a linear frequency-dependent anisotropic dielectric tensor ϵ . After a solution to Eqs. (5.2) for the perturbed potential ψ is found, Eqs. (5.2) can be used to calculate the perturbed density δn and perturbed fluid velocity $\delta \mathbf{v}$.

The normal mode problem requires a solution to Eq. (5.3) subject to the boundary condition that $\psi \rightarrow 0$ at infinity, which is a problem in the theory of electrostatics. Outside the plasma $\epsilon = 1$ and ψ satisfies Laplace's equation, $\nabla^2 \psi^{\text{out}} = 0$. Inside the plasma the dielectric tensor is anisotropic and the solution of Eq. (5.3a) is more compli-

cated. The inner and outer solutions must be matched across the plasma-vacuum boundary according to

$$\psi^{\text{in}} = \psi^{\text{out}}|_{\text{boundary}}, \quad (5.4a)$$

$$\hat{\mathbf{n}} \cdot \boldsymbol{\epsilon} \cdot \nabla \psi^{\text{in}} = \hat{\mathbf{n}} \cdot \nabla \psi^{\text{out}}|_{\text{boundary}}, \quad (5.4b)$$

where $\hat{\mathbf{n}}$ is a unit vector normal to the plasma-vacuum boundary.

Although the formulation of the problem as one in the theory of electrostatics is a step forward, simple solutions are generally available only in one of the standard geometries for which a separable solution exists, and this is not a standard geometry. The surface of the plasma is spheroidal, while the dielectric tensor is anisotropic with a different, cylindrical, symmetry. However, Ref. [29] showed that Eq. (5.3) does in fact have a separable solution in an unusual frequency-dependent coordinate system. This is the only known exact analytic solution for normal modes in a magnetized plasma of finite size. The solution for the mode potential is

$$\psi = \begin{cases} A Q_l^m(\xi_1/d) P_l^m(\xi_2) e^{i(m\phi - \omega t)} & (\text{outside plasma}), \\ B P_l^m(\bar{\xi}_1/\bar{d}) P_l^m(\bar{\xi}_2) e^{i(m\phi - \omega t)} & (\text{inside plasma}), \end{cases} \quad (5.5)$$

where A and B are constants and Q_l^m and P_l^m are associated Legendre functions. Outside the plasma, the solution is expressed in terms of spheroidal coordinates [49] (ξ_1, ξ_2, ϕ) defined by the relations

$$x \equiv [(\xi_1^2 - d^2)(1 - \xi_2^2)]^{1/2} \cos \phi,$$

$$y \equiv [(\xi_1^2 - d^2)(1 - \xi_2^2)]^{1/2} \sin \phi,$$

$$z \equiv \xi_1 \xi_2.$$

The coordinate ξ_1 is a generalized distance coordinate taking the value $\xi_1 \in [z_0, \infty)$ outside the cloud, ξ_2 is a generalized latitude in the range $[-1, 1]$ and ϕ is the usual azimuthal angle. Surfaces of constant ξ_1 are confocal spheroids with the surface of the cloud defined by $\xi_1 = z_0$, and surfaces of constant ξ_2 are confocal hyperboloids. The foci are a distance $2|d|$ apart, where $d^2 \equiv z_0^2 - r_0^2$. The coordinates (ξ_1, ξ_2, ϕ) become the usual spherical coordinates $(r, \cos \theta, \phi)$ when $z_0 = r_0$.

Inside the cloud the coordinates $(\bar{\xi}_1, \bar{\xi}_2, \phi)$ are employed in order to obtain a separable solution. These coordinates are transformed spheroidal coordinates defined by the equations

$$x \equiv [(\bar{\xi}_1^2 - \bar{d}^2)(1 - \bar{\xi}_2^2)]^{1/2} \cos \phi,$$

$$y \equiv [(\bar{\xi}_1^2 - \bar{d}^2)(1 - \bar{\xi}_2^2)]^{1/2} \sin \phi, \quad (5.6)$$

$$z(\epsilon_1/\epsilon_3)^{1/2} \equiv \bar{\xi}_1 \bar{\xi}_2.$$

where $\bar{d}^2 \equiv z_0^2 - r_0^2$ and $\bar{z}_0 \equiv z_0(\epsilon_1/\epsilon_3)^{1/2}$. These coordinates are frequency dependent; the different possible topologies of the coordinate surfaces are discussed in Ref. [29].

Returning to Eq. (5.5), we note that different normal modes are enumerated by the integers l and m , where $l \geq 0$ and $|m| \leq l$. In fact, values of $m < 0$ do not give rise to new modes if negative frequencies are allowed. Therefore $m \geq 0$ is assumed throughout, and negative frequen-

cies are allowed. For $m \neq 0$, positive and negative frequency modes rotate about the z axis in opposite directions. As discussed in Sec. III, we use the convention that modes with positive frequency rotate counterclockwise when viewed from above the x - y plane (so that $d\phi/dt > 0$ for $\omega > 0$). The two directions of rotation are not equivalent due to the applied magnetic field. The mode frequencies for positively and negatively charged particles differ by a minus sign.

For a given pair (l, m) the mode potential outside the cloud decays away like $s^{-(l-1)}$ at large distances s from the cloud center [because $Q_l^m(x) \rightarrow x^{-(l+1)}$ for large x and $\xi_1 \rightarrow s$ for large s]. The modes can also be differentiated by the number of oscillations in ψ . For example, there are $l - m$ zeros in the potential as one moves in ξ_2 along a given spheroid outside the plasma from one pole to the other [that is, from $\xi_2 = 1$ to -1 on a constant (ξ_1, ϕ) curve]. This is because $P_l^m(x)$ has $l - m$ zeros in the range $[-1, 1]$.

The variation of the potential outside the cloud is independent of the mode frequency, up to the overall constant A . However, inside the cloud, the frequency dependence of the coordinates (through their dependence on ϵ_1 and ϵ_3) implies that the behavior of the mode potential varies depending on the mode frequency, the plasma frequency and vortex frequency [except for two exceptional cases described in Eqs. (5.9) and (5.10) below]. This behavior can be understood qualitatively from the spatial Fourier transform of Eq. (5.3a),

$$\epsilon_1 \mathbf{k}_1^2 + \epsilon_3 k_z^2 = 0, \quad (5.7)$$

where \mathbf{k}_1 and k_z are the components of the wave vector perpendicular and parallel to the magnetic field, respectively. When ω/ω_p and Ω/ω_p are such that $\epsilon_1/\epsilon_3 < 0$, a solution of this equation exists with both \mathbf{k}_1 and k_z real, which is a propagating mode. However, when $\epsilon_1/\epsilon_3 > 0$, Eq. (5.7) implies that either \mathbf{k}_1 or k_z must be imaginary and the mode is evanescent. The frequency dependence of the ϵ 's implies that the propagating mode relation $\epsilon_1/\epsilon_3 < 0$ is satisfied by frequencies in the ranges $0 < |\omega| < \min[\omega_p, |\Omega_v|]$ and $\max[\omega_p, |\Omega_v|] < |\omega| < \Omega_u$, where $\Omega_u = (\omega_p^2 + \Omega_v^2)^{1/2}$ is the upper hybrid frequency. Modes in the first frequency range are called magnetized plasma oscillations, and modes in the second frequency range are called upper hybrid modes [50]. As we will see presently, evanescent modes occur only when $|\Omega_v| < \omega_p$, and such modes have frequencies in the range $|\Omega_v| < |\omega| < \omega_p$. These regimes are shown in Fig. 14 as a function of the rotation frequency. (Here, remember that both the vortex frequency and the plasma frequency are functions of ω_p .) Modes with frequencies falling in areas labeled A are magnetized plasma modes, modes falling in areas B are upper hybrid modes, and modes falling in C are evanescent.

Modes which are evanescent have a different potential variation within the cloud than modes which are propagating. Propagating modes reflect off the interior surface of the spheroid and set up a standing-wave pattern inside the cloud, whereas evanescent modes propagate along the cloud surface but decay with distance from the surface

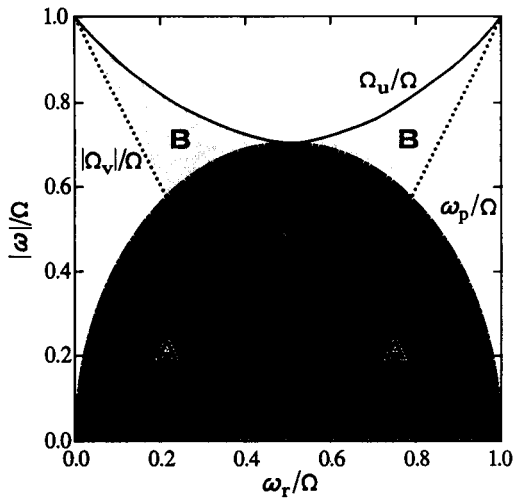


FIG. 14. Sketch showing the areas of allowed mode frequencies ω as a function of the rotation frequency ω_r . Modes in regions A, B, and C are, respectively, magnetized plasma, upper hybrid, and evanescent modes.

into the plasma. (Because of the curvature of the cloud's surface, this decay is algebraic rather than the exponential decay we would observe for an evanescent mode at a planar interface.)

For example, the zeros of the (2,0) mode potential within the cloud are shown in Fig. 15 for the case of a spherical plasma with $\Omega_v/\omega_p=0.5$. As discussed in Secs. III and IV, there are two possible forms for the potential corresponding to a high-frequency upper hybrid mode [labeled (a)] and a lower-frequency mode [labeled (b)]. The upper hybrid mode is propagating, but for this value of Ω_v/ω_p the lower-frequency mode is evanescent, decaying with distance into the plasma. This behavior is best observed in Figs. 15(c) and 15(d), which show the potential variation of the modes along $z=0$ and $r=0$, respectively.

Furthermore, either Fig. 15(a) or Figs. 15(c) and 15(d) show that the potential of the upper hybrid mode nearly vanishes along the cloud surface, so there is almost no potential variation exterior to the cloud. This is because as $\Omega_v/\omega_p \rightarrow 0$ (the Brillouin limit in a Penning trap or the condition for ions in a Paul trap) the upper hybrid modes have frequency $\omega = \omega_p$ and, as shown below, become bulk plasma oscillations with $\psi^{\text{out}}=0$. If $\Omega_v/\omega_p \rightarrow 0$ and $\omega \rightarrow \omega_p$, then $\epsilon=0$ and Eq. (5.4) implies $\nabla\psi^{\text{out}} \cdot \hat{n}=0$ along the plasma boundary. The only solution which satisfies both the boundary condition at the plasma and $\psi^{\text{out}} \rightarrow 0$ at infinity is $\psi^{\text{out}}=0$. Furthermore in the $\Omega_v/\omega_p \rightarrow 0$ limit the magnetized plasma modes disappear as their frequency $\omega \rightarrow 0$. Thus, only the evanescent modes with $\epsilon_1/\epsilon_3 > 0$ may be observable near the $\Omega_v/\omega_p \rightarrow 0$ limit if only electrostatic detection of the modes is employed. In this limit the evanescent modes satisfy $\nabla^2\psi^{\text{in}}=0$, so from Eq. (5.2) there is no density perturbation except at the surface of the cloud. In this limit the evanescent modes induce incompressible deformations of the cloud's shape, and for this reason they are often called surface modes.

As a second example, the interior potential variation of

the four possible (4,0) normal mode potentials are shown in Fig. 16, again for a spherical cloud with $\Omega_v/\omega_p=0.5$. Like the (2,0) modes, these modes could also be driven by in-phase oscillation of the end-cap potentials. There are now four zeros in the exterior potential as we move from pole to pole along the spheroid, as can be observed in Figs. 16(a)–16(d). Figures 16(a) and 16(b) correspond to upper hybrid modes, whereas Fig. 16(d) is a magnetized plasma mode and Fig. 16(c) is an evanescent mode. The decay of the evanescent mode with distance into the plas-

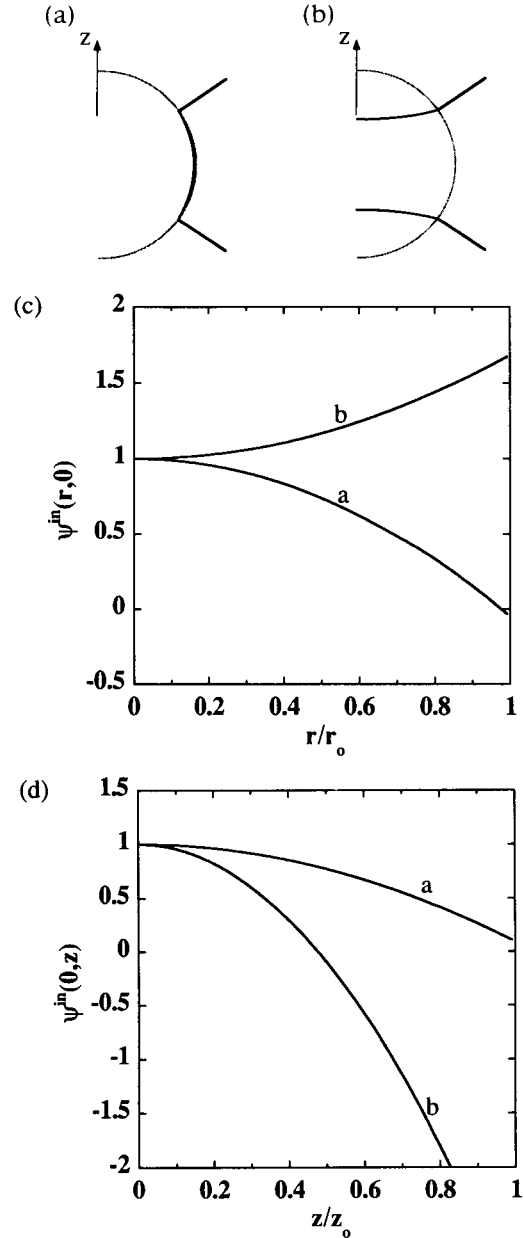


FIG. 15. (a) and (b) show the zeros of the potential for the two $l=2, m=0$ modes in a spherical plasma with $\Omega_v/\omega_p=0.5$. (a) is the upper hybrid mode and (b) is the plasma mode which is evanescent for these conditions. In (c) the variation of the mode potential (normalized to the potential at the plasma center) is shown as a function of cylindrical radius r in the $z=0$ plane, and in (d) the potential is shown as a function of z along $r=0$.

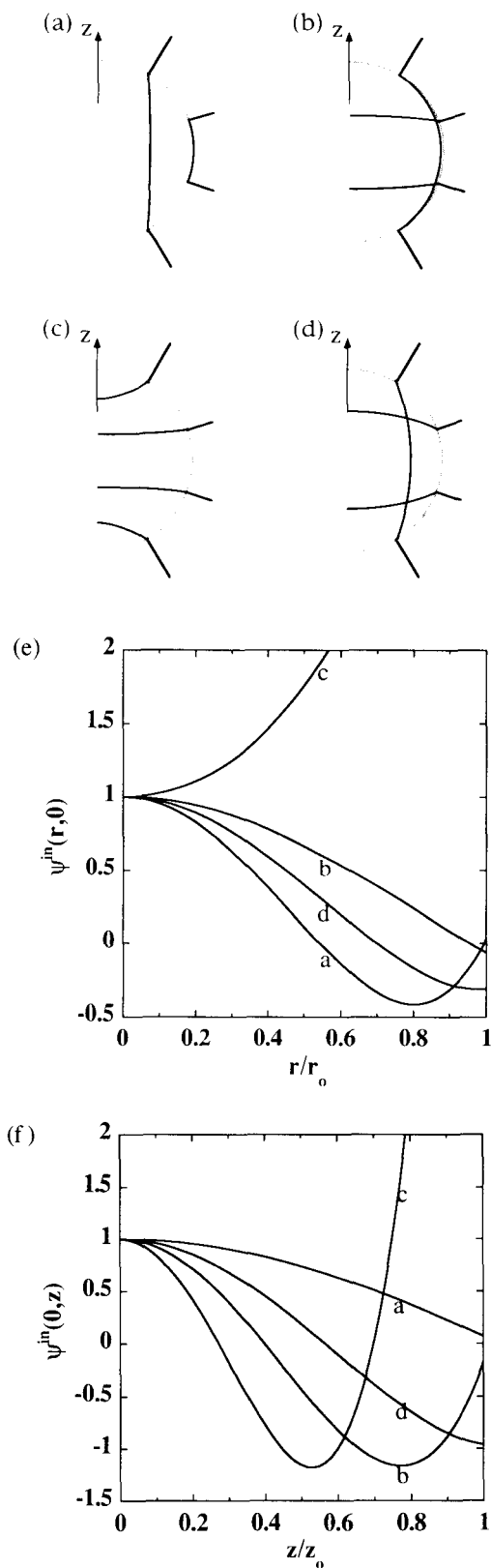


FIG. 16. (a)–(d) show the zeros of the potential for the four $l=4, m=0$ modes in a spherical plasma cloud with $\Omega_v/\omega_p=0.5$, in order of highest frequency (a) to lowest frequency (d). In (e) the variation of the mode potential (normalized to the potential at the plasma center) is shown as a function of cylindrical radius r in the $z=0$ plane, and in (f) the potential is shown as a function of z along $r=0$. The labels (a)–(d) correspond to Fig. 15(a)–15(d).

ma is most easily observed in Figs. 16(e) and 16(f). Just as with the (2,0) modes, for this relatively low value of Ω_v/ω_p the upper hybrid modes induce almost no potential variation outside the cloud, as opposed to the magnetized plasma mode or the evanescent mode.

Finally, there are two exceptional cases for which the form of the mode potential is independent of ω , ω_p , and Ω_v . When $l=m$ or $l=m+1$, we can substitute into Eq. (5.5) the general form of the Legendre function P_l^m ,

$$P_l^m(x) = \sum_{j=0}^{(l-m)/2} (1-x^2)^{m/2} p_j x^{l-m-2j}, \quad (5.8)$$

where the p_j 's are given numbers, and use Eq. (5.6) to show that

$$\psi_{(m,m)}^{\text{in}} = \bar{A} r^m e^{i(m\phi - \omega t)} \quad (5.9)$$

and

$$\psi_{(m+1,m)}^{\text{in}} = \bar{B} r^m z e^{i(m\phi - \omega t)}, \quad (5.10)$$

where \bar{A} and \bar{B} are constants. (In fact, for all l and m , ψ^{in} can be expressed as a finite-order multinomial in x , y , and z .) In the cases of Eqs. (5.9) and (5.10) the form of the mode potential is independent of ω , ω_p , and Ω_v , because the mode satisfies $\partial^2 \psi^{\text{in}} / \partial z^2 = 0$ and $\nabla_1^2 \psi^{\text{in}} = 0$ separately, and so Eq. (5.3a) is satisfied for any ϵ_1 and ϵ_3 . Furthermore, these particular modes satisfy $\nabla^2 \psi^{\text{in}} = 0$, so they cause incompressible deformations of the cloud for all ω_p and Ω_v ; that is, they are always surface modes. For example, for the case of the (2,1) mode, $\psi_{(2,1)}^{\text{in}} = \bar{B} e^{i(\phi - \omega t)} r z$, which is the potential inside a tilted cloud precessing at frequency ω , in agreement with the analysis of Sec. III. The (1,0) and (1,1) modes are also examples of incompressible cloud deformations, which correspond to the well-known axial center-of-mass and magnetron modes.

The (2,2) mode is an incompressible distortion of the cloud into a triaxial ellipsoid, leaving the length of the cloud fixed at $2z_0$. In general, the (l,l) modes are finite length extensions of the z -independent diocotron and upper hybrid surface modes of cylindrical non-neutral plasmas [51].

Although the $l=m$ and $l=m+1$ surface modes appear to be fundamentally different from other magnetized plasma, upper hybrid, and evanescent modes, in fact they display many characteristics which are similar to these modes. For example, when $\omega_r \ll \Omega$ two of the three (2,1) oscillations can be thought of as finite length versions of magnetized plasma modes in a cylindrical column. The modes (indicated by the upper two curves in Fig. 8) have $m=1$ and a half wavelength potential variation over the length of the column; they rotate in opposite directions around the column. Similarly, the other (2,1) mode is a finite length version of an upper hybrid oscillation which also has a half wavelength variation over the column length. Modes with larger values of l simply have more wavelengths fitted into the column length, and so are not fundamentally different. Indeed, we will soon see that the frequencies of these $l=m$ and $l=m+1$ modes behave in a qualitatively similar fashion as those of the other propagating and evanescent modes. When discussing the gen-

eral frequency dependence of the modes, we therefore do not need to make a distinction between these modes and modes with other values of l and m .

Turning now to the normal mode frequencies, Ref. [29] showed that substitution of Eq. (5.5) into Eq. (5.4) leads to two homogeneous linear equations for A and B which have a nontrivial solution only if

$$\epsilon_3 P_l^{m'} + m \alpha \left[\alpha^2 - \frac{\epsilon_3}{\epsilon_1} \right]^{1/2} P_l^m \epsilon_2 - \left[\frac{\alpha^2 - \epsilon_3/\epsilon_1}{\alpha^2 - 1} \right]^{1/2} P_l^m \frac{Q_l^{m'}}{Q_l^m} = 0. \quad (5.11)$$

$$x^{l-m-1} (1-x^2)^{m/2} \sum_{j=0}^{(l-m)/2} p_j x^{-2j} \left[m \alpha^2 (\epsilon_1 + \epsilon_2) + (l-m-2j) \epsilon_3 - \frac{\alpha}{(\alpha^2-1)^{1/2}} \frac{Q_l^{m'}}{Q_l^m} \right] = 0, \quad (5.12)$$

where $x = \alpha / (\alpha^2 - \epsilon_3/\epsilon_1)^{1/2}$. The factor before the sum is nonzero and can be discarded. Furthermore, since $x^{-2j} = (1 - \epsilon_3/\alpha^2 \epsilon_1)^j$, and ϵ_1 , ϵ_2 , and ϵ_3 are rational functions of ω , the sum itself may be expressed as a polynomial in ω . For example, $\epsilon_3/\epsilon_1 = (\omega^2 - \Omega_v^2)(\omega^2 - \omega_p^2) / [\omega^2(\omega^2 - \Omega_u^2)]$, and $\epsilon_1 + \epsilon_2 = (\omega^2 + \omega\Omega_v - \omega_p^2) / [\omega(\omega + \Omega_v)]$. Substitution of these results into Eq. (5.12) leads, after

Here $P_l^m \equiv P_l^m(\alpha / (\alpha^2 - \epsilon_3/\epsilon_1)^{1/2})$, $Q_l^m \equiv Q_l^m(\alpha / (\alpha^2 - 1)^{1/2})$, $\alpha \equiv z_0/r_0$, and the primes denote differentiation with respect to the entire argument.

The general behavior of the solutions to this equation was considered in Ref. [29]. Here, we discuss a simplification of Eq. (5.11) which aids in the determination of the solutions, and we consider some examples. Analysis of the roots of this nonlinear equation is aided by the fact that it can be expressed as a polynomial in the frequency ω . This polynomial can be derived by substitution of Eq. (5.8) into Eq. (5.11), which leads, after some algebra, to the expression

some further reduction, to the following polynomial equation:

$$\sum_{j=0}^{(l-m)/2} a_j b^j c^{\text{int}[(l-m)/2]-j} = 0, \quad (5.13)$$

where

$$a_j \equiv p_j \left[(\omega + \Omega_v) \left[(l-m-2j)(\omega^2 - \omega_p^2) - \frac{\alpha}{(\alpha^2-1)^{1/2}} \frac{Q_l^{m'}}{Q_l^m} \omega^2 \right] + m \alpha^2 \omega (\omega^2 - \omega_p^2 + \omega \Omega_v) \right],$$

$$b \equiv \alpha^2 \omega^2 (\omega^2 - \Omega_u^2) - (\omega^2 - \omega_p^2)(\omega^2 - \Omega_v^2),$$

and

$$c \equiv \alpha^2 \omega^2 (\omega^2 - \Omega_u^2).$$

The function $\text{int}[(l-m)/2]$ denotes the largest integer less than or equal to $(l-m)/2$.

This form of the dispersion relation (the dependence of ω on α for a given l, m) is considerably more simple to solve numerically than Eq. (5.12), using any polynomial-root-finding algorithm. Furthermore, the equation leads to some simple analytic results. For example, we can count the number of normal modes by determining the order of the polynomial. The order is $3 + 4 \text{int}[(l-m)/2]$; however, we must be careful to exclude any spurious roots generated in the derivation of Eq. (5.13) through multiplication by resonant denominators of ϵ_1 , ϵ_2 , or ϵ_3 . When $m=0$ and l is odd, there is a single spurious root at $\omega = -\Omega_v$ [due to the $(\omega + \Omega_v)$ term in a_j]. If $m=0$ and l is even there are three spurious roots at $\omega^2=0$ and $\omega = -\Omega_v$. Subtracting out these roots from the total, we find for $m=0$ there are $2l$ normal modes. However, when $m=0$, Eq. (5.13) is a polynomial of order l in ω^2 . The roots then come in l pairs at $\pm\omega$, and the pairs do not really correspond to two separate

modes; indeed, Eq. (5.5) shows that the mode potential is identical for both $\pm\omega$ when $m=0$.

When $m \neq 0$ and when $l-m$ is even, there is a single spurious root at $\omega=0$, while when $l-m$ is odd, there are no spurious roots. Thus, when $l-m$ is even there are $[2(l-m)+2]$ modes, and when $l-m$ is odd there are $[2(l-m)+1]$ modes. The roots no longer come in $\pm\omega$ pairs because, for $m \neq 0$, modes with positive and negative frequencies rotate in opposite directions around the z axis, and these directions are not equivalent because of the magnetic field.

Some simple analytic results are also possible for the mode frequencies when $l=m$ or $l=m+1$. In this case only the $j=0$ term survives from Eq. (5.13) and the modes are determined by the equation $a_0=0$. When $l=m$ this is a quadratic equation with roots given by

$$\omega_{l,l} = -\Omega_v/2 \pm \sqrt{\Omega_v^2/4 + \omega_p^2/[1 - (r_0/l\alpha d) Q_l^l/Q_l^l]}. \quad (5.14)$$

For $\Omega_v > 0$ the low-frequency mode (upper sign) corresponds to the diocotron mode of a cylindrical non-neutral plasma [51] and the high-frequency mode (lower sign) is a

surface mode in the upper hybrid frequency regime.

When $l = m + 1$, Eq. (5.13) becomes

$$(\alpha_l + \beta_l)\omega^2(\omega + \Omega_v) - \alpha_l\omega\omega_p^2 - \Omega_v\omega_p^2 = 0, \quad (5.15)$$

where $\alpha_l \equiv 1 + \alpha^2(l-1)$ and $\beta_l \equiv -[\alpha/(\alpha^2 - 1)^{1/2}]Q_l^{l-1}/Q_l^{l-1}$. There are three solutions for the mode frequency which, when $l=2$, are the same as the solutions of Eqs. (3.22)–(3.24) for the (2,1) mode. When $l=1$, one of the roots is spurious and the other two approach the single-particle axial bounce frequency $\omega_z = \omega_p/(1 + \beta_1)^{1/2}$ in agreement with Eq. (2.6); this is the axial center-of-mass mode.

Results for the frequencies when $l = m + 2$, $m + 3$, ... require the solution of even higher-order polynomial equations. We have found the solutions numerically, and some results are displayed in Figs. 17(a)–17(c) as functions of the rotation frequency ω_r . It is important to remember here that both Ω_v and ω_p are functions of the ω_r ; in fact, in the rotating frame the plasma becomes unmagnetized at the Brillouin limit $\Omega_v = 0$.

Examination of the mode frequencies at the Brillouin limit (equivalent to the case of ions in a Paul trap) shows that for given l and m there are two modes which become unmagnetized surface plasma oscillations. These surface mode frequencies are described by the particularly simple limiting form of Eq. (5.11), $\epsilon_3 = P_l^m Q_l^{m^2} / P_l^{m^2} Q_l^m$ [here the argument of the P_l^m 's simplifies to $\alpha/(\alpha^2 - 1)^{1/2}$]. Thus, when $\Omega_v = 0$ there are a pair of surface modes with frequencies of opposite sign. For $\Omega_v \neq 0$ but $|\Omega_v| < \omega_p$ and $l \rightarrow \infty$, these modes are evanescent, approaching the magnetized surface plasma frequencies $\pm\Omega_u/\sqrt{2}$. This result is independent of the shape of the cloud. However, for $|\Omega_v| > \omega_p$ the behavior of these two modes depends on m . When $m = 0$ the pair of modes remains in the magnetized plasma regime $\omega < \omega_p$, as shown in Figs. 17(b) and 17(c). When $m \neq 0$, however, only one mode remains in the magnetized plasma regime, while the other enters the upper hybrid range, as shown in Fig. 17(a).

The rest of the modes always remain in either the magnetized plasma or upper hybrid regime. Their numbers are as follows; when $m \neq 0$ there are $l - m$ magnetized plasma modes and $2 \text{int}[(l - m)/2]$ upper hybrid modes; when $m = 0$ there are $\text{int}[(l - 1)/2]$ pairs of magnetized plasma modes, and $\text{int}[l/2]$ pairs of upper hybrid modes. [These numbers can be determined by analysis of the solutions of Eq. (5.13) in the limits $\Omega_v \rightarrow \infty$ and $\Omega_v \rightarrow 0$.]

Finally, we compare the frequencies of (2,0) and (4,0) modes, which, like the (2,0) modes, can be excited using the technique described in Sec. IV. The frequency of the evanescent (4,0) mode, shown in Fig. 17(b) for the experimental value $\omega_z/\Omega = 0.151$, is quite different from the evanescent (2,0) frequency, which was measured experimentally. Evanescent branches with higher l are even further removed from the $l=2$ root, approaching $\Omega_u/\sqrt{2}$. This provides further evidence that the measured mode shown in Fig. 12 is in fact a (2,0) mode excitation and not a higher-order oscillation. However, it should be possible to excite other $m=0$ even l modes using the same experimental technique. For larger values of ω_z/Ω , however, the evanescent (2,0) mode becomes

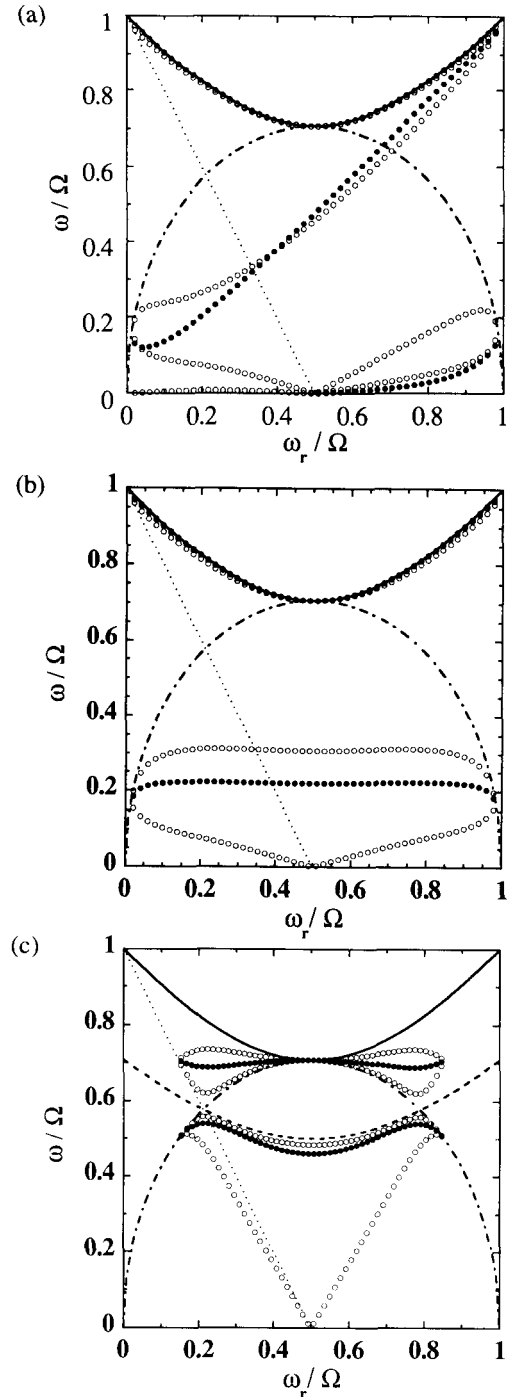


FIG. 17. Mode frequencies ω in the rotating frame vs rotation frequency ω_r for different values of (l, m) and ω_z . (From Sec. VB, $\omega^{\text{lab}} = \omega - m\omega_r$.) For $\omega < 0$ the diagrams should be reflected through the point $(\omega_r, \omega) = (\Omega/2, 0)$. Also shown for comparison are the upper hybrid frequency $\Omega_u(\omega_r)$ (solid curve), the vortex frequency $\Omega_v(\omega_r)$ (dotted curve), the plasma frequency $\omega_p(\omega_r)$ (dot-dashed curve), and in (c) the surface upper hybrid frequency $\Omega_u(\omega_r)/\sqrt{2}$ (dashed curve). All frequencies are expressed in units of the cyclotron frequency Ω . (a) $\omega_z/\Omega = 0.151$; $(l, m) = (2, 1)$, filled circles; $(l, m) = (5, 1)$, open circles. The (2,1) modes for this condition are also shown in Fig. 8 in the laboratory frame. (b) $\omega_z/\Omega = 0.151$; $(l, m) = (2, 0)$, filled circles; $(l, m) = (4, 0)$, open circles. The (2,0) modes for this condition are also shown in Fig. 6. They are the same in the laboratory or rotating frame. (c) $\omega_z/\Omega = 0.5$; $(l, m) = (2, 0)$, filled circles; $(l, m) = (4, 0)$, open circles.

nearly degenerate with the evanescent (4,0) mode [see Fig. 17(c)], making it more difficult to distinguish between modes with different values of l merely from frequency measurements.

B. Resonances between modes and static field errors

Now that the linear modes have been enumerated, we turn to the problem of modes driven by an external source. In particular, as we saw in Sec. IV, a static field error can drive to large amplitude a (2,1) mode, when the mode satisfies the linear resonance condition that it has zero frequency in the laboratory frame. In this section we consider the resonance between a static error and modes with general (l,m) .

In the rotating frame, modes have a variation proportional to $\exp(im\phi - i\omega t)$. The azimuthal angle ϕ as viewed in the rotating frame is related to the angle ϕ_L as viewed in the laboratory frame through the Galilean transformation $\phi = \phi_L + \omega_r t$. Therefore, the condition that a mode has zero frequency in the laboratory frame is

$$\omega = m\omega_r, \quad (5.16)$$

Solutions of this equation can be found graphically in Fig. 17 by finding the intersections of the line given by Eq. (5.16) and the curves of mode frequency versus rotation frequency. In general, for a given l and m there are $l - m$ intersections for $m \neq 0$ and no intersections when $m = 0$. [Equation (5.16) implicitly assumes $m \geq 0$ and positively charged, trapped particles as discussed earlier. With the sign convention used here where ω_r is always positive, the condition for negatively charged particles is $\omega = -m\omega_r$.]

For a given ω_z/Ω the solutions of Eq. (5.16) provide specific values of ω_r/Ω at which resonances can occur between a static error and a mode with given (l,m) . These values trace out curves as ω_z/Ω is varied; the curves are plotted for $m = 1$ and $m = 2$ in Fig. 18. Since modes with $l - m$ odd are odd in z , these modes will be excited (in linear theory) only by errors which are also odd in z , such as the error induced by a tilt of the electrodes with respect to the magnetic field. Similarly, errors which are even in z excite modes with $l - m$ even. Furthermore, only modes with the same value of m as the perturbation can be excited (in linear theory). This implies that the tilt field error, which (for small tilt angles) is

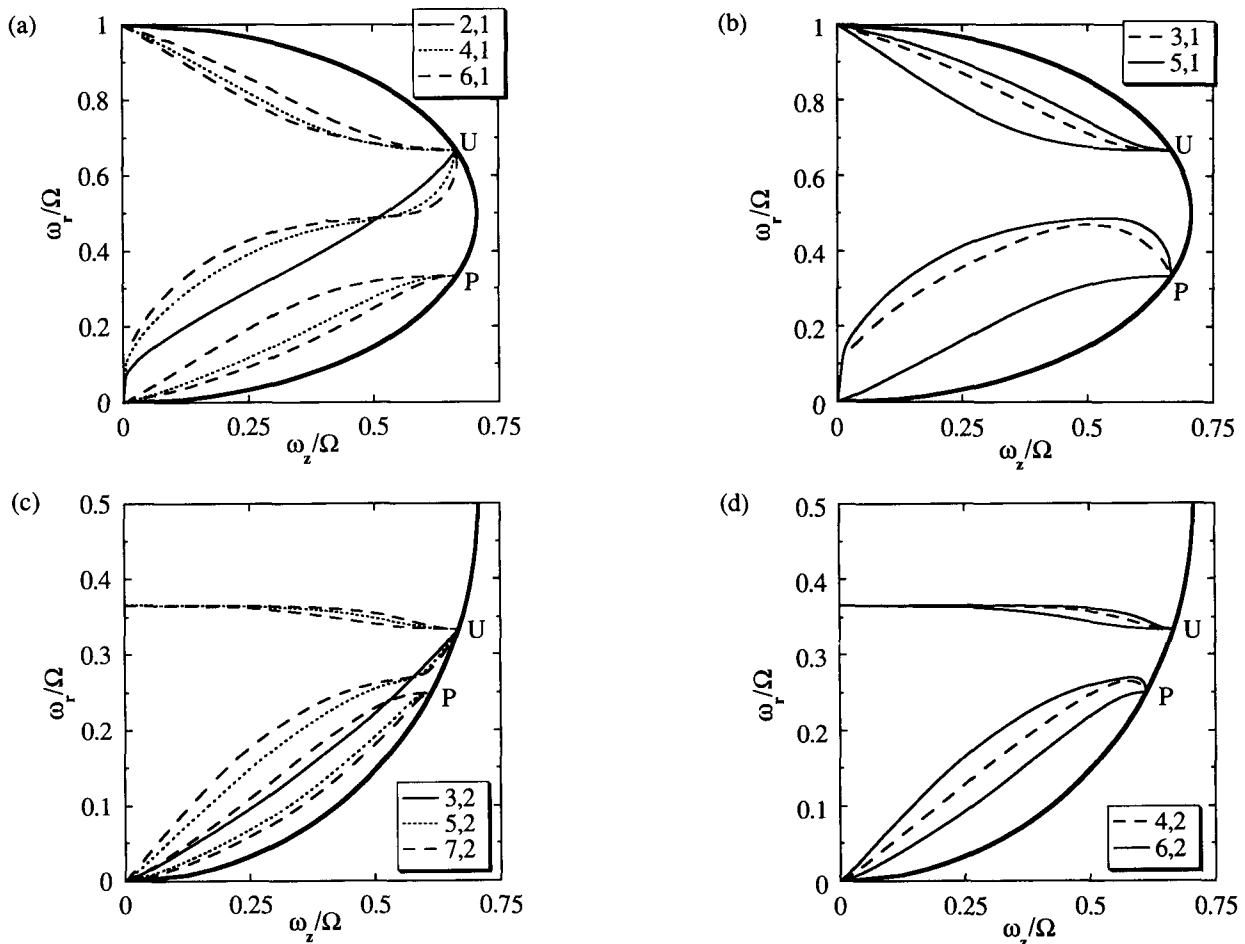


FIG. 18. Values of ω_r/Ω and ω_z/Ω for which different $m = 1$ and $m = 2$ modes become zero frequency in the laboratory frame. The limiting points U and P , which fall on the confinement boundary, are discussed in the text. The confinement boundary, defined by $\omega_r = \omega_m$ and $\omega_r = \Omega - \omega_m$, where ω_m is given by Eq. (2.10), is also drawn. The $m = 1$ modes are shown in (a) and (b), and the $m = 2$ modes are shown in (c) and (d). Modes odd in z are shown in (a) and (c) and modes even in z are shown in (b) and (d). The curve for the zero-frequency (2,1) mode in (a) is the curve in Fig. 10.

an $m=1$ perturbation that is odd in z , can linearly resonate only with the (2,1), (4,1), (6,1), . . . modes.

The (2,1) mode is most strongly excited since it has the slowest spatial variation and hence has the largest "overlap" with the slowly varying tilt error. Furthermore, the (4,1) and (6,1) resonance curves have quite different forms from the (2,1) curve, which indicates that the excitation observed in the experiments is in fact a (2,1) mode, not a higher-order excitation. However, the other resonances may also be measurable.

Turning now to the limiting behavior of the resonance curves, we observe that in the rotating-frame mode frequencies are always less than the upper hybrid frequency $\Omega_u = (\omega_p^2 + \Omega_v^2)^{1/2}$. Then Eq. (5.16) implies that resonant rotation frequencies must satisfy the relation

$$m\omega_r \leq \sqrt{\omega_p^2 + \Omega_v^2} = \sqrt{2\omega_r(\Omega - \omega_r) + (\Omega - 2\omega_r)^2},$$

which can be solved to give

$$\omega_r/\Omega \leq (\sqrt{m^2 - 1} - 1)/(m^2 - 2) = 1, 0.366, 0.261, \dots$$

This implies that as m increases the resonances become packed into a smaller and smaller region of the experimental operating regime. Since most experiments operate in the regime $\omega_r/\Omega \ll 1$, we may have cause to worry that these many resonances could have a deleterious effect on the plasma confinement. However, the mode resonances with smaller values of l and m are most dangerous since they are more easily excited by perturbations with slow spatial variation, and larger l and m modes may be heavily damped due to viscous effects or collisionless Landau damping [52].

Other limiting values of the resonance curves can also be found. For example, consider the limit in which the plasma becomes extremely oblate, that is, a thin disk or pancake. This occurs along the edge of the confinement region defined by the equations $\omega_r = \omega_m$ and $\omega_r = \Omega - \omega_m$, where ω_m is given by Eq. (2.10). In this limit, the mode frequencies approach either Ω_v or ω_p . In the former case resonances occur when $\Omega_v = m\omega_r$, or

$$\omega_r/\Omega = 1/(m+2) = \frac{1}{3}, \frac{1}{4}, \frac{1}{5}, \dots$$

This limit is labeled by the point P in Fig. 18. In the

latter case resonances occur when $\omega_p = m\omega_r$, which can be solved for ω_r to yield

$$\omega_r/\Omega = 2/(m^2 + 2) = \frac{2}{3}, \frac{1}{3}, \frac{2}{11}, \dots$$

This limit is labeled by the point U . Resonance curves which connect to the point P are due to magnetized plasma modes, whereas curves connecting to point U are due to resonances with upper hybrid modes.

Finally, we briefly discuss how the strength of these resonances should behave as the size or density of the plasma increases. Since the plasma is generally small compared to the distance to the electrodes, external field errors have slow spatial variation compared to the plasma size, and hence only the lowest-order l and m resonances should be observed. However, as the plasma increases in size higher-order modes have a larger "overlap" with the field error. Furthermore, as either plasma size or density is increased more electrostatic energy is liberated by radial expansion of the plasma due to the torque of the error acting on the cloud. Thus, we expect heating due to resonances to increase as more ions are trapped, and more resonances with higher values of l and m should be observable. This qualitative picture appears to agree with observations of higher density ion clouds. However, a quantitative analysis of this important question involves effects which are beyond the scope of this work, such as the effect of viscosity, Landau damping, laser light pressure, and nonlinearities on the saturation level of the mode amplitude. These issues need to be considered in a future paper.

ACKNOWLEDGMENTS

We thank John Schiffer for stimulating discussions on this subject and Steve Jefferts and Steve Barlow for their comments and careful reading of the manuscript. We gratefully acknowledge support by the U.S. Office of Naval Research Contract No. N00014-92-F-0038. D.H.E.D. acknowledges the support of the U.S. Office of Naval Research Contract No. N00014-89-J-1714 as well as National Science Foundation Grants No. PHY87-06358 and No. PHY91-20240.

*Current address: Department of Physics, University of Texas, Austin, TX 78712.

- [1] H. G. Dehmelt, *Adv. At. Mol. Phys.* **3**, 53 (1967); **5**, 109 (1969); D. J. Wineland, W. M. Itano, and R. S. Van Dyck, Jr., *ibid.* **19**, 135 (1983); R. C. Thompson, *Adv. At. Mol. Opt. Phys.* (to be published).
- [2] J. H. Malmberg and J. S. deGrassie, *Phys. Rev. Lett.* **35**, 577 (1975).
- [3] M. L. Gross and D. L. Rempel, *Science* **226**, 261 (1984); A. G. Marshall, *Acc. Chem. Res.* **18**, 316 (1985).
- [4] R. S. Van Dyck, Jr., P. B. Schwinberg, and S. H. Bailey, in *Atomic Masses and Fundamental Constants 6*, edited by J. A. Nolan, Jr. and W. Benenson (Plenum, New York, 1980), p. 173; R. S. Van Dyck, Jr., D. L. Farnham, and P. B. Schwinberg, *Phys. Scr.* **46**, 257 (1992).
- [5] E. A. Cornell, R. M. Weisskoff, K. R. Boyce, R. W.

- Flanagan, Jr., G. P. Lafyatis, and D. E. Pritchard, *Phys. Rev. Lett.* **63**, 1674 (1989).
- [6] G. Bollen, R. B. Moore, G. Savard, and H. Stolzenberg, *J. Appl. Phys.* **68**, 4355 (1990).
- [7] G. Gabrielse, X. Fei, L. A. Orozco, R. L. Tjoelker, J. Hass, H. Kalinowsky, T. A. Trainor, and W. Kells, *Phys. Rev. Lett.* **65**, 1317 (1990).
- [8] D. Hagena and G. Werth, *Europhys. Lett.* **15**, 491 (1991); J. Kern, T. Engel, D. Hagena, and G. Werth, *Phys. Scr.* **46**, 575 (1992).
- [9] R. S. Van Dyck, Jr., P. B. Schwinberg, and H. G. Dehmelt, *Phys. Rev. D* **34**, 722 (1986); *Phys. Rev. Lett.* **59**, 26 (1987).
- [10] M. Hubrich, H. Knab, K. H. Knoell, and G. Werth, *Z. Phys. D* **18**, 113 (1991).
- [11] *Frequency Standards and Metrology*, Proceedings of the

- Fourth Symposium on Frequency Standards and Metrology, Ancona, Italy, edited by A. De Marchi (Springer-Verlag, Berlin, 1989).
- [12] J. J. Bollinger, D. J. Heinzen, W. M. Itano, S. L. Gilbert, and D. J. Wineland, *Phys. Rev. Lett.* **63**, 1031 (1989); J. J. Bollinger *et al.*, *IEEE Trans. Instrum. Meas.* **40**, 126 (1991); D. J. Wineland, *et al.*, *IEEE Trans. Ultrason. Ferroelectrics Freq. Control* **37**, 515 (1990).
- [13] J. D. Prestage, G. J. Dick, and L. Maleki, *IEEE Trans. Instrum. Meas.* **40**, 132 (1991); L. S. Cutler, R. P. Giffard, P. J. Wheeler, and G. M. R. Winkler, in *Proceedings of the Forty-First Annual Frequency Symposium*, IEEE Catalog No. 87CH2427-3 (IEEE, New York, 1987), p. 12 (copies are available from NTIS, 5285 Port Royal Rd., Springfield, VA 22161); M. Jardino, M. Desaintfuscien, R. Barillet, J. Viennet, P. Petit, and C. Audoin, *Appl. Phys.* **24**, 107 (1981).
- [14] A. Muench, M. Berkler, Ch. Gerz, D. Wilsdorf, and G. Werth, *Phys. Rev. A* **35**, 4147 (1987).
- [15] D. A. Church, in *Physics of Electronic and Atomic Collisions*, edited by S. Datz (North-Holland, Amsterdam, 1982), p. 533; D. A. Church *et al.*, *Nuclear Instrum. Methods Phys. Res. Sect. B* **56/57**, 417 (1991).
- [16] J. H. Malmberg, C. F. Driscoll, B. Beck, D. L. Eggleston, J. Fajans, K. Fine, X.-P. Huang, and A. W. Hyatt, in *Non-Neutral Plasma Physics*, Proceedings of the Symposium on Non-Neutral Plasma Physics, edited by C. W. Roberson and C. F. Driscoll, AIP Conf. Proc. No. 175 (AIP, New York, 1988), p. 28.
- [17] C. F. Driscoll and K. S. Fine, *Phys. Fluids B* **2**, 1359 (1990).
- [18] C. F. Driscoll, J. H. Malmberg, and K. S. Fine, *Phys. Rev. Lett.* **60**, 1290 (1988).
- [19] D. L. Eggleston, T. M. O'Neil, and J. H. Malmberg, *Phys. Rev. Lett.* **53**, 982 (1984); D. L. Eggleston and J. H. Malmberg, *ibid.* **59**, 1675 (1987).
- [20] S. L. Gilbert, J. J. Bollinger, and D. J. Wineland, *Phys. Rev. Lett.* **60**, 2022 (1988).
- [21] D. J. Heinzen, J. J. Bollinger, F. L. Moore, W. M. Itano, and D. J. Wineland, *Phys. Rev. Lett.* **66**, 2080 (1991); **66**, 3087E (1991).
- [22] P. B. Schwinberg, R. S. Van Dyck, Jr., and H. G. Dehmelt, *Phys. Lett.* **81A**, 119 (1981).
- [23] C. M. Surko, M. Leventhal, and A. Passner, *Phys. Rev. Lett.* **62**, 901 (1989).
- [24] G. Gabrielse, X. Fei, L.A. Orozco, R. L.Tjoelker, J. Hass, H. Kalinowsky, T. A. Trainor, and W. Kells, *Phys. Rev. Lett.* **63**, 1360 (1989); **65**, 1317 (1990).
- [25] R. S. Van Dyck, Jr. and P. B. Schwinberg, *Phys. Rev. Lett.* **47**, 395 (1981); R. S. Van Dyck, Jr., F. L. Moore, D. L. Farnham, and P. B. Schwinberg, *Int. J. Mass Spectrom. Ion Processes* **66**, 327 (1985).
- [26] R. S. Van Dyck, Jr., F. L. Moore, D. L. Farnham, and P. B. Schwinberg, *Phys. Rev. A* **40**, 6308 (1989).
- [27] F. L. Walls and G. H. Dunn, *J. Geophys. Res.* **79**, 1911 (1974); R. A. Heppner, F. L. Walls, W. T. Armstrong, and G. H. Dunn, *Phys. Rev. A* **13**, 1000 (1976).
- [28] L. R. Brewer, J. D. Prestage, J. J. Bollinger, W. M. Itano, D. J. Larson, and D. J. Wineland, *Phys. Rev. A* **38**, 859 (1988).
- [29] D. H. E. Dubin, *Phys. Rev. Lett.* **66**, 2076 (1991).
- [30] S. A. Prasad and T. M. O'Neil, *Phys. Fluids* **22**, 278 (1979).
- [31] D. H. E. Dubin and T. M. O'Neil, *Phys. Rev. Lett.* **60**, 511 (1988).
- [32] J. H. Malmberg and T. M. O'Neil, *Phys. Rev. Lett.* **39**, 1333 (1977).
- [33] D. J. Wineland, J. J. Bollinger, W. M. Itano, and J. D. Prestage, *J. Opt. Soc. Am. B* **2**, 1721 (1985).
- [34] P. M. Morse and H. Feshbach, *Methods of Theoretical Physics* (McGraw-Hill, New York, 1963), Chap. 10.
- [35] J. B. Jeffries, S. E. Barlow, and G. H. Dunn, *Int. J. Mass Spectrom. Ion Processes* **54**, 169 (1983).
- [36] R. C. Davidson, in *Non-Neutral Plasma Physics* [16], p. 139.
- [37] J. S. deGrassie and J. H. Malmberg, *Phys. Fluids* **23**, 63 (1980).
- [38] S. A. Prasad and T. M. O'Neil, *Phys. Fluids* **26**, 665 (1983).
- [39] R. Keinigs, *Phys. Fluids* **24**, 860 (1981); **27**, 1427 (1984).
- [40] D. J. Wineland, J. C. Bergquist, M. W. Itano, and R. E. Drullinger, *Opt. Lett.* **5**, 245 (1980).
- [41] H. S. Lakkaraju and H. A. Schuessler, *J. Appl. Phys.* **53**, 3967 (1982).
- [42] D. J. Wineland, J. J. Bollinger, and W. M. Itano, *Phys. Rev. Lett.* **50**, 628 (1983); **50**, 1333E (1983).
- [43] W. M. Itano, L. R. Brewer, D. J. Larson, and D. J. Wineland, *Phys. Rev. A* **38**, 5698 (1988).
- [44] C. F. Driscoll, in *Low Energy Antimatter*, edited by David Cline (World Scientific, Singapore, 1986), pp. 184–195.
- [45] J. Yu, M. Desaintfuscien, and F. Plumelle, *Appl. Phys. B* **48**, 55 (1989).
- [46] C. F. Driscoll and J. H. Malmberg, *Phys. Rev. Lett.* **50**, 167 (1983).
- [47] L. S. Cutler, C. A. Flory, R. P. Giffard, and M. D. McGuire, *Appl. Phys. B* **39**, 251 (1986); L. S. Cutler, R. P. Giffard, and M. D. McGuire, *ibid.* **36**, 137 (1985).
- [48] R. C. Davidson, *Theory of Nonneutral Plasmas* (Benjamin, Reading, MA, 1974), pp. 14–16, and 43.
- [49] P. M. Morse and H. Feshbach, *Methods of Theoretical Physics* (McGraw-Hill, New York, 1963), Chap. 5.
- [50] F. F. Chen, *Introduction to Plasma Physics* (Plenum, New York, 1974), pp. 88–94.
- [51] R. C. Davidson, *Theory of Nonneutral Plasmas* [48], p. 62.
- [52] N. A. Krall and A. W. Trivelpiece, *Principles of Plasma Physics* (San Francisco Press, San Francisco, 1986), p. 386.

Electrostatic modes as a diagnostic in Penning-trap experiments

Carl S. Weimer, J. J. Bollinger, F. L. Moore,* and D. J. Wineland

Time and Frequency Division, National Institute of Standards & Technology, 325 Broadway, Boulder, Colorado 80303

(Received 4 October 1993)

A subset of the electrostatic modes of a cold cloud of electrons, a non-neutral electron plasma, trapped in a Penning trap has been observed and identified using a recent theoretical model. The detection of these modes is accomplished using electronic techniques which could apply to any ion species. The modes are observed in the low-density, low-rotation limit of the cloud where the cloud approaches a two-dimensional charged disk. We observe both axially symmetric and asymmetric drumhead modes. The shape, rotation frequency, and density of the cloud are found in a real-time nondestructive manner by measuring the frequency of these modes. In addition, it is found that radio-frequency sideband cooling compresses the cloud, increasing its density. The ability to measure and control the density of a trapped ion cloud might be useful for experiments on low-temperature ion-neutral-atom collisions, recombination rates, and studies of the confinement properties of non-neutral plasmas.

PACS number(s): 32.80.Pj, 35.80.+s, 52.25.Wz, 52.35.Fp

Penning ion traps have become an important tool in studies involving low-energy charged particles [1]. Recently, a theory of the electrostatic fluid modes of a plasma confined in a Penning trap (and Paul rf trap) was developed [2-4]. A number of these modes were observed experimentally in a plasma of Be^+ ions using optical fluorescence techniques [3,4]. By measuring the eigenfrequencies of two or more of these modes, plasma characteristics such as density, rotation frequency, and shape can be found nondestructively. Several types of experiment would benefit from this information. For example [1,4], experiments on recombination rates, ion-neutral-atom and ion-ion collisions, and strongly coupled systems depend on the ion sample density, size, and shape. These modes can also be used to study the confinement properties of the trap. However, a general method for detecting these modes is desired. Optical detection of the modes, as demonstrated in Ref. [3], is practical only for a small number of ion species. The method of characterizing the plasma by ejecting the plasma from the trap onto a set of charge collectors [5] has the disadvantage (for some experiments) of being a destructive measurement.

The object of the work reported here was to investigate detection techniques which would allow these mode frequencies to be measured nondestructively for any type of

ion species. To do this, we used electronic methods for detecting the modes and electron plasmas to test the methods. Related observations with trapped ions have been made by Barlow, Jeffries, and Dunn [6], and with electrons and positrons by Tinkle, Greaves, and Surko [7]. In the low-density, low-rotation limit of the electron plasmas we were able to detect a number of modes. By comparing the frequency dependence of the detected modes with the theoretical model by Dubin [2,4], an identification of the modes was made. This allowed us to calculate the density and aspect ratio of the electron plasmas and study their evolution. By combining this information with a measurement of the number of electrons, the plasma size could then be determined.

A second goal of this work was to find a way to manipulate and increase the plasma density. For trapped atomic ions, lasers can be used to apply a torque to the plasma, compressing it and increasing its density [3,4,8]. In addition, lasers can be used to cool the atomic ion plasma, reducing its temperature to below 10 mK [8]. The possibility of compression of a non-neutral plasma by wave excitation has also been discussed [9]. In the work reported here, we found that the parametric coupling technique called magnetron sideband cooling [10,11] increased the electron plasma density. This technique uses only radio-frequency fields, is independent of the internal structure of the ion, and therefore can be used for any type of ion. The ability to increase a trapped plasma's density and decrease its temperature is important for a number of experiments including proposals to produce antihydrogen [12]. A prominent candidate for antihydrogen formation is a three-body collision (e^+, e^+, \bar{p}) whose cross section scales as $n_0^2 T^{-9/2}$, where n_0 is the density and T the temperature [12,13].

*Present address: Dept. of Physics, University of Texas, Austin, TX 78712.

I. THEORY

A Penning trap [1,5,10,11] confines charged particles by combining static magnetic and electric fields. Referring to Fig. 1, a static voltage V_0 applied between the endcaps and ring forms a potential (in spherical coordinates),

$$\Phi(r, \theta, \phi) = V_0 \sum_{n=0}^{\infty} c_{2n} (r/d)^{2n} P_{2n}(\cos\theta), \quad (1)$$

where P_{2n} are the Legendre polynomials and c_{2n} are constants. Here $d = r_i/\sqrt{2}$ is a characteristic trap size, with r_i the ring's internal radius (for our trap, $d = 3.54$ mm). The electrode shapes are designed so that the dominant term in the electrostatic expansion is that labeled by c_2 . This results in a potential $V_0 c_2 [z^2 - (x^2 + y^2)/2]/2d^2$ which confines the electrons axially in a harmonic well. In this case, the axial center-of-mass (c.m.) motion of the electrons is the same as that of a single electron and has a frequency $\omega_z = (2c_2 q V_0 / m d^2)^{1/2}$ where q/m is the charge-to-mass ratio. A homogeneous axial magnetic field B_0 is superimposed on this electric potential ensuring radial confinement. In the radial plane the center-of-mass motion is composed of two superimposed circular motions: the $\mathbf{E} \times \mathbf{B}$ (or magnetron) motion at frequency ω_m , and the modified cyclotron motion at frequency $\omega'_c = \omega_c - \omega_m$, where $\omega_c = qB_0/m$ (SI units). In general, $\frac{1}{2}\omega_z^2 = \omega_m \omega'_c$, and for our experiments, $\omega_m \ll \omega_z \ll \omega'_c$.

Cryogenic cooling used in this work was capable of reducing the electron temperature to close to 4 K. For the magnetic fields used here, and with 4 K temperatures, the cyclotron radius of an electron was small compared with the distance of closest approach between two electrons. Under this condition the plasma is strongly magnetized and the coupling between motion parallel and perpendicular to the magnetic field is weak [14,15]. This may have resulted in two different temperatures for motion parallel and perpendicular to the magnetic field. Except for a possible difference in these temperatures, we assume the electrons had sufficient time to evolve (due to electron/electron collisions) to a state of thermal equilibrium. In an experiment [16] with electrons with eV energies, global equilibration times were measured to be about 1 s at $B_0 = 0.01$ T. This time should increase with larger magnetic fields. It may scale as B_0^2 or B_0 depending on the conditions of the plasma [16–18]. For our experiment the non-center-of-mass modes were not observed until times greater than 100 s.

Over long times, trapped plasmas have been observed to undergo a radial expansion resulting in a decrease in their aspect ratio and density with time and eventual gradual particle loss from the trap as the particles strike the ring electrode. In the absence of external torques, the total canonical angular momentum of the plasma is conserved [19], which places a limit on the radial expansion and the number of electrons that can be lost from the trap. Therefore, some external torque is responsible for this radial transport of particles and energy [20]. For experiments done in high vacuum apparatus (such as used

here), the most likely candidates for this external torque are azimuthally asymmetric components in the trapping electric or magnetic fields [14]. Resonant enhancement of this transport rate can occur if the static field asymmetries couple to collective modes [3].

In thermal equilibrium, a cold electron (or ion) plasma with dimensions much less than those of the Penning-trap electrodes can be modeled as a uniform density spheroid which rigidly rotates about \hat{z} at the rotation frequency ω_r , with $\omega_m \leq \omega_r \leq \omega'_c$ [3,4,21–23]. The density is $n_0 = 2\epsilon_0 m \omega_r (\omega_c - \omega_r) / q^2$ in the plasma interior and falls off at the plasma boundary over a distance approximately equal to the Debye length $\lambda_d = (\epsilon_0 kT / n_0 q^2)^{1/2}$, where k is Boltzmann's constant, T the temperature, and ϵ_0 the permittivity of free space. For a comparison of experiment with theory, we will assume that the plasma is sufficiently cold that the Debye length is much smaller than the cloud dimensions. The plasma frequency ω_p , defined by $\omega_p^2 = q^2 n_0 / m \epsilon_0$, is related to the rotation frequency by $\omega_p^2 = 2\omega_r (\omega_c - \omega_r)$. The maximum density occurs for $\omega_r = \omega_c / 2$, which is called the Brillouin limit.

The aspect ratio of the plasma, defined by $\alpha \equiv z_0 / r_0$ with $2z_0$ the cloud length and $2r_0$ its diameter, is a function of the rotation frequency and therefore the density [23]. As $\omega_r \rightarrow \omega_c / 2$ (Brillouin limit) the aspect ratio increases to its maximum value. If, in addition, $\omega_z \ll \omega_c$, the cloud is a long cigar shape (prolate spheroid) along z . For either $\omega_r \rightarrow \omega_m$ or $\omega_r \rightarrow \omega'_c$, α decreases and the cloud becomes a flat pancake shape (oblate spheroid). An exact expression relating α and ω_r is given in Refs. [4] and [23]. For $\alpha \ll 1$, this expression can be expanded to first order in α with the result $\omega_p \simeq \omega_z (1 + \pi\alpha/4)$.

We have neglected the effects of correlations in the plasma due to the electron/electron Coulomb interaction [24]. A measure of these correlations is the coupling constant $\Gamma \equiv q^2 / (4\pi\epsilon_0 a_s kT)$, where a_s is the Wigner-Seitz radius given by $4\pi a_s^3 n_0 / 3 = 1$. For $\Gamma \ll 1$, the plasma acts as a weakly interacting gas, so correlations can be ignored. For $\Gamma > 1$, the plasma correlation increases and the plasma becomes liquidlike. As Γ further increases, the plasma crystallizes into a rotating lattice. In a Penning trap, the onset of crystallization has been directly observed using laser-cooled Be^+ ions [25]. A similar crystallization has also been reported in other systems, for example, in Paul traps [26], electrons on liquid helium [27], and, in the high-density limit, electrons in GaAs junctions [28]. For the work here, $\Gamma \simeq 0.2$ was measured and therefore correlations can be ignored. In general, even in the presence of spatial correlations, if the electron/electron spacing is short compared to the wavelength of the modes, the plasma can be treated as a constant-density plasma.

The theory of the electrostatic fluid modes of a cold, constant-density, spheroidal plasma confined by a harmonic well was solved analytically for some simple cases in Refs. [3] and [4], and was solved for the general case by Dubin [2,4]. The theory, applied at the Brillouin limit, also applies to ion plasmas in the rf or Paul trap [4]. Dubin assumes that the plasma is in thermal equilibrium and its temperature sufficiently low that pressure effects can be ignored. In addition he assumes that a_s and λ_d

are much less than the plasma dimensions and the wavelength of the modes. By combining the continuity, momentum, and Poisson's equations, the differential equation for the electric potential was solved using scaled spheroidal coordinates. The solutions are a set of mode potentials expressed as products of associated Legendre functions P_l^m and Q_l^m and a factor $e^{i(m\phi - \omega t)}$, where ϕ is the azimuthal angle about the trap axis and ω is the mode frequency. Here l and m are integers which label the modes, with $l \geq |m|$. Without loss of generality, $m \geq 0$ may be assumed and negative frequencies allowed.

As examples of these modes [2-4] the $(l,m)=(1,0)$ mode is just the axial center-of-mass mode. There are two $(1,1)$ modes which are just the magnetron and cyclotron center-of-mass modes, so all the $l=1$ modes are center-of-mass modes. The $l=2$ modes correspond to quadrupole deformations of the plasma shape. For example, there are two $(2,0)$ modes. Here the plasma shape remains spheroidal, but the aspect ratio of the spheroid oscillates in time. The low-frequency $(2,0)$ mode is a quadrupole oscillation where the axial and radial extents of the plasma oscillate out of phase with each other. The high-frequency $(2,0)$ mode is similar, except that the axial and radial extents oscillate in phase as if the plasma were breathing. The three $(2,1)$ modes are azimuthally asymmetric modes. For these modes, for small amplitude, the z axis of the plasma tips and precesses relative to the magnetic axis. In general, since the mode potential is proportional to $e^{im\phi}$, modes with $m=0$ are azimuthally symmetric while those with $m > 0$ are azimuthally asymmetric. The $(1,0)$ and $(1,1)$ modes (center-of-mass modes) are commonly observed both with electronic and optical detection. The $(2,0)$ and $(2,1)$ modes have been observed using optical detection, and excitation of a $(2,1)$ mode by a static field asymmetry was observed to heat the cloud [3].

A polynomial equation for the mode eigenfrequencies in a frame rotating at frequency ω_r is given in Eq. (5.13) of Ref. [4]. The mode frequencies in the laboratory frame are related to those in the rotating frame by $\omega_{l,m}(\text{lab}) = \omega_{l,m}(\text{rotating}) - m\omega_r$, where the term $m\omega_r$ is due to the Doppler shift. For $\omega_r \ll \omega_z \ll \omega_c$, the modes fall into three frequency ranges: high-frequency modes with $\omega \approx \omega_c$, intermediate-frequency modes with $\omega \approx \omega_z$ (or ω_p), and low-frequency modes with $\omega \approx \omega_m$ (or ω_r). Because of our detection technique (described below), the modes which we detected were the intermediate-frequency modes. For $\omega_r, \omega_z \ll \omega_c$ (the case here), they are magnetized plasma modes [4]. Here we summarize the $m=0$ and $m=1$ intermediate mode frequencies with $l-m \leq 7$ in the $\alpha \ll 1$ (low-density) limit. This was obtained by solving Eq. (5.13) of Ref. [4] for each value of l and m , to first order in α in the limit $\omega \approx \omega_p \ll \omega_c$ [29]. In the laboratory frame

$$\begin{aligned} |\omega_{1,0}| &= \omega_z, \\ |\omega_{2,0}| &= \omega_p, \\ |\omega_{3,0}| &= \begin{cases} \omega_z [1 - \frac{5}{16}\pi\alpha] \\ \omega_p \end{cases} \end{aligned}$$

$$\begin{aligned} |\omega_{4,0}| &= \omega_p, \\ |\omega_{5,0}| &= \begin{cases} \omega_z [1 - \frac{161}{256}\pi\alpha] \\ \omega_p \end{cases}, \\ |\omega_{6,0}| &= \omega_p, \\ |\omega_{7,0}| &= \begin{cases} \omega_z [1 - \frac{969}{1024}\pi\alpha] \\ \omega_p \end{cases}, \\ |\omega_{2,1}| &= \omega_z \pm \omega_r - \frac{1}{8}\pi\alpha\omega_z, \\ |\omega_{3,1}| &= \omega_p \pm \omega_r, \\ |\omega_{4,1}| &= \begin{cases} \omega_z \pm \omega_r - \frac{29}{64}\pi\alpha\omega_z \\ \omega_p \pm \omega_r \end{cases}, \\ |\omega_{5,1}| &= \omega_p \pm \omega_r, \\ |\omega_{6,1}| &= \begin{cases} \omega_z \pm \omega_r - \frac{397}{512}\pi\alpha\omega_z \\ \omega_p \pm \omega_r \end{cases}, \\ |\omega_{7,1}| &= \omega_p \pm \omega_r, \\ |\omega_{8,1}| &= \begin{cases} \omega_z \pm \omega_r - \frac{8977}{8192}\pi\alpha\omega_z \\ \omega_p \pm \omega_r \end{cases} \end{aligned} \quad (2)$$

and in addition, for completeness,

$$|\omega_{1,1}| = \omega_m, \omega_c',$$

and to first order in α

$$\omega_p = \omega_z [1 + \frac{1}{4}\pi\alpha],$$

$$\omega_r = (\omega_z^2 / 2\omega_c) [1 + \frac{1}{2}\pi\alpha].$$

The braces and \pm signs indicate when there are more than one intermediate mode frequencies to first order in α . Notice that for all values of l and m (except for $l-m=1$) there are mode frequencies which decrease with decreasing α . In general, these frequencies occur for more than one mode; they are degenerate to first order in α . However, when $l-m$ is odd, there are also mode frequencies that increase with decreasing α . Each of these frequencies occurs for a single, nondegenerate mode. The center-of-mass modes $(1,0)$ and $(1,1)$ are independent of α and thus the density of the cloud. However, (1) anharmonic terms in the trapping potential [$n > 1$ in Eq. (1)], and (2) image charge shifts, which are neglected in these expressions, cause the c.m. frequencies to depend slightly on their amplitudes of oscillation as well as the spatial distribution of the plasma in the trap. As a result of these effects, as the plasma expands due to radial transport the c.m. mode frequencies will shift slightly.

By knowing ω_z and identifying and measuring the frequency of any non-center-of-mass mode (or alternatively by measuring the frequencies of any two non-center-of-

mass modes), the plasma's aspect ratio and therefore its rotation frequency and density can be calculated. We note that if modes that are azimuthally asymmetric ($m > 0$) can be resonantly excited, then it might be possible to change the rotation frequency and increase or decrease the density. This is because the $m > 0$ modes carry angular momentum. Therefore, by driving them it might be possible to apply to the plasma a torque which in turn could affect the plasma density.

The linewidths of the modes will be set by some combination of damping and dephasing processes. Mode damping could occur through resonant or nonresonant coupling to resistive elements making up the trap and support structure. Careful trap design can decrease (or increase) this loss mechanism. Coupling between electrostatic modes could also cause energy transfer out of any one mode, damping its amplitude. Landau damping of the modes has also been reported [7]. Dephasing of the modes, leading to line broadening, could occur because of small anharmonic terms in the trapping or mode potentials. In addition, electron/electron collisions could cause this dephasing.

II. EXPERIMENTAL APPARATUS

The trap used in this study was previously used to investigate the nonlinear excitation of a single trapped electron and the center-of-mass modes of electron clouds [30]. The trap electrodes (Fig. 1) were machined from oxygen-free copper and had an inner ring radius of 0.50 cm, resulting in $d = 0.35$ cm. When a voltage V_0 was applied between the endcaps and the ring, the resulting electric potential near the trap's center closely approximated a harmonic potential along the z direction (with $c_2 = 0.487$) [31]. The cylindrical symmetry of the electrodes minimized azimuthally asymmetric electric perturbations. The leading order perturbation to the potential was the term labeled by c_4 in Eq. (1). However, by applying a voltage V_g to the additional guard electrodes [32] and observing the axial c.m. mode line shape, this perturbation could be reduced to $|c_4| \leq 5 \times 10^{-5}$. For a precision hyperbolic trap without guard electrodes, typically $|c_4| \geq 10^{-3}$ [11]. The ring electrode was split into three

sectors (Fig. 1). Typical operating parameters for this trap were $V_0 = -10.45$ V, $B_0 = 0.110$ T, $\omega_z/2\pi = 61.54$ MHz, $\omega_m/2\pi = 615.0$ kHz, and $\omega'_c/2\pi = 3.079$ GHz.

The magnetic field B_0 was produced with a multifilament Nb-Ti superconducting magnet. The field homogeneity near the trap center was specified as $\Delta B/B_0 \leq 2 \times 10^{-5}$ for a 1-cm-diam volume. The magnetic field's long term drift was measured to be within $1 \times 10^{-5}/h - 7 \times 10^{-7}/h$ for $B_0 = 0.1$ T. The trap was mounted at the center of the magnet in a sealed copper vacuum container. The magnet and vacuum container shared a common liquid-helium bath. The large cryosorption rate of the liquid-helium cooled walls maintained the vacuum inside the trap. The background pressure in a similar system was measured to be less than 7×10^{-15} Pa (5×10^{-17} Torr) [33]. An additional set of Helmholtz coils whose axis was perpendicular to B_0 and whose center was common with the trap center was mounted external to the magnet dewar. These coils were used to minimize the angle Θ_0 between the trap magnetic and electric axes when $B_0 \approx 0.1$ T.

Electrons were loaded into the trap by using a field-emission point (FEP) aligned along the \hat{z} axis and mounted in one endcap. By applying a negative potential of 600 V to the FEP an electron beam which passed into the trap and back out through matching holes in the endcaps was formed. Inside the trap the electron beam ionized background gas, which in turn supplied the low-energy secondary electrons which were trapped. By varying the beam current, the loading rate was varied from 0.01 to 100 s^{-1} .

The electronic system (Fig. 2) used to detect the signal induced by the electron's motion was similar to that developed at the University of Washington [10,11,34,35]. At the heart of the system is a helical resonator tuned circuit (TC) with frequency ω_{TC} . The resonator is attached to one endcap and its frequency set such that $\omega_{TC} \approx \omega_z$. The current induced in this endcap by the electrons' axial motion produces a voltage drop across the tuned circuit which was then amplified with a dual gate GaAs FET preamplifier. Both the tuned circuit and preamplifier were immersed in the liquid helium. The real part of the tuned circuit impedance sets the damping rate and

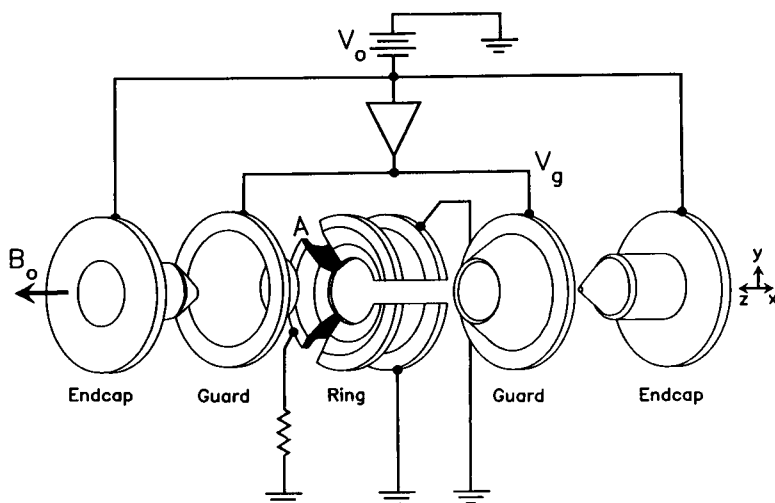


FIG. 1. A schematic diagram of our Penning trap. The electrodes have been separated along the axis to show details. The inner ring diameter is 1 cm.

linewidth of the axial c.m. motion [10,11,36]. The axial c.m. linewidth $\Delta\omega_z$ for our experiment was $\Delta\omega_z = N \times 19 \text{ s}^{-1}$ for $\omega_z = \omega_{\text{TC}}$, where N was the number of electrons. Therefore, an estimate for the number of electrons trapped was made by measuring $\Delta\omega_z$. The thermal amplitude of the axial c.m. motion (and the cyclotron c.m. motion via synchrotron radiation) had a characteristic temperature set by the liquid-helium bath, $T = 4 \text{ K}$.

Different detection methods were used in this study. The following is a brief description of each.

1. *Noise power.* In this detection method the noise induced in the endcap by the electrons' thermal motion was detected using a spectrum analyzer which acted as a square-law power detector [34,36]. When this spectrum analyzer was used to detect noise near the axial c.m. frequency, a noise decrease (or "dip") was observed for $\omega_z \approx \omega_{\text{TC}}$ as the electrons short circuited the tuned circuit's noise voltage [36]. A noise peak occurred for values of ω_z outside of the tuned circuit resonance [36]. The advantage of this detection technique was that it was passive, requiring no oscillating drive voltages to be applied to the trap.

A related detection method is sometimes called the "bolometric" method [6,34,36,37]. In this method, the spectrum analyzer's local oscillatory frequency is fixed so that only noise power around ω_z is observed. A parametric drive at $2\omega_z$ can be applied to heat the cloud increasing collisions and coupling between the modes. An oscillating drive voltage at frequency $\omega_d \neq \omega_z$ can simultaneously be applied to any of the trap electrodes. If the electrons absorb energy at ω_d , and if some of this energy is

coupled through some mechanism to the axial c.m. motion at ω_z , then an increase in the noise is observed.

2. *Coherent.* In this method, typically, the electrostatic well is modulated at a frequency $\omega_{\text{mod}}/2\pi = 1 \text{ MHz}$ producing frequency modulation sidebands on ω_z . A second drive of frequency ω_d is then applied to an endcap with $\omega_d \approx \omega_z + \omega_{\text{mod}}$. As ω_d is swept through resonance with the sideband ($\omega_d = \omega_z + \omega_{\text{mod}}$), the electrons' axial c.m. is excited, and this excitation in turn induces a signal in the other endcap near ω_z . This signal is then amplified and phase-sensitively (linearly) detected with a double-heterodyne receiver [10,11,35]. The modulation allows the drive to be applied at a frequency different than ω_{TC} , thus preventing saturation of the preamplifier. This method is very sensitive to small coherent changes in the axial c.m. amplitude.

3. *Axial frequency shift.* Because of imperfections in the static trap fields ($c_{2n} \neq 0$ for $n > 1$, and B_0 not homogeneous) and because of relativistic effects, the axial c.m. motion is slightly anharmonic and weakly coupled to the other degrees of freedom [10,30,38]. As an example, the axial c.m. frequency ω_z becomes dependent on the amplitude of oscillation of the c.m. magnetron motion. If the magnetron motion is excited, the axial frequency shifts because of the residual c_4 term in the trap potential. For a change of $r_m = 0 \rightarrow r_{m0}$ in the magnetron amplitude, the axial frequency shifts by $\delta\omega_z/\omega_z \approx 3c_4 r_{m0}^2 / (2c_2 d^2)$. To observe the axial frequency shift, an electronic servomechanism is used [10,38]. An axial drive is used to weakly excite the axial c.m. motion. The response to this drive is then detected and the output of the coherent phase detector is integrated and added (feedback) to V_0 with the correct sign. This effectively locks the axial frequency, holding it fixed relative to the (synthesized) drive and modulation frequencies. Any effect which would otherwise change the axial c.m. frequency is observable by monitoring the correction signal of the servo.

An additional experimental technique which was investigated was a parametric mode-coupling technique called magnetron sideband cooling [10,11,39], which is analogous to laser cooling [40]. It was first reported in experiments involving single electrons at the University of Washington [10]. The technique is used to reduce the metastable magnetron c.m. amplitude by parametrically coupling this motion to the axial c.m. motion which is damped by its coupling to the tuned circuit ($\omega_z = \omega_{\text{TC}}$). This parametric coupling is accomplished by applying a spatially inhomogeneous electric potential of the form $\phi(x, y, z) = V_p x z \cos(\omega_z + \omega_m)t$. The magnetron amplitude can be damped to a theoretical limit given by $r_m = 2[(\omega_m/\omega_z)\langle r_z^2 \rangle]^{1/2}$, where $\langle r_z^2 \rangle^{1/2}$ is the thermalized axial amplitude. Similarly, the magnetron motion can be damped through coupling to the cyclotron motion. Theoretical models of the cooling have not included plasma effects [11,39,41], although plasma models for parametric couplings between plasma modes might apply [42]. Evidence that sideband cooling affects the radial transport rate of a plasma has been found previously, in that, with the cooling on, cloud lifetimes are extremely long [33]. However, the effect of sideband cooling on the

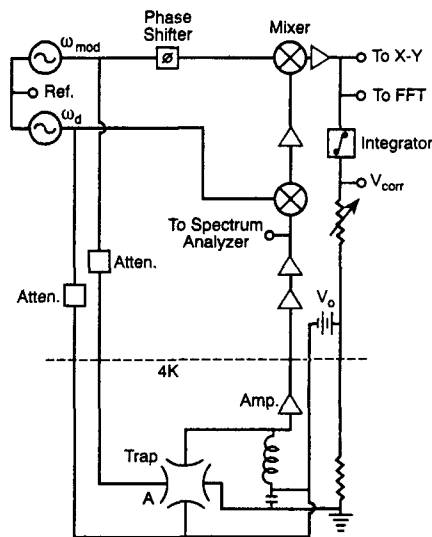


FIG. 2. A schematic diagram of the electronic detection system used in detecting the electrostatic modes of the electron plasma. The primary detection method was to look at the noise induced in one endcap using the spectrum analyzer, with the voltages at ω_d and ω_{mod} set to zero amplitude. In addition, the response of the plasma to the coherent drives ω_d and ω_{mod} was also detected and recorded by the X-Y recorder. A dynamic signal analyzer which recorded the fast Fourier transform (FFT) of the response was used as a diagnostic tool. V_{corr} is the servomechanism correction voltage.

aspect ratio and density of a plasma has not been studied before. For our trap the sideband cooling drive was applied to the ring sector *A*. The necessary axial dependence to the drive arose from the different impedances attached to the endcaps.

III. EXPERIMENTAL RESULTS

A. Observation of the modes from the noise power

Detection of the noise power of the induced currents in one endcap (method 1 above) gave the most definitive results, so we focused our attention there. After a cloud of electrons was loaded and the field emitter (and all drives) turned off, the axial c.m. motion with frequency $\omega_z = \omega_{1,0}$ could be seen in the noise spectrum (see inset in Fig. 3). Initially, the frequency of the c.m. motion decreased slightly with time. At a later point in time, noise peaks began to appear in the noise spectrum (Fig. 3). The frequencies of these noise peaks increased in time, with some crossing the axial c.m. frequency and others approaching it asymptotically (Fig. 4). If $\omega_z = \omega_{TC}$, so the axial c.m. signal was a noise dip, then as the peaks approached ω_z they too would change to noise dips, then back to peaks after the crossing. After the last crossing, the frequency of the axial c.m. mode would begin to increase slightly. Eventually, one by one, the amplitudes of the peaks decreased until they were no longer observable, with the axial c.m. mode typically the last to be seen. Surprisingly, it was found that the larger the value of $|c_4|$ the smaller the absolute frequency shift of the axial center of mass.

The number of noise peaks which were observed de-

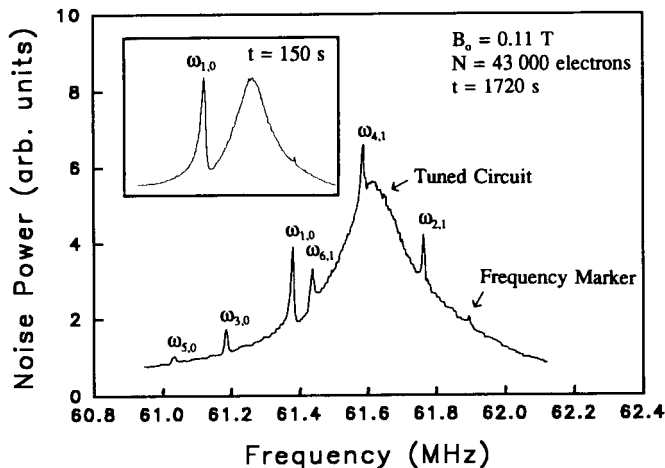


FIG. 3. The noise spectrum induced in one endcap as seen by the spectrum analyzer (resolution bandwidth is 10 kHz). The broad peak centered at 61.6 MHz is the axial tuned circuit resonance excited by thermal (≈ 4 K) noise. The inset shows the noise spectrum of a newly loaded cloud ($t = 150$ s after loading) in which only the axial center-of-mass mode and tuned circuit resonance are seen, and with ω_z slightly detuned from ω_{TC} . In the main figure the signals from six electrostatic modes including the axial center of mass mode can be seen at a later time ($t = 1720$ s after loading). Here $B_0 = 0.11$ T.

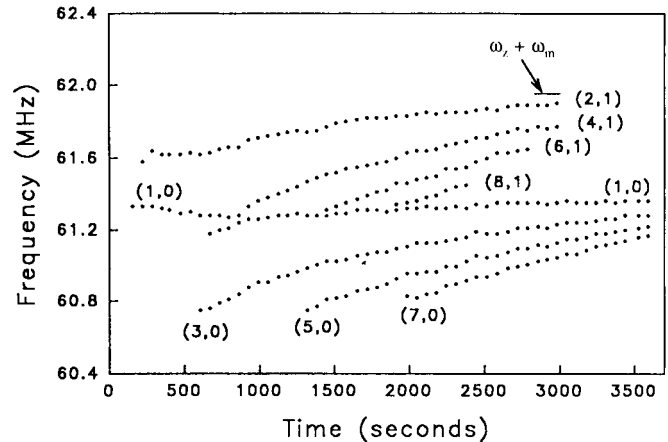


FIG. 4. A plot of the frequencies of the modes vs time after the cloud was loaded. The modes are labeled by their (l, m) values. These data were taken using a spectrum analyzer and were from the same data set as in Fig. 3. For these data the sideband cooling was off and the guard electrode voltage detuned so that $|c_4| \approx 4 \times 10^{-3}$. The measurement uncertainty in the frequency is less than the symbol size used in the plot and is the same for all points.

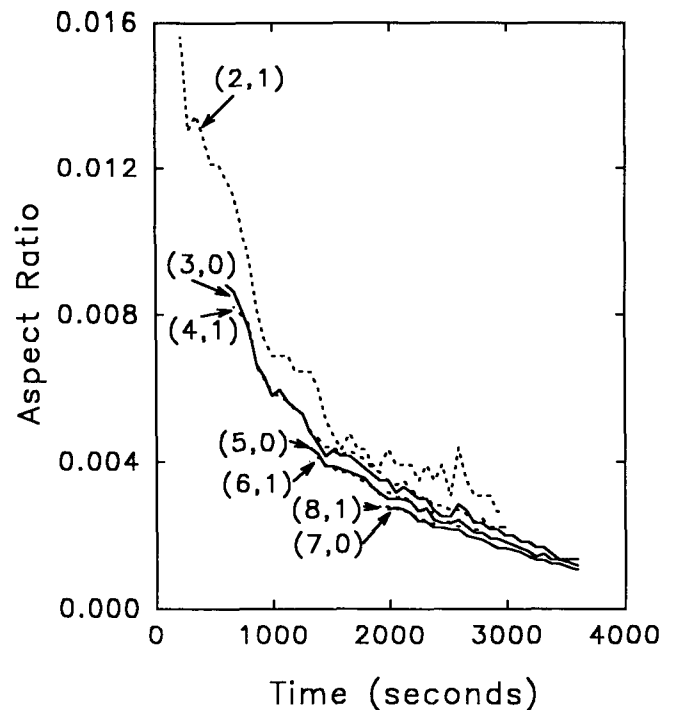
pendent most strongly on the number of electrons in a cloud. For clouds of 7000 electrons only the c.m. signal and one other peak were observed. For clouds of 70 000 electrons as many as ten peaks besides the axial c.m. peak were observed. The time at which the first additional noise peak appeared was found to be strongly dependent on the magnetic-field strength B_0 . For $B_0 = 0.11, 0.25,$ and 1.4 T (and for all N between 7000 and 70 000) the first peaks (other than the $\omega_{1,0} = \omega_z$ mode, which was seen immediately) appeared at the respective average times 520, 2000, and 15 800 s after loading. The modes were observed as the clouds' aspect ratio decreased below $\alpha \approx 0.02$. It was likely that the magnetic-field dependence was partly due to a slower radial expansion with larger magnetic fields. Also, the larger magnetic fields should have produced a more tightly confined electron beam that was used to load the electrons. This probably resulted in an initial cloud of smaller radial dimension.

Figure 4 shows a plot of the frequency of the noise peaks, including the axial center-of-mass peak, as a function of the elapsed time after an electron cloud was loaded into the trap. As discussed above, the frequency of the center-of-mass peak decreased slightly for early times after loading and then increased slightly. The figure shows two sets of noise peaks: those which asymptotically approach the axial center-of-mass frequency ω_z and those which asymptotically approach $\omega_z + \omega_m$. These peaks can be identified with some of the electrostatic mode frequencies of Eq. (2) for a pancake shaped (strongly oblate) plasma ($\alpha \ll 1$). The peaks which asymptotically approach ω_z can only be $m = 0$ modes. The peaks which asymptotically approach $\omega_z + \omega_m$ can only be $m = 1$ modes. In addition to the noise peaks shown in Fig. 4, some peaks were observed at early times and appeared to be $m = 2$ modes. These modes were only detected for a brief time which made their identification uncertain.

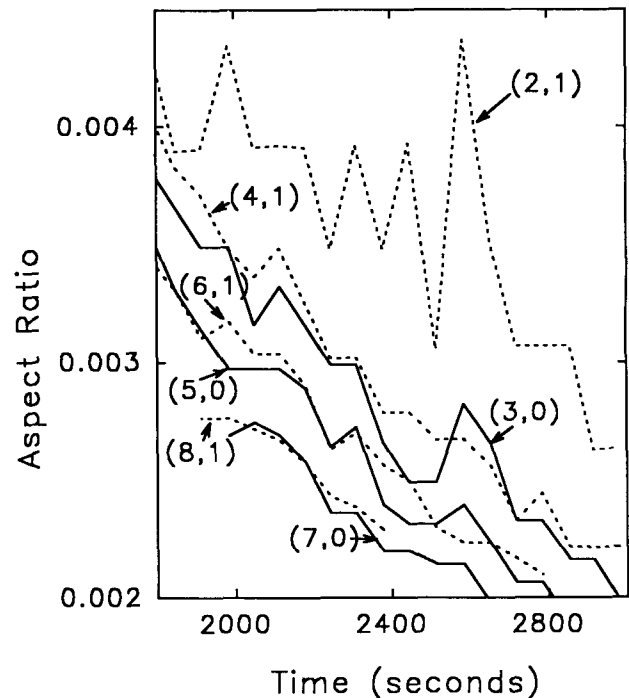
As discussed previously, azimuthal asymmetries in the trap cause a radial expansion of the plasma. The radial expansion should produce a decrease in the plasma's aspect ratio with increasing time. Therefore the mode frequencies detected in Fig. 4 apparently increase with decreasing aspect ratio (except the center-of-mass mode, whose frequency remains relatively constant). From Eqs. (2), only the frequencies of a subset of the modes with $l-m$ odd increase, or stay the same, for decreasing aspect ratio. For modes in this subset with $m=0$, the (1,0) mode has the highest frequency, the (3,0) mode has the next highest, the (5,0) the next, etc. For modes in this subset with $m=1$, the (2,1) mode has the highest frequency, the (4,1) the next highest, etc. In this manner, we were able to make the probable identification shown in Fig. 4 of the noise peaks.

The modes can be used to obtain information on the aspect ratio as a function of time. Following Dubin's cold fluid theory, we let $\omega_{1,0}$ be an estimate of ω_z . (This means our estimate of ω_z varies slightly as a function of time which disagrees with the ideal cold fluid theory.) Then, from Eqs. (2), every non-c.m. mode which we detected provides an estimate for the plasma aspect ratio α . Figure 5 shows the estimated aspect ratio as a function of time from the data of Fig. 4, using the measured value $\omega_c/2\pi=3080$ MHz. Fair agreement between the different estimates is obtained. Excluding the $\omega_{2,1}$ mode estimate, all the other estimates agree to better than 20%. It appears that the differences between the estimates are due to a systematic effect not included in the theory. In Fig. 5(b) it is seen that the estimated aspect ratio depends on $l-m$. As $l-m$ increases, the estimated aspect ratio decreases. For example, the (2,1) mode gives the highest estimated aspect ratio. The aspect ratio estimates from the (4,1) and (3,0) modes agree, but are less than the (2,1) estimate, and they are in turn greater than the (6,1) and (5,0) estimates. If the systematic dependence of the aspect ratio estimates on $l-m$ could be corrected, it appears that the mode frequencies could be used to calculate the plasma aspect ratio to better than 5%. We also note that the noise fluctuations in the estimates for the plasma aspect ratio decrease with increasing $l-m$. This is a result of the different sensitivities of α to the different mode frequencies [see Eqs. (2)].

The systematic shifts in the mode frequencies can also be seen in Fig. 4. From Eqs. (2), the intervals in Fig. 4 between neighboring $m=0$ noise peaks and also between neighboring $m=1$ noise peaks should equal $\omega_z\alpha$ to within a few percent. A visual inspection of Fig. 4 shows that the differences in these intervals are not equal within a few percent. In general, the intervals decrease in frequency as l increases. The smallest frequency intervals are 25–30% less than the largest frequency intervals. Similar results are found for $|c_4| < 5 \times 10^{-5}$. The discrepancy between the detailed predictions of Eqs. (2) and the observed noise peak frequencies of Fig. 4 may be due to (1) coupling of the modes with each other causing relative frequency shifts, (2) shifts due to image charges because the plasma radius is approaching the ring radius, and (3) the small thickness of the cloud. Because the detected modes appear to be two dimensional (discussed



(a)



(b)

FIG. 5. (a) Estimates of the cloud aspect ratio α as a function of the time since the cloud was loaded, for the data of Fig. 4. For each time, the (1,0) mode is used to estimate ω_z . Each (l,m) mode is then used to provide an estimate for α . The calculated values for α have been connected by straight lines for each mode. The values of α from $m=1$ ($m=0$) modes are connected by dashed (solid) lines. (b) An expanded view of (a) from 1800 to 3000 s showing the systematic dependence of the estimated aspect ratios on l and m .

below) the small thickness of the cloud should be less important. Evidence for the mode coupling is discussed below. The frequency variation of the (1,0) mode is possibly due to a combination of mode coupling, anharmonic effects, and image charge effects. If the size of the frequency variation of the (1,0) mode is used as an estimate of potential systematic shifts, then these shifts are sufficient to explain the apparent differences in the intervals between the mode frequencies.

As an example of what the mode frequencies infer about the plasmas, from Fig. 5 at time $t = 1720$ s, we find that $\alpha = 0.0039 \pm 0.0005$. The uncertainty here is equal to the scatter between the average aspect ratio estimate and the individual estimates. From the linewidth of the $\omega_{1,0}$ mode for $\omega_{1,0} = \omega_{TC}$ when first loaded, we determined $N = 43\,000$. The calculated electron density is then $4.7 \times 10^7 \text{ cm}^{-3}$, which implies an interparticle spacing of $17.2 \text{ }\mu\text{m}$ and cloud dimensions of $z_0 = 14.9 \text{ }\mu\text{m}$ and $r_0 = 3830 \text{ }\mu\text{m}$. Assuming the plasma was thermalized to $T = 4 \text{ K}$, the Debye length was $\lambda_d = 20.1 \text{ }\mu\text{m}$ and the coupling strength was $\Gamma = 0.24$.

The evolution of the mode frequencies was studied while varying different trap parameters. As discussed above and below, the two parameters which had the most profound effect on the plasma in this low-density limit were the magnetic-field strength and the application of a cooling drive. The appearance time of the mode peaks depended strongly on B_0 (the trap axial frequency was kept constant for all B_0). For all B_0 , the signals from the modes appeared when the plasmas' aspect ratios were approximately the same, $\alpha \approx 0.02$. This means the mode frequencies for different B_0 were also about the same. However, the rate at which the frequencies of these peaks changed in time due to radial expansion was found to be fairly insensitive to B_0 (see Fig. 6). This needs to be studied in more detail with better control over all other experimental parameters (such as Θ_0). Increasing the num-

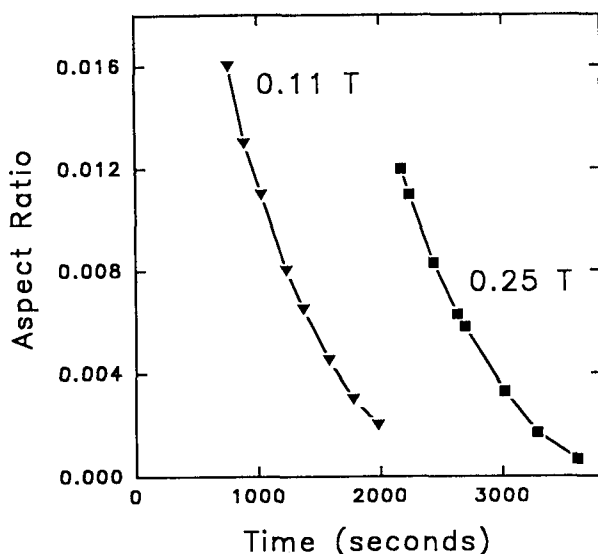


FIG. 6. The evolution of cloud aspect ratio as calculated from the frequencies of the $\omega_{3,0}$ mode and ω_z for two different magnetic fields. For $B_0 = 0.1 \text{ T}$, $N = 43\,000$ electrons and $\Theta_0 \leq 0.03^\circ$; and for $B_0 = 0.25 \text{ T}$, $N = 57\,000$ electrons and $\Theta_0 \approx 0.7^\circ$.

ber of trapped electrons from 7000 to 70 000 had little effect on the mode evolution. Changing the trap angle from $\Theta_0 < 0.030^\circ$ to $\approx 0.7^\circ$ (increasing the azimuthal asymmetry), distorting the electrostatic well by adding to 0.5 V to ring sector A (again, increasing the azimuthal asymmetry), or decreasing the resistance to ground of sector A from 105 to 16 Ω (which might change the radial damping) also had little or no effect on the mode evolution. Changing the guard voltage so that the trap was less harmonic (larger $|c_4|$) allowed the modes to be observed for a longer time after they appeared. It also slowed the rate of change of the aspect ratio, but by only a factor of 2.5 for a change of $|c_4| \leq 5 \times 10^{-5}$ to 4×10^{-3} . Having the cooling drive on or off during the initial loading had no effect on the mode evolution, nor did having ω_z tuned or detuned from ω_{TC} . We also tried to change the plasma's density by applying a drive to ring sector A resonant with the azimuthally asymmetric ($m > 0$) modes whose frequencies were near ω_z . No change in the mode frequencies was observed. Of these different control parameters, the only one which had any dramatic effect on the signal size, or number of observed modes, was the number of electrons in the plasma. We found that (as noted above) the larger the number of electrons, the larger the number of modes that were observed.

As mentioned previously, we detected only a subset of all of the possible modes with frequency near ω_z . Why we observed these modes and not others involves a number of factors. We found that by inspecting the mode potential [4] that the modes detected in Fig. 4 look like drumhead modes of a two-dimensional disk. At a given radius and azimuthal coordinate, all the electrons of the plasma oscillate axially in phase. Parts of the plasma with different radial positions and azimuthal coordinates oscillate with different phases. These modes are two dimensional and will exist in the limit that the thickness of the electron plasma is much less than the mean interparticle spacing. Modes which we did not detect have structure in the axial direction (the phase of the motion depends on z) which can be characterized by an effective wavelength which is less than, or on the order of, the plasma's axial extent. The continuous, fluid description of these modes breaks down when the interparticle spacing is comparable to or larger than this wavelength. In particular, when the plasma is very thin it is not clear how to think about these modes, and their calculation from the formulas of Refs. [2] and [4] is not correct.

In order to understand some of the other factors that determined which modes we observed, we require a better understanding of the detection mechanisms. There are at least two mechanisms by which the modes could couple to the endcap and be detected. The first is that, like the axial center of mass, the modes couple directly to the endcap by electrostatic coupling [6,43]. In general, the efficiency of inducing axial currents in the endcap depends on the radius of the plasma. Therefore, modes whose radial extent is on the order of r_i might induce a detectable current in the endcap even though the net axial velocity of the plasma is zero. For detection of an azimuthally asymmetric ($m > 0$) mode this requires that the cylindrical symmetry of the trap be broken by, for ex-

ample, a misalignment of the trap's electric and magnetic axes [44].

A second coupling mechanism for detection would be that the modes couple directly to the axial c.m. mode, which in turn couples to the endcap. This coupling could be by field asymmetries or mediated by image currents induced in the electrodes. For an ideal trap, small plasma size, and low mode excitation, all the modes are independent and therefore there would be no such coupling between the modes. However, Fig. 7 shows a narrow frequency span as the frequencies of two of the modes intersect that of the axial c.m. The (2,1) mode forms an anticrossing (or avoided crossing) with the axial center-of-mass mode; the mode frequencies never overlap. This is a general characteristic of two coupled oscillators [45]. Further evidence of the mode coupling was observed in the mode linewidths. Modes with frequencies different from ω_z by more than 150 kHz had full width at half maximum (FWHM) linewidths less than 10 kHz. These linewidths were observed to increase as the mode fre-

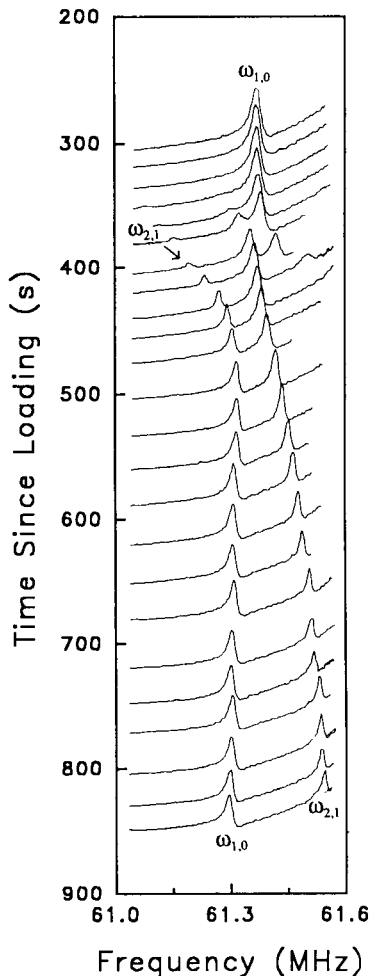


FIG. 7. A series of noise spectra (as in Fig. 3) of a cloud of 20 000 electrons (with $|c_4| \leq 5 \times 10^{-5}$, $B_0 = 0.11$ T) showing an avoided crossing between the axial center-of-mass mode and the ω_{21} mode (plus an avoided crossing of an unidentified mode at $t \approx 380$ s). As the modes approach each other they couple together resulting in the mode frequencies never becoming equal. The modes were identified by observing their behavior after the cloud was first loaded and also their asymptotic behavior for long times. The resolution bandwidth is 10 kHz.

quencies approached ω_z , as would be expected since the axial center-of-mass linewidth was larger.

These two detection mechanisms are not completely independent, making it difficult for us to differentiate between them. In addition, we might observe the modes through a combination of the two mechanisms. Additional evidence comes from the fact that we did not detect the $m = 1$ subset of modes whose frequencies went as $\omega_z - \omega_m - k(l)\alpha$, where $k(l)$ is a constant which depends on l [see Eq. (2)]. This was true for both $\omega_z - \omega_m \approx \omega_{TC}$ and $\omega_z - \omega_m < \omega_{TC}$. These modes have the same mode potential as the subset of modes whose frequencies went as $\omega_z + \omega_m - k(l)\alpha$, which we did detect. However, this subset of modes which we did detect crossed or had a small detuning from ω_z , while the others did not. Another important factor was that, when we purposely increased the trap azimuthal asymmetry (as discussed above), the signal size and number of observed $m = 1$ modes did not noticeably increase. Also, when we increased $|c_4|$ we were able to observe all the modes for a longer time. Together, these observations imply that coupling to the axial c.m. mode might have been the more important detection mechanism for us.

B. Effect of sideband cooling

The effects of sideband cooling were studied by first loading a cloud and allowing it to evolve to the point where some of the other modes besides the axial c.m. mode were observed. Then a strong sideband cooling drive was applied with frequency $\omega_z + \omega_m$ (for $\omega_z \approx \omega_{TC}$). After a few seconds, all the modes other than the c.m. mode disappeared. In addition, the c.m. mode frequency was back to its initial loading value. If the drive was then turned off, the other modes reappeared in approximately the same time, and in the same order, as a newly loaded cloud. This process was found to be very repeatable. Each time after the strong cooling drive was applied, the mode frequencies evolved at the same time and rate as that of a newly loaded cloud, except that the time was measured from when the drive was turned off. Thus, after each time the cooling was applied, the plasma density was reset back to the same value. Electrons were lost only when the cloud was allowed to expand radially until they struck the ring electrode before the cooling drive was applied. The point at which electrons began to be lost was consistent with the ring electrode radius being equal to the cloud radius as calculated from the mode frequencies. A typical drive strength to observe the effect of the sideband cooling drive was $V_A/V_0 \approx 10^{-4}$ at ring sector A for 10 000 electrons and $B_0 = 0.1$ T, where V_A is the voltage on A . Similar results were found for the different magnetic fields used, as well as with the cooling drive applied at frequency $\omega_d = \omega_z + 2\omega_m$ with a larger drive amplitude. With a weak cooling drive on continuously, additional modes were observed in the noise spectrum but they were not positively identified.

From these observations we conclude that the sideband cooling not only can stop radial expansion, but can reverse it by increasing the rotation frequency, and thus the aspect ratio and density, of the cloud. The rotation frequency was increased to approximately the same value as

the loading value. Applying the drive after the cloud expanded increased the aspect ratio by more than a factor of 20 from $\alpha < 0.001$ to $\alpha > 0.02$. For our conditions this implies an increase in the density of $\geq 3\%$. The mechanism for this compression of the cloud and what determines the limit to that compression are not known. One possibility is that the parametric coupling directly reduces the magnetron center-of-mass amplitude just as for a single electron. Then, anharmonic terms in the trapping potential might couple the magnetron c.m. mode to other non-c.m. modes [36] resulting in a compression. A second possible mechanism is that the parametric drive directly couples some other azimuthally asymmetric mode whose frequency is close to ω_m (like the lower frequency $\omega_{2,2}$ mode) to the axial center-of-mass mode. The cooling would then proceed until the azimuthally asymmetric mode frequency had shifted away from the resonance condition as the plasma density increased. Both of these mechanisms are possible in that we observed: (1) apparent electrostatic coupling between c.m. and azimuthally asymmetric non-c.m. modes (see Fig. 7) and (2) parametric coupling between a c.m. and an azimuthally asymmetric non-c.m. mode (discussed below).

C. Alternate detection methods

Detection of non-c.m. modes was also possible using the other techniques discussed in Sec. II. The "bolometric" technique (described in method 1 above) did not detect any modes, but it was not thoroughly tested. However, by using coherent detection (method 2 above) some of the modes were detected. Figure 8 shows the output of the phase-sensitive detector when the drive frequency was swept through $\omega_z + \omega_{\text{mod}}$. Two modes besides the axial c.m. mode are seen in the figure. This demonstrates that not only can we detect these modes coherently, but also that we can excite them with external drives.

Figure 9 shows the servo correction voltage in the axial frequency shift detection method (method 3 of above). Here the axial c.m. frequency was kept fixed by the servomechanism while a drive was applied to ring sector A. For $B_0 = 0.1$ T, a resonance appeared when the drive frequency was between ~ 100 and 500 kHz, and the resonance had a dispersive line shape. As time increased, this resonant frequency increased, always staying below ω_m . The resonance was very repeatable from cloud to cloud and was observable on clouds with as few as 300 electrons. As the drive strength was increased, the line shape became hysteretic, depending on the direction that the drive frequency was swept and the amplitude of the drive.

Evidence for the origin of this resonance was found when we simultaneously detected both the noise spectrum (method 1) and the axial frequency shift (method 3). We found that the resonant frequency of the dispersive resonance occurred at exactly the measured difference frequency between $\omega_z = \omega_{1,0}$ and $\omega_{2,1}$ for all the time the resonance could be observed. However, this dispersive resonance could be observed only after the $\omega_{2,1}$ mode had crossed over ω_z . Apparently the drive was capable of parametrically coupling together the (2,1) mode and the

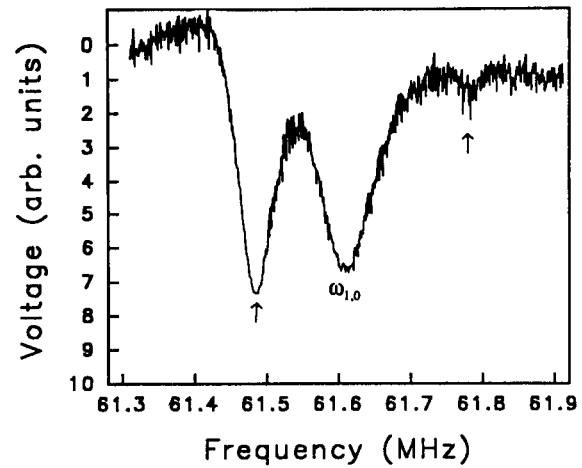


FIG. 8. Data taken using coherent detection (method 2 in the text) with $\omega_z \approx \omega_{\text{TC}}$ and a detection bandwidth of 10 Hz. The axial potential well was modulated at $\omega_{\text{mod}}/2\pi = 1$ MHz. A coherent drive applied to one endcap was swept across $\omega_z + \omega_{\text{mod}}$ and the response detected phase sensitively in the absorptive mode. These data were taken for $B_0 = 0.11$ T, $N = 26000$ electrons, and $|c_4| < 5 \times 10^{-5}$. The signals from the axial center-of-mass plus two other modes can be seen.

axial c.m. mode, similar to magnetron sideband cooling. This was done either directly by the parametric electric field or indirectly through the field's modulating the coherent axial motion necessary for the detection. This mode coupling might also explain the dispersive line shape since, as the modes become more strongly coupled

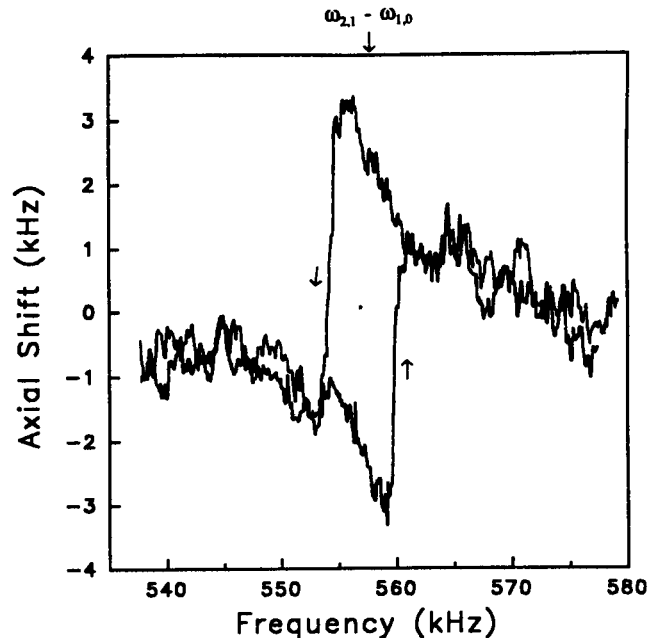


FIG. 9. The detection of the $\omega_{2,1}$ mode by monitoring the correction voltage to the locked axial center-of-mass frequency when a spatially inhomogeneous drive was applied through ring sector A and its frequency swept through $\omega_{2,1} - \omega_z$ (method 3 in the text). These data were taken for $B_0 = 0.11$ T, $N = 3000$ electrons, $|c_4| < 5 \times 10^{-5}$, and $\omega_m/2\pi = 615$ kHz. The arrows show the direction of the sweep. The hysteresis in this dispersive resonance can be seen. For sufficiently hard drives, the axial frequency could be shifted by much more than its linewidth.

together by the field, the modes would form an avoided crossing [45]. Our detecting just the frequency of the axial c.m. mode, while varying the coupling by sweeping the drive frequency, would result in a dispersive line shape. This line shape would become more hysteretic the stronger the coupling strength.

IV. DISCUSSION AND CONCLUSIONS

We have shown that it is possible to detect the electrostatic modes of a pure electron plasma in a Penning trap using nondestructive electronic methods. We detected several azimuthally symmetric and asymmetric modes in the low-density limit where the plasma approaches a two-dimensional charged disk. We observed these modes in the low-density limit because the noise power detection technique which we primarily used is facilitated by the mode frequencies being close to the axial center-of-mass frequency. This occurs for the intermediate frequency modes when the plasma density is low. We found that the frequencies of these modes fit Dubin's theoretical model [2,4] reasonably well. Also, we found that we could excite these modes directly with external drives, and in addition, by parametrically coupling modes together. The observation of these modes allowed the rotation frequency, shape, and density of the plasma to be determined. From auxiliary measurements of the electron number, we could then determine the plasma size. The detection techniques demonstrated here should work for any type of non-neutral trapped plasma, and should be applicable to the detection of modes other than the intermediate frequency modes. Other modes might also be detectable with a different geometry of electrodes to act as induced current detectors. The modes observed here may correspond to some of the features reported by Barlow [6], but a comparison is difficult because of differences in the detection.

In studying these modes we also observed behavior which departed from Dubin's model. This included a time dependence to the axial center-of-mass mode frequency due in part to the plasma radial expansion in an anharmonic trap. Also, we observed coupling between the axial center-of-mass mode and other modes evidenced, primarily, by avoided crossing behavior as their frequencies became degenerate. It is likely that this coupling is one cause for the deviations between observed and predicted mode frequencies, and will have to be studied further in order to get a more complete picture of the plasmas' characteristics. In addition, in comparing our data with Dubin's theory we found there to be a systematic shift in our measured aspect ratios as a function of $l - m$ where (l, m) is the mode used to determine the aspect ratio. To be able to measure plasma aspect ratios to much better than 20% will require this systematic effect to be understood and corrected for.

We also demonstrated that the parametric coupling technique called magnetron sideband cooling, which couples the magnetron and axial center-of-mass motions, not only stops the radial expansion of the plasma, but actual-

ly compresses the plasma increasing its density. The mechanism for this compression needs to be found in hopes of achieving higher densities with this technique. An interesting test would be to look for compression by sideband cooling when the coupling is between the magnetron and cyclotron motions. The ability to control the density without requiring optical methods might open new avenues for the study of cold non-neutral plasmas in Penning traps.

This study leaves a number of issues to be investigated. While the origin for the coupling between modes might be related to static electric field asymmetries, this needs to be studied further. Also, the mechanisms by which the modes are detected need not be positively identified. A detailed study of the signal amplitudes and linewidths of the modes would be a helpful first step towards solving these problems. A detailed study of the linewidths might also yield information on electron/electron collisions in trapped plasmas. If trapped, strongly coupled electron plasmas could be achieved, then these mode linewidths might be a measure of spatial correlations in the plasma. For example, in experiments on electrons localized near the surface of liquid helium, it has been demonstrated that the linewidth of shear wave resonances depended on Γ [46]. Similar results have been predicted for the electrostatic mode linewidths discussed here [47].

One important plasma parameter which we could not easily control was the plasma temperature T . Other groups have controlled their ion and electron plasmas' temperatures by introducing a buffer gas (e.g., Refs. [7], [43], and [48]). This has the disadvantages of applying an external torque on the cloud causing it to expand, being limited to temperatures greater than 4 K, and introducing what can be undesirable ion/neutral collisions affecting the physics to be studied. The problem of radial expansion due to the torque applied by the buffer gas can be eliminated by applying simultaneously a sideband cooling drive [48]. However, as noted in the introduction, there is also interesting physics to be studied for temperatures less than 4 K. Two methods which allow temperature control of the plasma for $T < 4$ K are using a dilution refrigerator, or sympathetic cooling by laser-cooled ions [49]. While both these methods are practical, they suffer from being expensive and difficult to implement. However, with advances in space-borne ^3He liquefiers, a liquefier well suited for cryogenic ion trap experiments has been developed [50]. These liquefiers act as both refrigerator and thermal isolator allowing the temperature to be varied within the range 0.3 to 30 K. While such a device would not give the lowest achievable temperature, it would give a useful control parameter.

ACKNOWLEDGMENTS

We gratefully acknowledge the support of ONR for this work. We would like to thank Dan Dubin for his help on the mode theory. We would also like to thank Steve Jefferts, Joseph Tan, and Matt Young for their comments on the manuscript.

- [1] For reviews see Fred L. Walls and Gordon H. Dunn, *Phys. Today* **27** (8), 30 (1974); *Phys. Scr.* **T22**, 21 (1988); *Int. J. Mass. Spectrom. Ion Proc.* **106**, 1 (1991); *J. Mod. Opt.* **39**, 193 (1992); *Phys. Scr.* **46**, 255 (1992); **46**, 544 (1992); *Hyperfine Interact.* **76**, 3 (1993); D.A. Church, *Phys. Rep.* **228**, 253 (1993); R. Thompson, *Adv. At. Mol. Phys.* **31**, 253 (1993).
- [2] Daniel H. E. Dubin, *Phys. Rev. Lett.* **66**, 2076 (1991).
- [3] D. J. Heinzen, J. J. Bollinger, F. L. Moore, Wayne M. Itano, and D. J. Wineland, *Phys. Rev. Lett.* **66**, 2080 (1991).
- [4] J. J. Bollinger, D. J. Heinzen, F. L. Moore, W. M. Itano, D. J. Wineland, and D. H. E. Dubin, *Phys. Rev. A* **48**, 525 (1993).
- [5] J. H. Malmberg and J. S. deGrassie, *Phys. Rev. Lett.* **35**, 577 (1975); A. J. Peurrung and J. Fajans, *Rev. Sci. Instrum.* **64**, 52 (1993).
- [6] Stephan Barlow, Ph.D. thesis, University of Colorado, 1984 (unpublished).
- [7] M. D. Tinkle, R. G. Greaves, C. M. Surko, R. L. Spencer, and G. W. Mason, *Phys. Rev. Lett.* **72**, 352 (1994).
- [8] D. J. Wineland, R.E. Drullinger, and F. L. Walls, *Phys. Rev. Lett.* **40**, 1639 (1978); Wayne M. Itano, L. R. Brewer, D. J. Larson, and D. J. Wineland, *Phys. Rev. A* **38**, 5698 (1988).
- [9] D. L. Eggleston, T. M. O'Neil, and J. H. Malmberg, *Phys. Rev. Lett.* **53**, 982 (1984).
- [10] Robert S. Van Dyck, Jr., Paul B. Schwinberg, and H. G. Dehmelt, in *New Frontiers in High Energy Physics*, edited by Behram Kursunoglu, Arnold Perlmutter, and Linda F. Scott (Plenum, New York, 1978).
- [11] Lowell S. Brown and Gerald Gabrielse, *Rev. Mod. Phys.* **58**, 233 (1986).
- [12] G. Gabrielse, S. L. Ralston, L. Haarsma, and W. Kells, *Phys. Lett. A* **129**, 38 (1988).
- [13] Michael E. Glinsky and Thomas M. O'Neil, *Phys. Fluids B* **3**, 1279 (1991).
- [14] A. W. Hyatt, C. F. Driscoll, and J. H. Malmberg, *Phys. Rev. Lett.* **59**, 2975 (1987).
- [15] M. E. Glinsky, T. M. O'Neil, M. N. Rosenbluth, K. Tsurata, and S. Ichimaru, *Phys. Fluids B* **4**, 1156 (1992).
- [16] C. F. Driscoll, J. H. Malmberg, and K. S. Fine, *Phys. Rev. Lett.* **60**, 1290 (1988).
- [17] T. M. O'Neil, *Phys. Rev. Lett.* **55**, 943 (1985).
- [18] D. H. E. Dubin and T. M. O'Neil, *Phys. Rev. Lett.* **60**, 1286 (1988).
- [19] T. M. O'Neil, *Phys. Fluids* **23**, 2216 (1980).
- [20] J. S. deGrassie and J. H. Malmberg, *Phys. Fluids* **23**, 63 (1980); C. F. Driscoll and J. H. Malmberg, *Phys. Rev. Lett.* **50**, 167 (1983).
- [21] S. A. Prasad and T. M. O'Neil, *Phys. Fluids* **22**, 278 (1979).
- [22] J. B. Jeffries, S. E. Barlow, and G. H. Dunn, *Int. J. Mass. Spectrom. Ion Proc.* **54**, 169 (1983).
- [23] L. R. Brewer, J.D. Prestage, J. J. Bollinger, Wayne M. Itano, D. J. Larson, and D. J. Wineland, *Phys. Rev. A* **38**, 859 (1988).
- [24] J. H. Malmberg and T. M. O'Neil, *Phys. Rev. Lett.* **39**, 1333 (1977).
- [25] S. L. Gilbert, J. J. Bollinger, and D. J. Wineland, *Phys. Rev. Lett.* **60**, 2022 (1988).
- [26] F. Diedrich, E. Peik, J. M. Chen, W. Quint, and H. Walther, *Phys. Rev. Lett.* **59**, 2931 (1987); D. J. Wineland, J. C. Bergquist, Wayne M. Itano, J. J. Bollinger, and C. H. Manney, *ibid.* **59**, 2935 (1987); Th. Sauter, M. Gilhaus, I. Siemers, R. Blatt, W. Neuhauser, and P. E. Toschek, *Z. Phys. D* **10**, 153 (1988); G. Birkel, S. Kassner, and H. Walther, *Nature* **357**, 310 (1992).
- [27] C. C. Grimes and G. Adams, *Phys. Rev. Lett.* **42**, 795 (1979).
- [28] Anil Khurana, *Phys. Today* **14** (12), 17 (1990).
- [29] Dr. D. H. E. Dubin has calculated a closed-form solution for the modes in this limit.
- [30] Carl S. Weimer, F. L. Moore, and D. J. Wineland, *Phys. Rev. Lett.* **70**, 2553 (1993).
- [31] Earl C. Beaty, *J. Appl. Phys.* **61**, 2118 (1987).
- [32] R. S. Van Dyck, Jr., D. J. Wineland, P. A. Ekstrom, and H. G. Dehmelt, *Appl. Phys. Lett.* **28**, 446 (1976).
- [33] G. Gabrielse, X. Fei, L. A. Orozco, R. L. Tjoelker, J. Haas, H. Kalinowsky, T. A. Trainor, and W. Kells, *Phys. Rev. Lett.* **65**, 1317 (1990).
- [34] H. G. Dehmelt and F. L. Walls, *Phys. Rev. Lett.* **21**, 127 (1968).
- [35] D. Wineland, P. Ekstrom, and H. Dehmelt, *Phys. Rev. Lett.* **31**, 1279 (1973).
- [36] D. J. Wineland and H. G. Dehmelt, *J. Appl. Phys.* **46**, 919 (1975).
- [37] R. S. Van Dyck, Jr., F. L. Moore, D. L. Farnham, P. B. Schwinberg, and H. G. Dehmelt, *Phys. Rev. A* **36**, 3455 (1987); J. Tan and G. Gabrielse, *Phys. Rev. Lett.* **67**, 3090 (1991).
- [38] F. L. Moore, L. S. Brown, D. L. Franham, S. Jeon, P. B. Schwinberg, and R. S. Van Dyck, Jr., *Phys. Rev. A* **46**, 2653 (1992).
- [39] D. Wineland and H. Dehmelt, *Int. J. Mass Spectrom. Ion Phys.* **16**, 338 (1975); Erratum **19**, 251 (1976).
- [40] D. J. Wineland and W. M. Itano, *Phys. Rev. A* **20**, 1521 (1979).
- [41] D. J. Wineland, *J. Appl. Phys.* **50**, 2528 (1979); Carl S. Weimer, Ph.D. thesis, Colorado State University, 1992 (unpublished).
- [42] John David Crawford and T. M. O'Neil, *Phys. Fluids* **30**, 2076 (1987).
- [43] S. E. Barlow, J. A. Luine, and G. H. Dunn, *Int. J. Mass Spectrom. Ion Proc.* **74**, 97 (1986).
- [44] G. W. Hart, *Phys. Fluids B* **3**, 2987 (1991); T. B. Mitchell, Ph.D. thesis, University of California at San Diego, 1993 (unpublished).
- [45] Claude Cohen-Tannoudji, *Metrologia* **13**, 161 (1977); Claude Cohen-Tannoudji, Bernard Diu, and Franck Laloe, *Quantum Mechanics I* (Wiley, New York, 1977), pp. 405–411; Eric A. Cornell, Robert Weisskoff, Kevin Boyce, and David E. Pritchard, *Phys. Rev. A* **41**, 312 (1990).
- [46] G. Deville, A. Valdós, E. Y. Andrei, and F. I. B. Williams, *Phys. Rev. Lett.* **53**, 588 (1984).
- [47] D. H. E. Dubin, in *Strongly Coupled Plasma Physics*, edited by H. M. Van Horn and S. Ichimaru (University of Rochester Press, Rochester, 1993), pp. 399–406.
- [48] G. Savard, St. Becker, G. Bollen, H. J. Kluge, R. B. Moore, Th. Otto, L. Schweikhard, H. Stolzenberg, and U. Wiess, *Phys. Lett. A* **158**, 247 (1991).
- [49] D. J. Larson, J. C. Bergquist, J. J. Bollinger, Wayne M. Itano, and D. J. Wineland, *Phys. Rev. Lett.* **57**, 70 (1986); D. J. Wineland, C. S. Weimer, and J. J. Bollinger, *Hyperfine Interac.* **76**, 115 (1993).
- [50] Franco Pavese and Danilo Ferri, in *Advances in Cryogenic Engineering*, edited by R. W. Fast (Plenum, New York, 1990), Vol. 35.

Long-Range Order in Laser-Cooled, Atomic-Ion Wigner Crystals Observed by Bragg Scattering

Joseph N. Tan, J. J. Bollinger, B. Jelenkovic,* and D. J. Wineland

Time and Frequency Division, National Institute of Standards and Technology, Boulder, Colorado 80303

(Received 26 June 1995)

We report the first observation of Bragg scattering from atomic ions confined in an electromagnetic trap. The results reveal long-range order and give evidence for bulk behavior in a strongly coupled collection of laser-cooled ${}^9\text{Be}^+$ ions in a Penning trap. Long-range order emerges in approximately spherical clouds with as few as 5×10^4 ions (cloud radius $r_0 \approx 37a$ where $a \equiv$ Wigner-Seitz radius). Bulk behavior is evident with 2.7×10^5 trapped ions ($r_0 \approx 65a$), with Bragg scattering patterns characteristic of a body-centered cubic lattice.

PACS numbers: 32.80.Pj, 52.25.Wz

Systems of crystallized charged particles have gained wide interest, with implications for the pure Coulomb systems of one-component plasmas [1], trapped atomic ions [1–3], ion storage rings [4], and dense astrophysical matter [5], and for the shielded Coulomb systems of colloidal suspensions [6] and dusty plasmas [7]. For example, Paul rf traps have been used to study crystallization and melting of small “Coulomb clusters” [8]. In both the rf and Penning traps, cold ions form shell structures when the dimensions of the system exceed a few interparticle spacings [9,10]. Such transitions of Coulomb fluids into crystal-like structures are examples of Wigner crystallization in the classical regime (i.e., the wave functions of the particles do not overlap). However, the pure Coulomb systems realized so far are not large enough to neglect surface effects and hence do not allow observation of infinite-volume or bulk behavior [11]. For example, the “micromotion” of ions in the rf trap, which generates the trapping potential, can cause heating which limits the smallest dimension of laser-cooled ion collections to a few interparticle spacings [3]. The drawback of the Penning trap (which uses static trapping fields) *vis-à-vis* the rf trap is that the ions rotate about the trap magnetic field—this has hindered imaging of the ion crystals as seen in Paul traps [3,8,10]. However, the Penning trap, which has no micromotion heating, can potentially store very large systems of laser-cooled ions and hence was used in the studies here.

In related works, optical lattices formed by the interference of intersecting laser beams have been used to localize and cool neutral atoms [12,13]. Unlike the ion Wigner crystals, optical lattices are not formed by the interaction of the confined atoms; rather, they conform to the periodic confinement wells created by the laser standing waves. Also, trapped ions differ from systems of colloidal suspensions and dusty plasmas in that the ions interact through a pure Coulomb (rather than a Yukawa-type) potential, and the charges (q) and masses (m) of the particles are identical.

A system of ions confined in a Penning trap (hereafter called an “ion cloud”) is an example of a one-component

plasma (OCP) [1]. A OCP is a system of identical charged particles that is neutralized by a uniform-density background of opposite charge. The thermodynamic properties of an ion OCP are fully characterized by the coupling parameter

$$\Gamma \equiv \frac{1}{4\pi\epsilon_0} \frac{q^2}{ak_B T}, \quad (1)$$

the ratio of the nearest-neighbor Coulomb interaction energy to the thermal energy ($k_B T$) of an ion. The Wigner-Seitz radius a , a measure of the interparticle spacing, is defined by $4\pi a^3 n_0/3 = 1$, where n_0 is the density of the neutralizing background (which is formally equivalent to the confinement fields in ion traps), and is equal to the ion density at low temperatures [1]. An unbounded OCP is predicted to exhibit liquidlike behavior for $\Gamma > 2$ and undergo a liquid-solid phase transition to a bcc lattice at $\Gamma = 172$ [14]. The OCP has become one of the most carefully studied models in statistical physics because the interaction is simple and because of its importance in understanding dense astrophysical plasmas [5]. In contrast to the growing number of theoretical works, there are few laboratory systems to test the models. Until now, only shell structures have been observed with $N < 1.5 \times 10^4$ ions in a Penning trap [9], and in a race-track rf trap [3,10]. This shell phase can be viewed as arising from the strong influence of the curved surface of a small cloud [11]. Simulation studies show that the ions in each shell form distorted (2D) hexagonal lattices, exhibiting short-range order with little correlation between shells [4,15].

We report here the first observation of Bragg scattering from laser-cooled ions in a trap [16]. In ion clouds with all dimensions much larger than the Wigner-Seitz radius, we find interesting departures from the earlier observed shell phase [9]. Shell structures are still observed with $N < 2 \times 10^4$ ions (or radii $r_0 < 27a$ for spherical clouds). Long-range order emerges with as few as $N \approx 5 \times 10^4$ ions ($r_0 \approx 37a$). We show that for $N \approx 2.7 \times 10^5$ ions ($r_0 \approx 65a$) the Bragg scattering pat-

tern is consistent with a bcc lattice. The ion crystals are estimated to be $>150 \mu\text{m}$ ($\sim 20a$) long on a side.

Theoretical estimates indicate that $r_0 \geq 50a$ is required for bulk behavior [11,17]. We have built a large Penning trap wherein clouds with $N \leq 2.7 \times 10^5$ ions ($r_0 \leq 65a$) and Γ values as high as 600 have been attained. The trap is formed by a 127 mm long stack of cylindrical electrodes with 40.6 mm inner diameter, in a 10^{-8} Pa vacuum. A NMR superconductive magnet provides a uniform magnetic field ($B_0 = 4.5$ T) parallel to the trap axis (z axis), confining the ions in orbits around this axis (cyclotron frequency of $\Omega/2\pi = qB_0/m = 7.55$ MHz). A static electric field, generated by applying $V_0 = 1$ kV between the end and central electrodes, confines the ions along the z axis near the center ($z = 0$) of the trap (a single ion oscillates at $\omega_z/2\pi = 795$ kHz).

The trapped ${}^9\text{Be}^+$ ions are cooled by a laser beam propagating along the z axis (Fig. 1) and are optically pumped into the $2s^2S_{1/2}(M_I = -\frac{3}{2}, M_J = -\frac{1}{2})$ state by tuning the laser frequency ($\lambda \approx 313$ nm) slightly below the $2s^2S_{1/2}(-\frac{3}{2}, \frac{1}{2}) \rightarrow 2p^2P_{3/2}(-\frac{3}{2}, -\frac{3}{2})$ resonance frequency [2]. A laser-cooled ion cloud first condenses into a bounded fluid state (a liquid drop). In a Penning trap with quadratic potential and negligible image charge effects, a laser-cooled ion cloud forms a uniform density spheroid bounded by $(x^2 + y^2)/r_s^2 + z^2/z_s^2 = 1$ (for a spherical cloud, $r_s = z_s \equiv r_0$) [18]. The residual thermal motions are superimposed upon a rigid rotation of the ion cloud about the z axis. The aspect ratio $\alpha \equiv z_s/r_s$ of the spheroid varies with its rigid rotation frequency ω_r [18,19]. A laser beam directed normal to the z axis (not shown in Fig. 1 and turned off during the Bragg scattering) can exert a torque and change ω_r within 40.8 kHz $< \omega_r/2\pi < 7.51$ MHz, thus controlling the shape and density of the cloud [18]. An $f/5$ imaging system along the

x axis, with a laser beam along the z axis (beam waist ~ 0.4 mm $\geq r_s$, power $\sim 200 \mu\text{W}$), gives a side-view image of the ion cloud, thus monitoring z_s and r_s which, in turn, yields α , a , ω_r , n_0 , and N [18].

Bragg scattering is used to study the spatial correlations because the rigid rotation of the ion cloud makes it difficult to image a crystal lattice. The photons resonantly scattered by the ions interfere to form Bragg-scattering peaks at certain angles determined by the crystal lattice. Because $\lambda/a \sim 0.04$, the diffraction pattern occurs very close to the laser beam direction (Fig. 1), within about 0.1 rad. Since the ions scatter far fewer photons than the vacuum windows, special care is needed to minimize this potentially strong background.

As shown in Fig. 1 (not to scale), the laser beam ($\mathbf{k}_i = 2\pi\hat{z}/\lambda$) propagates first through a linear polarizer 1, and then into the vacuum chamber. Upon exiting the ion trap, the laser beam is diverted away from the detector by a set of mirrors. The photons scattered by the ions ($\mathbf{k}_s = 2\pi\hat{\mathbf{k}}_s/\lambda$) are collected by lens 1 ($f = 19$ cm, $z = 25.5$ cm from the ions), forming an image of the ion cloud at a small aperture (A) to reduce the background. The diffraction pattern is then relayed by lens 2 ($f \approx 24$ cm) to the photocathode of a photon-counting imager ($z \approx 160$ cm). The linear polarizer 2 is inserted after the aperture. The polarization axes of polarizers 1 and 2 are crossed to attenuate, with extinction ratio $\geq 6 \times 10^5$, the stray light that leaks through the small aperture and has the same polarization as polarizer 1. The photons scattered from the ions, however, are attenuated only by a factor of 2 since they are mainly circularly polarized.

The Bragg scattering from ion clouds with $N \geq 5 \times 10^4$ ions ($r_0 \geq 37a$) exhibits long-range order characteristic of a crystal. Because of the ion cloud rotation ($\omega_r/2\pi \sim 10^5$ Hz), the dots in a crystalline Laue pattern are rotated into rings. (A ring pattern will also be produced by a crystalline powder or fluid.) Figure 2(a) gives an example of a Bragg scattering pattern obtained with $N = 2.7 \times 10^5$ trapped ions with long-range order. The circular intensity maxima are Bragg peaks, with radii inversely proportional to the Wigner-Seitz radius a . To facilitate analysis, a differential scattering cross section is generated from each diffraction pattern by averaging the photon counts azimuthally about the z axis, as illustrated in Fig. 2(b). A density-independent plot is obtained by using the dimensionless parameter Δka , where Δk is the length of the vector $\Delta\mathbf{k} = \mathbf{k}_i - \mathbf{k}_s$. This can be compared with the interference function [20] or the static structure factor $S(\Delta ka)$ calculated for various systems. For incoherent scattering, $S(\Delta ka) = 1$. The short correlation lengths ($\sim a$) of the fluid and shell phases are reflected in their $S(\Delta ka)$, shown in Fig. 2(c) [21], which have only one strong, narrow peak. In contrast, Fig. 2(b) has four strong, narrow peaks indicating the presence of a crystal. Similar diffraction patterns for

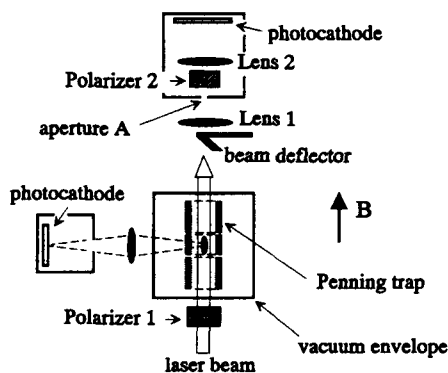


FIG. 1. Schematic diagram (not to scale) for detection of Bragg scattering from an ion cloud, shown as a small prolate spheroid, inside a Penning trap. An $f/5$ imaging system (left) monitors the shape of the cloud, thereby giving the ion density. The diffraction pattern is relayed to the upper photocathode, filtered by a small aperture (A) and crossed polarizers, as described in the text.

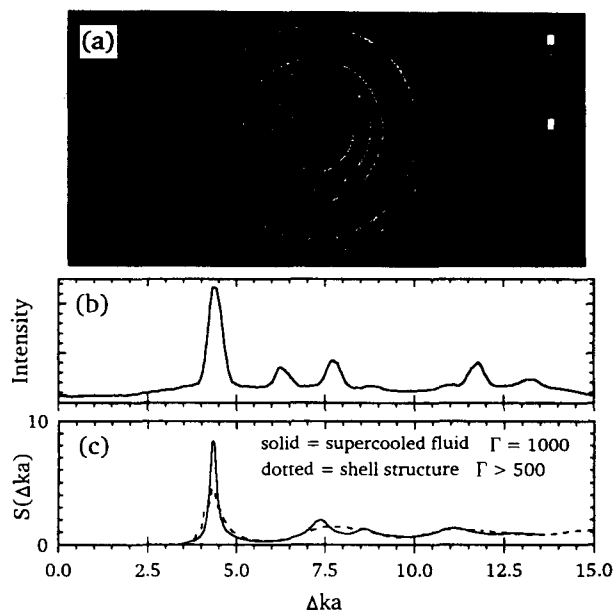


FIG. 2(color). Observed Bragg scattering from $N = 2.7 \times 10^5$ ions (a) and (b) compared with the $S(\Delta ka)$ calculated for a supercooled fluid and an $N = 5 \times 10^3$ ion cloud with shells (c) [21]. The diffraction pattern ions (a) is partially blocked, as indicated by a rectangular shadow due to the laser beam deflector and a square shadow due to a wire mech. The color scale is logarithmic. The total flux reaching the detector is $\approx 1 \times 10^8$ photons/s but is attenuated to avoid saturating the photocathode. The field of view subtends a 5.4° scattering angle from the z axis. The differential cross section (b) is obtained by azimuthally averaging (a) about the z axis.

$N > 5 \times 10^4$ ions ($r_0 > 37a$) have been obtained with up to nine narrow Bragg peaks. Such long-range order is not observed every time we cooled an ion cloud. In this case, if a crystal was formed, the reason it was not observed may be that some crystal orientations did not produce Bragg peaks.

The crystal structure may be determined from the positions of the Bragg peaks [22]. For an unbounded OCP the minimum-energy structure is a body-centered cubic (bcc) lattice [14]. However, there are metastable structures with slightly higher energies, such as the face-centered cubic (fcc) and the hexagonal close-packed (hcp) lattices [11,23]. In a bounded ion cloud, residual surface effects may determine which structure dominates. An analysis of data from a cloud with $N \approx 2.7 \times 10^5$ ions ($r_0 \approx 65a$) shows that the diffraction patterns are consistent with a bcc lattice. Figure 3(a), the evidence of bulk behavior, shows a histogram of the number of observed Bragg peaks (not intensity) as a function of Δka , constructed with no adjustable parameters from 14 diffraction patterns obtained from the same ion cloud ($N = 2.7 \times 10^5$ ions) with various Wigner-Seitz radii ($20 < a/\lambda < 27$). Typically the ion cloud was heated and recooled several times between each recorded pattern.

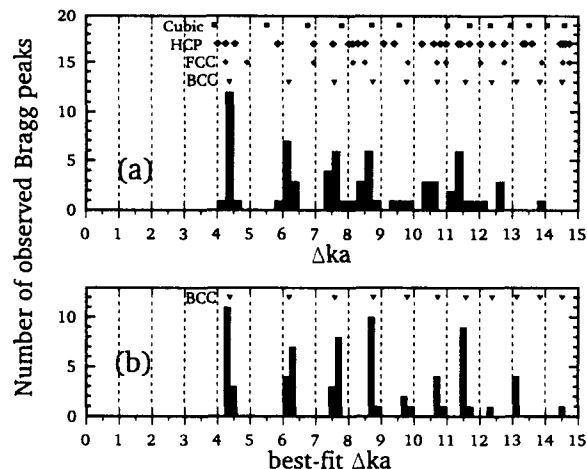


FIG. 3. Evidence of bulk behavior in an ion OCP. Histogram (a) counts the number of observed peaks (not intensity) from various diffraction patterns of the same cloud ($N = 2.7 \times 10^5$ ions), with no adjustable parameters (a is determined from the observed α). By fitting to the bcc lattice for the Wigner-Seitz radius a , even the high Δka peaks are observed to be consistent with a bcc lattice (b). The ticks indicate the location of Bragg peaks for various lattice types.

The scatter of the peak positions in Fig. 3(a) is consistent with the $\sim 5\%$ uncertainty in the determination of the Wigner-Seitz radius a from the observed value of the aspect ratio α . This uncertainty also makes comparison with known lattices difficult for $\Delta ka > 10$, where the density of Bragg peaks is higher. However, for $\Delta ka < 10$, the bcc lattice is the best match to the observed patterns. Having identified the lattice, we can also determine the Wigner-Seitz radius a by fitting each pattern to the calculated bcc peaks. With these fitted values of a , the histogram Fig. 3(b) matches the bcc lattice very well even as far as $\Delta ka \sim 14$.

The minimum size of the ion crystals can be estimated from the intensity widths of the Bragg peaks [see Fig. 2(b)]. For a perfect crystal of characteristic length L , the finite-size broadening of the Bragg peaks is estimated by the formula $L \approx \lambda/\Delta$, where Δ is the angular FWHM of the Bragg peak [24]. We find that, on average, $\Delta \sim 2$ mrad. This gives $L \sim 150 \mu\text{m}$ ($\sim 20a$). With the typical density ($n_0 \sim 5 \times 10^8/\text{cm}^3$), this corresponds to a few thousand ions per crystal. This is a lower limit since the observed widths can be instrumentally broadened, as suggested by the small change in Δ with N .

The relative intensity of the Bragg peaks indicates that the ions do not freeze into a "powdered" sample of randomly oriented crystals. For example, in some cases, peaks expected in such a powder pattern are missing. The crystallized region may be surrounded by at least ≈ 20 shells on the cloud surface (based on a simulation with 2×10^4 ions) [25]. For a cloud with 2.7×10^5 ions these boundary shells contain about 2.3×10^5 ions.

The scattering from the shells may contribute to the size of the first Bragg peaks, but will produce a fairly flat background [$S(\Delta ka) \sim 1$] for the other peaks. As shown in Fig. 2(b), the Bragg peaks are superimposed upon a broad background. Many of the observed Bragg peaks are often as large as, if not a few times larger than, the background. If these are Bragg peaks from a single crystal, the crystal must contain $N \sim 10^4$ ions (for $L \sim 240 \mu\text{m}$ or $35a$ on a side) in order to produce peak intensities greater than the background due to 2.3×10^5 ions.

In the future, we hope to remove the averaging due to the rigid rotation by stroboscopic detection of the Bragg scattering. This could be useful in determining whether the ions form more than one crystal. It may reveal other types of crystals in the ion OCP. Quasicrystals, for example, would produce a fivefold azimuthal symmetry in the diffraction pattern [26]. The uncertainty in Wigner-Seitz radius a can be reduced by measuring ω_r directly [18].

This work is supported by the Office of Naval Research. We acknowledge useful and stimulating discussions with D. H. E. Dubin, J. P. Schiffer, H. E. DeWitt, and S. Ichimaru. We thank J. P. Schiffer for providing simulation data of shell structure, D. H. E. Dubin for providing calculations of $S(\Delta ka)$ from shells and OCP fluids, and S. Ichimaru for permission to reproduce the fluidlike $S(\Delta ka)$ [plotted in Fig. 2(c)]. We thank S. Gilbert, S. Jefferts, H. J. M. Hanley and M. Young for useful comments on the manuscript.

*On leave from the Institute of Physics, University of Belgrade, Yugoslavia.

- [1] J. H. Malmberg and T. M. O'Neil, Phys. Rev. Lett. **39**, 1333 (1977).
- [2] J. J. Bollinger and D. J. Wineland, Phys. Rev. Lett. **53**, 348 (1993).
- [3] H. Walther, Adv. At. Opt. Phys. **31**, 137 (1993).
- [4] A. Rahman and J. P. Schiffer, Phys. Rev. Lett. **57**, 1133 (1986); J. P. Schiffer, Phys. Rev. Lett. **61**, 1843 (1988); D. Habs, Max-Planck Institut für Kernphysik, Heidelberg, Report No. MPI H-1987-V10, 1987 (unpublished).
- [5] S. Ogata and S. Ichimaru, Astrophys. J. **361**, 511 (1990); T. Strohmayer *et al.*, Astrophys. J. **375**, 679 (1991).
- [6] N. A. Clark, A. J. Hurd, and B. J. Ackerson, Nature (London) **281**, 57 (1979); C. A. Murray, W. O. Sprenger, and R. A. Weak, Phys. Rev. B **42**, 688 (1990); L. B. Chen *et al.*, Phys. Rev. Lett. **69**, 688 (1992).
- [7] J. H. Chu and Lin I, Phys. Rev. Lett. **72**, 4009 (1994); H. Thomas, G. E. Morfill, V. Demmel, and J. Goree, Phys. Rev. Lett. **73**, 652 (1994).
- [8] R. F. Wuerker *et al.*, J. Appl. Phys. **30**, 342 (1959); F. Diedrich *et al.*, Phys. Rev. Lett. **59**, 2931 (1987); D. J. Wineland *et al.*, Phys. Rev. Lett. **59**, 2935 (1987).
- [9] S. L. Gilbert, J. J. Bollinger, and D. J. Wineland, Phys. Rev. Lett. **60**, 2022 (1988).
- [10] G. Birkl, S. Kassner, and H. Walther, Nature (London) **357**, 310 (1992).
- [11] D. H. E. Dubin, Phys. Rev. A **40**, 1140 (1989).
- [12] P. Verkerk *et al.*, Phys. Rev. Lett. **68**, 3861 (1992); P. S. Jessen *et al.*, Phys. Rev. Lett. **69**, 49 (1992); A. Hemmerich and T. W. Hansch, Phys. Rev. Lett. **70**, 410 (1993).
- [13] D. R. Meacher *et al.*, Phys. Rev. Lett. **74**, 1958 (1995), and references therein.
- [14] W. L. Slatery, G. D. Doolen, and H. E. DeWitt, Phys. Rev. A **26**, 2255 (1982); D. H. E. Dubin, Phys. Rev. A **42**, 4972 (1990).
- [15] D. H. E. Dubin and T. M. O'Neil, Phys. Rev. Lett. **60**, 511 (1988); R. W. Hasse and J. P. Schiffer, Ann. Phys. (N.Y.) **203**, 419 (1990).
- [16] Some preliminary results are in J. N. Tan *et al.*, *Non-neutral Plasma Physics II*, edited by J. Fajans and D. H. E. Dubin (AIP Press, New York, 1995), p. 215.
- [17] R. W. Hasse and V. V. Avilov, Phys. Rev. A **44**, 4506 (1991).
- [18] J. J. Bollinger *et al.*, Phys. Rev. A **54**, 525 (1993).
- [19] L. R. Brewer *et al.*, Phys. Rev. A **38**, 859 (1988).
- [20] A. Guinier, *X-Ray Diffraction in Crystals, Imperfect Crystals, and Amorphous Bodies* (Dover Publications, Inc., New York, 1994), p. 29.
- [21] The supercooled fluid $S(\Delta ka)$, calculated for an unbounded system with $\Gamma = 1000$, is from Fig. 6(b) in S. Ichimaru *et al.*, Phys. Rep. **149**, 91 (1987). The shell phase $S(\Delta ka)$ is calculated from simulation data for an $N = 5000$ spherical cloud and $\Gamma > 500$, received from J. P. Schiffer. Similar shells $S(\Delta ka)$ have been calculated by D. H. E. Dubin.
- [22] N. W. Ashcroft and N. D. Mermin, *Solid State Physics* (Holt, Reinhart, and Winston, Philadelphia, 1976), pp. 104–107.
- [23] S. Ogata, Phys. Rev. A **45**, 1122 (1992).
- [24] Guinier (Ref. [20]), pp. 125–130.
- [25] J. P. Schiffer, in *Non-neutral Plasma II*, edited by J. Fajans and D. H. E. Dubin (AIP, New York, 1995), p. 191.
- [26] M. V. Jaric, Phys. Rev. B **34**, 4685 (1986); S. Ogata and S. Ichimaru, Phys. Rev. A **39**, 1333 (1989); H. C. Jeong and P. J. Steinhardt, Phys. Rev. Lett. **73**, 1943 (1994).

OBSERVATION OF LONG-RANGE ORDER IN TRAPPED ION PLASMAS BY BRAGG SCATTERING[†]

JOSEPH N. TAN, J.J. BOLLINGER, B. JELENKOVIC*, WAYNE
M. ITANO, and D.J. WINELAND
National Institute of Standards and Technology
325 Broadway, Boulder, CO 80303

ABSTRACT

We have detected long-range order (crystal lattices) in atomic ions confined in a Penning trap. The crystals were observed by the Bragg scattering of nearly resonant laser light at small ($1-5^\circ$) scattering angles. Long-range order was observed in approximately spherical plasmas with as few as 5×10^4 ions (plasma radius $r_o \approx 37 a_{WS}$ where $a_{WS} \equiv$ Wigner-Seitz radius). With 2.7×10^5 trapped ions ($r_o \approx 65 a_{WS}$), Bragg scattering patterns were obtained that were consistent with a body-centered cubic lattice.

1. Introduction

Charged particles in a trap form a realistic model of a classical one-component plasma (OCP). For example, in a Penning trap under conditions of thermal equilibrium the trapping fields provide a uniform background of opposite charge.¹ With Doppler laser-cooling on trapped ions, temperatures of a few millikelvins can be obtained with densities greater than 10^8 cm^{-3} which results in couplings $\Gamma = q^2 / (4\pi\epsilon_o a_{WS} k_B T) > 250$.^{2,3} Here q is the ion charge, ϵ_o is the permittivity of the vacuum, a_{WS} is the Wigner-Seitz radius, k_B is Boltzmann's constant, and T is the ion temperature. These couplings are larger than the predicted liquid-solid phase transition ($\Gamma \sim 172$)⁴ for an infinite OCP and enable trapped ion plasmas to be used to study strongly coupled one-component plasmas. However, in the trapped ion experiments to date, the boundary and relatively small size of the ion plasmas have strongly affected the observed spatial correlations. In plasmas where the smallest dimension is only a few interparticle spacings, the ions form curved shells which approximately conform with the boundary of the plasma.⁵⁻⁷ These shell structures have been observed with imaging techniques in both the Penning and rf traps.⁸⁻¹⁰

In this manuscript we describe some recent experiments on approximately spherical plasmas of up to 4.7×10^5 Be^+ ions whose dimensions are large compared to a_{WS} . Through Bragg scattering we occasionally observe the presence of long-range order or crystal lattices in the ion plasmas. Crystal lattices have been observed in the shielded Coulomb systems of colloidal suspensions¹¹ and dusty plasmas¹². However, we believe this is the first observation¹³ of crystal lattices in a pure Coulomb strongly coupled

[†]Work of the US Government; not subject to US copyright

*On leave from the Institute of Physics, University of Belgrade, Yugoslavia

plasma. We use the Penning trap in this work because it permits dimensionally large plasmas to be laser-cooled. The Penning trap¹⁴ uses a uniform, static magnetic field to confine ions in directions perpendicular to the magnetic field. A static electric field is used to confine ions in the direction parallel to the magnetic field. Due to the axial magnetic field and the radial electric field in a Penning trap, the ion plasma rotates about the magnetic field axis of the trap. The plasma rotation makes it difficult to directly image the ions in a crystal. However, Bragg scattering can still be used to observe the crystals. In the final section of this manuscript we also discuss a time-resolved experiment where the Bragg scattering signal is used to measure the plasma rotation frequency.

In an infinite, homogeneous one-component plasma, the body-centered cubic (bcc), face-centered cubic (fcc), and hexagonal close-packed (hcp) lattices have the same Madelung energy within 1 part in 10^4 , with the bcc lattice the energetically favored configuration.¹⁵ For a finite system, the surface energy and details of the boundary also determine the energetically favored configuration. Dubin¹⁶ considered a zero-temperature model which was infinite and homogeneous in two dimensions but bounded and confined in the third direction by a quadratic potential. He found that if the system was greater than ~ 60 lattice planes (in the bounded direction), a bcc-like structure was the minimum energy configuration. However, with less than 60 lattice planes the minimum energy configuration depended sensitively on the exact number of lattice planes. This calculation indicates that a trapped ion plasma may need to be larger than 60 lattice spacings along its smallest dimension to exhibit behavior which is not strongly influenced by the plasma boundary. A different analytical method developed by Hasse gives a comparable prediction.¹⁷ With a spacing of $\sim 1.5a_{ws}$ between typical low order lattice planes,¹⁶ a spherical plasma with a diameter of $60 \times 1.5a_{ws}$ consists of $\sim 9 \times 10^4$ ions. We have observed long-range order (crystals) in approximately spherical plasmas with greater than 5×10^4 ions. With 2.7×10^5 ions, the observed Bragg scattering pattern was predominantly consistent with a bcc lattice, the expected infinite volume structure.

2. Experimental Set-up

Figure 1 shows a sketch of our experimental set-up. The Penning trap is formed by a 127 mm stack of cylindrical electrodes with 40.6 mm inner diameter, in a 10^{-8} Pa vacuum (133 Pa = 1 Torr). A superconductive magnet provides a uniform magnetic field ($B_0 = 4.5$ T) parallel to the symmetry axis (${}^9\text{Be}^+$ cyclotron frequency of $\Omega/2\pi = qB_0/m = 7.55$ MHz, where m is the ion mass). The static electric field is generated by applying $V_0 = 1$ kV between the end and central electrodes of the trap (a single ion oscillates at $\omega_z/2\pi = 795$ kHz).

The trapped ${}^9\text{Be}^+$ ions are laser-cooled and optically pumped into the $2s^2S_{1/2}(M_I = -3/2, M_J = -1/2)$ state by tuning the laser frequency ($\lambda \approx 313$ nm) slightly below the $2s^2S_{1/2}(-3/2, -1/2) \rightarrow 2p^2P_{3/2}(-3/2, -3/2)$ resonance frequency.^{2,18} A laser-cooled ion plasma in thermal equilibrium forms a uniform density plasma (number density n_0) with sharp boundaries. In a Penning trap with quadratic potential ($\Phi =$

$m\omega_z^2[2z^2-r^2]/[2q]$) and in which image charge effects from the trap electrodes are negligible, the boundary is a spheroid given by $(x^2+y^2)/r_s^2 + z^2/z_s^2 = 1$ (for a spherical plasma $r_s=z_s\equiv r_0$). The residual thermal motions of the ions are superimposed upon a rigid rotation of the plasma about the magnetic field axis (z-axis) at a frequency ω_r . The aspect ratio $\alpha\equiv z_s/r_s$ of the spheroid varies with ω_r .^{18,19} A laser beam directed normal to the z-axis (not shown in Fig. 1 and turned off during the Bragg scattering) can exert a torque that changes ω_r within 40.8 kHz $< \omega_r/(2\pi) < 7.51$ MHz, thus controlling the shape and density of the plasma.¹⁹

An $f/5$ imaging system along an axis perpendicular to the z-axis, with a laser beam along the z-axis (beam waist ~ 0.4 mm, power ~ 200 μ W), gives a side-view image of the ion plasma, thus monitoring z_s and r_s , which, in turn, yield α , ω_r , n_0 , a_{ws} , and the number N of trapped ions.¹⁹ Typical values for these parameters in the work described here are $\alpha\sim 1$, $\omega_r/(2\pi)\sim 125$ kHz, $n_0\sim 4\times 10^8$, $a_{ws}\sim 8.4$ μ m. (The measurement of ω_r and therefore most of these parameters is significantly improved by an autocorrelation measurement of the Bragg-scattered light described in the last section.)

The laser beam along the z-axis in Fig. 1 is used both to laser-cool the ions and also to perform the Bragg scattering. Because $\lambda/a_{ws}\sim 0.04$, the diffraction pattern occurs at small angles (a few degrees) relative to the initial beam direction. The main purpose of the Bragg scattering apparatus in Fig. 1 is to detect the light scattered at small angles by the ions while hiding from the forward-scattered light from the vacuum windows. The incident laser beam ($\mathbf{k}_i=2\pi\hat{z}/\lambda$) first passes through linear polarizer 1, and then into the vacuum chamber. Upon exiting the ion trap, the laser beam is diverted away from the detector by a set of mirrors. The photons scattered by the ions ($\mathbf{k}_s=(2\pi/\lambda)\hat{\mathbf{k}}_s$) are collected by lens 1 ($f=19$ cm, $z=25.5$ cm from the ions), forming an image of the ions at a small aperture (A) to reduce the background. The diffraction pattern is then relayed by lens 2 ($f\approx 24$ cm) to the photocathode of a photon-counting imaging tube ($z\approx 160$ cm). Linear polarizer 2 is inserted after the aperture. The polarization axes of polarizers 1 and 2 are crossed to attenuate, with extinction ratio $> 10^5$, stray light which leaks through the small aperture and has the same polarization as polarizer 1. The photons from the ions are attenuated by only a factor of 2 since they are mainly circularly polarized. The angular acceptance of the system is limited by lens 1 to be $\pm 5.4^\circ$. For plasmas of a few hundred thousand ions, the ion fluorescence is

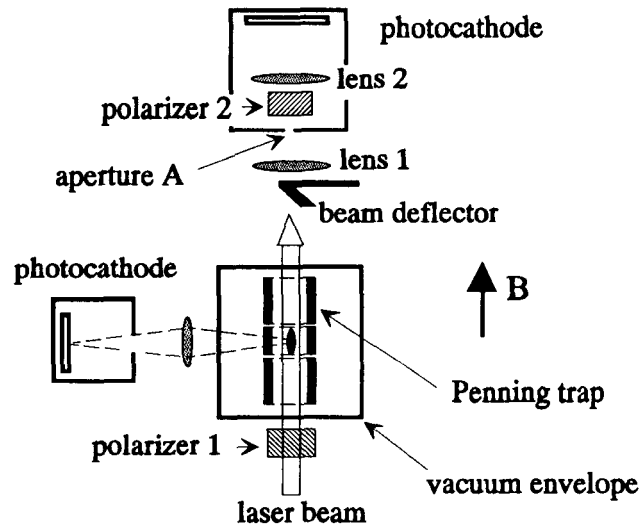


Figure 1. Schematic diagram (not to scale) of the experimental set-up for detection of the Bragg scattering as described in the text.

strong enough that it was necessary to insert a 10-20 dB attenuator in front of the photon-counting imaging tube.

3. Bragg Scattering Results

The following procedure was typically used in obtaining a Bragg scattering pattern. First, the perpendicular (to the z-axis) laser beam was used to set the density and aspect ratio of the cloud. Typical densities were $n_0 \sim 4 \times 10^8 \text{ cm}^{-3}$ with aspect ratios close to spherical (between 0.5 and 2). The perpendicular beam was then blocked and the parallel beam unblocked with its frequency well below atomic resonance where little scattering takes place. The frequency of the parallel beam was then increased to near resonance and a Bragg scattering pattern was recorded. The laser frequency was then detuned and increased again (or perhaps the laser was blocked and then unblocked) and another pattern was recorded. The expansion of the plasma was slow enough that this process could be repeated many times before the perpendicular beam was used to reset the plasma density and aspect ratio. On some occasions we observed Bragg scattering patterns that consisted of several sharp rings such as shown in Fig. 2a. Patterns like this with up to 9 narrow rings were observed with as few as $N \approx 6 \times 10^4$ trapped ions. The circular intensity maxima in Fig. 2a are Bragg peaks. The radius of a Bragg peak is inversely proportional to a_{ws} , a fact which was verified by changing the Wigner-Seitz radius using laser torque. Figure 2b is a differential scattering cross section generated from Fig. 2a by averaging the photon counts azimuthally about the z-axis (the laser beam axis which is normal to the figure). Figure 2b is qualitatively different from the static structure factor $S(q)$ in Fig. 2c for the quenched OCP fluid and shell structure,²⁰ both of which exhibit short range order characteristic of a fluid. Here $q = |\mathbf{k}_i - \mathbf{k}_s| = (4\pi/\lambda)\sin(\theta/2)$ where θ is the scattering angle. The fluid-like patterns have only one strong narrow peak. In contrast, Fig. 2b has 4 narrow peaks which indicate the formation of a crystal lattice. As mentioned earlier, such long-range order was not observed every time we cooled an ion plasma. We have not determined whether this was because a crystal had not formed or a crystal had formed but was not observed (because, for example, the crystal orientation did not produce Bragg peaks).

In order to compare the Bragg peak positions with the calculated positions for the bcc, fcc and hcp lattices, the radii of the Bragg rings must be calibrated in terms of the scattering angle. This was done for a set of 14 diffraction patterns which were obtained on a plasma of 2.7×10^5 ions. For each pattern, a_{ws} was determined with about 5% uncertainty from the measured α . Figure 3a shows a histogram of the number of observed Bragg peaks as a function of qa_{ws} . For $qa_{ws} < 10$, the histogram shows 5 groups of peaks. These groups are consistent with a bcc lattice but not an fcc lattice. (They are also nominally consistent with a subset of hcp peaks, but if many hcp crystals were forming randomly, we would expect to see more groups or at least broader groups of peaks.) Comparison of the groups of peaks with different calculated Bragg peaks for $qa_{ws} > 10$ is limited by the uncertainty in the determination of a_{ws} . However, if a_{ws} is determined by fitting each diffraction pattern used in Fig. 3a to the calculated bcc peaks,

we see from Fig. 3b that with 2.7×10^5 trapped ions the Bragg peaks are consistent with a bcc lattice even as far as $qa_{ws} \sim 14$.

A lower limit on the size of the ion crystals can be obtained from the widths of the Bragg peaks as observed in Fig. 2b. A crystal with dimension L has a Bragg-peak width of $\Delta \sim \lambda/L$, where Δ is the angular FWHM of the Bragg peak. We find that, on

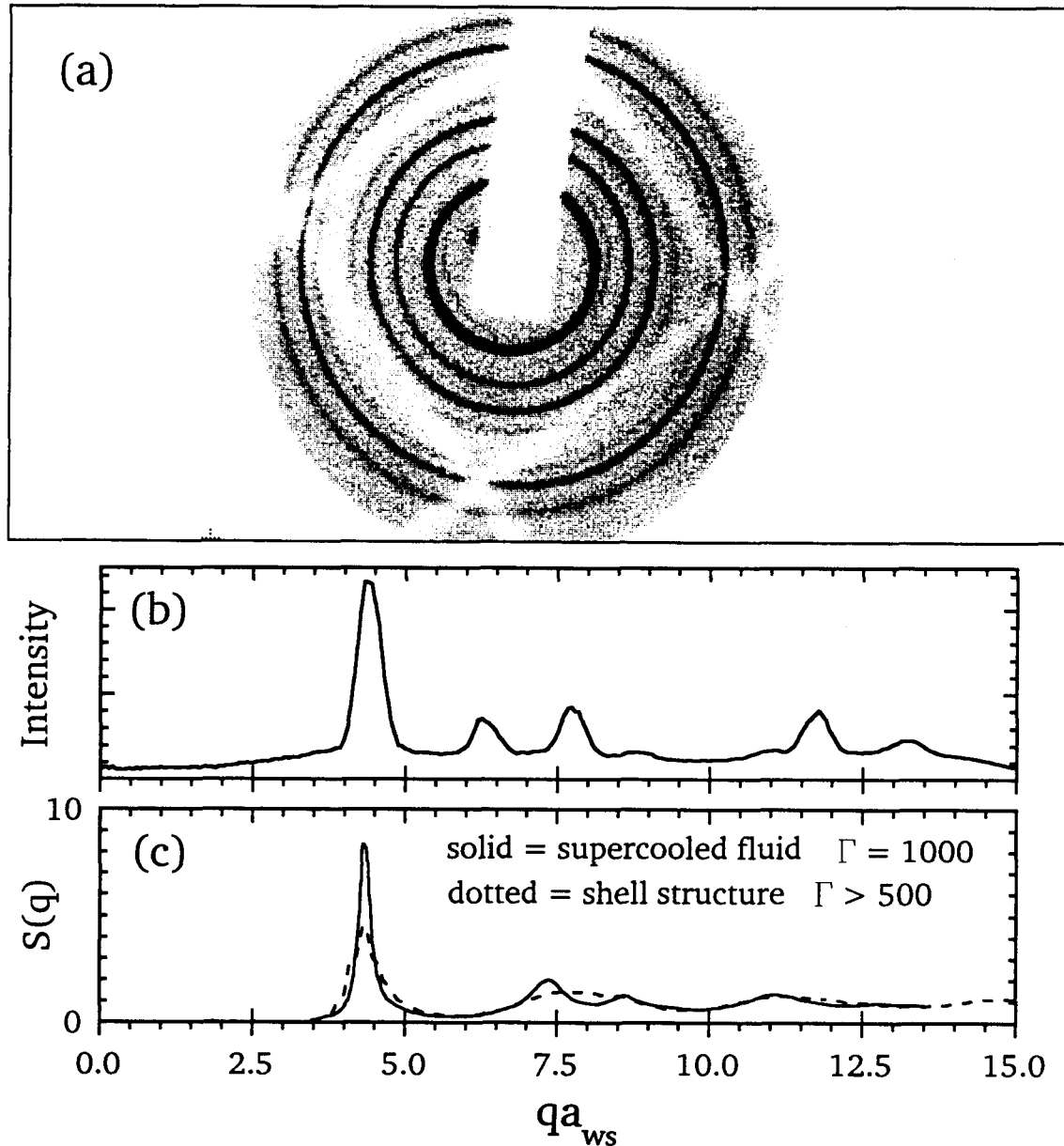


Figure 2. (a) Bragg scattering pattern observed from 2.7×10^5 ions showing the presence of a crystal(s). The diffraction pattern is partially blocked by a rectangular shadow due to the laser beam deflector and a square shadow due to a wire mesh. (b) Differential cross-section obtained from an azimuthal average of (a) about the z-axis. (c) Fluid-like $S(q)$ calculated for a super-cooled OCP and an $N=5 \times 10^3$ ion cloud with shells.²⁰

average, $\Delta \sim 2$ mrad, which gives $L \sim 150 \mu\text{m}$ ($\sim 20a_{\text{ws}}$) and a few thousand ions per crystal. This is a lower limit, since the observed widths could be instrumentally broadened. The negligible change measured in Δ with N supports such broadening. In addition, the intensity in the Bragg peaks increased with N , which indicates that the crystal size is growing with the number of trapped ions. The crystallized region is probably surrounded by at least ~ 20 shells (based on a simulation with 2×10^4 ions).²¹ For a plasma with 2.7×10^5 ions, this corresponds to about 2.3×10^5 ions or a large fraction of the total plasma in these boundary shell layers. The positions of these ions are correlated only over a few interparticle spacings and may be the source of the background signal in Fig. 2b. If the peaks in Fig. 2b are due to Bragg scattering off a single crystal, we estimate that the crystal must contain $\sim 10^4$ ions in order to produce peak intensities greater than the uncorrelated background due to 2.3×10^5 ions.

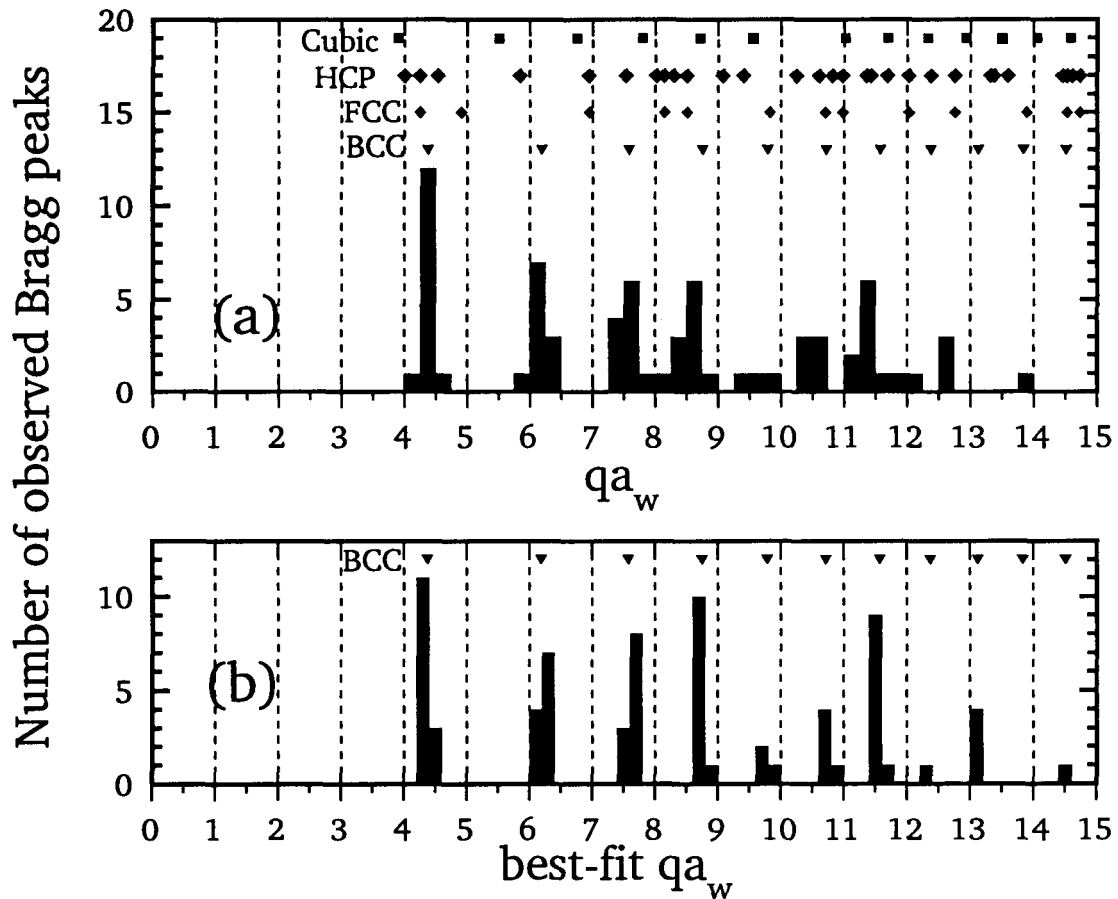


Figure 3. The number of observed peaks (not intensity) from 14 diffraction patterns with $N \approx 2.7 \times 10^5$ ions. In (a) there are no adjustable parameters (a_{ws} is determined from the observed α). In (b), a_{ws} is determined by fitting the diffraction patterns used in (a) to a bcc lattice. The ticks indicate the location of Bragg peaks for the simple cubic, hcp, fcc, and bcc lattices.

4. Time-Resolved Experiments

The Bragg scattering pattern from a single, stationary crystal consists of dots (a Laue pattern). In our experiment the crystal rotates ($\omega_r/(2\pi) \approx 125$ kHz) about the magnetic field axis (which is aligned with the laser beam axis to within 0.5°). This rotation turns the Laue pattern of dots into rings. At any given point on a ring, the light intensity should be modulated at the rotation frequency or a multiple of the rotation frequency if the ring consists of more than one dot. The experimental set-up in Fig. 1 was modified to look for a time dependence of the Bragg-scattered light. The camera in Fig. 1 was replaced with a mirror which made a 45° angle with respect to the laser beam axis (the z-axis). The mirror had a small hole drilled parallel to the z-axis which could be positioned on one of the Bragg rings. The light which passed through this hole was detected by a photomultiplier tube. A pulse from the photomultiplier triggered a multichannel scaler. The multichannel scaler then measured the arrival times of photomultiplier pulses for ~ 0.5 ms after the trigger. The Bragg scattering pattern reflected from the 45° mirror was re-imaged onto the camera.

Figure 4a shows an example of an autocorrelation pattern obtained on the first ring from a plasma of 4.7×10^5 trapped ions. The pattern indicates that the ring consists of 4 equally spaced dots of unequal intensity. From the side-view image of the plasma, $2\pi/\omega_r$ is determined within $\sim 15\%$, which unambiguously identifies the period of the autocorrelation pattern. However, a strong autocorrelation signal can be used to improve the measurement of ω_r to $\sim 0.1\%$ with less than 10 s of averaging. The output of the phototube was also used to "trigger" the camera recording the Bragg-scattered light. A pulse from the phototube would enable the position of a photon to be recorded if it arrived within a window (duration much less than $2\pi/\omega_r$) that was a fixed delay after the photomultiplier pulse. Figure 4b shows the gated image that was recorded simultaneously with the autocorrelation pattern in Fig. 4a. The gated Laue pattern provides more information for determining the crystal type and the crystal orientation relative to the laser beam. So far most, but not all, of the Laue patterns we have observed are consistent with a single crystal.

The data in Fig. 4 can be understood as Bragg scattering off a single bcc or fcc crystal as follows. First, Bragg scattering is observed at small ($1-5^\circ$) scattering angles. This means that the planes which give rise to Bragg-scattered light are nearly vertical (parallel to the z-axis). Second, a Bragg ring with momentum transfer q will persist over an angular change in crystal orientation of $\sim (2\pi/L)/q$. For low-order planes, $q \sim (2\pi/a)$, where a is the lattice constant ($a[\text{bcc}] = 2.03a_{\text{WS}}$; $a[\text{fcc}] = 2.56a_{\text{WS}}$). For our small crystals, this means the crystal can be tilted with respect to the z-axis over a range $a/L \sim 0.1$ rad or 5° and still give rise to the same Bragg peak. This means a low order, nearly vertical plane will produce two Laue dots separated by 180° . The four equally spaced dots making up the first Bragg ring in Fig. 4 are therefore produced by two vertical planes which are 90° from each other. This rules out the hcp lattice as a possibility; however the planes could be bcc 110 planes or fcc 200 planes where the laser beam is approximately aligned with a 4-fold symmetry axis of the cubic cell. The rest of the

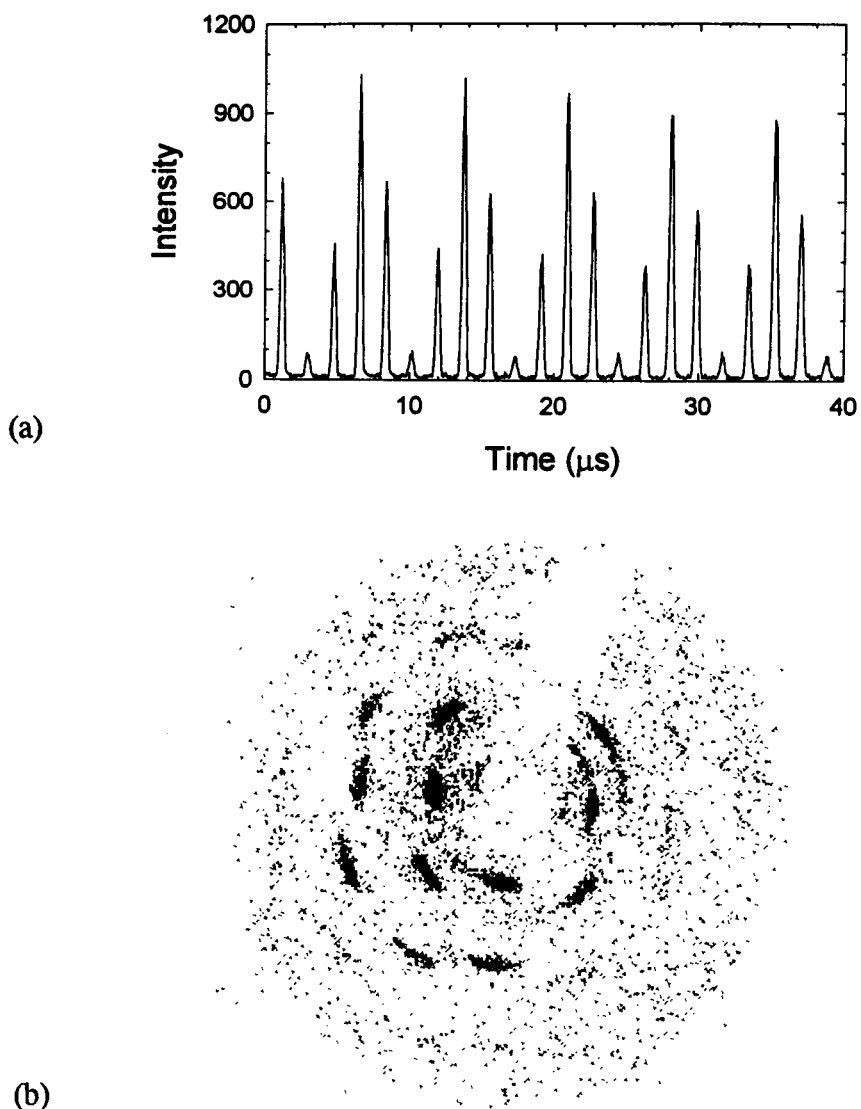


Figure 4. (a) Autocorrelation pattern and (b) gated image simultaneously obtained on 4.7×10^5 trapped ions. The photomultiplier tube was sampling counts from the first ring.

Laue pattern in Fig. 4b is consistent with this interpretation. To distinguish between bcc and fcc in this case, an absolute angular calibration of the rings must be done. We are doing this with the time resolved set-up as well as analyzing other Laue patterns. This will enable us to check with increased confidence that the lattice most frequently formed with a few hundred thousand trapped ions is bcc.

5. Acknowledgements

We gratefully acknowledge the support of the US Office of Naval Research. We acknowledge stimulating discussions with D.H.E. Dubin, J.P. Schiffer, H.E. DeWitt,

and S. Ichimaru. We thank J.P. Schiffer for providing simulation data of shell structure, D.H.E. Dubin for providing calculations of $S(q)$ from shells and OCP fluids, and S. Ichimaru for permission to reproduce $S(q)$ for the supercooled OCP fluid (Fig. 2c). We also thank D. Berkeland, F. Cruz, and M. Young for carefully reading the manuscript.

6. References

1. J.H. Malmberg and T.M. O'Neil, *Phys. Rev. Lett.* **39** (1977) 1333.
2. J.J. Bollinger and D.J. Wineland, *Phys. Rev. Lett.* **53** (1984) 348.
3. J.J. Bollinger, D.J. Wineland, and D.H.E. Dubin, *Phys. Plasmas* **1** (1994) 1403.
4. E.L. Pollock and J.P. Hansen, *Phys. Rev.* **A8** (1973) 3110; W.L. Slattery, G.D. Doolen, and H.E. DeWitt, *Phys. Rev.* **A26** (1982) 2255; S. Ogata and S. Ichimaru, *Phys. Rev.* **A36** (1987) 5451; D.H.E. Dubin, *Phys. Rev.* **A42** (1990) 4972.
5. A. Rahman and J.P. Schiffer, *Phys. Rev. Lett.* **57** (1986) 1133.
6. H. Totsuji, in *Strongly Coupled Plasma Physics*, ed. F.J. Rogers and H.E. Dewitt (Plenum, New York, 1987) p. 19.
7. D.H.E. Dubin and T.M. O'Neil, *Phys. Rev. Lett.* **60** (1988) 511.
8. S.L. Gilbert, J.J. Bollinger, and D.J. Wineland, *Phys. Rev. Lett.* **60** (1988) 2022.
9. G. Birkl, S. Kassner, and H. Walther, *Nature* **357** (1992) 310.
10. R.F. Wuerker, H. Shelton, and R.V. Langmuir, *J. Appl. Phys.* **30** (1959) 342; F. Diedrich, E. Peik, J.M. Chen, W. Quint, and H. Walther, *Phys. Rev. Lett.* **59** (1987) 2931; D.J. Wineland, J.C. Bergquist, W.M. Itano, J.J. Bollinger, and C.H. Manney, *Phys. Rev. Lett.* **59** (1987) 2935; Th. Sauter, H. Gilhaus, W. Neuhauser, R. Blatt, and P. Toschek, *Europhys. Lett.* **7** (1988) 317.
11. N.A. Clark, A.J. Hurd, and B.J. Ackerson, *Nature* **281** (1979) 57; C.A. Murray and D.G. Grier, *Amer. Sci.* **83** (1995) 238; L.B. Chen, C.F. Zukoski, B.J. Ackerson, H.J.M. Hanley, G.C. Straty, J. Barker and C.J. Glinka, *Phys. Rev. Lett.* **69** (1992) 688.
12. J.H. Chu and Lin I, *Phys. Rev. Lett.* **72** (1994) 4009; H. Thomas, G.E. Morfill, V. Demmel, and J. Goree, *Phys. Rev. Lett.* **73** (1994) 652.
13. Preliminary results are in J.N. Tan, J.J. Bollinger, A.S. Barton, and D.J. Wineland, in *Non-Neutral Plasma Physics II*, ed. J. Fajans and D.H.E. Dubin (AIP Press, New York, 1995) p. 215.
14. H.G. Dehmelt, *Adv. At. Mol. Phys.* **3** (1967) 53; **5** (1969) 109.
15. S.G. Brush, H.L. Sahlin, and E. Teller, *J. Chem. Phys.* **45** (1966) 2102.
16. D.H.E. Dubin, *Phys. Rev.* **A40** (1989) 1140.
17. R.W. Hasse and V.V. Avilov, *Phys. Rev.* **A44** (1991) 4506.
18. L.R. Brewer, J.D. Prestage, J.J. Bollinger, W.M. Itano, D.J. Larson and D.J. Wineland, *Phys. Rev.* **A38** (1988) 859.
19. J.J. Bollinger, D.J. Heinzen, F.L. Moore, W.M. Itano, D.J. Wineland, and D.H.E. Dubin, *Phys. Rev.* **A48**, (1993) 525.
20. The supercooled $S(q)$, calculated for an unbounded OCP with $\Gamma=1000$, is from Fig. 6b in S. Ichimaru, H. Iyetomi, and S. Tanaka, *Phys. Rep.* **149** (1987) 91. The shell

structure $S(q)$ is calculated from the simulation data, received from J.P. Schiffer, for an $N=5000$ spherical plasma with $\Gamma > 500$. Similar shell $S(q)$ have been calculated by D.H.E. Dubin.

21. J.P. Schiffer, in *Non-Neutral Plasma Physics II*, ed. J. Fajans and D.H.E. Dubin (AIP Press, New York, 1995) p. 191.

Laser-cooled positron source [☆]

D.J. Wineland, C.S. Weimer and J.J. Bollinger

Time and Frequency Division, NIST, Boulder, CO 80303, USA

We examine, theoretically, the feasibility of producing a sample of cold (≤ 4 K), high-density ($\approx 10^{10}/\text{cm}^3$) positrons in a Penning trap. We assume ${}^9\text{Be}^+$ ions are first loaded into the trap and laser-cooled to approximately 10 mK where they form a uniform density column centered on the trap axis. Positrons from a moderator are then injected into the trap along the direction of the magnetic field through an aperture in one endcap of the trap so that they intersect the ${}^9\text{Be}^+$ column. Positron/ ${}^9\text{Be}^+$ Coulomb collisions extract axial energy from the positrons and prevent them from escaping back out the entrance aperture. Cooling provided by cyclotron radiation and sympathetic cooling with the laser-cooled ${}^9\text{Be}^+$ ions causes the positrons to eventually coalesce into a cold column along the trap axis. We present estimates of the efficiency for capture of the positrons and estimates of densities and temperatures of the resulting positron column. Positrons trapped in this way may be interesting as a source for antihydrogen production, as an example of a quantum plasma, and as a possible means to produce a bright beam of positrons by leaking them out along the axis of the trap.

1. Introduction

1.1. MOTIVATION AND BACKGROUND

For over a decade, slow positron beams using moderators [1–3] have found use in diverse areas such as the formation of positronium, measurement of atomic scattering cross sections, and surface studies. In addition to the importance of slow positron beams, it would be useful to have an accumulator and reservoir of cold positrons for various experiments. An important application of such a reservoir might be for forming antihydrogen by passing cold antiprotons through the positron reservoir and relying on three-body recombination [4]. Since the recombination rate is expected to scale as $n^2 T^{-9/2}$, where n and T are the positron density and temperature [4,5], it is important to achieve as high a density and as low a temperature as possible in the reservoir.

A cold positron reservoir has other potential applications. Surko et al. [6] point out possible applications such as the study of electron/positron recombination, the

[☆] Contribution of the National Institute of Standards and Technology; not subject to US copyright.

study of resonances in electron/positron scattering [6,7], a positron source for accelerators, a diagnostic for fusion plasmas, and studies of basic plasma physics. With the techniques described here, the resulting positron plasma may reach the conditions for a quantum plasma [8] in the sense that $\hbar\omega_p > k_B T$ where ω_p is the plasma frequency and k_B is the Boltzmann constant. The techniques described here may also be useful for providing a reservoir of cold high- Z ions or other ions which are difficult to cool by other means.

If cold positrons are extracted from the reservoir, a beam source with high brightness might be obtained. Such a source might be useful in atomic scattering experiments which seek to observe positron/atom scattering resonances, diffraction from atoms, and high angular resolution [3].

Several other groups have already investigated and demonstrated trapping of positrons in Penning traps. Schwinberg, Van Dyck, and Dehmelt have captured small numbers of positrons in a Penning trap by injecting positrons from a ^{22}Na source through an aperture in one endcap of the trap and extracting the axial energy by resistive damping of the currents induced in the electrodes [9]. Gabrielse and Brown have discussed a similar idea with potential increased loading efficiency by use of a moderated positron source [10]. Surko et al. have achieved a nonneutral positron plasma stored in a Penning trap [6]. In this work, positrons from a moderator are injected into the trap and their energy reduced by collisions with background gas. Conti, Ghaffari, and Steiger have trapped positrons in a Penning trap by injecting positrons from a moderator through one endcap while ramping the voltage of the trap [11]. Mills has discussed a scheme for positron accumulation in a magnetic bottle [12].

In this paper, we investigate the feasibility of making a positron accumulator and reservoir by injecting positrons from a moderator through an aperture in one endcap of a Penning trap and extracting axial energy from them through collisions with a simultaneously trapped laser-cooled ion plasma.

1.2. BASIC IDEA

The basic idea of the scheme is illustrated in fig. 1. We assume that $^9\text{Be}^+$ ions are first loaded into a Penning trap and laser-cooled by established techniques [13]. With only $^9\text{Be}^+$ ions in the trap, the ions form a uniform density nonneutral ion plasma (temperature $T(^9\text{Be}^+) \approx 10$ mK) which rotates about the trap axis at frequency ω . We will assume the Debye length of the plasma is small compared to its dimensions. Therefore, the potential inside the plasma is independent of the axial coordinate. We assume that positrons from a moderator are injected through an off-axis aperture in one endcap (endcap 1) with just enough energy to pass through the center of the aperture. The potential at the center of the aperture is less than the potential V_1 of endcap 1 because of the proximity of the tube (held at potential $V_T < V_1$) between the moderator and endcap 1. The diameter of the $^9\text{Be}^+$ plasma is assumed to be large enough that the incoming positrons pass through the $^9\text{Be}^+$

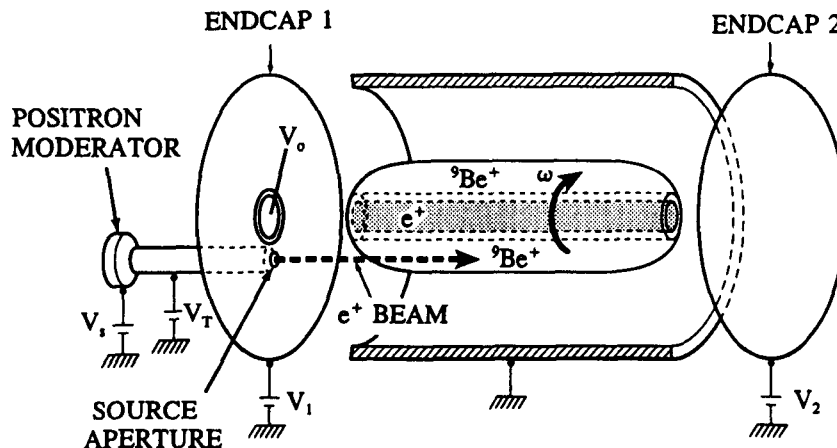


Fig. 1. Schematic diagram of a possible Penning trap apparatus for capturing and cooling positrons injected into the trap from a moderator. The trap magnetic field (not shown) is assumed parallel to the axis of the electrodes. The ${}^9\text{Be}^+$ ions damp the motion of the positrons along the B field direction causing them to be trapped. As the positrons are cooled, they are forced inside the ${}^9\text{Be}^+$ ions where they eventually form a cold column centered on the trap axis.

ion plasma. The other trap endcap (endcap 2) is biased at a potential V_2 which is sufficient to reflect the positrons back through the ${}^9\text{Be}^+$ plasma. Positrons inside the ${}^9\text{Be}^+$ plasma also rotate about the trap axis at approximately frequency ω . If ω is large enough and/or the ${}^9\text{Be}^+$ plasma is sufficiently long, the positrons will have been displaced azimuthally when they approach endcap 1 from inside the trap and are reflected by the potential V_1 back through the ${}^9\text{Be}^+$ plasma. As the positrons pass through the ${}^9\text{Be}^+$ ions they undergo Coulomb collisions which extract axial energy from them. At the low energies we consider, positron annihilation by collisions with the ${}^9\text{Be}^+$ ions is suppressed by Coulomb repulsion. Initially, the positrons' axial energy is primarily transferred into their cyclotron motion energy since the recoil energy of the ${}^9\text{Be}^+$ ions is small. If these collisions extract enough axial energy before the positrons encounter the entrance aperture again, they will be trapped. If the entrance aperture is mounted off axis, the positrons can make many oscillations along the trap axis (and through the ${}^9\text{Be}^+$ ions) before encountering the entrance aperture again. This is the same idea proposed by Dehmelt et al. [14] and used successfully by Schwinberg et al. [9] except we assume the axial energy is extracted by $e^+ / {}^9\text{Be}^+$ collisions rather than resistive damping.

Once trapped, the positrons cool by cyclotron radiation and sympathetic cooling with the cold ${}^9\text{Be}^+$ ions. When sufficiently cooled, the positrons coalesce to a uniform density plasma column along the trap axis which co-rotates with the ${}^9\text{Be}^+$ plasma (both at frequency ω) as shown in fig. 1 [8,15,16]. At low temperatures, the

${}^9\text{Be}^+$ plasma separates from the positron plasma forming an annular region outside the positron plasma [8,15,16]. Qualitatively, the separation occurs because of the larger outward centrifugal force on the ${}^9\text{Be}^+$ ions. The positron cyclotron motion is strongly coupled to the ambient temperature T_0 (4 K assumed here) by cyclotron radiation. At temperatures below about 10 K, the positron axial motion decouples from the cyclotron motion [17] and we expect the positron axial or “parallel” motion temperature T_{\parallel} to be reduced to less than T_0 by the Coulomb interaction with the cold ${}^9\text{Be}^+$ ions. Therefore we expect the parallel temperature T_{\parallel} to be lower than the cyclotron or “perpendicular” temperature T_{\perp} . For $\omega < \Omega/2$, the positron and ${}^9\text{Be}^+$ plasma densities will be approximately equal [8] and limited by the maximum attainable ${}^9\text{Be}^+$ plasma density (Brillouin density). Here we will make the approximation $n(e^+) \approx n({}^9\text{Be}^+) \equiv n$. Since the Brillouin density for an ion species of mass M scales as B^2/M , where B is the magnitude of the Penning trap magnetic field, we want B as large as possible and M as small as possible. This is the reason for choosing ${}^9\text{Be}^+$ ions; other ions would work in the scheme described here, but ${}^9\text{Be}^+$ has the smallest mass of any of the positive ions which can be easily laser cooled therefore giving the highest density ($n \approx 10^{10} \text{ cm}^{-3}$ for $B = 6 \text{ T}$).

1.3. USEFUL FEATURES OF A LASER-COOLED POSITRON SOURCE

If this reservoir of cold positrons can be achieved, it should have some interesting features compared to those of other schemes. (1) Under the assumptions described below, the efficiency of capturing moderated positrons can be very high, approaching unity. (2) Relatively direct visual information is available on the positron plasma. By use of imaging techniques, the ${}^9\text{Be}^+$ plasma can be observed in real time [13,18]. The positron plasma is then observed by the “hole” it creates in the image of the ${}^9\text{Be}^+$ plasma. In this way we obtain fairly direct information on the size and shape of the positron plasma. (3) If there is sufficient Coulomb coupling between the positrons and ${}^9\text{Be}^+$ ions, the density and temperature of both species can be determined by spectroscopic techniques [13,18]. (4) The density of both plasmas can be varied by controlling the angular momentum imparted to the ${}^9\text{Be}^+$ plasma by the laser [13,18]. (5) The apparatus can be operated at high vacuum, thereby reducing positron loss due to annihilation or positron formation with neutral background gas.

1.4. APPROXIMATIONS

The calculations contained here are, admittedly, based on approximations. In addition, the availability of a moderated source with certain characteristics (in particular a small energy spread, $\Delta E_i = 0.1 \text{ eV}$) is freely assumed. The purpose of these notes is to give an estimate of what might be achievable with the proposed technique.

2. Positron capture

2.1. POSITRON INJECTION

We assume positrons are emitted from a moderator (fig. 1) with axial energy spread and cyclotron energy spread both equal to ΔE_i . They enter the Penning trap along magnetic field lines through a tube held at potential V_T . We assume they enter the trap through a circular aperture in endcap 1 which is offset from the trap axis by distance R_A . Near the center of the aperture the potential is between V_1 and V_T ; we consider an area $A_1 (= \pi r_A^2)$ centered on the aperture which is smaller than the geometrical area of the aperture. The area A_1 is such that V_1 minus the potential within A_1 is larger than ΔE_i . We make the approximation that over A_1 the potential is constant and equal to V_A , where $V_1 > V_A > V_T$ and $V_1 - V_A > \Delta E_i$. Outside A_1 , we assume the potential is equal to V_1 . We assume the potential V_s is adjusted so that the positrons have just enough axial energy to spill over the potential V_A and enter the trap. The positrons then are accelerated to an energy E_i by the potential difference between V_A and the ${}^9\text{Be}^+$ plasma potential $\phi_p(R_A)$ at radius R_A ; we have $E_i = q(V_A - \phi_p(R_A)) + E_o$, where q is the positron charge and E_o ($\approx \Delta E_i$) is the mean axial kinetic energy of the positrons at the aperture. When the positrons enter the plasma they drift through it with a velocity $(2E_i/m)^{1/2}$, where m is the positron mass. Positrons exit the far side of the plasma and are then reflected back by endcap 2. They then traverse the plasma in the opposite direction and approach endcap 1. If the length of the plasma is long compared to the spacings between the plasma and the endcaps, the positrons spend most of their time in the plasma. Therefore, upon returning to endcap 1 for the first time, they rotate an azimuthal angle

$$\Delta\theta \approx 2\omega h(2E_i/m)^{-1/2} = 0.18(\omega/(\Omega/2))hBE_i^{-1/2}, \quad (1)$$

where $\Delta\theta$ is in radians, ω is the plasma rotation frequency, and in the last expression the plasma length h is expressed in cm, B in T, E_i in eV and Ω is the ${}^9\text{Be}^+$ cyclotron frequency. We have $\Omega/2\pi = 1.70 \times B[\text{T}]$ MHz when B is expressed in T. If $\Delta\theta$ is larger than the angle subtended by the effective entrance aperture θ_A ($\approx 2r_A/R_A$), then positrons are again reflected back into the plasma where they have a greater chance to lose axial energy [14]. As long as $\Delta\theta > \theta_A$, the positrons typically take $2(2\pi/\theta_A)$ passes through the ${}^9\text{Be}^+$ plasma before encountering the entrance aperture again. If $\Delta\theta < \theta_A$, only a fraction of the positrons which enter the trap make multiple bounces [19]. In order to have all of the positrons enter the trap we want $E_i > \Delta E_i$. We would like E_i to be as small as possible to satisfy the condition $\Delta\theta > \theta_A$ and to make the positrons scatter through the largest angles.

If the length of the positron/ ${}^9\text{Be}^+$ plasma is much longer than its diameter, the potential inside the plasma as a function of radius is approximately equal to that of an infinitely long uniformly charged cylinder inside of a concentric grounded cylinder. Therefore the potential at radius r inside the plasma is approximately equal to

$$\phi_p(r) \approx \pi q n r_p^2 [2 \ln(r_w/r_p) + 1 - (r/r_p)^2], \quad (2)$$

where r_p is the plasma radius, and r_w is the radius of the grounded outer cylindrical "wall" electrode. Since the potential inside the plasma is independent of the axial coordinate, to keep the plasma confined along the axis, we require $V_o, V_2 > \phi_p(0)$, where V_o is the potential on the central portion of endcap 1 as shown in fig. 1. We adjust V_o and V_1 (and V_T and V_s) so that E_i is kept small. This implies $V_o > V_1$ and that the end of the plasma bulges out towards endcap 1 at the radius R_A . The ${}^9\text{Be}^+$ plasma density n is related to the rotation frequency ω by [20]

$$n = \frac{M\omega(\Omega - \omega)}{2\pi q^2} = 2.95 \times 10^8 B^2 \left(\frac{\omega}{\Omega/2} \right) \left(2 - \frac{\omega}{\Omega/2} \right), \quad (3)$$

where M is the ${}^9\text{Be}^+$ mass and in the last expression B is expressed in T. The maximum density, called the Brillouin density, is obtained when $\omega = \Omega/2$.

2.2. POSITRON DAMPING

We assume that the positrons initially lose axial kinetic energy by Coulomb scattering off the ${}^9\text{Be}^+$ ions. This transfers some of the initial positron axial kinetic energy E_i into cyclotron motion energy. We assume that the cyclotron motion energy is predominantly extracted by cyclotron radiation in the first stages of cooling. In the first stages of the cooling, a good approximation is to assume that the ${}^9\text{Be}^+$ ions are stationary and infinitely heavy; cooling of the positrons by the recoil of the ${}^9\text{Be}^+$ ions is negligible. We assume that the positrons scatter through a net angle θ_s (relative to the magnetic field direction) before encountering the entrance aperture from inside the plasma. The scattering angle θ_s results primarily from multiple small angle scattering of the positrons in the ${}^9\text{Be}^+$ plasma. The mean scattering angle $\langle \theta_s \rangle = 0$. The mean-squared scattering angle is nonzero and given by [21]

$$(\Delta\theta_s)^2 \equiv \langle \theta_s^2 \rangle = \frac{2\pi n L q^4}{E_i^2} \ln(b_{\max}/b_{\min}), \quad (4)$$

where L is the effective length of the plasma. When $\Delta\theta > \theta_A$, L is equal to $2h(2\pi/\theta_A)$. For a weakly magnetized plasma b_{\max}/b_{\min} is given by r_c/b , where r_c is the positron cyclotron radius and b is the distance of closest approach ($b = q^2/k_B T$) [22]. For the plasma to be weakly magnetized, we require $r_c/b \gg 1$. We assume that $\frac{1}{2}m\Omega_p^2 r_c^2 \approx \Delta E_i$, where Ω_p is the positron cyclotron frequency. Therefore, we can write

$$r_c/b = 2320 \frac{E_i \Delta E_i^{1/2}}{B}, \quad (5)$$

where the energies are expressed in eV and the field in T. Therefore, when $\Delta\theta > \theta_A$, we can write eq. (4) in the form

$$\Delta\theta_s = 1.28 \times 10^{-6} [\ln(r_c/b)nh/\theta_A]^{1/2}/E_i, \quad (6)$$

where the angles are expressed in radians, h in cm, n in cm^{-3} , and E_i in eV.

From simple geometric considerations, the axial energy lost before re-encountering the entrance aperture (assuming the initial cyclotron energy is much less than E_i) is

$$\Delta E_s = E_i \sin^2 \theta_s. \quad (7)$$

We will make the approximation that the positrons are captured if $\Delta E_s > \Delta E_i$. Therefore from eq. (7), positrons are captured if they scatter through angles greater than θ_c where

$$\theta_c = \sin^{-1}(\Delta E_i/E_i)^{1/2}. \quad (8)$$

If we assume that the distribution of angles θ_s is Gaussian, the fraction of positrons which enter the trap and are captured is given by

$$\eta_c = 1 - \text{erf}(\theta_c/(2^{1/2}\Delta\theta_s)). \quad (9)$$

In table 1, we list values of η_c for various positron and ${}^9\text{Be}^+$ plasma parameters.

3. Beam source

In addition to using this configuration as a cold positron reservoir, it might also be possible to use it as a positron beam source by leaking positrons out a hole in endcap 2, which is centered on the trap axis. If the positrons are injected into the trap at an arbitrarily slow rate, they can be extracted as a beam with an internal temperature governed by the final equilibrium conditions achieved for the reservoir discussed in the previous section. For a beam source we would like as high a throughput as possible. Therefore it is useful to estimate the temperature of the ex-

Table 1

Calculated values of $\Omega/2\pi$, θ_A , $\Delta\theta$, n , $\theta_p(0)$, r_c/b , η_c , and $T - T_o$ for various values of input parameters. We assume $h = 10$ cm and $\Delta E_i = 0.1$ eV for all entries. The last column for $(T - T_o)$ applies only for the positron beam source described in the text (for all rows we assume $dN/dt = 10^7 \text{ s}^{-1}$). The first row gives a high value of η_c but requires a very high trap potential ($> \phi_p(0)$). The last two rows assume the entrance aperture for positrons is centered on the trap axis.

B (T)	E_i (eV)	r_A (cm)	R_A (cm)	r_p (cm)	r_w (cm)	$2\omega/\Omega$	$\Omega/2\pi$ (MHz)	θ_A (rad)	$\Delta\theta$ (rad)	n (10^{10} cm^{-3})	$\phi_p(0)$ (V)	r_c/b	η_c	$(T - T_o)$ (K)
10	1	0.05	0.5	0.7	2.0	0.5	17	0.2	9.0	2.2	15200	73	0.91	0.013
5	1	0.05	0.25	0.4	2.0	0.1	8.5	0.4	0.9	0.14	427	147	0.55	2.52
5	10	0.025	0.25	0.3	1.0	0.1	8.5	0.2	0.28	0.14	194	1470	0.27	44.8
10	10	-	-	0.1	1.0	0.5	17	2π	-	2.2	560	734	0.11	6.38
10	10	-	-	0.1	0.5	0.1	17	2π	-	0.56	107	734	0.001	25.2

tracted beam versus throughput. As a conservative estimate we will assume that the positron energy is extracted only by cyclotron radiation. In steady state, energy balance is therefore described by the expression $(dE/dt)_{\text{in}} \simeq (dE/dt)_{\text{c}} + (dE/dt)_{\text{b}}$, where $(dE/dt)_{\text{in}}$ is the energy input from the incoming positron beam, $(dE/dt)_{\text{c}}$ is the energy extracted by cyclotron radiation, and $(dE/dt)_{\text{b}}$ is the energy removed by the extracted beam. The cyclotron energy decays at the rate $\gamma_{\text{c}} \simeq 0.39B^2[\text{T}] \text{ s}^{-1}$. This rate is lower than the equilibration rate between T_{\parallel} and T_{\perp} for temperatures down to about 10 K (for $n \approx 10^9$, $B \approx 6$ T, see fig. 3 of ref. [23]), therefore above this temperature $T_{\parallel} = T_{\perp} \equiv T$. In this case, the expression for energy balance can be written

$$(dN/dt)E_i = \frac{2}{3}\gamma_{\text{c}}Nk_{\text{B}}(T - T_0) + \frac{3}{2}k_{\text{B}}T(dN/dt), \quad (10)$$

where (dN/dt) is the positron flux, N is the total number of trapped positrons, and T_0 is the ambient temperature. This equation yields the solution

$$T - T_0 \approx 4.43 \times 10^4 \frac{(dN/dt)E_i}{NB^2}, \quad (11)$$

where E_i is given in eV and B in T. Examples are included in table 1. Similar considerations must be addressed to ensure that the laser beams can remove the (canonical) angular momentum and energy input to the ${}^9\text{Be}^+$ ions due to the incoming positrons. With care these requirements can be satisfied. For small values of dN/dt , the parallel and perpendicular motions become decoupled [22] and we expect $T_{\parallel} \ll T_{\perp} \simeq 4$ K. In this case the positron plasma is expected to be strongly coupled. Under these conditions, it may be possible to extract a ‘‘string’’ of positrons which is located on the axis of the trap [18]. For these positrons, the angular momentum is zero, so when the positrons are extracted from the B field, the transverse energy can be quite small. In the extraction to zero magnetic field, the cyclotron energy is converted to axial energy spread. At $B \approx 6$ T and $T_{\perp} \simeq 4$ K, the cyclotron energy is concentrated in the $n = 0$ and 1 quantum levels, so the axial energy of the extracted positrons is concentrated in two energy peaks.

4. Experiments

Cooling positrons with ${}^9\text{Be}^+$ ions has not been tried yet. However, some important aspects of the scheme have been demonstrated by using one laser-cooled ion species to sympathetically cool another ion species. In fig. 2 we show an image taken by viewing along the z axis of a Penning trap [13,18]. In this (UV) photograph, a column of ${}^9\text{Be}^+$ ions, centered on the trap axis, is sympathetically cooled by laser-cooled Mg^+ ions at a magnetic field $B \approx 0.82$ T [24]. We have also demonstrated the use of laser torque to control the shape and density of a ${}^9\text{Be}^+$ ion plasma, reaching densities very near the Brillouin density ($n \approx 10^{10} \text{ cm}^{-3}$ for $B \approx 6$ T) [13].

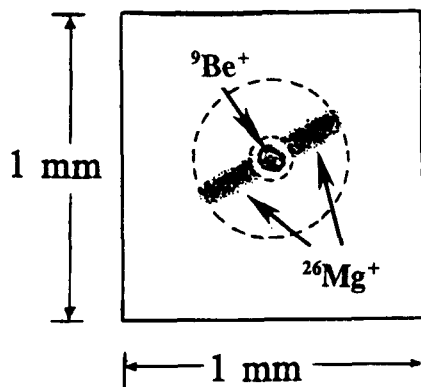


Fig. 2. Ultraviolet photograph showing the light scattered from laser beams which intersect a ${}^9\text{Be}^+ / {}^{26}\text{Mg}^+$ plasma confined in a Penning trap ($B = 0.82$ T). The view is along the direction of the trap axis (and B field) as described in refs. [13,18]. The laser beam for the Mg^+ ions intersects only a portion of the Mg^+ plasma whose boundary is indicated by the dashed lines. The separation of the species is probably exaggerated because the photograph required a double exposure. The optics were refocused between the 313 nm (${}^9\text{Be}^+$) and 280 nm (Mg^+) images. This probably resulted in different magnifications of the two wavelengths. The separation between plasmas is expected to be approximately equal to the interparticle spacing for low rotation frequencies ($\omega \ll \Omega/2$) [15,16].

5. Discussion

If the configuration above can be achieved, antihydrogen formation from three-body recombination with cold antiprotons passed through the positron plasma should be very efficient. If the positron plasma is strongly magnetized, the recombination rate should depend on T_{\parallel} as $n^2 T_{\parallel}^{-9/2}$. In this case the probability of antihydrogen formation might be unity for one pass of cold antiprotons through the positron plasma [4,5]. Similarly, for the positron plasma to be quantized we require $\hbar\omega_p > k_B T_{\parallel}$.

On the theoretical side, more exact calculations are required to achieve better estimates of η_c and other parameters. We have omitted any details of the positron cooling for $T < 10$ K. For example, for $\omega \ll \Omega$, the separation between plasmas is approximately the interparticle spacing. As ω approaches Ω , the separation becomes large compared to the interparticle spacing and the Debye length [8,15]. In this case, we expect the thermal coupling between the positron axial motion and the ${}^9\text{Be}^+$ ions to become weak. If the coupling between the positron axial motion and the ${}^9\text{Be}^+$ ions remains relatively weak compared to the coupling between parallel and perpendicular positron motions for $T \approx 4$ K, then T_{\parallel} will not be significantly below T_{\perp} . In principle, we could decouple the positrons' cyclotron motion from the ambient temperature by avoiding the resonances of the cavity formed by the trap electrodes [25]. However, this decoupling will be more difficult to achieve for plasmas whose dimensions are large compared to the cyclotron wavelength.

On the experimental side, we have assumed narrow energy distributions ΔE_i from the moderator, which we have implicitly assumed is in the trap magnetic field. These values of ΔE_i must be demonstrated experimentally. Use of a transmission moderator would be desirable; the high energy particles from the moderator could perhaps be rejected with an $E \times B$ filter.

The long ${}^9\text{Be}^+$ plasmas assumed here ($h = 10$ cm) have not been demonstrated yet. This is an important question which must be resolved experimentally; in general, longer plasmas are more prone to mode excitation from static field azimuthal asymmetry which limits their density [13]. Currently we are assembling a new apparatus which should allow us to investigate the storage of large plasmas. If the desired long plasmas are difficult to achieve, it should be possible to stack shorter plasmas with traps stacked along the axis of the system. This configuration may also have the advantage that between the trap sections, $E \times B$ azimuthal drift section could be configured to increase $\Delta\theta$ for the incident positrons.

The ideas presented here should apply to the trapping of other ions such as multiply charged ions which are difficult to cool by other means. In principle, these ideas would apply to cooling of antiprotons or other negative ions. This would require use of simultaneously stored laser-cooled negative ions. Unfortunately, laser cooling of negative ions has not been achieved so far because of the apparent lack of a suitable optical transition in a negative ion. Sympathetic laser cooling of negative ions might be achieved using a coupled trap geometry [26].

Acknowledgement

We thank the US Office of Naval Research for support. We thank S. Gilbert, S. Jefferts, T. Steiger, D. Sullivan and M. Young for helpful comments on the manuscript. We acknowledge helpful discussion with B.R. Beck, R.S. Conti, G. Gabrielse, M.E. Glinsky, A.P. Mills, T.M. O'Neil, T.D. Steiger, T.S. Stein and C.M. Surko.

References

- [1] A.P. Mills Jr., Hyp. Int. 44 (1988) 107;
P.J. Schultz and K.G. Lynn, Rev. Mod. Phys. 60 (1988) 701, and references therein.
- [2] A. Rich, R.S. Conti, D.W. Gidley, M. Skalsey, J. Van House and P.W. Zitzewitz, Hyp. Int. 44 (1988) 125.
- [3] L. Dou, W.E. Kauppila, C.K. Kwan and T.S. Stein, Phys. Rev. Lett. 68 (1992) 2913;
T.S. Stein, private communication.
- [4] G. Gabrielse, S.L. Rolston, L. Haarsma and W. Kells, Phys. Lett. A129 (1988) 38.
- [5] M.E. Glinsky and T.M. O'Neil, Phys. Fluids B3 (1991) 1279.
- [6] C.M. Surko, M. Leventhal, A. Passner and F.J. Wysocki, in: *Non-neutral Plasma Physics*, eds. C.W. Roberson and C.F. Driscoll (AIP Press, New York, 1988) p. 75;
C.M. Surko, M. Leventhal and A. Passner, Phys. Rev. Lett. 62 (1989) 901;
T.J. Murphy and C.M. Surko, Phys. Rev. Lett. 67 (1991) 2954.

- [7] T.E. Cowan et al., *Bull. Am. Phys. Soc.* 34 (1989) 1812.
- [8] J.J. Bollinger, L.R. Brewer, J.C. Bergquist, W.M. Itano, D.J. Larson, S.L. Gilbert and D.J. Wineland, in: *Intense Positron Beams*, eds. E.H. Ottewitte and W. Kells (World Scientific, Singapore, 1988) p. 63.
- [9] P.B. Schwinberg, R.S. Van Dyck and H.G. Dehmelt, *Phys. Lett.* 81A (1981) 119.
- [10] G. Gabrielse and B.L. Brown, in: *The Hydrogen Atom*, eds. G.F. Bassani, M. Inguscio and T.W. Hänsch (Springer, Berlin, 1989) p. 196.
- [11] R.S. Conti, B. Ghaffari and T.D. Steiger, *Nucl. Instr. Meth. Phys. Res. A*299 (1990) 420; B. Ghaffari, R.S. Conti and T.D. Steiger, *Bull. Am. Phys. Soc.* 37 (1992) 1148.
- [12] A.P. Mills Jr., in: *Positron Scattering in Gases*, eds. J.W. Humberston and M.R.C. McDowell (Plenum Press, New York, 1984) p.121.
- [13] D.J. Heinzen, J.J. Bollinger, F.L. Moore, W.M. Itano and D.J. Wineland, *Phys. Rev. Lett.* 66 (1991) 2080; erratum 66 (1991) 3087.
- [14] H.G. Dehmelt, P.B. Schwinberg and R.S. Van Dyck Jr., *Int. J. Mass Spectrom. Ion Phys.* 26 (1978) 107.
- [15] T.M. O'Neil, *Phys. Fluids* 24 (1981) 1447.
- [16] D.J. Larson, J.C. Bergquist, J.J. Bollinger, W.M. Itano and D.J. Wineland, *Phys. Rev. Lett.* 57 (1986) 70.
- [17] T.M. O'Neil and P.G. Hjorth, *Phys. Fluids* 13 (1985) 3241.
- [18] S.L. Gilbert, J.J. Bollinger and D.J. Wineland, *Phys. Rev. Lett.* 60 (1988) 2022.
- [19] P.B. Schwinberg, Thesis, Department of Physics, University of Washington, USA.
- [20] J.H. Malmberg and T.M. O'Neil, *Phys. Rev. Lett.* 39 (1977) 1333.
- [21] N.A. Krall and T.W. Trivelpiece, *Principles of Plasma Physics* (McGraw-Hill, New York, 1973) p. 292.
- [22] M.E. Glinsky, T.M. O'Neil, M.N. Rosenbluth, K. Tsuruta and S. Ichimaru, *Phys. Fluids B*4 (1992) 1156.
- [23] B.R. Beck, J. Fajans and J.H. Malmberg, *Phys. Rev. Lett.* 68 (1992) 317.
- [24] J.J. Bollinger, D.J. Heinzen, W.M. Itano, S.L. Gilbert and D.J. Wineland, *IEEE Trans. Instr. Measurement* 40 (1991) 126.
- [25] J. Tan and G. Gabrielse, *Phys. Rev. Lett.* 67 (1991) 3090.
- [26] D.J. Heinzen and D.J. Wineland, *Phys. Rev. A*42 (1990) 2977.

High-Order Multipole Excitation of a Bound Electron

Carl S. Weimer,^(a) F. L. Moore,^(b) and D. J. Wineland

Time and Frequency Division, National Institute of Standards and Technology, Boulder, Colorado 80303
(Received 9 November 1992)

The nonlinear resonant response of a bound electron to a time-varying spatially inhomogeneous electric field was studied experimentally. By use of the artificial atom "geonium" (an electron bound in a Penning trap), we observed up to ninth-order multipole (pentacosiododecapole) coherent excitation of the electron's magnetron motion, and up to third-order (octupole) excitation of the cyclotron motion. Also, by applying two fields simultaneously, we have observed coherent stimulated Raman excitation of the electron's motion.

PACS numbers: 42.65.Ky, 36.90.+f, 42.79.Nv

The interaction of an electromagnetic field with a medium is, in general, nonlinear. There are three common origins of the nonlinearity [1-3]: (1) the interaction of the charges with the spatial inhomogeneity of the excitation fields, (2) the anharmonic binding of the medium's charges, and (3) the interaction of the medium with the magnetic component of the field. A number of resonant nonlinear effects have been studied, for example, harmonic generation, multiwave mixing, and multiphoton absorption. These nonlinear effects have almost exclusively relied on electric dipole transitions (with notable exceptions [4]), and the origin of the nonlinearities falls primarily into the second category. The first nonlinear mechanism, which corresponds to excitation of higher-order multipole transitions, is less common. Although multipole excitation is observed in some atomic and nuclear physics experiments, the excitation and detection are usually incoherent. We have studied this nonlinear mechanism by using an artificial atom [5]: an electron bound in a Penning trap [6-8]. This has provided for the first time a means to excite and detect, coherently, high-order multipole transitions, and observe high-order subharmonic generation. We have also observed several degenerate and nondegenerate nonlinear parametric processes which have been discussed by Kaplan and Ding [2,3]. Our observations complement the body of work on coherent harmonic excitation and multiwave mixing in atoms.

An electron bound in a Penning trap can be thought of as the artificial atom "geonium" [6-8]. The "nucleus" of geonium (the trap) is created with the electrodes (and fields) shown schematically in Fig. 1. A static voltage V_0 applied between the end caps and ring forms a potential (in spherical coordinates)

$$\Phi(r, \theta, \phi) = V_0 \sum_{n=0}^{\infty} C_{2n} (r/d)^{2n} P_{2n}(\cos\theta), \quad (1)$$

where the P_{2n} are the Legendre polynomials and the C_{2n} are constants. Here $d = r_0/\sqrt{2} = 3.54$ mm is a characteristic trap size, with r_0 the ring internal radius. The term labeled by C_2 forms a harmonic well along the \hat{z} axis. Our trap is designed to have $C_2 = 0.477$, and $C_4 = C_6 = 0$ [9]. Applying a voltage V_g to two additional guard electrodes [10] allows C_4 to be varied; in practice,

$|C_4| < 5 \times 10^{-5}$. Although $|C_4|$ was small, it remains the dominant electrostatic perturbation to our harmonic potential term. The leading perturbation to an applied homogeneous magnetic field $B_0 \hat{z}$ is a magnetic quadrupole bottle [6-8] of order $B_2/B_0 = 7 \times 10^{-5} \text{ cm}^{-2}$ due to magnet imperfections and the copper electrode diamagnetism. B_0 was measured to have a minimum long term drift rate of $|(dB_0/dt)/B_0| = 7 \times 10^{-7} \text{ h}^{-1}$, and for times on the order of 1 min, field fluctuations of $\Delta B_0/B_0 \approx 3 \times 10^{-7}$ for $B_0 = 0.1$ T.

The motion of a nonrelativistic electron bound in an ideal Penning trap ($C_n = 0$ for $n > 2$, B_0 homogeneous) is composed of three independent modes [6-8]. The axial (z) motion is harmonic with amplitude r_z and frequency $\omega_z = (2C_2 q V_0 / m d^2)^{1/2}$ where q/m is the electron's charge-to-mass ratio. In the radial (x - y) plane the motion is two superimposed circular motions: the magnetron motion of radius r_m and frequency ω_m corresponding to the $\mathbf{E} \times \mathbf{B}$ drift of the electron, and the cyclotron motion of radius r_c and frequency $\omega'_c = \omega_c - \omega_m$ where $\omega_c = qB_0/mc$. For $V_0 = -10.45$ V and $B_0 = 0.1$ T we obtain $\omega_z/2\pi = 61.5$ MHz, $\omega_m/2\pi = 615$ kHz, $\omega'_c/2\pi = 3.08$ GHz, and in general we maintain $\omega'_c \gg \omega_z \gg \omega_m$. The axial energy is damped [Γ_z (measured) $\approx 20 \text{ s}^{-1}$] by connecting a resonant tuned circuit to one of the end cap electrodes (analogous to a two-level atom in a resonant optical cavity) [6-8,11]. The magnetron motion is meta-

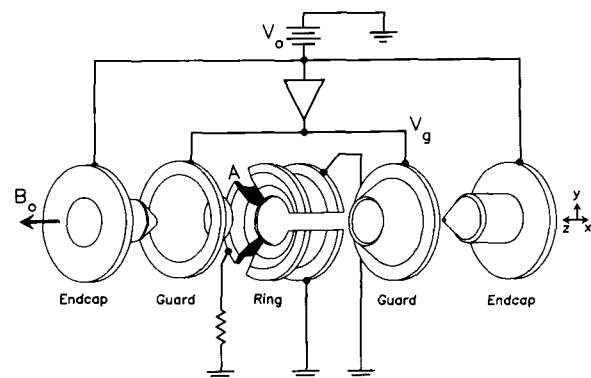


FIG. 1. A schematic diagram of the Penning trap used in the experiment. The electrodes have been separated along the z axis to show details.

stable. However, its amplitude can be damped at a variable rate of $0 \leq \Gamma_m \leq \frac{1}{2} \Gamma_z$ to a theoretical limit of $r_m = 2[(\omega_m/\omega_z)\langle r_z^2 \rangle]^{1/2}$ [where $\langle r_z^2 \rangle^{1/2}$ is the thermalized ($T=4$ K) axial amplitude] by the use of sideband cooling [6-8]. The cyclotron energy is radiatively damped at the free space rate modified by the presence of the trap and secondary electrodes [12] [$\Gamma_c(\text{measured}) \approx 0.1 \text{ s}^{-1}$ (1 s^{-1}) for $B_0 \approx 0.1 \text{ T}$ (1.4 T)]. Three main factors lead to deviations from the ideal motion: (1) anharmonic terms in the electrostatic potential ($C_n \neq 0, n > 2$), (2) relativistic effects, and (3) inhomogeneity of the magnetic field [6-8,13]. These cause the electron's modes of motion to be slightly anharmonic and weakly coupled together.

A single electron is loaded into the trap using established techniques [6-8,11]. The frequencies $\omega_z, \omega_m, \omega_c'$ are measured by applying oscillating drive potentials to different electrodes and observing a resonant response of the electron's motion. For the axial motion, the electron's response is observed by measuring the image currents induced in one end cap using a phase sensitive heterodyne detector (analogous to phase sensitive detection of atomic resonance fluorescence) [6-8,11]. We chose to detect the magnetron or cyclotron excitations via their coupling to the axial motion [6-8]. Specifically, the observed axial frequency depended upon the magnetron amplitude due to the electrostatic C_4 term, and it depended on the cyclotron amplitude due to the slight magnetic field inhomogeneity B_2 . For example, for a magnetron excitation ($r_m = 0 \rightarrow r_{m0}$), $\Delta\omega_z/\omega_z \approx -3C_4(r_{m0})^2/2C_2d^2$. The shift

$\Delta\omega_z$ is effectively observed by monitoring the correction voltage of an electronic servomechanism that locks the axial frequency to an external reference [6-8]. If, in addition to the driven oscillation (at frequency ω_d) there is a free (or thermally excited) oscillation at ω_m , then an interference beat note at $\omega_d - \omega_m$ will be observable in the correction voltage [7,14]. If a second coherent drive field is applied with frequency ω_0 , then three beat notes can be observed with frequencies $\omega_d - \omega_m$, $\omega_0 - \omega_m$, and $\omega_d - \omega_0$. The magnetron and cyclotron motions are excited by applying a drive voltage to sector A of the ring electrode (Fig. 1). To estimate the $(x-y)$ drive field the electrode geometry is approximated by a box with sides of length $(l_x, l_y, l_z) = 2d(\sqrt{2}, \sqrt{2}, 1)$. One side of the box perpendicular to \hat{x} (representing sector A) is assumed to be at a potential V_d with respect to the other sides. This model gives the resulting potential (in the $x-y$ plane)

$$\Phi_d(x, y, 0) = V_d \sum_m \sum_n a_{m,n} (x/d)^m (y/d)^n, \quad (2)$$

with $a_{m,n}$ constants [15].

A quantum description of the nonlinear excitation involves calculating amplitudes for processes like those in the insets in Figs. 2 and 3. However, in our experiment the mean occupation numbers of the electron's quantized motion were much larger than 1, so a classical model suffices [2,3]. When excited by a homogeneous field, the magnetron and cyclotron motions can be treated as one-

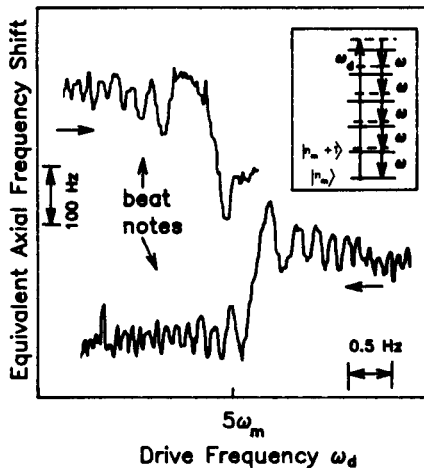


FIG. 2. The subharmonic response of order $\omega_d/\omega_m \approx 5$ of the center-of-mass magnetron motion of a cloud of approximately seventy electrons. Baselines for the two traces have been offset for clarity. The arrows show the direction the drive frequency was swept (at a rate of 0.1 Hz/s). The axial frequency shifts due to the magnetron excitation (the vertical steps) and the beat note between the free oscillation at ω_m and the subharmonically excited oscillation at $\omega_d/5$ are observed. For this figure the sideband cooling was off and the magnetron amplitude had been initialized in a large orbit. The inset shows a representation of this coherent process for particular quantum levels.

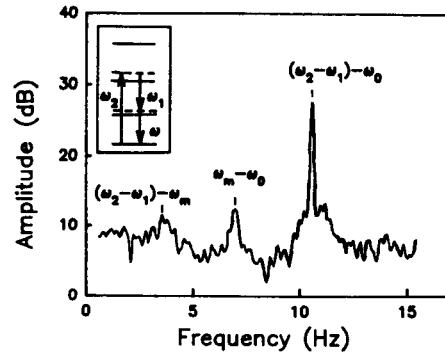


FIG. 3. The Fourier transform of the response of the magnetron motion of a single electron to drive fields at frequencies ω_0 , ω_1 , and ω_2 . The magnetron free oscillation is at frequency ω_m , and the driven oscillations are at $\omega_0 = \omega_m - 2\pi(7 \text{ Hz})$ and $\omega_2 - \omega_1 = \omega_m + 2\pi(4 \text{ Hz})$, with $\omega_1 = \omega_m + 2\pi(97 \text{ Hz})$. Three interference beat notes are observed. For short averaging times, $\tau < 10 \text{ s}$, the amplitudes and widths of the three beat notes were comparable. For longer averaging times ($\tau = 100 \text{ s}$ is shown here) the beat note responses between the driven and free oscillations (left two peaks) broaden and decay because of the magnetic field noise affecting the free oscillation. The beat between two driven oscillations (right peak) is unaffected (other than an amplitude modulation noise pedestal) and its width remains limited by the resolution of the dynamic signal analyzer (FFT). When measured with a phase detector, this peak showed that the nonlinear response was phase coherent with the drives. The inset shows a representation of this stimulated Raman response at $\omega_2 - \omega_1$.

dimensional harmonic oscillators. For an inhomogeneous drive field this is no longer true, but the main effect of the field inhomogeneity is to modify somewhat the strength and phase of the force. We therefore assume that the x components of the magnetron and cyclotron motions obey the approximate equations of motion (ignoring mode coupling)

$$\ddot{x} + \Gamma_j \dot{x} + \omega_j^2 x [1 + \xi(t) + \beta_2(x/d)^2 + \beta_4(x/d)^4 + \dots] = a_j F_d [a_0 + a_1(x/d) + a_2(x/d)^2 + \dots] \cos(\omega_d t), \quad (3)$$

where $F_d = qV_d/md$, $a_0 = 0.19$, $a_1 = 0.35$, $a_2 = 0.29$, and $a_3 = 0.13$ [from Eq. (2)], and j refers to either the cyclotron or magnetron motion. This equation neglects the y and z dependence of the force. However, since the a_i are only approximate, this further simplification should not significantly affect the results. For the magnetron motion $\omega_j = \omega_m$, $a_j = \omega_m/(\omega_m - \omega_c') \approx -\omega_m/\omega_c'$, and $\beta_i \propto C_{i+2}$. For the cyclotron motion $\omega_j = \omega_c'$, $a_j \approx \omega_c'/(\omega_c' - \omega_m) \approx 1$, and the β_i arise from the relativistic mass shift [13]. The term $\xi(t)$ is a multiplicative noise term [16] which, in our experiment, is caused primarily by the magnetic field fluctuations. The magnetic component of the drive fields [category (3) of the introduction] can be shown to be negligible here. Equation (3) holds also for the center-of-mass motion of small clouds of electrons (cloud size $\ll d$); experimentally, both small clouds and single electrons were used.

Equation (3) is solved by assuming solutions of the form $x(t) = A(t)\cos[\omega t + \phi(t)]$ where $A(t)$ and $\phi(t)$ are slowly varying. Nearly resonant excitation ($\omega \approx \omega_j$) of the motion can occur when $\omega_d \approx n\omega_j$, n an integer, in which case $\omega = (1/n)\omega_d$. This corresponds to subharmonic excitation (i.e., frequency division). It can be caused by (1) the electron's motion in the inhomogeneous drive field [a_i in Eq. (3)], and/or (2) the anharmonic motion of the electron [β_i in Eq. (3)], as noted in the introduction. The first is due to electric multipole transitions of frequency $n\omega_j$. The second is due to dipole transitions of frequency $n\omega_j$ which arise from mixing of the quantum oscillator levels due to the anharmonicity. Since $\beta_{n-1} \ll n^2 a_{n-1}/a_0$ for our experiment, Eq. (3) can be used to show that the first mechanism dominates. Parametric excitation ($n=2$) has been observed previously in traps for the axial motion of a single electron [11] and clouds of electrons [17-19].

If we neglect β_i with $i > 2$, Eq. (3) reduces to Duffing's equation [3] driven by a nonlinear force. Subharmonic response of order n exhibits both hysteresis and n stable phases of response relative to the phase of the drive [2,3]. In addition, from Eq. (3), a steady state response requires [for $\xi(t) = 0$] [3,20]

$$\left| \frac{a_j a_{n-1} F_d}{2^{n-1} \omega_j d} (A/d)^{n-2} \right| \geq \Gamma_j. \quad (4)$$

Therefore F_d and A must exceed certain threshold values

F_{dt} and A_t . The origin of these thresholds is that the energy supplied by the drive at ω_d to the oscillation at ω_d/n is dependent upon the amplitude A of that oscillation and must overcome the damping. No such threshold exists for harmonic excitation (frequency multiplication), $\omega_d \approx \omega_j/m$. The initial amplitude A_t necessary for subharmonic response can be generated by a resonant homogeneous drive ($\omega_d \approx \omega_j$), a thermal drive, or a free oscillation. When frequency noise is included [$\xi(t) \neq 0$], Γ_j in Eq. (4) is replaced by an effective damping rate which depends upon the form of the noise [16], and the frequency sweep rate of the drive. However, the ratios of Eq. (4) for different orders of n should be insensitive to Γ_j .

Subharmonic excitation of the magnetron motion was observed for $n=1-9$ on samples of up to about seventy electrons when the magnetron amplitude was initialized in a large orbit. Both the frequency shift and modulation of the axial frequency (by the beat notes) were observed as the magnetron amplitude resonantly increased. This is seen in Fig. 2 for $n=5$, where the beat note is due to the interference between the magnetron free oscillation and the subharmonically excited driven oscillation.

With a single electron the threshold values for subharmonic response for $n=2, 3$, and 4 were measured with the initial magnetron amplitude cooled to its minimum value (set by the sideband cooling). Independently, we determined the magnetron amplitude at its sideband cooling limit by varying C_4 and measuring the resulting change in ω_m [8,14]. This gave $r_m = 220 \pm 140 \mu\text{m}$, or $r_m = (55 \pm 35)r_{\text{theo}}$, where r_{theo} is the theoretical cooling limit. This disagreement with theory is consistent with measurements made by other groups, and its origin is not known [7,8,14]. We measured the threshold values $V_d(n=2) = 6 \mu\text{V}$, $V_d(n=3) = 300 \mu\text{V}$, and $V_d(n=4) = 6 \text{mV}$, for $\omega_m/2\pi = 615.0 \text{ kHz}$ ($B_0 = 0.1 \text{ T}$, sideband cooling off, sweep rate 0.1 Hz/s). From these measurements and Eq. (4), we calculated $a_1/a_2 = 1.6 \pm 1.0$ and $a_1/a_3 = 1.0 \pm 0.8$. These agree with the values given by the electrostatic model [Eq. (2)] within the measurement uncertainty. Similar results were found for $\omega_m/2\pi = 47.34 \text{ kHz}$ ($B_0 \approx 1.4 \text{ T}$).

The origin of the subharmonic response at $n=3$ was experimentally investigated. This response could arise from the excitation of the octupole moment of the magnetron orbit, or from a weakly allowed dipole transition due to the C_4 anharmonic term in the trap electrostatic potential. Changing the guard voltage allowed C_4 to be varied in small steps from $C_4 < 5 \times 10^{-5}$ to $> 4 \times 10^{-4}$. No change in the required threshold drive strength was observed. If the subharmonic response had been due to the anharmonic component of the magnetron motion, this threshold drive strength would be proportional to $|C_4^{-1}|$.

The more general resonance condition [21] $\omega_d = (n/m)\omega_m$, $m, n \neq 1$ was also investigated. We observed resonant excitation when $\omega_d = \frac{2}{3}\omega_m$ (for $V_d = 3 \text{ mV}$, $\omega_m/2\pi = 615.0 \text{ kHz}$, and the same conditions as above), which corresponds to three-photon excitation of the quadrupole

resonance.

For two drive fields we observed stimulated Raman excitation of the magnetron motion when $\omega_2 = q\omega_1 = r\omega_m$ with $(q=1, r=1,2,3)$ and $(q=1,2,3, r=1)$. These resonances could be observed either with the sideband cooling (damping) on or off, and typical detunings $\Delta = \omega_1 - \omega_m = 2\pi(1 \text{ to } 150 \text{ Hz})$. Resonant enhancement of the response was observed as Δ was decreased. The beating between these excitations and the free magnetron oscillation was observed as well as the anharmonic pulling of the magnetron frequency. When another driven oscillation near $\omega_0 \approx \omega_m$ was generated, three beat notes were observed, two between the driven and free oscillations, and one between the two driven oscillations near ω_m (see Fig. 3). The observation of these beat notes allows the magnetron responses (linear or nonlinear) to be measured in a continuous phase sensitive manner [20].

We observed subharmonic excitation of order $n=2$ and 3 for a single electron's cyclotron motion ($\omega_c'/2\pi \approx 3 \text{ GHz}$). Since $\omega_c' \gg \omega_m$, magnetic field drift and noise caused significantly more dephasing of the cyclotron motion than that of the magnetron motion; this resulted in poor quantitative agreement between the cyclotron results and the simple theory. When two drive fields were applied with frequencies ω_2 and ω_1 , stimulated Raman excitation of the cyclotron motion of a single electron was observed for $\omega_2 - \omega_1 \approx \omega_c'$ with $\omega_1 = \omega_c' + \Delta$. Resonant enhancement of the response was observed as the detuning Δ was decreased; typically $\Delta/2\pi = 100 \text{ to } 600 \text{ kHz}$. Magnetic field noise prevented us from observing beat notes between the different cyclotron excitations.

In summary, we have observed, coherently, high-order nonlinear resonant excitation of a single bound electron's motion as well as that of the center-of-mass motion of a cloud of electrons. These effects were observed in the limit where the nonlinearity was dominated by the multipole interaction between the electron and the drive field. Initial comparisons with a simple one-dimensional theory show quantitative agreement for excitation of the magnetron motion. Detailed quantitative comparisons between experiment and theory requires better magnetic field stability, better estimates for the shape of the drive fields (the α_i) and orbit amplitudes, as well as the extension of Eq. (3) to three dimensions. In addition, the effects of mode coupling and noise-induced fluctuations of the mode frequencies must be included in the nonlinear analysis, especially because they can inhibit very high-order excitation. Experimentally, it should be possible to greatly reduce the magnetic field noise, which in turn should facilitate high-order subharmonic excitation of the cyclotron motion. If very high-order subharmonic response can be observed $\omega = \omega_d/n$ with $n \approx 10^4$, the system could have applications in frequency metrology [3,22]. In general, this system might be useful in studies of the effect of noise on nonequilibrium phase transitions [16], as well as chaotic behavior in the transition from classical to quantum dynamics.

We thank J. Bergquist, J. Bollinger, R. Fox, S. Jefferts,

D. Sullivan, and M. Young for their comments on the manuscript. We gratefully acknowledge the support of the Office of Naval Research and the U.S. Air Force Office of Scientific Research.

^(a)Also at Colorado State University, Fort Collins, CO 80523.

^(b)Current address: Physics Department, University of Texas at Austin, Austin, TX 78712.

- [1] N. Bloembergen, *Nonlinear Optics* (Benjamin, New York, 1965).
- [2] A. E. Kaplan, Phys. Rev. Lett. **56**, 456 (1986).
- [3] A. E. Kaplan, Opt. Lett. **12**, 489 (1987); Alexander E. Kaplan and Yu J. Ding, IEEE J. Quantum Electron. **24**, 1470 (1988), and references therein.
- [4] D. C. Hanna, M. A. Yuratic, and D. Cotter, *Nonlinear Optics of Free Atoms and Molecules* (Springer-Verlag, Berlin, 1979), and references therein.
- [5] Marc A. Kastner, Phys. Today **46**, No. 1, 24 (1993).
- [6] Robert S. Van Dyck, Jr., Paul B. Schwinberg, and Hans G. Dehmelt, Phys. Rev. D **34**, 722 (1986).
- [7] Robert S. Van Dyck, Jr., Paul B. Schwinberg, and Hans G. Dehmelt, in *New Frontiers in High-Energy Physics*, edited by Behram Kursunoglu, Arnold Perlmutter, and Linda F. Scott (Plenum, New York, 1978).
- [8] Lowell S. Brown and Gerald Gabrielse, Rev. Mod. Phys. **58**, 233 (1986).
- [9] Earl C. Beaty, J. Appl. Phys. **61**, 2118 (1987), and unpublished calculations.
- [10] R. S. Van Dyck, Jr., D. J. Wineland, P. A. Ekstrom, and H. G. Dehmelt, Appl. Phys. Lett. **28**, 446 (1976).
- [11] D. Wineland, P. Ekstrom, and H. Dehmelt, Phys. Rev. Lett. **31**, 1279 (1973).
- [12] R. S. Van Dyck, Jr., P. B. Schwinberg, and H. G. Dehmelt, in *Atomic Physics 9*, edited by R. S. Van Dyck, Jr. and E. N. Fortson (World Scientific, Singapore, 1984); Gerald Gabrielse and Hans Dehmelt, Phys. Rev. Lett. **55**, 67 (1985).
- [13] Gerald Gabrielse, Hans Dehmelt, and William Kells, Phys. Rev. Lett. **54**, 537 (1985).
- [14] F. L. Moore, L. S. Brown, D. L. Farnham, S. Jeon, P. B. Schwinberg, and R. S. Van Dyck, Jr., Phys. Rev. A **46**, 2653 (1992).
- [15] J. D. Jackson, *Classical Electrodynamics* (Wiley, New York, 1975), 2nd ed.
- [16] R. L. Stratonovich, *Topics in the Theory of Random Noise* (Gordon and Breach, New York, 1967), Vol. II; A. Schenzle and H. Brand, Phys. Rev. A **20**, 1628 (1979); H. Haken, *Synergetics* (Springer-Verlag, Berlin, 1978).
- [17] H. G. Dehmelt and F. L. Walls, Phys. Rev. Lett. **21**, 127 (1968).
- [18] R. S. Van Dyck, Jr., F. L. Moore, D. L. Farnham, P. B. Schwinberg, and H. G. Dehmelt, Phys. Rev. A **36**, 3455 (1987).
- [19] J. Tan and G. Gabrielse, Phys. Rev. Lett. **67**, 3090 (1991).
- [20] Carl S. Weimer, Ph.D. thesis, Colorado State University, 1992.
- [21] N. N. Bogoliubov and Y. A. Mitropolsky, *Asymptotic Methods in the Theory of Non-Linear Oscillations* (Hindustan, Delhi, India, 1961).
- [22] D. J. Wineland, J. Appl. Phys. **50**, 2528 (1979).

Coaxial-resonator-driven rf (Paul) trap for strong confinement

S. R. Jefferts, C. Monroe, E. W. Bell,* and D. J. Wineland

National Institute of Standards and Technology, Boulder, Colorado 80303

(Received 22 August 1994)

We describe a variant of the quadrupole rf (Paul) ion trap capable of localization of a trapped ion to much less than an optical wavelength (Lamb-Dicke regime). The trapping potentials are generated by a high- Q , vacuum-compatible, quarter-wave resonator driven at about 240 MHz. The binding strength of the trap has been characterized. The trap contains compensation electrodes which allow the cancellation of stray static electric fields within the trap. Secular frequencies of tens of megahertz have been achieved for trapped magnesium and beryllium ions.

PACS number(s): 32.80.Pj

I. INTRODUCTION

In this paper we describe an ion trap apparatus capable of very strong confinement. Strong confinement is important in several applications. In optical atomic spectroscopy, strong confinement allows the attainment of the Lamb-Dicke condition whereby the extent of the atom's motion is less than $\lambda/2\pi$, where λ is the wavelength of the exciting radiation [1]. Attainment of the Lamb-Dicke condition is important because it suppresses broadening due to the first-order Doppler effect, which, in harmonically bound atoms, takes the form of motion-induced sidebands [2–5]. It also suppresses the fluctuations of the “carrier” from measurement to measurement [6]. More recently, strong confinement has been suggested as a way to observe the effects of super and subradiance for two closely spaced atoms under well-controlled conditions [7]. Achievement of the Lamb-Dicke limit also suggests experiments on single-atom cavity QED and nonclassical atomic fluorescence features under controlled conditions [8,9].

With strong confinement, we should be able to achieve resolved sideband cooling [10,11] using allowed electric-dipole transitions. Previously, resolved sideband cooling has been achieved using weakly allowed optical transitions [11]. For resolved sideband cooling, we require that the trap is made deep enough that the atom oscillation frequencies (ω_i , $i=x,y,z$) satisfy $\omega_i \gg \gamma$, where γ is the linewidth of the transition. Use of resolved sidebands on allowed electric-dipole transitions has the potential advantage that cooling to the ground state of motion can be achieved very rapidly. Resolved sidebands should also facilitate precise measurement of the lifetimes of rapidly decaying levels by measuring the linewidth of the resolved carrier.

In a Penning trap [12], single-ion confinement is limited by the strength of binding along the magnetic-field direction, which we can characterize by the (harmonic)

binding frequency ω_z . For stable trapping in the radial direction, we must have $\omega_z < \omega_c/\sqrt{2}$, where ω_c is the ion cyclotron frequency. This implies $2\pi\nu_z \equiv \omega_z < 2^{-1/2}QB/M$, where Q is the ion charge, B is the magnetic-field strength, and M is the ion mass. For $B=10$ T, $Q=1e$, and $M=9$ u (e.g., ${}^9\text{Be}^+$), $\nu_z < 12$ MHz. In this paper, we discuss only the Paul trap because, for practical field strengths, the binding should be stronger.

For a single ion bound in a quadrupole rf Paul trap [12], the axial or z frequency ω_z must satisfy $\omega_z \leq \Omega/2$, where Ω is the rf drive frequency. If we assume that the static potential applied between the electrodes is zero, then, at the Mathieu stability limit ($q_z=0.908$) [12,13] in an axially symmetric trap, $\omega_z(\text{max})=\Omega/2$ and the radial secular frequency is given by $\omega_r(\text{max})\simeq 0.35\omega_z(\text{max})$. The maximum secular frequencies can then be characterized by the expression for $\nu_z(\text{max})$ [12,13]

$$\nu_z(\text{max}) = \frac{\Omega/2\pi}{2} = \frac{1}{2\pi d_0} \left[\frac{QV_0}{0.908M} \right]^{1/2}, \quad (1)$$

where Q is the ion charge, V_0 is the peak rf potential applied between the ring and end caps, M is the ion mass, and d_0 is the characteristic trap dimension. For a trap with hyperbolic electrodes, $2d_0^2 \equiv r_0^2 + 2z_0^2$, where r_0 is the inner radius of the ring electrode and $2z_0$ is the inner end-cap to end-cap distance. Using $Q=1e$, $M=9$ u, $V_0=2$ kV, and $d_0=0.15$ mm, we find $\nu_z(\text{max})\simeq 164$ MHz and $\nu_r(\text{max})\simeq 58$ MHz. These conditions would allow resolved sidebands on the $S \rightarrow P$ transition in ${}^9\text{Be}^+$, where $\gamma/2\pi=19.4$ MHz. If we assume $\nu_r=58$ MHz and the ion is cooled to the ground state of motion, the Lamb-Dicke parameter is $2\pi x_0/\lambda=0.063$, where x_0 is the spread of the zero-point wave function.

From Eq. (1), to achieve strong confinement, we require large values of V_0 and small values of d_0 . Implicitly, we assume that Ω is adjusted to give stable trapping, that is, $\Omega > 2\omega_z$. Large values of V_0 can be limited by electric-field breakdown or arcing. Also, if the high voltage is generated external to the required vacuum enclosure for the trap, the voltage at the trap is reduced by the capacitance of the vacuum feedthroughs. This problem becomes more difficult for the required high values of Ω .

As the trap dimensions are reduced, it becomes more

*Present address: National Institute of Standards and Technology, Building 221, Gaithersburg, MD 20899.

difficult to machine the desired electrode shapes. This problem can be minimized by using simpler electrode shapes where the leading anharmonic terms in the trap potential can be nulled for appropriate electrode shapes. For example, nominally quadrupolar electrodes with simple conical surfaces can be used [14]. "Planar" traps formed with holes in parallel plates [15,16] or with conducting rings [16] simplify construction even further. These electrodes have the advantage that they can be made small by using lithographic techniques [16].

As multielectrode traps (such as the conventional quadrupole trap) become smaller, the relative electrode positions also become more difficult to maintain. One way to eliminate this problem is to keep either the ring or end-cap electrodes small and let the complementary electrode(s) recede to large distances. The Paul-Straubel or "ring" trap [17] is essentially a ring electrode with the end caps at large distances. This trap has been analyzed [16,18,19] and demonstrated for Ba^+ ions [18] and In^+ ions [19]. For this kind of trap, an efficiency ϵ can be defined as the ratio of the rf voltage required in a quadrupole trap with hyperbolic electrodes to the voltage required in the ring trap (of the same internal ring diameter) which gives the same secular frequency. References [16,18,19] find ϵ in the range of 0.1–0.2. In a similar spirit, Janik, Prestage, and Maleki [20] have analyzed the case of a linear trap with two and three electrodes rather than four electrodes as for the quadrupole linear trap. For the two-electrode trap they find $\epsilon \approx 0.25$.

The "end-cap" trap is complementary to the Paul-Straubel trap in that it has closely spaced end cap electrodes with the ring receding to infinity. Schrama *et al.* [19] analyzed and demonstrated a version of this trap using Mg^+ ions. They find an efficiency ϵ in the range of 0.2–0.5. Both the Paul-Straubel or ring trap and the end-cap trap additionally provide a more open optical access for collecting ion fluorescence light than the conventional quadrupole trap.

In the work described below [21], we discuss a strategy for achieving large values of V_0 and Ω and small values of d_0 in a trap with nominal quadrupolar geometry where $\epsilon \approx 1$.

II. DESCRIPTION

The trap described here is very simple; it consists of two thin sheets of metal: the first, the ring, has a hole, the second, perpendicular to the first, has a slit and acts as the end caps. The arrangement is illustrated in Fig. 1. One trap constructed with this geometry is used for trapping $^{24}\text{Mg}^+$ ions and has a ring inner diameter $2r_0$ of 0.43 mm. The end-cap slit width $2z_0$ is 0.32 mm. The molybdenum sheet from which the trap was constructed was 0.13 mm thick. As shown in Fig. 1, the relative position of the trap electrodes is maintained by ceramic positioning rods.

The trap is mounted at the end of an ultrahigh-vacuum-compatible coaxial quarter-wave resonant transmission line. This oxygen-free high-conductivity copper quarter-wave line is installed inside a vacuum enclosure which has fused silica windows to allow the pas-

sage of uv laser beams for cooling and probing the atom and resonance fluorescence light from the ions. The transmission line is resonant at a frequency of approximately 240 MHz and has an unloaded quality factor Q_u on the order of 2000. The transmission line is excited with a small loop antenna at the base of the transmission line. The area of the loop is adjusted so that, on resonance, the antenna plus resonator presents a 50- Ω load to the driving amplifier. With some care adjusting the coupling, voltage standing-wave ratios of less than 1.05 can be achieved. With 1 W of incident rf power, the calculated rf trapping voltage V_0 at the trap is about 700 V peak, neglecting the trap capacitance and end effects of the resonator. From the modeled trap parameters (Sec. III) and the measured secular frequencies (below), we calculate the actual voltage between the ring and end caps to be $V_0 \approx 600$ V for 1 W of incident power. We have been unable to apply voltage much beyond 1 kV due to a vacuum discharge problem which we are attempting to solve.

One advantage of this type of design results from the fact that the rf voltage at the vacuum feedthrough is small, thus minimizing problems associated with high-voltage breakdown at or before the feedthrough as well as reduction of the resonator Q by the vacuum feedthrough. An extension of the design would be to mount the "ring" electrode at the antinode of a half-wave transmission line resonator with the end caps attached to the outer wall of the transmission line. This geometry would allow a direct current to be passed through the ring electrode to evaporate any contaminants on the trap ring [18].

Uncontrolled static electric fields arising from contact potentials or charged patches can cause significant problems in miniature rf traps. These fields displace ions from the zero of the rf trapping fields, thereby leading to undesirable increases in the "micromotion" amplitudes [18]. A common scheme for dealing with these problems is the introduction of "compensation electrodes," which are used to cancel the stray electric fields in the trapping regions. We have included compensation electrodes, similar to those used by Nagourney [22], in the manner shown in Fig. 1. Static potentials applied to various combinations of the compensation electrodes allow for cancellation of static electric fields in an arbitrary direction in the trapping region.

With zero static potential between the electrodes and in the pseudopotential approximation, the secular (motional) frequencies of a trapped ion can be expressed as

$$\omega_i = \alpha_i \frac{\sqrt{2}QV_0}{md_0^2\Omega}, \quad (2)$$

where α_i is a numerical constant for ion motion along the i th axis ($i = x, y, z$; see Fig. 1). In the case of a quadrupolar hyperbolic ion trap, the constant α_i is $\frac{1}{2}$ for the x and y directions and 1 for the z direction. The trap described here breaks the symmetry about the z direction, causing $\omega_x < \omega_y$. In the pseudopotential approximation, with zero static electric field between the trap electrodes, $\omega_x + \omega_y = \omega_z$. Measured ion motional frequencies for this trap fall in the ratios of $\omega_x/\omega_z = 0.40$ and $\omega_y/\omega_z = 0.60$.

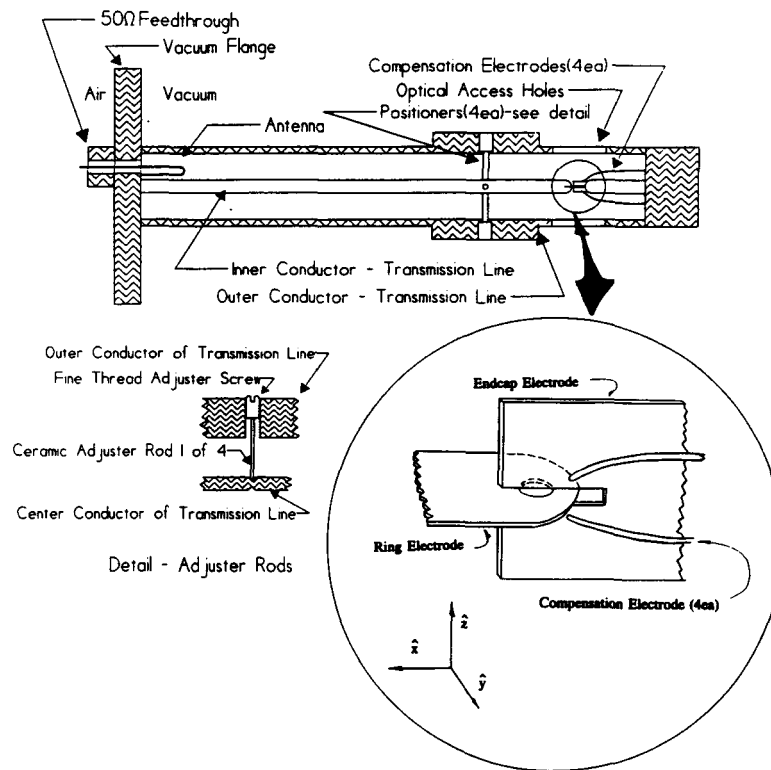


FIG. 1. Approximate scale drawing of the coaxial resonator and rf trap electrodes (shown in an expanded view in the lower right of the figure). The ring electrode is attached to the inner conductor at the position of the antinode of the quarter-wave line. The end cap electrode is held near the rf ground by the short section of center conductor at the right-hand side of the resonator. The resonator is driven by a coaxial line external to the vacuum system shown at the left. The area of the loop antenna is adjusted so the resonator (on resonance) presents a matched load ($50\ \Omega$) to the input line. The resonator is surrounded by a vacuum envelope (not shown in the figure) which has quartz windows to allow the passage of uv laser beams and fluorescence light. The position of the ring electrode relative to the end cap electrode is maintained by four adjustable ceramic rods (alumina) shown in the detail in the lower left of the figure. Static potentials are applied to four compensation electrodes to compensate for stray electric fields due to contact potentials and charge buildup on the trap electrodes. For a proper selection of compensation potentials, the average position of a single trapped ion coincides with the position of a zero rf electric field. The two compensation electrodes in front of the end cap electrode are shown in the expanded view in the lower right of the figure. Two more compensation electrodes (behind the end cap electrode) are not shown in the figure.

The secular frequencies of trapped $^{24}\text{Mg}^+$ ions were measured by monitoring the intensity of scattered laser-cooling light ($\lambda \approx 280\ \text{nm}$) as an rf drive was applied to one of the compensation electrodes and swept over the frequency range which included the secular motion frequencies. Data taken with a single trapped $^{24}\text{Mg}^+$ ion and $V_0 \approx 450\ \text{V}$ at frequency Ω are shown in Fig. 2. The measurements of ion secular frequencies at a given rf voltage in Ω yield the efficiency of this trap relative to the normal hyperbolic rf trap. From these measurements, we can assign a trap efficiency factor ϵ of about 0.9 for the axial (z) direction of this trap. This compares favorably with the efficiency factor of about 0.13 for the single-ring trap [18] and between 0.2 and 0.5 for the multiring trap [16], or end cap trap [19]. We have constructed a similar but slightly smaller trap ($r_0 = 0.15\ \text{mm}$, $z_0 = 0.10\ \text{mm}$), for $^9\text{Be}^+$ ions; this trap has demonstrated confinement with secular axial frequencies in excess of $50\ \text{MHz}$ ($\Omega/2\pi = 230\ \text{MHz}$), the largest secular frequency reported to date to our knowledge. Previously, secular frequen-

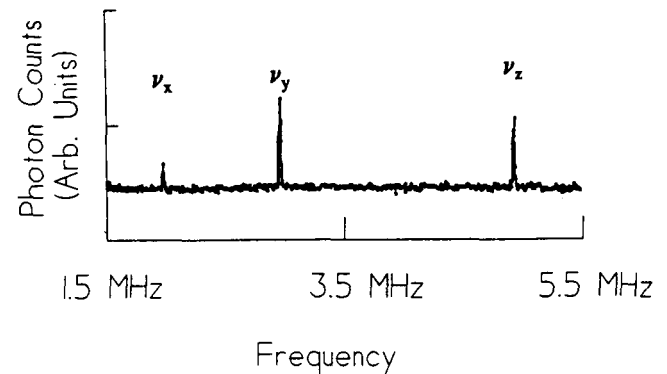


FIG. 2. Response of a single $^{24}\text{Mg}^+$ ion to an oscillating potential applied to one of the compensation electrodes shown in Fig. 1. The cooling laser for $^{24}\text{Mg}^+$ ions is tuned several linewidths to the red of the $^2S_{1/2} \rightarrow ^2P_{3/2}$ transition. When the ion is excited by the oscillating electric field, the Doppler shift caused by its increased velocity leads to an increase in fluorescence scattering. The three resonances shown correspond to excitation of the three secular frequencies ω_x , ω_y , and ω_z .

cies of approximately 10 MHz have been reported for Ba^+ ions [16,18]. In this second trap the secular frequency was inferred by measuring the ion-ion spacing at low rf-drive levels, which calibrates the "spring" constant of the trap, and then scaling the spring constant to higher rf-trapping voltages. This measurement, coupled with the modeled electric potential in the trap (below) and the results from the first trap using trapped $^{24}\text{Mg}^+$, allows the assignment of the secular frequencies at arbitrary values of the rf-trapping voltage. The secular frequencies will be limited by the requirement that $\omega_z < \Omega/2$ for stable trapping (Mathieu stability limit). To increase ω_z , one must increase Ω ; one way this can be accomplished with no change to the apparatus is by driving the transmission line at the first overtone, thereby raising Ω , and hence the limit on ω_z , by a factor of 3.

III. MODELING

This trap design does not lend itself well to analytic methods of solution for the electric potential in the trapping region, so the trap potential must be modeled using a computer program which can describe the full three-dimensional extent of the trap electrodes. We have performed modeling of the three-dimensional trap structure using the MAFIA [23] computer program.

The ring and end-cap electrodes of the $^{24}\text{Mg}^+$ trap were discretized on a cubical mesh whose overall side was 1.02 mm on a side with a distance between individual mesh points of 0.013 mm. The mesh axes lay along the same coordinate system as the trap coordinate system shown in Fig. 1, with the origin centered on the trap. The compensation electrodes were not included in the model. The mesh spacing was chosen so there were a sufficient number of mesh points to describe the smallest feature of the trap. The electrostatic field was then calculated and the secular frequencies determined from the field. The calculated motional frequencies are in the ratios $\omega_x/\omega_z=0.44$ and $\omega_y/\omega_z=0.63$, in reasonable agreement with the measured ratios of $\omega_x/\omega_z=0.40$ and $\omega_y/\omega_z=0.60$. The relatively coarse grid used in the trap modeling limits the accuracy of the modeled trap potential thus causing the calculated ω_x and ω_y to not sum exactly to ω_z .

Higher-order terms in the potential are also of importance. These have also been estimated by fitting the MAFIA results to the expansion (in spherical coordinates)

$$\Phi(r, \theta, \phi) = V_0 \sum_{n=0}^{\infty} C_{2n} \left[\frac{r}{d_0} \right]^{2n} P_{2n}(\cos\theta). \quad (3)$$

As a result of the reflection symmetry in \hat{z} , the odd order terms in the expansion have been eliminated. The constant C_2 is the coefficient of the quadrupolar trapping potential and is of order 1. The C_4 term in the expansion, the lowest-order correction to the described quadrupole potential, is less than 0.3. Higher-order even terms in the expansion have not been calculated.

Due to the small size of the trap, significant misalignment of the trap electrodes is a possibility. To determine the sensitivity of the trapping potential to this effect, possible misalignments of the components of the trap were modeled. Several cases where the end caps were shifted up to 0.13 mm relative to the ring in the y and z directions were computed. This distance corresponds to about one-third of the ring diameter and represents a "worst" case misalignment. The predicted motional frequencies for maximal misalignment differed by less than 5% from the frequencies for the aligned case. This calculated shift is approximately the uncertainty introduced due to discretizing the trap on the finite mesh used. Therefore, it seems that small misalignments of the trap electrodes do not significantly alter the characteristics of the trap.

IV. CONCLUSIONS

This trap has demonstrated the highest secular frequencies for trapped ions reported to date and can be extended to even higher frequencies. Unlike some other designs, it retains the trapping efficiency of conventional hyperbolic quadrupolar designs, thereby allowing larger traps to be built to achieve a given secular frequency and thus relaxing dimensional tolerance requirements. Use of a coaxial-resonator-based design minimizes problems associated with high-voltage breakdown and facilitates the attainment of high values of the drive frequency Ω .

ACKNOWLEDGMENTS

Support for this project has been provided by the ONR. S.R.J. and C.M. received financial support from the National Research Council. We thank J. C. Bergquist for help in setting up the cooling laser used in these experiments. A. S. Barton provided significant help in the early stages of this work. We thank the AT-7 code group at Los Alamos National Laboratories for the use of the MAFIA modeling program. We thank R. Blatt, J. Miller, and M. Young for helpful comments on the manuscript.

-
- [1] R. H. Dicke, Phys. Rev. **89**, 472 (1953).
 [2] D. J. Wineland and W. M. Itano, Phys. Rev. A **20**, 1521 (1979); J. C. Bergquist, W. M. Itano, and D. J. Wineland, *ibid.* **36**, 428 (1987).
 [3] W. Neuhauser, M. Hohenstatt, P. E. Toschek, and H. G.

- Dehmelt, Phys. Rev. A **22**, 1137 (1980).
 [4] G. Janik, W. Nagourney, and H. Dehmelt, J. Opt. Soc. Am. **2**, 1251 (1985).
 [5] A. A. Madej, K. J. Siemsen, J. D. Sankey, R. F. Clark, and J. Vanier, IEEE Trans. Instrum. Meas. **42**, 234 (1993).

- [6] H. Dehmelt, *Bull. Am. Phys. Soc.* **18**, 1521 (1973).
- [7] R. G. DeVoe and R. G. Brewer, *Bull. Am. Phys. Soc.* **38**, 1140 (1993).
- [8] *Fundamental Systems in Quantum Optics*, Proceedings of the Les Houches Summer School of Theoretical Physics, Session LIII, Les Houches, France, 1990, edited by J. Dalibard, J. M. Raimond, and J. Zinn-Justin (Elsevier, Amsterdam, 1992).
- [9] W. Vogel, *Phys. Rev. Lett.* **67**, 2450 (1991); W. Vogel and R. Blatt, *Phys. Rev. A* **45**, 3319 (1992).
- [10] D. J. Wineland and H. Dehmelt, *Bull. Am. Phys. Soc.* **20**, 637 (1975).
- [11] F. Diedrich, J. C. Bergquist, W. M. Itano, and D. J. Wineland, *Phys. Rev. Lett.* **62**, 403 (1989).
- [12] H. G. Dehmelt, *Adv. At. Mol. Phys.* **3**, 53 (1967); **5**, 109 (1969); D. J. Wineland, W. M. Itano, and R. S. Van Dyck, Jr., *ibid.* **19**, 135 (1983); R. C. Thompson, *ibid.* **31**, 63 (1993).
- [13] R. F. Wuerker, H. Shelton, and R. V. Langmuir, *J. Appl. Phys.* **30**, 342 (1959).
- [14] E. C. Beaty, *J. Appl. Phys.* **61**, 2118 (1987).
- [15] M. H. Prior and H. A. Shugart, *Phys. Rev. Lett.* **27**, 902 (1971).
- [16] R. G. Brewer, R. G. DeVoe, and R. Kallenbach, *Phys. Rev. A* **46**, R6781 (1992).
- [17] H. Straubel, *Naturwissenschaften* **18**, 506 (1955).
- [18] N. Yu, W. Nagourney, and H. Dehmelt, *J. Appl. Phys.* **69**, 3779 (1991).
- [19] C. A. Schrama, E. Peik, W. W. Smith, and H. Walther, *Opt. Commun.* **101**, 32 (1993).
- [20] G. R. Janik, J. D. Prestage, and L. Maleki, *J. Appl. Phys.* **67**, 6050 (1990).
- [21] S. R. Jefferts, C. Monroe, A. S. Barton, and D. J. Wineland, *Bull. Am. Phys. Soc.* **39**, 1167 (1994).
- [22] W. Nagourney (private communication).
- [23] T. Weiland, MAFIA (Release 3.1), October 1991, CST, Ohlystrasse 69, D-6100 Darmstadt, Germany.

NIST Technical Publications

Periodical

Journal of Research of the National Institute of Standards and Technology—Reports NIST research and development in those disciplines of the physical and engineering sciences in which the Institute is active. These include physics, chemistry, engineering, mathematics, and computer sciences. Papers cover a broad range of subjects, with major emphasis on measurement methodology and the basic technology underlying standardization. Also included from time to time are survey articles on topics closely related to the Institute's technical and scientific programs. Issued six times a year.

Nonperiodicals

Monographs—Major contributions to the technical literature on various subjects related to the Institute's scientific and technical activities.

Handbooks—Recommended codes of engineering and industrial practice (including safety codes) developed in cooperation with interested industries, professional organizations, and regulatory bodies.

Special Publications—Include proceedings of conferences sponsored by NIST, NIST annual reports, and other special publications appropriate to this grouping such as wall charts, pocket cards, and bibliographies.

Applied Mathematics Series—Mathematical tables, manuals, and studies of special interest to physicists, engineers, chemists, biologists, mathematicians, computer programmers, and others engaged in scientific and technical work.

National Standard Reference Data Series—Provides quantitative data on the physical and chemical properties of materials, compiled from the world's literature and critically evaluated. Developed under a worldwide program coordinated by NIST under the authority of the National Standard Data Act (Public Law 90-396). NOTE: The Journal of Physical and Chemical Reference Data (JPCRD) is published bi-monthly for NIST by the American Chemical Society (ACS) and the American Institute of Physics (AIP). Subscriptions, reprints, and supplements are available from ACS, 1155 Sixteenth St., NW, Washington, DC 20056.

Building Science Series—Disseminates technical information developed at the Institute on building materials, components, systems, and whole structures. The series presents research results, test methods, and performance criteria related to the structural and environmental functions and the durability and safety characteristics of building elements and systems.

Technical Notes—Studies or reports which are complete in themselves but restrictive in their treatment of a subject. Analogous to monographs but not so comprehensive in scope or definitive in treatment of the subject area. Often serve as a vehicle for final reports of work performed at NIST under the sponsorship of other government agencies.

Voluntary Product Standards—Developed under procedures published by the Department of Commerce in Part 10, Title 15, of the Code of Federal Regulations. The standards establish nationally recognized requirements for products, and provide all concerned interests with a basis for common understanding of the characteristics of the products. NIST administers this program in support of the efforts of private-sector standardizing organizations.

Consumer Information Series—Practical information, based on NIST research and experience, covering areas of interest to the consumer. Easily understandable language and illustrations provide useful background knowledge for shopping in today's technological marketplace.

Order the above NIST publications from: Superintendent of Documents, Government Printing Office, Washington, DC 20402.

Order the following NIST publications—FIPS and NISTIRs—from the National Technical Information Service, Springfield, VA 22161.

Federal Information Processing Standards Publications (FIPS PUB)—Publications in this series collectively constitute the Federal Information Processing Standards Register. The Register serves as the official source of information in the Federal Government regarding standards issued by NIST pursuant to the Federal Property and Administrative Services Act of 1949 as amended, Public Law 89-306 (79 Stat. 1127), and as implemented by Executive Order 11717 (38 FR 12315, dated May 11, 1973) and Part 6 of Title 15 CFR (Code of Federal Regulations).

NIST Interagency Reports (NISTIR)—A special series of interim or final reports on work performed by NIST for outside sponsors (both government and non-government). In general, initial distribution is handled by the sponsor; public distribution is by the National Technical Information Service, Springfield, VA 22161, in paper copy or microfiche form.

U.S. Department of Commerce
National Institute of Standards and Technology
325 Broadway
Boulder, Colorado 80303-3328

Official Business
Penalty for Private Use, \$300